Cold Cap Glass-Melt Migration for Radioactive Waste Vitrification at the Hanford Site

Jessica C. Rigby

A thesis submitted in partial fulfilment of the requirements of Sheffield Hallam University

For the degree of Doctor of Philosophy

September 2022

Declaration

I hereby declare that:

1. I have not been enrolled for another award of the University, or other academic or professional organisation, whilst undertaking my research degree.

2. None of the material contained in the thesis has been used in any other submission for an academic award.

3. I am aware of and understand the University's policy on plagiarism and certify that this thesis is my own work. The use of all published and other sources of material consulted have been properly and fully acknowledged.

4. The work undertaken in this thesis has been conducted in accordance with the SHU Principles of Integrity in Research and the SHU Research Ethics Policy.

5. The word count of the thesis is 61,005

Name	*Jessica C. Rigby*
Award:	*Doctor of Philosophy*
Date of Submission	*September 2022*
Faculty	*College of Business Technology and Engineering*
Director of Studies	*Professor Paul A. Bingham*

Dedication

Always for Agnes and Dave Owen.

Acknowledgements

For the wisdom supplied through the entire PhD process, and the encouragement, patience and flexibility while writing this thesis, my greatest thanks goes to my director of studies, Paul Bingham. This PhD, and everything that follows, is because of his eye for opportunity and belief that I could meet the task.

Great appreciation goes to all of the technical staff at MERI, but in particular, to my second supervisor, Anthony Bell, for providing invaluable technical knowledge with a side-order of classic beamline tales. Additionally, special thanks goes to Paul Allender and Francis Sweeney for the endless hours spent SEM searching for meaning in dull grey and slightly less dull grey. I gratefully acknowledge the staff at BM28 beamline at ESRF and B18 at Diamond for their technical expertise and support with beamline operation in the dawn of remote working.

I would like to acknowledge Sheffield Hallam University and US Department of Energy for funding this work and giving me the opportunity to collaborate with researchers all over the globe. Much of this work would not have got off the ground without researchers at PNNL, and UCT Prague. Albert Kruger, Derek Dixon, Derek Cutforth, Jamie George, Will Eaton, José Marical, Stephen Luksic, Richard Pokorny, Pavel Hrma, Jarda Kloužek, thank you all for the technical advice, encouragement and the thrilling 2 hours of entertainment of a Wednesday evening, with a dash of science.

I am very grateful that James Eales was navigating this PhD alongside me, and to Alex Scrimshire, we are all indebted to you for walking before us and sticking around to warn us. I would still be on the first page if it were not for having the two of them to bounce ideas off, and I might have finished a while ago if it were not for their constant distractions. Thank you to the rest of Paul's group, past and present, who have made this experience so enjoyable.

I am extraordinarily grateful for my family and friends for their confidence in me and for bringing balance to the last 4 years. Particularly for Mum and Dad, thank you for always hiding the final puzzle piece. You really knew what you were doing.

Finally, for the incredible support and patience of my best friend and loving husband, Lloyd. Thank you for keeping me sane all those times the world went insane, and for reminding me of what's important every day. I am the most grateful to have you on my team for everything in life.

Abstract

With public and environmental pressure to clean-up the 200,000 m^3 of radioactive wastes at the Hanford site, WA, USA, in a timely manner, many pathways to efficient processing of the wastes are being explored. One avenue, rife for exploration, is the waste feed-to-glass transition that occurs within a "cold cap" layer inside the melters, used to vitrify the wastes into stable glass wasteforms, for long-term immobilisation of the radioactive isotopes. Foaming beneath the cold cap, caused by the trapping of evolving gases in the glass-forming melt, can restrict heat-transfer from the glass melt to the reacting feed, thus reducing the efficiency of the melters, and the clean-up project.

For a high-foaming, high-iron waste feed, HLW-NG-Fe2, a series of laboratory-scale representations of the cold cap were examined for the original feed, a reduced iron raw material ($FeC_2O_4 \cdot 2H_2O$), as well as added sucrose, graphite, coke, formic acid and HEDTA. The $FeC_2O_4 \cdot 2H_2O$ raw material reduced foaming by 50 ± 2%, with minimal change to the final glass structure. Graphite and coke were most effective additives in foam reduction, reducing foaming by 51 ± 3 and 54 ± 3%, respectively.

The effect of the reductants on the redox behaviour of Fe, Cr, Mn and Ce with temperature was explored, as well as the contribution to O_2 evolution. Manipulation of the structure of the iron in the melt influenced the level of precipitation of Fe, Mn, Cr and Ni -bearing spinel crystals. The final graphite and coke glasses had Fe^{2+} content above the contract limit, and a structural change identified in most of the glasses, requiring further examination, appears to influence the chemical durability and glass transition temperature. Evidence is presented to suggest adoption of the reductants is feasible for mitigation of excessive foaming, pending further optimisation, although thus far, there is no indication that they offer improved melting rates.

List of Publications

Bell, A. M. T., Backhouse, D. J., Deng, W., Eales, J. D., Kilinc, E., Love, K., Rautiyal, P., Rigby, J. C., Stone, A. H., Vaishnav, S. and Wie-Addo, G. and Bingham, P. A. (2020) "X-ray fluorescence analysis of feldspars and silicate glass: effects of melting time on fused bead consistency and volatilisation" 2020. *Minerals*, *10*(5), p. 442.

Rigby, J. C, Dixon, D. R., Cutforth, D. A., Kloužek, J., Pokorný, R., Kruger, A. A., Marcial, J., Scrimshire, A., Bell, A. M. T. and Bingham, P. A. (2022) "Alternative reductants for efficient vitrification of radioactive wastes high in multivalent species" 2022, *Waste Management Symposia*, Phoenix, Arizona, US.

Rigby, J. C., Eales, J. D., Skerratt-Love, K., Scrimshire, A., Rautiyal, P., Radford, J. T., Spencer, J. Harrison, M. T., Hollands, L., Corkhill, C., Hyatt, N., Hand, R. and Bingham, P. A. (2022) "AFCP: Improved Glass Formulations for Advanced Oxide Fuels – Glasses with Lower Processing Temperatures" 2022. *Waste Management Symposia*, Phoenix, Arizona, US.

Calas, G., Galoisy, L., Hunault, M. O. J. Y., Love, K., Rautiyal, P. Rigby, J. C., Bingham, P. A. (2022) "Spectroscopic investigation of historical uranium glasses." *SSRN*. 4144995.

Rigby, J. C, Dixon, D. R., Cutforth, D. A., Marcial, J., Kloužek, J., Pokorný, R., Kruger, A. A., Scrimshire, A., Bell, A. M. T., and Bingham, P. A. (2022) "Melting behaviour of simulated radioactive waste as functions of different redox iron-bearing raw materials." *Journal of Nuclear Materials*. 569, 153946.

Conferences

MERI Research Symposium 2019, Sheffield, UK. "Understanding REDOX reactions in the cold cap for nuclear waste vitrification at the Hanford Site" Poster.

Society of Glass Technology 2019, Cambridge, UK. "Understanding cold cap – glass melt conversion for vitrification at the Hanford Site, USA" Presentation.

MERI Research Symposium 2021, Sheffield, UK. "Alternative reductants for vitrification of high-iron high-level radioactive waste streams" Presentation.

International Conference on the Applications of Mössbauer 2021, Brasov, Romania. "Evolution of iron redox and partitioning during vitrification of high-level radioactive waste" Poster.

Waste Management 2022, Arizona, USA. "Improved glass formulations for advanced oxide fuels – Glasses with lower processing temperatures." Presentation.

Waste Management 2022, Arizona, USA. "Alternative reductants for efficient vitrification of radioactive wastes high in multivalent species." Poster.

Physics of Non-Crystalline Solids 2022, Canterbury, UK. "Alternative foam reductants for the vitrification of high-iron Hanford High Level Waste (HLW) feeds." Presentation.

Prizes and Awards

ICG Travel Award: Awarded for travel to Wuhan, China for the International Commission on Glass Winter School 2018 for post-graduate students in the field of Glass Science.

1st Place Oldfield Award: Awarded by Society of Glass Technology at SGT 2019 for best taught master's research project.

1st Place Poster Award: MERI symposium 2019, at Sheffield Hallam University, awarded for technical content and presentation.

HRI Grant Scholar: Awarded the Henry Royce Institute PGR Access Scheme Grant Scholarship.

Contents

List of Abbreviations 11
List of Figures 13
List of Tables 19
1 Introduction 21
1.1 Background 21
1.2 Aims and Scope 23
1.3 Thesis Outline 24
1.4 References 26
2 Literature Review 30
2.1 Nuclear fuel and nuclear weapons production 30
2.2 Glasses and glass ceramics for waste immobilisation 39
2.3 The Hanford Site 52
2.4 The Cold Cap 58
2.5 HLW-Al-19 Simulated Waste Feed 67
2.6 HLW-NG-Fe2 Simulated Waste Feed 72
2.7 Redox behaviour in glass melts 78
2.8 Redox control during vitrification 85
2.9 References 91
3 Research Methods 134
3.1 Overview 134
3.2 Sample Compositions 135
3.3 Sample Preparation 138
3.4 Glass Characterisation Techniques 145
3.5 Foaming and Melting Behaviour 149
3.6 Structural Analysis 152
3.7 Morphological Analysis 169
3.8 Glass Product Testing 173
3.9 References 176
4 Comparison of Raw Materials in High-Iron High-Level Waste Feeds 189
4.1 Overview 189
4.2 Sample Properties 190
4.3 Foaming and Gas Evolution 192
4.4 Structure of the feeds during melting 199
4.5 Laboratory-scale melter study 214
4.6 Summary 221
4.7 References 225
5 Alternative Reductants – Foaming and Gas Evolution 233

5.1 Overview 233
5.2 Graphite Study 235
5.3 Feed Volume Expansion 236
5.4 Thermal Analysis 238
5.5 Gas Evolution 242
5.6 Melt Rate Correlation 248
5.7 Summary 249
5.8 References 252
6 Alternative Reductants: Structural changes during melting 255
6.1 Overview 255
6.2 XRD and phase evolution during melting 256
6.3 Raman Spectroscopy 259
6.4 ^{57}Fe Mössbauer Spectroscopy 265
6.5 Summary 271
6.6 References 275
7 Alternative Reductants: Redox behaviour of multivalent species 279
7.1 Overview 279
7.2 Expected redox behaviour 280
7.3 Fe K-edge X-ray Absorption Near-Edge Spectroscopy 281
7.4 Mn K-edge X-ray Absorption Near-Edge Spectroscopy 286
7.5 Cr K-edge X-ray Absorption Near-Edge Spectroscopy 289
7.6 Ce L_{III}-edge X-ray Absorption Near-Edge Spectroscopy 292
7.7 Ni K-edge X-ray Absorption Near-Edge Spectroscopy 295
7.8 Partial Pressure of Oxygen 296
7.9 Revised O_2 Balance 297
7.10 Summary 299
7.11 References 304
8 Alternative Reductants: Final Glass Product 312
8.1 Overview 312
8.2 Glass Characterisation 314
8.3 Iron Redox 316
8.4 Spinel Phase Precipitation 318
8.5 Thermal Properties 324
8.6 Product Consistency Test 327
8.7 Summary 330
8.8 References 333
9 Discussion 340
9.1 Overview 340
9.2 Effect of carbon content and source on melting behaviour 341

9.3 Evolution of the local environment of multivalent species during melting.....345
9.4 Application and scale-up of the range of foam controlling techniques.....352
9.5 References.....361
10 Conclusions.....372
11 Appendices.....375

List of Abbreviations

BO	Bridging oxygen
BSE	Backscattered Electron
CCIM	Cold Crucible Induction Melting
CS	Centre Shift
DTA	Differential Thermal Analysis
DTG	Derivative of Thermogravimetric Analysis
DWPF	Defense Waste Processing Facility
EDS/EDX	Energy Dispersive Electron Spectroscopy
EGA	Evolved Gas Analysis
EPA	United States Environmental Protection Agency
ESRF	European Synchrotron Radiation Facility
EXAFS	X-ray Absorption Fine Structure
$f(O_2)$	Oxygen Fugacity
Fe_T	Total iron (ΣFe)
FDSS	Fast-Dried Slurry Solids
FET	Feed Volume Expansion Test
HEDTA	N'(-2 hydroxyethyl) ethylenediamine-NNN' triacetic acid
HLW	High-Level Waste
HLW-Al-19	(or HWI-Al-19) High-alumina simulated waste feed
HLW-NG-Fe2	High-iron simulated waste feed
IAEA	International Atomic Energy Agency
ICDD	International Centre for Diffraction Data
ICP-MS	Inductively Coupled Plasma-Mass Spectrometry
IM	Induction Melting
JHCM	Joule-Heated Ceramic Melter
LAW	Low-Activity Waste
LCF	Linear Combination Fitting
LSM	Laboratory Scale Melter
MAS-NMR	Magic Angle Spinning – Nuclear Magnetic Resonance
MRC	Melt-Rate Correlation

NBO	Non-bridging oxygen
nc-AFM	Non-contact Atomic Force Microscopy
NPT	Non-Proliferation of Nuclear Weapons Treaty
NWS	Nuclear Weapon holding States
ORNL	Oak Ridge National Laboratory
ORP	Office of River Protection
$p(O_2)$	Partial Pressure of Oxygen
PCT-B	Product Consistency Test Method B
PNNL	Pacific Northwest National Laboratory
QS	Quadrupole Splitting
REDOX	Reduction/Oxidation
SE	Secondary Electron
SEM	Scanning Electron Microscopy
SHU	Sheffield Hallam University
SoM	Stages of Melting
SRNL	Savannah River National Laboratory
T_{FB}	Temperature of Foam Bottom
T_{FM}	Temperature of Foam Maximum
T_g	Glass Transition Temperature
TGA	Thermogravimetric Analysis
TG-MS	Thermogravimetric Mass Spectrometry
T_L	Liquidus Temperature
T_{MO}	Melter Operating Temperature
US DoE	United States Department of Energy
VSL	Vitreous State Laboratory
XANES	X-ray Absorption Near Edge Spectroscopy
XAS	X-ray Absorption Spectroscopy
X-ray CT	X-ray Computed Tomography
XRD	X-ray Powder Diffraction
XRF	X-ray Fluorescence Spectroscopy
WTP	Waste Treatment Plant

List of Figures

Figure 2.1.1. The “once-thru” nuclear fuel cycle used for plutonium production in the US (U.S. Department of Energy 2009). 32
Figure 2.1.2. The decay behaviour of some radionuclides in HLW from 1 t of SNF (Spent Nuclear Fuel) (I. W. Donald 2015). 37
Figure 2.1.3. Illustration of the Classification of Wastes and disposal requirements by half-life and activity content (IAEA 2009b). 38
Figure 2.2.1 Effect of temperature on enthalpy of a glass forming melt (Shelby 2005, 4). 40
Figure 2.2.2. Example of (a) a glass network containing network formers (SiO_2), and network modifiers (Na_2O) and (b) also containing network intermediates (PbO) from (Smallman and Bishop 1999). 43
Figure 2.2.3. Phase diagram of Na_2O/B_2O_3 showing eutectic temperatures (C. Wang et al. 2003). 48
Figure 2.2.4. Phase diagram of FeO/Fe_2O_3 showing formation and melting regions of magnetite with temperature and iron redox state (Shi et al. 2020). 49
Figure 2.2.5. ^{57}Fe Mössbauer spectroscopy at (A) 300 K and (B) 77 K, for Fe_3O_4, showing the sextets representative of the A ($^{VI}Fe^{2+}$) and B ($^{[IV,VI]}Fe^{3+}$) sites (Oh, Cook, and Townsend 1998). 51
Figure 2.3.1. Aerial view of key waste vitrification facilities at the Hanford Site (Goel et al. 2019). 56
Figure 2.4.1. Schematic diagram of the cold cap, optical microscopy image and summary of feed-to-glass reactions occurring at different temperature stages (Chun et al. 2013). 58
Figure 2.4.2. Melting rate of 5 feeds measured in the DM100 melter and estimated using the melt-rate correlation equation (Hrma et al. 2018; Lee, Hrma, Pokorný, Kloužek, et al. 2019). 66
Figure 2.5.1. Normalised pellet area (A_T) as a function of temperature for 6 variations of the HLW-Al-19 feed (Harris et al. 2017). 69
Figure 2.5.2. Evolved Gas Analysis (EGA) for the High-Alumina HLW-Al-19 feed with iron hydroxide $Fe(OH)_3$ and iron oxalate dihydrate $FeC_2O_4{\cdot}2H_2O$ as raw materials for Fe (Guillen et al., 2020). 71
Figure 2.6.1. Feed volume expansion of the HLW-NG-Fe2 feed at heating rates of 10, 20 and 40 K min^{-1} (Lee, Hrma, Pokorný, Traverso, et al. 2019). 73
Figure 2.6.2. Decomposition of $FeC_2O_4{\cdot}2H_2O$ in air by TG-DTA at a heating rate of 2 °C min^{-1} (Angermann and Töpfer 2008). 76
Figure 2.6.3. ^{57}Fe Mössbauer Spectroscopy of a) $FeC_2O_4{\cdot}2H_2O$ and $FeC_2O_4{\cdot}2H_2O$ isothermally heated at 350 °C for b) 8 minutes, c) 12 minutes, d) 60 minutes, e) 120 minutes, and f) 180 minutes (Smrčka et al. 2016). 76
Figure 2.7.1. Relationship between oxygen fugacity and redox ratio of Fe in SRL-131 melt, with 1 wt% (circles and triangles) and 5 wt% (squares) Fe (left) and 10 wt% Fe (right) over a range of temperatures (Schreiber et al. 1986). 80
Figure 2.7.2. Relationship between oxygen fugacity and redox ratio of a range of redox species in the SRL-131 melt (Schreiber and Hockman 1987). 81
Figure 3.3.1. Sample types explored in this study. a) slurry feed, b) SoM samples, c) glass samples, d) fast-dried slurry solids and e) Laboratory Scale Melter sample. 139
Figure 3.3.2. Demonstration of creating an FDSS sample in an aluminium foil wrapped alumina mould on a hotplate with incoming feed from above. 142
Figure 3.3.3. Comparison of scale of laboratory scale melters, research scale melters and the WTP LAW melter, with a surface area of 10 m^2 (Dixon et al. 2022). 143
Figure 3.3.4. Schematic of the LSM (Dixon et al. 2015b). 144
Figure 3.4.1. Production of characteristic radiation from (Brouwer 2010) 146
Figure 3.4.2. Instrumental components of an ICP-MS system (Thomas 1978). 147

Figure 3.5.1. TG/DTA study on the oxidation of nickel concentrate (Yu and Utigard 2012)...150
Figure 3.6.1. Schematic of Bragg's law showing incident X-rays interacting with the crystal lattice (Chatterjee 2001).....152
Figure 3.6.2. Refinement a diffraction pattern of a glass-ceramic sample containing Si powder standard. A phase identified as Fe-bearing spinel was fitted to the diffraction pattern, the residual of the fit is shown in the lower image.....154
Figure 3.6.3. Energy level diagram clarifying the difference between Anti-Stokes Raman Scattering, Rayleigh Scattering and Stokes-Raman Scattering (Almieda & Santos, 2015). 155
Figure 3.6.4. Four Raman spectra collated from different regions on the HLW-NG-Fe2-S sample quenched at 1000 ℃. 157
Figure 3.6.5. Raman spectra for HLW-NG-Fe2 and HLW-NG-Fe2-II samples melted in Pt and Al_2O_3 crucibles.....157
Figure 3.6.6. Example XAS of Cr K-edge (Turner 2017). 159
Figure 3.6.7. Schematic view of a synchrotron radiation facility (Balerna and Mobilio 2015).160
Figure 3.6.8. XMaS BM28 beamline optics hutch and experimental hutch. 161
Figure 3.6.9. Example pre-edge fitting for HLW-NG-Fe2-S 600 ℃ sample.....164
Figure 3.6.10. (left) Fe K-edge XANES for HLW-NG-Fe2-S quenched at 600, 800, 1000 and 1150 ℃. (right) Fitted pre-edges for HLW-NG-Fe2-S spectra. 164
Figure 3.6.11. Example linear combination fitting of the Cr K-edge in the HLW-NG-Fe2-S 600 ℃ sample with the $^{IV}Cr^{6+}$ and $^{IV}Cr^{3+}$ reference spectra. 165
Figure 3.6.12. Generic set-up for transmission ^{57}Fe Mössbauer spectrometer (Stevens, Travis, and DeVoe 1972).....168
Figure 3.7.1. Interaction volume within a sample for secondary and backscattered electrons and X-rays in SEM analysis (Hafner & Hafner, 2007). 169
Figure 3.8.1. Typical sequential ICP-OES (Tyler 2001). 174
Figure 4.3.1. Timing and temperatures of photographs of pellets ramped at 10 ℃ min^{-1}. Photographs taken every 100 ℃ initially, then more frequently when volume changes began to occur. 192
Figure 4.3.2. Feed expansion test images of HLW-NG-Fe2 showing initial expansion of the feed pellet between 500 and 700 ℃, followed by collapse of the foam up to melt temperature. Some large bubbles seem to emerge between 850 and 870 ℃ after the initial collapse. 193
Figure 4.3.3. Feed expansion test images of HLW-NG-Fe2-II showing initial expansion of the feed pellet between 600 and 700 ℃ followed by steady collapse of the foam. 194
Figure 4.3.4. Normalised volume expansion to the volume of glass, V/V_g, during melting of a pellet of the HLW-NG-Fe2 feed with iron hydroxide (black) and iron oxalate dihydrate (red) raw materials showing reduction of peak and overall foaming in the HLW-NG-Fe2-II feed...195
Figure 4.3.5. Gas evolution by 1st derivative of the TGA mass loss curve (red), showing and increase in total gas evolution for the HLW-NG-Fe2-II feed. DTA (black) for the HLW-NG-Fe2 and HLW-NG-Fe2-II feeds showing distinctive endothermic peaks in the HLW-NG-Fe2 feed between 700 and 900 ℃ are not present in the HLW-NG-Fe2 feed.....197
Figure 4.3.6. EGA of O_2, NO, CO and SO_2 (left axis) and CO_2 (right axis) for the HLW-NG-Fe2 feed. Gases evolved above 600 ℃ are primarily O_2, SO_2 and residual CO_2.....197
Figure 4.3.7. EGA of NO, CO, CO_2, O_2 and SO_2 for the HLW-NG-Fe2-II feed. There is no SO_2 or O_2 evolution above ~600 ℃, only residual CO_2. 198
Figure 4.4.1. Comparison of XRD patterns for HLW-NG-Fe2 (black) and HLW-NG-Fe2-II (red) SoM samples quenched at 600, 700, 800, 900, 1000, 1100 and 1150 ℃. Peaks identified belonging to Fe_2O_3, Haematite (H) ICDD; 04-015-7029, SiO_2, Quartz (Q) ICDD; 01-070-3755, and Fe_3O_4, Magnetite (S) ICDD; 04-009-8433. 199
Figure 4.4.2. Comparison of quantity of phases present during melting by refinement of XRD patterns in (a) HLW-NG-Fe2 and (b) HLW-NG-Fe2-II. Quartz ICDD: 01-070-3755, Haematite ICDD: 04-015-7029, ICDD: 04-007-2132. “Spinel” incorporates cubic spinels based on the magnetite system, Fe_3O_4. The only significant difference between the two feeds can be seen in the form of iron during melting.....200

Figure 4.4.3. Backscattered electron image (top) and elemental maps of the spinel crystals in HLW-NG-Fe2 quenched at 1150 ℃, showing presence of Mn, Ni and Cr, as well as Fe within the spinels. 202
Figure 4.4.4. Backscattered electron image (top) and elemental maps of the spinel crystals in HLW-NG-Fe2-II quenched at 1150 ℃, showing presence of Mn, Ni and Cr, as well as Fe within the spinels. 203
Figure 4.4.5. Raman spectra of the HLW-NG-Fe2 feed during melting at 600, 700, 800, 900, 1000, 1100 and 1150 ℃, showing the dissolution of sharp crystalline materials and emergence of the Q^n species region with increasing temperature. 205
Figure 4.4.6. Raman spectra of the HLW-NG-Fe2-II feed during melting at 600, 700, 800, 900, 1000, 1100 and 1150 ℃, showing the emergence of the borosilicate glass network with an intense band at 610 cm^{-1}, which remains present in the 1150 ℃ sample. 205
Figure 4.4.7. Raman Difference spectrum for HLW-NG-Fe2-II compared with HLW-NG-Fe2. The main difference between the two glass samples is in the 610 cm^{-1} band. 207
Figure 4.4.8. Raman spectra of the HLW-NG-Fe2 glass, and the HLW-NG-Fe2-II glasses melted for 1 hour and 24 hours, showing reduction in the 610 cm^{-1} peak in the 24 h sample equilibrating towards the HLW-NG-Fe2 sample. 208
Figure 4.4.9. Room temperature ^{57}Fe Mössbauer spectra for SoM samples at 600, 800, 1000 and 1150 ℃ fitted with Lorentzian functions for the HLW-NG-Fe2 and HLW-NG-Fe2-II feeds. CS relative to α-Fe. Fe^{3+} magnetic structures in the 600 ℃ HLW-NG-Fe2 sample and paramagnetic Fe^{2+} and Fe^{3+} in the 600 ℃ HLW-NG-Fe2-II sample converge to almost entirely paramagnetic Fe^{3+} in the final 1150 ℃ samples with some remaining sextets attributed to Fe-bearing spinel. 210
Figure 4.4.10. Room temperature ^{57}Fe Mössbauer spectrum for HLW-NG-Fe2-II glass sample heated to 1150 ℃ for 24 hours fitted with Lorentzian functions. CS relative to α-Fe. Identified paramagnetic doublets are Fe^{3+} iron and the sextets are iron-bearing spinel. 213
Figure 4.5.1. Fast-dried slurry solid samples of the HLW-NG-Fe2 feed (left) and HLW-NG-Fe2-II feed (right) showing the difference in colour and texture of the two feeds. 214
Figure 4.5.2. Image of the final HLW-NG-Fe2-II LSM sample broken from the crucible showing the porous dried feed, small bubbles and large cavities and the glass melt encased in the fused silica vessel. 215
Figure 4.5.3. Secondary electron images of the top (a), middle (b) and bottom (c) of the HLW-NG-Fe2-II LSM sample, and the 800 ℃ (d), 1000 ℃ (e) and 1150 ℃ (f) HLW-NG-Fe2 SoM samples. Region (a) on the LSM sample correlates most to (e) the 1000 ℃ sample, with scattered bubbles in an inhomogeneous matrix, the bottom glass and sample (f) both appear mostly homogenous. 216
Figure 4.5.4. EDX mapping of the bottom glass region (c) of the HLW-NG-Fe2-II LSM sample showing a number of spinel crystals containing Fe, Mn, Cr and Ni in an otherwise amorphous glassy matrix. 217
Figure 4.5.5. Montage of X-ray Tomography images of the HLW-NG-Fe2-II LSM sample, from the top porous feed region in the top left image, through the feed-to-glass transition. Showing the different densities of the feed and glass, and emergence of large and smaller bubbles. The bottom right image shows the homogenous glass in the bottom of the silica crucible. 218
Figure 4.5.6. Closed porosity of the LSM sample by image analysis of X-ray Tomography, in ImageJ, showing large peak porosity followed by sustained lower porosity further down in the sample. 220
Figure 4.5.7. Average bubble size (black) and circularity (red) through slices of the LSM sample by X-ray Tomography showing large bubbles at the surface of the sample as well as in the centre. Those at the sample surface are least circular. 220
Figure 5.2.1. XRD patterns of the HLW-NG-Fe2 glass with varying levels of graphite added to the feed. An Fe_3O_4 spinel is identified in all samples (S) and the main peak for Fe in this region (Fe) emerges for the 5 and 6 wt% samples. 235

Figure 5.3.1. Normalised volume of pellets during Feed Expansion Test with different reductant and raw material feeds showing the evolution of primary foaming and foam collapse for the HLW-NG-Fe2-R feeds. Both primary and secondary foaming are considerably supressed in the HLW-NG-Fe2-G and -C feeds. 236
Figure 5.3.2. Normalised maximum foam volume of HLW-NG-Fe2 and HLW-NG-Fe2-R feeds with carbon content of reductant g^{-1}. A linear fit of the data with a $R^2 = 0.903$. 237
Figure 5.4.1. Derivative of the TGA (DTG) of some of the reductants (top) and feeds with added reductants (bottom) between room temperature and 1150 ℃. Sucrose and HEDTA decompose between 200 and 500 ℃, where coke does not decompose in the temperature range measured and graphite only begins to react in the feed ~1050 ℃. 238
Figure 5.4.2. DTA of the HLW-NG-Fe2 and HLW-NG-Fe2-R feeds from room temperature to 600 ℃, showing endothermic dehydration reactions up to 350 ℃ and connection of the glass-forming melt between 550 and 600 ℃. 240
Figure 5.4.3. DTA of the HLW-NG-Fe2 and HLW-NG-Fe2-R feeds from 600 to 1150 ℃ showing the enthalpy of melting for each of the feeds. Endothermic peaks indicating high-temperature reactions, 700-900 ℃, are absent in the HLW-NG-Fe2-S and -G feeds. 240
Figure 5.5.1. CO_2 evolution from the feeds by gas chromatography. The main CO_2 peak evolution is similar for all feeds, however HLW-NG-Fe2-G and -C have sustained CO_2 evolution up to ~1100 ℃. 244
Figure 5.5.2. CO evolution from the feeds by gas chromatography. CO is evolved at temperatures above foam collapse in the HLW-NG-Fe2-H, -G and -C feeds, evolution in the -G and -C feeds is up to melting temperature. 244
Figure 5.5.3. NO evolution from the feeds by gas chromatography, showing earlier evolution of NO in the HLW-NG-Fe2-S and -F feeds. 245
Figure 5.5.4. SO_2 evolution from the feeds by gas chromatography, showing much greater overall evolution in the HLW-NG-Fe2-G and -C feeds. 245
Figure 5.5.5. O_2 evolution from the feeds by gas chromatography showing suppression of O_2 evolution in all of the HLW-NG-Fe2-R feeds. 246
Figure 6.2.1. XRD patterns for HLW-NG-Fe2-S, G, C, F and H 600, 800 1000 and 1150 ℃ showing quartz (Q) and haematite (H) phases present up to 1150 ℃ in the HLW-NG-Fe2-S and -F samples compared to the HLW-NG-Fe2-G and -H samples were there is little to no remaining quartz or haematite at 1000 ℃. Spinels (S) are present in all feeds up to 1150 ℃. . 257
Figure 6.2.2. Quantity of phases determined by semi-quantitative analysis of refined phases identified in XRD patterns, compared with 5 wt% Si powder as an internal standard, for each of the feeds studied at 600, 800 1000 and 1150 ℃. Quartz dissolution and amorphization of the melt occur at similar temperatures in all feeds, the feeds vary in the form of iron with temperature: the ratio of haematite to spinel. 258
Figure 6.3.1. Raman spectra for HLW-NG-Fe2, HLW-NG-Fe2-II and HLW-NG-Fe2-R feeds of samples quenched at 600 ℃ (top), 800 ℃ (bottom left) and 1000 ℃ (bottom right). Raman mode assignments are labelled H = haematite, B = borate/borosilicate structures, Q = Q^n species and O = O – O in molecular oxygen. The spectra show the evolution from sharp crystalline peaks and haematite bands to the emergence of borosilicate structures, notably the 610 cm^{-1} band and the Q^n species region. 260
Figure 6.3.2. Raman spectra of HLW-NG-Fe2, -II and -R 1150 ℃ samples. More detailed Raman mode assignments are labelled including individual borate and silicate modes. The 610 cm^{-1} peak is the main difference between the spectra. There is no defined shift in Q^n species and other modes remain similar between the spectra. 262
Figure 6.3.3. Raman spectra (left) and difference spectra (right) between 200-800 cm^{-1} showing the main difference in the spectra low wave-number region is the 610 cm^{-1} peak which is most intense in the HLW-NG-Fe2-C spectra followed by -II, -S, -G and -H. The feature is absent from the HLW-NG-Fe2 and -F spectra. 263
Figure 6.3.4. Raman spectra for HLW-NG-Fe2 and HLW-NG-Fe2-G for 0.5 – 6 wt% Graphite collected on samples quenched at 1150 ℃ showing the increase in intensity of the 610 cm^{-1}

band up to most intense at 4 wt% graphite addition, at 5 and 6 wt% addition the band is no longer visible.....264
Figure 6.4.1. ^{57}Fe Mössbauer spectra of the HLW-NG-Fe2, HLW-NG-Fe2-S and -F feeds quenched at 600, 800, 1000 and 1150 ℃ showing the evolution of the form of iron during melting from magnetic to paramagnetic. Fe^{2+} is observed in the HLW-NG-Fe2-S sample at 1000 ℃, but only Fe^{3+} is resolvable at 1150 ℃. 266
Figure 6.4.2. ^{57}Fe Mössbauer spectra of the HLW-NG-Fe2-G, HLW-NG-Fe2-C and -H feeds quenched at 600, 800, 1000 and 1150 ℃, showing the presence of Fe^{2+} iron in all of the feeds during melting resolvable by 800 ℃. Magnetic components remain prevalent up to 1150 ℃ indicating high levels of spinel present. 269
Figure 7.3.1. Fe K-edge XANES Spectra for HLW-NG-Fe2 and HLW-NG-Fe2-R samples quenched at 600, 800, 1000 and 1150 ℃. 281
Figure 7.3.2. Integrated intensity and centroid positions of Fe K-edge pre-edge peaks for each of the HLW-NG-Fe2 and -R feeds and the measured standards labelled. The position of the datapoints indicate that most of the samples are $^{VI}Fe^{3+}$ or high in Fe_2O_3, those that contain considerable amounts of Fe^{2+} are -G at 800 and 1150 ℃, -H from 800 - 1150 ℃ and -S at 800 ℃. 283
Figure 7.4.1. Mn K-edge XANES Spectra for HLW-NG-Fe2 and HLW-NG-Fe2-R samples quenched at 600, 800, 1000 and 1150 ℃. 287
Figure 7.4.2. Mn K-edge positions plotted as a linear function of the reference standards and associated oxidation states for each of the HLW-NG-Fe2 and HLW-NG-Fe2-R samples at 600, 800, 1000 and 1150 ℃. Mn reduces from Mn^{4+} to Mn^{2+} with temperature, reduction is at higher temperature in the HLW-NG-Fe2, -S and -F feeds.....288
Figure 7.5.1. Cr K-edge XANES Spectra for the HLW-NG-Fe2 and HLW-NG-Fe2-R samples quenched at 600, 800, 1000 and 1150 ℃, with the reference standards for Cr^{3+} (Cr_2O_3) and Cr^{6+} ($NaCr_2O_4$). The sharp pre-edge feature reduces with melt temperature. 289
Figure 7.5.2. Cr K-edge positions plotted as a linear function of the standards and associated oxidation states for the samples at 600 - 1150 ℃. Oxidation of Cr^{3+} to Cr^{6+} is observed between 600 and 800 ℃ in the HLW-NG-Fe2, -S and -F samples, followed by reduction. Reoxidation may have occurred in the HLW-NG-Fe2-G sample at 1150 ℃. 290
Figure 7.6.1. Ce L_{III}-edge XANES Spectra for the HLW-NG-Fe2 and HLW-NG-Fe2-R samples quenched at 600 - 1150 ℃, with the reference standards for Ce^{3+} ($Ce_2(C_2O_4)_3$) and Ce^{4+} (CeO_2). The two absorption edge features converge with temperature. 292
Figure 7.6.2. Ce L_{III}-edge positions plotted as a linear function of the standards and associated oxidation states for each of the samples at 600, 800, 1000 and 1150 ℃. Reduction to Ce^{3+} occurs by 1000 ℃ for the HLW-NG-Fe2-S, -G, -C, and -H samples. In the HLW-NG-Fe2 sample complete reduction to Ce^{3+} is not reached at 1150 ℃. 294
Figure 7.7.1. Ni K-edge XANES Spectra for HLW-NG-Fe2 feed samples heated to 600, 800, 1000 and 1150 ℃ and the NiO reference material. 295
Figure 7.9.1. Summary of the net contributions to O_2 evolutions by all of the multivalent species for the HLW-NG-Fe2, HLW-NG-Fe2-II and HLW-NG-Fe2-R samples, showing the Mn redox change contributes most to O_2 evolution for all but the HLW-NG-Fe2-G feed, for which it is equivalent to Fe within error. 298
Figure 7.10.1. Maximum normalised foam volume with Fe^{3+}/Fe_T by ^{57}Fe Mössbauer spectroscopy of the final glasses for the HLW-NG-Fe2 and HLW-NG-Fe2-R feeds showing that the samples containing reduced Fe correlated to reduced foam volume.....299
Figure 7.10.2. Summary of the percentage of Fe, Cr, Mn, Ni and Ce in the reduced state, Fe^{2+}, Cr^{3+}, Mn^{2+}, Ce^{3+} and Ni^{2+} for the HLW-NG-Fe2 and HLW-NG-Fe2-R feeds at 600, 800, 1000 and 1150 ℃. Errors are shown in the filled area around each line. Where the error area is not visible, the errors are within the lines shown. The reduction of the Cr precedes, Mn and Ce. Fe is the least reduced in all of the samples. 302

Figure 8.3.1. Evolution and retention of sulphates in the final glass samples as a function of redox state of Fe, showing that the evolved SO_2 and retained SO_3 do not correlate. Evolved SO_2 is highest for the feeds with the lowest final iron redox states. 317
Figure 8.4.1. Quantity of crystalline phases identified by XRD patterns as a function of carbon content g^{-1} of reductant added. 319
Figure 8.4.2. Elemental maps by EDX of the HLW-NG-Fe2-C showing dispersed spinel crystals rich in Fe, Mn, Ni and Cr in an inhomogeneous matrix. 320
Figure 8.4.3. Elemental maps by EDX of the HLW-NG-Fe2-S showing regions rich in O, Fe, Mn and Ni, and Cr, as well as regions of only O, Fe, Mn and Ni. Si and O rich regions are also observed. 321
Figure 8.4.4. Elemental point identification of the crystalline phases on the backscattered electron image HLW-NG-Fe2-S quenched at 1150 ℃ identifying SiO_2 crystals and spinels containing mixtures of Fe, Mn, Cr and Ni. 321
Figure 8.4.5. Crystalline phase wt% by XRD of the heat-treated glass samples. Highest spinel phase precipitation and lowest haematite in the HLW-NG-Fe2-G and -C samples. 322
Figure 8.5.1. DTA of HLW-NG-Fe2, HLW-NG-Fe2-II and HLW-NG-Fe2-R glass samples. Insert magnified curves showing onset of T_g. The temperatures of T_g onset are lower in the HLW-NG-Fe2-S, -G, -C and -H samples than the HLW-NG-Fe2 sample. 324
Figure 8.5.2. Temperature of onset of T_g, for HLW-NG-Fe2, HLW-NG-Fe2-II and HLW-NG-Fe2-R glass samples showing a decrease in T_g for the samples with lower Fe^{3+} contents in the final glasses. 326
Figure 8.6.1. Average normalised elemental mass loss by calculations of values from ICP-OES of leachate samples following a 7-day PCT-B showing high losses of Al, P and Ni as well as the B and Li. 329
Figure 9.3.1. Area of the 610 cm^{-1} danburite-like ring peak for each of the HLW-NG-Fe2 glasses made with each of the reductants. Above 6 wt% Fe^{3+} content there is a negative relationship in the area of the peak with increasing iron content. HLW-NG-Fe2-G has low Fe^{3+} content but a moderate peak area. 348
Figure 9.4.1. Summary of the measured glass properties of the HLW-NG-Fe2-R feeds, along with the contract limits for these properties employed at the Waste Treatment Plants, and the maximum normalised foam volume for each of the feeds during melting. 355

List of Tables

Table 2.1.1. CO_2 emissions produced by different energy sources (Köne and Büke 2010). 31
Table 2.2.1. Selected network formers, intermediates and modifiers in oxide glass networks (Smallman and Bishop 1999). 41
Table 2.2.2. Characteristics of Q^n units for alkali silicates from (Shelby 2005, 88). 44
Table 2.2.3. Lattice constants of common iron-bearing spinel structures (Biagioni and Pasero 2014). 50
Table 2.3.1. Breakdown of waste tanks at Hanford and confirmed/assumed leaks (Templeton 2018). 54
Table 2.5.1. HLW-Al-19 simulated glass composition (Joseph et al. 2010). 68
Table 2.6.1. HLW-NG-Fe2 simulated glass composition developed by the VSL to immobilise the C-106/AY-102 high-iron tank waste (Matlack et al. 2012). 72
Table 2.7.1. Reduction potentials for redox states of multivalent species in the HLW-NG-Fe2 feed, for borosilicate melts at 1150 ℃ (Schreiber and Balazs 1985). 83
Table 2.7.2. Mutual interactions of redox couples via electron exchange (Schreiber et al. 1987). 84
Table 2.8.1. Properties of some carbonaceous reducing agents for waste glass melting, reproduced from (Ryan 1995). 88
Table 3.2.1. HLW-NG-Fe2 composition developed by the VSL to immobilise the C-106/AY-102 high-iron tank waste (Matlack et al. 2012). 136
Table 3.2.2. Source of iron in the nominal HLW-NG-Fe2 simulated glass composition with iron hydroxide $Fe(OH)_3$ and iron oxalate $FeC_2O_4 \cdot 2H_2O$, HLW-NG-Fe2-II 136
Table 3.2.3. Raw materials and reductants used for each of the feeds studied and the associated carbon content g^{-1} of compound. 137
Table 3.3.1. A summary of sample types for each composition used in the study 138
Table 3.3.2. Melting conditions for glasses made at Pacific Northwest National Laboratory (PNNL) and Sheffield Hallam University (SHU). 140
Table 4.2.1. Analysed compositions of HLW-NG-Fe2 and HLW-NG-Fe2-II glasses by XRF and ICP-OES compared with the nominal composition. 191
Table 4.3.1. Foaming behaviour in the HLW-NG-Fe2 and HLW-NG-Fe2-II feeds during melting from FETs. 196
Table 4.3.2. Total evolved gases during melting of the HLW-NG-Fe2 and HLW-NG-Fe2-II feeds by integration of the EGA curves. 198
Table 4.4.1. Spinel composition determined by average point scans by EDX. 204
Table 4.4.2. Raman bands common to borosilicate structures and crystalline and amorphous iron-bearing structures identified in the HLW-NG-Fe2 -II spectra. 206
Table 4.4.3. ^{57}Fe Mössbauer spectra hyperfine splitting parameters of SoM samples at 800, 1000 and 1150 ℃ for HLW-NG-Fe2 (NG-Fe2) and HLW-NG-Fe2-II (NG-Fe2-II). CS relative to α-Fe. CS ± 0.02 mm s^{-1}, QS ± 0.02 mm s^{-1}, H ± 0.5 T, Area ± 2 %. 211
Table 4.4.4. Hyperfine fitting parameters for ^{57}Fe Mössbauer spectra of the HLW-NG-Fe2-II glass sample heated to 1150 ℃ for 24 hours. CS relative to α-Fe. CS ± 0.02 mm s^{-1}, QS ± 0.02 mm s^{-1}, H ± 0.5 T, Area ± 2 %. 213
Table 5.3.1. Foaming behaviour of feeds during melting from FETs. 237
Table 5.4.1. Enthalpy of reacting feed by DTA 241
Table 5.5.1. Calculated evolved gases based on stoichiometric calculations of the HLW-NG-Fe2 feed, and HLW-NG-Fe2-R feeds. 243
Table 5.5.2. Evolved gases by EGA for the HLW-NG-Fe2 and HLW-NG-Fe2-R feeds. 246
Table 5.5.3. Evolution of O_2 by evolved SO_2 measured by EGA. 247
Table 5.5.4. Expected NO_2 evolution based on measured NO evolved by EGA. 247
Table 5.5.5. Expected O_2 evolution based on measured CO and CO_2 evolved. 247

Table 5.6.1. Expected melting rate from the measured parameters for the MRC. 248
Table 5.7.1. Comparison of evolved O_2 with expected O_2 based on batched feed raw materials and evolution of O_2 by reactions with SO_x, NO_x and CO_x measured by EGA.....250
Table 6.3.1. Relative proportions of Q^n species by Raman spectral deconvolution.....262
Table 6.4.1. ^{57}Fe Mössbauer fit parameters for HLW-NG-Fe2, HLW-NG-Fe2-S, and HLW-NG-Fe2-F SoM samples. CS, relative to α-Fe, ± 0.02 mm s^{-1}. QS, ± 2 mm s^{-1}, H, ± 0.5 T, Area ± 2 %.....267
Table 6.4.2. ^{57}Fe Mössbauer fit parameters for HLW-NG-Fe2-G and HLW-NG-Fe2-C. CS, relative to α-Fe, ± 0.02 mm s^{-1}. QS, ± 2 mm s^{-1}, H, ± 0.5 T, Area ± 2 %. 270
Table 6.5.1. O_2 contributions from the formation of Fe_3O_4 over Fe_2O_3 measured by XRD. The net O_2 evolution by the change in crystalline phase of iron is shown in bold. 272
Table 6.5.2. Redox state in the amorphous phase in each sample measured by ^{57}Fe Mössbauer spectroscopy and estimated O_2 evolution contribution from these redox changes. The net O_2 evolution by the change in redox state of iron is shown in bold. 274
Table 7.2.1. Theoretical O_2 evolution if multivalent species were reduced g kg^{-1} glass, calculated by taking the contributions of each reduction reaction weighted by the quantity of the oxidised species in the batch. While Fe contributes most to the theoretical O_2 evolution, Mn is still a considerable quantity. 280
Table 7.3.1. Table of comparison of the ^{57}Fe Mössbauer and Fe K-edge XANES redox state predictions.....285
Table 7.8.1. Estimated -log(f_{O_2}) at 1150 °C by Fe^{3+}/Fe_T by ^{57}Fe Mössbauer spectroscopy, Cr K-edge, Ce L_{III}-edge and Mn K-edge XANES spectroscopy (Schreiber and Hockman 1987; Schreiber et al. 1986). 296
Table 7.9.1. O_2 evolution from redox reactions observed by XANES and ^{57}Fe Mössbauer spectroscopy.....297
Table 7.9.2. O_2 balance measured by EGA, with O_2 evolution from batched feed raw materials and redox reactions of Fe, Mn, Cr and Ce by XANES and ^{57}Fe Mössbauer.....298
Table 8.2.1. Analysed compositions of HLW-NG-Fe2 and reductant-added glasses by XRF spectroscopy compared with the nominal composition. 315
Table 8.2.2. Measured density of the HLW-NG-Fe2 and HLW-NG-Fe2-R glasses as well as wt% crystalline phase by XRD. 315
Table 8.3.1. Redox state of iron in the final HLW-NG-Fe2, -II and -R glasses.....316
Table 8.4.1. Spinel composition by average point scans by EDX and average spinel size. 320
Table 8.4.2. Measured density of the HLW-NG-Fe2 and HLW-NG-Fe2-R glasses, compared with the samples heat treated to 950 °C for 24 hours as well as wt% crystalline phase by XRD. 323
Table 8.4.3. Crystalline phase vol% in heat-treated glass samples. 323
Table 8.5.1. Temperature of T_g onset and midpoint for the HLW-NG-Fe2, HLW-NG-Fe2-II and HLW-NG-Fe2-R glasses measured by DTA. 325
Table 8.6.1. pH measurements of the leachates before and after the 7-day PCT-B test.....327
Table 8.6.2. Average normalised concentrations (NC_i), of elements leached during 7-day PCT-B test.....328

1 Introduction

The Waste Treatment Plants (WTPs) at the Hanford Site, USA, will process ~204,400 m^3 of radioactive legacy wastes from plutonium production for the Manhattan Project, the Cold War and subsequent nuclear power ventures. These wastes were historically stored in 177 steel tanks, some decades past their design lives (Bernards et al. 2020). High-level wastes (HLW) and Low-activity wastes (LAW) containing volatile radionuclides such as caesium-137, strontium-90, and technetium-99 are to be processed by vitrification in Joule-Heated Ceramic Melters (JHCMs) (McCarthy et al. 2018; Guillen et al. 2018). The first phase of the project over the next 10 years will be Direct-Feed LAW (DF-LAW) processing (Bernards et al. 2020). Once LAW sustained operations are underway, efforts will turn to HLW vitrification in JHCMs. The final HLW wasteforms are to be stored in geological repositories so long-term durability and radioactive stability of the glasses produced is essential (Goel et al. 2019; Colburn and Peterson 2021). The safety and efficiency of the project at Hanford depends on two major factors; waste loading and glass production rate (Hrma and Pokorný 2016). Due to variability in the feed compositions, the rate-controlling reactions are not well understood (Matlack et al. 2011), particularly the Reduction/Oxidation (REDOX) reactions for which the impact on foaming behaviour is presently unclear (Perez et al. 2001; Hrma et al. 2018; Jantzen et al. 2003).

1.1 Background

The volatility of radioactive components during vitrification is inhibited by the presence of a batch blanket (Xu et al. 2015) on top of the melt pool within the JHCMs. This "cold cap" covers 90 to 95 % of the glass melt surface (Hrma and Pokorný 2016; Marcial et al. 2014b; Hrma, Kruger, and Pokorný 2012). While necessary for restricting radionuclide volatility, the cold cap may hinder the rate of melting and therefore glass

production (Guillen and Agarwal 2013; Marcial, Kloužek, et al. 2021; Kruger et al. 2008). Pokorný and Hrma (2011) (Pokorný and Hrma 2011) outlined a mathematical model to understand the cold cap and optimize melting conditions to process each of the tank waste compositions. Their current model is being verified by simulated melter studies (Guillen and Agarwal 2013; Abboud, Guillen, and Pokorný 2016) and laboratory scale experiments (Lee, Hrma, Pokorný, et al. 2017; Dixon et al. 2015a, 2016).

The steps necessary to model the batch-to-glass process were outlined in a 2016 report (Hrma and Pokorný 2016); highlighted in this report is the lack of understanding of "cold cap" behaviour. As waste feed slurry and glass forming chemicals are fed into the melter the cold cap forms, covering the surface of the melt. The cold cap is made up of 4 layers, the reaction layer, primary foam, gas cavities and secondary foam (Hrma and Pokorný 2016). Foaming, caused by trapped gases from the melt pool such as O_2, CO_2 and NO_x, is dependent on the feed composition, operating conditions and the use of forced bubblers, which aid homogenisation of the melt. One-dimensional simulations have been developed to model the temperature gradient and rheology throughout the depth of the cold cap (McCarthy et al. 2018; Pokorný and Hrma 2011; Dixon et al. 2015a, 2015b). The objective of these efforts is to ensure the safety and efficiency of the JHCM process and ultimately the waste clean-up efforts at the Hanford site (Dixon et al. 2015b).

The HLW-NG-Fe2 waste glass composition was designed to immobilise the high-iron C-106/AY-102 tank waste from the Hanford site. The feed is a particularly high foaming HLW feed, which also provides an interesting basis to study the effects of multivalent species on melting and foaming behaviour due to the presence of Mn, Cr, Ni and Ce oxides in the feed as well as Fe (Matlack et al. 2012). Redox behaviour is recognised as a rate controlling parameter in the processability of waste streams

(Kruger, Matlack, Pegg, et al. 2012; Pinet, Hugon, and Mure 2014), however previous algorithms for controlling redox in high-nitrate LAW feeds through addition of sucrose are insufficient to predict the behaviour of HLW feeds (Kruger, Matlack, Pegg, et al. 2012). Further work is required to better understand the relationship between sources of carbon and the redox behaviour of HLW feeds (Kruger, Matlack, Pegg, et al. 2012).

1.2 Aims and Scope

The aim of the presented work is to investigate the melting behaviour of the HLW-NG-Fe2 simulated waste stream in the cold cap, using representative laboratory-scale experiments. This study aims to investigate the causes of the vigorous foaming and explore methods of reducing foaming that have little effect on the quality of the final glass product. Although research on the additions of carbon-based reductants has been carried out since the 1980s no single studies exist that compare carbon-based reductants on equal wt% bases in HLW streams. Optimising the processing rate through addition of the appropriate type and level of reductant for foam reduction could lead to improved efficiency at the Hanford site.

The objective is to deliver a variety of reductant options for use in the HLW-NG-Fe2 feed at the Hanford site, and a comparison of their effects on the behaviour during melting and the properties of the final glasses. The range of samples based on the high-iron HLW-NG-Fe2 feed also provides an interesting matrix to explore the behaviour of multivalent species during melting under the influence of different reductants, and therefore different redox conditions. The in-depth study of glasses with mixed multivalent species will be relevant, not just to the Hanford site, but also the wider glass manufacturing industry.

1.3 Thesis Outline

The literature review follows this chapter, Chapter 2, in which early vitrification processes are discussed, through to the current understanding of the cold cap behaviour in Hanford specific melter models. The chapter reviews carbon-based reductants from both previous radioactive waste programs and industrial glass plants, used to reduce foaming. Redox behaviour in a variety of different glass melts is discussed, building from first principles of a single multivalent species in simple glasses to mixed multivalent species in complex waste glasses.

Chapter 3 describes the approach to fulfilling the objectives outlined in 1.2. Sample types and compositions are described, and how they represent regions of the cold cap. Analytical techniques to characterise the samples are described in sufficient detail that the work is reproducible. Where protocols have been conducted to standards of quality assurance defined by the Hanford site or ASTM standards, these are noted.

Chapter 4 compares the original HLW-NG-Fe2 feed to an equivalent feed using a reduced iron raw material, ferrous oxalate. Comparisons are made between their melting and foaming behaviour, exploring the structure during melting and the redox behaviour of the iron. This chapter aims to underpin the main contributions to foaming in the HLW-NG-Fe2 feed and provides the basis to explore reductant additions to the feed in the following chapters. A representative sample of a static cold cap was produced using the ferrous oxalate feed in a Laboratory Scale Melter, and comparisons are made of the structure and morphology of the sample with the structural studies of quenched feed samples, demonstrating scale-up of the crucible studies.

Chapter 5 introduces the 5 reductants, sucrose, graphite, coke, formic acid, and N'(-2 hydroxyethyl) ethylenediamine-NNN' triacetic acid (HEDTA), the rationale for choosing the type and added amounts of each reductant and their effects on foaming and gas evolution. Analysis of evolved gases during melting aims to reveal the contributions

to foaming, and mechanisms of foam reduction. Feed parameters from experimental tests of volume expansion and thermal analysis compare the melting rates of the feeds using mathematical models discussed in Chapter 2.

The reductant-added feeds are investigated in a "stages of melting" study in Chapter 6, where the feeds are quenched at selected temperatures representative of temperatures of foaming onset, collapse and melting. This aims to understand the structure and chemistry of the feeds at the foaming temperatures, and any variations that lead to differences in the foaming or melting behaviour obtained in Chapter 5.

Chapter 7 reports the redox behaviour of the feeds during melting using X-ray absorption near edge spectroscopy (XANES). Analysis of each of the samples shows the evolution of the redox states of key species, Fe, Cr, Mn and Ce. Their behaviour is compared to previous studies of mixed multivalent species in complex glass compositions. Net changes in redox state, as well as intermediate redox changes, are compared with the gas evolution profiles from Chapter 5, aiming to uncover the role of redox changes in the total gas balance and gas evolution temperatures.

For the purpose of application of any methods of foam reduction presented in Chapters 4 through to 7, the properties of the final glasses are investigated in Chapter 8. Standard methods are used to determine whether the properties of the glasses are suitable for processing and geological disposal, based on criteria outlined by the Hanford site.

A complete discussion of the results is provided in Chapter 9, in which the variations in melting behaviour between each of the feeds are compared. The application of the results to the real-world scenario is discussed in both its scope and limitations. Finally, Chapter 10 draws together the main conclusions from the work presented, and the implications of the work to the Hanford site and to the wider research landscape. Potential further options are presented for advancements in the field of study and optimisation of the processes discussed.

1.4 References

Abboud, A. W., Post Guillen, D. and Pokorný, R. (2016) 'Heat Transfer Model of a Small-Scale Waste Glass Melter with Cold Cap Layer', in 11th International Topical Meeting on Nuclear Thermal Hydraulics, Operation and Safety. (NURETH-11), Avignon (France).

Bernards, J. K., Hersi, G. A., Hohl, T. M., Jasper, R. T., Mahoney, P. D., Pak, N. K., Reaksecker, S. D., Schubick, A. J., West, E. B., Bergmann, L. M., Golcar, G. R., Praga, A. N., Tilanus, S. N. and Crawford, T. W. (2020) 'River Protection Project System Plan: Safely, Effectively and Efficiently Treat Tank Waste and Close Hanford Tanks Rev. 9.' ORP-11242. U.S. Department of Energy, Office of River Protection. Richland, WA (United States).

Colburn, H. A., and Peterson, R. A. (2021) 'A History of Hanford Tank Waste, Implications for Waste Treatment, and Disposal.' Environmental Progress and Sustainable Energy, 40:e13567.

Dixon, D. R., Schweiger, M. J., Lee, S., Heilman-Moore, J. S. and Hrma, P. (2016) 'Effect of Feed Composition on Cold-Cap Formation in Laboratory-Scale Melter.' in WM2016, Phoenix, AZ (United States).

Dixon, D. R., Schweiger, M. J., Riley, B. J., Pokorný, R. and Hrma, P. (2015) 'Cold-Cap Temperature Profile Comparison between the Laboratory and Mathematical Model', in WM2015 Conference. Phoenix, AZ (United States).

Dixon, D. R., Schweiger, M. J., Riley, Brian J., Pokorný, R. and Hrma, P. (2015) 'Temperature Distribution within a Cold Cap during Nuclear Waste Vitrification', Environmental Science and Technology, 49(14), pp. 8856–8863.

Goel, A., McCloy, J. S., Pokorný, R. and Kruger, A. A. (2019) 'Challenges with Vitrification of Hanford High-Level Waste (HLW) to Borosilicate Glass – An Overview.' Journal of Non-Crystalline Solids: X, 4: 100033.

Guillen, D. P., Pokorný, R., Eaton, W. C., Dixon, D. R., Fox, K. and Kruger, A. A. (2018) 'Development of a Validation Approach for an Integrated Waste Glass Melter Model', Nuclear Technology. Taylor & Francis, 203(3), pp. 244–260.

Guillen, D. P. and Agarwal, V. (2013) 'Incorporating Cold Cap Behavior in a Joule-heated Waste Glass Melter Model.' INL/EXT-13-29794. Idaho National Laboratory. Idaho Falls, ID. (United States).

Hrma, P. and Kruger, A. A. (2008) 'Nuclear Waste Glasses: Continuous Melting and Bulk Vitrification', Advanced Materials Research, 39–40, pp. 633–640.

Hrma, P., Kruger, A. A. and Pokorný, R. (2012) 'Nuclear waste vitrification efficiency: Cold cap reactions', Journal of Non-Crystalline Solids, 358(24), pp. 3559–3562.

Hrma, P. and Pokorný, R. (2016) 'The Office of River Protection Cold Cap and Melt Dynamics Technology Development and Research Plan.' PNNL-25350. Pacific Northwest National Laboratory, Richland, WA (United States).

Hrma, P., Pokorný, R., Lee, S. M. and Kruger, A. A. (2018) 'Heat transfer from glass melt to cold cap: Melting rate correlation equation.' International Journal of Applied Glass Science, (August) pp. 1–8.

Jantzen, C. M. (2011) 'Development of glass matrices for high level radioactive wastes. In Handbook of Advanced Radioactive Waste Conditioning Technologies' 1st ed. Aiken, SC (United States): Woodhead Publishing Limited. pp. 230–292.

Jantzen, C. M., Koopman, D. C., Herman, C. C., Pickett, J. B. and Zamecni, J. R. (2003) 'Electron Equivalents Redox Model for High Level Waste Vitrification. In Symposium on Waste Management Technologies' in Ceramic and Nuclear Industries, American Ceramic Society. Westerville, Ohio (United States): Westinghouse Savannah River Company.

Kruger, A. A., Gan, H., Pegg, I. L., Matlack, K. S., Chaudhuri, M., Bardakci, T., Gong, W. and Kot, W. K. (2008) 'Melt Rate Enhancement for High Aluminum HLW

Glass Formulations.' ORP-56292. Office of River Protection, Richland, WA (United States).

Kruger, A. A., Matlack, K. S., Pegg, I. L., Kot, W. K. and Joseph, I. (2012) 'Redox Control for Hanford HLW Feeds.' VSL-12R2530-12. Office of River Protection, Richland, WA (United States).

Lee, S., Hrma, P., Pokorný, R., Kloužek, J., VanderVeer, B. J., Dixon, D. R., Luksic, S. A., Rodriguez, C., Chun, J., Schweiger, M. J. and Kruger, A. A. (2017) 'Effect of melter feed foaming on heat flux to the cold cap', Journal of Nuclear Materials. 496, pp. 54–65.

Marcial, J. Chun, J., Hrma, P. and Schweiger, M. J. (2014) 'The Effect of Foaming and Silica Dissolution on Melter Feed Rheology during Conversion to Glass-14473', in WM2014 Conference. Phoenix, AZ (United States).

Marcial, J., Kloužek, J., Vernerová, M., Ferkl, P., Lee, S., Cutforth, D., Hrma, P., Kruger, A. and Pokorný, R. (2021) 'Effect of Al and Fe sources on conversion of high-level nuclear waste feed to glass', Journal of Nuclear Materials, 559(153423).

Matlack, K. S., Gan, H., Chaudhuri, M., Kot, W. K., Pegg, I. L., Joseph, I. and Kruger, A. A. (2012) 'Melter Throughput Enhancements for High-Iron HLW.' ORP-54002. Vitreous State Laboratory, Washington, D. C. (United States).

Matlack, K. S., Muller, I. S., Callow, R. A., D'Angelo, N., Bardakci, T., Joseph, I. and Pegg, I. L. (2011) 'Improving Technetium Retention in Hanford LAW Glass - Phase 2.' VSL-11R2260-1. Vitreous State Laboratory, Washington, D. C. (United States).

McCarthy, B. P., George, J. L., Dixon, D. R., Wheeler, M., Cutforth, D. A., Hrma, P. R., Linn, D., Chun, J., Hujová, M., Kruger, A. A. and Pokorný, R. (2018) 'Rheology of simulated radioactive waste slurry and cold cap during

vitrification', Journal of the American Ceramic Society, 101(11), pp. 5020–5029.

Perez, J. M., Bickford, D. F., Day, D. E., Kim, D. -S., Lambert, S. L., Marra, S. L., Strachan, D. M., Triplett, M. B. and Vienna, J. D. (2001) 'High-Level Waste Melter Study Report.' PNNL - 13582. Pacific Northwest National Laboratory, Richland, WA (United States).

Pinet, O., Hugon, I. and Mure, S. (2014) 'Redox Control of Nuclear Glass', Procedia Materials Science, 7, pp. 124–130.

Pokorný, R. and Hrma, P. (2011) 'Mathematical Model of Cold Cap — Preliminary One-Dimensional Model Development.' PNNL-20278. Pacific Northwest National Laboratory, Richland, WA (United States).

Xu, K., Hrma, P., Rice, J., Riley, B. J., Schweiger, M. J. and Crum, J. V. (2015) 'Melter Feed Reactions at T ≤ 700 °C for Nuclear Waste Vitrification', Journal of the American Ceramic Society, 98(10), pp. 3105–3111.

2 Literature Review

2.1 Nuclear fuel and nuclear weapons production

2.1.1 The History of Nuclear Fuel Production

With the inception of the Manhattan Project in October 1939, the rush to develop the atomic bomb created a whole new industry that by 1950 would be the biggest in the USA (Harvey 2000; Groves 1983). Uranium and plutonium fuelled weapons were developed for use during WW2. The first atomic bomb dropped on Hiroshima, in Japan, was uranium fuelled and the second, on Nagasaki, was plutonium fuelled. Uranium was produced at Oak Ridge National Laboratory (ORNL), Tennessee and plutonium at the Hanford Site, Washington State, USA (Groves 1983; Hege Howes and Herzenberg 2003; Gosling 1999). Following WW2 more countries armed themselves with a nuclear arsenal, the Soviet Union developed its own nuclear weapons during the Cold War (Myrdal 1977; Haslam 1989), and the UK, France and China produced nuclear weapons during the 1950s to 80s. Alongside the USA, these states make up the current five nuclear weapon holding states, under the Non-Proliferation of Nuclear Weapons Treaty (NPT), with other states including India, Pakistan, Israel and North Korea having not disclosed their nuclear arsenals (Scheffran 2018; Norris and Kristensen 2010). The Cold War saw an increase in weapons grade plutonium and uranium production at the Hanford site. The reactors ceased to operate in 1987 (Gephart 2010).

The NPT enforced in 1970 and signed by 191 states has prevented the use of atomic bombs and promoted the disarmament of nuclear weapons. The treaty encourages cooperation between states for the peaceful use of nuclear technology (United Nations 2020). The UK, USA and Russia began to develop the technology for controlled nuclear reactions and commercial nuclear power production (Scurlock 2007), with the first full-scale nuclear power station built at Calder Hall in the UK (Hinton 1958). Nuclear

energy has become a popular “green energy” source (World Nuclear Association 2011; International Atomic Energy Agency 2017; Adamantiades and Kessides 2009) with 456 nuclear power plants operational in 2019 (Pioro and Duffey 2019; Siqueira et al. 2019). Nuclear power accounted for 11 % of the electricity generated worldwide in 2016 (IAEA, 2017), as an alternative to high CO_2 emitting sources shown in Table 2.1.1; this percentage is expected to increase in the coming years (Köne and Büke 2010). The nuclear energy industry produces significantly less CO_2 emissions than fossil fuels. This data, however, does not consider CO_2 emissions from nuclear waste processing.

Table 2.1.1. CO_2 emissions produced by different energy sources (Köne and Büke 2010).

Source	**CO_2 Emissions (MTonnes CO_2 TWh^{-1})**
Wind	0.020
Solar	0.200
Hydro	0.004
Nuclear	0.025
Natural Gas	0.380
Oil	0.760
Hard Coal	0.790
Lignite	0.910

The lifecycle CO_2 emissions of nuclear power are addressed in a study by the World Nuclear Association that compares 14 sources, some of which include the CO_2 emitted from waste processing, and show significantly higher CO_2 emissions, up to 130 tonnes CO_2e GWh^{-1}, compared with a mean of 29 tonnes CO_2e GWh^{-1}. Both of these values are still significantly lower than the reported values fossil fuels, with mean estimates for lignite and coal of 1054 CO_2e GWh^{-1} and 888 CO_2e GWh^{-1}, respectively (World Nuclear Association 2011), following the trend for direct emissions shown in Table 2.1.1.

A sector built on producing weapons of mass destruction, with a history of high impact disasters in recent memory, will have to take into account public attitudes towards risk to further advance nuclear fuel cycles (Boscarino 2019). With the development of new technology, many safety aspects of nuclear power generation have been addressed and confidence in nuclear power has increased (Adamantiades and Kessides 2009; Oltra et al. 2019). The clean-up of nuclear waste and decommissioning of nuclear power plants were not an area of much concern when reactors were initially built: this has led to more safety issues in recent years that must be addressed before nuclear power generation can develop (Ewing, Weber, and Clinard 1995; Ojovan and Lee 2014a). At the Hanford site, WA, USA only interim storage was considered, and this decision is costing an estimated $16 Bn (2018 estimation) (R. A. Peterson et al. 2018), the construction of facilities up to the size of 2 nuclear power plants, and decades of research (Ojovan and Lee 2014a).

2.1.2 The Nuclear Fuel Cycle

The stages of the front end of the nuclear fuel cycle employed for plutonium production at the Hanford site are shown in Figure 2.1.1. Sections 2.1.2.1 - 2.1.2.4 give a brief overview of the earlier steps employed at the Hanford site in particular.

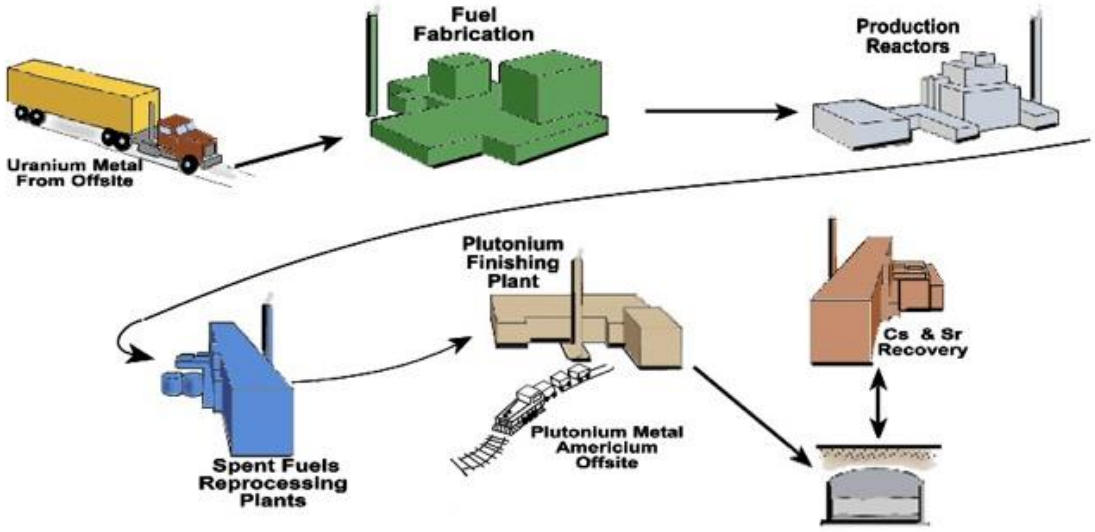

Figure 2.1.1. The “once-thru” nuclear fuel cycle used for plutonium production in the US (U.S. Department of Energy 2009).

2.1.2.1 Uranium and Plutonium Production

For commercial nuclear power stations ^{235}U is the most common isotope for sustained nuclear chain reactions. Natural uranium contains 0.07 % ^{235}U so it is concentrated by leaching, precipitation, solvent extraction or ion exchange before purification. Uranium, as a fuel for energy production, must be enriched up to about 3 % ^{235}U for modern light water reactors. As a fuel for nuclear weapons, the uranium must be highly enriched, for lower than 10 % enrichment the critical mass required for explosion would be "essentially infinite" (Krass et al. 1983). A device called "the calutron" which deflected beams of ^{235}U and ^{238}U ions by slightly different amounts was used to enrich the uranium for the "Little Boy" bomb dropped on Hiroshima (Yergey and Yergey 1997).

Plutonium production removes the requirement for highly enriched uranium (Krass et al. 1983; Adamantiades and Kessides 2009). The bismuth-phosphate carrier process technique discovered in 1942 (Seaborg 1962) and developed by the Clinton Laboratories (later ORNL) (Benedict, Pigford, and Levi 1981) in 1943, enabled the successful isolation of plutonium. By 1945 the process was in large-scale operation at the Hanford site (Gerber 1996).

2.1.2.2 Nuclear Reactor

A fission reaction is initiated by an incident neutron on a fissile nucleus (usually ^{235}U) which then splits, generating the nuclei of lighter elements (fission products) and a further 2.43 neutrons on average (S. K. Sharma 2004, 366–75; Hore-Lacy 2010, 47). In a nuclear fission bomb these neutrons interact with other ^{235}U nuclei compacted within the bomb causing an uncontrolled chain reaction. Each fission event of a ^{235}U nuclei releases around 200 MeV of energy (Yang and Hamilton 2010, 590). Commercial power reactors generally submerge fuel-rods in a moderator (usually heavy water or carbon) with a coolant running through to slow the neutrons released from the decay of the fuel to speeds at which they can be reabsorbed for a controlled chain reaction. The

coolant carries the heat generated by the reactors to the generator, most commonly a steam generator (S. K. Sharma 2004, 366–75; Hore-Lacy 2010, 40; Semat 1973, 532–35).

Plutonium is produced as a product of the decay of a ^{238}U nucleus by the following reaction pathway:

$$^{238}U + {}^{1}n \rightarrow {}^{239}U^{*} \rightarrow {}^{239}Np + e^{-} \quad (1)$$

$$^{239}Np \rightarrow {}^{239}Pu + e^{-} \quad (2)$$

Where * indicates an unstable nucleus (Benedict, Pigford, and Levi 1981, 5; Reed 2005). Spent nuclear fuel rods contain uranium and plutonium and a number of primary fission decay products, some stable and some unstable, leading to further decay products such as minor actinides. The half-lives of the products vary between less than a few days and thousands of years (Jansson et al. 2002; Dobson and Phillips 2006).

2.1.2.3 Reprocessing: The PUREX Process

Spent nuclear fuel can be reprocessed by separating the U and Pu from the other minor actinides. This process is called the Plutonium Uranium Extraction (PUREX) process (Dey and Bansal 2006; Corkhill and Hyatt 2018). The PUREX process was developed at Knolls Atomic Power Laboratory and developed at ORNL between 1950-1952 (Legget 2012). Irradiated fuel was dissolved in nitric acid to oxidise the UO_2 to uranyl nitrate ($UO_2NO_3)_2 \cdot xH_2O$) and plutonium oxidised to $Pu(NO_3)_4$ and then solvent extraction was used to extract all of the uranium and plutonium from the aqueous phase, leaving the fission products in solution (Benedict, Pigford, and Levi 1981). Extraction of the uranium and plutonium from the minor actinides and fission products reduces the activity of the waste product by 80 % compared to the “single-pass” cycle (Gerber 1996). The PUREX process was operational at the Hanford site between 1956 and 1990 (Gephart 2003) replacing the previous REDOX process, which was the initial attempt at

solvent extraction developed at the Argonne National Laboratory in Chicago, IL (Benedict, Pigford, and Levi 1981).

2.1.2.4 Closing the Nuclear Fuel Cycle

Due to the reprocessing of nuclear fuel, the nuclear fuel cycle for commercial energy is considered a "closed" cycle, although there are still radioactive wastes that cannot be reprocessed and must be safely disposed (Ojovan and Lee 2014a; Rodríguez-Penalonga and Yolanda Moratilla Soria 2017). The aim of the initial nuclear reactors, including those built at the Hanford site, USA, was to produce plutonium for atomic bombs. These "single-pass reactors", with open fuel cycles, eventually shut down in 1971 and the production of electricity as well as plutonium closed the nuclear fuel cycle as the uranium could then be reprocessed and reused (Gerber 1996).

These cycles generates a large amount of high-level (HLW) and low-activity (LAW) wastes that need to be disposed of. The clean-up of nuclear waste is of high priority in many nuclear power generating countries (Rao 2001; Sengupta, Kaushik, and Dey 2013; Nuclear Decommissioning Authority 2016; Blowers and Sundqvist 2010) leading to an international effort to develop vitrification technologies, aided by the International Atomic Energy Agency (IAEA) and other organisations (Washington Department of Ecology State of Washington 2018; International Atomic Energy Agency 1992; Ojovan and Lee 2014a; Krass et al. 1983). Each waste clean-up operation is unique in waste composition, quantities and surrounding infrastructure; and none are quite as large or complex as the Hanford site (Guillen et al. 2018; Guillen and Agarwal 2013; Harvey 2000; Washington Department of Ecology State of Washington 2018).

2.1.3 Waste Management and Disposal Strategies

International policies are broadly similar in that it is agreed that radioactive waste should be chemically and thermally stable before it is stored (Gin et al. 2013). The agreed strategy for dealing with radioactive waste long-term is to convert it into a solid

wasteform with long-term mechanical, chemical, thermal and radioactive stability and durability (Ojovan and Lee 2014a). The solid wasteform is then to be stored in deep geological repositories for high-level waste (HLW) and shallower repositories for low and intermediate level wastes. The solid matrix for the waste-form must be able to incorporate the wide range of elements present in the waste and minimise the final volume of the wasteform as much as possible for practical and economic considerations (Corkhill and Hyatt 2018).

2.1.3.1 Classification of Wastes

Radioactive wastes differ between countries and individual nuclear plants, depending on reactor type, nuclear fuel source and the nature of reprocessing flowsheets, amongst other variables (Mohapatra et al. 2014). By the IAEA Classification of Wastes (IAEA 2009b), low level waste (LLW) is waste that is "suitable for near surface disposal" and does not generate significant heat (IAEA 2009a); intermediate level waste "contains long-lived radionuclides in quantities that need a greater degree of containment"; and high level waste (HLW) "contains such large concentrations of both short and long lived radionuclides" that "deep geological disposal" is necessary, with typical levels of activity in the range of 10^4 – 10^6 TBg m^{-3} (IAEA 2009a).

The decay behaviour of some radionuclides is shown in Figure 2.1.2. While a large majority of the radioactive decay occurs in the first few hundred years, there is still a significant amount of activity up to 10^7 years. Plans for immobilisation of these high-level streams must take these timescales into account (I. W. Donald 2015). Classifications of waste by activity is the standard for the International Atomic Energy Agency, as shown in Figure 2.1.3 (IAEA 2009b).

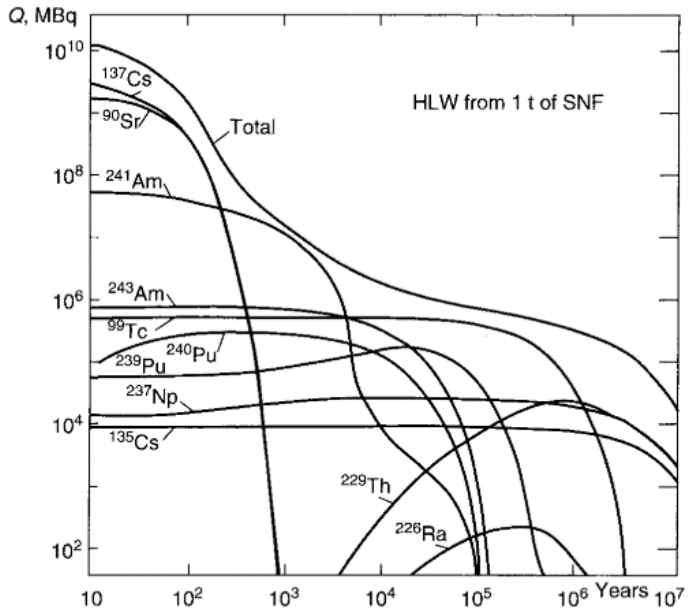

Figure 2.1.2. The decay behaviour of some radionuclides in HLW from 1 t of SNF (Spent Nuclear Fuel) (I. W. Donald 2015).

The US defines its radioactive wastes as HLW or LAW, based on the origin of the waste. HLW is "the irradiated fuel from a nuclear reactor and the waste generated when that fuel is processed to extract other products." The remainder of the tank waste is LAW, which makes up 90 % of the volume of waste (Office of Civilian Radioactive Waste Management 2004; International Atomic Energy Agency 2000; U.S. Environmental Protection Agency 2003).

As stated in 2.1.3, a solid wasteform, capable of withstanding pressures and geological conditions for hundreds of thousands of years, is the requirement for disposal of HLW. The material must also be processable at reasonable temperatures and by well-understood methods (Plodinec 2000). For these reasons, along with the ability to incorporate a wide range of elements into their microstructure, offer long-term thermal and radiation stability and high corrosion resistance, glass is the internationally agreed and desired final wasteform material for HLW immobilisation (Caurant et al. 2009; Gin et al. 2013; Vienna et al. 2013; Ojovan and Lee 2014a; I. W. Donald 1997).

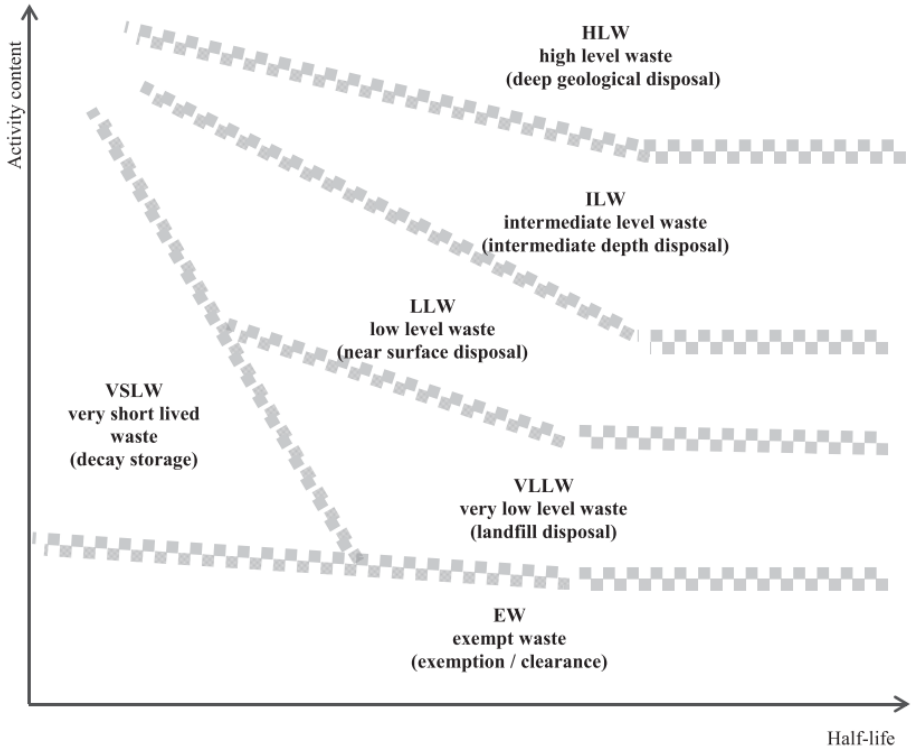

Figure 2.1.3. Illustration of the Classification of Wastes and disposal requirements by half-life and activity content (IAEA 2009b).

2.2 Glasses and glass ceramics for waste immobilisation

While ceramic and glass-ceramic materials have been investigated for immobilisation of radioactive species (Ewing and Lutze 1991; Caurant et al. 2009; Orlova and Ojovan 2019) vitrification is the selected method worldwide for the immobilisation of HLW, due to the ability of glass to remain durable for extended periods of time while incorporating a wide range of species into its network (Ojovan and Lee 2014a). The process that has been demonstrated for thousands of years and the fundamental method of melting and forming glasses using silica-based materials has not changed dramatically from the industrial glass works of 1500 BC Egypt (Kurkjian and Prindle 1998), giving insight into the long-term durability of vitrified nuclear wasteforms.

The process of immobilisation by vitrification was first investigated using alkali borosilicate glass formers, in Canada, in the 1950s (Corkhill and Hyatt 2018; Caurant et al. 2009). By the 1980s the UK, France, Germany, Italy, Canada, USA and Russia were immobilising wastes in borosilicate matrices (I. W. Donald 1997; Caurant et al. 2009). Russia also used phosphate glass matrices (Ojovan and Lee 2011). The first phase of immobilisation of Hanford wastes will be Direct-Feed LAW (DF-LAW) vitrification (Bernards et al. 2020). Once sustained LAW processing is underway, the HLW will be also be processed by vitrification (Vienna, Kim, Muller, Piepel, Kruger, et al. 2014; Rodriguez et al. 2017). The following sections will describe the structure of glasses and the role of key elements in glass formation, followed by the mechanisms of crystal precipitation and structures that commonly form during vitrification of HLW.

2.2.1 Crystalline and non-crystalline materials

Crystals are defined as a “solid composed of atoms, ions or molecules arranged in a pattern that is periodic in three dimensions” (ASM International 2004). Whereas, the definition of a glass is “any product of fusion that has been cooled from a liquid state to a rigid state without crystallising” (ASTM C162-05 2015). The product is “amorphous

and completely lacking in long-range, periodic atomic structure, and exhibiting a region of glass transition behaviour" according to Shelby (Shelby 2005, 3) This behaviour is not limited to inorganic oxide materials, but anything that "exhibits glass transformation behaviour" (Shelby 2005, 3). A description of the glass transformation behaviour is given in the diagram in Figure 2.2.1. Upon cooling of a liquid to below the melting temperature, a glass will continue to rearrange its structure until eventually the viscosity is so high that it can no longer change. If the liquid were to crystallise, this would be an abrupt increase in ordering, matched with an abrupt decrease in enthalpy and volume (i.e., increase in density). Since viscosity is a kinetic property, the rate at which the liquid is cooled determines when the enthalpy deviates from the equilibrium, and ultimately whether it crystallises or remains a supercooled liquid. The temperature of the onset to the glass transformation region when heating a glass is called the glass transformation temperature, T_g, and is different for different glass compositions (Jiang and Zhang 2014; Shelby 2005).

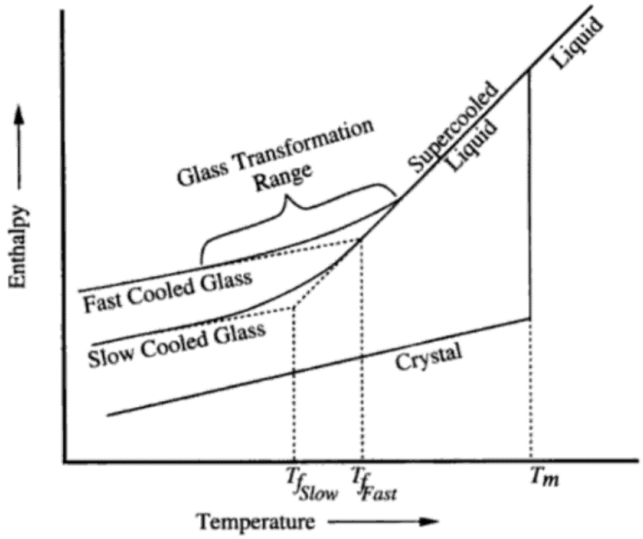

Figure 2.2.1 Effect of temperature on enthalpy of a glass forming melt (Shelby 2005, 4).

2.2.2 Glass Structure

While glasses are random networks with no long-range periodic order, their properties are based on the short-range structure, which explains why two glasses of the same

composition will have the same properties despite their random structures (Shelby 2005, 74). Most technical and commercial glasses are based on oxides, however in some cases metallic species and carbonates can be incorporated into the glass network, or in fact, form glasses themselves (Swallen et al. 2007; W. H. Wang, Dong, and Shek 2004; Ashby and Greer 2006; Ojovan and Lee 2011). For the purpose of this report, the majority of species in the glass structures will be in the form of oxides. Zachariasen divided oxides based on their glass forming ability into the following categories: network formers, network modifiers and network intermediates (Zachariasen 1932). Examples of each of these categories, relevant to the waste glasses discussed here, are given in Table 2.2.1.

Table 2.2.1. Selected network formers, intermediates and modifiers in oxide glass networks (Smallman and Bishop 1999).

Network formers	Intermediates	Network Modifiers
SiO_2	Al_2O_3	Na_2O
B_2O_3	Fe_2O_3	Li_2O
P_2O_5	ZrO_2	CaO
GeO_2	PbO	MgO
	ZnO	SrO
	MnO	BaO
	Cr_2O_3	K_2O
	CeO_2	La_2O_3
	NiO	

Network formers can readily form a glass by forming random networks on their own. They are usually characterised by 3 or 4 coordination and small atomic radii of the cation (Vogel 1994; Zachariasen 1932). Network modifiers are generally alkali and alkaline earth metal oxides, with large atomic radii, Table 2.2.1. These depolymerise the network and have the effect of reducing the melting temperature and viscosity of the glass. They usually have coordination numbers greater than 6 (Jiang and Zhang 2014; Greaves, Binsted, and Henderson 1984; Vogel 1994; Chemarin and Champagnon 1999). Network intermediates cannot usually produce glasses alone, but can replace glass formers in the network when they are 4-coordinated. They can also act as glass

modifiers, for coordination numbers 6-8 (Vogel 1994). Aluminium is perhaps the best-known and most technologically-important intermediate (Jiang and Zhang 2014; Osipov et al. 2016). Typically transition metals such as Fe, Cr and Mn also act as network intermediates, Table 2.2.1, taking the role of either network formers or modifiers depending on the redox state of the element (Farges et al. 2005). Examples of how network formers, modifiers and intermediates can exist in the glass structure are shown schematically in Figure 2.2.2.

2.2.2.1 Oxygen

For oxide glasses, oxygen bonding is a useful way of describing the connectivity of the network. Bridging oxygens (BO) are those that connect two network forming elements, or a network former and intermediate acting as a network former. Non-bridging oxygens (NBO) connect network forming and network modifying elements. The bonds between oxygens and elements acting as network formers are mostly covalent (stronger) and those between oxygens and network modifiers are ionic (weaker). Increasing the amount of NBOs in a glass network generally decreases the chemical durability of the glass (Bragg 2002, 25; Shelby 2005, 190).

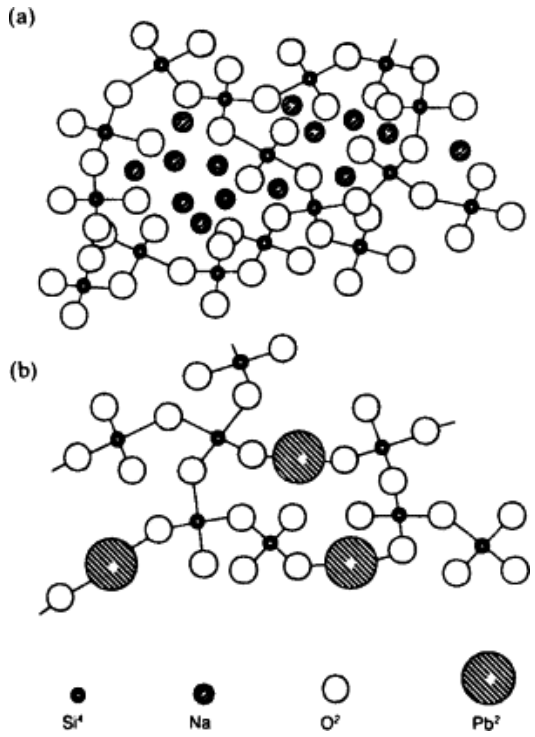

Figure 2.2.2. Example of (a) a glass network containing network formers (SiO_2), and network modifiers (Na_2O) and (b) also containing network intermediates (PbO) from (Smallman and Bishop 1999).

2.2.2.2 Silicon

The most common glass network former, SiO_2 forms a three-dimensional network of tetrahedral units, where each Si cation is connected to 4 oxygen anions. Oxygens are shared between tetrahedra, giving the net neutral charge and formula SiO_2 (Bragg 2002, 24–25). A pure silica glass has high chemical durability and mechanical stability, however, it requires melting temperatures > ~2000 ℃ to form into shapes, so modifiers are often added to reduce glass melting temperature to more technically and economically viable levels (Shelby 2005, 25).

Alkalis such as sodium or lithium are added as modifiers to the silicate network. Every alkali oxide molecule added creates two NBOs in the network, decreasing the connectivity of the melt (Shelby 2005, 82), therefore decreasing melting point and viscosity of the melt. The number of NBOs per silica tetrahedron is given in Q^n notation, where n is the number of BOs. A Q^4 unit is a silica tetrahedral unit completely

linked to the silicate network, where a Q^0 unit has no BOs, a full description of Q^n species is given in Table 2.2.2 (Brawer and White 1975; Matson, Sharma, and Philpotts 1983; Shelby 2005, 83–88). The Q^n speciation in a glass is often determined by Raman or Nuclear Magnetic Resonance spectroscopies (Lai et al. 2016; Ollier et al. 2004; M. Wang et al. 2011; Jiang and Zhang 2014; Hannon, Vessal, and Parker 1992; Belton, Deschaume, and Perry 2012).

Table 2.2.2. Characteristics of Q^n units for alkali silicates from (Shelby 2005, 88).

Characteristic	Q^4	Q^3	Q^2	Q^1	Q^0
BO per tetrahedron	4	3	2	1	0
NBO per tetrahedron	0	1	2	3	4
Oxygens per tetrahedron	2.0	2.5	3.0	3.5	4.0
Bridges per tetrahedron	4	3	2	1	0

2.2.2.3 Boron

Boron oxide is also a network former and can readily form a glass on its own (Avramov, Vassilev, and Penkov 2005; Alderman 2018; Meera and Ramakrishna 1993; Bengisu 2016). Glasses prepared with boron oxide as the main network former have significantly lower melting and softening temperatures than silica-based glasses: the melting temperature of pure B_2O_3 is 450 °C (Bengisu 2016). Borate glasses are preferable to silicate glasses in optical applications (Ehrt 2000), battery applications (Bengisu 2016; Yadav and Singh 2015; Velez, Tuller, and Uhlmann 1982) and many biomedical applications (Bengisu 2016).

Vitreous boron oxide networks are primarily built up of boroxol ring structures and borate superstructural units on the intermediate range order scale (Konijnendijk 1975; Bødker et al. 2019). Alkali additions to the vitreous B_2O_3 network initiates formation of BO_4 tetrahedra from BO_3 tetrahedra up to ~20 mol % (Konijnendijk 1975), beyond which point diborate structures form and are destroyed (~20 – 60 mol%) and then NBOs at ~29 mol% (Mamoshin et al. 1998; Doweidar 1990; Shelby 1983). The evolution of

the borate species with alkali content leads to a ”minimum” in the thermal expansion coefficient, known as the “borate anomaly” (Huang et al. 2021; Avramov, Vassilev, and Penkov 2005; Doweidar 1990; Mamoshin et al. 1998). Raman spectroscopy has shown the formation of diborate, metaborate, pyroborate and orthoborate units at high alkali content (35 – 50 mol%) (Hubert and Faber 2014; Konijnendijk and Stevels 1975).

Borate glasses are not generally considered suitable for waste immobilisation due to their lower chemical durability compared to silicate glasses (Bengisu 2016). However, when added to a silicate glass network, boron decreases the melting temperature by decreasing the amount of Q^4 units for silica and becoming 3-coordinated at high temperatures, acting as a glass modifier (Ojovan and Lee 2014a, 334–35). Borosilicate glasses are a system of borate and silicate cationic network formers and alkali oxides, alkali borosilicate glasses are discussed in the following section.

2.2.2.4 Alkali Borosilicates

Alone, the binary system of borate and silicate will act as two separate networks. With the addition of alkali oxides the borosilicate network forms (Konijnendijk 1975; Hubert and Faber 2014). For the system (R)M_2O·(K) SiO_2·B_2O_3, alkali oxides preferentially associate with the boron oxide for low alkali content, R < 0.5, converting some of the boron from a coordination of 3 to 4, as discussed in section 2.2.2.3 (Koroleva, Shabunina, and Bykov 2011; Hubert and Faber 2014). At higher alkali contents, the alkali is partitioned between the boron and silica creating NBOs (Varshneya and Mauro 2019). This behaviour was comprehensively modelled using by ^{11}B Nuclear Magnetic Resonance (NMR) by Yun and Bray (Yun and Bray 1978), and later updated to form the Yun-Bray-Dell model (Dell, Bray, and Xiao 1983; Manara, Grandjean, and Neuville 2009b). The model was adapted more recently to include the behaviour of danburite-like units with tetra-coordinated boron atoms (Manara, Grandjean, and Neuville 2009b).

Due to their high chemical and thermal stability and moderate processing temperatures, ~ 1000 to 1650 ℃ depending on modifier content (Neyret et al. 2015; Cassingham et al. 2008; Varshneya and Mauro 2019), alkali borosilicate glasses are widely used for the immobilisation of HLW in the UK, France and USA (Cunnane et al. 1994; Plodinec 2000; Ojovan and Lee 2011). The USA also plans to immobilise LAW in borosilicate based glasses (Vienna, Kim, Muller, Piepel, Kruger, et al. 2014; Matlack, Pegg, et al. 2011). Borosilicate glasses have shown acceptable long-term durability in many studies (Harrison and Brown 2018; Wu et al. 2018; Matyáš et al. 2017; Peeler and Edwards 2004). The random structure of the borosilicate glass network allows the flexibility to accommodate the complexity of waste compositions (Matyáš et al. 2017).

2.2.3 Iron in the glass network

Glasses containing < 5 wt% iron are the most often studied (S. B. Donald, Swink, and Schreiber 2006; Ceglia et al. 2015; Meechoowas et al. 2012), as small quantities of iron contamination can drastically change the colour of a colourless glass (Glass for Europe 2006). Glasses containing significantly larger quantities of iron have also been studied, particularly pertaining to immobilisation of industrial and radioactive wastes (Chinnam et al. 2013; Ahmadzadeh, Scrimshire, Bingham, Goel, et al. 2018).

Iron is a network intermediate - network forming and network modifying depending on its local structure in the glass (Farges et al. 2005; Ahmadzadeh, Scrimshire, Bingham, Goel, et al. 2018; Cochain et al. 2012). Generally observed in borosilicate glasses, is network-forming tetrahedrally-coordinated Fe^{3+} and network modifying octahedrally-coordinated Fe^{2+} (Cochain et al. 2012; Cochain and Neuville 2008; Shaharyar et al. 2016; Mysen and Virgo 1989; Greaves, Binsted, and Henderson 1984). Most glasses will be formed with Fe^{3+} iron raw materials, (Karamanov et al. 2000), however, there is a tendency for the reduction of Fe^{3+} to Fe^{2+} to proceed with increasing melt temperature (Johnston 1964). The redox state of iron in the final glass is dependent on the redox

state of the batch, the oxygen partial pressure, f_{O2}, the furnace atmosphere, optical basicity (Duffy 1996; Duffy and Ingram 1976) and the melt temperature (Beerkens 1999; Pinet, Hugon, and Mure 2014). Further discussion of the factors effecting the redox state of glasses is given in section 2.7.1.

The structure of iron in glass networks has been studied by many techniques, including X-ray Absorption Near Edge Spectroscopy (Farges et al. 2005; Wilke et al. 2004, 2001; Alderman et al. 2017) and ^{57}Fe Mössbauer spectroscopy. Once study claimed that the oxidation state of iron in a borosilicate glass could be determined using Raman spectroscopy, by examining the effect of iron speciation on the Si-O stretching region of the spectra (800-1200 cm^{-1}) (Cochain and Neuville 2008). Depletion in the 980 cm^{-1} band associated with iron tetrahedral units $^{IV}Fe^{3+}$-O bonds aligns with the reduction of the ratio Fe^{3+}/Fe_T, where Fe_T is the total iron (Cochain and Neuville 2008), and previous studies of silicate systems (Magnien et al. 2008, 2006). A follow-up study (Cochain et al. 2012) also observed a distinct change in a borosilicate (danburite-like: $Na_2O{\cdot}B_2O_3{\cdot}2SiO_2$) ring structure peak at ~630 cm^{-1} and at high wavenumber 1450 cm^{-1}, in the stretching of B-O^- bonds. At ~630 cm^{-1} there is a higher intensity band with higher Fe^{2+} content, or less total Fe content. In the 1450 cm^{-1} band there is a shift to lower wavenumber with increasing iron content and oxidation (Cochain et al. 2012; Osipov, Osipova, and Eremyashev 2013). This interpretation is based on the updated Yun-Bray-Dell model (Manara, Grandjean, and Neuville 2009b) discussed in section 2.2.2.4, however in this case the increase the Na^+ cations preferentially charge compensate the Fe^{3+}, decreasing the abundance of danburite-like ring structures and increasing the number of BO_4 units (Barth and Feltz 1989; Yun and Bray 1978).

2.2.4 Crystallisation mechanisms

In this thesis both the mechanisms of crystal dissolution into an amorphous matrix, and precipitation of crystals on cooling of a melt, are of importance. In the first instance the

dissolution of crystalline raw materials occurs lower than the melt temperature for the individual crystal, this is due to the low-temperature melting eutectic mixtures of crystals, for example ratios of B_2O_3 and Na_2O will become liquid at lower temperatures than either of the melting temperatures of the individual species, shown in the phase diagram, in Figure 2.2.3 (C. Wang et al. 2003). The rate of dissolution of silica is diffusion controlled and is effected by the melt viscosity (Shaw 2006), the grain size (Doi et al. 2019; Ueda et al. 2021). Haematite either dissolves into the glass matrix by diffusion (I. W. M. Brown 1982; Pokorny et al. 2013) or forms magnetite-like spinel depending on temperature and redox the melt, the phase diagram for Fe_2O_3/FeO mixtures as a function of temperature is given in Figure 2.2.4 (Shi et al. 2020). Spinels also dissolve into the melt with increasing temperature (Kruger et al. 2009; Alton, Plaisted, and Hrma 2002).

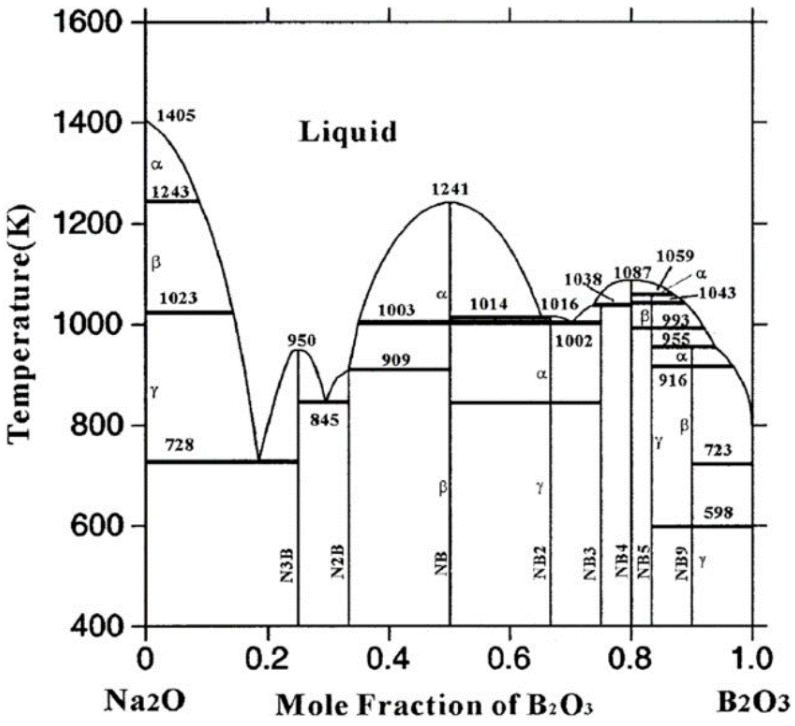

Figure 2.2.3. Phase diagram of Na_2O/B_2O_3 showing eutectic temperatures (C. Wang et al. 2003).

Precipitation of crystals or secondary amorphous phases during cooling of a homogeneous glass melt is usually avoided when dealing with vitrification of radioactive isotopes, particularly when the crystals or secondary phases are water soluble, or less mechanically, thermally or chemically stable than the desired glass. However, in some cases waste components are better housed in a desired, stable, crystalline phase where the solubility is limited in the glass (Caurant et al. 2009). In this case glass-ceramic materials are obtained by controlled crystallisation of desired phases in bulk glass trough the nucleation and growth mechanism (Schmelzer 2008).

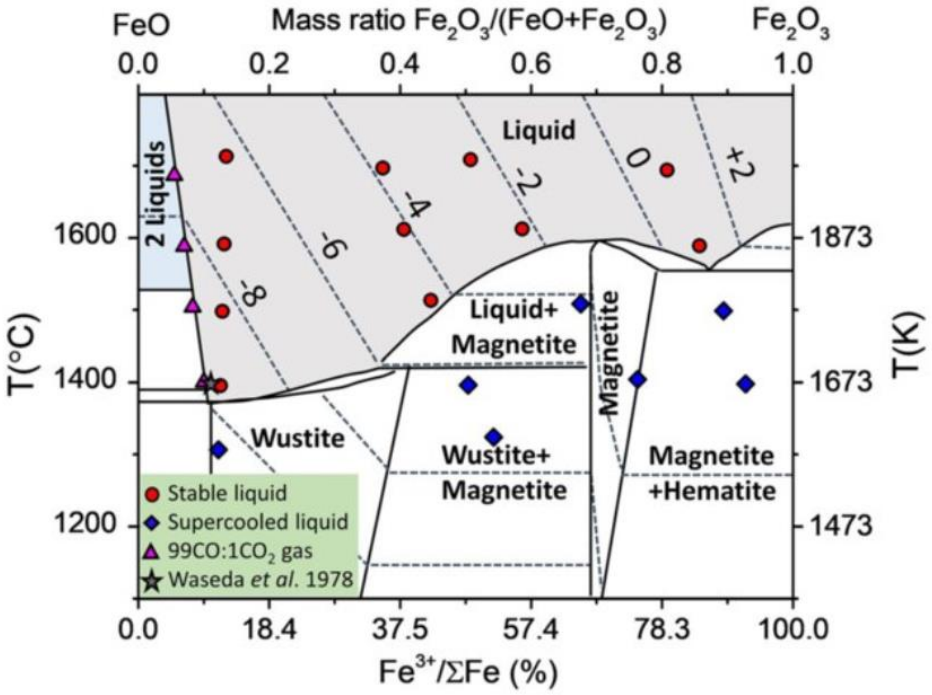

Figure 2.2.4. Phase diagram of FeO/Fe_2O_3 showing formation and melting regions of magnetite with temperature and iron redox state (Shi et al. 2020).

2.2.5 Spinel crystallisation in iron-bearing glasses

In high-iron, -alumina and other multivalent species glass compositions, formation of crystalline spinel phases is common, forming quenching, when the temperature reaches $< T_L$ (Alton, Plaisted, and Hrma 2002). Pertinent to the present work is crystallisation of iron-bearing spinels from Fe_2O_3 in the glass melt/glass-forming melt, as described in section 2.2.4. These iron-bearing spinels are thermally, chemically and mechanically

stable, however they can have an adverse effect on melter performance and processing due to accumulation and settling inside the melter (I. W. Donald 2015; Pokorny et al. 2013; Hrma, Schill, and Nemec 2001).

Spinel is a cubic structure with the formula AB_2O_4, there are both octahedral and tetrahedral sites, where the quantity of octahedral sites is always twice that of tetrahedral. In magnetite, Fe_3O_4 the A site is occupied by $^{VI}Fe^{2+}$ and the B site by $^{VI}Fe^{3+}$ and $^{IV}Fe^{3+}$. Where other multivalent species, such as Cr, Mn and Ni, are present in iron-bearing spinels they replace different sites on the spinel depending on their valency, i.e. $(Fe,Ni,Mn)^{[3+]}(Cr,Fe)^{[2+]}{}_2O_4$. In pure spinel oxides, the site occupancies can be determined by cell refinement of X-ray diffraction patterns of pure spinel oxides, lattice parameters, a = b = c, of common Fe-bearing spinels are given in Table 2.2.3 (Biagioni and Pasero 2014).

Table 2.2.3. Lattice constants of common iron-bearing spinel structures (Biagioni and Pasero 2014).

Species	**Phase Chemistry**	**Lattice Constants (Å)**
Magnetite	$Fe^{2+}Fe^{3+}{}_2O_4$	8.397
Jacobsite	$Mn^{2+}Fe^{3+}{}_2O_4$	8.496
Trevorite	$Ni^{2+}Fe^{3+}{}_2O_4$	8.347
Chromite	$Fe^{2+}Cr^{3+}{}_2O_4$	8.376

^{57}Fe Mössbauer spectroscopy has been performed on pure iron-bearing spinels, Fe_3O_4 (Oh, Cook, and Townsend 1998), $MnFe_2O_4$ (Sawatzky, Van Der Woude, and Morrish 1969), and $NiFe_2O_4$ (Sepela´k et al. 2007). The spectrum for magnetite is shown in Figure 2.2.5, at 300 K and 77 K, where the sextets characteristic of the A and B sites shown. Spinels with Fe^{3+} occupying the B site, such as $Ni_{0.6}Zn_{0.4}FeO_4$, produce sextets with CS ~ 0.25 and 0.36 mm s^{-1} and H = 49.1 and 52.4 T (Arboleda et al. 2018). Similarly, for $MnFe_2O_4$, with negligible Fe^{2+} ions in the A site, sextets with average CS ~ 0.51-0.57 mm s^{-1} and H ~ 410-460 kOe (Sawatzky, Van Der Woude, and Morrish

1969) have been observed. Chromite ($FeCr_2O_4$), wherein Fe^{2+} occupies the A site and Cr^{3+} the B site, presents itself as a Mössbauer singlet with a high CS ~0.937 mm s^{-1} in room temperature Mössbauer spectra (Dézsi, Szucs, and Sváb 2000; Nakamura and Fuwa 2015; Sijo 2018; Sijo et al. 2019), the presence of Cr^{3+} ions generally reduces the strength of the A-O-B magnetic interactions, instead coupling anti-ferromagnetically with the Fe ions (Sijo 2018; Sijo et al. 2019).

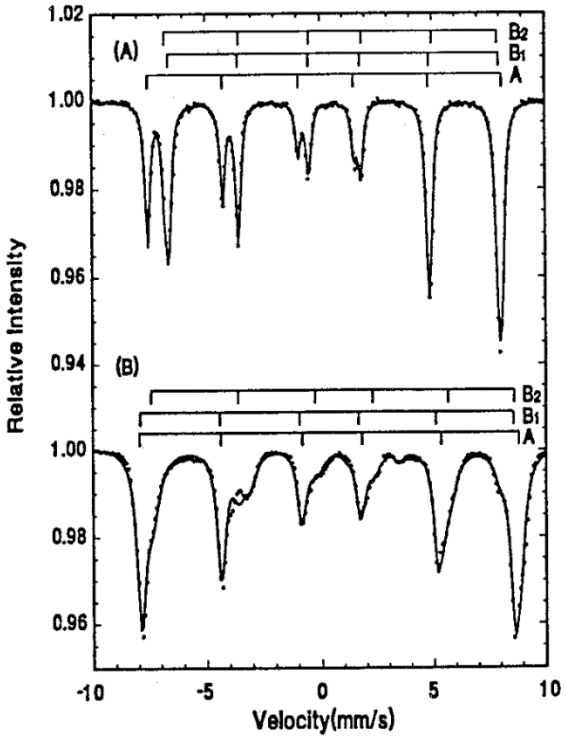

Figure 2.2.5. ^{57}Fe Mössbauer spectroscopy at (A) 300 K and (B) 77 K, for Fe_3O_4, showing the sextets representative of the A ($^{VI}Fe^{2+}$) and B ($^{[IV,VI]}Fe^{3+}$) sites (Oh, Cook, and Townsend 1998).

2.3 The Hanford Site

2.3.1 History of the Hanford Site

The Hanford desert, on the banks of the Columbia River in Washington, USA, was chosen as a plutonium production site during the Manhattan Project due to its sparse settlements, mild climate, access to water from the Columbia River, electricity, a railroad line and hills for security purposes (Gephart 2010). The Hanford site produced plutonium for the world's first nuclear explosion at the Trinity Site, New Mexico, in July 1945 and for the bomb dropped on Nagasaki, Japan in August 1945. The Trinity test was less than 2 years after the demonstration of the first controlled chain reaction in December 1943, It is clear that the "pressure of world war" meant that the site was constructed "without extensive laboratory research" (Gephart 2010; Edgemon et al. 2009; Washington Department of Ecology State of Washington 2018). Throughout Hanford's plutonium production lifetime, from 1944 to 1988, over 61,000 kg of plutonium was produced, along with ~200,000 m^3 of radioactive wastes (Gephart 2010). In May, 1989, the US DoE, US Environmental Protection Agency (EPA) and the Washington State Department of Ecology entered into an agreement to clean up the radioactive waste at Hanford (Gephart 2010). The wastes were historically stored in 177 single-walled steel tanks and their compositions have not been well-documented, making this the world's most complex clean-up effort (I. W. Donald 2015; Rushton 2006; McCabe, Wilmarth, and Nash 2013).

2.3.2 Waste Inventory

149 single-shell steel tanks were built from 1943-1964 with a design life of 20 years. In 1968, 28 double-shell carbon-steel tanks were built with design-lives of 50 years (Gephart 2010). Liquid wastes were transferred from some of the old tanks to the new tanks (Gephart 2010; Bernards et al. 2020). Today 153 of the 177 original underground

carbon-steel tanks contain mixed radioactive waste from 4 decades of weapons and fuel production at the site (Xu et al. 2016; Guillen et al. 2020; Gephart 2010; Bernards et al. 2020). In total the tanks contain 204,400 m^3 of waste (Perez et al. 2001), with suspected leakages up to a volume of 2,800 m^3.

In the inventory of the tank waste, the types of waste are separated into “sludge”, “saltcake” and “supernatant” (Colburn and Peterson 2021). Sludge is defined as “insoluble metal oxides and fission products from fuel reprocessing” and is characterised by “low-porosity, reduced interstitial liquid drainability, and mud-like texture” (R. A. Peterson et al. 2018; Templeton 2018). Saltcake is “soluble salts formed by evaporation of liquid waste from reactor fuels reprocessing” and is characterised by “high-porosity, interstitial liquid drainability, and crystalline texture” (Lambert and Kim 1994; Templeton 2018). Supernatant is defined as the “liquid above the solids or in large liquid pools” (Lambert and Kim 1994; Templeton 2018). The tanks are separated into 18 tank farms: the summary of the 18 tank farms shown in Table 2.3.1 gives the amount of sludge, saltcake and supernatant in each of the tanks and whether they are suspected or confirmed to have leaked (Templeton 2018).

The contents of the tanks are “extremely complex and diverse” (R. A. Peterson et al. 2018). This complexity derives from the number of different waste processing techniques used at the Hanford Site over the decades, the decay and self-induced heating of some of the radioactive material over time, amongst other processes. Regular samples of the waste are analysed and compared with the inventories taken over the years of operation (Kupfer et al. 1998; Colton, Orth, and Aitken 1993). Despite the differences in composition compared to some of the inventories, it is possible to predict the content of a tank with confidence using a combination of sampling and modelling (Agnew 1997).

Table 2.3.1. Breakdown of waste tanks at Hanford and confirmed/assumed leaks (Templeton 2018).

Tank Farm	Number of Tanks	Tanks	Assumed/ Confirmed Leak
A	6 Single-Shell	A-101 to 106	Yes
AN	7 Double Shell	AN-101 to 107	No
AP	8 Double Shell	AP-101 to 108	No
AW	6 Double Shell	AW-101 to 106	No
AX	4 Single Shell	AX-101 to 104	No
AY	2 Double Shell	AY-101 and 102	Yes
AZ	2 Double Shell	AZ-101 to 102	No
B	16 Single Shell	B-101 to 112 and B-201 to 204	Yes
BX	12 Single Shell	BX-101 to 112	Yes
BY	12 Single Shell	BY-101 to 112	Yes
C	16 Single Shell	C-101 to 112 and C-201 to 204	Yes
S	12 Single Shell	S-101 to 112	No
SX	15 Single Shell	SX-101 to 115	Yes
SY	3 Double Shell	SY-101 to 103	No
T	16 Double Shell	T-101 to 112 and T-201 to 204	Yes
TX	18 Single Shell	TX-101 to 118	Yes
TY	6 Single Shell	TY-101 to 106	Yes
U	16 Single Shell	U-101 to 112 and U-201 to 204	Yes

Volume reduction by vitrification of the HLW is limited by high levels of SO_3, P_2O_5, Al_2O_3, Fe_2O_3, Cr_2O_3 and to some extent Na_2O and mixtures of CaO and P_2O_5. The LAW feeds are limited by the high alkali content, mostly Na_2O but also K_2O in some feeds, as well as the SO_3 and P_2O_5 concentrations (Vienna et al. 2013; Kruger, Pegg, et al. 2012). The limiting properties of high-Fe_2O_3 glasses include spinel or nepheline formation and viscosity (Ahmadzadeh, Scrimshire, Bingham, Goel, et al. 2018). Al_2O_3 and Cr_2O_3 are also "major spinel-forming components" (Kruger et al. 2009). Na_2O in combination with high Al_2O_3 tends to crystallise aluminosilicate phases such as nepheline and sodalite, and high alkali content reduces flexibility in the glass formation (Matlack et al. 2007). The solubility limit of P_2O_5 in the borosilicate glass matrix is around 5 – 6 wt% (Achigar et al. 2021), beyond which point phase separation may occur followed by crystallisation of species such as $NaCaPO_4$ and $NaLi_2PO_4$ (Achigar et

al. 2021; I. W. Donald 2015). Above the SO_3 solubility limit salts can accumulate on the melt surface, increasing melter corrosion and potentially volatilisation of technetium and caesium (Vienna, Kim, Muller, Piepel, Kruger, et al. 2014). A sulphur saturated melt may also form water-soluble salt layers on in the final glasses (Vienna, Kim, Muller, Piepel, Kruger, et al. 2014).

2.3.3 Waste Treatment Plants

When the tri-party agreement was signed in 1989 (Washington Department of Ecology State of Washington 2018; U.S. Department of Energy 2019; Gephart 2003) a 10-30 year timeline for clean-up was estimated and many of the complex issues which have arisen with a radioactive waste clean-up of this magnitude were not anticipated (Gephart 2010). The agreement is regularly updated to adapt to new complications with extended timelines and budgets (U.S. Department of Energy, U.S. Environmental Protection Agency, and Washington State Department of Ecology 2018, 2020). In 2022 the clean-up was estimated to reach near the end of the current century, and cost at least $300.2 billion (Richland Operations Office 2022). Pressure from the government and the public over concerns of waste leakage and the costs of the clean-up (Macuglia 2017) is driving research and innovation, and worldwide support, to improve the safety, efficiency and lifespan of this project (Mann 1999; Kruger 2011).

The pre-treatment flowsheet at the pre-treatment facility, Figure 2.3.1, will include the following processes: waste receipt, evaporation, ultrafiltration and separation of HLW, transport to the HLW Vitrification Plant, removal of caesium by ion exchange, evaporation of some excess water, and transport of the LAW to the LAW Vitrification Plant, Figure 2.3.1 (Kruger, Kim, and Goel 2015; Pegg 2015). Each stream of waste slurry is then to be mixed with glass forming chemicals (GFCs) upon entry to the melter (Lee, Hrma, Kloužek, et al. 2017; Kelly 2011).

Figure 2.3.1. Aerial view of key waste vitrification facilities at the Hanford Site (Goel et al. 2019).

The compositions of GFCs to be added to the waste prior to vitrification are designed for each individual waste stream based on rigorous laboratory-based testing and modelling of composition, structure and properties of the final glass wasteform (Vienna et al. 2016, 2013). Property constraints considered include temperature restrictions imposed by the melter technology, crystal tolerance limits, leach rates and chemical durability, viscosity and processability (Vienna et al. 2016, 2013). Constraints have been placed on Hanford HLW glass vitrification operating parameters for the purpose of safety, processability and long-term immobilisation of the wastes (Matlack et al. 2012; Piepel et al. 2008, 2007). Those constraints that are relevant to the present work are:

- Melt viscosity 1 - 15 Pa.s at 1100 ℃ (Piepel et al. 2007)
- Spinel phase precipitation < 1 vol% at 950 ℃ (Matlack et al. 2012; Piepel et al. 2007; Gan et al. 2009)
- Leach rates < 4 g L^{-1} (2 g m^{-2}) by Product Consistency Test Method B (PCT-B) of Si, B and Na (Piepel et al. 2007; Kirkbride et al. 2009; Piepel et al. 2005; Muller et al. 2013)
- $0.09 < Fe^{2+}/Fe_T < 0.33$ (Larson 1996; Jantzen 2011; Peeler and Edwards 2004)

2.3.4 Melter Technology

Joule-Heated Ceramic Melting (JHCM) is the selected technique for vitrification of the Hanford wastes. It is suggested that the WTPs under construction at the Hanford site will have the capability to vitrify all of the HLW and a minimum of one-third of the LAW in their expected lifetimes. Vitrification of the remainder of the LAW is yet to be agreed upon; a second vitrification plant or grouting of the LAW in a cementitious wasteform as a supplementary technique are the likely approaches (National Academies of Sciences Engineering and Medicine 2019). Direct feed (DF) vitrification in Joule-Heated Ceramic Melters (JHCMs) was also the chosen technology at Savannah River and West Valley in the USA, Mayak and Radon in Russia, PAMELA in Belgium, VEK in Germany, Tokai in Japan and WIP in India (Ojovan and Lee 2014a, 273; Kelly 2011).

Unlike in the induction melting (IM) process, the technology adopted by Sellafield in the UK and the R7T7 in France (Crum et al. 2014; M. Kim et al. 2018; J. C. Marra and Kim 2014; Sakai et al. 2017), in DF-vitrification, the waste and GFCs enter the melter as an uncalcined slurry containing 40 – 60 % water (Hujová, Kloužek, et al. 2018; Hujová, Pokorný, and Kloužek 2018; Matlack, Kot, et al. 2015). Water is added to the batch to combine the grains of the GFCs and waste stream and prevent segregation (Kocarkova 2011). The cost and practicality associated with removing the calcination and glass fritting steps are a driver for the JHCM method (Sakai et al. 2017; Pinet et al. 2021; Aloy 2011). The JHCM may also increase glass product homogeneity, compared to IM, due to more uniform heating throughout the melt (Sakai et al. 2017; Kelly 2011; Matlack, Joseph, et al. 2009). Both methods produce a wasteform with large waste volume reduction, typically 20 – 50% (Geeting and Kurath 1830; Ojovan and Lee 2014b; Gervasio et al. 2018), however can be up to 90 % (Jantzen, Pickett, and Ramsey 1993).

2.4 The Cold Cap

Inside the JHCM, Figure 2.4.1, a slurry of waste and GFCs is fed into the top of a sealed, refractory-lined melter vessel (Kruger et al. 2013; I. W. Donald 1997). The melter vessel is heated by nickel-chromium alloy electrodes to 1150 °C and the slurry forms a molten glass (Ojovan and Lee 2011; Jantzen 2011; Bickford, Hrma, and Bowan 1990). The glass melt is lifted through the air lift glass-discharge port and poured into steel canisters to cool (Hrma and Pokorný 2016; Schweiger et al. 2010).

Unique to the JHCM process employed at the Hanford WTPs, section 2.3.4, a batch layer called the "cold cap" is created on top of the melt pool when incoming, un-calcined waste and glass forming chemicals (GFCs) are fed into the melter (Hrma, Kruger, and Pokorný 2012). The cold cap, Figure 2.4.1, is formed by the reacting batch during melting, where decomposition of raw materials, gas-evolving reactions and formation of a glass melt, occur.

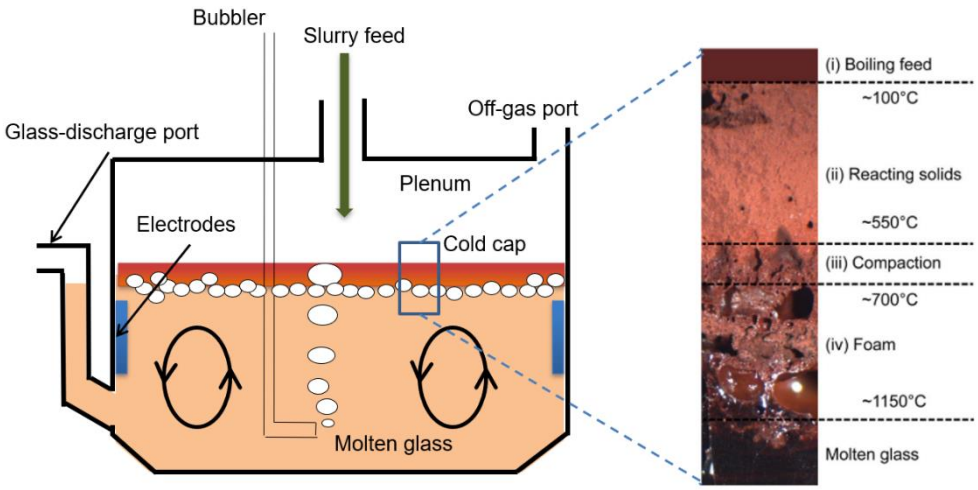

Figure 2.4.1. Schematic diagram of the cold cap, optical microscopy image and summary of feed-to-glass reactions occurring at different temperature stages (Chun et al. 2013).

The cold cap covers 90-95 % of the melt surface (Hrma and Pokorný 2016; Marcial et al. 2014b; Hrma, Kruger, and Pokorný 2012). While the presence of a cold cap helps to

insulate the melt pool and hinders the release of volatile elements during melting, which would otherwise enter the off-gas system (Kruger et al. 2013), it also slows the melting rate, reducing the efficiency of the melter and thus glass throughput (Hrma and Pokorný 2016; Hujová, Pokorný, and Kloužek 2018). Excessive foaming of the cold cap can also cause blockages to off-gas components (Bricker et al. 2012; Seymour 1995). So, while the continuous, direct-feed (DF) vitrification may improve the overall processing rates compared with induction melting (IM), the actual glass production rate may in some cases be lower due to the presence of the cold cap. The risk of corrosion of the electrodes due to the cold cap also limits the processing temperature (Lee, Hrma, Pokorný, et al. 2017; I. W. Donald 2015).

In the Advanced Waste Glass Research and Development Plan, the Office of River Protection highlighted the "complex series of reactions" within the cold cap, and referred to the mechanism as "perhaps the least understood" in the process of DF melting (Peeler et al. 2015). The plan states that "a fundamental understanding of these key phenomena will lead to strategic methods to minimise (or eliminate) the potential negative effects during facilities operations" (Peeler et al. 2015). Substantial ongoing work between Idaho National Laboratory (INL) and Pacific Northwest National Laboratory (PNNL) aims to develop computational models of simplified melter systems and feed behaviour, with improvements in accuracy and complexity derived from experimental results (Hrma and Pokorný 2016). Understanding cold cap batch-to-melt conversion will allow a more complete process control model for the JHCMs and improvements in melting rate, leading to reduced cost and lifetime of the facility operations (Guillen and Agarwal 2013; Marcial, Kloužek, et al. 2021; Kruger et al. 2008). The ORP plan summarises the desired outcome for cold cap research thus: to "demonstrate effective glass processing in scaled melter tests for glass compositions across the full WTP compositional envelope" (Peeler et al. 2015).

2.4.1 Cold Cap Structure

The cold cap is a continuum of material from waste feed slurry through to glass melt with many complex intermediate phases widely varying in density, viscosity and chemical properties (Hrma and Kruger 2008; Abboud and Guillen 2016). It is often divided into four key areas; boiling feed slurry, open-porosity reaction layer, primary foaming and secondary foaming (Hrma and Pokorný 2016). Cavities are included in some cold cap models where foaming is particularly vigorous and forms large bubbles that are trapped between the primary and secondary foam (Pokorný and Hrma 2014). The thermal boundary layer beneath the cold cap is also included for some thermodynamic models of the cold cap (Hrma et al. 2018). The temperature gradient in the cold cap is complex due to its varying thickness and gradient of around 1000 °C (Pokorný and Hrma 2011). The chemical and physical profiles of each of the layers of the cold cap are also difficult to understand and it is nearly impossible to fully replicate the cold cap conditions in a lab-based experiment without the use of a nearly-full-scale melter (Guillen, Abboud, and Pokorný 2019; Hrma 2014; Matlack, Gan, et al. 2009; Kruger et al. 2006), and moreover the cold cap is extremely difficult to observe in situ (R. A. Peterson et al. 2018; I. M. Peterson et al. 2019; Luksic et al. 2020). However, research has been performed in both of these areas to replicate the JHCM on a research scale at the Catholic University of America and to observe the cold cap in situ at a laboratory-based scale using X-ray Tomography (Harris et al. 2017; Luksic et al. 2020).

2.4.1.1 Boiling Slurry Layer

Water is present in the feed slurry from 40 – 60 wt % depending on the waste stream (Hujová, Kloužek, et al. 2018; Hujová, Pokorný, and Kloužek 2018; Matlack, Kot, et al. 2015). When this slurry lands on the surface of the cold cap, which is at a temperature of ~100 °C, most of this physical water is immediately boiled off, so long as the layers below are thin enough to facilitate sufficient heat transfer to this layer (Hujová,

Kloužek, et al. 2018; Dixon et al. 2015b). The feed is dried and creates a relatively solid layer at the very top of the reaction layer (McCarthy et al. 2018; Guillen et al. 2020).

2.4.1.2 Reaction Layer

The reaction layer varies in temperature from 100 ℃ near the top to around 600-800 ℃ at the bottom (Dixon et al. 2015b), this is where most of the batch-to-glass reactions take place (Hrma et al. 2010; Hrma, Marcial, et al. 2011; Rodriguez et al. 2014). The reaction layer has open porosity since little connected melt has formed, so gases from batch reactions in this region are free to escape (Hujová, Pokorný, et al. 2018; Hrma and Pokorný 2016; Hujová, Kloužek, et al. 2018). Reactions in this region include (Xu et al. 2015): dehydration of hydrated raw materials and waste products at 105 ℃ < T < 400 ℃, melting and decomposition of oxy-ionic salts and borates 100 ℃ < T < 350 ℃, evolution of CO_2 and NO_x from decomposition of raw materials and waste products at 400 ℃ < T < 700 ℃, formation of early amorphous borate phase, not yet connected, between 400 ℃ < T < 700 ℃, and formation of intermediate crystalline phases throughout the reaction layer (Xu et al. 2016, 2015; Dixon et al. 2015b). Further reactions such as dissolution of silica in the melt, evolution of SO_2 and redox reactions occur at higher temperatures once the main melt has formed (Marcial et al. 2014b; Hrma, Marcial, et al. 2011).

2.4.2 Foaming in the Cold Cap

The connectivity of the melt phase above ~700 ℃ leads to trapping of evolving gases (Hrma and Pokorný 2016; Hujová, Pokorný, et al. 2018; Marcial, Kloužek, et al. 2021). The initial melt has a relatively low viscosity (Hrma 2014; Rodriguez et al. 2014) so gases can easily escape but as the temperature increases, and more material dissolves into the melt, the viscosity increases and causes primary foaming at ~700 ℃ (Fedorov and Pilon 2002; Harris et al. 2017). The viscosity of the melt at gas-evolving temperatures is thought to be the most influential factor in the amount of foam

produced, followed by the gas evolution rate (Lee, Hrma, Pokorný, Kloužek, et al. 2019). The stability of the foam is dependent on the feed composition, feeding rate, operating conditions and the use of forced bubblers which aid in homogenisation of the melt (Pokorný et al. 2015; Abboud and Guillen 2016; Abboud, Guillen, and Pokorný 2016). Of these parameters the feed composition is the most complex to work with, since the feed is likely to vary widely with the different types of wastes (Xu et al. 2016; Hrma et al. 2010).

2.4.2.1 Primary Foaming

Residual CO_2 from decarbonation reactions is usually the main contribution to the primary foam, between temperatures of ~700 – 1000 ℃ (Xu et al. 2015; Hrma 2014) and while most of the CO_2 evolves at lower temperature regions where there is open porosity, there remains sufficient residual gas evolution to cause the significant foaming observed in many waste feeds (Hujová, Pokorný, et al. 2018; Lee, Hrma, Pokorný, et al. 2017). NO is another gas evolved in the lower end of the 700 – 1000 ℃ temperature range, up to ~750 ℃ (Luksic et al. 2020; Guillen et al. 2020; Appel et al. 2019) and makes some contribution to the foaming, varying with the amount of nitrates in the initial composition (Lee, Hrma, Pokorný, et al. 2017). Some feeds also have O_2 contributions to foaming at this temperature range (Lee, Hrma, Pokorný, Kloužek, et al. 2019). As the number of gas evolving batch reactions increases, the trapped bubbles begin to coalesce and form channels through the reaction layer so that gases can escape (Choi et al. 2017). This causes the collapse of the primary foam above ~800 ℃. The exact temperature of the primary foam collapse is different for different glass compositions and heating rates (Hrma 2009).

2.4.2.2 Secondary Foaming

Secondary foaming occurs due high temperature reactions such as sulphate decomposition and O_2 released via redox reactions, after the collapse of the primary

foam (Lee, Hrma, Pokorný, et al. 2017; Lee, Hrma, Kloužek, et al. 2017). At this point the melt is much more viscous and secondary foam does not collapse as readily as primary foam (Henager et al. 2011; Guillen and Agarwal 2013). Secondary foam bubbles will eventually merge with cavities and some primary foam and escape through the vent holes created (Lee, Hrma, Pokorný, et al. 2017). Small shifts in the redox ratio of iron in particularly high-iron glass melts can produce large volumes of O_2 in the secondary foaming region (Hrma 1990a).

Other multivalent species present in waste feeds that are likely to affect the oxidation state of the melt include Cr, S, Mn, Ni, Mo, and Ce (Pinet, Hugon, and Mure 2014). Higher quantities of multivalent species and sulphates in the melt lead to more secondary foaming. In feeds high in multivalent species the O_2 evolution, associated with secondary foam, overlaps with the primary foaming as redox reactions occur at lower temperatures. These feeds do not have distinct primary foaming and secondary foaming regions in the cold cap, but rather a continuum in which secondary foaming impedes the collapse of the primary foaming (Lee, Hrma, Pokorný, et al. 2017; Hrma et al. 2010).

2.4.3 Models of the Cold Cap

Mathematical models have been developed for the melting behaviour of the waste feeds to optimise glass production, predict any issues during melter operation and ensure the safety and efficiency of the process before the WTPs are operational. Models for melting behaviour of commercial glasses cannot simply be applied to the Hanford waste treatment operation due to the variability and complexity of the waste slurries that are to be vitrified (Hujová, Pokorný, and Kloužek 2018). A full predictive model of the cold cap, that can be implemented into wider Joule-Heated Ceramic Melter models, is the objective of much current research (Guillen 2015; Guillen et al. 2018; Abboud, Guillen, and Pokorný 2016).

A one-dimensional cold cap model has been developed (Pokorný and Hrma 2011; Pokorný et al. 2015) building on a previous one-dimensional thermodynamic model (Freeman 1996) to include the effect of bubblers. This model makes a prediction of the melting rate of a generic waste slurry which is in reasonable agreement with laboratory scale experimental tests. The model, thus far, is based on results from "a particular waste stream" and is most applicable when primary foaming occurs, but secondary foaming is negligible (Dixon et al. 2015a). In order to incorporate the properties of a wider range of feeds into the mathematical models, the Melt Rate Correlation (MRC) equation was derived from previous thermodynamic models by Hrma et al. (Hrma et al. 2018). Based on the thermodynamics of a particle moving vertically downward through the cold cap, the rate of melting is “reliably measured” for constant parameters such as rate of bubbling and total energy input. The equation is given in the form:

$$\mathrm{Q\ (kWm^{-2})} = \mathrm{\Delta H\ (kJg^{-1})\ j\ (gm^{-2}s^{-1})} \tag{3}$$

or,

$$\mathrm{j} = \xi_0 \left(\frac{\eta_{MO}}{\eta_R}\right)^{-\alpha} \left(1 + \frac{u_B}{u_0}\right)^{\beta} (T_{MO} - T_{FB}) \Delta H^{-1} \tag{4}$$

where Q is the total heat flux to the cold cap, ΔH is the specific melting heat per unit mass of glass and j is the melting rate of the glass. Q can be given in terms of bubbling rate, u_B, melter operating temperature, T_{MO}, temperature of cold cap bottom, T_{FB}, and viscosity at melter operating temperature, η_{MO}. T_{FB} can currently only be determined by feed expansion tests (FETs) although it is often disputed whether this temperature correlates to the collapse of the primary foam or that of the total foam (Hrma et al. 2018; Lee et al. 2020; Lee, Hrma, Pokorný, Kloužek, et al. 2019). From Hrma et al. (2018), the definition used for this data is $T_{FB} = T_{FM}$, the foam bottom temperature is defined as the temperature at the start of the collapse of primary foam, or the foam maximum. Reference viscosity, η_R, is equal to 1, to ensure correct units. Reference

bubbling rate, u_0, refers to the bubbling rate due to natural convection. ξ_0, is a coefficient related to a particular melter and type of glass. The equation is being validated for multiple feeds by the DM100 melter at the Vitreous State Laboratory (VSL), at the Catholic University of America, Washington D.C., USA (Hrma et al. 2018; Lee et al. 2020; Lee, Hrma, Pokorný, Kloužek, et al. 2019). For the data collected so far, least squares regression analysis of the melting rate resulted in the following parameters for the high-level waste feeds in the laboratory scale melter (LSM), DM100 melter and DM1200 melter, with a bubbling rate of u_B = 9.0 L min $^{-1}$, ξ_0 = 74.40 kg.s^{-3}.K^{-1}, α = 0.889, β = 0.699 and u_0 = 0.234 m.h^{-1} (Hrma et al. 2018; D. S. Kim et al. 2012).

Correlation between the measured melting rate and the melting rate estimated by the MRC for 5 simulated Hanford waste feeds: HLW-E-Al-27, HWI-Al-19, HLW-E-M-09, HLW-NG-Fe2 and HWI-Al-28, are shown in Figure 2.4.2**.** For these feeds the equation provides a good fit to the measured data, and "covers the influential variables", with the glass viscosity being the most influential within the range of data studied (Hrma et al. 2018; Lee, Hrma, Pokorný, Kloužek, et al. 2019), however it is also stated that an exact theory "would need to consider the effect of the gas cavities carried by the melt flow, the gas bubbles from redox, and the dissolving residues of solid particles" (Hrma et al. 2018). In a study of a broader envelope of HLW feeds and processing conditions, the feeds that were overestimated for melting rate by the MRC were HLW-E-ANa-22, HLW-98-86, HLW-E-M09 and HLW-NG-Fe2. The HLW-E-ANa-22 and HLW-E-M-09 are the highest Cr_2O_3 containing HLW feeds (Kruger et al. 2009; Kruger, Pegg, et al. 2012), HLW-98-86 is high in both Fe_2O_3 and MnO (Kruger, Pegg, et al. 2012) and HLW-NG-Fe2 is the highest Fe_2O_3 feed.

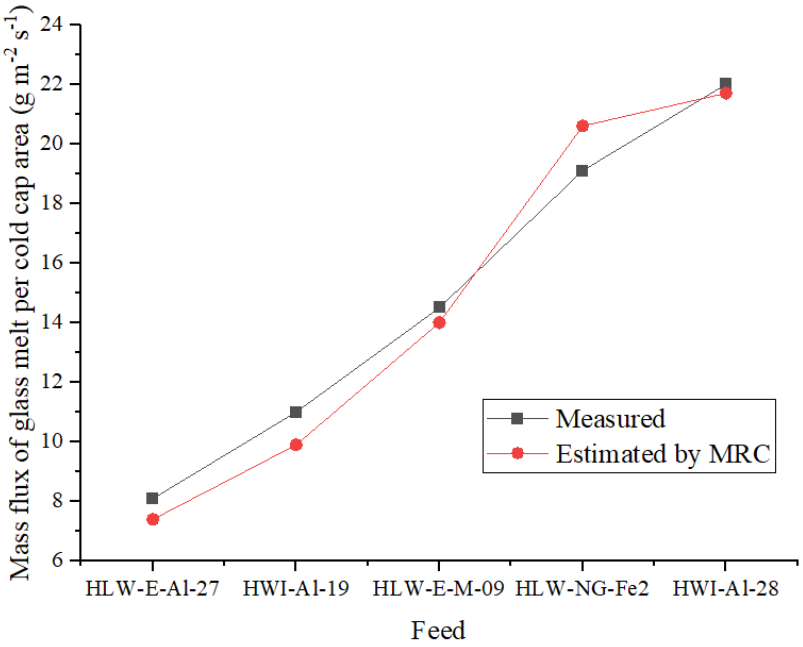

Figure 2.4.2. Melting rate of 5 feeds measured in the DM100 melter and estimated using the melt-rate correlation equation (Hrma et al. 2018; Lee, Hrma, Pokorný, Kloužek, et al. 2019).

While the MRC predicts the melting rate well for all of the five feeds, it slightly overestimates for the HLW-NG-Fe2 feed and underestimates the other 4 feeds. This single data point alone cannot be used to draw any conclusions, however, there is a possibility that the use of $T_{FM} = T_{FB}$, where the HLW-NG-Fe2 feed shows significant foaming at higher temperatures, does not sufficiently describe the melting behaviour (Guillen et al. 2020).

2.5 HLW-Al-19 Simulated Waste Feed

Of the feeds used to validate the MRC equation discussed in section 2.4.3, (Hrma et al. 2018), HLW-Al-19 (referred to as HWI-Al-19 in that study), is one of the most deeply-studied waste streams in the cold cap (Matlack, Gan, et al. 2009; Hujová, Kloužek, et al. 2018; McCarthy et al. 2018; Mitchell and Guillen 2016; Chun et al. 2013). The glass composition, Table 2.5.1, is limited by the high-alumina content, however, in terms of foaming behaviour, by all experiments performed so far, it is a "regular" high-level waste feed (Lee, Hrma, Pokorný, Kloužek, et al. 2019). Studies of raw material changes, melting rates and bubbling rates, and foam expansion during melting have been performed with this feed to give an idea of how a generic HLW feed will behave inside a melter and it is often used to compare with irregularly foaming feeds (Lee, Hrma, Pokorný, Kloužek, et al. 2019; Hrma et al. 2018).

In an investigation of cold cap analysis techniques, a simplified version of the HLW-Al-19 feed, the A0 feed (Xu et al. 2016; Dixon et al. 2015b), was used to correlate the temperature regions of stages of melting (SoM) samples, where feed was quenched at various temperatures during melting to provide snapshots of the melting behaviour, with a sample produced in an LSM (Dixon et al. 2015b). Results from this study made it possible to compare SoM samples to a more representative cold cap system by employing Scanning Electron Microscopy (SEM) and Energy Dispersive Spectroscopy (EDX), as well as X-ray Powder Diffraction (XRD) and optical microscopy to compare chemical and morphological structures in the samples and produce a temperature distribution curve of the LSM sample.

Table 2.5.1. HLW-Al-19 simulated glass composition (Joseph et al. 2010).

Raw Material	**Oxide**	**Batch 100 g^{-1}**	**wt%**	**Raw Material**	**Oxide**	**Batch 100 g^{-1}**	**wt%**
$Al(OH)_3$	Al_2O_3	37.18	24.53	$Ni(OH)_2$	NiO	0.50	0.41
H_3BO_3	B_2O_3	34.16	19.41	PbO	PbO	0.42	0.42
$CaCO_3$	CaO	1.09	0.61	$Fe(H_2PO_2)_3$	Fe_2O_3	1.25	0.40
$Fe(OH)_3$	Fe_2O_3	7.44	5.61		P_2O_5		1.07
Li_2CO_3	Li_2O	8.92	3.64	NaF	Na_2O	1.50	0.41
NaOH	Na_2O	1.99	1.55		F		0.34
SiO_2	SiO_2	22.15	22.35	Na_2CO_3	Na_2O	10.66	6.29
$Zr(OH)_4 \cdot 0.65H_2O$	ZrO_2	0.55	0.40	$NaNO_2$	Na_2O	0.35	0.16
Na_2SO_4	Na_2O	0.36	0.16	$NaNO_3$	Na_2O	1.24	0.46
	SO_3		0.20	$Na_2C_2O_4$	Na_2O	0.13	0.06
Bi_2O_3	Bi_2O_3	1.17	1.18	$CaSiO_3$	CaO	9.71	4.73
$Cr_2O_3 \cdot 1.5H_2O$	Cr_2O_3	0.62	0.53		SiO_2		5.07
				Total		141.366	100

2.5.1 Foaming Behaviour

As discussed above, the HLW-Al-19 feed is considered a regular foaming HLW feed. Previous Feed Expansion Tests have shown the feed to foam up to a peak foaming volume of 2-5 times its original volume (Lee, VanderVeer, Hrma, et al. 2017; Lee, Hrma, Pokorný, Kloužek, et al. 2019; Guillen et al. 2020; Lee, Hrma, Pokorný, Traverso, et al. 2019). The variation in peak foam height arises from various parameters such as quartz particle size, viscosity and heating rate, it has been shown that the melting rate does not alter significantly the peak foam volume, but does change the temperature of peak foam and foam collapse, with the higher melting rate peaking at a higher temperature (Lee, VanderVeer, Hrma, et al. 2017). Both feed viscosity and the quartz particle size change the amount of foam produced during melting, with the higher viscosity causing more foaming overall and peaking at a higher temperature, while the smaller quartz particles produce the most foam but the temperature profile was similar throughout the particle sizes (Lee, VanderVeer, Hrma, et al. 2017).

2.5.2 X-ray Computed Tomography

The HLW-Al-19 feed was the subject of a few studies investigating the use of X-ray computed tomography (X-ray CT) on expanding pellets during melting (Mitchell and Guillen 2016; Harris et al. 2017; Luksic et al. 2020; Hrma and Pokorný 2016). X-ray CT has the ability to uncover information about the bubbles forming within the melt during melting and foaming by mapping phases of various densities within a 3D bulk sample with 2D images throughout its volume (Hrma and Pokorný 2016). In a study of variations on the HLW-Al-19 feed pellets, using different ratios of glass-forming chemicals, with the foaming profiles shown in Figure 2.5.1, images of the pellets provided data on the bubble size and morphology during foaming (Harris et al. 2017). Generally observed in X-ray CT of pellet tests; the largest bubbles contribute most to peak foaming and there are smaller secondary bubbles at higher temperatures (Harris et al. 2017; Luksic et al. 2020).

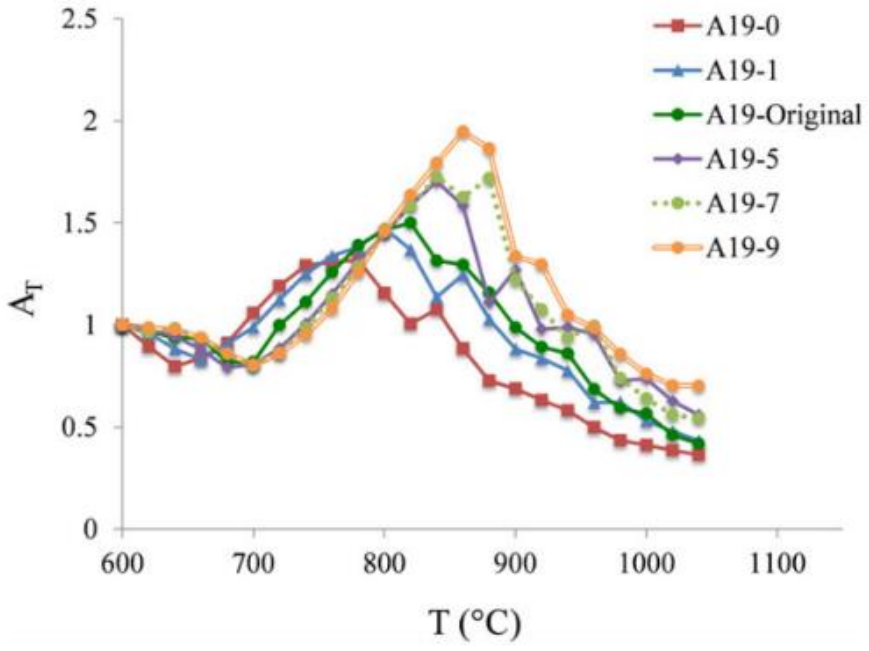

Figure 2.5.1. Normalised pellet area (A_T) as a function of temperature for 6 variations of the HLW-Al-19 feed (Harris et al. 2017).

In X-ray CT studies of pellet expansion the maximum bubble size is limited by the size of the pellet. The foam morphology inside a pressed pellet is likely to be different to

that inside a cold cap due to the interactions between layers of the cold cap and bubbles rising due to buoyancy from the glass melt, and ongoing work aims to use this technique in dynamic melter systems where bubbles are more representative (Harris et al. 2017; Guillen et al. 2018; Choi et al. 2017).

2.5.3 Impact of Raw Materials

The influence of quartz particle size on the melting and foaming behaviour of the HLW-Al-9 feed is discussed in section 2.5.1 (Lee, VanderVeer, Hrma, et al. 2017), however, other raw material alterations have also been examined and it is clear that the make-up of the feed is an influential parameter in predicting the foaming behaviour (Hrma et al. 2010). Boehmite (γ-AlO(OH)) and corundum (Al_2O_3) have been explored as alternatives to gibbsite ($Al(OH)_3$) as the aluminium source, showing changes in the temperatures of CO_2, SO_2 and O_2 evolution profiles and even influencing the Fe redox state through the oxygen partial pressure above the melt (Lee, Hrma, Kloužek, et al. 2017). A 25 % increase in the rate of melting was observed in the feed using AlO(OH) as the alumina source, compared to $Al(OH)_3$ (Pokorný and Hrma 2014; Hrma 2014), whereas corundum produced substantially more foam (Pierce et al. 2012). Overall, it appears that the rate of Al_2O_3 incorporation into the glass-forming melt dictates the melting rate of the glass, which can be affected by both the raw material source and the particle size (Marcial, Kloužek, et al. 2021).

Despite the HLW-Al-19 glass only containing 5.9 wt% Fe_2O_3, the source of Fe_2O_3 has also been shown to have significant impacts on the melting behaviour of the feed (Marcial, Kloužek, et al. 2021; Guillen et al. 2020). Melting of the feed with magnetite (Fe_3O_4), goethite (FeOOH), and haematite (Fe_2O_3) replacing the iron hydroxide ($Fe(OH)_3$) raw material showed little difference in the foaming behaviour (Marcial, Kloužek, et al. 2021), however, the use of a completely reduced iron source, iron oxalate dihydrate ($FeC_2O_4 \cdot 2H_2O$), did show significant reduction in the feed volume

expansion (Guillen et al. 2020). The Fe_3O_4 feed evolved less O_2 than the Fe^{3+} iron sources (Marcial, Kloužek, et al. 2021), and the $FeC_2O_4 \cdot 2H_2O$ feed showed a complete suppression of O_2 evolution, Figure 2.5.2 (Guillen et al. 2020).

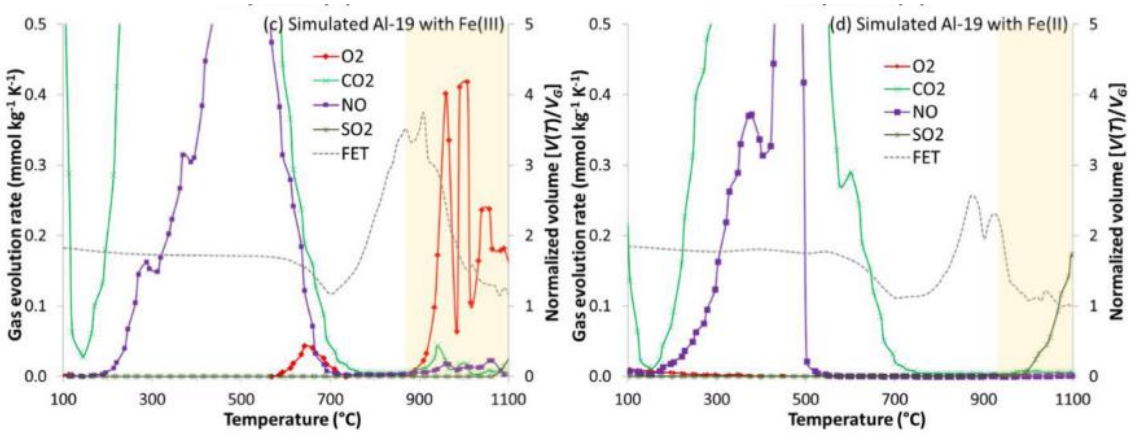

Figure 2.5.2. Evolved Gas Analysis (EGA) for the High-Alumina HLW-Al-19 feed with iron hydroxide $Fe(OH)_3$ and iron oxalate dihydrate $FeC_2O_4 \cdot 2H_2O$ as raw materials for Fe (Guillen et al., 2020).

2.6 HLW-NG-Fe2 Simulated Waste Feed

The HLW-NG-Fe2 feed is much higher in Fe than the HLW-Al-19 feed and foams significantly more than the "regular" HLW-Al-19 feed, and most other HLW feeds (Guillen et al. 2020; Lee, Hrma, Pokorný, Kloužek, et al. 2019). The HLW-NG-Fe2 glass composition, given in Table 2.6.1, was developed by the VSL at the Catholic University of America to immobilise the high-iron C-106/AY-102 tank waste (Matlack et al. 2012; Chekhmir, Gribetz, and Shore 2011). The final vitrified HLW-NG-Fe2 glass composition has 42 wt% waste loading and an average glass production rate of 1650 kg m^{-2} day^{-1} in the DM100 research scale melter system at the VSL (Matlack et al. 2012; E. C. Smith et al. 2011).

Table 2.6.1. HLW-NG-Fe2 simulated glass composition developed by the VSL to immobilise the C-106/AY-102 high-iron tank waste (Matlack et al. 2012).

Raw Material	**Oxide**	**Batch 100 g^{-1}**	**Wt%**	**Raw Material**	**Oxide**	**Batch 100 g^{-1}**	**Wt%**
$Al(OH)_3$	Al_2O_3	8.61	5.59	$FePO_4 \cdot 2H_2O$	P_2O_5	1.71	0.65
H_3BO_3	B_2O_3	0.56	13.57		Fe_2O_3		0.73
$Na_2B_4O_7 \cdot 10H_2O$	Na_2O	37.16	6.04	PbO	PbO	0.63	0.63
	B_2O_3		0.32	Na_2SiO_3	SiO_2	8.03	3.95
$CaCO_3$	CaO	0.94	0.52		Na_2O		4.08
CeO_2	CeO_2	0.12	0.12	Na_2SO_4	SO_3	0.39	0.22
$Cr_2O_3 \cdot 1.5H_2O$	Cr_2O_3	0.30	0.25		Na_2O		0.17
$Fe(OH)_3$	Fe_2O_3	20.54	15.35	SiO_2	SiO_2	37.33	37.33
$La(OH)_3$	La_2O_3	0.11	0.09	$SrCO_3$	SrO	0.28	0.20
Li_2CO_3	Li_2O	3.87	1.56	ZnO	ZnO	0.03	0.03
$Mg(OH)_2$	MgO	0.24	0.16	$Zr(OH)_4 \cdot 0.654H_2O$	ZrO_2	1.57	1.13
MnO_2	MnO_2	3.98	3.98	$NaNO_2$	Na_2O	0.01	0.00
NaOH	Na_2O	0.81	0.63	$NaNO_3$	Na_2O	0.45	0.16
Na_2CO_3	Na_2O	4.04	2.36	$H_2C_2O_4 \cdot 2H_2O$		0.06	
$Ni(OH)_2$	NiO	0.59	0.47				
					Total	132.36	100.00

As well as the high Fe_2O_3 content, the presence of Cr_2O_3, MnO_2, NiO and CeO_2 in the wastes may also impact the melting behaviour, particularly in the oxygen balance during melting (Lee, Hrma, Kloužek, et al. 2017), and the formation of spinel compounds such as magnetite, trevorite and chromite in the final glass (Matyáš et al. 2017; Hrma, Schill, and Nemec 2002; Lonergan et al. 2022).

2.6.1 Foaming Behaviour

The maximum foam volume during melting in the HLW-NG-Fe2 feed has been measured as up to ~ 10 times its original volume at a heating rate of 10 °C min^{-1} (Guillen et al. 2020; Lee, Hrma, Pokorný, Traverso, et al. 2019; Marcial, Kloužek, et al. 2021). An example of the feed expansion at different heating rates is shown in Figure 2.6.1. As well as the vigorous peak foaming there is considerable secondary foaming above primary foam collapse, between 800 and 1100 °C, Figure 2.6.1, which as discussed in section 2.4.2.2 is caused by mainly SO_2, O_2 and residual CO_2 evolution.

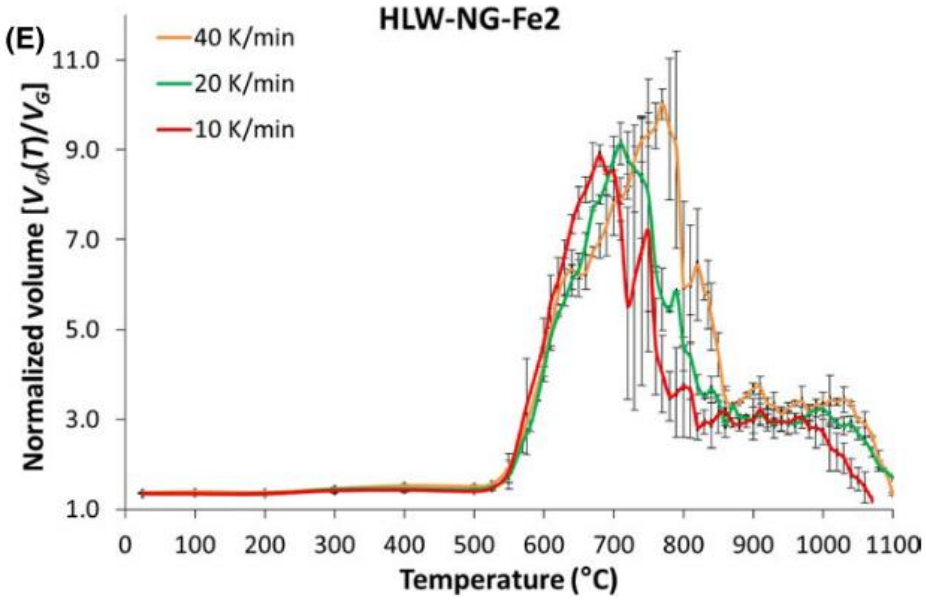

Figure 2.6.1. Feed volume expansion of the HLW-NG-Fe2 feed at heating rates of 10, 20 and 40 K min^{-1} (Lee, Hrma, Pokorný, Traverso, et al. 2019).

Given the large quantity of Fe_2O_3, as well as other multivalent species, it is likely that O_2 evolution from redox reactions contributes to the secondary foaming. A reduction in

average Fe oxidation state was observed during melting of the HLW-NG-Fe2 feed, accompanied by a significant evolution of O_2 compared with the HLW-Al-19 feed (Guillen et al. 2020), therefore a likely source of O_2 evolution can be attributed to the following decomposition reaction (Pokorný and Hrma 2014; Hrma et al. 2010):

$$2Fe_2O_3 \rightarrow 4FeO + O_2 \quad (5)$$

2.6.2 Impact of Raw Materials

Due to "significant uncertainty" in the form of iron in the real waste feeds, it is possible that it will be present in "a number of amorphous forms, minerals and oxidation states" (Matlack, Kot, et al. 2015). The VSL ran melter tests on the HLW-NG-Fe2 feed with the same four iron sources as discussed in the HLW-Al-19 feed (Marcial, Kloužek, et al. 2021), section 2.5.3: iron hydroxide $Fe(OH)_3$, goethite (FeOOH), haematite (Fe_2O_3) and magnetite (Fe_3O_4) (Matlack, Kot, et al. 2015). In terms of melting rate the Fe_2O_3 had the highest melting rate at 1910 kg m^{-2} day^{-1}, followed by Fe_3O_4 at 1830 kg m^{-2} day^{-1}, and finally FeO(OH) at 1725 kg m^{-2} day^{-1} (Matlack, Viragh, et al. 2015). However, an investigation of the foaming behaviour (Marcial, Kloužek, et al. 2021) showed that the foam volume increased in the order Fe_3O_4 < FeOOH < $Fe(OH)_3$ < Fe_2O_3. The foam volume does not directly correlate to the melting rate. The viscosity of the feed containing $Fe(OH)_3$ was an order of magnitude greater than the viscosities of any of the other feeds tested (Matlack, Viragh, et al. 2015), which is consistent with the sensitivity study showing the viscosity to be the most influential factor on melting rate (Lee, Hrma, Pokorný, Kloužek, et al. 2019). A correlation between the chemically-bound water in the iron source and reduced melt viscosity could also explain these results (Marcial, Kloužek, et al. 2021). Despite the 33.3 % Fe^{2+} content in the Fe_3O_4 iron source, there does not appear to be a correlation in this case between the redox state of the iron source and the rate of melting (Matlack, Viragh, et al. 2015), although there may be some impact on the foaming behaviour (Marcial, Kloužek, et al. 2021).

2.6.3 Reduced Fe Raw Material

Given the large difference in behaviour of the HLW-Al-19 feed during melting using the $FeC_2O_4 \cdot 2H_2O$, discussed in section 2.5.3 (Hujová, Pokorný, et al. 2018; Guillen et al. 2020), there is potential that the $FeC_2O_4 \cdot 2H_2O$ raw material could have an even greater effect on the HLW-NG-Fe2 feed. Iron oxalate dihydrate, $FeC_2O_4 \cdot 2H_2O$ contains iron in the 2+ oxidation state. Thermal decomposition of iron oxalate by DTA-TGA-EGA, (López, Tirado, and Pérez Vicente 2013; Carles et al. 1999; Ogasawara and Koga 2014) suggests the following potential decomposition pathways during heating:

$$FeC_2O_4 \cdot 2H_2O \rightarrow FeC_2O_4 + 2H_2O \quad (6)$$

$$FeC_2O_4 \rightarrow FeO + CO + CO_2 \quad (7)$$

$$CO + \frac{1}{2}O_2 \rightarrow CO_2 \quad (8)$$

$$2FeO + \frac{1}{2}O_2 \rightarrow Fe_2O_3 \quad (9)$$

or,

$$3FeC_2O_4 \rightarrow Fe_3O_4 + 4CO + 2CO_2 \quad (10)$$

The O_2 consumption in these decomposition pathways explains the lack of O_2 evolution in the HLW-Al-19 feed made with $FeC_2O_4 \cdot 2H_2O$ compared to the original $Fe(OH)_3$ slurry source (Guillen et al. 2020), reducing the effect of O_2 evolution on secondary foaming. There is, however, an increase in CO_2 and potentially CO evolved. The decomposition of $FeC_2O_4 \cdot 2H_2O$ in air at 200-250 is observed using DTA in Figure 2.6.2 (Angermann and Töpfer 2008). and when held at 350 °C by ^{57}Fe Mössbauer spectroscopy, in Figure 2.6.3 (Smrčka et al. 2016).

The room temperature ^{57}Fe Mössbauer spectra sample shows a single Fe^{2+} doublet. By the first heat treatment to 350 °C held for 8 minutes most of the paramagnetic iron is

now amorphous Fe_2O_3, with a small remaining Fe^{2+} doublet. Magnetically ordered Fe^{3+} phases, identified as haematite and maghemite, begin to form, and increase in relative abundance with heat treatment time, supporting equations (6-9) as decomposition pathways.

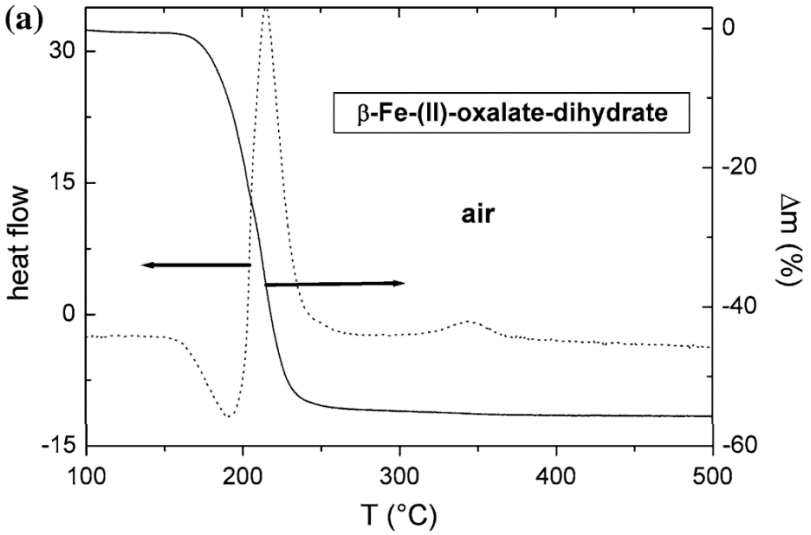

Figure 2.6.2. Decomposition of $FeC_2O_4 \cdot 2H_2O$ in air by TG-DTA at a heating rate of 2 °C min^{-1} (Angermann and Töpfer 2008).

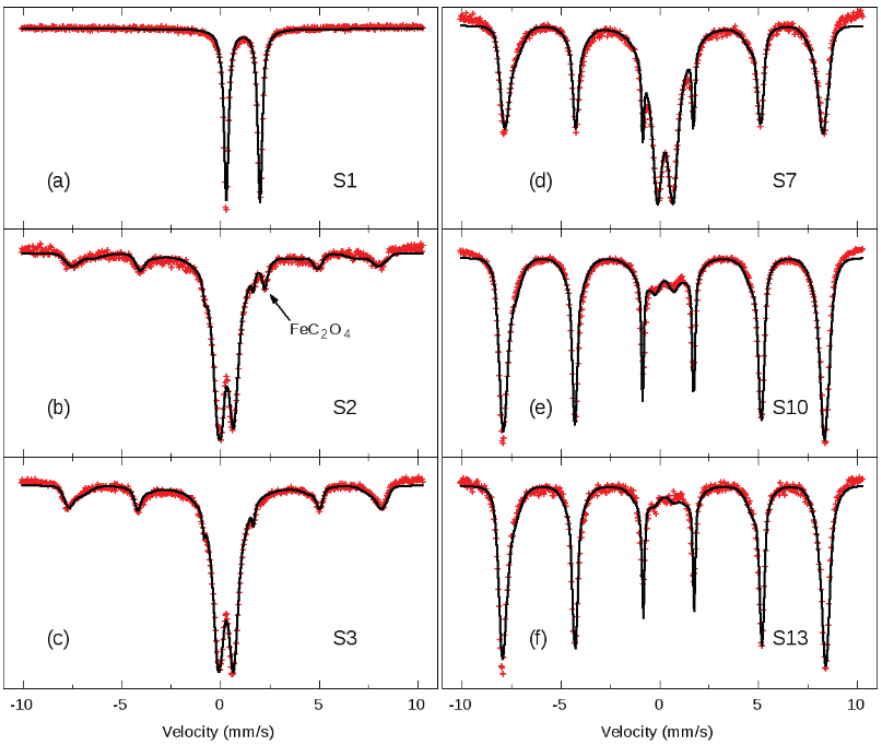

Figure 2.6.3. ^{57}Fe Mössbauer Spectroscopy of a) $FeC_2O_4 \cdot 2H_2O$ and $FeC_2O_4 \cdot 2H_2O$ isothermally heated at 350 °C for b) 8 minutes, c) 12 minutes, d) 60 minutes, e) 120 minutes, and f) 180 minutes (Smrčka et al. 2016).

2.6.4 Redox Control

A study exploring varying nitrate and oxalate levels in the C-106/AY-102 simulated feed (HLW-NG-Fe2), found that increased nitrate content decreased the rate of glass production, and additions of oxalate at 50-75 g kg^{-1} glass resulted in more than 10 % Fe^{2+}/Fe_T (Kruger, Matlack, Pegg, et al. 2012). It concluded that oxalate content should be limited in the feed to avoid precipitation of secondary phases. The study also concluded that the management of organics in the high-iron HLW feed is important for controlling production rates and glass properties. However, algorithms used to determine the amount of sugar to add to high-nitrate LAW feeds as a reducing agent need to be modified and require further testing to better define the relationship between sources of carbon (Kruger, Matlack, Pegg, et al. 2012). In Hanford waste glasses, limits have been set on the iron redox ratio in the glass, $0.09 < Fe^{2+}/Fe^{3+} < 0.3$, with the justification of controlling gas release and foaming, while avoiding precipitation of metals, spinel and sulphide species in the melt (Lambert and Kim 1994).

In the HLW-NG-Fe2 feed, a DM100 melter test produced glass with 0.65 vol% of spinel crystals, containing Fe, Mn, Cr, and Ni, at 950 ℃ for 72 hours (Matlack, Viragh, et al. 2015), leaving some room for increases in spinel content under the current limitations.

2.7 Redox behaviour in glass melts

The redox state of the glass-melt has an effect on O_2 evolution and secondary foaming (Kocarkova 2011; Lee, Hrma, Kloužek, et al. 2017) as well as the solubility of certain species (including SO_3) (Soderquist et al. 2014; Vienna, Kim, Muller, Piepel, Kruger, et al. 2014; Langowski, Darab, and Smith 1996; Bibler et al. 2000), furnace refractory corrosion, crystallinity and settling of metallic species, glass product durability (Peeler and Edwards 2004), electrical melt conductivity amongst other parameters (Goldman 1986). With the diversity of waste compositions at the Hanford site, understanding the redox in the cold cap and glass melt is essential to reduce uncertainties in final glass quality and melt behaviour in the JHCMs (Pinet, Hugon, and Mure 2014).

2.7.1 Modelling Redox Behaviour in Glass Melts

The factors that affect the redox state of the melt include oxygen fugacity, or partial pressure, f_{O2}, above the glass melt (Lee, Hrma, Kloužek, et al. 2017; Kloužek and Rohanová 1999), melt temperature, *T*, and the glass composition (Pinet, Hugon, and Mure 2014). The oxygen fugacity is determined by the raw materials and their decomposition, glass composition and the furnace conditions. The melt temperature is set at 1150 ℃ for vitrification at the Hanford site (Vienna et al. 2016; Jantzen 2011).

The optical basicity is determined by both the glass composition, and the local environment of oxygen atoms (Duffy 1996; Duffy and Ingram 1976). The basicity of a melt can be considered as its "tendency to liberate oxide ions" (Duffy 1996). This depends on the number on BOs and NBOs in silicate melts, and therefore the quantity of alkali modifiers. The optical basicity of a glass, Λ, has been shown to correlate with oxygen partial pressure (Thiemsorn et al. 2008a) and $\log(Fe^{2+}/Fe^{3+})$ (Duffy 1996; Pinet et al. 2008). The glass composition is thus a highly influential parameter in the redox state of the melt (Pinet, Hugon, and Mure 2014).

^{57}Fe Mossbauer spectroscopy has been used to indicate the redox state of iron in the melt or glass (Goldman 1986; Cassingham et al. 2008; Glazkova et al. 2015; Muller et al. 2009). While iron is often the most abundant multivalent species in HLW feeds, the contributions of all multivalent species must be considered (Jantzen and Stone 2007). X-ray absorption spectroscopy (XAS) studies have also been used to identify the redox states of further multivalent species in HLW feeds including Mn and Cr (McKeown et al. 2002; Guillen et al. 2020; Gan et al. 2009). In order to begin to understand the interactions between redox species in a melt, the following sections 2.7.2 and 2.7.3, describe work performed on single multivalent species and multiple multivalent species in glass melts, and attempts to model their behaviour.

2.7.2 Single multivalent species in glass melt

Schreiber and co-workers performed predictive work on redox behaviour in both industrial and nuclear waste glasses using empirical data and modelling (Schreiber and Hockman 1987; Schreiber 1986, 1980, 1983; Schreiber and Todd Coolbaugh 1995; Schreiber et al. 1994, 1990). For a single multivalent element in a glass-forming melt, the simplest equation to describe the behaviour is (Schreiber et al. 1986):

$$4\mathrm{M}^{\mathrm{m+}}_{\mathrm{(melt)}} + 2\mathrm{nO}^{2-}_{\mathrm{(melt)}} \rightleftharpoons 4\mathrm{M}^{(\mathrm{m-n})+}_{\mathrm{(melt)}} + \mathrm{nO}_{2\mathrm{(gas)}} \qquad (11)$$

Where M^{m+}, and $M^{(m-n)+}$, are the oxidised and reduced element, M, respectively, and n is the number of transferred electrons in the reaction (Schreiber et al. 1986).

For a constant b, which incorporates all terms relating to temperature and melt composition, the following equation can be used to calculate the oxygen fugacity, f_{O_2}:

$$-\log(fO_2) = \frac{4}{n}\log[\frac{M^{(m-n)+}}{M^{m+}}] + b \qquad (12)$$

This relationship is used to plot linear relationships between -log(f_{O2}) and log(M(m-n)+/Mm+) for many multivalent elements in synthesized glass compositions at constant

temperature. Relevant to the present work is the calculations made with the SRL-131 glass from the Defence Waste Processing Facility (DWPF) at Savanah River, SC, USA (Schreiber et al. 1986). Relationships between the redox state and oxygen fugacity by equation (12) are applied to the SRL-131 glass in Figure 2.7.1, for various Fe^{2+}/Fe^{3+} and Fe^{2+}/metallic Fe, at melt temperatures from 850 – 1150 ℃ at 1, 5 and 10 wt% Fe.

The oxygen fugacity required to reduce Fe from either Fe^{3+} to Fe^{2+}, or Fe^{2+} to metallic Fe, is lower for higher melt temperatures (Beerkens 1999; Lee, Hrma, Kloužek, et al. 2017; Kloužek and Rohanová 1999; Sugawara et al. 2016). The gradient of the line decreases for Fe^{2+}/metallic Fe, but at 1150 ℃ it there is no metallic reduction up to $-log(f_{O2})$ = 12 to 14. For one-electron transfer, Fe^{3+} to Fe^{2+}, governed by equation (12), the difference between 1 and 5 wt% Fe is a shift to higher $-log(f_{O2})$ with $log(Fe^{2+}/Fe^{3+})$. For 10 wt% Fe the relationship for the one-electron transfer is not accurately predicted by equation (12), attributed to the effect of the high-iron concentration on the "basicity of the melt with changing oxygen fugacity" (Schreiber et al. 1986).

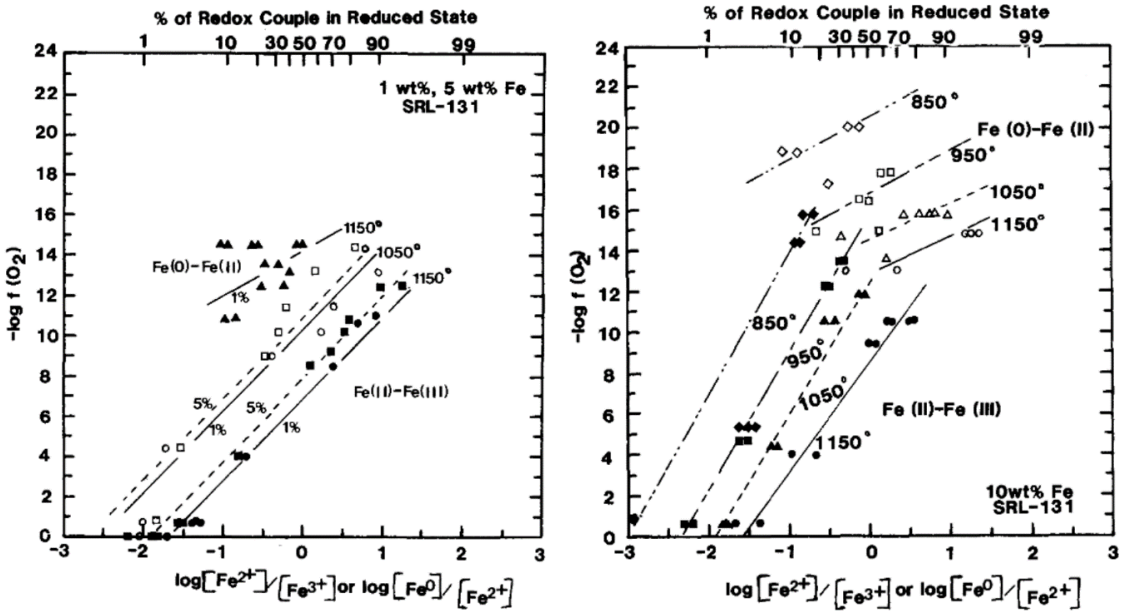

Figure 2.7.1. Relationship between oxygen fugacity and redox ratio of Fe in SRL-131 melt, with 1 wt% (circles and triangles) and 5 wt% (squares) Fe (left) and 10 wt% Fe (right) over a range of temperatures (Schreiber et al. 1986).

From this linear relationship, equation (12), – assuming the differences in the rest of the composition are minimal – an estimation for the oxygen fugacity can be made for other waste glass compositions containing Fe up to 5 wt%, as well as finding the limits of Fe2+/FeT before the onset of potential precipitation of metallic species. For higher iron contents more empirical data or measurements of glass basicity may be required (Schreiber et al. 1986; Kloužek and Rohanová 1999).

As well as the diversion from the simplest model owing to the high-iron content (Schreiber et al. 1986; Seymour 1995), the HLW-NG-Fe2 feed also contains 2.5 wt% Mn, 0.2 wt% Cr, 0.1 wt% Ce and 0.4 wt% Ni. For the SRL-131 glass redox states were given for all of the redox-active species present in the melt with imposed oxygen fugacity at 1150 °C, Figure 2.7.2 (Schreiber and Hockman 1987).

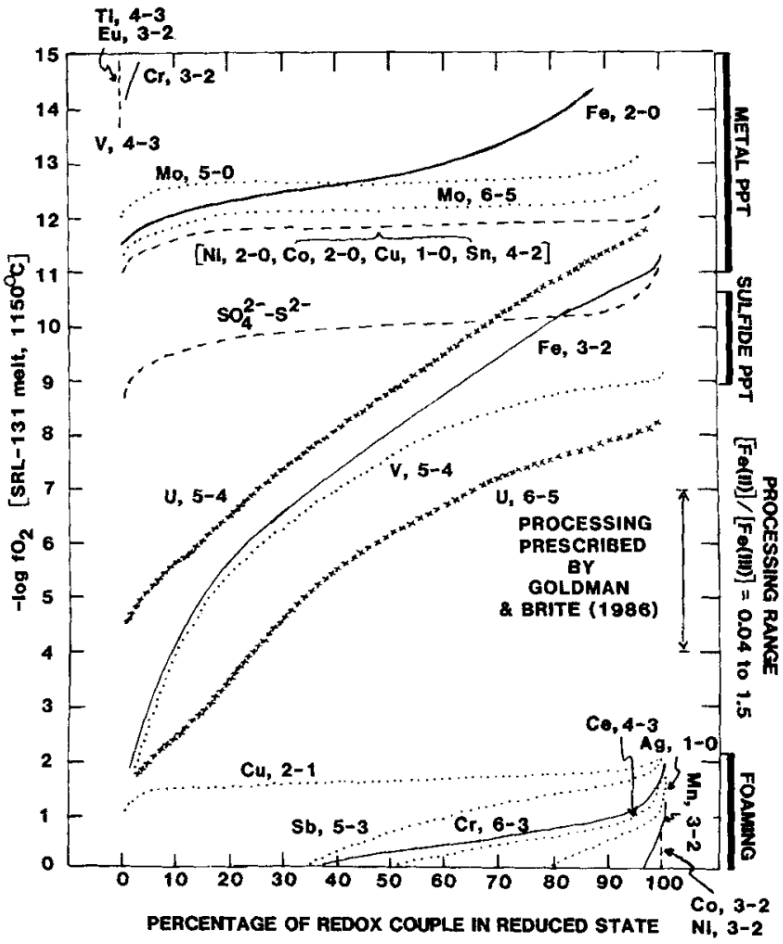

Figure 2.7.2. Relationship between oxygen fugacity and redox ratio of a range of redox species in the SRL-131 melt (Schreiber and Hockman 1987).

2.7.3 Multiple multivalent species in glass melt

Little predictive modelling has been performed on mixtures of multivalent species in glass melts, although it has been noted that predictability is necessary for redox control during vitrification of radioactive wastes (Bickford and Diemer Jr 1986; Seymour 1995; Peeler, Lorier, and Vienna 2001). Full understanding of mutual redox reactions becomes more complex with addition of each new species. In 1960, Tress (Tress 1960) provided the reaction series in aqueous materials, by which any ion with a lower reduction potential, E°, will be oxidised by any ion with a higher E° (Schreiber and Haskin 1976). The reduction potential, E_M^*, is defined as the y-intercept on the linear graph of $-log(f_{O_2})$ and *log(redox state)*, equation (13) (Berry and O'Neill 2004; Schreiber and Balazs 1985):

$$-\log(fO_2) = \frac{4}{n}\log\left[\frac{M^{(m-n)+}}{M^{m+}}\right] - E_M^* \qquad (13)$$

This electrochemical series was found to be adequate in predicting redox states in alkali silicate glasses, but inadequate in alkali borate glasses (Paul and Douglas 1966). In sodium-silicate glasses, species with significantly different reduction potentials behaved as predicted, however, with a change in alkali content, the effective electrochemical potentials of Fe, V and Cu changed order in the series (Paul and Douglas 1966).

Schreiber and Balazs evaluated the reduction potentials in the borosilicate SRL-131 glass melt (Schreiber and Balazs 1985), as well as a range of other silicate glasses in comparison to water, showing a variation in the electrochemical potentials of many redox active species in each medium, as well as variation in the series, even between glass melt compositions (Schreiber and Balazs 1985). The resulting reduction potentials calculated for the relevant species in borosilicate glass melts are given in Table 2.7.1 (Brückner 1985; Schreiber and Balazs 1985).

Table 2.7.1. Reduction potentials for redox states of multivalent species in the HLW-NG-Fe2 feed, for borosilicate melts at 1150 ℃ (Schreiber and Balazs 1985).

Element	Initial Oxidation State	Final Oxidation State	Reduction Potential
Chromium	Cr^{3+}	Cr^{2+}	-1.38
	Cr^{6+}	Cr^{3+}	-0.04
Cerium	Ce^{4+}	Ce^{3+}	-0.03
Iron	Fe^{2+}	Fe^{0}	-1.27
	Fe^{3+}	Fe^{2+}	-0.68
Manganese	Mn^{3+}	Mn^{2+}	0.33
Nickel	Ni^{2+}	Ni^{0}	-1.06
	Ni^{3+}	Ni^{2+}	0.69

Electron exchange between individual redox ions may not occur in the glass melt, due to buffering by the melt, they may, in fact, occur during cooling (Brückner 1985; Schreiber et al. 1987; Borisov 2016). High-precision measurements at melt temperature showed up to a 20 % variation in the measured enthalpy of the redox reactions; however, in that study there was no diversion from the overall series (Brückner 1985).

Equilibrium for two redox couples in a glass forming melt can be expressed as (Schreiber et al. 1987):

$$\mathrm{sM}^{m+}_{(melt)} + \mathrm{nR}^{(r-s)}_{(melt)} \rightleftharpoons \mathrm{sM}^{(m-n)+}_{(melt)} + \mathrm{nR}^{(r+)}_{(melt)} \tag{14}$$

where n and s are the number of electrons transferred from multivalent elements M and R, respectively (Schreiber et al. 1987). The net reaction potential term, ΔE^*, where

$$\Delta E^* = sE^*_M - nE^*_R \tag{15}$$

governs the degree of mutual interaction. In the SRL-131 melt, for values of $\Delta E^* < 0.7$, there is negligible electron exchange between the redox couples, for $0.7 < \Delta E^* < 1.5$ electron exchange occurs but the reaction is incomplete, and for $\Delta E^* > 1.5$ there is a completed interaction (Schreiber et al. 1987). Some mutual redox interactions relevant to the present work are presented in Table 2.7.2. For three redox couples, the results were sequential (Schreiber et al. 1987).

Table 2.7.2. Mutual interactions of redox couples via electron exchange (Schreiber et al. 1987).

Reactants		*ΔE**	Degree of Mutual Interaction
Mn^{3+}	Fe^{2+}	2.5	To completion
Fe^{3+}	Cr^{2+}	1.7	Near completion
Ce^{4+}	Fe^{2+}	1.6	Near completion
Mn^{3+}	Ce^{3+}	0.9	Small degree of interaction
Ce^{4+}	Cr^{3+}	0.0	Equally likely in either direction, or none at all

Schreiber's work continues to provide a basis for exploration of mixed multivalent species redox reactions in complex glass compositions. In nuclear waste vitrification, Goldman examined redox control during vitrification of high-level radioactive wastes at the Hanford site (Goldman 1985), using the premise that the redox ratio of iron, Fe^{3+}/Fe_T, could be used to indicate the glass oxidation state, and how the redox state influenced the foam stability (Goldman 1986). Cassingham et al. used Schreiber's understanding of mutual redox reactions to explain preferential oxidation of Fe^{2+} by Ce^{4+} present in the melt (Cassingham et al. 2008), and two studies have used the relationships to explain the oxidation of Cr^{3+} by SO_4^{2-} and the implications for sulphate immobilisation (Kaushik et al. 2004; Manara et al. 2007). Mutual interactions of Fe, S and Cr have been investigated in a high-alumina HLW feed, in relation to their O_2 evolution and foaming behaviour (Lee, Hrma, Kloužek, et al. 2017). The electron equivalents model for further Hanford HLW feeds was developed based on Schreiber's principles, explaining the redox controlling reactions that occur between formate salts and nitrate salts in the cold cap (Jantzen et al. 2003). A predictive model for the redox state of the nuclear waste glasses containing iron, cerium, chromium, manganese, nickel and ruthenium has more recently been developed based on estimations of the oxygen partial pressure which predicted the redox state reasonably well for both single multivalent oxides and mixtures of multivalent oxides (Pinet et al. 2008).

2.8 Redox control during vitrification

In nuclear waste feeds both oxidising agents such as nitrates and reducing agents such as organic compounds are present, leading to both evolution and consumption of O_2. Schreiber describes how the presence of carbon dioxide, water and sulphur dioxide gases, and dissolution into the melt can change the redox equilibrium through the uptake of oxide ions, forming more reduced species (Schreiber 1986). However, the reverse of these reactions is also possibly true in the production of CO_2 and SO_2 gases from dissolved sulphates and carbonates in the melt, which leaves O_2 in the melt to oxidise species (Schreiber 1986).

In order to reduce foaming, carbon has been added as a foam reductant in the form of sucrose or formic acid in nuclear waste treatment plants (Hrma et al. 2010; Bibler and Fellinger 2001; Henager et al. 2011; P. A. Smith, Vienna, and Hrma 1995; Matlack, Joseph, et al. 2009; Bickford, Hrma, and Bowan 1990), by reducing the nitrates at low temperatures and therefore reducing primary foam. Sucrose has been studied in high-nitrate LAW feeds for the Hanford Site (Soderquist et al. 2014; Hrma et al. 2010; Appel et al. 2019; Kruger et al. 2013), and is the baseline reductant selected for all feeds with foaming issues at the WTPs (Matlack, Muller, et al. 2011). Studies of the effect of reductants on HLW feeds are much less prevalent as many of the feeds do not generally contain high nitrate concentrations that contribute to the more prominent primary foaming (Matlack et al. 2007; Henager et al. 2011). Caution must be taken not to over-reduce the melt which could cause precipitation of crystalline and metallic species (Bingham et al. 2011; Appel et al. 2019); metallic species are particularly detrimental to the melter lifetime and crystalline phases can reduce the quality of the final glass product (Matlack, Joseph, et al. 2009).

2.8.1 Effect of reducing agents

The use of carbonaceous materials during vitrification of radioactive waste dates back to the 1970s (Bickford and Diemer Jr 1986; Goldman 1986; Drobnik 1972; Ross 1978; Blair 1976; Straub 1973), and in the industrial glass melting industry, their use is reported back to earlier 20th Century (Adams 1942; Cable 2005; Silverman 1932; Fuwa 1936). A patent filed in 1942 describes the "common practice" of throwing organic matter such as "potatoes, apples, coal, charcoal or the like" into melts to "liberate large volumes of gases" (Adams 1942). A later patent filed in 1991 referred to the earlier method as an "erratic technique" that is "not considered suitable for a large scale, continuous, glass melting operation" (Knavish and Harrell 1991). This patent describes the need for a reducing agent that does not dissociate before it is necessary, "i.e. after the initial melting of the batch materials, as the melt enters the zone of peak temperature" in order to reduce the amount of reducing agent needed (Knavish and Harrell 1991). Some forms of carbon reducing agents dissociate as soon as they are exposed to the heat of the furnace, the continual introduction of the reducing agent to the melt is suggested so as to shift the redox conditions in the high-temperature region (Knavish and Harrell 1991).

Addition of carbon to a glass batch is likely to increase the volume of gas released overall, however, there are benefits to promoting gas release earlier in the glass melting process (Ryan 1995). When investigating secondary foaming, Fedorov et al. (2002) suggested that carbon addition to the batch could reduce secondary foaming while promoting primary foaming (Fedorov and Pilon 2002).

Different forms of carbon have been studied for their effectiveness in reducing glass foams, such as: powdered anthracite coal (Muschik et al. 2005), fine coke particles (Vernerová, Kloužek, and Němec 2015), spraying oil, natural gas or other combustible materials (Fedorov and Pilon 2002), pulsing CO into the atmosphere or through the melt

(Fedorov and Pilon 2002; Adams 1942). Petroleum coke and powdered graphite are reported to be the most effective additions in controlled foaming the slag in the steelmaking process compared to other forms of carbon (Sahajwalla et al. 2006).

2.8.2 Reductant Selection

In the early evaluation of different reductants on the Hanford waste glasses, particularly using carboxylic acids, the effect on redox behaviour of mixed multivalent species feeds was not well understood, and Seymour, 1995, suggested that fine tuning of the interrelationship of the complex redox chemistry of the cold cap and melt pool should be pursued (Seymour 1995). Requirements to be considered when selecting an appropriate reductant include low cost, low toxicity, minimal effects on the quality of the final glass product and ease of handling (Ryan 1995). Care must be taken when formaldehyde, formic acid or sugar are applied to avoid violent chemical reactions (Appel et al. 2019; International Atomic Energy Agency 1992). The temperature of foaming is important when choosing a suitable reductant; if primary foaming is the dominant foam mechanism, and it collapses < 850 °C, early CO_2 release and denitration are sufficient for reducing foaming (Bickford, Hrma, and Bowan 1990), which has been demonstrated by the addition of sucrose (Henager et al. 2011; Hrma, Marcial, et al. 2011; Hrma et al. 2010; Appel et al. 2019). Reduction of O_2 and SO_2 evolution at higher temperatures may require alternative reductants based on the temperature at which each redox reaction becomes energetically favourable (Kruger et al. 2013; Ryan 1995; Seymour 1995).

In a 1995 review of the effects of raw materials and reducing agents on the redox and foaming behaviour in generic Hanford Tank waste (Ryan 1995), reductants such as semi-metallic elements, carbon in the form of coke, coal or graphite, and other organic compounds are discussed (Ryan 1995). A summary of the properties of some of the carbon-based reductants is provided in Table 2.8.1.

Table 2.8.1. Properties of some carbonaceous reducing agents for waste glass melting, reproduced from (Ryan 1995).

Compound	Average Carbon Oxidation State	Reducing Equivalents mol^{-1}	Reducing Equivalents g^{-1} of Compound
Oxalic Acid	3.00	2	0.0222
Formic Acid	2.00	2	0.0435
Glyoxylic Acid	2.00	2	0.0541
Tartaric Acid	1.5	10	0.0667
Malonic Acid	1.33	8	0.0769
Glycolic Acid	1.00	6	0.0789
Pyruvic Acid	0.67	10	0.114
Acetic Acid	0.00	8	0.133
Sucrose	0.00	44	0.129
Graphite	0.00	4	0.333
Propionic Acid	-0.67	14	0.212
Polyethylene	-2.00		0.429
HEDTA*	0.20	38**	0.139

* N'(-2 hydroxyethyl) ethylenediamine-NNN' triacetic acid.
** Based on the assumption that the nitrogen atoms present do not change oxidation state and in doing so also act as reductants.

Sucrose has the highest reducing equivalent per mole from the potential reductant sources in Table 2.8.1, however, per gramme of substance acetic acid, graphite, propionic acid, N'(-2 hydroxyethyl) ethylenediamine-NNN' triacetic acid (HEDTA) and polyethylene are more effective. The effect of sucrose on the reduction of nitrates in LAW feeds has been shown on multiple occasions (Appel et al. 2019; Muller et al. 2009; Hujová, Pokorný, et al. 2018; Hrma, Pokorný, et al. 2011), however, the iron redox ratio, Fe^{3+}/Fe_T, has rarely been provided for these compositions. Goldman (Goldman 1986) described the link between sucrose addition, foam stability and Fe redox state in a large compositional range of nuclear waste glass melts at 1150 °C. Above ~90 g L^{-1} sucrose addition to the melts, the foam became unstable and the proportion Fe^{2+} increased from $Fe^{2+}/Fe^{3+} < 0.2$ up to 0.8-1.0, summarising that foam generated under reducing melt conditions is unstable (Goldman 1986).

One study showed an small increase in Fe^{2+} content throughout melting with sucrose addition to a LAW AZ-102 feed compared to a baseline sample, with a larger difference

at 900 °C, however, the feed also contained Fe^{2+} iron oxalate ($FeC_2O_4 \cdot 2H_2O$) instead of Fe_2O_3 as the iron source, which renders the effect of sucrose difficult to interpret (George, Kim, and Kruger 2020). A DM100 melter report shows a variation of <1–78 % Fe^{2+} concentration with different stoichiometric carbon ratios from 0.5 – 1.25 (0.5 = 1 mole sucrose per 16 mole NO_x) in a simulant LAWA44 waste glass (Kruger et al. 2013), other reports have also shown extreme reduction in Fe at high C/N ratios (Matlack, Gong, and Pegg 2003; Matlack et al. 2001, 2000). The use of sucrose in LAW feeds high in nitrates has been proven effective across a wide envelope of feeds (Matlack et al. 2006; Muller et al. 2009; Hrma, Pokorný, et al. 2011; Appel et al. 2019). Its use in HLW feeds is nominally based on the same conditions as LAW feeds, 1.5 moles of organic carbon per mole of nitrate (Matlack, Gan, et al. 2009). As discussed in section, 2.6.5., there is a need for updated algorithms to support redox control in HLW streams (Kruger, Matlack, Pegg, et al. 2012; Matlack, Kruger, et al. 2011) as the mechanism of foam production is not the same as in LAW feeds.

Formic acid is a common reductant due to its influence on foam rheology as well as reducing ability (Ryan 1995; Bickford, Hrma, and Bowan 1990; Seymour 1995). Its effectiveness in reducing the iron redox ratio of feeds and early elimination of nitrate was reported at the DWPF (Bickford, Hrma, and Bowan 1990). One study observed that the low-temperature decomposition of formic acid, 100 – 400 °C precludes efficient high-temperature reduction of multivalent species (P. A. Smith, Vienna, and Merz 1996), however, other studies have shown a significant effect on ferrous iron content, up to $Fe^{3+}/Fe_T = 0$ at 3.1 $g.mol.lb^{-1}$ of dried sludge solids (Bickford and Diemer Jr 1986), and $Fe^{3+}/Fe_T \sim 0.4$ for a ratio of formic acid/NO_3 of 7 to 11 (Weimers 1998).

N'(-2 hydroxyethyl) ethylenediamine-NNN' triacetic acid (HEDTA) has been found in some of the Hanford waste tanks (Kruger et al. 2013; Matlack, Gong, and Pegg 2003; Kelly 2011; Agnew 1997). Thus far, the effects of HEDTA addition on the redox state

of glasses has not been explored in the literature, beyond the suggestion of its use in reduction of oxidising species in glass melting in 1995 (Ryan 1995). Where HEDTA is in waste Hanford streams, studies on these feeds have also included sucrose additions, so the specific redox reactions involving HEDTA are not discernible (Kruger, Matlack, Gong, et al. 2012; Matlack, Gong, and Pegg 2003; Matlack et al. 2006).

Graphite is a common reductant in slag furnaces (Shibata, Egawa, and Nakamura 2002; Yu et al. 2014). Additions of graphite powder to glass batches or melts are scarce, however, a few studies report its use in controlled precipitation of metallic particles from glass (Jiménez 2016), and immobilisation of graphite wastes (Mayzan et al. 2014). Two studies on waste glasses report oxidation of the graphite by Fe reduction (Bickford, Hrma, and Bowan 1990), reduction of partial pressure in the melt, earlier sulphate decomposition and increased rate of silica dissolution (Matyáš and Hrma 2005).

The use of coke addition in redox control of nuclear waste vitrification has been suggested (Pinet, Hugon, and Mure 2014; D'agostini and Horan 2018), based on the studies of reducing effects at high temperature, effecting the SO_2 redox state and consequent retention/evolution (D'agostini and Horan 2018; Beerkens 1999; Ryan 1995). No studies have been found to report the redox ratio of Fe in glasses with coke additions. The 1995 report suggested that hypothetically coke could have a greater affect than some reductants at higher temperatures, above the temperatures of glass-forming and foaming (Ryan 1995). Given that coke is a common waste product from other industries, the use of it in glass melting could have multiple benefits (Devasahayam et al. 2019; Nemanova et al. 2014; Babich and Senk 2018) and indeed coke is a widely-used raw material in the manufacture of amber container glass, for example (Reiner and Schaeffer 1987; Beerkens 1999; Simpson and Myers 1978).

2.9 References

Abboud, A. W. and Guillen, D. P. (2016) 'Computational fluid dynamics modeling of bubbling in a viscous fluid for validation of waste glass melter modeling', International Topical Meeting on Advances in Thermal Hydraulics 2016, ATH 2016, pp. 527–538.

Abboud, A. W., Post Guillen, D. and Pokorný, R. (2016) 'Heat Transfer Model of a Small-Scale Waste Glass Melter with Cold Cap Layer', in 11th International Topical Meeting on Nuclear Thermal Hydraulics, Operation and Safety. (NURETH-11), Avignon (France).

Achigar, Sophie, Caurant, D. Régnier, E. and Majérus, O. (2021) 'Dismantling Nuclear Waste Rich in P_2O_5, MoO_3 and ZrO_2: How Do These Oxides Incorporate in Aluminoborosilicate Glasses?' Journal of Nuclear Materials 544(152731).

Adamantiades, A. and Kessides, I. (2009) 'Nuclear power for sustainable development: Current status and future prospects.' Energy Policy. 37(12), pp. 5149–5166.

Adams, F. W. (1942) 'Fining of Glass.' United States: United States Patent Office: US2274643.

Agnew, S. F. (1997) 'Hanford Tank Chemical and Radionuclide Inventories: HDW Model Rev. 4.' LA-UR-96-3860. Los Alamos, NM (United States).

Ahmadzadeh, M., Scrimshire, A., Bingham, P. A. and Goel, A. (2018) 'Structural Role of Iron in Nepheline-based Aluminosilicates for Nuclear Waste Applications.' WM2018 Conference. Phoenix, AZ (United States).

Alderman, O. (2018) 'Borate Melt Structure: A Short Review.' Physics and Chemistry of Glasses: European Journal of Glass Science and Technology Part B. 59(1), pp. 1–10.

Alderman, O. L. G., Wilding, M. C., Tamalonis, A., Sendelbach, S., Heald, S. M., Benmore, C. J., Johnson, C. E., Johnson, J. A., Hah, H. Y. and Weber, J. K. R.

(2017) ‘Iron K-edge X-ray absorption near-edge structure spectroscopy of aerodynamically levitated silicate melts and glasses.’ Chemical Geology, 453, pp. 169–185.

Aloy, A. S. (2011) ‘Calcination and vitrification processes for conditioning of radioactive wastes.’ in ‘Handbook of Advanced Radioactive Waste Conditioning Technologies,’ Chapter 5. Cambridge (UK): Woodhead Publishing Limited.

Angeli, F., Villain, O., Schuller, S., Charpentier, T., De Ligny, D., Bressel, L. and Wondraczek, L. (2012) ‘Effect of temperature and thermal history on borosilicate glass structure.’ Physical Review B - Condensed Matter and Materials Physics, 85(5), pp. 1–15.

Angermann, A. and Töpfer, J. (2008) ‘Synthesis of Magnetite Nanoparticles by Thermal Decomposition of Ferrous Oxalate Dihydrate.’ Journal of Materials Science, 43 (15), pp. 5123–30.

Alton, J., Plaisted, T. J. and Hrma, P. (2002) ‘Dissolution and growth of spinel crystals in a borosilicate glass’, Journal of Non-Crystalline Solids, 311(1), pp. 24–35.

Appel, C. J., Kloužek, J., Jani, N. Lee, S., Dixon, D. R., Hrma, P., Pokorný R., Kruger A. A. and Schweiger, M. J. (2019) ‘Effect of sucrose on foaming and melting behavior of a low-activity waste melter feed.’ Journal of the American Ceramic Society, 102(12), pp. 7594–7605.

Arboleda, J. D. Arnache, O. Aguirre, M. H. Ramos, R. Anadón, A. Ibarra, M. R. (2018) ‘Evidence of the spin Seebeck effect in Ni-Zn ferrites polycrystalline slabs.’ Solid State Commun. 270, 140–146.

ASTM. (2015) ‘Standard Terminology of Glass and Glass Products.’ C162-05. United States. https://compass.astm.org/document/?contentCode=ASTM%7CC0162-05R15%7Cen-US (Accessed 05 September 2022).

ASM International (2004) Glossary of Terms. In Vander Voort, G. F. (ed) 'ASM Handbook: Metallography and Microstructures.' Vol. 9. ASM International ®.

Ashby, M. F. and Greer, A. L. (2006) 'Metallic glasses as structural materials.' Scripta Materialia, 54(3), pp. 321–326.

Avramov, I., Vassilev, T. and Penkov, I. (2005) 'The glass transition temperature of silicate and borate glasses.' Journal of Non-Crystalline Solids, 351, pp. 472–476.

Babich, A. and Senk, D. (2018) 'Coke in the iron and steel industry', in Suárez-Ruiz, I., Diez, M. A., and Rubiera, F. (eds) 'New Trends in Coal Conversion: Combustion, Gasification, Emissions, and Coking.' 1st ed. Duxford, UK: Elsevier, pp. 367–404.

Barth, S. and Feltz, A. (1989) 'Structure and ionic conduction in solids. VII. Ion conducting glasses in the system $Na_2ONb_2O_5P_2O_5$.' Solid State Ion. 34, 41–45.

Beerkens, R. (1999) 'Redox and sulphur reactions in glass melting processes.' Ceramics - Silikaty, 43(3), pp. 123–131.

Belton, D. J., Deschaume, O. and Perry, C. C. (2012) 'An overview of the fundamentals of the chemistry of silica with relevance to biosilicification and technological advances.' FEBS Journal, 279(10), pp. 1710–1720.

Benedict, M., Pigford, T. H. and Levi, H. W. (1981) 'Nuclear Chemical Engineering.' 2nd edn. Heiberg, D. D. (Ed.) New York, NY (United States): McGraw-Hill Book Company.

Bengisu, M. (2016) 'Borate glasses for scientific and industrial applications: a review.' Journal of Materials Science, 51(5), pp. 2199–2242.

Bernards, J. K., Hersi, G. A., Hohl, T. M., Jasper, R. T., Mahoney, P. D., Pak, N. K., Reaksecker, S. D., Schubick, A. J., West, E. B., Bergmann, L. M., Golcar, G. R., Praga, A. N., Tilanus, S. N. and Crawford, T. W. (2020) 'River Protection Project System Plan: Safely, Effectively and Efficiently Treat Tank Waste and

Close Hanford Tanks ORP-11242 Rev. 9.' U.S. Department of Energy, Office of River Protection. Richland, WA (United States).

Berry, A. J. and O'Neill, H. S. C. (2004) 'A XANES determination of the oxidation state of chromium in silicate glasses.' American Mineralogist, 89(5–6), pp. 790–798.

Biagioni, C, and Pasero. M. (2014) 'The Systematics of the Spinel-Type Minerals: An Overview.' American Mineralogist 99 (7): 1254–64.

Bibler, N. E., Fellinger, T. L., Marra, S. L., O'Driscoll, R. J., Ray, J. W. and Boyce, W. T. (2000) 'Tc-99 and Cs-137 volatility from the DWPF production melter during vitrification of the first macrobatch of HLW sludge at the Savannah River Site', in Materials Research Society Symposium - Proceedings. Aiken, SC (United States), pp. 697–702.

Bibler, N. E. and Fellinger, T. L. (2001) 'DWPF Vitrification - Characterisation of the radioactive glass being produced during immobilization of the second batch of HLW sludge', in WM2001 Conference. Tuscon, AZ (United States).

Bickford, D. F. and Diemer Jr, R. B. (1986) 'Redox control of electric melters with complex feed compositions I. Analytical methods and models.' Journal of Non-Crystalline Solids, 84, pp. 276–284.

Bickford, D. F., Hrma, P. and Bowan, B. W. (1990) 'Control of Radioactive Waste Glass Melters: II, Residence Time and Melt Rate Limitations.' Journal of the American Ceramic Society, 73(10), pp. 2903–2915.

Bickford, D. F. and Jantzen, C. M. (1986) 'Devitrification of defense nuclear waste glasses: Role of melt insolubles.' Journal of Non-Crystalline Solids, 84(1–3), pp. 299–307.

Bingham, P. A. Connelly, A. J., Hyatt, N. C. and Hand, R. J. (2011) 'Corrosion of glass contact refractories for the vitrification of radioactive wastes: a review.' International Materials Reviews, 56(4), pp. 226–242.

Blair, H. T. (1976) 'Vitrification of Nuclear Waste Calcines by In-Can Melting.' BNWL-2061. Battelle-Northwest, Pacific Northwest National Laboratories, Richland, WA (United States).

Blowers, A. and Sundqvist, G. (2010) 'Radioactive waste management - technocratic dominance in an age of participation.' Journal of Integrative Environmental Sciences, 7(3), pp. 149–155.

Bødker, M. S., Mauro, J. C., Youngman, R. E. and Smedskjaer, M. M. (2019) 'Statistical Mechanical Modeling of Borate Glass Structure and Topology: Prediction of Superstructural Units and Glass Transition Temperature.' Journal of Physical Chemistry B 123 (5). pp. 1206–13.

Borisov, A. A. (2016) 'Mutual interaction of redox pairs in silicate melts: Equilibria involving metallic phases', Petrology, 24(2), pp. 117–126.

Boscarino, J. E. (2019) 'From Three Mile Island to Fukushima: the impact of analogy on attitudes toward nuclear power.' Policy Sciences, 52(1), pp. 21–42.

Bragg, W. (2002) 'The Glassy State', in Rao, K. J. (ed.) 'Structural Chemistry of Glasses.' Oxford, (UK): Elsevier Science Ltd.

Brawer, S. A. and White, W. B. (1975) 'Raman spectroscopic investigation of the structure of silicate glasses. I. The binary alkali silicates. The Journal of Chemical Physics, 63(6), pp. 2421–2432.

Bricker, J. M., Fellinger, T. L., Staub, A. V., Smith, M. E. and Iaukea, J. F. (2012) 'Control of the Reduction/Oxidation State of the High Level Waste Form in the Defense Waste Processing Facility at the Savanah River Site - 12451', in WM2012 Conference. Phoenix, AZ (United States).

Brown, I. W. M. (1982) ‘A Mössbauer Study of Hematite Dissolution and Devitrification in Float Glass.’ Journal of Non-Crystalline Solids, 50 (2). pp. 233-252.

Brückner, R. (1985) ‘Redox Ratio Shifts and Electrical Transport Properties in Redox Pairs Containing Glasses.’ Journal of Non-Crystalline Solids, 71, pp. 49–57.

Cable, M. (2005) ‘A Century of Developments in Glassmelting Research.’ Journal of the American Ceramic Society, 81(5), pp. 1083–1094.

Carles, V., Alphonse, P., Tailhades, P. and Rousset, A. (1999) ‘Study of thermal decomposition of $FeC_2O_4.2H_2O$ under hydrogen.’ Thermochimica Acta, 334(1–2), pp. 107–113.

Cassingham, N. J., Bingham, P. A., Hand, R. J. and Forder, S. D. (2008) ‘Property modification of a high level nuclear waste borosilicate glass through the addition of Fe_2O_3.’ Glass Technology: European Journal of Glass Science and Technology Part A, 49 (1), 21–26, 49(1), pp. 21–26.

Caurant, D., Loiseau, P., Majerus, O., Aubin-Chevaldonnet, V., Bardez, I. and Quintas, A. (2009) ‘Glasses, Glass-Ceramics and Ceramics for Immobilization of Highly Radioactive Nuclear Wastes.’ New York (United States): Nova Science Publishers, Inc.

Ceglia, A., Nuyts, G., Meulebroeck, W., Cagno, S., Silvestri, A., Zoleo, A., Nys, K., Janssens, K., Thienpont, H. and Terryn, H. (2015) ‘Iron speciation in soda-lime-silica glass: a comparison of XANES and UV-vis-NIR spectroscopy.’ Journal of Analytical Atomic Spectrometry, 30(7), pp. 1552–1561.

Chekhmir, A., Gribetz, A. and Shore, L. (2011) ‘A New Approach to Glass Formulation Generates Improved Waste Loadings for Hanford HLW/LAW and Savannah River Site HLW - 11093’, in WM2011 Conference. Phoenix, AZ (United States).

Chemarin, C. and Champagnon, B. (1999) ‘Medium range order in sodium silicate glasses: Role of the network modifier.’ Journal of Non-Crystalline Solids, 243, pp. 281–284.

Chinnam, R. K., Francis, A. A., Will, J., Bernardo, E. and Boccaccini, A. R. (2013) ‘Review. Functional glasses and glass-ceramics derived from iron rich waste and combination of industrial residues.’ Journal of Non-Crystalline Solids, 365, pp. 63–74.

Choi, A. S., Miller, D. H., Immel, D. M. and Smith, F. G. (2017) ‘Investigation of high-level waste glass melting using X-ray computed tomography.’ International Journal of Applied Glass Science, 8(2), pp. 165–176.

Chun, J., Pierce, D. A., Pokorný, R., Hrma, P. (2013) ‘Cold-cap reactions in vitrification of nuclear waste glass: Experiments and modelling.’ Thermochimica Acta, 559, pp. 32–39.

Cochain, B., Neuville, D. R., Henderson, G. S., McCammon, C. A., Pinet, O. and Richet, P. (2012) ‘Effects of the iron content and redox state on the structure of sodium borosilicate glasses: A Raman, Mössbauer and boron K-edge XANES spectroscopy study.’ Journal of the American Ceramic Society, 95(3), pp. 962–971.

Cochain, B. and Neuville, D. R. (2008) ‘Determination of iron redox ratio in borosilicate glasses and melts from Raman spectra’, in Atalante, Montpellier (France).

Colburn, H. A. and Peterson, R. A. (2021) ‘A history of Hanford tank waste, implications for waste treatment, and disposal.’ Environmental Progress and Sustainable Energy, 40(1). pp. 1-12.

Colton, N. G., Orth, R. J. and Aitken, E. A. (1993) ‘Tank Waste Processing Analysis: Database Development, Tank-by-Tank Processing Requirements, and Examples

of Pretreatment Sequences and Schedules as Applied to Hanford Double-shell Tank Supernatant Waste - FY 1993.' PNL-10134. Pacific Northwest National Laboratory, Richland, WA (United States).

Corkhill, C. L. and Hyatt, N. C. (2018) 'Nuclear Waste Management.' Bristol (UK): IOP Publishing Ltd 2018.

Crum, J., Maio, V., McCloy, J., Scott, C., Riley, B., Benefiel, B., Vienna, J. D., Archibald, K., Rodriguez, C., Rutledge, V., Zhu, Z., Ryan, J. and Olszta, M. (2014) 'Cold crucible induction melter studies for making glass ceramic waste forms: A feasibility assessment. Journal of Nuclear Materials.' Elsevier B.V., 444(1–3), pp. 481–492.

Cunnane, J. C., Bates, J. K., Bradley, C. R., Buck, E. C., Ebert, W. L., Feng, X., Mazer, J. J., Wronkiewicz, D. J., Sproull, J., Bourcier, W. L., McGrail, B. P. and Altenhofen, M. K. (1994) 'High Level Waste Borosilicate Glass: A Compendium of Corrosion Characteristics Volume 2' Office of Waste Management, United States Department of Energy. Argonne National Laboratory, IL (United States).

D'agostini, M. D. and Horan, B. (2018) 'Optimization of energy efficiency, glass quality and NO_x emissions in oxy-fuel glass furnaces through advanced oxygen staging.' Ceramic Transactions, 267, pp. 101–115.

Dell, W. J., Bray, P. J. and Xiao, S. Z. (1983) '^{11}B NMR Studies and Structural Modeling of $Na_2OB_2O_3SiO_2$ Glasses of High Soda Content.' Journal of Non-Crystalline Solids 58 (1). pp. 1–16.

Devasahayam, S., Singh Raman, R. K., Chennakesavulu, K. and Bhattacharya, S. (2019) 'Plastics–Villain or hero? Polymers and recycled polymers in mineral and metallurgical processing–A review.' Materials, 12(4). 1–36.

Dey, P. K. and Bansal, N. K. (2006) ‘Spent fuel reprocessing: A vital link in Indian nuclear power program.’ Nuclear Engineering and Design, 236(7–8), pp. 723–729.

Dézsi, I., Szucs, I. and Sváb, E. (2000) ‘Mossbauer spectroscopy of spinels.’ Journal of Radioanalytical and Nuclear Chemistry, 246(1), pp. 15–19.

Dixon, D. R., Schweiger, M. J., Riley, B. J., Pokorný, R. and Hrma, P. (2015) ‘Cold-Cap Temperature Profile Comparison between the Laboratory and Mathematical Model’, in WM2015 Conference. Phoenix, AZ (United States).

Dixon, D. R., Schweiger, M. J., Riley, Brian J., Pokorný, R. and Hrma, P. (2015) ‘Temperature Distribution within a Cold Cap during Nuclear Waste Vitrification.’ Environmental Science and Technology, 49(14), pp. 8856–8863.

Dobson, A. J. and Phillips, C. (2006) ‘High Level Waste Processing in the U.K.–Hard Won Experience that can Benefit U.S. Nuclear Cleanup Work.’ WM2006 Conference, Tucson, AZ (United States).

Doi, Y. Yano, T. McCarthy, B. P. Schweiger, M. J. and Hrma. P. (2019) ‘Effects of Particle Size and Briquetting of Soda-Lime-Silicate Glass Batch on Viscosity during Batch-to-Melt Conversion.’ International Journal of Applied Glass Science, 10 (1), pp. 115-24.

Donald, I. W. (1997) ‘Review: The immobilization of high level radioactive wastes using ceramics and glasses.’ Journal of Materials Science, 32(22), pp. 5851–5887.

Donald, I. W. (2015) ‘Waste immobilisation in glass and ceramic based hosts.’ West Sussex, (UK): John Wiley & Sons, Ltd.

Donald, S. B., Swink, A. M. and Schreiber, H. D. (2006) ‘High-iron ferric glass.’ Journal of Non-Crystalline Solids, 352 (6-7), pp. 539–543.

Doweidar, H. (1990) ‘Consideration of the boron oxide anomaly.’ Journal of Materials Science, 25(1), pp. 253–258.

Drobnik, S. (1991) ‘Method of removing nitric acid, nitrate ions and nitrite ions out of aqueous waste solutions.’ United States: United States Patent Office: US3,673,086

Duffy, J. A. (1996) ‘Optical Basicity: A Practical Acid-Base Theory for Oxides and Oxyanions.’ Journal of Chemical Education 73 (12). pp. 1138–42.

Duffy, J. A. and Ingram, M. D. (1976) ‘An Interpretation of Glass Chemistry in Terms of The.’ Journal of Non-Crystalline Solids 21. pp. 373–410.

Edgemon, G. L. Anda, V. S., Berman, H. S., Johnson, M. E. and Boomer, K. D. (2009) ‘History and Operation of the Hanford High-Level Waste Storage Tanks.’ Corrosion in Nuclear Waste Systems, 65(3), pp. 163–174.

Ehrt, D. (2000) ‘Structure, properties and applications of borate glasses.’ Glass Technology, 41(6), pp. 182–185.

Ewing, R. C., Weber, W. J. and Clinard, F. W. (1995) ‘Radiation effects in nuclear waste forms for high-level radioactive waste.’ Progress in Nuclear Energy, 29(2), pp. 63–127.

Farges, F., Rossano, S., Lefrère, Y., Wilke, M. and Brown, G. E. (2005) ‘Iron in silicate glasses: A systematic analysis of pre-edge, XANES and EXAFS features.’ Physica Scripta T, T115, pp. 957–959.

Fedorov, A. G. and Pilon, L. (2002) ‘Glass foams: Formation, transport properties, and heat, mass, and radiation transfer.’ Journal of Non-Crystalline Solids, 311(2), pp. 154–173.

Freeman, C. J. (1996) ‘Melt Rate Predictions for Slurry-Fed Glass Melters.’ PNNL-11012. Pacific Northwest National Laboratory. Richland, WA (United States).

Fuwa, K. (1936) ‘Glasses Containing Iron Oxide.’ Dainippon Ceramics Association Magazine 44(521), pp. 297–306.

Gan, H., Viragh, C., McKeown, D. A., Muller, I. S., Cecil, R., Kot, Wing K., Joseph, I., Wang, C., Pegg, I. L., Chaudhuri, M., Zhao, W. and Feng, Z. (2009) 'Crystal Settling, Redox, and High Temperature Properties of ORP HLW and LAW Glasses.' VSL-09R1510-1. Vitreous State Laboratory, Washington, D. C. (United States).

Geeting, J. G. H., and Kurath, D. E. (1993) 'Preliminary Assessment of Blending Hanford Tank Wastes.' PNL-8589. Pacific Northwest National Laboratory. Richland, WA (United States).

George, J. L., Kim, D. -S and Kruger, A. A. (2020) 'Effects of iron oxalate on rhenium incorporation into low-activity waste glass.' Journal of Non-Crystalline Solids. Elsevier, 545(June), p. 120257.

Gephart, R. E. (2003) 'A Short History of Hanford Waste Generation, Storage, and Release.' PNNL-13605. Pacific Northwest National Laboratory. Richland, WA (United States).

Gephart, R. E. (2010) 'A short history of waste management at the Hanford Site.' Physics and Chemistry of the Earth. Elsevier Ltd, 35(6–8), pp. 298–306.

Gerber, M. S. (1996) 'Plutonium production story at the Hanford site: processes and facilities history.' WHC-MR-0521. Westinghouse Hanford Company, Richland, WA (United States).

Gervasio, V., Kim, D. S., Vienna, J. D., and Kruger, A. A. (2018) 'Impacts of Process and Prediction Uncertainties on Projected Hanford Waste Glass Amount.' PNNL-26996. Pacific Northwest National Laboratory. Richland, WA (United States).

Gin, S. Abdelouas, A., Criscenti, L. J., Ebert, W. L., Ferrand, K., Geisler, T., Harrison, M. T., Inagaki, Y., Mitsui, S., Mueller, K. T., Marra, J. C., Pantano, C. G., Pierce, E. M., Ryan, J. V., Schofield, J. M., Steefel, C. I. and Vienna, J. D. (2013) 'An

international initiative on long-term behavior of high-level nuclear waste glass.' Materials Today. Elsevier Ltd., 16(6), pp. 243–248.

Glass for Europe (2006) 'The status of Flat Soda Lime Silicate Glass and its raw materials under REACH (Regulation (EC) No 1907 /2006).' Brussels (Belgium).

Glazkova, Y. S., Kalmykov, S. N., Presnyakov, I. A., Stefanovskaya, O. I. and Stefanovsky, S. V. (2015) 'The structural state of iron in multicomponent aluminum iron borosilicate glass depending on their composition and synthesis conditions.' Glass Physics and Chemistry, 41(4), pp. 367–377.

Goel, A., McCloy, J. S., Pokorný, R. and Kruger, A. A. (2019) 'Challenges with Vitrification of Hanford High-Level Waste (HLW) to Borosilicate Glass – An Overview.' Journal of Non-Crystalline Solids: X, 4: 100033.

Goldman, D. S. (1985) 'Investigation of Potential Analytical Methods for Redox Control of the Vitrification Process' PNL-5581. Pacific Northwest National Laboratory, Richland, WA (United States).

Goldman, D. S. (1986) 'Melt foaming, foam stability and redox in nuclear waste vitrification.' Journal of Non-Crystalline Solids, 84(1–3), pp. 292–298.

Gosling, F. G. (1999) 'The Manhattan Project: Making the Atomic Bomb.' Darby, PA: DIANE Publishing Co.

Greaves, G. N., Binsted, N. and Henderson, C. M. B. (1984) 'The Environments of Modifiers in Oxide Glasses', EXAFS and Near Edge Structure III. Springer Proceedings in Physics., 2, pp. 297–301.

Groves, L. R. (1983) 'Now It Can Be Told: The Story of the Manhattan Project.' New Ed. Boston, MA: Da Capo Press.

Guillen, D. P. (2015) 'Bubbling behavior in a waste glass melter', in 8th International Conference on Computational and Experimental Methods in Multiphase Flow. Valencia (Spain).

Guillen, D. P. Lee, S., Hrma, P., Traverso, J., Pokorny, R., Kloužek, J. and Kruger, A. A. (2020) 'Evolution of chromium, manganese and iron oxidation state during conversion of nuclear waste melter feed to molten glass', Journal of Non-Crystalline Solids. Elsevier, 531(December 2019), p. 119860.

Guillen, D. P., Abboud, A. W. and Pokorný, R. (2019) 'Computational experiments to characterize bubble formation and movement in waste glass foam layer.' INL/CON-18-52050-Rev-0. Idaho National Laboratory. Idaho Falls, ID. (United States).

Guillen, D. P., Pokorný, R., Eaton, W. C., Dixon, D. R., Fox, K. and Kruger, A. A. (2018) 'Development of a Validation Approach for an Integrated Waste Glass Melter Model', Nuclear Technology. Taylor & Francis, 203(3), pp. 244–260.

Guillen, D. P. and Agarwal, V. (2013) 'Incorporating Cold Cap Behavior in a Joule-heated Waste Glass Melter Model.' INL/EXT-13-29794. Idaho National Laboratory. Idaho Falls, ID. (United States).

Hannon, A. C., Vessal, B. and Parker, J. M. (1992) 'The structure of alkali silicate glasses', Journal of Non-Crystalline Solids, 150(1–3), pp. 97–102.

Harris, W. H., Guillen, D. P., Kloužek, J., Pokorný, R., Yano, T., Lee, S., Schweiger, M. J. and Hrma, P. (2017) 'X-ray tomography of feed-to-glass transition of simulated borosilicate waste glasses', Journal of the American Ceramic Society, 100(9), pp. 3883–3894.

Harrison, M. T. and Brown, G. C. (2018) 'Chemical durability of UK vitrified high level waste in Si-saturated solutions', Materials Letters, 221, pp. 154–156.

Harvey, D. (2000) 'History of the Hanford Site, Pacific Northwest National Laboratory.' G. O'Connor. (Ed.) Pacific Northwest National Laboratory, Richland, WA (United States).

Haslam, J. (1989) ‘The Soviet Union and the Politics of Nuclear Weapons in Europe, 1969-87: The Problem of the SS-20.’ 1st ed. Basingstoke, Hampshire, (UK): The Macmillan Press Ltd.

Hege Howes, R. and Herzenberg, C. L. (2003) ‘Their Day in the Sun: Women of the Manhattan Project.’ Philadelphia, PA (United States): Temple University Press.

Henager, S. H., Hrma, P., Swearingen, K. J., Schweiger, M. J., Marcial, J. and TeGrotenhuis, N. E. (2011) ‘Conversion of batch to molten glass, I: Volume expansion’, Journal of Non-Crystalline Solids. Elsevier B.V., 357(3), pp. 829–835.

Hinton, S. C. (1958) ‘Atomic Power in Britain’, Scientific American, 198(3), pp. 29–35.

Hore-Lacy, I. (2010) ‘Nuclear Energy in the 21st Century: World Nuclear University Press.’ London, (UK): Elsevier.

Hrma, P. (1990) ‘Melting of Foaming Batches: Nuclear Waste Glass’, in Advances in Fusion and Processing of Glass. Richland, WA (United States).

Hrma, P. (2009) ‘Effect of heating rate on glass foaming: Transition to bulk foam’, Journal of Non-Crystalline Solids. Elsevier B.V., 355(4–5), pp. 257–263.

Hrma, P. (2014) ‘Conversion of Nuclear Waste into Nuclear Waste Glass: Experimental Investigation and Mathematical Modeling’, Procedia Materials Science. Elsevier B.V., 7, pp. 117–123.

Hrma, P. R., Alton, J., Plaisted, T., Kloužek, J., Matyáš, J., Mika, M., Schill, P., Trochta, M. and Nemec, L. (2001) ‘Increasing High-Level Waste loading in glass without changing the baseline melter technology’, WM2001 Conference. Tuscon, AZ (United States).

Hrma, P., Marcial, J., Swearingen, K. J., Henager, S. H., Schweiger, M. J., and Tegrotenhuis, N. E. (2011) ‘Conversion of batch to molten glass, II: Dissolution

of quartz particles', Journal of Non-Crystalline Solids. Elsevier B.V., 357(3), pp. 820–828.

Hrma, P., Pokorný, R., Lee, S. and Kruger, A. A. (2018) 'Heat transfer from glass melt to cold cap: Melting rate correlation equation', International Journal of Applied Glass Science, (August), pp. 1–8.

Hrma, P. and Kruger, A. A. (2008) 'Nuclear Waste Glasses: Continuous Melting and Bulk Vitrification', Advanced Materials Research, 39–40, pp. 633–640.

Hrma, P. and Kruger, A. A. (2009) 'Crystallization in Multicomponent Glasses.' ORP-42447. Office of River Protection. Richland, WA (United States).

Hrma, P., Kruger, A. A. and Pokorný, R. (2012) 'Nuclear waste vitrification efficiency: Cold cap reactions', Journal of Non-Crystalline Solids, 358(24), pp. 3559–3562.

Hrma, P. and Pokorný, R. (2016) 'The Office of River Protection Cold Cap and Melt Dynamics Technology Development and Research Plan.' PNNL-25350. Pacific Northwest National Laboratory, Richland, WA (United States).

Hrma, P. R. Schweiger, M. J., Humrickhouse, C. J., Moody, J. A., Tate, R. M., Rainsdon, T. T., Tegrotenhuis, N. E., Arrigoni, B. M., Marcial, J., Rodriguez, C. P. and Tincher, B. H. (2010) 'Effect of glass-batch makeup on the melting process', Ceramics - Silikaty, 54(3), pp. 193–211.

Hrma, P. R. Pokorny, R., Pierce, D. A., Kruger, A. A. (2011) 'Thermal Analysis Of Waste Glass Melter Feeds.' ORP-50828. Office of River Protection. Richland, WA (United States).

Hrma, P., Schill, P. and Nemec, L. (2002) 'Settling of Spinel in a High-Level Waste Glass Melter.' PNNL-13747. Pacific Northwest National Laboratory, Richland, WA (United States).

Huang, Q., Liu, J., He, X., Liu, T. and Lu, A. (2021) ‘Analysis of structure evolution and performance in alkali-free glass substrates via XPS and infrared: Boron-aluminum anomaly’, Journal of Non-Crystalline Solids, 555(120531).

Hubert, M. and Faber, A. J. (2014) ‘On the structural role of boron in borosilicate glasses’, Physics and Chemistry of Glasses: European Journal of Glass Science and Technology Part B, 55(3), pp. 136–158.

Hujová, M., Kloužek, J., Cutforth, D. A., Lee, S., Miller, M. D., McCarthy, B. P., Hrma, P., Kruger, A. A. and Pokorný, R. (2018) ‘Cold-cap formation from a slurry feed during nuclear waste vitrification’, Ceramics International. 45(5), pp. 6405–6412.

Hujová, M., Pokorný, R., Kloužek, J., Lee, S., Traverso, J. J., Schweiger, M. J., Kruger, A. A. and Hrma, P. (2018) ‘Foaming during nuclear waste melter feeds conversion to glass: Application of evolved gas analysis’, International Journal of Applied Glass Science, 9(4), pp. 487–498.

Hujová, M., Pokorný, R. and Kloužek, J. (2018) ‘Vitrification of nuclear waste: Exploring the cold cap’, Sklář a keramik, (195), pp. 195–201.

International Atomic Energy Agency (1992) ‘Design And Operation Of High Level Waste Vitrification And Storage Facilities’, Technical Report Series No. 339, Vienna (Austria).

International Atomic Energy Agency (2000) ‘Report 1: National waste class definitions versus the IAEA’s proposed waste classes. Responses to the 1997/1998 WMDB Questionnaire (created 2000-03-21).’ Vienna (Austria).

International Atomic Energy Agency (2009a) ‘Geological Disposal of Radioactive Waste: Technological Implications for Retrievability.’ IAEA Nuclear Energy Series. Vienna (Austria).

International Atomic Energy Agency (2009b) ‘Safety Standards: Classification of Radioactive Waste - No. GSG-1.’ General Safety Guide, IAEA. Vienna (Austria). p. 68.

International Atomic Energy Agency (2017) ‘Energy, Electricity and Nuclear Power Estimates for the Period up to 2050.’ Series No. 1 Vienna (Austria).

Jansson, P., Håkansson, A., Bäcklin, A. and Jacobsson, S. (2002) ‘Gamma-ray spectroscopy measurements of decay heat in spent nuclear fuel’, Nuclear Science and Engineering, 141(2), pp. 129–139.

Jantzen, C. M. (2011) ‘Development of glass matrices for high level radioactive wastes’, in Handbook of Advanced Radioactive Waste Conditioning Technologies. 1st ed. Aiken, SC (United States): Woodhead Publishing Limited, pp. 230–292.

Jantzen, C. M., Koopman, D. C., Herman, C. C., Pickett, J. B. and Zamecni, J. R. (2003) ‘Electron Equivalents Redox Model for High Level Waste Vitrification’, in Symposium on Waste Management Technologies in Ceramic and Nuclear Industries, American Ceramic Society. Westerville, Ohio: WSRC-MS-2003-00547. Westinghouse Savannah River Company, Aiken, SC (United States).

Jantzen, C. M., J. B. Pickett, and W. G. Ramsey. (1993) ‘Reactive Additive Stabilization Process (RASP)* for Hazardous and Mixed Waste Vitrification (U).’ WSRC-MS-93-118. Westinghouse Savannah River Company, Aiken, SC (United States).

Jantzen, C. M. and Stone, M. E. (2007) ‘Role of Manganese Reduction/Oxidation (REDOX) on Foaming and Melt Rate in High Level Waste (HLW) Melters (U).’ WSRC-STI-2006-00066. Savannah River National Laboratory, Aiken, SC (United States).

Jiang, Z. H. and Zhang, Q. Y. (2014) 'The structure of glass: A phase equilibrium diagram approach', Progress in Materials Science. Elsevier Ltd, 61(August 2013), pp. 144–215.

Jiménez, J. A. (2016) 'Carbon as reducing agent for the precipitation of plasmonic Cu particles in glass', Journal of Alloys and Compounds, 656, pp. 685–688.

Johnston, W. D. (1964) 'Oxidation-Reduction Equilibria in Iron-Containing Glass', Journal of the American Ceramic Society, 47(4), pp. 198–201.

Joseph, I., Bowan, B. W., Kruger, A. A., Gan, H., Kot, W. K., Matlack, K. S. and Pegg, I. L. (2010) 'High Aluminum HLW Glasses for Hanford's WTP ORP-42448-FP', in WM2010 Conference. Phoenix, AZ (United States).

Karamanov, A., Pisciella, P., Cantalini, C. and Pelino, M. (2000) 'Influence of Fe^{3+}/Fe^{2+} Ratio on the Crystallization of Iron-Rich Glasses Made with Industrial Wastes', Journal of the American Ceramic Society, 83(12), pp. 3153–3157.

Kaushik, C. P., Mishra, R. K., Thorat, V., Ramchandran, M., Kumar, A., Ozarde, P. D., Raj, K. and Das, D. (2004) 'Development of a Glass Matrix for Vitrification of Sulphate Bearing High Level Radioactive Liquid Waste.' BARC--2004/E/018. Bhabha Atomic Research Centre, Mumbai (India).

Kelly, S. E. (2011) 'A Joule-Heated Melter Technology for the Treatment and Immobilization of Low-Activity Waste.' RPP-48935. Washington River Protection Solutions Report. Richland, WA (United States).

Kim, D. -S., Schweiger, M. J., Buchmiller, W. C. and Matyáš, J. et al. (2012) 'Laboratory scale melter for determination of melting rate of waste glass feeds.' PNNL-21005. Pacific Northwest National Laboratory, Richland, WA (United States).

Kim, M. Corkhill, C. L., Hyatt, N. C. and Heo, J. (2018) 'Development, characterization and dissolution behavior of calcium-Aluminoborate glass wasteforms to immobilize rare-earth oxides', Scientific Reports. 8(1), pp. 1–8.

Kirkbride, R. A., Allen, G. K., Lowy, R. M. and Bergmann, L. M. (2009) 'Hanford Tank Waste Operations Simulator (HTWOS) Model Design.' RPP-17152. Richland, WA (United States).

Kloužek, J. and Rohanová, D. (1999) 'The measurement of oxygen partial pressure and characterisation of oxidation-reduction equilibria in glass melts', Ceramics - Silikaty, 43(3), pp. 94–98.

Knavish, L. A. and Harrell, W. C. (1991) 'Melting Glass with Oxidation Control and Lowered Emissions.' United States. United States Patent Office: US5006144

Kocarkova, H. (2011) 'Stability of glass foams: experiments at the bubble scale and on vertical film', PhD Thesis. Université Paris-Est. (France).

Köne, A. I. and Büke, T. (2010) 'Forecasting of CO_2 emissions from fuel combustion using trend analysis', Renewable and Sustainable Energy Reviews, 14(9), pp. 2906–2915.

Konijnendijk, W. L. (1975) 'The Structure of Borosilicate Glasses.' PhD Thesis. Technische Hogeschool Eindhoven. (Netherlands).

Konijnendijk, W. L. and Stevels, J. M. (1975) 'The structure of borate glasses studied by Raman scattering', Journal of Non-Crystalline Solids, 18(3), pp. 307–331.

Koroleva, O. N., Shabunina, L. A. and Bykov, V. N. (2011) 'Structure of borosilicate glass according to Raman spectroscopy data', Glass and Ceramics (English translation of Steklo i Keramika), 67(11–12), pp. 340–342.

Krass, A. S. et al. (1983) 'Uranium enrichment and nuclear weapon proliferation International Affairs.' London (UK): Taylor & Francis.

Kruger, A. A., Gan, H., Pegg, I. L., Kot, W. K. and Feng, Z. (2006) 'Final Report - Sulfate Solubility in RPP-WTP HLW Glasses.' ORP-56325, Office of River Protection, Richland, WA (United States).

Kruger, A. A., Gan, H., Pegg, I. L., Matlack, K. S., Chaudhuri, M., Bardakci, T., Gong, W. and Kot, W. K. (2008) 'Melt Rate Enhancement for High Aluminum HLW Glass Formulations.' ORP-56292. Office of River Protection, Richland, WA (United States).

Kruger, A. A., Pegg, I. L., Matlack, K. S., Chaudhuri, M., Kot, W. and Lutze, W. (2009) 'Effects of High Spinel and Chromium Oxide Crystal Contents on Simulated HLW Vitrification in DM100 Melter Tests.' VSL-09R1520-1 Rev. 0. Office of River Protection, Richland, WA (United States).

Kruger, A. A. (2011) 'Waste loading enhancements for Hanford Low-Activity Waste glasses', Proceedings of the International Conference on Radioactive Waste Management and Environmental Remediation, ICEM, (PARTS A AND B), pp. 753–754.

Kruger, A. A., Matlack, K. S., Pegg, I. L., Kot, W. K. and Joseph, I. (2012) 'Redox Control for Hanford HLW Feeds.' VSL-12R2530-12. Office of River Protection, Richland, WA (United States).

Kruger, A. A., Matlack, K. S., Gong, W., and Pegg, I. L. (2012) 'Small-Scale Melter Testing with LAW Simulants to Assess the Impact of Higher Temperature Melter Operations.' ORP-51809, VSL-04R4980-1. Office of River Protection, Richland, WA (United States).

Kruger, A. A., Matlack, K. A., Pegg, Ian L. and Gong, W. (2013) 'Final Report - Glass Formulation Testing to Increase Sulfate Volatilization from Melter.' VSL-04R4970-1, Rev. 0. Office of River Protection, Richland, WA (United States).

Kruger, A. A., Kim, D. -S. and Goel, A. (2015) 'Technetium incorporation in glass for the Hanford tank waste treatment and immobilization plant', in WM2015 Conference. Phoenix, AZ (United States).

Kruger, A. A., Pegg, I. L., Kot, W., Matlack, K. S. and Gan, H. (2012) 'Enhanced Sulfate Management in HLW Glass Formulations.' VSL12R2540. Office of River Protection, Richland, WA (United States).

Kupfer, M. J., Boldt, A. L., Hodgson, K. N., Shelton, L. W., Simpson, B. C., Watrous, R. A., LeClair, M. D., Borsheim, G. L., Winward, R. T., Colton, N. G., Lambert, S. L., Place, D. E. and Schulz, W. W. (1998) 'Standard Inventories of Chemicals and Radionuclides in Hanford Site Tank Wastes.' HNF-SD-WM-TI-740, Lockheed Martin Hanford Corporation, Richland, WA (United States).

Kurkjian, C. R. and Prindle, W. R. (1998) 'Perspectives on The History of Glass Composition', Journal of the American Ceramic Society, 81(4), pp. 795–813.

Lai, Y., Zeng, Y., Tang, X., Zhang, H., Han, J. and Su, H. (2016) 'Structural investigation of calcium borosilicate glasses with varying Si/Ca ratios by infrared and Raman spectroscopy.' RSC Advances. Royal Society of Chemistry, 6(96), pp. 93722–93728.

Lambert, S. L. and Kim, D. -S. (1994) 'Tank Waste Remediation System High-Level Waste Feed Processability Assessment Report.' WHC-SP-1143. Westinghouse Hanford Company, Richland, WA (United States).

Langowski, M. H., Darab, J. G. and Smith, P. A. (1996) 'Volatility Literature of Chlorine, Iodine, Strontium, Technetium, and Rhenium: Technetium and Rhenium Volatility Testing.' PNNL-11052. Pacific Northwest National Laboratory, Richland, WA (United States).

Larson, D. E. (1996) 'Hanford High-Level Waste Vitrification Program at the Pacific Northwest National Laboratory: Technology Development - Annotated

Bibliography.' Pacific Northwest National Laboratory, Richland, WA (United States).

Lee, S., Hrma, P. R., Kloužek, J., Pokorný, R., Hujová, M., Dixon, D. R., Schweiger, M. J. and Kruger, A. A. (2017) 'Balance of oxygen throughout the conversion of a high-level waste melter feed to glass', Ceramics International, 43(16), pp. 13113–13118.

Lee, S., Hrma, P., Pokorný, R., Kloužek, J., VanderVeer, B. J., Dixon, D. R., Luksic, S. A., Rodriguez, C., Chun, J., Schweiger, M. J. and Kruger, A. A. (2017) 'Effect of melter feed foaming on heat flux to the cold cap', Journal of Nuclear Materials. 496, pp. 54–65.

Lee, S., VanderVeer, B. J., Hrma, P., Hilliard, Z. J., Heilman-Moore, J. S., Bonham, C. C., Pokorný, R., Dixon, D. R., Schweiger, M. J. and Kruger, A. A. (2017) 'Effects of heating rate, quartz particle size, viscosity, and form of glass additives on high-level waste melter feed volume expansion', Journal of the American Ceramic Society, 100(2), pp. 583–591.

Lee, S., Hrma, P., Pokorný, R., Kloužek, J., Eaton, W. C. and Kruger, A. A. (2019) 'Glass production rate in electric furnaces for radioactive waste vitrification', Journal of the American Ceramics Society. 102(10). pp. 5828–5842.

Lee, S, Hrma, P., Pokorný, R., Traverso, J. J., Kloužek, J., Schweiger, M. J. and Kruger, A. A. (2019) 'Heat transfer from glass melt to cold cap: Effect of heating rate', International Journal of Applied Glass Science, (February), pp. 1–13.

Lee, S. Ferkl, P., Pokorný, R., Kloužek, J., Hrma, P., Eaton, W. C. and Kruger, A. A. (2020) 'Simplified melting rate correlation for radioactive waste vitrification in electric furnaces', Journal of the American Ceramic Society, 103(10), pp. 5573–5578.

Legget, C. J. (2012) ‘Thermodynamic Investigations of Aqueous Ternary Complexes for Am/Cm Separation.’ PhD Thesis. University of California, Berkeley, CA (United States).

Lonergan, C. E., Rice, J., Skidmore, C., Schweiger, M. J. and Hrma, P. (2022) ‘The effects of mixing multi-component HLW glasses on spinel crystal size’, Journal of Nuclear Materials. Elsevier B.V., 558, p. 153318.

López, M. C., Tirado, J. L. and Pérez Vicente, C. (2013) ‘Structural and comparative electrochemical study of M(II) oxalates, M = Mn, Fe, Co, Ni, Cu, Zn’, Journal of Power Sources, 227, pp. 65–71.

Luksic, S. A., Pokorný, R., George, J., Hrma, P., Varga, T., Reno, L. R., Buchko, A. C. and Kruger, A. A. (2020) ‘In situ characterization of foam morphology during melting of simulated waste glass using X-ray computed tomography’, Ceramics International. 46(11), pp. 17176–17185.

Macuglia, D. (2017) ‘Talking about secrets: The Hanford nuclear facility and news reporting of silence, 1945-1989’, in Mellor, F. and Webster, S. (eds) ‘The Silence of Science: Gaps and Pauses in the Communication of Science.’ New York, NY: Routledge. (United States).

Magnien, V., Neuville, D. R., Cormier, L., Roux, J., Hazemann, J. L., Pinet, O. and Richet, P. (2006) ‘Kinetics of iron redox reactions in silicate liquids: A high-temperature X-ray absorption and Raman spectroscopy study’, Journal of Nuclear Materials, 352, pp. 190–195.

Magnien, V., Neuville, D. R., Cormier, L., Roux, J., Hazemann, J. L., de Ligny, D., Pascarelli, S., Vickridge, I., Pinet, O. and Richet, P. (2008) ‘Kinetics and mechanisms of iron redox reactions in silicate melts: The effects of temperature and alkali cations’, Geochimica et Cosmochimica Acta, 72, pp. 2157–2168.

Mamoshin, V. L., Batalov, N. N., Zelyutin, G. V., Kozyreva, E. A. and Nepomiluev, A. M. (1998) 'Sodium-Conducting Glass for Electrochemical Equipment.' Glass and Ceramics. 55(9–10) pp. 299–302.

Manara, D., Grandjean, A. and Neuville, D. R. (2009) 'Structure of Borosilicate Glasses and Melts: A Revision of the Yun, Bray and Dell Model.' Journal of Non-Crystalline Solids 355 (50–51) pp. 2528–31.

Manara, D., Grandjean, A., Pinet, O., Dussossoy, J. L. and Neuville, D. R. (2007) 'Sulfur behavior in silicate glasses and melts: Implications for sulfate incorporation in nuclear waste glasses as a function of alkali cation and V_2O_5 content', Journal of Non-Crystalline Solids, 353, pp. 12–23.

Mann, F. M. (1999) 'Scenarios for the Hanford Immobilized Low-Activity Waste (ILAW) Performance Assessment.' HNF-EP-0828. Fluor Daniel Hanford, Inc. Richland, WA (United States).

Marcial, J. Chun, J., Hrma, P. and Schweiger, M. J. (2014) 'The Effect of Foaming and Silica Dissolution on Melter Feed Rheology during Conversion to Glass-14473', in WM2015 Conference. Phoenix, AZ (United States).

Marcial, J., Kloužek, J., Vernerová, M., Ferkl, P., Lee, S., Cutforth, D., Hrma, P., Kruger, A. and Pokorný, R. (2021) 'Effect of Al and Fe sources on conversion of high-level nuclear waste feed to glass', Journal of Nuclear Materials, 559(153423).

Marra, J. C. and Kim, D. -S. (2014) 'Towards Increased Waste Loading in High Level Waste Glasses: Developing a Better Understanding of Crystallization Behavior', Procedia Materials Science. Elsevier B.V., 7(803), pp. 87–92.

Marra, S. L., Andrews, M. K. and Cicero, C. A. (1993) 'Phase Stability Determinations of DWPF Waste Glasses.' WSRC-TR-93-00227. Westinghouse Savannah River Company, Aiken, SC (United States).

Matlack, K. S., Buechele, A. C., McKeown, D. A., Perez-Cardenas, F., Hojaji, H., Pegg, I. L., Muller, I. S., Macedo, P. B. and Morgan, S. (2000) 'Final Report: Melter Tests with LAW Envelope B Simulants to Support Enhanced Sulfate Incorporation.' VSL-00R3501-1, Rev 0. Vitreous State Laboratory, Washington, D. C. (United States).

Matlack, K. S., Perez-Cardenas, F., Pegg, I. L., Macedo, P. B., Buechele, A. C., Hojaji, H., Muller, I. S., Morgan, S. P. (2001) 'Final Report : Melter Tests with LAW Envelope A and C Simulants to Support Enhanced Sulfate Incorporation.' VSL-01R2501-2. Vitreous State Laboratory, Washington, D. C. (United States).

Matlack, K. S., Muller, I. S., Gong, W., Pegg, I. L. and Kruger, A. A. (2006) 'Final Report - DuraMelter 100 Tests to Support LAW Glass Formulation Correlation Development.' VSL-06R6480-1. Vitreous State Laboratory, Washington, D. C. (United States).

Matlack, K. S., Gan, H., Gong, W., Pegg, I. L., Champman, C. C., Joseph, I. and Kruger, A. A. (2007) 'Final Report - High Level Waste Vitrification System Improvements' VSL-07R1010-1, Rev 0, dated 04/16/07. Vitreous State Laboratory, Washington, D. C. (United States).

Matlack, K. S., Gan, H., Chaudhuri, M., Kot, W. K., Gong, W., Bardakci, T., Pegg, I. L. and Innocent, J. (2009) 'DM100 and DM1200 Melter Testing with High Waste Loading Glass Formulations for Hanford High-Aluminum HLW Streams.' VSL-09T1690-1. Vitreous State Laboratory, Washington, D. C. (United States).

Matlack, K. S., Joseph, I., Gong, W., Muller, I. S. and Pegg, I. L. (2009) 'Glass Formulation Development and DM10 Melter Testing with ORP LAW Glasses.' VSL-09R1510-2. Vitreous State Laboratory, Washington, D. C. (United States).

Matlack, K. S., Muller, I. S., Callow, R. A., D'Angelo, N., Bardakci, T., Joseph, I. and Pegg, I. L. (2011) 'Improving Technetium Retention in Hanford LAW Glass -

Phase 2.' VSL-11R2260-1. Vitreous State Laboratory, Washington, D. C. (United States).

Matlack, K. S., Gan, H., Chaudhuri, M., Kot, W. K., Pegg, I. L., Joseph, I. and Kruger, A. A. (2012) 'Melter Throughput Enhancements for High-Iron HLW.' ORP-54002. Vitreous State Laboratory, Washington, D. C. (United States).

Matlack, K. S., Viragh, C., Kot, W. K., Pegg, I. L. and Joseph, I. (2015) 'Effect of the Form of Iron on HLW Melt Rate.' VSL-15R3430-1. Vitreous State Laboratory, Washington, D. C. (United States).

Matlack, K. S., Kot, W. K., Pegg, I. L. and Joseph, I. (2015) 'Support for HLW Direct Feed - Phase 2.' VSL-15R3440-1. Vitreous State Laboratory, Washington, D. C. (United States).

Matlack, K. S., Gong, W. and Pegg, I. L. (2003) 'Final Report: Compositional Variation Tests on DuraMelter 100 with LAW Sub-Envelope A3 Feed in Support of the LAW Pilot Melter.' VSL-01R62N0-1, Rev. 2. Vitreous State Laboratory, Washington, D. C. (United States).

Matlack, K. S., Kruger, A. A., Gong, W., Bardakci, T., D'Angelo, N. A., Kot, W. K. and Pegg, I. L. (2011) 'Integrated DM1200 Melter Testing of HLW C-106/AY-102 Composition Using Bubblers.' VSL-03R3800-1. Vitreous State Laboratory, Washington, D. C. (United States).

Matson, D. W., Sharma, S. K. and Philpotts. J. A. (1983) 'The Structure of High-Silica Alkali Silicate Glasses. A Raman Spectroscopic Investigation.' Journal of Non-Crystalline Solids (58)

Matyáš, J., Gervasio, V., Sannoh, S. E. and Kruger, A. A. (2017) 'Predictive modeling of crystal accumulation in high-level waste glass melters processing radioactive waste', Journal of Nuclear Materials, 495, pp. 322–331.

Matyáš, J. and Hrma, P. (2005) ‘Sulfate Fining Chemistry in Oxidized and Reduced Soda-Lime-Silica Glasses (G Plus Project for Visteon Inc.).’ PNNL - 15175. Pacific Northwest National Laboratory, Richland, WA (United States).

Mayzan, M. Z. H., Stennett, M. C., Hyatt, N. C. and Hand, R. J. (2014) ‘Graphite immobilisation in iron phosphate glass composite materials produced by microwave and conventional sintering routes’, Journal of Nuclear Materials. Elsevier B.V., 454(1–3), pp. 343–351.

McCabe, D. J., Wilmarth, W. R. and Nash, C. A. (2013) ‘Waste Treatment Technology Process Development Plan for Hanford Waste Treatment Plant Low Activity Waste Recycle’, SRNL-STI-2013-00351. Savannah River National Laboratory, Aiken. SC (United States).

McCarthy, B. P., George, J. L., Dixon, D. R., Wheeler, M., Cutforth, D. A., Hrma, P. R., Linn, D., Chun, J., Hujová, M., Kruger, A. A. and Pokorný, R. (2018) ‘Rheology of simulated radioactive waste slurry and cold cap during vitrification’, Journal of the American Ceramic Society, 101(11), pp. 5020–5029.

McCloy, J. S., Schweiger, M. J., Rodriguez, C. and Vienna, J. D. (2011) ‘Nepheline Crystallization in Nuclear Waste Glasses : Progress Toward Acceptance of High-Alumina Formulations’, Applied Glass Science. 2(3), pp. 201–214.

McKeown, D. A., Muller, I. S., Matlack, K. S. and Pegg, I. L. (2002) ‘X-ray absorption studies of vanadium valence and local environment in in borosilicate waste glasses using vanadium sulfide, silicate, and oxide standards’, Journal of Non-Crystalline Solids, 298, pp. 160–175.

Meechoowas, E., Ketboonruang, P., Tapasa, K. and Jitwatcharakomol, T (2012) ‘Improve melting glass efficiency by Batch-to melt conversion’, in Procedia Engineering, 32, pp. 956–961.

Meera, B. N. and Ramakrishna, J. (1993) 'Raman spectral studies of borate glasses', Journal of Non-Crystalline Solids, 159, pp. 1–21.

Mitchell, L. and Post Guillen, D. (2016) 'Cold Cap Bubble Topology Report.' INL/EXT-16-38473. Idaho National Laboratory. Idaho Falls, ID. (United States).

Mohapatra, M., Mishra, R. K., Kaushik, C. P. and Tomar, B. S. (2014) 'Investigation of Radiation Damage in Trombay Nuclear Waste Glasses by ESR and Photoluminescence Techniques', Procedia Materials Science. Elsevier B.V., 7(December), pp. 247–251.

Muller, I. S., Gilbo, K., Joseph, I. and Pegg, Ian L. (2013) 'Final Report- Enhanced LAW Glass Property-Composition Models- Phase 1.' VSL-13R2940-1. Richland, WA (United States).

Muller, I. S., Viragh, C., Gan, H., Matlack, K. S. and Pegg, I. L. (2009) 'Iron Mössbauer redox and relation to technetium retention during vitrification', Hyperfine Interactions, 191(1–3), pp. 17–24.

Muschik, W., Römer, H., Eichholz, K., Kissl, P., Collignon, J. and Zintl, R. (2005) 'Method of Making Glass, A Method and Device for the Control and Setting of the Redox State of Redox Fining Agents in a Glass Melt.' United States: United States Patent Office: US6871514 B2.

Myrdal, A. (1977) 'The Game of Disarmament: How the United States and Russia Run the Arms Race.' 1st ed. Manchester (UK): Manchester University Press.

Mysen, B. O. and Virgo, D. (1989) 'Redox equilibria, structure, and properties of Fe-bearing aluminosilicate melts; relationships among temperature, composition, and oxygen fugacity in the system Na_2O-Al_2O_3-SiO_2-FeO', American Mineralogist, 74(1–2), pp. 58–76.

Nakamura, S. and Fuwa, A. (2015) 'Spin Order in $FeCr_2O_4$ Observed by Mössbauer Spectroscopy.' Phys. Procedia 75, pp. 747–754.

National Academies of Sciences Engineering and Medicine (2019) 'Review of the final draft analysis of supplemental treatment approaches of Low-Activity Waste at the Hanford Nuclear Reservation, Review #3.' Washington, D. C. (United States): The National Academic Press.

Nemanova, V., Abedini, A., Liliedahl, T. and Engvall, K. (2014) 'Co-gasification of petroleum coke and biomass', Fuel. Elsevier Ltd, 117(A), pp. 870–875.

Neyret, M., Lenoir, M., Grandjean, A., Massoni, N., Penelon, P. and Malki, M. (2015) 'Ionic Transport of Alkali in Borosilicate Glass. Role of Alkali Nature on Glass Structure and on Ionic Conductivity at the Glassy State.' Journal of Non-Crystalline Solids 410. pp. 74–81.

Norris, R. S. and Kristensen, H. M. (2010) 'Global nuclear weapons inventories, 1945-2010', Bulletin of the Atomic Scientists, 66(4), pp. 77–83.

Nuclear Decommissioning Authority (2017) 'Radioactive Wastes in the UK: A summary of the 2016 Inventory.' ISBN: 978-1-905985-33-3 Cumbria (UK).

Office of Civilian Radioactive Waste Management (2004) 'The Nuclear Waste Policy Act of 1982 - As amended with Appropriations Acts Appended.' Washington, D. C. (United States). Available at: https://inis.iaea.org/search/search.aspx?orig_q=RN:25059339. (Accessed: 25 July 2022).

Ogasawara, H. and Koga, N. (2014) 'Kinetic modeling for thermal dehydration of ferrous oxalate dihydrate polymorphs: A combined model for induction period-surface reaction-phase boundary reaction', Journal of Physical Chemistry A, 118(13), pp. 2401–2412.

Oh, S. J., Cook, D. C. and Townsend, H. E. (1998) 'Characterisation of iron oxides commonly formed as corrosion products on steel', Hyperfine Interactions, 112, pp. 59–65.

Ojovan, M. I. and Lee, W. E. (2011) ‘Glassy Wasteforms for Nuclear Waste Immobilization’, Metallurgic and Materials Transactions A, 42(April), pp. 837–852.

Ojovan, M. I. and Lee, W. E. (2014) ‘Principles of Nuclear Waste Management’, in An Introduction to Nuclear Waste Immobilisation. Oxford, (UK): Elsevier, pp. 65–74.

Ojovan, M. I. and Lee, W. E. (2014) ‘Waste Processing Schemes’, in An Introduction to Nuclear Waste Immobilisation. Oxford, (UK): Elsevier, pp. 117-35.

Ollier, N., Charpentier, T., Boizot, B., Wallez, G. and Ghaleb, D. (2004) ‘A Raman and MAS NMR study of mixed alkali Na-K and Na-Li aluminoborosilicate glasses’, Journal of Non-Crystalline Solids, 341(1–3), pp. 26–34.

Orlova, A. I., and Ojovan. M. I. (2019) ‘Ceramic Mineral Waste-Forms for Nuclear Waste Immobilization.” Materials 12 (16), pp. 1-45.

Oltra, C. et al. (2019) ‘Trust perceptions among residents surrounding nuclear power plants: A descriptive and explanatory study’, Progress in Nuclear Energy. 113, pp. 1–6.

Osipov, A. A., Eremyashev, V. E., Mazur, A. S., Tolstoi, P. M. and Osipova. L. M. (2016) ‘Coordination State of Aluminum and Boron in Barium Aluminoborate Glass.’ Glass Physics and Chemistry 42(3). pp. 230–37.

Osipov, A. A., Osipova, L. M. and Eremyashev, V. E. (2013) ‘Structure of alkali borosilicate glasses and melts according to Raman spectroscopy data’, Glass Physics and Chemistry, 39(2), pp. 105–112.

Paul, A. and Douglas, R. W. (1966) ‘Mutual interaction of different redox pairs in glass’, Physics and Chemistry of Glasses, 7(1), pp. 1–13.

Peeler, D. K., Vienna, J. D., Schweiger, M. J. and Fox, K. M. (2015) ‘Advanced High-Level Waste Glass Research and Development Plan.’ Pacific Northwest National Laboratory. Richland, WA (United States).

Peeler, D. K. and Edwards, T. B. (2004) ‘Impact of redox on glass durability: the glass selection process.’ WSRC-TR-2004-00135, Savannah River Technology Center, Aiken, SC (United States).

Peeler, D. K., Lorier, T. H. and Vienna, J. D. (2001) ‘Melt Rate Improvement for DWPF MB3: Foaming Theory and Mitigation Techniques.’ WSRC-RP-2001-00351. Savannah River Site. Aiken, SC (United States).

Pegg, I. L. (2015) ‘Behavior of technetium in nuclear waste vitrification processes’, Journal of Radioanalytical and Nuclear Chemistry, 305(1), pp. 287–292.

Perez, J. M., Bickford, D. F., Day, D. E., Kim, D. -S., Lambert, S. L., Marra, S. L., Strachan, D. M., Triplett, M. B. and Vienna, J. D. (2001) ‘High-Level Waste Melter Study Report.’ PNNL - 13582. Pacific Northwest National Laboratory, Richland, WA (United States).

Peterson, I. M., Shi, Y., Ma, D., Rygel, J. L., Wheaton, B., Whitfield, P. S., Wright, J. and Carlineo, M. (2019) ‘In situ measurements of reactions in a glass-forming batch by X-ray and neutron diffraction’, Journal of the American Ceramic Society, 102(3), pp. 1495–1506.

Peterson, R. A. Buck, E. C., Chun, J., Daniel, R. C., Herting, D. L., Ilton, E. S., Lumetta, G. J. and Clark, S. B. (2018) ‘Review of the Scientific Understanding of Radioactive Waste at the U.S. DOE Hanford Site’, Environmental Science and Technology, 52(2), pp. 381–396.

Piepel, G., Cooley, S. K., Muller, I. S., Gan, H., Joseph, I. and Pegg, I. L. (2007) ‘ILAW PCT, VHT, Viscosity, and Electrical Conductivity Model Development. VSL-07R1230-1, Rev. 0’, (June 2017).

Piepel, G. F., Amidan, B. G., Heredia-langner, A., Weier, D. R. and Cooley, S. K. (2005) ‘Statistical Methods and Results for WTP IHLW and ILAW

Compliance.' PNWD-3568. Battelle—Pacific Northwest Division Richland, WA. (United States).

Piepel, G. F., Cooley, S. K., Heredia-langner, A. Landmesser, S. M., Kot, W. T., Gan, H. and Pegg, I. L. (2008) 'Final Report IHLW PCT, Spinel $T_{1\%}$, Electrical Conductivity, and Viscosity Model Development.' VSL-07R1240-4, Pacific Northwest National Laboratory, Richland, WA. (United States).

Pierce, D. A., Hrma, P., Marcial, J., Riley, B. J. and Schweiger, M. J. (2012) 'Effect of alumina source on HLW-feed melting process', International Journal of Applied Glass Science, 3, pp. 59–68.

Pinet, O. Guirat, R., Phalippou, J., Advocat, T. (2008) 'Development of Models to Predict the Redox State of Nuclear Waste Containment Glass', in Nuclear fuel cycle for a sustainable future. Atalante, Montpellier (France).

Pinet, O., Vernaz, E., Conradt, R., Ladirat, C. and Gin, S. (2021) 'Nuclear Waste Vitrification', in Richet, P. et al. (eds) Encyclopedia of Glass Science, Technology, History, and Culture. 1st ed. Hoboken, NJ (United States): Wiley-American Ceramic Society.

Pinet, O., Hugon, I. and Mure, S. (2014) 'Redox Control of Nuclear Glass', Procedia Materials Science, 7, pp. 124–130.

Pioro, I. and Duffey, R. (2019) 'The Present Status of Electricity Generation in the World; how important it is, which industrial methods of electricity generation world uses, how efficient they are, how they interact in an electrical grid.' in Managing Global Warming. Letcher, T. M. (Ed.) Academic Press, London, (UK): Elsevier. Chapter 3. pp. 67–114.

Plodinec, M. J. (2000) 'Borosilicate Glasses for Nuclear Waste Immobilization', Glass Technology, 41(6), pp. 186–192.

Pokorný, R., Hilliard, Z. J., Dixon, D. R., Schweiger, M. J., Guillen, D. P., Kruger, A. A. and Hrma, P. (2015) 'One-Dimensional Cold Cap Model for Melters with Bubblers', Journal of the American Ceramic Society, 98(10), pp. 3112–3118.

Pokorný, R. and Hrma, P. (2011) 'Mathematical Model of Cold Cap — Preliminary One-Dimensional Model Development.' PNNL-20278. Pacific Northwest National Laboratory, Richland, WA (United States).

Pokorný, R. and Hrma, P. R. (2014) 'Model for the conversion of nuclear waste melter feed to glass', Journal of Nuclear Materials, 445(1–3), pp. 190–199.

Rao, K. R. (2001) 'Radioactive waste: The problem and its management', Current Science, 81(12), pp. 1534–1546.

Reed, B. C. (2005) 'Understanding Plutonium Production in Nuclear Reactors', The Physics Teacher, 43(4), pp. 222–224.

Reiner, K., and Schaeffer, H. A. (1987) 'Oxidation States of Glass Melts.' Defect and Diffusion Forum 53. 325–34.

Richland Operations Office. (2022) '2022 Hanford Lifecycle Scope, Schedule and Cost Report.' DOE/RL-2021-47. Richland Operations Office, U.S. Department of Energy, Richland, WA (United States). Retrieved from: http://www.hanford.gov/files.cfm/2016_LCR_Fact_Sheet_Final.pdf. (Accessed 01 August 2022).

Rodriguez, C. Kruger, A. A., Pierce, D. A., Chun, J., Schweiger, M. J. and Hrma, P. (2014) 'Kinetics of Cold-Cap Reactions for Vitrification of Nuclear Waste Glass Based on Simultaneous Differential Scanning Calorimetry -Thermogravimetry (DSC-TGA) and Evolved Gas Analysis (EGA).' ORP-56005-FP. Office of River Protection, Richland, WA (United States).

Rodriguez, C., Chun, J., Crum, J. V., Canfield, N. L., Ronnebro, E., Vienna, J. D. and Kruger, A. A. (2017) 'Thermal properties of simulated Hanford waste glasses', Journal of the American Ceramic Society, 100(6), pp. 2533–2542.

Ross, W. A. (1978) 'Process for solidifying high-level nuclear waste.' United States: United States Patent Office: US4,094,809.

Rushton, M. J. D. (2006) 'Simulations of Glass and Ceramic Systems for Nuclear Waste Applications', PhD Thesis. Imperial College of Science Technology and Medicine, London (UK).

Ryan, J. L. (1995) 'Redox Reactions and Foaming in Nuclear Waste Glass Melting.' PNL-10510. Pacific Northwest National Laboratory. Richland, WA (United States).

Sahajwalla, V., Rahman, M., Hong, L., Saha-Chaudhury, N. and Spencer, D. (2006) 'Influence of Carbonaceous Materials on Slag Foaming Behavior during EAF Steelmaking', Iron and Steel Technology, I, pp. 639–650.

Sakai, A., Koiegami, H., Roth, G., Weisenburger, S., Kanehira, N. and Komamine, S. (2017) 'Comparison of Advanced Melting Process for HLW Vitrification, Joule Heated-Ceramic-Lined Melter (JHCM) and Cold-Crucible Induction Melter (CCIM)', Proceedings of the 25th International Conference on Nuclear Engineering. Shanghai (China) pp. 1–12.

Sawatzky, G. A., Van Der Woude, F. and Morrish, A. H. (1969) 'Mössbauer study of several ferrimagnetic spinels', Physical Review, 187(2), pp. 747–757.

Scheffran, J. (2018) 'Verification and security of transformation to a nuclear-weapon-free world: The framework of the treaty on the prohibition of nuclear weapons', Global Change, Peace and Security, 30(2), pp. 143–162.

Schmelzer, J. W. P. (2008) 'Crystal Nucleation and Growth in Glass-Forming Melts: Experiment and Theory.' Journal of Non-Crystalline Solids 35(2–9), pp. 269–78.

Schreiber, H. D. (1980) ‘Properties of redox ions in glasses: An interdisciplinary perspective’, Journal of Non-Crystalline Solids, 42(1–3), pp. 175–183.

Schreiber, H. D. (1983) ‘The characterisation of individual redox ions in glasses’, in Rossington, D. R., Condrate, R. A., and Snyder, R. L. (eds) Advances in Materials Characterisation, Materials Science Research. Boston, MA (United States): Springer, pp. 647–658.

Schreiber, H. D., Kozak, S. J., Merkel, R. C., Balazs, G. B. and Jones, P. W. (1986) ‘Redox equilibria and kinetics of iron in a borosilicate glass-forming melt’, Journal of Non-Crystalline Solids, 84(1–3), pp. 186–195.

Schreiber, H. D. (1986) ‘Redox processes in glass-forming melts’, Journal of Non-Crystalline Solids, 84(1–3), pp. 129–141.

Schreiber, H. D. Merkel Jr., R. C., Schreiber, V. L. and Balazs, G. B. (1987) ‘Mutual Interactions of Redox Couples Via Electron Exchange in Silicate Melts: Models for Geochemical Melt Systems’, Journal of Geophysical Research, 92(B9), pp. 9233–9245.

Schreiber, H. D., Schreiber, C. W., Riethmiller, M. W. and Sloan Downey, J. (1990) ‘The effect of temperature on the redox constraints for the processing of high-level nuclear waste into a glass waste form’, Materials Research Society Symposium - Proceedings, 176(419).

Schreiber, H. D., Kochanowski, B. K., Schreiber, C. W., Morgan, A. B., Coolbaugh, M. T. and Dunlap, T. G. (1994) ‘Compositional dependence of redox equilibria in sodium silicate glasses’, Journal of Non-Crystalline Solids, 177(C), pp. 340–346.

Schreiber, H. D. and Balazs, G. B. (1985) ‘An Electromotive Force Series for Redox Couples in a Borosilicate Melt: The Basis for Electron Exchange Interactions of the Redox Couples’, Journal of Non-Crystalline Solids, 71, pp. 59–67.

Schreiber, H. D. and Haskin, L. A. (1976) ‘Chromium in basalts: Experimental determination of redox states and partitioning among synthetic silicate phases’, in Proceedings of the Lunar and Planetary Science Conference 7th. Houston, Texas (United States): Pergamon Press.

Schreiber, H. D. and Hockman, A. L. (1987) ‘Redox Chemistry in Candidate Glasses for Nuclear Waste Immobilization’, Journal of the American Ceramic Society, 70(8), pp. 591–594.

Schreiber, H. D. and Todd Coolbaugh, M. (1995) ‘Solvations of redox ions in glass-forming silicate melts’, Journal of Non-Crystalline Solids, 181(3), pp. 225–230.

Schweiger, M. J., Hrma, P., Humrickhouse, C. J., Marcial, J., Riley, B. J. and TeGrotenhuis, N. E. (2010) ‘Cluster formation of silica particles in glass batches during melting’, Journal of Non-Crystalline Solids. Elsevier B.V., 356(25–27), pp. 1359–1367.

Scurlock, J. (2007) ‘A Concise History of the Nuclear Industry Worldwide’, in Elliot D. (eds) Nuclear or Not? Energy, Climate Change and the Environment Series. London (UK): Palgrave Macmillan, pp. 24–33.

Seaborg, G. T. (1962) ‘The First Nuclear Reactor, the Production of Plutonium and Its Chemical Extraction’, Atomic Energy Commission, 4, pp. 15-17.

Semat, H. (1973) ‘Introduction to Atomic and Nuclear Physics: 5th edition.’ London (UK): Chapman and Hall Ltd.

Sengupta, P., Kaushik, C. P. and Dey, G. K. (2013) ‘Imobilization of High Level Nuclear Wastes: The Indian Scenario’, in Ramkumar, M. (ed) ‘On a Sustainable Future of the Earth’s Natural Resources.’ Heidelberg (Germany): Springer Berlin. Chapter 2. pp. 25–51.

Šepelák, V., Bergmann, I., Feldhoff, A., Heitjans, P., Krumeich, F., Menzel, D., Litterst, F., Campbell, S. J. and Becker, K. D. (2007) ‘Nanocrystalline Nickel Ferrite,

$NiFe_2O_4$: Mechanosynthesis, Nonequilibrium Cation Distribution, Canted Spin Arrangement, and Magnetic Behavior', Journal of Physical Chemistry, 111, pp. 5026–5033.

Seymour, R. G. (1995) 'Evaluation of Alternative Chemical Additives for High-Level Waste Vitrification Feed Preparation Processing.' WHC-SD-WM-SP-009. Westinghouse Hanford Company, Oak Ridge, TN (United States).

Shaharyar, Y., Cheng, J. Y., Han, E., Maron, A., Weaver, J., Marcial, J., McCloy, J. S. and Goel, A. (2016) 'Elucidating the Effect of Iron Speciation (Fe^{2+}/Fe^{3+}) on Crystallization Kinetics of Sodium Aluminosilicate Glasses', Journal of the American Ceramic Society, 99(7), pp. 2306–2315.

Sharma, S. K. (2004) 'Atomic and Nuclear Physics.' New Dehli, (India): Pearson Education India.

Shaw, C. S. J. (2006) 'Effects of Melt Viscosity and Silica Activity on the Rate and Mechanism of Quartz Dissolution in Melts of the CMAS and CAS Systems.' Contributions to Mineralogy and Petrology, 151(6), pp. 665–80.

Shelby, J. E. (1983) 'Thermal Expansion of Mixed Alkali Borate Glasses.' Journal of the American Ceramic Society 66 (3), pp. 225–27.

Shelby, J. E. (2005) 'Introduction to Glass Science and Technology', Cambridge, (UK): The Royal Society of Chemistry.

Shi, C., Alderman, O. L. G., Tamalonis, A., Weber, R., You, J. and Benmore, C. J. (2020) 'Redox-Structure Dependence of Molten Iron Oxides.' Communications Materials 1(80), pp. 1–8.

Shibata, E., Egawa, S. and Nakamura, T. (2002) 'Reduction behavior of chromium oxide in molten slag using aluminum, ferrosilicon and graphite', ISIJ International, 42(6), pp. 609–613.

Sijo, A. K. (2018) ‘Tailoring of the Magnetic and Structural Properties of Nanosized Ferrites.’ in Recent Advances in Porous Ceramics, Basheer Al-Naib, U. M. (Ed.) 97, London (UK): IntechOpen.

Sijo, A. K., Jha, V. K., Kaykan, L. S. & Dutta, D. P. (2019) ‘Structure and cation distribution in superparamagnetic $NiCrFeO_4$ nanoparticles using Mössbauer study.’ Journal of Magnetism and Magnetic Materials. 497, pp. 166047

Silverman, A. (1932) ‘Use of Electrochemical By-Products in Glass Making: I. Arsenic, Selenium, Tellurium.’ Transactions of The Electrochemical Society, 61(1), pp. 101-112

Simpson, W. and Myers, D. D. (1978) ‘Redox Number Concept and Its Use By the Glass Technologist.’, Glass Technology, 19(4), pp. 82–85.

Siqueira, D. S., de Almeida Meystre, J., Hilário, M. Q., Rocha, D. H. D., Menon, G. J. and da Silva, R. J. (2019) ‘Current perspectives on nuclear energy as a global climate change mitigation option’, Mitigation and Adaptation Strategies for Global Change, 24(5), pp. 749–777.

Smallman, R. E. and Bishop, R. J. (1999) ‘Atomic arrangements in materials’, in Modern Physical Metallurgy and Materials Engineering. 6th edn. Oxford (UK): Butterworth Heinemann, pp. 11–41.

Smith, E. C., Butler, T. A., Ciorneiu, B., Bowan, B. W., Matlack, K. S. and Pegg, I. L. (2011) ‘Advanced Joule Heated Melter Design to Reduce Hanford Waste Treatment Plant Operating Costs - 11131’, in WM2011 Conference. Phoenix, AZ (United States).

Smith, P. A., Vienna, J. D. and Hrma, P. (1995) ‘The effects of melting reactions on laboratory-scale waste vitrification’, Journal of Materials Research, 10(8), pp. 2137–2149.

Smith, P. A., Vienna, J. D. and Merz, M. D. (1996) 'NCAW Feed Chemistry: Effect of Starting Chemistry on Melter Offgas and Iron Redox.' PNL-10517. Pacific Northwest National Laboratory, Richland, WA (United States).

Smrčka, D., Procházka, V., Novák, P., Kašlík, J. & Vrba, V. (2016) 'Iron oxalate decomposition process by means of Mössbauer spectroscopy and nuclear forward scattering.' American Institute of Physics Conference Proceedings. 1781, 020012

Soderquist, C. Z., Schweiger, M. J., Kim, D. -S., Lukens, W. W. and McCloy, J. S. (2014) 'Redox-dependent solubility of technetium in low activity waste glass', Journal of Nuclear Materials. Elsevier B.V., 449(1–3), pp. 173–180.

Straub, C. P. (1973) 'Radioactive Wastes.' Water Pollution Control Federation, 45(6), pp. 1202–1215.

Sugawara, T., Ohira, T., Komamine, S. and Ochi, E. (2016) 'Estimation of redox condition of simulated high-level waste glass based on the chemical composition of crystalline phases of platinum-group elements', Transactions of the Atomic Energy Society of Japan, 15(1), pp. 43–52.

Swallen, S. F., Kearns, K. L., Mapes, M. K., Kim, Y. S., McMahon, R. J., Ediger, M. D., Wu, T., Yu, L. and Satija, S. (2007) 'Organic Glasses with Exceptional Thermodynamic and Kinetic Stability', Science Mag, 315, pp. 98–101.

Templeton, A. M. (2018) 'Waste Tank Summary Report for Month Ending November 30, 2018.' HNF-EP-0182, Rev. 371. Washington River Protection Solutions. Richland, WA (United States).

Thiemsorn, W., Keowkamnerd, K., Phanichphant, S., Suwannathada, P., and Hessenkemper, H. (2008) 'Influence of Glass Basicity on Redox Interactions of Iron-Manganese-Copper Ion Pairs in Soda-Lime-Silica Glass.' Glass Physics and Chemistry 34 (1). pp. 19–29.

Tress, H. J. (1960) ‘A thermodynamic approach to redox equilibria in glasses’, Physics and Chemistry of Glasses, 1(6), pp. 196–97.

U.S. Department of Energy (2019) ‘Hanford Lifecycle Scope, Schedule and Cost Report.’ DOE/RL-2018-45. Richland Operations Office, Richland, WA (United States).

U.S. Department of Energy, U.S. Environmental Protection Agency and Washington State Department of Ecology (2020) ‘Hanford Federal Facility Agreement and Consent Order.’ Richland, WA (United States). Available at: https://www.hanford.gov/page.cfm/TriParty/TheAgreement (Accessed: 25 July 2022).

U.S. Department of Energy (2009) ‘Hanford Cleanup Progress Washington State Legislature.’ Richland, WA (United States). Available at: http://www.hanford.gov/page.cfm/HanfordCleanup. (Accessed 09 August 2022).

U.S. Environmental Protection Agency. (2003) ‘Low-Activity Radioactive Wastes, Radiation Protection.’ Available at: https://www.epa.gov/radiation/low-activity-radioactive-wastes (Accessed: 25 July 2022).

Ueda, N., Vernerová, M., Kloužek, J., Ferkl, P., Hrma, P., Yano, T. and Pokorný. R. (2021) ‘Conversion Kinetics of Container Glass Batch Melting.’ Journal of the American Ceramic Society, 104 (1), pp. 34–44.

United Nations (2022) ‘Treaty on the Non-Proliferation of Nuclear Weapons (NPT), Treaty on the Non-Proliferation of Nuclear Weapons (NPT).’ Available at: https://www.un.org/disarmament/wmd/nuclear/npt/text/ (Accessed: 25 July 2022).

Varshneya, Arun K., and John C. Mauro. (2019) ‘Fundamentals of Inorganic Glasses. Fundamentals of Inorganic Glasses.’ 3rd ed. Amsterdam, (Netherlands): Elsevier.

Velez, M. H., Tuller, H. L. and Uhlmann, D. R. (1982) ‘Chemical durability of lithium borate glasses’, Journal of Non-Crystalline Solids, 49, pp. 351–362.

Vernerová, M., Kloužek, J. and Němec, L. (2015) ‘Reaction of soda-lime-silica glass melt with water vapour at melting temperatures’, Journal of Non-Crystalline Solids, 416, pp. 21–30.

Vienna, J. D., Skorski, D. C., Kim, D. -S. and Matyáš, J. (2013) ‘Glass Property Models and Constraints for Estimating the Glass to be Produced at Hanford by Implementing Current Advanced Glass Formulation Efforts.’ PNNL-22631, Rev. 1, Pacific Northwest National Laboratory, Richland, WA (United States).

Vienna, J. D., Kim, D. -S., Muller, I. S., Piepel, G. F. and Kruger, A. A. (2014) ‘Toward Understanding the Effect of Low-Activity Waste Glass Composition on Sulfur Solubility’, Journal of the American Ceramic Society. 97(10), pp. 3135–3142.

Vienna, J. D., Stanfill, B. A., Piepel, G. F., Riley, B. J., Kim, D. -S., Cooley, S. K., Crum, J. V., Jin, T. and Lonergan, C. E. (2016) ‘2016 Update of Hanford Glass Property Models and Constraints for Use in Estimating the Glass Mass to be Produced at Hanford by Implementing Current Enhanced Glass Formulation Efforts.’ PNNL-25835 2016. Pacific Northwest National Laboratory, Richland, WA (United States).

Virgo, D. and Mysen, B. O. (1985) ‘The structural state of iron in oxidized vs. reduced glasses at 1 atm: A ^{57}Fe Mössbauer study’, Physics and Chemistry of Minerals, 12(2), pp. 65-76.

Vogel, W. (1994) ‘Classical Theories of Glass Structure’, in Glass Chemistry. 2nd ed. Berlin, (Germany): Springer-Verlag, pp. 41–56.

Wang, C., Yu, H., Liu, H. and Jin, Z. (2003) ‘Thermodynamic Optimization of the Na_2O-B_2O_3 Pseudo-Binary System.’ Journal of Phase Equilibria, 24 (1), pp. 12–20.

Wang, M., Cheng, J., Li, M. and He, F. (2011) 'Raman spectra of soda-lime-silicate glass doped with rare earth', Physica B: Condensed Matter., 406(20), pp. 3865–3869.

Wang, W. H., Dong, C. and Shek, C. H. (2004) 'Bulk metallic glasses', Materials Science and Engineering R: Reports, 44(2–3), pp. 45–89.

Washington Department of Ecology State of Washington (2018) 'Cleanup Progress at Hanford.' (Richland, WA (United States). Available at: www.hanford.gov/ (Accessed: 25 July 2022).

Weimers, K. D. (1998) 'The Effect of HWVP Feed Nitrate and Carbonate Content on Glass Redox Adjustment.' PNNL-11044. Pacific Northwest National Laboratory, Richland, WA (United States).

Wilke, M., Farges, F., Petit, P. E., Brown, G. E. and Martin, F. (2001) 'Oxidation state and coordination of Fe in minerals: An Fe K-XANES spectroscopic study.' American Mineralogist, 86(5–6). pp. 714–730.

Wilke, M., Partzsch, G. M., Bernhardt, R. and Lattard, D. (2004) 'Determination of the iron oxidation state in basaltic glasses using XANES at the K-edge.' Chemical Geology, 213(1–3), pp. 71–87.

World Nuclear Association (2011) 'Comparison of Lifecycle Greenhouse Gas Emissions of Various Electricity Generation Sources, WNA Report.' Available at: https://gssd.mit.edu/search-gssd/site/comparison-lifecycle-greenhouse-gas-61507-tue-10-31-2017-2350 (Accessed: 25 July 2022).

Wu, L., Xiao, J., Wang, X., Teng, Y., Li, Y. and Liao, Q. (2018) 'Crystalline phase, microstructure, and aqueous stability of zirconolite–barium borosilicate glass-ceramics for immobilization of simulated sulfate bearing high-level liquid waste', Journal of Nuclear Materials. 498, pp. 241–248.

Xu, K., Hrma, P., Rice, J., Riley, B. J., Schweiger, M. J. and Crum, J. V. (2015) 'Melter Feed Reactions at T ≤ 700 ℃ for Nuclear Waste Vitrification', Journal of the American Ceramic Society, 98(10), pp. 3105–3111.

Xu, K., Hrma, P., Rice, J. A., Schweiger, M. J., Riley, B. J., Overman, N. R. and Kruger, A. A. (2016) 'Conversion of Nuclear Waste to Molten Glass: Cold-Cap Reactions in Crucible Tests', Journal of the American Ceramic Society, 99(9), pp. 2964–2970.

Yadav, A. K. and Singh, P. (2015) 'A review of the structures of oxide glasses by Raman spectroscopy', RSC Adv. Royal Society of Chemistry, 5(83), pp. 67583–67609.

Yang, F. and Hamilton, J. H. (2010) 'Modern Atomic and Nuclear Physics: Revised.' Toh Tuck Link, (Singapore): World Scientific Publishing Co.

Yergey, A. L. and Yergey, A. K. (1997) 'Preparative scale mass spectrometry: A brief history of the calutron', Journal of the American Society for Mass Spectrometry, 8(9), pp. 943–953.

Yu, D., Zhu, M., Utigard, T. A. and Barati, M. (2014) 'TG/DTA study on the carbon monoxide and graphite thermal reduction of a high-grade iron nickel oxide residue with the presence of siliceous gangue', Thermochimica Acta, 575, pp. 1–11.

Yun, Y. H. and Bray, P. J. (1978) 'Nuclear magnetic resonance studies of the glasses in the system $K_2OB_2O_3P_2O_5$.' Journal of Non-Crystalline Solids. 30, pp. 45–60.

Zachariasen, W. H. (1932) 'The atomic arrangement in glass', Journal of the American Chemical Society, 54(10), pp. 3841–3851.

3 Research Methods

3.1 Overview

Experiments were designed to investigate the fundamental mechanisms of the batch-to-glass conversion process within a cold cap, with particular focus on redox and structural changes during melting. A wide array of sample types, sample compositions and analysis techniques has been used to generate the results in this work. Analysis techniques for cold cap samples are discussed in the literature review, in Chapter 2, section 2.4, 2.5 and 2.6. The limitations of these techniques, and the potential improvement of cold cap analysis becoming more representative of melter systems, are explored throughout the following work. The following sections describe the types of samples generated for the study and methods of sample preparation, followed by the laboratory-based analysis techniques used to investigate melting and thermal behaviour, structural and physical changes, foaming behaviour and redox behaviour during melting of the simulated waste stream compositions.

3.2 Sample Compositions

The following Hanford Analogue compositions were based on the glass compositions developed by the ORP, VSL and PNNL, based on composition-property models (Vienna, Kim, and Hrma 2002; G. L. Smith et al. 2001; Kruger et al. 2008), to immobilise Hanford tank waste (Templeton 2018; Vienna et al. 2013; D. S. Kim 2015; Vienna, Kim, and Hrma 2002). The compositions are those currently accepted for each waste stream and are being tested and optimised based on melter runs and laboratory-based analysis techniques.

The HLW-NG-Fe2 glass was selected for the in-depth study of the redox behaviour and foaming behaviour due to its high contents of Fe and other multivalent species (Matlack et al. 2012). Previous work on the HLW-NG-Fe2 feed, section 2.6.2, found that little change was experienced in the foaming or gas evolution in the feed with alternative raw materials for iron, however, thus far, a completely reduced Fe raw material has not been explored in this feed. Following on from results in the study which used a reduced Fe source, $FeC_2O_4 \cdot 2H_2O$ in the HLW-Al-19 feed, with success in reducing foam and suppressing oxygen evolution (Guillen et al. 2020), the same method is applied in the following work. Iron hydroxide, $Fe(OH)_3$, is the Fe^{3+} raw material used in the original feed, and iron oxalate dihydrate, $FeC_2O_4 \cdot 2H_2O$, is used here for the Fe^{2+} raw material in the comparative feed: this feed is denoted HLW-NG-Fe2-II for this work.

Table 3.2.1. HLW-NG-Fe2 composition developed by the VSL to immobilise the C-106/AY-102 high-iron tank waste (Matlack et al. 2012).

Raw Material	**Batch 100 g^{-1}**	**Oxide**	**Wt%**
$Al(OH)_3$	8.61	Al_2O_3	5.59
H_3BO_3	0.56	B_2O_3	13.79
$Na_2B_4O_7 \cdot 10H_2O$	37.16	Na_2O	13.36
$CaCO_3$	0.94	CaO	0.52
CeO_2	0.12	CeO_2	0.12
$Cr_2O_3 \cdot 1.5H_2O$	0.30	Cr_2O_3	0.25
$Fe(OH)_3$	20.54	Fe_2O_3	16.12
$La(OH)_3$	0.11	La_2O_3	0.09
Li_2CO_3	3.87	Li_2O	1.56
$Mg(OH)_2$	0.24	MgO	0.16
MnO_2	3.98	MnO_2	3.98
NaOH	0.81		
Na_2CO_3	4.04		
$Ni(OH)_2$	0.59	NiO	0.47
$FePO_4 \cdot 2H_2O$	1.71	P_2O_5	0.78
PbO	0.63	PbO	0.63
Na_2SiO_3	8.03	SiO_2	41.02
Na_2SO_4	0.39	SO_3	0.22
SiO_2	37.33		
$SrCO_3$	0.28	SrO	0.20
ZnO	0.03	ZnO	0.03
$Zr(OH)_4 \cdot 0.654H_2O$	1.57	ZrO_2	1.13
$NaNO_2$	0.01		
$NaNO_3$	0.45		
$H_2C_2O_4 \cdot 2H_2O$	0.06		
Total	132.36	Total	100.00

Table 3.2.2. Source of iron in the nominal HLW-NG-Fe2 simulated glass composition with iron hydroxide $Fe(OH)_3$ and iron oxalate $FeC_2O_4 \cdot 2H_2O$, HLW-NG-Fe2-II

Raw Material	**Oxide**	**HLW-NG-Fe2 Batch 100 g^{-1} glass**	**HLW-NG-Fe2-II Batch 100 g^{-1} glass**	**wt%***
$Fe(OH)_3$	Fe_2O_3	20.54	0	16.08
$FeC_2O_4 \cdot 2H_2O$	Fe_2O_3	0	34.58	16.08

* Including 0.73 wt% from $FePO_2 \cdot 2H_2O$.

Additionally the use of reductants has been widely-explored in the LAW feeds, particularly the use of sucrose to promote early denitration to reduce foaming (Matlack, Muller, et al. 2011), however, evidence suggests that in HLW feeds that are low in nitrates, alternative reductants may be more applicable (Kruger et al. 2013; Ryan 1995). For this reason, a series of alternative reductants have been studied in the HLW-NG-Fe2 batch, at 3 wt% addition to the batch, with examination of the melting and foaming behaviour.

Table 3.2.3. Raw materials and reductants used for each of the feeds studied and the associated carbon content g^{-1} of compound.

Feed Name	**Reductant Carbon Source**	**Carbon content g^{-1} compound**
HLW-NG-Fe2	None	0
HLW-NG-Fe2-II	Fe^{2+} raw material ($FeC_2O_4 \cdot 2H_2O$)	0.32
HLW-NG-Fe2-S	Sucrose ($C_{12}H_{22}O_{11}$)	0.42
HLW-NG-Fe2-G	Graphite (C)	1.0
HLW-NG-Fe2-C	Coke (93 % C)	0.93
HLW-NG-Fe2-F	Formic Acid (CH_2O_2)	0.26
HLW-NG-Fe2-H	$C_{10}H_{16}N_2O_8$	0.43

3.3 Sample Preparation

In order to examine the cold cap behaviour, a variety of laboratory-based analysis techniques for sample formulation and observation were employed, which are described in this section. Since in-situ analysis of the cold cap is difficult to obtain, the following sample preparation techniques were designed to simulate different aspects of cold cap behaviour and structure.

Glass samples are used to represent the bottom of the cold cap and the final wasteform product, SoM samples represent the different layers of the cold cap corresponding to quenching temperatures, fast-dried slurry solid samples (FDSS) represent the top portion of the cold cap and the initial dehydration reactions and laboratory scale melter (LSM) samples are quenched full cold cap samples which are representative of the entire system. In Table 3.3.1, the sample types are shown for each of the feeds used in the study, where HLW-NG-Fe2-II represents the HLW-NG-Fe2 feed batched with $FeC_2O_4 \cdot 2H_2O$ instead of $Fe(OH)_3$, and HLW-NG-Fe2-R represents the HLW-NG-Fe2 feeds batched with the reductants outlined in section 2.8.2. Example sample types are shown in Figure 3.3.1.

Table 3.3.1. A summary of sample types for each composition used in the study.

Sample Type	**Feed compositions**
Glass Samples	HLW-NG-Fe2, HLW-NG-Fe2-II, HLW-NG-Fe2-R
SoM Samples	HLW-NG-Fe2, HLW-NG-Fe2-II, HLW-NG-Fe2-R
FDSS Samples	HLW-NG-Fe2, HLW-NG-Fe2-II
LSM Sample	HLW-NG-Fe2-II

Figure 3.3.1. Sample types explored in this study. a) slurry feed, b) SoM samples, c) glass samples, d) fast-dried slurry solids and e) Laboratory Scale Melter sample.

3.3.1 Batching and Feed Preparation

For preparation of the Hanford analogues slurry feed, raw materials were weighed on a 2 d.p. scale and all raw materials used had a purity >99 %. The iron hydroxide source was an iron hydroxide slurry with 13 wt% $Fe(OH)_3$, the silica source was <75 μm crushed quartz. Chemicals were mixed with deionised water and stirred continuously during batching in a glass beaker, as shown in Figure 3.3.1 (a). Each feed was batched with ~2 L of water. The target glass yield was 400 g L^{-1} for the HLW-NG-Fe2-II, and 290 g L^{-1} for the HLW-NG-Fe2 feed and derivative HLW-NG-Fe2-R feeds, due to the rheology of the iron hydroxide slurry. Once batched, some of the feed was dried in an oven at 105 ℃ for 24 hours and then milled for analysis and for use in the SoM study. The remainder of the slurry was stored in a plastic container for FDSS samples and the LSM run.

3.3.2 Glass Samples

All feeds were batched at Pacific Northwest National Laboratory, USA (PNNL), as described in section 3.3.1. HLW-NG-Fe2 and HLW-NG-Fe2-II glasses were formed at PNNL by melting in electric furnaces. HLW-NG-Fe2-R feeds were mixed with the reductants in slurry form, dried, and melted in air in electric furnaces at Sheffield Hallam University, UK (SHU). A comparison of the melting conditions used at the two laboratories are given in Table 3.3.2. Apart from the furnace and potential differences in the furnace atmospheres, the only difference between the melting conditions is the use of platinum (PNNL) or alumina (SHU) crucibles. To ensure that results were consistent, both the HLW-NG-Fe2 and HLW-NG-Fe2-II batches were also melted at SHU in alumina crucibles and the glasses were compared for structure, with those melted in platinum crucibles, by Raman spectroscopy. The results of this study are given in section 3.6.2.1. All glasses were poured into steel moulds in the shape of rings, Figure 3.3.1 (c) or rectangular blocks, depending on the shape required for analysis. Some of each glass sample was milled to a fine powder for analysis, in a Retsch vibratory disc mill RS200 at 700 rpm in a hardened steel sample holder.

Table 3.3.2. Melting conditions for glasses made at Pacific Northwest National Laboratory (PNNL) and Sheffield Hallam University (SHU).

Laboratory	**Crucible**	**Melt Temp (°C)**	**Ramp Rate (°C min^{-1})**	**Dwell (hours)**	**Annealing (hours)**
SHU	Alumina	1150	10	1	0
PNNL	Platinum	1150	10	1	0

The ramp rate of 10 °C min^{-1} was chosen for heating the batches based on previous work on the effect of heating rate on foaming in nuclear waste feeds (Lee, Hrma, Pokorný, Traverso, et al. 2019), as higher melting rates cause higher foam porosity. The choice not to dwell or anneal the Hanford analogue melts was made so as to avoid any

further loss of volatile components from the complex compositions, and represent only the bottom of the cold cap and not the final glass product which will undergo a certain residence time in the WTP melter (Bickford, Hrma, and Bowan 1990).

3.3.3 Stages of Melting Samples

Quenched Stages of Melting (SoM) samples, Figure 3.3.1 (b), represent different temperatures regions within, and therefore different layers of, the cold cap (Pokorný et al. 2015; Guillen et al. 2020; Deng et al. 2018). They are used in this work to analyse the crystalline phases present and the redox states of multivalent species in the different layers of the cold cap. The results of these tests were used to indicate the reactions occurring, as well as the amount of glass forming melt at different layers, and to qualify the general structure and morphology of the cold cap. Quench temperatures of 600, 700, 800, 900, 1000, 1100 and 1150 ℃ were used for the HLW-NG-Fe2 and HLW-NG-Fe2-II feeds, and 600, 800, 1000 and 1150 ℃ for the HLW-NG-Fe2-R feeds. These temperatures are representative of the onset of foaming through to the fully molten glass (Dixon et al. 2015b).

To form the samples 20 g of dried, milled, feed were placed in small alumina crucibles and ramped at 10 ℃ min^{-1} in an electric furnace to the desired temperatures, at which they were held for 10 minutes before quenching. Samples were then carefully removed from the crucibles and part of each sample was milled for analysis.

3.3.4 Fast-Dried Slurry Solid Samples

Fast-Dried Slurry Solid (FDSS) samples, Figure 3.3.1 (d), represent the top portion of the cold cap. These samples reach temperatures of 200-300 ℃ so they represent both the dehydration and the beginning of some reactions in the reaction layer. For the most part FDSSs remain in the open porosity region, although excessive foaming has been observed in some samples suggesting some melt has connected (McCarthy et al. 2018; Hujová et al. 2017).

Figure 3.3.2. Demonstration of creating an FDSS sample in an aluminium foil wrapped alumina mould on a hotplate with incoming feed from above.

To generate the samples the feed slurry was pumped through 3.1 mm Tygon tubing at a variable rate between 2-10 ml/min onto an aluminium foil-lined alumina mould, placed on a 650 W hotplate, shown in Figure 3.3.2. The hotplate temperature did not exceed 300 ℃. Feeding duration varied from 60-80 minutes to get a sufficient sample covering the area of the 10 cm diameter mould with a height of ~1 in. Once feeding was stopped the hotplate remained on to boil off remaining water. The mould was then removed from the hotplate and allowed to cool to room temperature on a copper quench block. The dried sample was then removed from the foil. The process is described in great detail in Hujová et al. (2018) (Hujová, Kloužek, et al. 2018). One of the main purposes of generating an FDSS, particularly in the present study, is to demonstrate the ability to feed the waste slurry through the pumping system, which is then used to feed into the LSM. Feeds with minimal feeding issues or blockages are suitable for the LSM (D. S. Kim et al. 2012).

3.3.5 Laboratory Scale Melter Samples

Laboratory Scale Melter (LSM) samples, Figure 3.3.1 (e), are the most representative samples we were able to access at the laboratory scale, without in situ observation (Guillen, Abboud, and Pokorný 2019). The diagram in Figure 3.3.3 compares the scales of different melters used to represent the WTP LAW melter (Dixon et al. 2022). The LSM used in this study is 10 cm in diameter, the Continuous Laboratory Scale Melter (CLSM) in the diagram is ~13 cm in diameter (D. S. Kim et al. 2012; R. A. Peterson et al. 2017). The WTP LAW melter has a 10 m^2 surface area, and the WTP HLW melter has a 3.75 m^2 surface area (Ramsay et al. 2011).

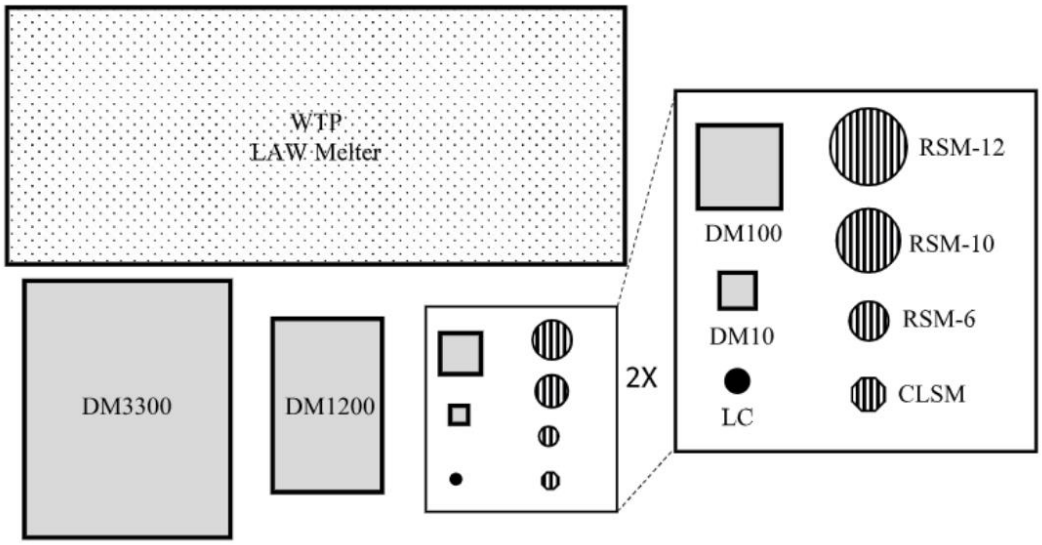

Figure 3.3.3. Comparison of scale of laboratory scale melters, research scale melters and the WTP LAW melter, with a surface area of 10 m^2 (Dixon et al. 2022).

For an LSM run, 200 g of the desired composition is melted in the bottom of the crucible to form the melt pool. Continuously stirred slurry feed is pumped at 7-10 mL min^{-1}, through 3.1 mm Tygon ® tubing, into the top of the melter system, landing on top of the melt pool. Variable height of the crucible, shown in Figure 3.3.4, allows control of the temperature gradient in the feed-to-glass transition region, so a cold cap layer can form on top of the melt pool. Feeding usually occurs for 1-2 hours to generate a

sufficient cold cap sample. During the run thermocouples record the temperature of the plenum and glass melt every 20 s. The thermocouple readings are monitored regularly to ensure the melt is around 1150 °C and the plenum temperature remains consistent, signalling sufficient cold cap coverage. Once feeding is stopped the tubes are removed, and the entire crucible removed from the melter and quenched immediately on a copper block. Once cooled the top of the crucible without any sample is removed and the remaining portion is the encased cold cap sample (D. S. Kim et al. 2012).

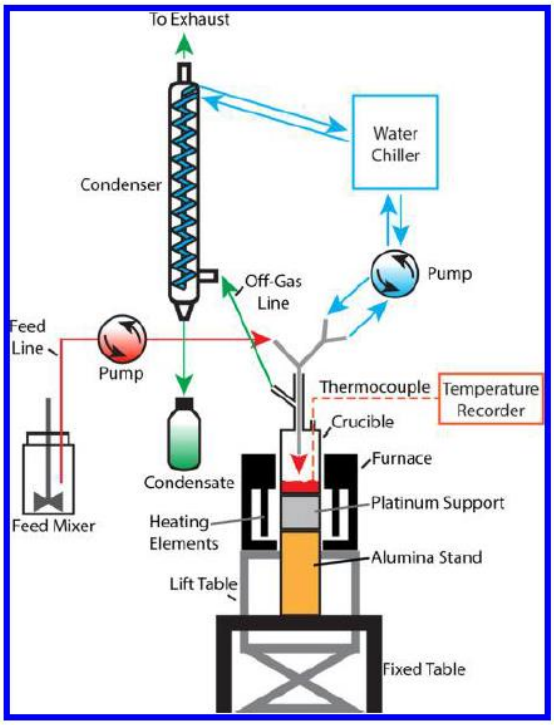

Figure 3.3.4. Schematic of the LSM (Dixon et al. 2015b).

Quenching of the cold cap may affect some of the bubble morphology and internal structure, however, the bulk structure will remain the same and it is unlikely that many major reactions will occur during cooling. The Laboratory Scale Melter at PNNL (D. S. Kim et al. 2012) was used to create LSM samples of the modified Hanford analogue HLW-NG-Fe2-II feed. Analysis of the temperature regions in the LSM sample is not feasible directly from the sample which is why supplementary analysis such as SoM samples and FDSS samples with defined temperature histories have been developed (Dixon et al. 2015b).

3.4 Glass Characterisation Techniques

The final glass product is not the main focus of this aspect of the research, and all of the simulant waste glasses undergo extensive testing for chemical durability, mechanical stability, radiation stability and thermal stability at PNNL and other laboratories in the US (G. L. Smith et al. 2001; Kruger et al. 2008). The focus of this work is the melting behaviour of the waste feeds and understanding characterising the cold cap. However, all of the glasses generated were analysed using thermal analysis by DTA; any crystalline phases by XRD; elemental composition by X-ray Fluorescence spectroscopy (XRF) and ICP-MS; to ensure consistency between the glasses created and the quality assessed glasses that will be generated at the Hanford site. Density measurements were taken to calculate the crystal volume in the glasses, and further heat-treated glass samples for quality assurance purposes introduced in Chapter 2, section 2.3.3.

3.4.1 X-Ray Fluorescence Spectroscopy

X-ray fluorescence spectroscopy (XRF) is a non-destructive technique, providing information on the elemental composition of a sample. Incident X-rays on the surface of a sample will excite electrons from inner orbitals of the elements present (Beckhoff et al. 2006; Brouwer 2010). When these electrons return to their ground state, the wavelength of the X-ray emitted is characteristic of the element it is emitted from, due to the unique energy differences between the excited and ground state. Collection of these X-rays can give quantitative elemental information on the sample (Beckhoff et al. 2006). The simplicity of the process allows for the analysis of many different types of samples using different sample preparation techniques (Potts 1987; Merdanovica 2009; West et al. 2012).

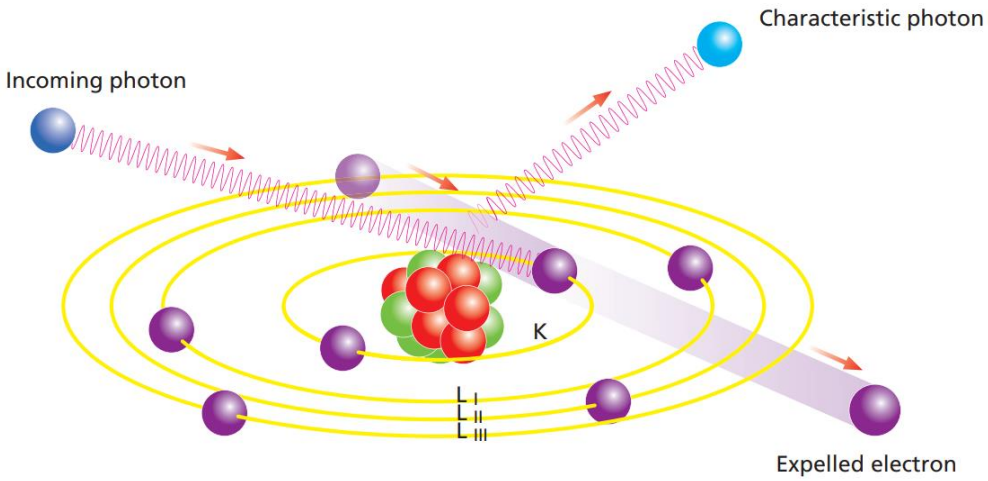

Figure 3.4.1. Production of characteristic radiation from (Brouwer 2010)

Due to the high X-ray energies required to remove electrons from inner orbitals of light elements, the spectrometer used for this work can generally only detect elements as light as fluorine (Kikongi, Salvas, and Gosselin 2017; Kregsamer et al. 1999). Oxygen cannot be detected, therefore, for oxide glass samples the constituents detected are assumed to be oxides and analysed using the Glass OXI program developed for this purpose (Giles, Hurley, and Webster 1995a). For non-glass samples the PANalytical SuperQ IQ+ software was used to identify elements.

The technique is surface sensitive due to the low penetration depth of the incoming X-rays, so sample preparation is critical to ensuring the measured surface is representative of the entire sample. All glass samples in this study were analysed using the PANalytical MagiX PRO XRF spectrometer. Samples were prepared as fused beads. Fused beads were made by incorporating 1 g of powdered sample into dissolved lithium borate, $Li_2B_2O_7$ doped with 0.5 wt% LiI anti-cracking agent (Merdanovica 2009; Bell et al. 2020). Li, B and O all have atomic masses lower than F so they will not be detected. The combination was mixed by rocking motions during melting in a 5 % Au- 95 % Pt crucible during melting in a Claisse LeNeo fused bead maker. The mixture was held at to 1065 °C for 6 minutes, to ensure the temperature was stable and then mixed for 11 mins, before pouring into a 5 % Au- 95 % Pt disc-shaped mould to air cool.

3.4.2 ICP-MS

Since B and Li cannot be detected by XRF, glass samples were also subject to Inductively Coupled Plasma-Mass Spectrometry (ICP-MS) at Sheffield Assay Office to quantify these elements. ICP-MS can detect ppm levels of elements in samples depending on the matrix. The technique is more accurate than XRF due to the lack of chemical interference in the inert plasma substance analysed (Mirti et al. 2009; Jenner et al. 1990; Corzo et al. 2018).

For inductively coupled plasma (ICP) techniques, liquid samples are most economical for nebulization (Ammann 2007). Liquid is pumped into a nebuliser to form a fine aerosol, and the finest aerosol droplets are transported into the ICP torch, Figure 3.4.2. An intense magnetic field in the plasma torch on a tangential flow of argon gas ionises the gas. The gas is then seeded with a source of electrons from a high-voltage spark to form a high-temperature plasma discharge. The ions produced are then directed towards the mass spectrometer (Thomas 1978).

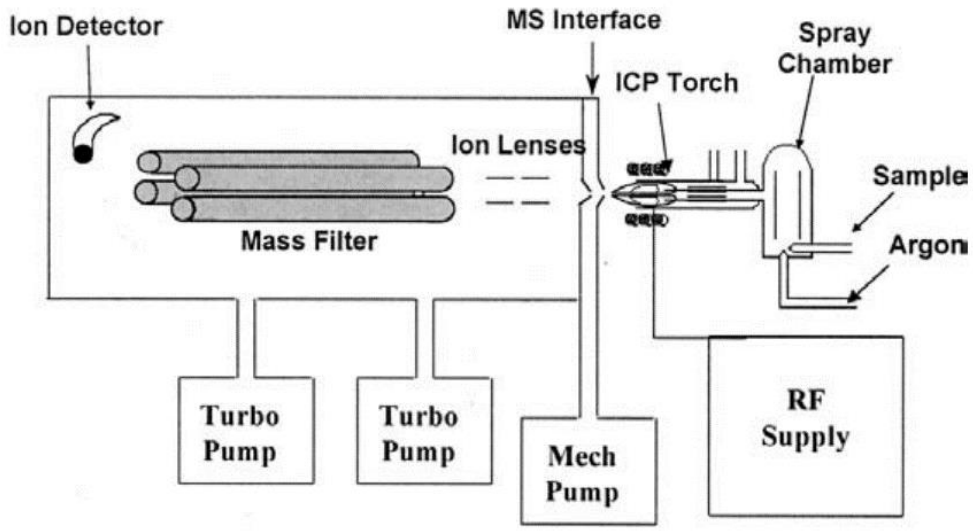

Figure 3.4.2. Instrumental components of an ICP-MS system (Thomas 1978).

Extraction was conducted on three trials of 500 mg of each powdered glass sample using an acid mixture of $4HNO_3$ + 3HF + 2HCl + $2H_2O$ using an Anton Paar microwave digestion system. Following digestion, 2 samples were diluted to 50 ml and

the other was spiked with a known quantity of Li and B. The spiked sample was used to calculate the recovery factor for the sample. All samples were then measured using ICP-MS on a Perkin Elmer ® Nexion-1000 ICP-MS. The concentrations were determined by subtracting acid blanks and the correction factor from the spiked sample.

The mass spectrometer has the ability to detect ppm levels of species, based on the mass to charge ratio of the ions. Calibration of the instrument with known gaseous species allows for quantification of the elements in the gas.

3.4.3 Density

Density measurements were taken using the Archimedes method (hydrostatic weighing) on calibrated scales. Measurements of samples weight were taken in air and in deionised water. The density of water at 22 °C is 0.998 g cm^{-3}. The volume of the sample, V_S, is derived from the mass of water displaced, M_w, and the density of the water, ρ_W by,

$$V_S = \frac{M_W}{\rho_W} \tag{16}$$

Then the density of the sample ρ_A is equal to the mass in air M_a divided by the V_S,

$$\rho_a = \frac{M_a}{V_S} \tag{17}$$

Additionally, the molar volume of a glass, V_m, can be calculated from the density by

$$V_m = M_m \rho_a \tag{18}$$

Where M_m is the molar mass of the total composition. Density measurements are used to compare the levels of crystallinity in the glass samples with heat treated samples.

3.5 Foaming and Melting Behaviour

3.5.1 Feed Expansion Tests

The aim of the Feed Expansion Test (FET) test is to determine the amount of foaming during melting of a feed, and the dynamics of foam growth and collapse to be applied to mathematical models of the cold cap (Hrma et al. 2010, 2018). Pressed pellets were prepared for the HLW-NG-Fe2, HLW-NG-Fe2-II and HLW-NG-Fe2-R feeds, at 13 mm in diameter and 1.5 g of batch. The pellets were held under 10 MPa pressure for 180 s. These pellets were then heated in an electric furnace with a viewport up to 1150 ℃, and images were taken with a camera at certain intervals, increasing in frequency when the volume expansion began. Images were then processed in Photoshop ® for the area of each pellet in the 2-D image, and the volume extrapolated assuming rotational symmetry. The volumes of the pellets were then normalised to the initial volume to provide FET curves. Averages of 3 FETs were taken for each of the feeds.

3.5.2 Evolved Gas Analysis

Evolved gas analysis (EGA) measures the quantity of gases evolving from a sample in a given temperature range, by simultaneous gas chromatography and mass spectrometry, described in section 3.4.2. The release rates of evolved gases were measured using a gas chromatograph and Agilent 6890/5973N mass spectrometric detector, at the Laboratory of Inorganic Materials, University of Chemistry and Technology, Prague. The equipment was connected to a silica tube inside a furnace containing each sample. The furnace heated the sample to 1150 ℃ at 10 K min^{-1} under He, flowing at 50 ml min^{-1}.

3.5.3 Thermal Analysis

Differential thermal analysis (DTA) was used in the analysis of the batch to glass process to determine the temperatures of key glass-forming reactions. By measuring the temperature difference between a sample and a reference material during controlled

heating, exothermic and endothermic reactions occurring during heating present themselves on a plot of temperature difference against time (or control temperature) (Bhadeshia 2002). Endothermic reactions, absorbing heat, present themselves as troughs on a DTA curve, while exothermic reactions, giving off heat, present as peaks, as shown in the example DTA curve in Figure 3.5.1. For example, melting requires heat input, therefore reactions associated with the melting of raw materials would present as an endothermic peak on a DTA curve (Boettinger et al. 2006).

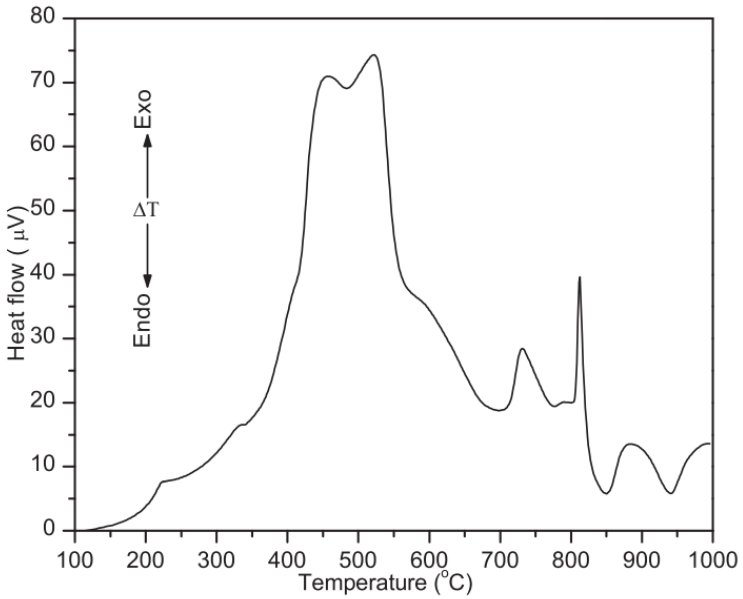

Figure 3.5.1. TG/DTA study on the oxidation of nickel concentrate (Yu and Utigard 2012).

Thermogravimetric Analysis (TGA) measures the mass loss of the sample compared to the reference sample during heating, and the derivative of this curve gives the evolution of gases at each temperature. In combination with the Evolved Gas Analysis these data were used to evaluate the total loss of mass from the feeds during melting, and the temperatures at which gases evolved.

Simultaneous TGA/DTA was performed on a TA Instruments SDT 650 DSC/TGA. For each run, calibrations of the alumina sample pans were performed, as well as a reference sample with a similar amount of Al powder to the sample of interest to be applied as a

buoyancy correction. Powdered feed samples were heated from 30 – 1150 ℃ and held at 1150 ℃ for 10 minutes. Processing of the spectra was performed in the TRIOS ® software.

For determination of the glass transition temperature, T_g, of each of the final glasses. DTA was performed on ~30 mg of powdered glass sample heated at a ramp rate of 5 ℃ min^{-1} up to 520 ℃ (50 ℃ higher than the expected T_g onset) then cooled to 200 ℃, before a second ramp to 1150 ℃, similar to the standard test method for assignment of the glass transition temperature by DSC (ASTM E1356-08 2014). Data processing to find T_g was performed in the TRIOS ® software, using the same procedure described in the ASTM standard (ASTM E1356-08 2014).

3.6 Structural Analysis

3.6.1 X-ray powder diffraction

X-ray powder diffraction (XRD) is a technique that identifies crystalline phases by the interplanar, *d*, spacings in the lattice by manipulating Bragg's Law:

$$2dsin\theta = n\lambda \tag{19}$$

Incident monochromatic X-rays, of known wavelength, λ, are diffracted by the sample and the constructive interference caused by X-rays that are in phase with the d-spacings are detected by a detector scanning through a range of possible angles, 2θ, as shown in Figure 3.6.1.

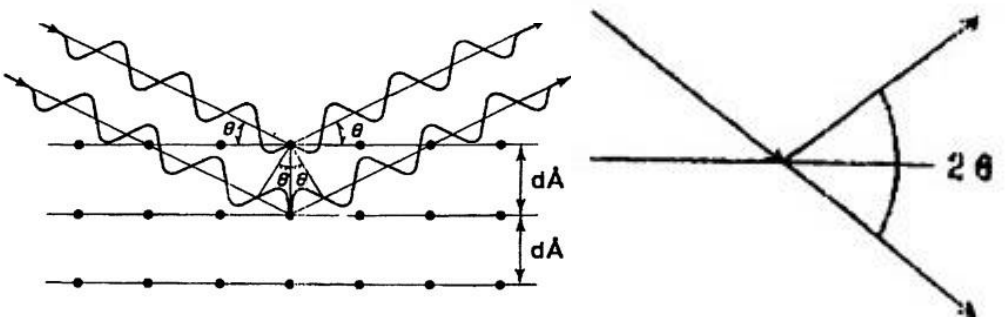

Figure 3.6.1. Schematic of Bragg's law showing incident X-rays interacting with the crystal lattice (Chatterjee 2001).

Using the PANalytical X'Pert Pro X-Ray Powder Diffractometer an incident beam of X-rays from a 40 kV and 40 mA, copper anode X-ray tube, of wavelengths λ = 1.540560 (Cu Kα1) Å and 1.544390 (Cu Kα2) Å, were incident on each sample. Finely ground samples were placed in circular disk sample holders in a sample changer, samples were rotated at 15 rpm to improve coverage of the sample and, therefore, improve the powder average. A mask was inserted between 5 and 20 mm depending on the size of the sample and divergence slits were inserted to optimise the peak resolution. Anti-scatter slits were also inserted to lower the background on the XRD data.

The diffractometer scanned between 5 º and 80 º 2θ giving the distribution of the characteristic angles. The pattern generated is a combination of diffraction patterns for all of the crystalline phases in a sample and any amorphous phase is given by a broad "hump" region due to random scattering of X-rays. Crystalline phases were identified using the International Centre for Diffraction Data (ICDD) (Gates-Rector and Blanton 2019) in the HighScore Plus analysis software (Degen et al. 2014). The samples were mixed with 5 wt% Si SRM:640c powder to compare the intensity of the Si diffraction pattern with the phases identified, allowing for quantification of the crystalline phases present as well as the remaining amorphous phase fraction (De La Torre, Bruque, and Aranda 2001)

3.6.1.1 Refinement of XRD patterns

Rietveld refinement (Rietveld 1969) is a method of least squares refinement of a calculated powder diffraction from a model crystal structure by comparison with observed powder diffraction data. Refined structural parameters include atomic coordinates, atomic site occupancies, and atomic displacement (temperature) factors, background parameters and peak shapes. Lattice parameters can also be refined by the method. In multiphase samples, comparisons of the refined scale factors for each phase can be used to determine phase proportions (Rietveld 1969; Young 1993).

The Rietveld refinement function, in the HighScore Plus analysis software (Degen et al. 2014), was used to refine the modelled diffraction patterns for each of the phases identified in the samples. ICDD references for the starting models used for each of the 1150 ℃ samples for which the patterns were refined, and the final lattice parameters are given in Appendix A Table 11. An example of the peak refinement is shown in Figure 3.6.2 showing the refined peak fit and residual. For each sample the global parameters for the background and shift in the pattern were refined, which are determined by the bulk sample properties. Where peak positions were well modelled, allowing for

determination of the unit cell parameters, the peak shapes were refined, which are a function of the domain size, stress/strain and defects, as well as the instrument geometry (Mccusker et al. 1999). A complete structural model was not achieved for the samples, refinement of the site occupancies values was hindered by the presence of a minimum of 2 phases in each sample along with amorphous component. Precise Rietveld refinement of the site occupancies for the crystalline phases identified was unattainable.

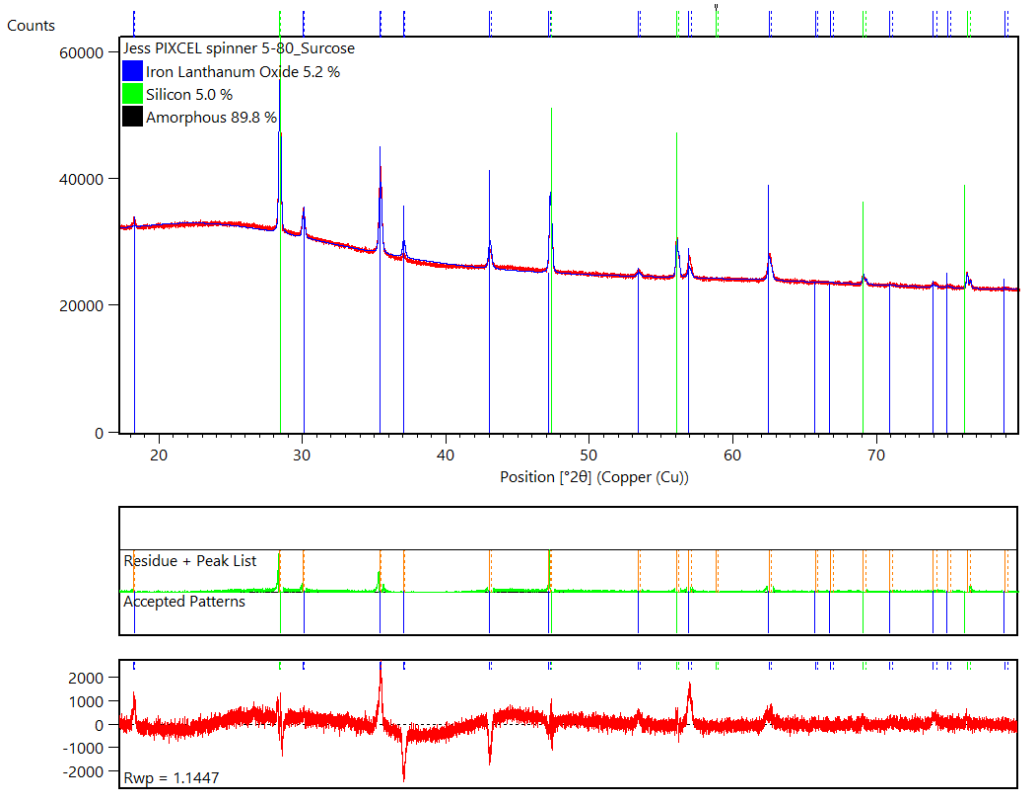

Figure 3.6.2. Refinement a diffraction pattern of a glass-ceramic sample containing Si powder standard. A phase identified as Fe-bearing spinel was fitted to the diffraction pattern, the residual of the fit is shown in the lower image.

3.6.2 Raman Spectroscopy

Raman spectroscopy exploits the phenomenon “Stokes-Raman Scattering” which gives the change in energy between an excited state of a molecule and its original state (Raman 1929). A laser light incident on the sample excites the vibrating molecules. When they return to their original state, the photon emitted may have a different energy than the original,

$$\Delta E = h(v_0 - v_1) \tag{20}$$

where ν_0 and ν_1 are the initial and scattered frequency respectively, and h is Planck's constant. If the frequency does not change the photon is emitted in with the same energy (elastic scattering). This is Rayleigh scattering, and occurs for most of the photons incident on the sample. However, those that do change in frequency (inelastic scattering) are scattered in all directions, they either have more or less energy than the original photon, corresponding to Anti-Stokes Raman scattering and Stokes Raman scattering, respectively, as shown in Figure 3.6.3. This modified spectrum represents the frequencies of the vibrational or rotational transitions of the molecules, which are specific to the individual bond and its vibrational modes (Chalmers & Dent, 1997).

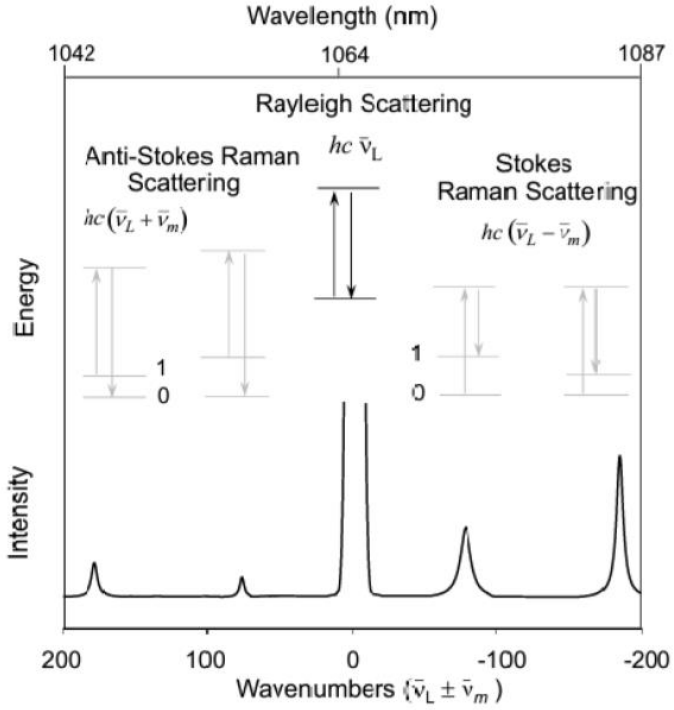

Figure 3.6.3. Energy level diagram clarifying the difference between Anti-Stokes Raman Scattering, Rayleigh Scattering and Stokes-Raman Scattering (Almieda & Santos, 2015).

The molecular polarizability is governed by the cloud of electrons, the dipole moment induced by an incident electric field (monochromatic laser), is a product of the molecule's polarizability and the strength of the electric field:

$$\mu = \alpha E\ r \quad (21)$$

where μ is the induced dipole moment and α is the molecular polarizability. When the molecules are displaced by this dipole moment and released, they perform superimposed vibrations of their normal modes. Each normal mode of a molecule has its own vibrational frequency. Once a spectrum of these vibrational frequencies is collected, the position of individual bands and the overall shape of the spectrum gives information on the molecules within the sample, their normal modes and the strength and size of the bonds between them (Almieda & Santos, 2015).

Raman spectroscopy is a non-destructive technique and samples are prepared as disks with a flat surface for analysis. For analysis of structural changes during melting, polished SoM samples, and glass samples for all HLW-NG-Fe2 and derivative feeds, were analysed with a Renishaw InVia Raman Spectrometer with a CCD detector, using a 532 nm laser at 10 mW power and X10 objective lens. Multiple Raman spectra were collected for each sample between 100 and 3000 cm^{-1} with up to 200 accumulations and an exposure time of 5-20 s. All spectra underwent a baseline correction, a 5^{th} order polynomial fluorescence correction, and a temperature and frequency dependent scattering intensity correction as described in (Neuville and Mysen 1996).

3.6.2.1 Sample validation

Point Raman spectra were collected on multiple areas of each of the samples in the SoM study. This was important to capture a wider sample size in the inhomogeneous, partially crystalline samples, quenched at 600, 800 and 1000 ℃. Averages of the multiple scans are displayed in this chapter for comparison between samples. This is still a limited sample size compared to methods of bulk characterisation such as XRD. An example of the variety between points in a sample is shown in the HLW-NG-Fe2-S 1000 ℃ spectra collected in Figure 3.6.4.

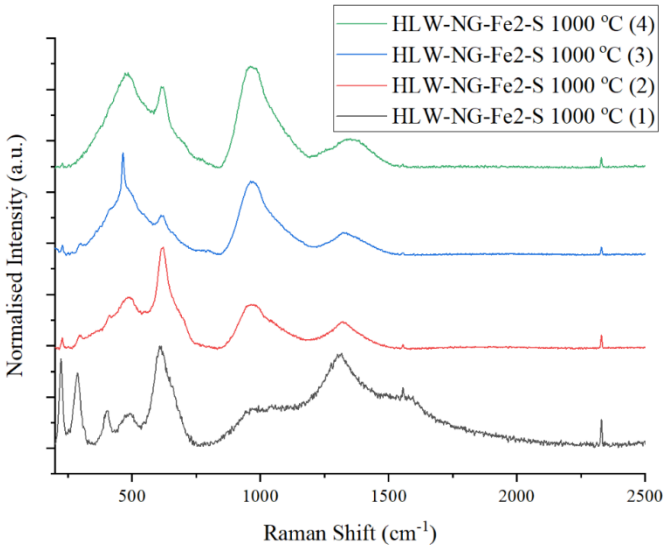

Figure 3.6.4. Four Raman spectra collated from different regions on the HLW-NG-Fe2-S sample quenched at 1000 ℃.

The HLW-NG-Fe2 and HLW-NG-Fe2-II original SoM study was performed in platinum crucibles, while the HLW-NG-Fe2-R SoM samples were melted in alumina crucibles. Raman spectra were collected on remelted HLW-NG-Fe2 and HLW-NG-Fe2-II samples in alumina crucibles to ensure they were structurally consistent with those melted in platinum, Figure 3.6.5. It was determined that any minor spectral differences between the samples was negligible compared to difference in spectra between multiple scans of the same sample.

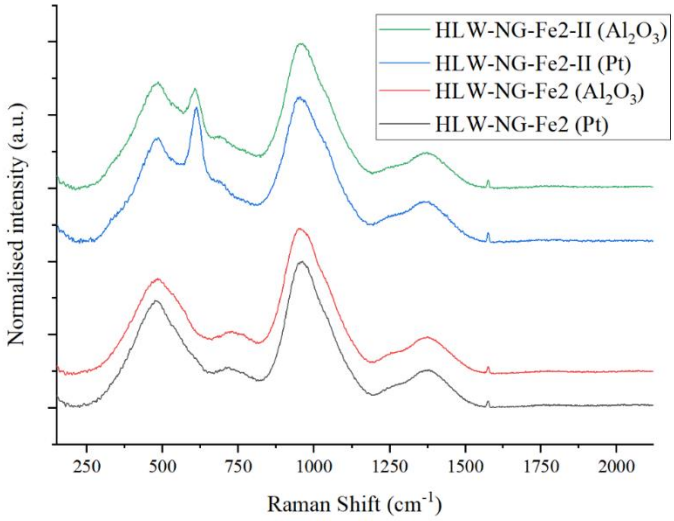

Figure 3.6.5. Raman spectra for HLW-NG-Fe2 and HLW-NG-Fe2-II samples melted in Pt and Al_2O_3 crucibles.

3.6.3 X-Ray Absorption Near Edge Spectroscopy (XANES)

3.6.3.1 X-ray Absorption Spectroscopy

X-ray Absorption Spectroscopy (XAS) studies the local structures of materials by examining energy shifts in core and valance electrons of individual elements in a compound (Belli et al. 1980; Chalmin, Farges, and Brown 2009). When incoming X-ray energy is equal to or greater than the binding energy of an electron the X-ray can be absorbed, and an electron liberated form the core of an atom. The relaxation of an electron into the hole created emits a characteristic photon, equal in energy to that of the energy difference between the two transition states. The spectra collected from the emission of these photons is the fluorescence XAS spectra (Turner 2017), the intensity of the X-rays transmitted through the sample, after interaction with the sample, creates the transmission XAS spectra (Henderson, De Groot, and Moulton 2014). The intensity of the transmitted electrons is given by Beer-Lambert's Law of X-ray intensity (Kelkar, Boushey, and Okos 2015):

$$\frac{I_T}{I_0} = e^{(-\mu x)} \tag{22}$$

Where I_T is the intensity of the beam after transmission through the sample at distance x, I_0 is incident X-ray energy. Rearranging for the absorption coefficient, μ, for X-ray energy, E, is given by,

$$\mu(\mathrm{E}) = \frac{-\ln\left(\frac{\mathrm{I_x}}{\mathrm{I_0}}\right)}{\mathrm{x}} \tag{23}$$

When the incident X-ray energy is equal to the binding energy of the core electron, there is a sharp rise in absorption, creating the absorption edge (Turner 2017). Transmission spectra are highly sensitive to the thickness of a sample, due to the attenuation length of less than 1 μm, and require a high concentration of absorber atoms. Fluorescence spectra are often collected for samples with a low concentration of the

absorber atoms (Henderson, De Groot, and Moulton 2014; Mastelaro and Zanotto 2018).

The Extended X-ray Absorption Fine Structure (EXAFS) portion of the absorption spectra, Figure 3.6.6, contains information on the final state of the generated photoelectron, and any neighbouring atoms will distort the outgoing spherical wave pattern of energies created (Mastelaro and Zanotto 2018), providing information on the local structure of the number and type of neighbouring atoms. The XANES region, Figure 3.6.6, contains the pre-edge and the main absorption edge. In transition metal absorbers these features contain information on the valance of the absorber atoms.

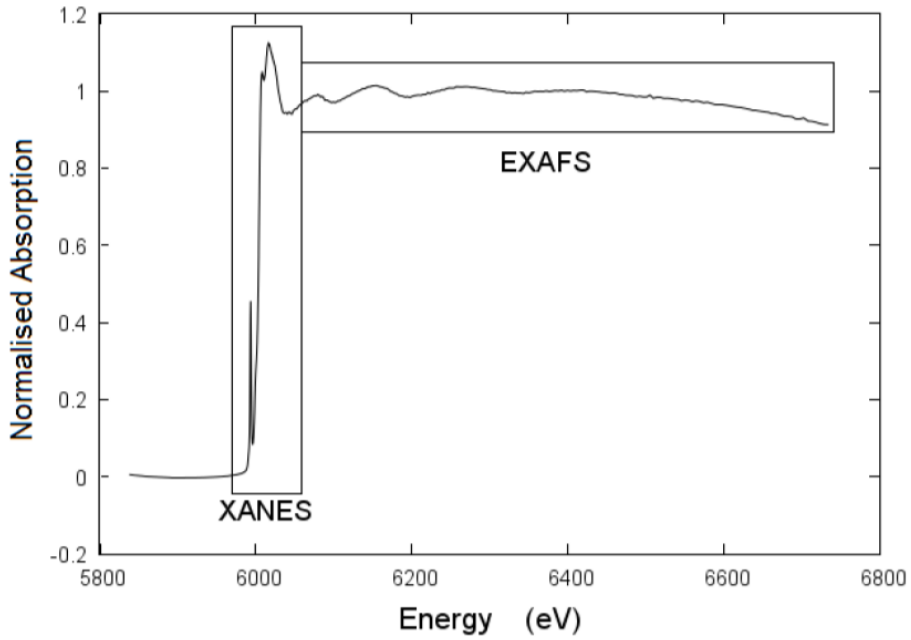

Figure 3.6.6. Example XAS of Cr K-edge (Turner 2017).

3.6.3.2 Synchrotron Radiation

Synchrotron X-ray sources are used for XAS due to the high X-ray flux and tunable energies required to probe specific elements (Luo and Zhang 2010). Synchrotron radiation is the name given to the electromagnetic radiation emitted by charged particles moving at relativistic velocities in a curved trajectory (Elder, Langmuir, and Pollock 1948; Ternov, Mikhailin, and Khalilov 1985). Synchrotron radiation is produced in

large accelerators, now called synchrotrons (Ternov, Mikhailin, and Khalilov 1985; Margaritondo 2017). In a modern synchrotron, electrons (or positrons) are produced and enter a linear accelerator, they are then circulated through a booster ring to increase the acceleration up to the order of GeV using bending magnets, and subsequently accelerated in the storage ring, held in a vacuum (Kulipanov 2007; Wille 1991; Wiedemann 2015, 815–17). A planar diagram of a typical third generation synchrotron is shown in Figure 3.6.7.

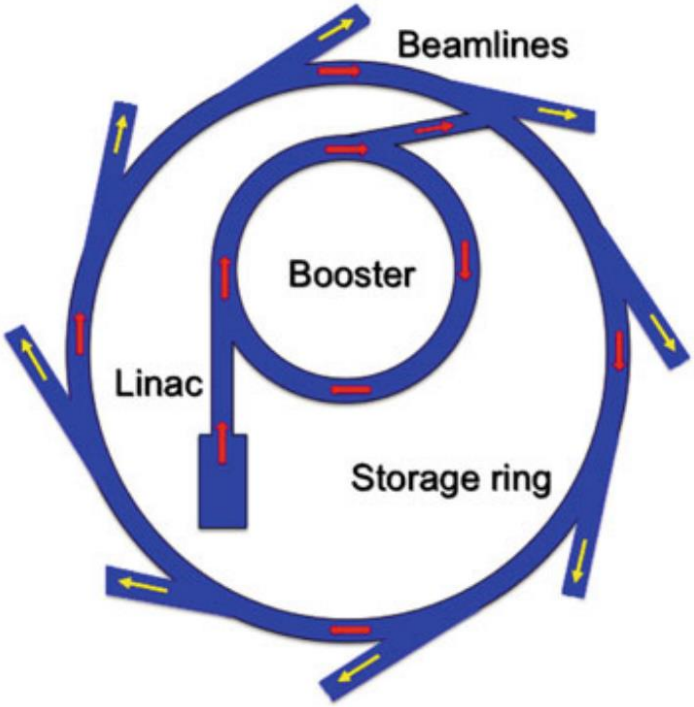

Figure 3.6.7. Schematic view of a synchrotron radiation facility (Balerna and Mobilio 2015).

Beamlines are situated at certain points on the storage ring, shown in Figure 3.6.7., exploiting the focussed path of the intense beam of deflected synchrotron radiation (Attwood, Halbach, and Kim 1985). This provides directional, tunable, high-flux X-ray sources for a wide range of analytical techniques including XRF, X-ray microscopy, XRD and XAS experiments and many more (Mao et al. 1988; Mino et al. 2018; Beckhoff et al. 2006; Cotte et al. 2010; Fiori et al. 2004). High-flux synchrotron

radiation makes it possible to explore elements in the X-ray Near Edge Absorption Spectroscopy region discussed in section 3.6.3.

3.6.3.3 Beamlines

The BM28 XMaS beamline is situated on a 6 GeV bending magnet on the ESRF third generation synchrotron source (Giuli et al. 2011; Luo and Zhang 2010; Mino et al. 2018). The beamline energy can be tuned within the range of 3 – 15 keV, the maximum achievable flux for a beam energy of 10 keV and beam dimensions 0.8 x 0.3 mm is ~5 x 10^{12} photons s^{-1} (S. D. Brown et al. 2001). The optical and experimental hutch at the BM28 XMaS beamline is shown schematically in Figure 3.6.8. A double-crystal Si (111) monochromator is situated 24.5 m from the source point. The rhodium coated toroidal mirror, curved to a radius of 5.5 km focusses the beam to a small tunable spot on the sample (S. D. Brown et al. 2001).

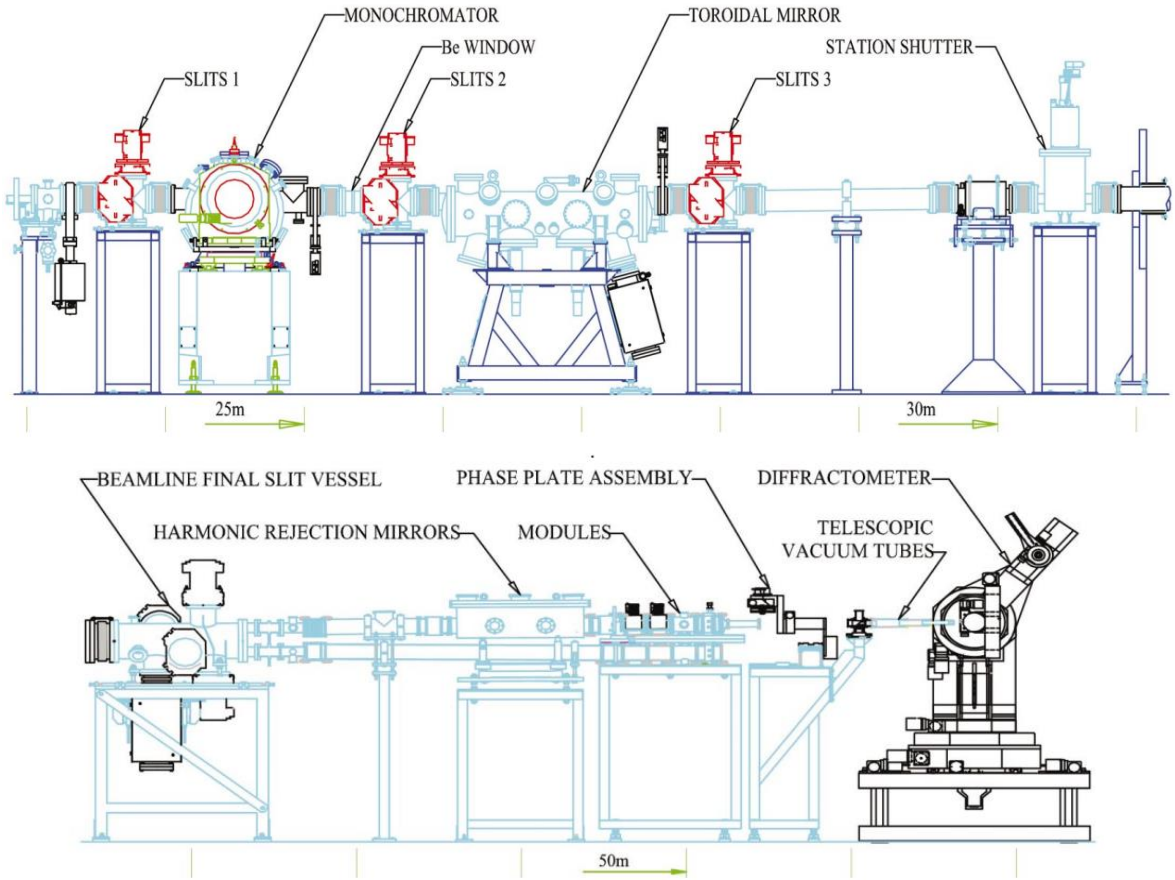

Figure 3.6.8. XMaS BM28 beamline optics hutch and experimental hutch.

The B18 Core XAS beamline is situated on a 3 GeV bending magnet on the Diamond Light Source third generation synchrotron source (Mino et al. 2018). The energy range of the beamline is 2.1 – 35 keV. The flux is on the order of 10^{11} photons s^{-1} (Dent et al. 2009). A Si(111) double crystal monochromator and a Si(311) double crystal monochromator allow for the low energy and high energy ranges to be reached, respectively. Beam focusing is achieved using a focussing mirror configuration consisting of toroidal mirrors with 38 mm radius, a 1.2 m chromium and platinum coated flat bent silicon collimator, and a monolithic chromium and platinum coated double toroidal mirror (Diaz-Moreno et al. 2018). The B18 beamline is a high-throughput beamline with continuous scanning and fast acquisition of the full energy range (Dent et al. 2009; Diaz-Moreno et al. 2018).

3.6.3.4 Experimental set up

HLW-NG-Fe2, HLW-NG-Fe2-II, HLW-NG-Fe2-S and HLW-NG-Fe2-G feeds were measured on the BM28 XMaS beamline at the European Synchrotron Radiation Facility (ESRF) in France (S. D. Brown et al. 2001), and the HLW-NG-Fe2-C, H and F feeds were collected at the B18 XAS beamline at the Diamond Light Source in the UK (Dent et al. 2009). Pressed pellets, 10 mm diameter and ~0.5 mm thick, were prepared of powdered glass samples mixed with cellulose acetate, at appropriate ratios to maximise the signal of the element. K-edge spectra of Fe, Cr, Mn and Ni were collected as well as L_{III}-edge Ce.

All spectra were collected in simultaneous fluorescence and transmission mode. Energy was selected using the Si (111) monochromator. Only Fe was present in the sample in sufficient quantities to attain useful transmission data. Spectra were collected ~150 eV before the absorption edge and up to 250 eV beyond the absorption edge. Energy calibration was performed for each sample element of interest using Fe, Mn, Cr, Ce and Ni foil. Resolutions of 0.15 eV over the pre-edge features was attainable at the BM28

beamline at ESRF and steps of 2 eV were used before and after the edge. At the B18 beamline at Diamond, 0.3 eV steps were available for the entire spectra. Up to 5 repeat measurements were performed at the BM28 beamline at ESRF and up to 20 repeat measurements were attainable at the B18 beamline at Diamond, due to the high throughput rate, improving signal to noise. Reference materials for each likely oxidation state were measured at each beamline, Cr_2O_3, $Na_2Cr_2O_7$, Fe_2O_3, FeO, NiO, Mn-foil, MnO, MnO_2, Mn_2O_3, CeO_2, $Ce_2(C_2O_4)_3$, for iron further reference materials, Fe_3O_4, berlinite, grandidierite and aegirine were measured for different iron coordination.

3.6.3.5 Analysis of collected spectra

For all spectra collected, processing was performed in Athena ® (0.9.26) (Ravel and Newville 2005). Processing of each scan included a deglitching, background corrections, normalisation, alignment with the standards, and merging of multiple scans, in that order. The integrated self-absorption correction was applied to the fluorescence spectra of the Fe edges.

The Fe K-edge XANES spectra provides information on the $1s \rightarrow 3d$ (pre-edge), $1s \rightarrow 4s$ (shoulder), and $1s \rightarrow 4p$ (edge crest) transitions (Berry et al. 2003; Wilke et al. 2001). The energy separation between the $1s \rightarrow 3d$ transition (pre-edge) and the absorption edge is the key determinant for the ratio of Fe^{3+} to Fe^{2+} in a sample: the lower the energy of the pre-edge the more Fe^{2+} in the sample (Berry et al. 2003; Wilke et al. 2001). Transitions for tetrahedrally coordinated Fe are more intense than for octahedrally coordinated Fe (Berry et al. 2003). For processing of Fe K-edge data, spectra were calibrated using the standard materials and known edge positions. The pre-edge feature was fitted to a tangent and then deconvoluted with the minimum number of Gaussian components to achieve a $R^2 > 0.95$.

Deconvolution of the pre-edge was performed in OriginPro ® graphing software. An example of the pre-edge peak deconvolution is shown in Figure 3.6.9 for the HLW-NG-

Fe2-S 600 °C sample, and for the HLW-NG-Fe2-S series in Figure 3.6.10. First, a tangent was subtracted from the baseline to the absorption edge, and then multiple peaks were fitted beneath the tangent subtracted data (the minimum number of peaks was used to achieve an R^2 value of 0.95 or greater). The pre-edge fits were plotted and compared with the standards for oxidation state and coordination (Wilke et al. 2001).

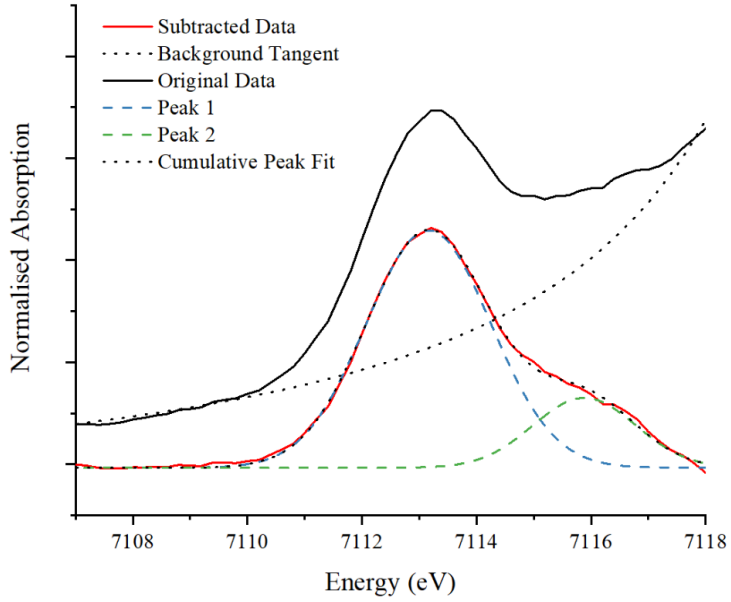

Figure 3.6.9. Example pre-edge fitting for HLW-NG-Fe2-S 600 °C sample.

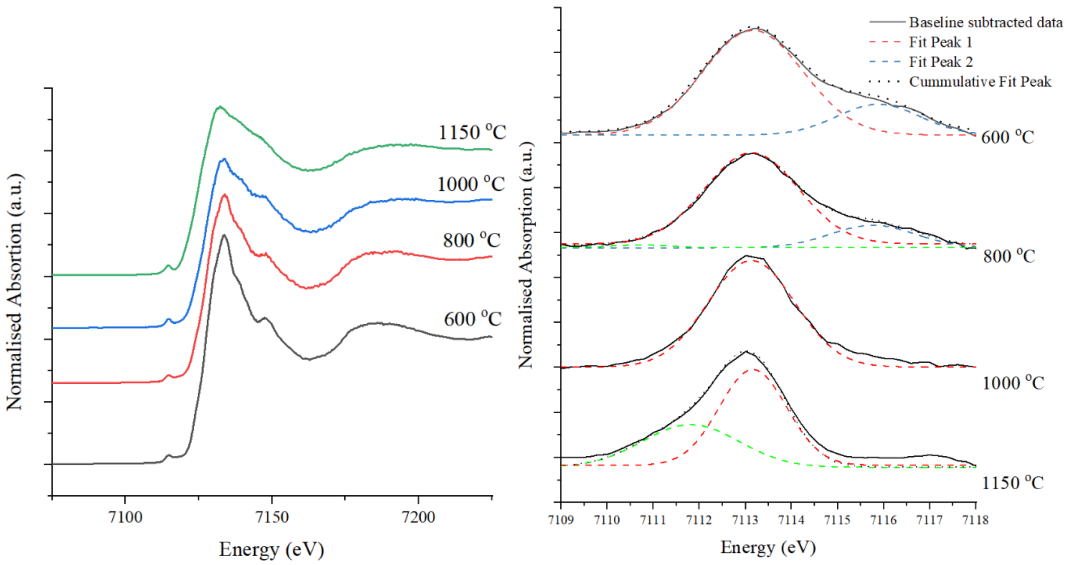

Figure 3.6.10. (left) Fe K-edge XANES for HLW-NG-Fe2-S quenched at 600, 800, 1000 and 1150 °C. (right) Fitted pre-edges for HLW-NG-Fe2-S spectra.

The manganese valence state was determined by the position of the absorption edge, as near edge features can be shielded by the nuclear charge of valence electrons (Chalmin, Farges, and Brown 2009). For processing of Mn K-edge data, spectra were calibrated by calibrating the standards to the referenced literature and then shifting each spectrum by the same energy. The absorption edge in Mn spectra shifts linearly with the oxidation state (Chalmin, Farges, and Brown 2009; McKeown et al. 2003). The first inflection point in each of the spectra was plotted against the first inflection point of each of the standards and the known oxidation state.

For processing of Ce L_{III} and Cr K edges, spectra were calibrated by calibrating the standards to the referenced literature and shifting each spectrum by the same amount. The linear combination fitting (LCF) function in Athena ® (Cui et al. 2014; Ma et al. 2015) was used to fit each of the standards to each spectra to determine the proportion of the elements in each oxidation state. An example LCF for a Cr K-edge spectra is shown in Figure 3.6.11 using standard data.

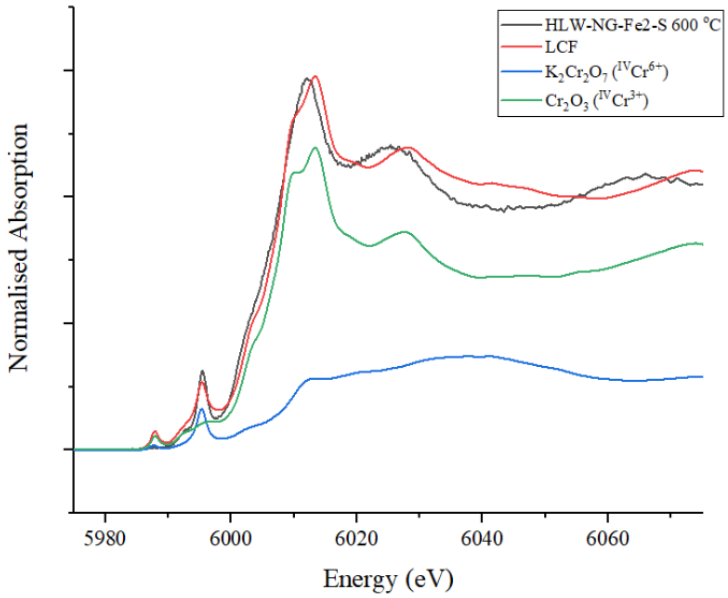

Figure 3.6.11. Example linear combination fitting of the Cr K-edge in the HLW-NG-Fe2-S 600 °C sample with the $^{IV}Cr^{6+}$ and $^{IV}Cr^{3+}$ reference spectra.

The Ni K-edge spectra all contained high levels of noise due to the low amount of Ni present in the feed. Little XANES work has been published on the Ni K-edge in glasses and glass-ceramic materials (Tirez et al. 2011; Kuzmin, Purans, and Rodionov 1997; Galoisy et al. 2001). Throughout melting and between the different reductants, the Ni oxidation state, Ni^{2+}, and coordination did not appear to change, but with limited resolution it is difficult to be certain. For this reason, the Ni K-edge data were not further processed.

3.6.4 ^{57}Fe Mössbauer Spectroscopy

^{57}Fe Mössbauer spectroscopy is a technique used to probe the local structure and environment of Fe in a solid matrix. An in-depth quantum mechanical approach to understanding the theory and development of ^{57}Fe Mössbauer spectroscopy is provided in the literature (Tuthill et al. 1967; Fultz 2012; Johnson, Ridout, and Cranshaw 1963). The key features of the theory are outlined in this section, particularly focussing on those that allow for appropriate sample selection and preparation and interpretation of the data collected.

The Mössbauer effect is the recoil-free emission and resonant absorption of γ-rays in a solid matrix (Kurkjian 1970; Bearden 1963; Fultz 2012; Wertheim 1964). It can be performed with numerous isotopes (Fultz 2012; Kurkjian 1970), but for this study we will focus on ^{57}Fe Mössbauer spectroscopy. In principle, an isolated, free atom, emitting a γ-ray recoils with kinetic energy:

$$R = \frac{{E_0}^2}{2Mc^2} \tag{24}$$

Where E_0, is the energy of the transition within the nucleus and M is the mass of the nucleus. (Wertheim 1964). This recoil energy is much smaller than the γ-ray energy, so in a free atom the energy of the nuclear transition is $\gg$ R and no resonant absorption occurs (Kurkjian 1970). However, in a solid matrix, the essentially recoil-free state,

resonant absorption can occur, by taking into account the macroscopic mass of the entire crystal rather than the singular atom (Kurkjian 1970; Wertheim 1964; Solomatova 2017). The recoil-free resonant absorption of γ-rays in ^{57}Fe Mössbauer spectroscopy gives rise to detection of hyperfine interactions, caused by interactions between the electrons and the nucleus of the absorber atom.

In practise, a beam of γ-rays generated by a vibrating source is incident on a solid sample, and the intensity of the beam transmitted through the sample is measured by a detector (I. W. Donald 2015). The vibrating source gives rise to Doppler shifting effects. At velocities that correspond to the resonant energy levels of the samples material some of the γ-rays are absorbed giving rise to a drop in the measured intensity and therefore a change in the spectrum (I. W. Donald 2015). An unstable ^{57}Co atom is used as a γ-ray emitter in ^{57}Fe Mössbauer spectroscopy. The ^{57}Co nucleus absorbs and inner-shell electron, forming an ^{57}Fe nucleus in its first excited state, and emits a 122-keV γ-ray. The excited ^{57}Fe nucleus decays with a half-life of ~141 s by the emission of a 14.41 keV γ-ray (Fultz 2012; Kurkjian 1970).

A Mössbauer spectrum is obtained by counting the number of γ-ray photons passing through a sample as a function of the γ-ray energy, at energies where the resonant absorption occurs, there are dips in the Mössbauer spectrum (Fultz 2012).

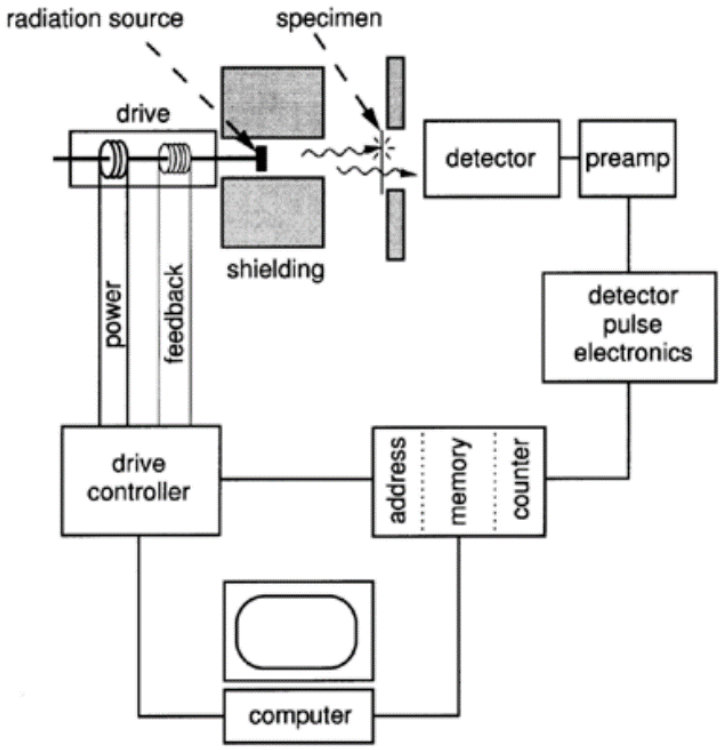

Figure 3.6.12. Generic set-up for transmission ^{57}Fe Mössbauer spectrometer (Stevens, Travis, and DeVoe 1972).

The velocity of the vibrating source atom determines the range of energies that can be observed (Fultz 2012; Kurkjian 1970). Five measurable quantities are available from ^{57}Fe Mössbauer spectroscopy, the recoil free fraction, *f*, and three hyperfine interactions, the isomer shift (or centre shift), CS, the quadrupole splitting (QS), the hyperfine magnetic splitting H and the Linewidth, Γ (Fultz 2012).

For analysis of the structure and redox state of the iron during melting, samples heated to 600 ℃, 800 ℃, 1000 ℃ and 1150 ℃ for each of the feeds were powdered for room temperature ^{57}Fe Mössbauer spectroscopy. 14.4 keV γ-rays from decay of 25 mCi ^{57}Co source in Rh matrix oscillated at constant acceleration and were absorbed by the sample. ^{57}Fe Mössbauer spectra were collected in the velocity range of ±12 mm s^{-1} relative to α-Fe. Signal to noise was improved with collection times of up to two weeks. Recoil software was used to fit Lorentzian doublets and sextets to the data. The assumption was made that the recoil-free fraction ratio $f(Fe^{3+}/Fe^{2+})=1.0$.

3.7 Morphological Analysis

3.7.1 Scanning Electron Microscopy/Electron Dispersive X-ray Spectroscopy

Scanning electron microscopy (SEM) provides high resolution images of surface microstructure. Coupled with Electron Dispersive X-ray Spectroscopy, the technique can map both morphological and elemental changes on the surface of a sample. Electrons are used as a probe in SEM and EDX. They are generated by inducing a voltage across a tungsten tip. Electrons are then accelerated down a column towards the sample and focussed by lenses, all within a vacuum chamber. The electrons interact with the sample in a 3D interaction volume, shown in Figure 3.7.1, which includes electrons from inelastic collisions with K-orbital electrons in the sample (secondary electrons), elastic collisions with the atoms just below the surface (backscattered electrons) and X-rays from excited atoms further into the sample.

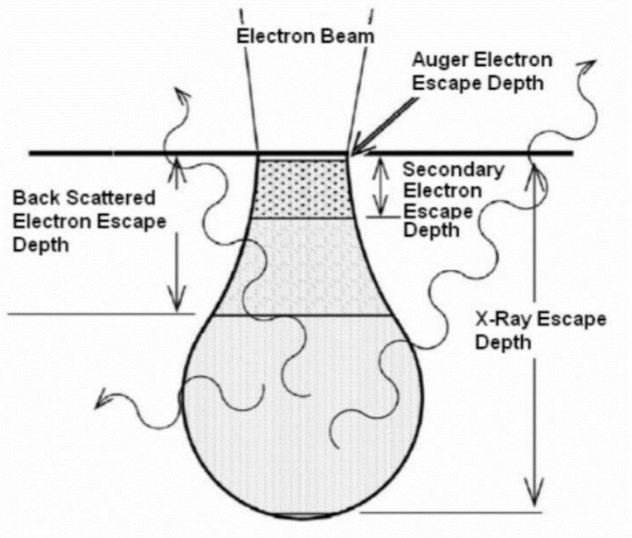

Figure 3.7.1. Interaction volume within a sample for secondary and backscattered electrons and X-rays in SEM analysis (Hafner & Hafner, 2007).

Secondary electrons (SEs) give topological detail of the surface of the sample, and are detected by a positive biased faraday cage to the side of the sample. The intensity of

backscattered electrons (BSE) is dependent on the atomic number of the atoms within the sample, therefore can be used to give elemental and phase information. BSEs are collected by a detector around the lens. The intensity of electrons is processed to give a greyscale image for SEs or BSEs, giving different perspectives of the same area of the sample.

In order to get an accurate surface analysis, the samples were prepared by mounting in Conductive Cold Mount epoxy resin and hardener for 24 hours, inside a cylindrical mould. The cylinders were removed and the samples ground using SiC grinding paper, from grit size 400 to 2500, until the sample surface was entirely flat. The surface was then polished down to 1-micron with CeO_2 polish. The sample was attached to an aluminium stub with Agar silver paint, from the sample to the base, to ensure conduction of electrons to the base. It was then coated with carbon up to a maximum of 26 nm thick, to ensure conductivity. The FEI Quanta 3D FEG/FIB ESEM was used for analysis of glass samples, SoM samples and the LSM sample. EDX provides collection, and spatial resolution of elemental data (Falk 2004; Maleki et al. 2017).

In the interaction volume, an incident electron of the correct energy ejects a 1s shell electron from the atom, causing a 2p shell electron to drop into its place and release a characteristic X-ray photon of the element. Characteristic X-rays from within the sample are collected by the single silicon detector, and then spatially resolved to a produce quantitative elemental analysis at different regions of the sample. Both point elemental analysis and the collection of elemental maps were employed on the samples in this study, analysed in the Aztec software platform.

3.7.2 X-Ray CT

X-ray CT is based on Beer-Lambert's Law of X-ray intensity, as discussed in section 3.6.3.1, when passing through an object (Kelkar, Boushey, and Okos 2015). The total spectrum attenuation, μ, for X-ray energy, E, is given by:

$$\mu = \rho\alpha\frac{Z^k}{E^l} + \beta\rho \quad (25)$$

Where ρ is density, $\rho\alpha\frac{Z^k}{E^l}$ is the photoelectric absorption term, α is the photoelectric constant and Z is the atomic number of the absorption term and $\beta\rho$ is the Compton Scattering term. By mapping the X-ray densities transmitted through the sample in 2D images slices throughout an axis of the sample a 3D model of the sample can be reproduced in greyscale. This is useful for "seeing inside" LSM samples, investigating bubble sizes and morphologies and observing different densities of material in the feed-to-glass transition.

A section of the HLW-NG-Fe2-II LSM sample was carefully broken apart from the rest, to produce a suitably sized sample for X-ray CT that contains all layers of the cold cap within the sample. The sample represents about ½ of the entire sample, it is assumed that the sample generally has rotational symmetry about the vertical axis. A whole LSM sample had a diameter of 10 cm and a height ~ 3-4 cm.

X-ray CT was performed at the Henry Royce Institute (HRI) University of Manchester, UK. Samples, inside a plastic box with foam supporting the sample, were loaded into the Nikon Xtek XTH225kV X-ray CT, with a maximum power of 225 W, and Varian 4030, 14-bit, 2300 x 3200 detector. Both the plastic and foam had very low X-ray attenuations and therefore did not appear in any of the scans. X-ray CT scans were taken with a minimum pixel size of 0.027 mm^2 throughout the sample, at a X-ray power of 190 kV and 105 μA.

3.7.3 Image Analysis

Analysis of the X-ray CT images was performed for the HLW-NG-Fe2-II portioned sample. For each sample a stack of 2D X-ray images were provided that form the 3D image. For each of the stacks of images a global scale was applied using the Scale

function in ImageJ ®, allowing quantification of volumes and areas using direct values. Various noise filters were used on the images leading to some smaller bubbles being excluded as they could not be segregated from the noise in the image. Best efforts were made to remove noise without compromising the bubble count. The limit of detection on bubbles was also limited by the size of 1 voxel (a 3D pixel) which was 27 μm^3.

Thresholding of the images allowed segregation of the gas and condensed phase. The condensed phase in the LSM images were combinations of feed, glass and the intermediate feed-to-glass transition. Segregation was difficult due to the various densities causing a continuum of contrasts in the condensed phase. Less dense areas of the condensed phase, particularly where there was mostly feed present, had overlapping contrast with some of the bubbles. In order to compare the results between samples the same greyscale threshold was used throughout, carefully balancing the small bubble count and noise contributions. Bubble count and size per scan image was collected via the measure and analyse function, giving a distribution of the bubbles in 2D in the area of each image. The final macro used is given in Appendix A, M1.

From the stack of 2D images, the "Measure and Analyse" function in ImageJ generated data on the bubble count and shape for each image. From this, distributions and morphology of bubbles can be described as a function of depth in the cold cap. All of the steps described were automated by ImageJ so the entire stacks of images could be processed in the same way, free from user bias. Once bubbles were isolated, a 3D reconstruction of just the bubbles was generated. This allowed for measurements of bubble volumes and positions in 3D space.

3.8 Glass Product Testing

As described in Chapter 2, section 2.3.3, candidate glasses for the WTPs are subject to stringent contract limits to ensure that the waste glass compositions are suitable for processing in the melters and the final glass products are suitable for long-term immobilisation of the radioactive waste. The following sections describe two of the tests performed on the final glasses to ensure they meet the standards outlined in section 2.3.3, the standard test methods were followed where practical. The other tests performed in this work was analysis of the redox states of iron in the final glasses, performed using ^{57}Fe Mössbauer spectroscopy, described in section 3.6.4, and the measurement of glass transition temperature, T_g, values of the glasses by DTA, described in section 3.5.3, for an indication of the glass viscosity.

3.8.1 Product Consistency Test-B

The Product Consistency Test-B (PCT-B) method, as defined by the ASTM (ASTM C1285-21 2021), is employed to assess the chemical durability of nuclear waste glasses and glass ceramics. The test involves static leaching of glass powders over the course of a 7-day test at 90 ℃. The protocol involved powdered glass samples, sieved between 100 and 200 mesh (0.15 mm to 0.075 mm), washed and dried. Triplicates of each sample were placed in DI water, at a ratio of 10 ml to 1 g of sample, resulting in a surface area to volume ratio of 2000 m^{-1}. The samples were sealed in TFE-fluorocarbon vessels, in an oven at 90 ± 2 ℃ for 7 days ± 2 %. 3 “blank” samples containing only DI water were also placed in the oven at the same time. Measurements of liquid mass, sample mass and pH were taken before and after the 7-day test. Once removed from the oven, the remaining leachate samples, after the pH measurement, were filtered, and 10 ml of the leachate was sampled and acidified with 1 % HNO_3 for analysis by ICP-OES, to determine the concentration of Al, B, Ca, Cr, Fe, Li, Mg, Mn, Na, Ni, P, Pb, S, Si, Sr, and Zr.

Elemental concentration in the leachate samples were collected on a SPECTROGREEN ICP-OES, similarly to ICP-MS described in section 3.4.2. However, instead of utilizing MS on the ions created by the ICP, the spectral emission of the excited ions returning to ground state is measured by optical emission spectroscopy, in a typical spectral range of 165-1800 nm (Tyler 2001). The typical set-up of the OES is shown in Figure 3.8.1.

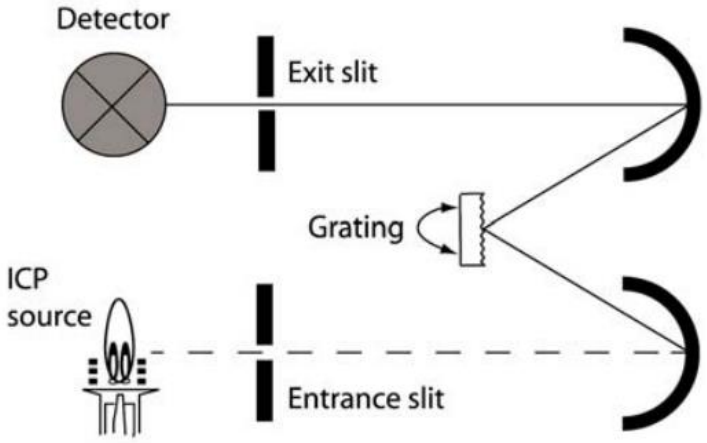

Figure 3.8.1. Typical sequential ICP-OES (Tyler 2001).

The SPECTROGREEN ICP-OES instrument was calibrated using a blank (1 % nitric acid), and 5 and 10 ppm standards of the elements Al, B, Cr, Fe, Li, Mn, Ni, Pb, Si, Sr and Zr, and 12.5 and 25 ppm standards of the elements Ca, Mg, Na, P and S. The plasma power of the instrument was 1150 W with a coolant flow of 13 L min^{-1}. The auxiliary flow and nebuliser flow were both 0.8 L min^{-1} with a sample flow rate of 2 ml min^{-1}.

The ICP-OES values for the leachate samples were corrected for the blank samples, and the test response was determined to be the values which were greater than 3 standard deviations from the blank sample values for each element. The normalised release of the elements were calculated by averaging the concentrations of the elements in the leachate solutions measured by ICP-OES and normalising them to the measured quantities of the element in the glasses measured by XRF, section 3.4.1, or ICP-MS, section 3.4.2, (for B and Li).

3.8.2 Heat Treatment

To determine whether the samples were within the crystal tolerance limit of <1 vol% at 950 °C (Matlack et al. 2012; Kruger et al. 2009; Matlack, Kot, et al. 2015), 10 g of each of HLW-NG-Fe2, HLW-NG-Fe2-II and R glasses were subject heated to 950 °C at 10 °C min^{-1} in an electric furnace and held for 24 hours. Samples were removed at temperature and left to cool. Density measurements were taken for each of the samples, as in section 3.4.3 and then portions of the samples were milled for determination of phase percentage in wt% by XRD, as in section 3.6.1. Using the wt% of crystalline phase in the sample, M_C, and the density of the phase, ρ_C, both determined by refinement of the XRD patterns the vol% of crystallinity, V_C, was determined by:

$$V_C = \frac{M_C}{\rho_C} \tag{26}$$

This was verified by comparing the density of the heat-treated sample to the un-heat-treated glass sample, to compare the volume change due to increased crystallinity. For selected samples, SEM/EDX, section 3.7.1, was also performed to investigate the morphology and elemental composition of the crystals formed.

3.9 References

Almieda, R. M. and Santos. L. F. (2015) 'Raman Spectroscopy of Glasses.' In Modern Glass Characterisation, edited by Mario Affatigato, 125–63. Hoboken, New Jersey (United States): The American Ceramic Society and John Wiley & Sons.

Ammann, A. A. (2007) 'Inductively coupled plasma mass spectrometry (ICP MS): a versatile tool.' Journal of Mass Spectrometry, 42. pp. 419–427.

ASTM. (2014) 'Standard Test Method for Assignment of the Glass Transition Temperatures by Differential Scanning Calorimetry.' E1356-08. United States. https://compass.astm.org/document/?contentCode=ASTM%7CE2602-22%7Cen-US (Accessed 05 September 2022)

ASTM. (2021) 'Standard Test Methods for Determining Chemical Durability of Nuclear, Hazardous, and Mixed Waste Glasses and Multiphase Glass Ceramics: The Product Consistency Test (PCT)' C1285-21. United States. https://www.astm.org/c1285-21.html (Accessed 22 July 2022)

Attwood, D., Halbach, K. and Kim, K. J. (1985) 'Tunable coherent X-rays.' Science, 228(4705). pp. 1265–1272.

Balerna, A. and Mobilio, S. (2015) 'Introduction to Synchrotron Radiation.' in S. Mobilio, F. Boscherini and C. Meneghini (eds.), 'Synchrotron Radiation: Basics, Methods and Applications' (pp. 1–799). Heidelberg, (Germany): Springer Berlin.

Bearden, A. J. (1963) 'The Mössbauer effect.' Physics Today, 16(12). pp. 46–48.

Beckhoff, B., Kanngießer, B., Langhoff, N., Wedell, R. and Helmut, W. (2006) 'Handbook of Practical X-Ray Fluorescence Analysis.' Heidelberg, (Germany): Springer Berlin.

Bell, A. M. T., Backhouse, D. J., Deng, W., Eales, J. D., Kilinc, E., Love, K., Rautiyal, P., Rigby, J. C., Stone, A. H., Vaishnav, S., Wei-Addo, G. and Bingham, P. A.

(2020) ‘X-ray fluorescence analysis of feldspars and silicate glass: Effects of melting time on fused bead consistency and volatilisation.’ Minerals, 10(5). pp. 1–17

Belli, M., Scafati, A., Bianconi, A., Mobilio, S., Palladino, L., Reale, A. and Burattini, E. (1980) ‘X-ray absorption near edge structures (XANES) in simple and complex Mn compounds.’ Solid State Communications, 35(4). pp. 355–361.

Berry, A. J., O’Neill, H. S. C., Jayasuriya, K. D., Campbell, S. J. and Foran, G. J. (2003) ‘XANES calibrations for the oxidation state of iron in a silicate glass.’ American Mineralogist, 88(7). pp. 967–977.

Bhadeshia, H. K. D. H. (2002) ‘Thermal Analysis Techniques.’ University of Cambridge, Materials Science & Metallurgy. Available at: www.msm.cam.ac.uk/phase-trans/2002/Thermal1.pdf (Accessed: 26 July 2022).

Bickford, D. F., Hrma, P. and Bowan, B. W. (1990) ‘Control of Radioactive Waste Glass Melters: II, Residence Time and Melt Rate Limitations.’ Journal of the American Ceramic Society, 73(10). pp. 2903–2915.

Boettinger, W. J., Kattner, U. R., Moon, K.-W. and Perepezko, J. H. (2006) ‘NIST Recommended Practice Guide: DTA and Heat-Flux DSC Measurements of Alloy Melting and Freezing.’ Elsevier, Kidlington, -1 Available at: https://tsapps.nist.gov/publication/get_pdf.cfm?pub_id=901091 (Accessed: 26 July 2022).

Brouwer, P. (2010) ‘Theory of XRF.’ Almelo: PANalytical B.V. (Netherlands).

Brown, S. D., Bouchenoire, L., Bowyer, D., Kervin, J., Laundy, D., Longfield, M. J., Mannix, D., Paul, D. F., Stunault, A., Thompson, P., Cooper, M. J., Lucas, C. A., Stirling, W. G. (2001) ‘The XMaS beamline at ESRF: Instrumental developments and high resolution diffraction studies.’ Journal of Synchrotron Radiation, 8(6). pp. 1172–1181.

Chalmin, E., Farges, F. and Brown, G. E. (2009) ‘A pre-edge analysis of Mn K-edge XANES spectra to help determine the speciation of manganese in minerals and glasses.’ Contributions to Mineralogy and Petrology, 157(1). pp. 111–126.

Chatterjee, A. K. (2001) ‘X-Ray Diffraction.’ In V. S. Ramachandran & J. J. Beaudoin (eds.), ‘Handbook of Analytical Techniques in Concrete Science and Technology.’ William Andrew Inc. Norwich, NY. (United States). pp. 275–332.

Corzo, R., Hoffman, T., Weis, P., Franco-Pedroso, J., Ramos, D. and Almirall, J. (2018) ‘The use of LA-ICP-MS databases to calculate likelihood ratios for the forensic analysis of glass evidence.’ Talanta, 186. pp. 655–661.

Cotte, M., Susini, J., Dik, J. and Janssens, K. (2010) ‘Spectroscopy for Art Conservation : Looking Back.’ Accounts of Chemical Research, 43(6), pp. 705–714.

Cui, D., Zhang, P., Ma, Y., He, X., Li, Y., Zhang, J., Zhao, Y. and Zhang, Z. (2014) ‘Effect of cerium oxide nanoparticles on asparagus lettuce cultured in an agar medium.’ Environmental Science: Nano, 1(5), pp. 459-465.

De La Torre, A. G., Bruque, S. and Aranda, M. A. G. (2001) ‘Rietveld Quantitative Amorphous Content Analysis.’ Journal of Applied Crystallography 34 (2). pp. 196–202.

Degen, T., Sadki, M., Bron, E., König, U. and Nénert, G. (2014) ‘The high score suite. Powder Diffraction.’ Cambridge University Press. 29(S2). pp. S13–S18.

Deng, W., Wright, R., Boden-Hook, C. and Bingham, P. A. (2018) ‘Melting behavior of waste glass cullet briquettes in soda-lime-silica container glass batch.’ International Journal of Applied Glass Science, 10. pp. 125–137.

Dent, A. J., Cibin, G., Ramos, S., Smith, A. D., Scott, S. M., Varandas, L., Pearson, M. R., Krumpa, N. A., Jones, C. P. and Robbins, P. E. (2009) ‘B18: A core XAS

spectroscopy beamline for Diamond.' Journal of Physics: Conference Series, 190. 012039.

Diaz-Moreno, S., Amboage, M., Basham, M., Boada, R., Bricknell, N. E., Cibin, G., Cobb, T. M., Filik, J., Freeman, A., Geraki, K., Gianolio, D., Hayama, S., Ignatyev, K., Keenan, L., Mikulska, I., Mosselmans, J. F. W., Mudd, J. J. and Parry, S. A. (2018) 'The Spectroscopy Village at Diamond Light Source.' Journal of Synchrotron Radiation, 25(4). pp. 998–1009.

Dixon, D. R., Hall, M. A., Lang, J. B., Cutforth, D. A., Stewart, C. M. and Eaton, W. C. (2022) 'Retention analysis from vitrified low-activity waste and simulants in a laboratory-scale melter.' Ceramics International, 48(5). pp. 5955–5964.

Dixon, D. R., Schweiger, M. J., Riley, B. J., Pokorný, R. and Hrma, P. R. (2015) 'Temperature Distribution within a Cold Cap during Nuclear Waste Vitrification.' Environmental Science and Technology, 49(14). pp. 8856–8863.

Donald, I. W. (2015) 'Waste immobilisation in glass and ceramic based hosts.' West Sussex, (UK): John Wiley & Sons, Ltd.

Elder, F. R., Langmuir, R. V. and Pollock, H. C. (1948) 'Radiation from electrons accelerated in a synchrotron.' Physical Review, 74(1). pp. 52–56.

Falk, L. K. L. (2004) 'Imaging and microanalysis of liquid phase sintered silicon-based ceramic microstructures.' Journal of Materials Science, 39(22). pp. 6655–6673.

Fiori, F., Albertini, G., Girardin, E., Giuliani, A., Manescu, A. and Rustichelli, F. (2004) 'Neutron and synchrotron radiation non-destructive methods for the characterisation of materials for different applications.' Journal of Alloys and Compounds, 382(1–2). pp. 39–45.

Fultz, B. (2012) 'Mössbauer Spectrometry.' In E. N. Kaufman (ed.), 'Characterisation of Materials.' Hoboken, MJ (United States): John Wiley & Sons, Ltd.

Galoisy, L., Cormier, L., Calas, G. and Briois, V. (2001) ‘Environment of Ni, Co and Zn in low alkali borate glasses: Information from EXAFS and XANES spectra.’ Journal of Non-Crystalline Solids, 293–295(1). pp. 105–111.

Gates-Rector, S. D. and Blanton, T. N. (2019) ‘The Powder Diffraction File: A Quality Materials Characterisation Database.’ Powder Diffraction, 34(4). pp. 352–360.

Giles, H. L., Hurley, P. W. and Webster, H. W. M. (1995) ‘Simple approach to the analysis of oxides, silicates and carbonates using X-ray fluorescence spectrometry.’ X-Ray Spectrometry, 4(24). pp. 205–218.

Giuli, G., Paris, E., Hess, K. U., Dingwell, D. B., Cicconi, M. R., E Eeckhout, S. G., Fehr, K. T. and Valenti, P. (2011) ‘XAS determination of the Fe local environment and oxidation state in phonolite glasses.’ American Mineralogist, 96(4). pp. 631–636.

Guillen, D. P., Lee, S., Hrma, P., Traverso, J., Pokorný, R., Kloužek, J. and Kruger, A. A. (2020) ‘Evolution of chromium, manganese and iron oxidation state during conversion of nuclear waste melter feed to molten glass.’ Journal of Non-Crystalline Solids, 531, 119860.

Guillen, Donna P., Abboud, A. W. and Pokorný, R. (2019) ‘Computational experiments to characterize bubble formation and movement in waste glass foam layer.’ INL/CON-18-52050-Rev. 0. Idaho National Laboratory, ID. (United States).

Henderson, G. S., De Groot, F. M. F. and Moulton, B. J. A. (2014) ‘X-ray absorption near-edge structure (XANES) spectroscopy.’ Reviews in Mineralogy and Geochemistry, 78(February) pp. 75–138.

Hrma, P., Pokorný, R., Lee, S. M. and Kruger, A. A. (2018) ‘Heat transfer from glass melt to cold cap: Melting rate correlation equation.’ International Journal of Applied Glass Science, (August) pp. 1–8.

Hrma, P. R. Schweiger, M. J., Humrickhouse, C. J., Moody, J. A., Tate, R. M., Rainsdon, T. T., Tegrotenhuis, N. E., Arrigoni, B. M., Marcial, J., Rodriguez, C. P. and Tincher, B. H. (2010) 'Effect of glass-batch makeup on the melting process', Ceramics - Silikaty, 54(3), pp. 193–211.

Hujová, M., Kloužek, J., Cutforth, D. A., Lee, S., Miller, M. D., McCarthy, B. P., Hrma, P., Kruger, A. A. and Pokorný, R. (2018) 'Cold-cap formation from a slurry feed during nuclear waste vitrification', Ceramics International. 45(5), pp. 6405–6412.

Hujová, M., Pokorný, R., Kloužek, J., Dixon, D. R., Cutforth, D. A., Lee, S., McCarthy, B. P., Schweiger, M. J., Kruger, A. A. and Hrma, P. (2017) 'Determination of heat conductivity of waste glass feed and its applicability for modeling the batch-to-glass conversion.' Journal of the American Ceramic Society, 100(11). pp. 5096–5106.

Jenner, G. A., Longerich, H. P., Jackson, S. E. and Fryer, B. J. (1990) 'ICP-MS — A powerful tool for high-precision trace-element analysis in Earth sciences: Evidence from analysis of selected U.S.G.S. reference samples.' Chemical Geology, 83(1–2). pp. 133–148.

Johnson, C. E., Ridout, M. S. and Cranshaw, T. E. (1963) 'The Mössbauer effect in iron alloys.' Proceedings of the Physical Society, 81(6). pp. 1079–1090.

Kelkar, S., Boushey, C. J. and Okos, M. (2015) 'A Method to Determine the Density of Foods using X-ray Imaging.' Journal of Food Engineering, 159. pp. 36–41.

Kikongi, P., Salvas, J. and Gosselin, R. (2017) 'Curve-fitting regression: improving light element quantification with XRF.' X-Ray Spectrometry, 46(5). pp. 347–355.

Kim, D. -S., Schweiger, M. J., Buchmiller, W. C. and Matyáš, J. (2012) 'Laboratory scale melter for determination of melting rate of waste glass feeds.' PNNL-21005. Pacific Northwest National Laboratory, Richland, WA. (United States).

Kim, D. -S. (2015) 'Glass property models, constraints, and formulation approaches for vitrification of high-level nuclear wastes at the US Hanford site.' Journal of the Korean Ceramic Society, 52(2). pp. 92–102.

Kregsamer, P., Streli, C., Wobrauschek, P., Gatterbauer, H., Pianetta, P., Palmetshofer, L. and Brehm, L. L. (1999) 'Synchrotron Radiation-excited Glancing Incidence XRF for Depth Profile and Thin-Film Analysis of Light Elements.' X-Ray Spectrometry, 28(4). pp. 292–296.

Kruger, A. A., Gan, H., Pegg, I. L., Matlack, K. S., Chaudhuri, M., Bardakci, T., Gong, W. and Kot, W. K. (2008) 'Melt Rate Enhancement for High Aluminum HLW Glass Formulations.' ORP-56292. Office of River Protection, Richland, WA (United States).

Kruger, A. A., Matlack, K. A., Pegg, Ian L. and Gong, W. (2013) 'Final Report - Glass Formulation Testing to Increase Sulfate Volatilization from Melter.' VSL-04R4970-1, Rev. 0. Office of River Protection, Richland, WA (United States).

Kruger, A. A., Pegg, I. L., Matlack, K. S., Chaudhuri, M., Kot, W. and Lutze, W. (2009) 'Effects of High Spinel and Chromium Oxide Crystal Contents on Simulated HLW Vitrification in DM100 Melter Tests.' VSL-09R1520-1 Rev. 0. Office of River Protection, Richland, WA (United States).

Kulipanov, G. N. (2007) 'Ginzburg's invention of undulators and their role in modern synchrotron radiation sources and free electron lasers.' Physics-Uspekhi, 50(4). pp. 368–376.

Kurkjian, C. R. (1970) 'Mössbauer spectroscopy in inorganic glasses.' Journal of Non-Crystalline Solids, 3(2). pp. 157–194.

Kuzmin, A., Purans, J. and Rodionov, A. (1997) ‘X-ray absorption spectroscopy study of the Ni K edge in magnetron-sputtered nickel oxide thin films.’ Journal of Physics Condensed Matter, 9(32). pp. 6979–6993.

Lee, S., Hrma, P., Pokorný, R., Traverso, J. J., Kloužek, J., Schweiger, M. J. and Kruger, A. A. (2019) ‘Heat transfer from glass melt to cold cap: Effect of heating rate.’ International Journal of Applied Glass Science, (February). pp. 1–13.

Luo, L. and Zhang, S. (2010) ‘Applications of synchrotron-based X-ray techniques in environmental science.’ Science China Chemistry, 53(12). pp. 2529–2538.

Ma, Y., Zhang, P., Zhang, Z., He, X., Li, Y., Zhang, J., Zheng, L., Chu, S., Yang, K., Zhao, Y. and Chai, Z. (2015) ‘Origin of the different phytotoxicity and biotransformation of cerium and lanthanum oxide nanoparticles in cucumber.’ Nanotoxicology, 9(2). pp. 262–270.

Maleki, A., Aghaei, M., Hafizi-Atabak, H. R. and Ferdowsi, M. (2017) ‘Ultrasonic treatment of $CoFe_2O_4@B_2O_3$-SiO_2 as a new hybrid magnetic composite nanostructure and catalytic application in the synthesis of dihydroquinazolinones.’ Ultrasonics Sonochemistry, 37. pp. 260–266.

Mao, H. K., Jephcoat, A. P., Hemley, R. J., Finger, L. W., Zha, C. S., Hazen, R. M. and Cox, D. E. (1988) ‘Synchrotron X-ray Diffraction Measurements of Single-Crystal Hydrogen to 26.5 Gigapascals.’ Science, 239(4844). pp. 1131–1134.

Margaritondo, G. (2017) ‘Synchrotron light: a success story over six decades.’ La Rivista Del Nuovo Cimento, (40). pp. 411–471.

Mastelaro, V. R. and Zanotto, E. D. (2018) ‘X-ray Absorption Fine Structure (XAFS) studies of oxide glasses-A 45-year overview.’ Materials, 11(2).

Matlack, K. S., Muller, I. S., Callow, R. A., D'Angelo, N., Bardakci, T., Joseph, I. and Pegg, I. L. (2011) ‘Improving Technetium Retention in Hanford LAW Glass -

Phase 2.' VSL-11R2260-1. Vitreous State Laboratory, Washington, D. C. (United States).

Matlack, K. S., Gan, H., Chaudhuri, M., Kot, W. K., Pegg, I. L., Joseph, I. and Kruger, A. A. (2012) 'Melter Throughput Enhancements for High-Iron HLW.' ORP-54002. Vitreous State Laboratory, Washington, D. C. (United States).

Matlack, K. S., Kot, W. K., Pegg, I. L. and Joseph, I. (2015) 'Support for HLW Direct Feed - Phase 2.' VSL-15R3440-1. Vitreous State Laboratory, Washington, D. C. (United States).

McCarthy, B. P., George, J. L., Dixon, D. R., Wheeler, M., Cutforth, D. A., Hrma, P. R., Linn, D., Chun, J., Hujová, M., Kruger, A. A. and Pokorný, R. (2018) 'Rheology of simulated radioactive waste slurry and cold cap during vitrification', Journal of the American Ceramic Society, 101(11), pp. 5020–5029.

McCusker, L. B., Von Dreele, R. B., Cox, D. E., Louër, D. and Scardi, P. (1999) 'Rietveld Refinement Guidelines.' Journal of Applied Crystallography, 32(1), pp. 36–50.

McKeown, D. A., Kot, W. K., Gan, H. and Pegg, I. L. (2003) 'X-ray absorption studies of manganese valence and local environment in borosilicate waste glasses.' Journal of Non-Crystalline Solids, 328. pp. 71–89.

Merdanovica, S. (2009) 'XRF Spectrometer sample preparation by using fused beads technique.' 13th International Research/Expert Conference: Trends in the Development of Machinery and Associated Technology, Hammamet (Tunisia).

Mino, L., Borfecchia, E., Segura-Ruiz, J., Giannini, C., Martinez-Criado, G. and Lamberti, C. (2018) 'Materials characterization by synchrotron X-ray microprobes and nanoprobes.' Reviews of Modern Physics, 90(2), 25007.

Mirti, P., Pace, M., Malandrino, M. and Ponzi, M. N. (2009) ‘Sasanian glass from Veh Ardašīr: new evidences by ICP-MS analysis.’ Journal of Archaeological Science, 36(4). pp. 1061–1069.

Neuville, D. R. and Mysen, B. O. (1996) ‘Role of aluminium in the silicate network: In situ, high-temperature study of glasses and melts on the join SiO_2-$NaAlO_2$.’ Geochimica et Cosmochimica Acta, 60(10). pp. 1727–1737.

Peterson, R. A., Eaton, W. C., Fiskum, S. K. and Geeting, J. (2017) ‘Functions and Requirements of the Waste Test Platform.’ PNNL-26322. Pacific Northwest National Laboratory, Richland, WA (United States).

Pokorný, R., Hilliard, Z. J., Dixon, D. R., Schweiger, M. J., Post Guillen, D., Kruger, A. A. and Hrma, P. (2015) ‘One-Dimensional Cold Cap Model for Melters with Bubblers.’ Journal of the American Ceramic Society, 98(10). pp. 3112–3118.

Potts, P. J. (1987) ‘X-ray fluorescence analysis: principles and practice of wavelength dispersive spectrometry.’ In ‘A Handbook of Silicate Rock Analysis.’ Dordrecht: Springer, Dordrecht (Netherlands). pp. 226–285.

Raman, C. V. (1929) ‘Investigation of Molecular Structure by Light Scattering.’ Transactions of the Faraday Society, 25. pp. 781–92.

Ramsay, W. G., M. F. Gray, R. B. Calmus, J. A. Edge, and B. G. Garret. (2011) ‘Next Generation Melter(s) for Vitrification of Hanford Waste: Status and Direction.’ In WM2011 Conference. Phoenix, AZ (United States).

Ravel, B. and Newville, M. (2005) ‘ATHENA and ARTEMIS: Interactive graphical data analysis using IFEFFIT.’ Physica Scripta T, T115. pp. 1007–1010.

Rietveld, H. M. (1969) ‘A profile refinement method for nuclear and magnetic structures.’ Journal of Applied Crystallography, 2. pp. 65–71.

Ryan, J. L. (1995) ‘Redox Reactions and Foaming in Nuclear Waste Glass Melting.’ PNL-10510. Pacific Northwest National Laboratory. Richland, WA (United States).

Smith, G. L. Bates, D. J., Goles, R. W., Greenwood, L. R., Lettau, R. C., Piepel, G. F., Schweiger, M. J., Smith, H. D., Urie, M. W., Wagner, J. J. (2001) ‘Vitrification and Product Testing of C-104 and AZ-102 Pretreated Sludge Mixed with Flowsheet Quantities of Secondary Wastes.’ PNNL-13452. Pacific Northwest National Laboratory. Richland, WA (United States).

Solomatova, N. V. (2017) ‘Iron-bearing Oxides, Silicate Glasses and Carbonates at Lower Mantle Pressures.’ PhD Thesis. California Institute of Technology, Pasadena, CA. (United States).

Stevens, J. G., Travis, J. C. and DeVoe, J. R. (1972) ‘Mössbauer Spectrometry.’ Analytical Chemistry, 44(5). pp. 384–406.

Templeton, A. M. (2018) ‘Waste Tank Summary Report for Month Ending November 30, 2018 (Vol. December).’ HNF-EP-0182, Rev. 371. Washington River Protection Solutions. Richland, WA. (United States).

Ternov, I. M., Mikhailin, V. V. and Khalilov, V. R. (1985) ‘Synchrotron Radiation and Its Applications.’ (Translated from Russian: Amoretty, S. J. ed.). Glasgow, (UK): Harwood Academic Publishers.

Thomas, R. (1978) ‘Practical Guide to ICP-MS.’ New York, NY (United States): Marcel Dekker, Inc.

Tirez, K., Silversmit, G., Vincze, L., Servaes, K., Vanhoof, C., Mertens, M., Bleux, N. and Berghmans, P. (2011) ‘Speciation and fractionation of nickel in airborne particulate matter: Comparison between selective leaching and XAS spectroscopy.’ Journal of Analytical Atomic Spectrometry, 26(3). pp. 517–527.

Turner, S. P. (2017) ‘XAS Measurements of Chromium Redox in Proton Damaged Glass.’ PhD Thesis. Aberystwyth University, (UK).

Tuthill, E. J., Weth, G. G., Emma, L. C., Strickland, G. and Hatch, L. P. (1967) ‘Phosphate Glass Process for Disposal of High Level Radioactive Wastes.’ I&EC Process Design and Development, 6(3).

Tyler, G. (2001) ‘ICP-OES, ICP-MS and AAS Techniques Compared.’ Technical Note 05: ICP Optical Spectroscopy, (3). pp. 1–11.

Vienna, J. D., Kim, D.-S. and Hrma, P. (2002) ‘Database and Interim Glass Property Models for Hanford HLW Glasses.’ PNNL-14060. Pacific Northwest National Laboratory, Richland. WA. (United States).

Vienna, J. D., Skorski, D. C., Kim, D. -S. and Matyáš, J. (2013) ‘Glass Property Models and Constraints for Estimating the Glass to be Produced at Hanford by Implementing Current Advanced Glass Formulation Efforts.’ PNNL-22631, Rev. 1. Pacific Northwest National Laboratory, Richland, WA (United States).

Wertheim, G. K. (1964) ‘Mössbauer Effect: Principles and Applications.’ New York, NY (United States): Academic Press Inc.

West, M., Ellis, A. T., Potts, P. J., Streli, C., Vanhoof, C., Wegrzynek, D. and Wobrauschek, P. (2012) ‘Atomic spectrometry update - X-ray fluorescence spectrometry.’ Journal of Analytical Atomic Spectrometry, 27(10). pp. 1603–1644.

Wiedemann, H. (2015) ‘Particle accelerator physics.’ Graduate Texts in Physics (4th ed.). (Switzerland): Springer International Publishing.

Wilke, M., Farges, F., Petit, P. E., Brown, G. E. and Martin, F. (2001) ‘Oxidation state and coordination of Fe in minerals: An Fe K-XANES spectroscopic study.’ American Mineralogist, 86(5–6). pp. 714–730.

Wille, K. (1991) ‘Synchrotron radiation sources.’ Reports on Progress in Physics, 54. pp. 1005–1068.

Young, R. A. (1993) ‘The Rietveld Method. International Union of Crystallography Monographs on Crystallography.’ 1st ed. Oxford, (UK): Oxford University Press.

Yu, D. and Utigard, T. A. (2012) ‘TG/DTA study on the oxidation of nickel concentrate.’ Thermochimica Acta, 533(April 2012). pp. 56–65.

4 Comparison of Raw Materials in High-Iron High-Level Waste Feeds

4.1 Overview

In studying the evolution of oxidation states during melting in the HLW-Al-19 feed with Fe^{2+} iron oxalate dihydrate, ($FeC_2O_4 \cdot 2H_2O$) and Fe^{3+} iron hydroxide ($Fe(OH)_3$) raw materials, there was a significant reduction in the O_2 evolved at high temperatures measured by Evolved Gas Analysis (EGA), contributing to a reduction in the secondary foam (Guillen et al. 2020). The HLW-Al-19 feed is a "regular" foaming feed without a significant secondary foaming peak, so the overall reduction in foaming does not have a substantial impact on the processability (Lee, Hrma, Pokorný, Kloužek, et al. 2019). The high-iron HLW-NG-Fe2 waste feed foams up to 10 times its original volume based on previous Feed Expansion Tests (FETs), which is anomalous for a HLW feed. This chapter describes the study proposed to test the hypothesis that using the reduced raw material for iron would have a more significant impact on the O_2 evolution, foaming behaviour and processability of the HLW-NG-Fe2 feed compared with the HLW-Al-19 feed studied previously, due to the higher iron content.

4.2 Sample Properties

HLW-NG-Fe2 and HLW-NG-Fe2-II feed slurries were batched as described in the research methods, section 3.3.1, on a 2 d.p. scale at the Pacific Northwest National Laboratory, the raw materials for iron in the two feeds, Table 3.2.2, were calculated such that the final Fe_2O_3 content in the glass was equal.

Glass samples were created by heating the slurry feed in platinum crucibles in an electric furnace up to 1150 ℃, at a rate of 10 ℃ min^{-1}. The melt dwelled for 1 hour before being poured and annealed at 500 ℃ for 3 hours. SoM samples were produced by the same procedure, with each sample quenched at 600, 700, 800, 900, 1000, 1100, and 1150 ℃, and not annealed. Compositions of the final glasses were measured using XRF and ICP-OES to ensure they were consistent with the nominal composition.

4.2.1 Glass compositions

The glass compositions are compared in Table 4.2.1 to the target composition using XRF and ICP-MS for Li_2O and B_2O_3. Samples were prepared as fused beads as described in the research methods, section 3.4.1. Nominal values were used for the CeO_2, ZnO and La_2O_3 as these were not available in the OXI program used (Giles, Hurley, and Webster 1995b). Consistency between the two analysed glasses is satisfactory. Deviation from the target composition is most prominent in the reduction of the Na_2O, which is likely due to the detection limits of the instrument rather than volatilisation during melting since there is little volatilisation of Li or B by ICP-OES. MgO is not detected in the HLW-NG-Fe2-II glass, the current explanation for this is the detection limits of lighter elements and errors associated with low-Z elements. The SO_3 has not been retained in either of the glasses within the limits of detection of XRF; its evolution may arise during either sample melting, or XRF sample preparation (Bell et al. 2020), or both.

Table 4.2.1. Analysed compositions of HLW-NG-Fe2 and HLW-NG-Fe2-II glasses by XRF and ICP-OES compared with the nominal composition.

Oxide	Nominal (wt%)	HLW-NG-Fe2 (wt%)	HLW-NG-Fe2-II (wt%)
SiO_2	41.02	41.2(2)	41.1(2)
Na_2O	13.36	10.1(2)	11.1(2)
B_2O_3	13.79	15.49*	14.46*
Li_2O	1.56	1.18*	1.38*
MgO	0.16	0.36(2)	0.00(2)
Fe_2O_3	16.12	17.94(3)	17.86(3)
Al_2O_3	5.59	6.58(1)	6.03(1)
CaO	0.52	0.61(1)	0.60(1)
ZrO_2	1.13	0.94(03)	1.18(03)
SrO	0.20	0.16(01)	0.16(01)
SO_3	0.22	0.00	0.00
P_2O_5	0.78	0.60(3)	0.65(3)
MnO_2	3.98	3.20(1)	3.63(1)
PbO	0.63	0.66(05)	0.73(05)
NiO	0.47	0.45(04)	0.54(04)
Cr_2O_3	0.25	0.25(1)	0.29(1)
CeO_2	0.12	0.12**	0.12**
ZnO	0.03	0.03**	0.03**
La_2O_3	0.09	0.09**	0.09**
Sum	100.00	100.00	100.00

* ICP-OES negligible errors

** Nominal values where values were not available in the OXI program used

4.3 Foaming and Gas Evolution

4.3.1 Feed Expansion Tests

Feed expansion tests (FETs) indicated the amount a particular feed will foam during melting. The pressed pellets used in this test have limited applicability to the material inside a cold cap (Marcial, Pokorný, et al. 2021; Pokorný, Kruger, and Hrma 2014), however parameters derived from FETs can be used to predict the melting rate of feeds with good correlation (Pokorný, Kruger, and Hrma 2014; Jin et al. 2018; Pokorný and Hrma 2011; Marcial et al. 2014a; Hrma et al. 2018).

During melting in the observation furnace, photographs were taken at 100 °C intervals initially, and then at 10 °C intervals once the pellets began to change shape, the timing of the images is given in Figure 4.3.1. Averages of three feed expansion tests were taken for each feed. Example photographs taken of each feed during melting are shown in Figure 4.3.3.

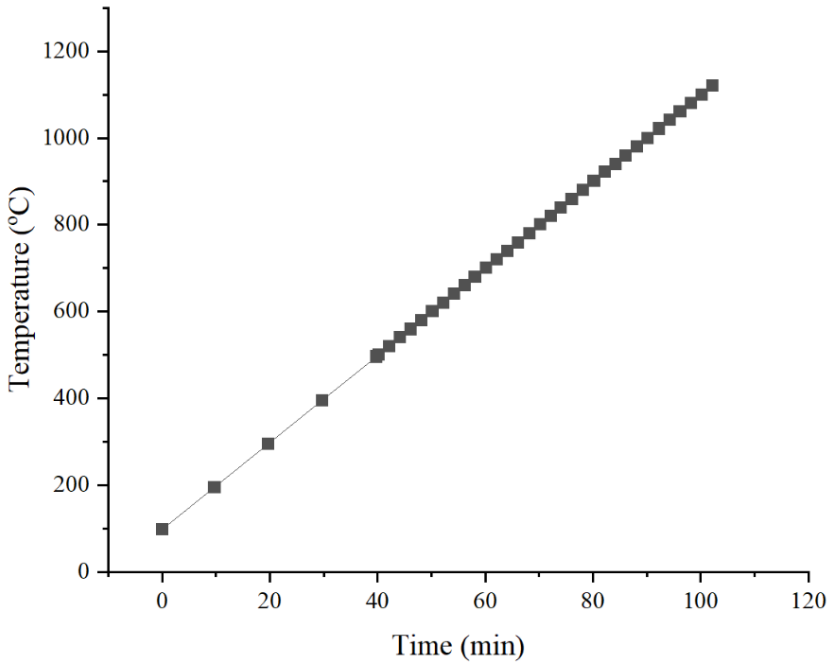

Figure 4.3.1. Timing and temperatures of photographs of pellets ramped at 10 °C min^{-1}. Photographs taken every 100 °C initially, then more frequently when volume changes began to occur.

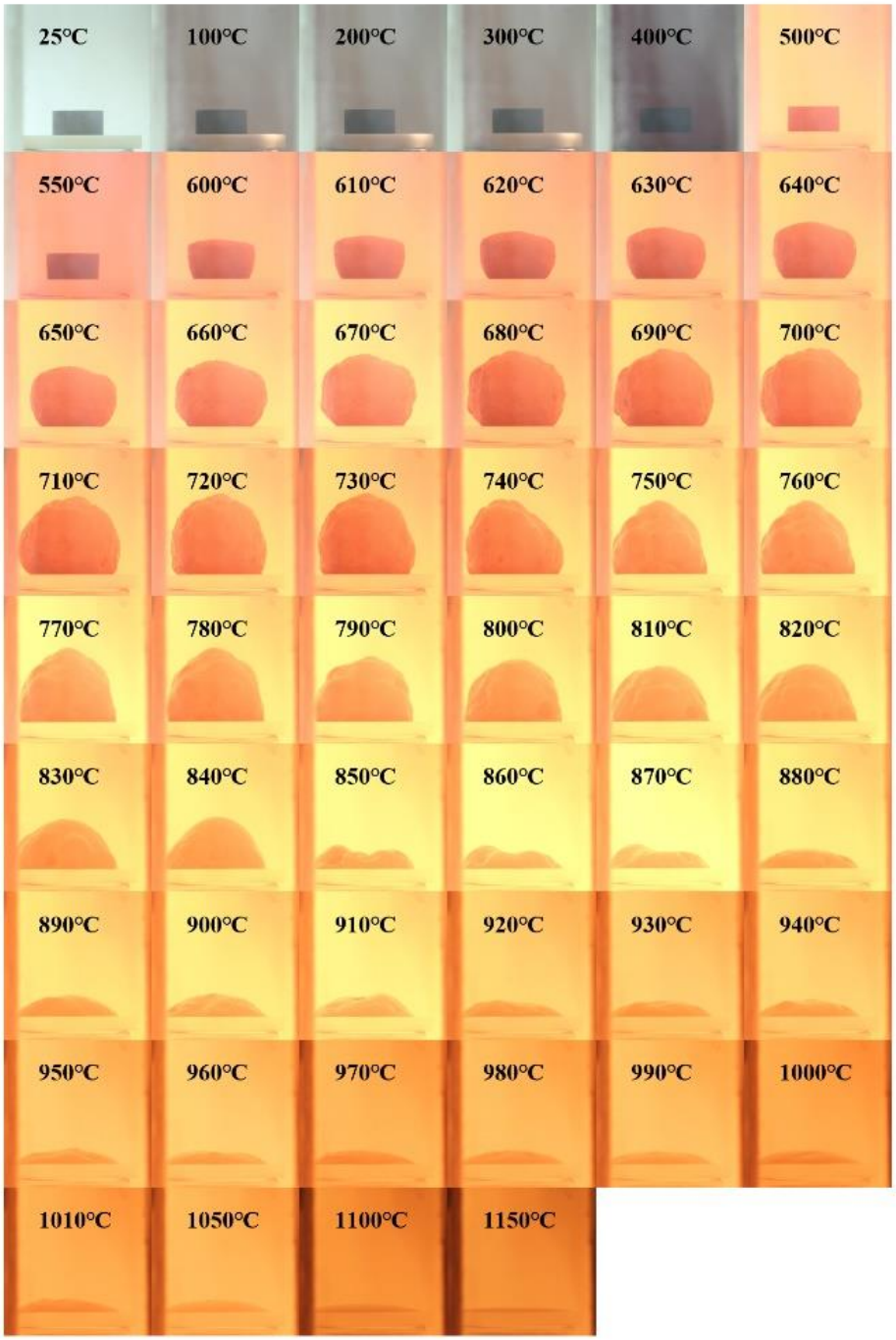

Figure 4.3.2. Feed expansion test images of HLW-NG-Fe2 showing initial expansion of the feed pellet between 500 and 700 ℃, followed by collapse of the foam up to melt temperature. Some large bubbles seem to emerge between 850 and 870 ℃ after the initial collapse.

Figure 4.3.3. Feed expansion test images of HLW-NG-Fe2-II showing initial expansion of the feed pellet between 600 and 700 °C followed by steady collapse of the foam.

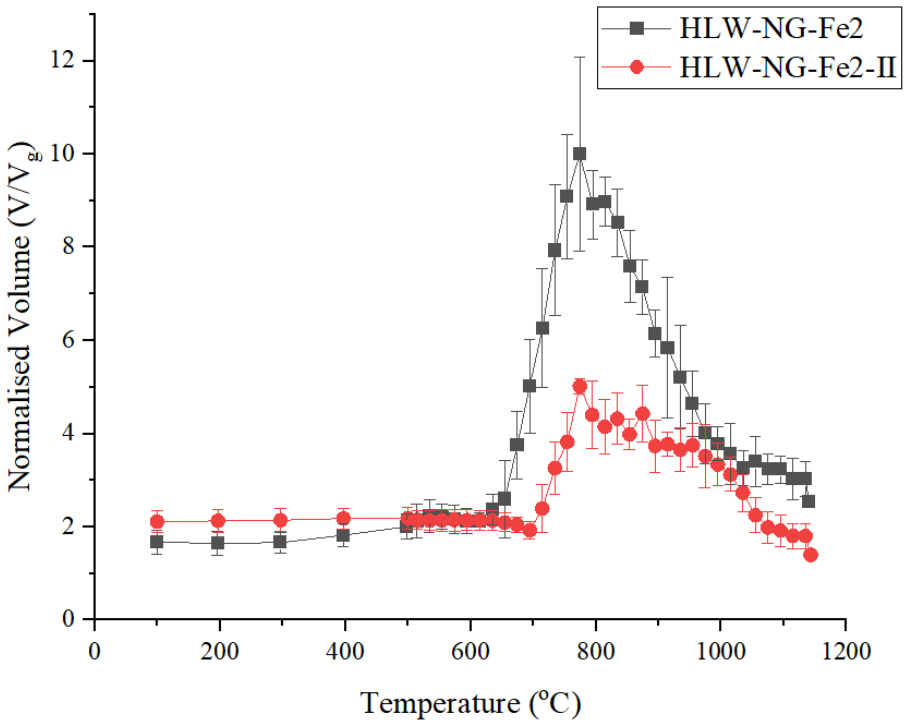

Figure 4.3.4. Normalised volume expansion to the volume of glass, V/V_g, during melting of a pellet of the HLW-NG-Fe2 feed with iron hydroxide (black) and iron oxalate dihydrate (red) raw materials showing reduction of peak and overall foaming in the HLW-NG-Fe2-II feed.

As experienced in previous FET experiments with HLW-NG-Fe2, the maximum volume expansion is ~10 times the original pellet volume (Lee, Hrma, Pokorný, Kloužek, et al. 2019; Guillen et al. 2020). There is a 50 ± 2 % reduction in maximum volume expansion using $FeC_2O_4{\cdot}2H_2O$. From calculations of the FET curves, parameters used in the Melt Rate Correlation Equation can be devised. The temperature at foam collapse, T_{FB}, is one of the parameters used. There is no difference in the values of T_{FB}, between the two samples during melting, so if the melt viscosity and heat transfer were equated, there would be no significant difference in melting rate between the two feeds, by:

$$j = \xi_0 \left(\frac{\eta_{MO}}{\eta_R}\right)^{-\alpha} \left(1 + \frac{u_B}{u_0}\right)^{\beta} (T_{MO} - T_{FB})\Delta H^{-1}. \quad (27)$$

Table 4.3.1. Foaming behaviour in the HLW-NG-Fe2 and HLW-NG-Fe2-II feeds during melting from FETs.

	HLW-NG-Fe2	**HLW-NG-Fe2-II**
Normalised Maximum Foam Volume	10.0 ± 2.1	5.0 ± 0.2
Temperature foam onset (℃)	600 ± 10	700 ± 10
Temperature foam collapse* (℃)	774 ± 10	775 ± 10

*Measured at peak foam height.

4.3.2 Gas Evolution

The total gas evolved in each feed, obtained from the derivative of the mass loss from TGA, Figure 4.3.5 shows a 62.9 ± 2.8 % increase during melting in the HLW-NG-Fe2-II feed compared with the original, and no significant gas evolution above ~600 ℃, suggesting a small relative amount of gas evolution contributes a large amount to the foaming observed in Figure 4.3.4. The main dehydration of raw materials in both feeds is observed as an endothermic reaction at ~300 ℃, with a smaller peak release of physical water at 100-200 ℃. The second large peak in the 400-600 ℃ temperature range in the HLW-NG-Fe2-II feed is likely exothermic organic reactions with the excess carbon in the feed. Beyond this temperature the steep drop in DTA suggests the sample is melting which requires a significant heat input. The main difference in the spectra passed 600 ℃ is the sharp endothermic reactions in the HLW-NG-Fe2 feed that are barely present in the HLW-NG-Fe2-II feed. Further structural studies were required to understand this difference in melting behaviour. Evolved gas analyses of the two feeds, shown in Figure 4.3.6 and Figure 4.3.7, by EGA the CO and CO_2 evolution continues beyond 600 ℃, potentially because of the difference in atmosphere of the two experiments. The HLW-NG-Fe2-II shows a 451 ± 65 % increase in total CO_2 evolution during melting of the HLW-NG-Fe2-II feed compared to HLW-NG-Fe2 feed and substantial CO evolution, at 35.2 g kg^{-1} of glass, compared to 10.8 mg kg^{-1} of glass in

the HLW-NG-Fe2 feed. Peak evolution of both CO and CO_2 occurs before the foam onset temperature of 600 °C in the HLW-NG-Fe2-II feed.

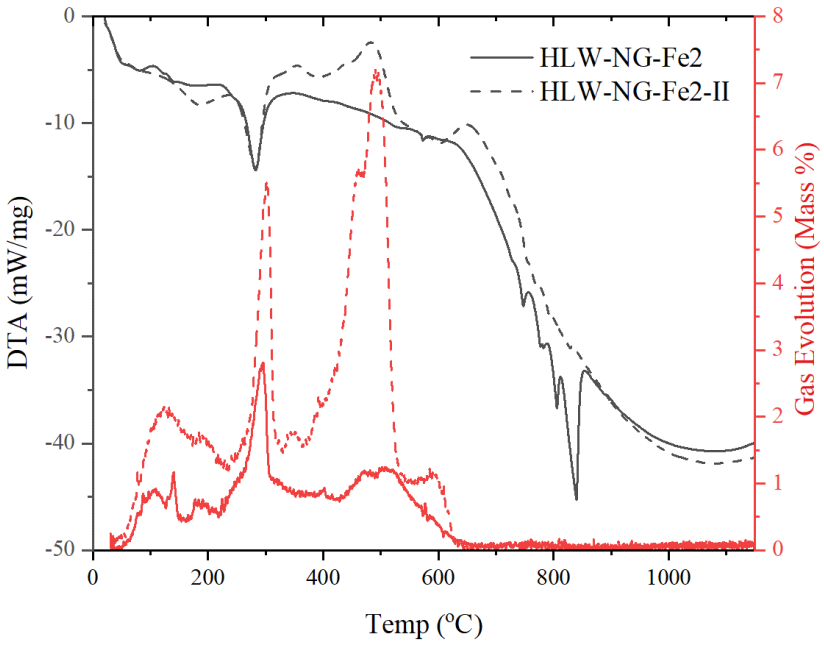

Figure 4.3.5. Gas evolution by 1st derivative of the TGA mass loss curve (red), showing and increase in total gas evolution for the HLW-NG-Fe2-II feed. DTA (black) for the HLW-NG-Fe2 and HLW-NG-Fe2-II feeds showing distinctive endothermic peaks in the HLW-NG-Fe2 feed between 700 and 900 °C are not present in the HLW-NG-Fe2 feed.

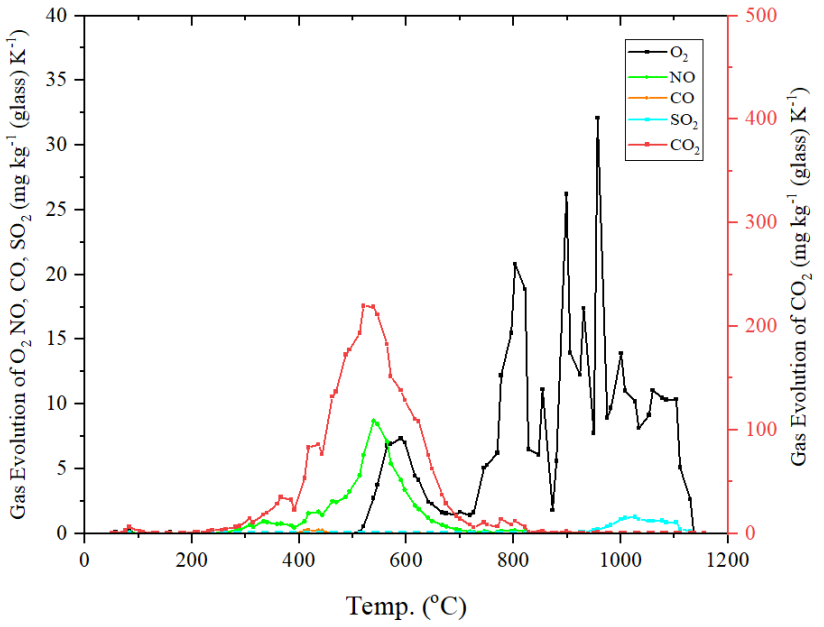

Figure 4.3.6. EGA of O_2, NO, CO and SO_2 (left axis) and CO_2 (right axis) for the HLW-NG-Fe2 feed. Gases evolved above 600 °C are primarily O_2, SO_2 and residual CO_2.

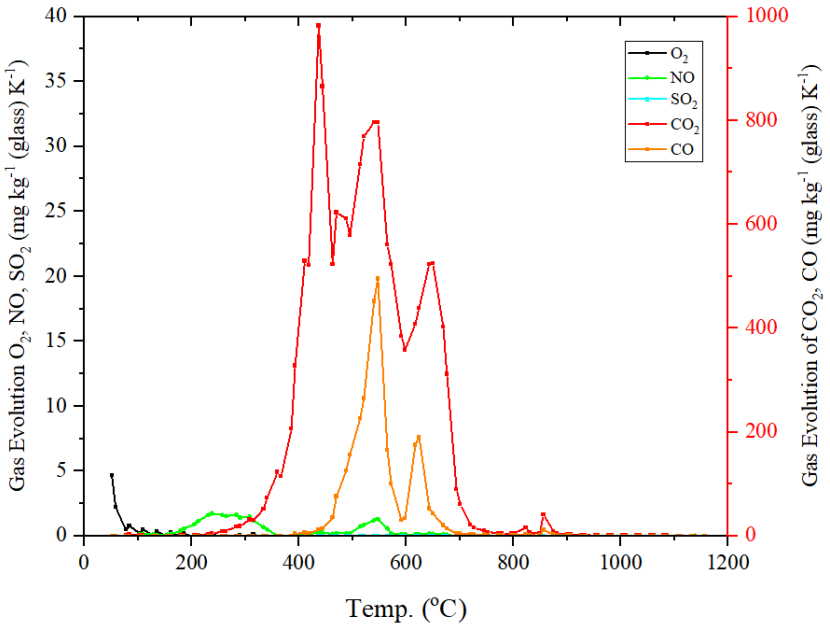

Figure 4.3.7. EGA of NO, CO, CO_2, O_2 and SO_2 for the HLW-NG-Fe2-II feed. There is no SO_2 or O_2 evolution above ~600 ℃, only residual CO_2.

There is suppression of O_2 and SO_2 evolution in the HLW-NG-Fe2-II feed compared to the 5.12 g kg^{-1} of glass evolved during melting of the HLW-NG-Fe2. O_2 evolution in the HLW-NG-Fe2 feed is recorded in spikes that may correspond to the sharp changes observed in the DTA data. The O_2 evolution continues in the HLW-NG-Fe2 feed up to the glass melting temperature, 1150 ℃.

Table 4.3.2. Total evolved gases during melting of the HLW-NG-Fe2 and HLW-NG-Fe2-II feeds by integration of the EGA curves.

	Total evolved gas (mg kg^{-1} glass)	
Gases	**HLW-NG-Fe2**	**HLW-NG-Fe2-II**
CO_2	40240	181340
CO	10	35180
O_2	5120	0
SO_2	150	0
NO	1030	320

4.4 Structure of the feeds during melting

4.4.1 XRD

The phase assemblage of the samples produced during the SoM study, between foam onset and melting temperatures (600-1150 °C), were analysed by XRD with phase identification and refinement for estimation of the relative abundances of the crystalline phase and the amorphous phase content. Figure 4.4.1 shows the XRD patterns for the SoM samples of each feed, quenched between 600 and 1150 °C, and Figure 4.4.2 shows the quantity of each of the phases identified these samples, as well as the amorphous phase fraction.

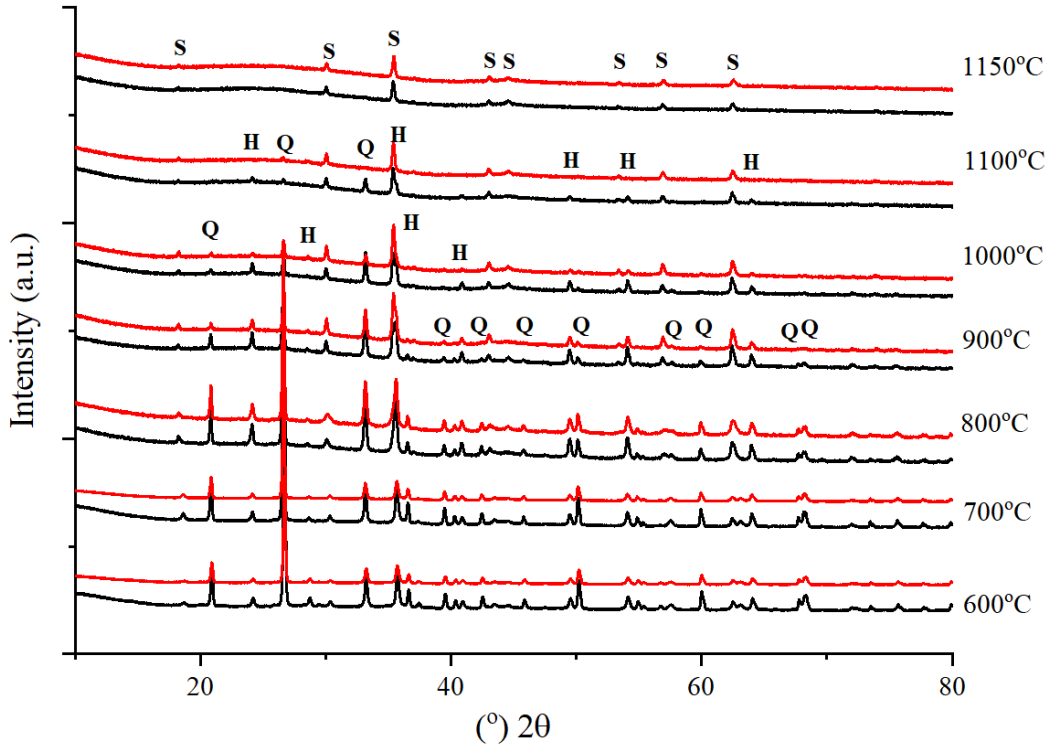

Figure 4.4.1. Comparison of XRD patterns for HLW-NG-Fe2 (black) and HLW-NG-Fe2-II (red) SoM samples quenched at 600, 700, 800, 900, 1000, 1100 and 1150 °C. Peaks identified belonging to Fe_2O_3, Haematite (H) ICDD; 04-015-7029, SiO_2, Quartz (Q) ICDD; 01-070-3755, and Fe_3O_4, Magnetite (S) ICDD; 04-009-8433.

All of the diffraction patterns show evidence of crystallinity. The amorphous "hump" begins to protrude clearly at around 1000 °C where at least some of the amorphous

silica structure of the glass has formed, it further increases in size with temperature, reflected in the identified phase proportions, Figure 4.4.2. All quantitified phases are given in Appendix B, Table 1.

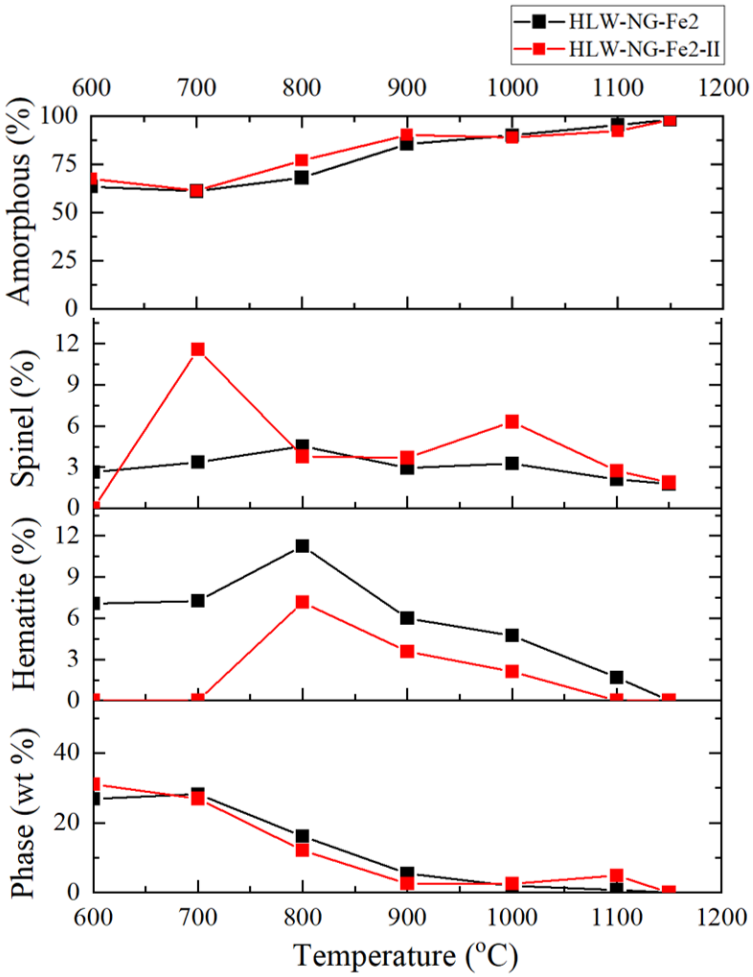

Figure 4.4.2. Comparison of quantity of phases present during melting by refinement of XRD patterns in (a) HLW-NG-Fe2 and (b) HLW-NG-Fe2-II. Quartz ICDD: 01-070-3755, Haematite ICDD: 04-015-7029, ICDD: 04-007-2132. “Spinel” incorporates cubic spinels based on the magnetite system, Fe_3O_4. The only significant difference between the two feeds can be seen in the form of iron during melting.

Total amorphous quantity and quartz dissolution is similar in both feeds and compares with the previous measurements (Marcial, Kloužek, et al. 2021). At 1150 °C the quartz and haematite have completely dissolved in both feeds. Haematite, present from 600 °C to 1100 °C in the HLW-NG-Fe2 feed, indicates that the decomposition of the $Fe(OH)_3$ raw material has been completed below 600 °C. In the HLW-NG-Fe2-II samples there

are no crystalline Fe-containing phases present at 600 ℃. At 700 ℃ there is a significant amount of spinel phase formed and less haematite and more magnetite are present in the HLW-NG-Fe2-II samples from 800-1150 ℃.

All of the spinel structures identified are $Fd\bar{3}m$ cubic spinels in the magnetite series (Sickafus, Wills, and Grimes 1999), in the typical structure AB_2O_4, discussed in 2.2.5, (Andrzejewski et al. 2014; Garcia-Muñoz et al. 2020). At 1150 ℃ both glasses contained phases identified as Magnetite (Fe_3O_4) with lattice constants (a = b = c) of 8.401(4) Å for the HLW-NG-Fe2 glass and 8.389(2) Å for the HLW-NG-Fe2-II glass, by refinement of the peak shapes and positions using the Rietveld refinement function in HighScore Plus. These are close to the referenced lattice constants for Fe_3O_4 at 8.394 Å (Brik, Suchocki, and Kamińska 2014). The slight difference in the lattice parameters leaves uncertainty around whether other elements such as Cr, Ni or Mn may be present as solid solutions with Fe within these compounds.

4.4.2 SEM/EDX

Electron dispersive X-ray spectroscopy of the glass samples shows presence of Fe, Mn, Cr and Ni in the spinel crystals in both 1150 ℃ samples, Figure 4.4.3 and Figure 4.4.4. A qualitative estimate of the proportion of each element in the spinels was calculated for an average of the spectra of 5-10 point scans on the spinels. The background glass phase was subtracted from the average composition detected in the spinels, to account for the amorphous phase in the interaction volume, discussed in Chapter 3, section 3.7.1. A scaled average composition of 5-10 point scans of homogenous glass phase was subtracted from the average composition. The scale factor used was determined by the difference in Si, Al and Na detected between the spinels and the glass phase.

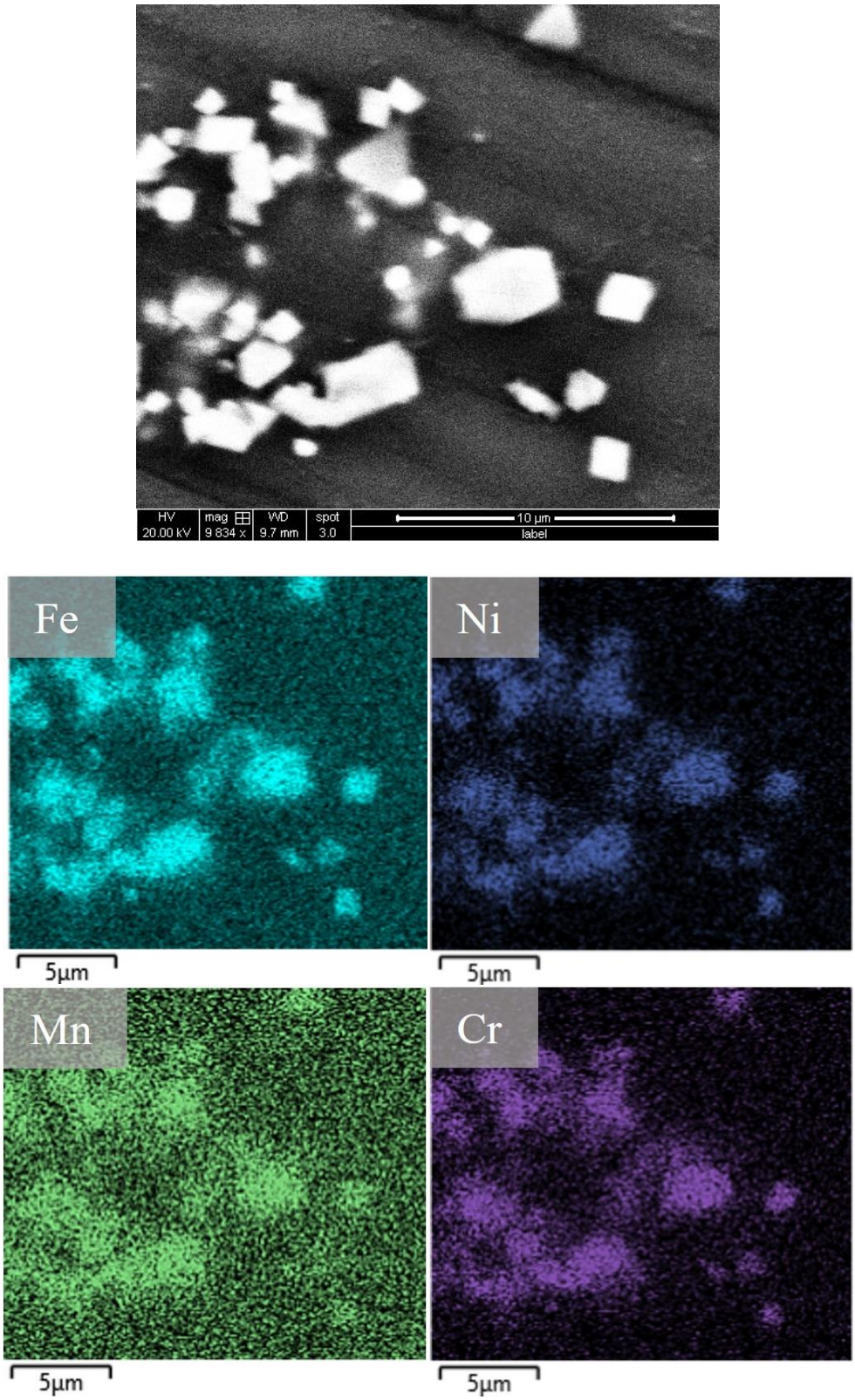

Figure 4.4.3. Backscattered electron image (top) and elemental maps of the spinel crystals in HLW-NG-Fe2 quenched at 1150 °C, showing presence of Mn, Ni and Cr, as well as Fe within the spinels.

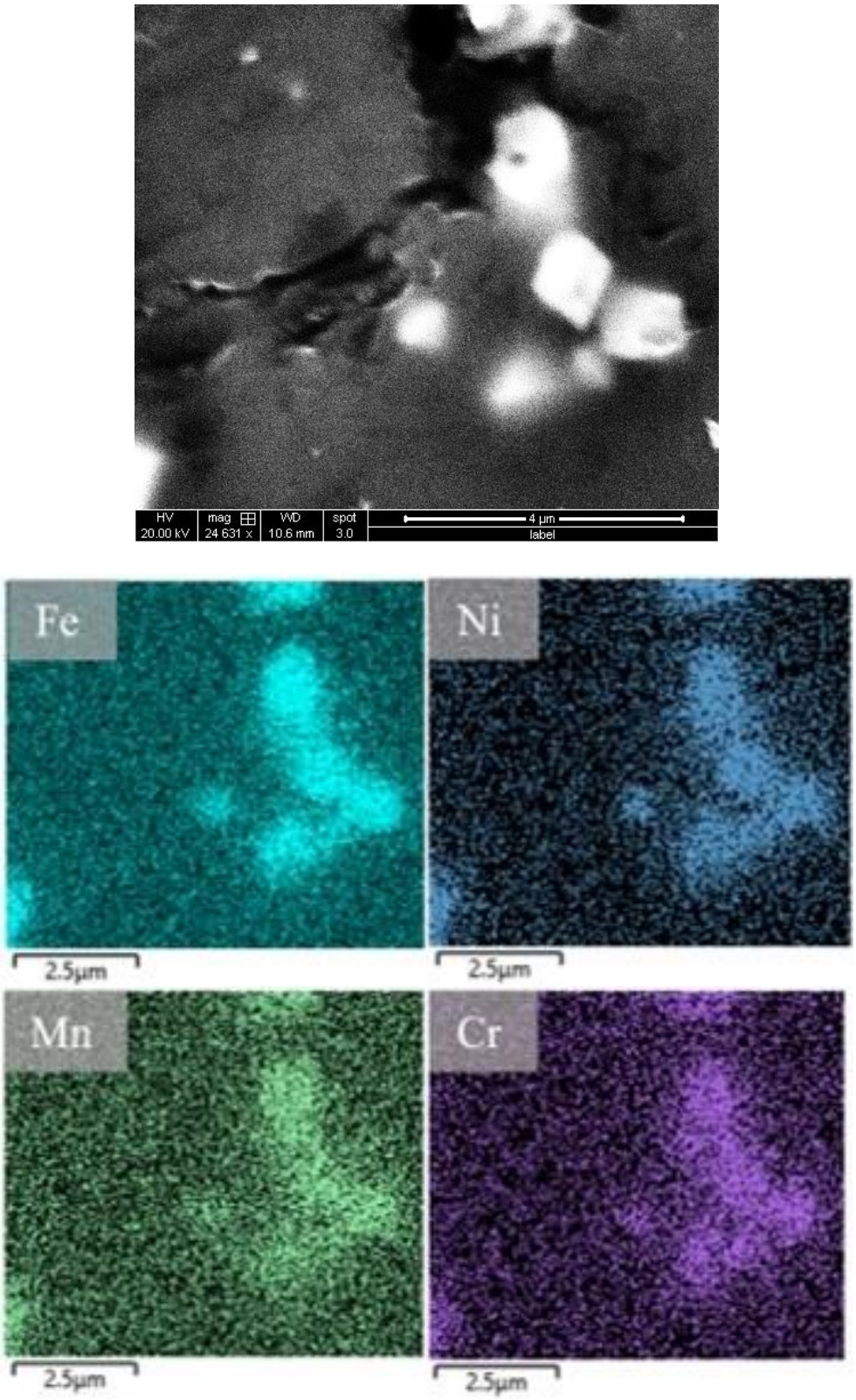

Figure 4.4.4. Backscattered electron image (top) and elemental maps of the spinel crystals in HLW-NG-Fe2-II quenched at 1150 ℃, showing presence of Mn, Ni and Cr, as well as Fe within the spinels.

The results of the proportions of Fe, Mn, Ni, Cr and O detected in the spinels are tabulated in Table 4.4.1, In the HLW-NG-Fe2 sample the average Fe is around 48 wt%, from the information in section 2.2.5, it is therefore expected that the Fe is mostly on the 3+ site, and the 2+ site has a combination of Ni^{2+} and Mn^{2+}. Cr^{2+} is unlikely, so this may sit on some of the Fe^{3+} sites. There is a lower quantity of Cr and higher quantity of Mn and Ni in the spinels in the HLW-NG-Fe2-II glass, which suggests a greater ratio of Fe^{3+} to Fe^{2+} filled sites, than in the HLW-NG-Fe2 spinels, and less Fe is incorporated into the spinels total.

Table 4.4.1. Spinel composition determined by average point scans by EDX.

Element	**HLW-NG-Fe2 1150 ℃**		**HLW-NG-Fe2-II 1150 ℃**	
	wt%	**mol%**	**wt%**	**mol%**
O	22.0 ± 3.0	49.5 ± 6.8	22.7 ± 1.8	50.7 ± 4.0
Fe	47.7 ± 5.6	30.8 ± 3.6	44.1 ± 6.9	28.2 ± 4.4
Cr	8.5 ± 1.9	5.9 ± 1.3	5.7 ± 1.2	3.9 ± 0.8
Mn	8.5 ± 1.1	5.5 ± 0.8	10.8 ± 1.6	7.0 ± 1.0
Ni	13.4 ± 2.1	8.2 ± 1.3	16.7 ± 4.0	10.1 ± 2.5

4.4.3 Raman Spectroscopy

Raman spectroscopy was performed on each of the SoM samples as described in section 3.6.2. Full deconvolution of the spectra would be very difficult, given the number of components and the presence of both amorphous and crystalline phases, indicators of bonding within the borosilicate glass network are obtained from the profile of the Raman spectra for feeds heated to 1000 ℃ and above.

Consistent with the XRD data, (Figure 4.4.1 and Figure 4.4.2), the wide Raman Si-O (Al-O, Fe-O) Q-species region, between ~800 and 1200 cm^{-1} (Parkinson et al. 2008; Yadav and Singh 2015), shows the emergence of the amorphous phase as the temperature increases, as well as bands due to the (boro)silicate network between 350

and 600 cm^{-1} and ~1200 to 1500 cm^{-1} expected for borosilicate glasses (Parkinson et al. 2008; Yadav and Singh 2015). Identifiable modes are tabulated in Table 4.4.2.

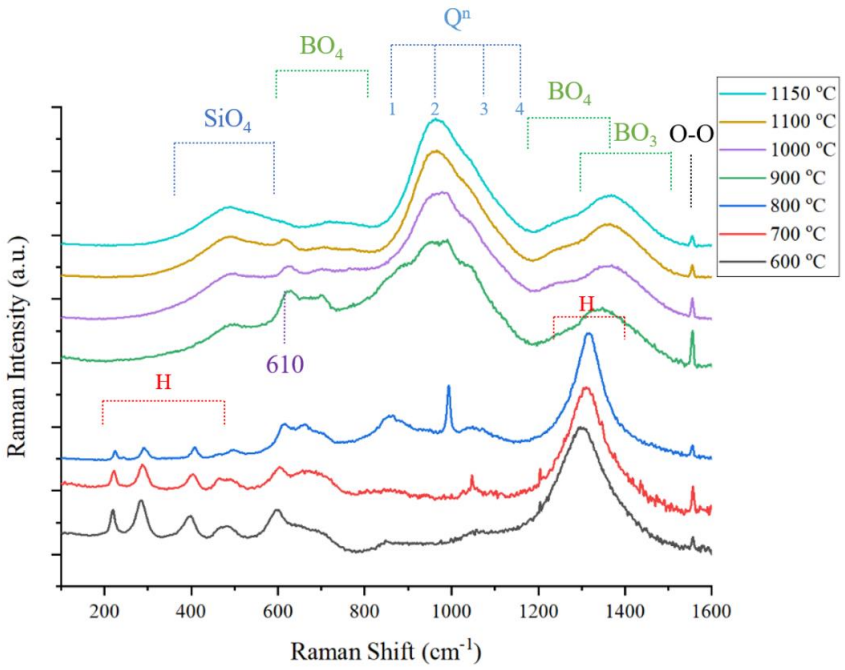

Figure 4.4.5. Raman spectra of the HLW-NG-Fe2 feed during melting at 600, 700, 800, 900, 1000, 1100 and 1150 °C, showing the dissolution of sharp crystalline materials and emergence of the Q^n species region with increasing temperature.

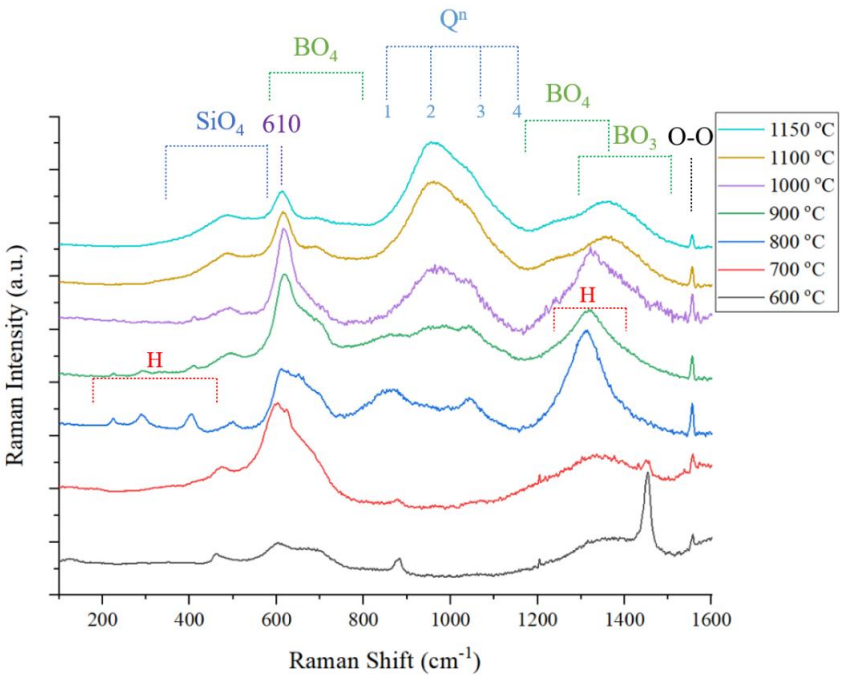

Figure 4.4.6. Raman spectra of the HLW-NG-Fe2-II feed during melting at 600, 700, 800, 900, 1000, 1100 and 1150 °C, showing the emergence of the borosilicate glass network with an intense band at 610 cm^{-1}, which remains present in the 1150 °C sample.

Table 4.4.2. Raman bands common to borosilicate structures and crystalline and amorphous iron-bearing structures identified in the HLW-NG-Fe2 -II spectra.

Raman Shift (cm^{-1})	**Raman modes**
226, 292	Haematite (Krolop et al. 2019; de Faria and Lopes 2007)
350-600	Borosilicate structures: reedmerginerite $[BSi_3O_8]^-$. SiO_4 modes: O-Si-O bending, mixed stretching and bending modes of Si-O-Si (Yadav and Singh 2015)
610	danburite $[B_2Si_2O_8]^{2-}$ -like ring structures (Cochain and Neuville 2008; Cochain et al. 2012)
970	$^{IV}Fe^{3+}$-O stretching (Cochain et al. 2012)
800-1200	Si-O, Al-O and Fe-O Q^n species (Parkinson et al. 2008; Yadav and Singh 2015)
1200-1400	BO_2O-BO_3 units (Osipov, Osipova, and Eremyashev 2013)
1320	Haematite (Krolop et al. 2019; de Faria and Lopes 2007)
1550	O-O bond in molecular oxygen (Chen et al. 2016).

Between 900 ℃ and 1150 ℃ the most significant difference between the two feeds is the narrow Raman band at 610 cm^{-1}. The Raman difference spectra for the 1150 ℃ HLW-NG-Fe2-II glass compared with the 1150 ℃ HLW-NG-Fe2 glass, shown in Figure 4.4.7, displays the large difference between the two samples in this spectral region, and also more minor shifts in the convoluted bands in the ~800-1200 cm^{-1} (Si-O Q^n) region and some changes at higher Raman shifts of ~1200-1500 cm^{-1}.

Crystalline magnetite exhibits its main, narrow band at ~670 cm^{-1} (Slavov et al. 2010; Li and Huan 2000; Jubb and Allen 2010; Testa-Anta et al. 2019), with other bands much less intense. However, the spinel contents are not significantly different between the two samples, by XRD, section 4.4.1, yet the intensity of the Raman band at 610 cm^{-1} is substantially different, suggesting other origins. The studies, discussed in Chapter 2, section 2.2.3, attribute this band to danburite-like ring structures (Testa-Anta et al. 2019; Cochain and Neuville 2008; Cochain et al. 2012). These structures tend to

increase with reduction of Fe^{3+} in the glass (Cochain and Neuville 2008; Cochain et al. 2012), the Na^{+} cations will preferentially charge-compensate Fe^{3+} in tetrahedral coordination (Barth and Feltz 1989; Yun and Bray 1978).

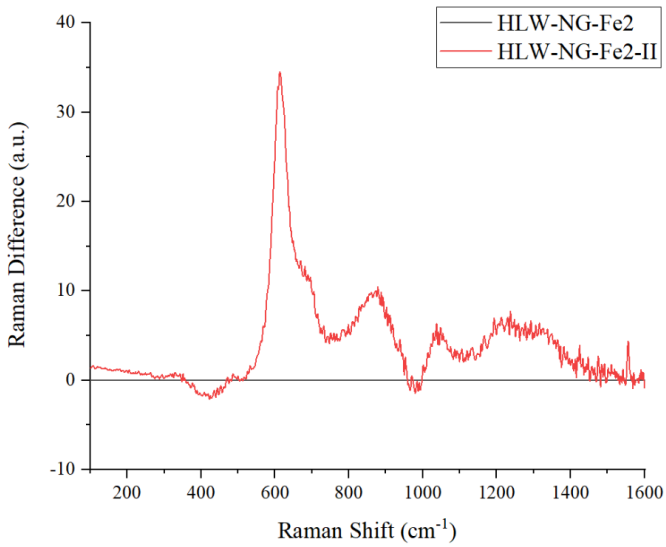

Figure 4.4.7. Raman Difference spectrum for HLW-NG-Fe2-II compared with HLW-NG-Fe2. The main difference between the two glass samples is in the 610 cm^{-1} band.

To investigate further, the HLW-NG-Fe2-II sample was remelted at 1150 ℃ for 24 hours to determine whether the behaviour of the ~610 cm^{-1} Raman band was transient or remained after longer melting times. Figure 4.4.8 shows a comparison between the Raman spectra of the original HLW-NG-Fe2-II glass melted at 1150 ℃ for one hour, and the remelted glass at 1150 ℃ for 24 hours. Some decrease in the intensity of the 610 cm^{-1} peak is observed, which may suggest that some form of relaxation or equilibration may be taking place and the glass. Within the typical melter residence time of the JHCM, 65 hours (Bickford et al. 1990; Hrma, Schill, and Nemec 2001; Nelson 2010), such equilibrations may occur (Schreiber et al. 1986), but further research is required to elucidate the behaviour of this Raman band and its origin.

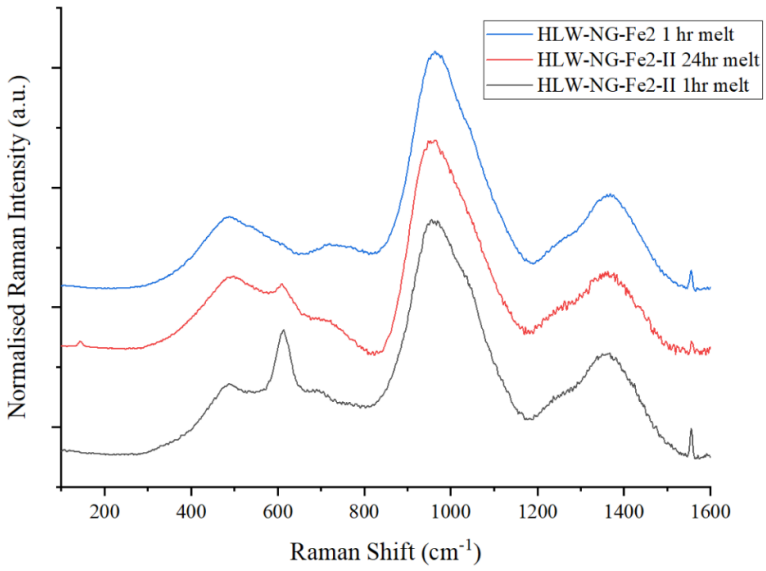

Figure 4.4.8. Raman spectra of the HLW-NG-Fe2 glass, and the HLW-NG-Fe2-II glasses melted for 1 hour and 24 hours, showing reduction in the 610 cm^{-1} peak in the 24 h sample equilibrating towards the HLW-NG-Fe2 sample.

4.4.4 Mössbauer Spectroscopy

SoM samples quenched at 600, 800, 1000 and 1150 ℃ for each feed were powdered for room temperature ^{57}Fe Mössbauer spectroscopy, as described in 3.6.4. For the original HLW-NG-Fe2 feed the iron in the sample heated to 600 ℃ is mostly present in crystalline magnetic phases, with sextets corresponding to α-Fe_2O_3 (Oh, Cook, and Townsend 1998) and spinel structures (Darby Dyar et al. 2006; Bonnenfant et al. 1982; Deshkar et al. 2019), consistent with the results of XRD. The content of paramagnetic phase, with a relative spectral area of 9 ± 2 %, in the HLW-NG-Fe2 feed at 600 ℃, has centre shift (CS) and quadrupole splitting (QS) values of 0.33 and 1.12, consistent with tetrahedrally coordinated Fe^{3+} (Darby Dyar et al. 2006; Bonnenfant et al. 1982; Deshkar et al. 2019) which may reside within the amorphous phase shown to be present (Figure 4.4.1 and Figure 4.4.2).

As temperature increases, the relative abundance of paramagnetic phase increases (consistent with increasing amorphous content), Figure 4.4.9, and a second doublet emerges with CS and QS parameters of 0.27 ± 0.02 mm s^{-1} and 0.79 ± 0.02 mm s^{-1},

respectively, also consistent with tetrahedral Fe^{3+} (Darby Dyar et al. 2006; Deshkar et al. 2019; Darby Dyar 1985; K. Sharma et al. 2009), while the sextets arising from the crystalline phases decrease in intensity, up to 1150 ℃.

For the reduced feed HLW-NG-Fe2-II at 600 ℃, the iron in the sample can be fitted by 3 Lorentzian paramagnetic doublets. Two of these doublets are consistent with octahedral Fe^{3+} in the amorphous phase, while the third is associated with tetrahedral Fe^{2+}. Fe^{2+} ions are octahedrally coordinated in FeC_2O_4 at room temperature, a doublet is expected with an CS ~ 1.12 mm s^{-1} and QS ~ 1.72 mm s^{-1} (Smrčka et al. 2016; D'Antonio et al. 2009). The Fe^{2+} doublet presented here has CS ~ 0.89 ± 0.02 mm s^{-1} and QS ~ 2.59 ± 0.02 mm s^{-1}, suggesting that the Fe^{2+} ions are tetrahedrally coordinated. The distortion in the geometry affecting QS; and the CS is more representative of unstable FeO (Fultz 2012; Shrotri et al. 1986).

At 800 ℃ crystalline haematite and spinel phases are present (Figure 4.4.1 and Figure 4.4.2). Haematite has a higher relative abundance at 800 ℃ than it does in the 800 ℃ HLW-NG-Fe2 spectra, however, at 1000 ℃ the haematite in the HLW-NG-Fe2-II sample has decreased more significantly, reflecting the relative abundances of the phases determined by XRD (Figure 4.4.1 and Figure 4.4.2).

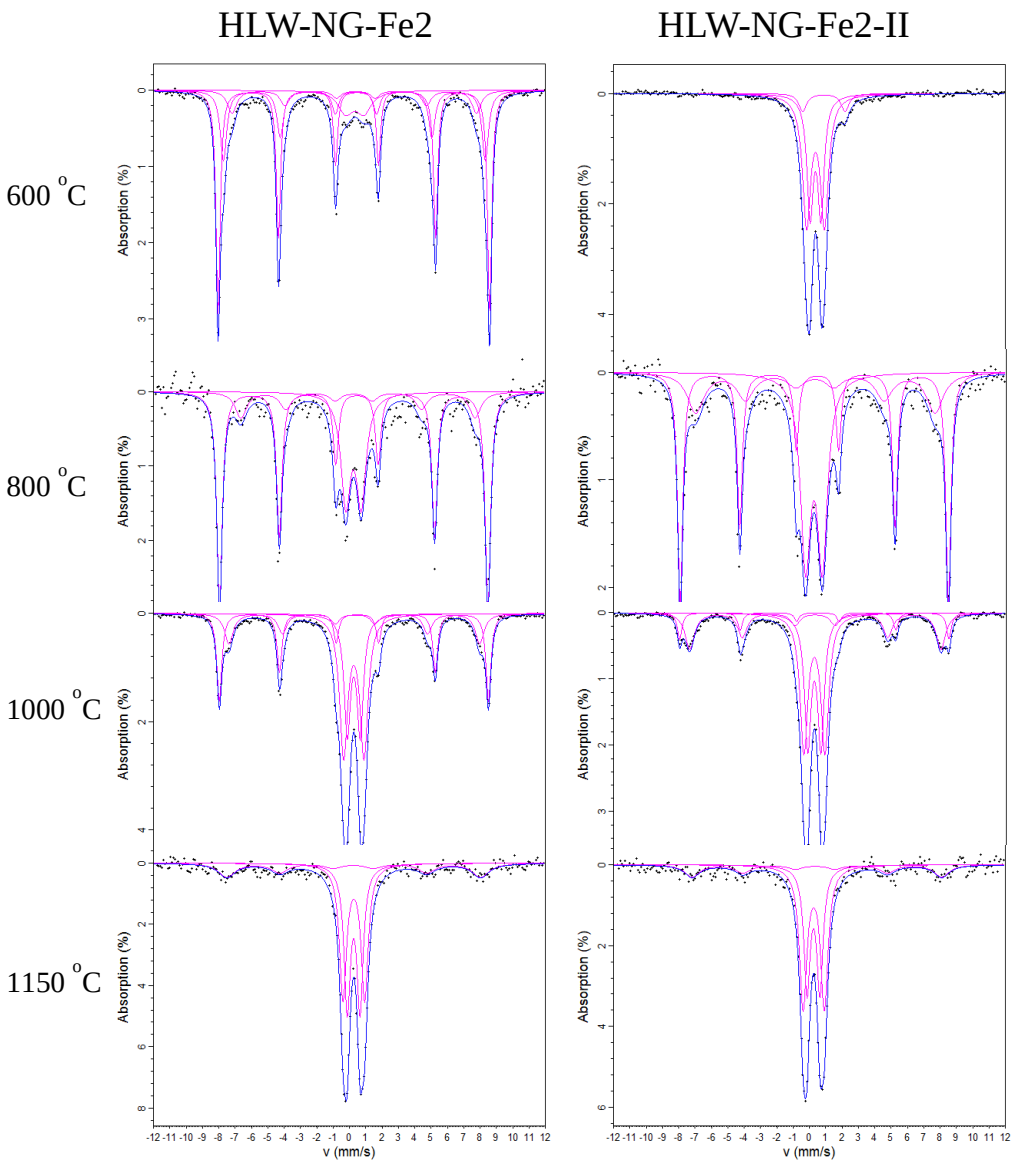

Figure 4.4.9. Room temperature ^{57}Fe Mössbauer spectra for SoM samples at 600, 800, 1000 and 1150 ℃ fitted with Lorentzian functions for the HLW-NG-Fe2 and HLW-NG-Fe2-II feeds. CS relative to α-Fe. Fe^{3+} magnetic structures in the 600 ℃ HLW-NG-Fe2 sample and paramagnetic Fe^{2+} and Fe^{3+} in the 600 ℃ HLW-NG-Fe2-II sample converge to almost entirely paramagnetic Fe^{3+} in the final 1150 ℃ samples with some remaining sextets attributed to Fe-bearing spinel.

Table 4.4.3. ^{57}Fe Mössbauer spectra hyperfine splitting parameters of SoM samples at 800, 1000 and 1150 ℃ for HLW-NG-Fe2 (NG-Fe2) and HLW-NG-Fe2-II (NG-Fe2-II). CS relative to α-Fe. CS ± 0.02 mm s^{-1}, QS ± 0.02 mm s^{-1}, H ± 0.5 T, Area ± 2 %.

Feed	**Temperature ℃**	**Component**	**CS (mm s^{-1})**	**QS (mm s^{-1})**	**H (T)**	**Area (%)**
NG-Fe2	600	Doublet 1	0.33	1.12		9.1
		Sextet 1	0.37		51.6	53.0
		Sextet 2	0.36		49.7	26.0
		Sextet 3	0.35		46.4	11.9
NG-Fe2-II	600	Doublet 1	0.38	0.66		38.8
		Doublet 2	0.38	1.09		53.8
		Doublet 3	0.89	2.59		7.4
NG-Fe2	800	Doublet 1	0.25	0.95		25.8
		Sextet 1	0.37		60.0	59.3
		Sextet 2	0.40		44.5	15.0
NG-Fe2-II	800	Doublet 1	0.25	1.03		33.4
		Sextet 1	0.37		50.8	43.0
		Sextet 2	0.32		45.4	23.6
NG-Fe2	1000	Doublet 1	0.27	1.25		34.3
		Doublet 2	0.27	0.79		23.0
		Sextet 1	0.38		51.1	26.5
		Sextet 2	0.33		47.6	16.1
NG-Fe2-II	1000	Doublet 1	0.28	1.29		37.3
		Doublet 2	0.28	0.80		30.0
		Sextet 1	0.39		51.0	8.50
		Sextet 2	0.33		47.6	24.2
NG-Fe2	1150	Doublet 1	0.26	0.78		39.0
		Doublet 2	0.27	1.33		41.0
		Sextet 1	0.41		47.4	20.0
NG-Fe2-II	1150	Doublet 1	0.25	0.79		35.4
		Doublet 2	0.27	1.30		48.2
		Sextet 1	0.41		47.7	16.4

At 1150 ℃ the paramagnetic phases in each sample are consistent with tetrahedrally coordinated Fe^{3+} in the bulk amorphous glass (Darby Dyar et al. 2006; Nishida 1994).

The remaining sextets fitted to spectra for both samples are almost identical. Both have CS and QS that are similar to values for the two sites of Fe_3O_4, which has an A-site at CS = 0.32 mm s^{-1} and H = 49.5 T, and a B site at CS = 0.66 mm s^{-1} and H = 45.6 T (Oh, Cook, and Townsend 1998; Gorski and Scherer 2010; Ahmadzadeh, Scrimshire, Bingham, and Goel 2018; Deshkar et al. 2019; Winsett et al. 2019; Petrova et al. 2019). In the spectra shown in Figure 4.4.9, the sextet indicates that at least some Fe^{3+} occupies the B site in the spinel, from the literature in section 2.2.5. The relative amounts of spinel to paramagnetic phase, is extremely low (Figure 4.4.1 and Figure 4.4.2), which limits the resolution of the spinel sextet in the Mössbauer spectra.

After 24 hours of melting of the HLW-NG-Fe2 sample, Figure 4.4.10, there is an increase in the proportion of the doublet with the higher QS ~1.3 ± 0.02 mm s^{-1}, suggesting some equilibration towards the HLW-NG-Fe2 sample. However, further xVBF fits of the HLW-NG-Fe2-II 24-hour melt spectra and the and HLW-NG-Fe2 spectra, there is no significant difference in partitioning of the iron in the total paramagnetic phase, with CS = 0.26 ± 0.02 and QS = 1.06 ± 0.02 in the HLW-NG-Fe2-II sample compared with CS = 0.27 ± 0.02 and QS = 1.07 ± 0.02 in the 24-hour melt sample. This suggests that the partitioning observed in the Lorentzian doublets is almost certainly statistical. There total paramagnetic Fe decreases in the 24 hour sample to 72 ± 2 %, compared to 84 ± 2 % in the 1-hour melt sample, coupled with an increase in the relative abundance of the magnetic spinel phase, for which two sextets are now resolved with magnetic field strength, H, values corresponding to Magnetite (Fe_3O_4) (Oh, Cook, and Townsend 1998). There is no suggestion that the structure of Fe in the HLW-NG-Fe2-II glass phase approaches the structure in the HLW-NG-Fe2 glass with 24 hours melting time, as the Raman would suggest, the main structural change with melting time is the increase in the relative abundance of magnetic phase.

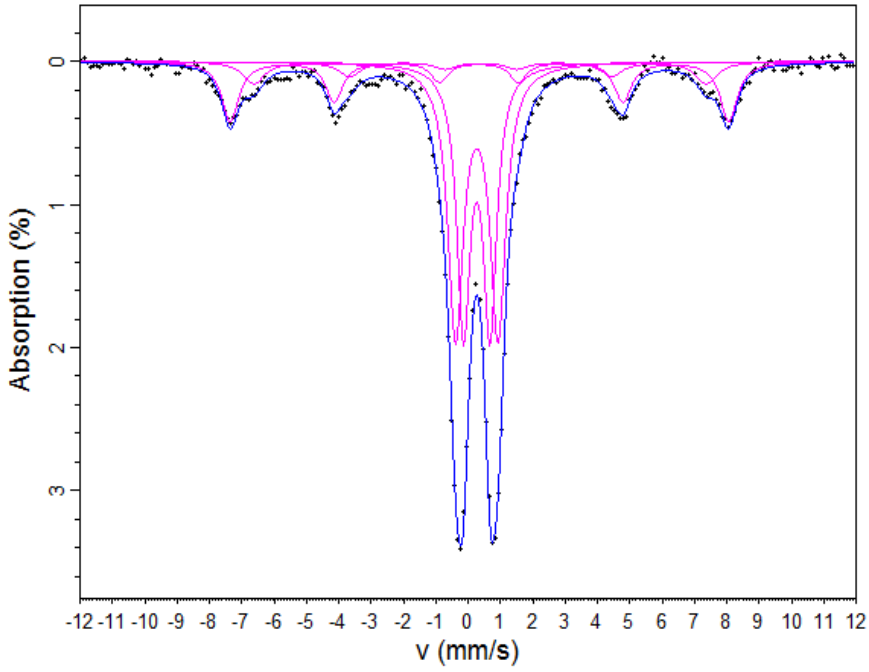

Figure 4.4.10. Room temperature ^{57}Fe Mössbauer spectrum for HLW-NG-Fe2-II glass sample heated to 1150 ℃ for 24 hours fitted with Lorentzian functions. CS relative to α-Fe. Identified paramagnetic doublets are Fe^{3+} iron and the sextets are iron-bearing spinel.

Table 4.4.4. Hyperfine fitting parameters for ^{57}Fe Mössbauer spectra of the HLW-NG-Fe2-II glass sample heated to 1150 ℃ for 24 hours. CS relative to α-Fe. CS ± 0.02 mm s^{-1}, QS ± 0.02 mm s^{-1}, H ± 0.5 T, Area ± 2 %.

Feed	**Temperature**	**Component**	**CS (mm s^{-1})**	**QS (mm s^{-1})**	**H (T)**	**Area (%)**
NG-Fe2-II 24-hour melt	1150 ℃	Doublet 1	0.27	0.82		32.6
		Doublet 2	0.27	1.31		39.0
		Sextet 1	0.35		47.8	19.4
		Sextet 2	0.38		43.4	9.0

4.5 Laboratory-scale melter study

4.5.1 Feed properties

Fast-dried slurry solid (FDSS) samples were generated, as described in Chapter 3, section 3.3.4, for both the HLW-NG-Fe2 and HLW-NG-Fe2-II feeds. Images of the samples, showing the distinct difference in colour and material properties are given in Figure 4.5.1. The purpose of generating these samples was to test the feeding behaviour through the Tygon tubing used in the Laboratory Scale Melter (LSM) system. As described in Chapter 3, section 3.3.1., the HLW-NG-Fe2 feed had a significantly different rheology to the HLW-NG-Fe2-II feed, meaning more water needed to be added to the HLW-NG-Fe2 feed to allow the feed to flow. During the run for the HLW-NG-Fe2 sample there were multiple occasions where the tubing was blocked by the highly viscous feed. The HLW-NG-Fe2-II sample experienced no feeding issues throughout the creation of the sample.

Figure 4.5.1. Fast-dried slurry solid samples of the HLW-NG-Fe2 feed (left) and HLW-NG-Fe2-II feed (right) showing the difference in colour and texture of the two feeds.

4.5.2 LSM Run

The process of creating the laboratory scale melter sample is described in Chapter 3 section 3.3.5. The HLW-NG-Fe2-II feed was used to produce an LSM sample, based on the FDSS tests of feed properties (D. S. Kim et al. 2012), section 4.5.1. The stirred feed was fed into the top of the LSM, on top of 200 g of pre-melted HLW-NG-Fe2-II glass,

for ~1 hour at an average rate of 9 mL min^{-1}. Thermocouples recorded the temperature of the melt and plenum every 20 s during feeding to ensure that the melt temperature stayed at ~1150 ℃, while the plenum temperature indicated cold cap coverage. A graph of the thermocouple readings during the run is given in Appendix B, Figure 1. Feeding was halted after a sufficient cold cap was generated. After a further 25 minutes of dwelling the entire melter vessel removed from the furnace and quenched immediately in air. Once cooled the sample was removed from the silica crucible and divided into two sections, shown in Figure 4.5.2, for analysis by SEM/EDX (section 4.5.3) and X-Ray CT (section 4.5.4).

Figure 4.5.2. Image of the final HLW-NG-Fe2-II LSM sample broken from the crucible showing the porous dried feed, small bubbles and large cavities and the glass melt encased in the fused silica vessel.

4.5.3 SEM/EDX

A portion of the LSM sample was cut apart and ground to 1 mm grain size using SiC, and then polished to 1 μm using diamond paste. SEM/EDX was performed on three key regions of the sample: (1) top porous feed region (2) middle feed-to-glass transition region (3) lower glass region. SEM images were taken in backscattered and secondary electron modes at an electron voltage of 20 kV. The secondary electron images are

compared in Figure 4.5.3, with the SoM samples for morphology and structure of the glasses. The 1000 ℃ SoM sample, Figure 4.5.3, I has a similar morphology to the top of the LSM sample, Figure 4.5.3 (a), where there are a significant number of bubbles in a partially glassy matrix. The 1150 ℃ sample, Figure 4.5.3 (f), showing some crystalline inclusions on a mostly glassy matrix, is most similar to the bottom of the LSM sample, Figure 4.5.3 (c). We approximate the image taken of the middle feed-to-glass region reached within the temperature range 800-1000 ℃ where the glassy matrix has formed and there are few bubbles remaining, but still large undissolved particles, such as the haematite and quartz phases found in section 4.4.1. The 800 ℃ sample is largely inhomogeneous, and the bulk structure of the melt does not appear to have formed. A section of the LSM sample that had reached this temperature would likely have been too easily removed during the sample preparation, Chapter 3, section 3.7.1.

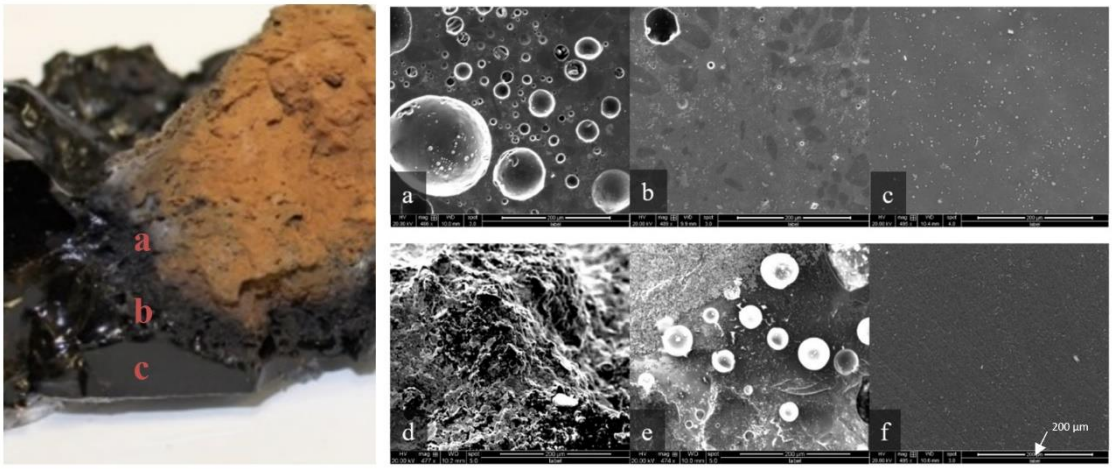

Figure 4.5.3. Secondary electron images of the top (a), middle (b) and bottom (c) of the HLW-NG-Fe2-II LSM sample, and the 800 ℃ (d), 1000 ℃ (e) and 1150 ℃ (f) HLW-NG-Fe2 SoM samples. Region (a) on the LSM sample correlates most to (e) the 1000 ℃ sample, with scattered bubbles in an inhomogeneous matrix, the bottom glass and sample (f) both appear mostly homogenous.

EDX maps of spinels present in the lower portion, section (c) in the micrographs in Figure 4.5.3, of the LSM sample, are shown in Figure 4.5.4. Similar to those in the 1150

°C sample, they contain Fe, Ni, Mn and Cr. EDX maps of the top feed region (a) and middle feed-to-glass region (b) are in Appendix D, Figure 1-2.

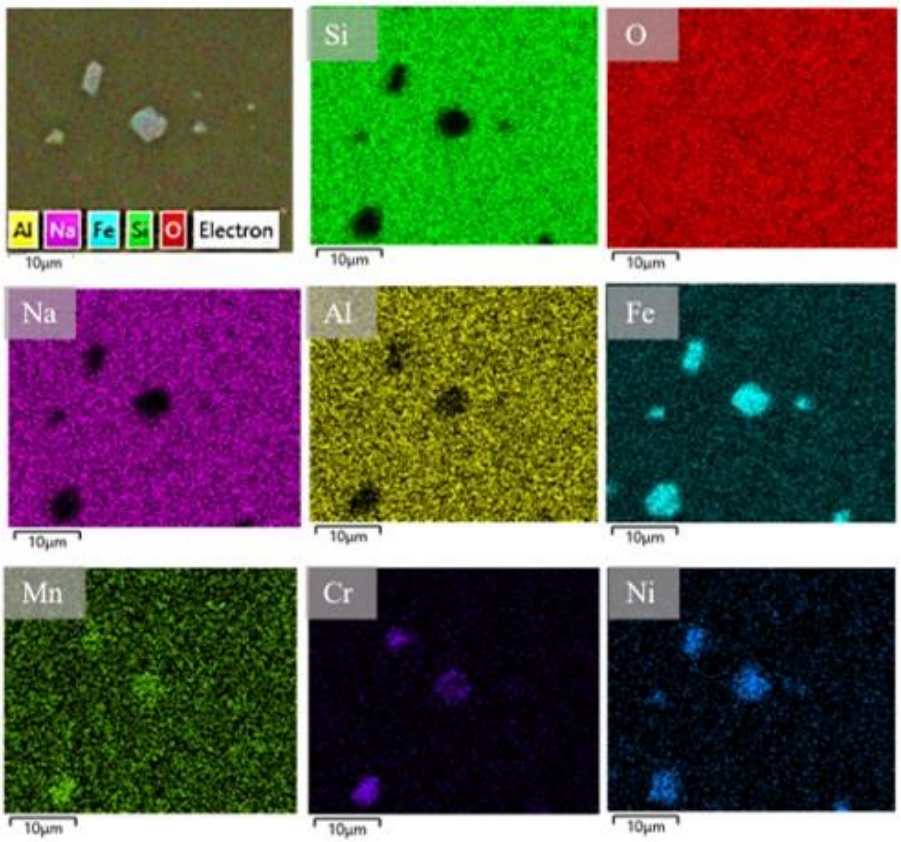

Figure 4.5.4. EDX mapping of the bottom glass region (c) of the HLW-NG-Fe2-II LSM sample showing a number of spinel crystals containing Fe, Mn, Cr and Ni in an otherwise amorphous glassy matrix.

4.5.4 X-ray CT

X-ray CT was performed on a portion of the HLW-NG-Fe2-II LSM sample, and image slices were analysed in ImageJ. Of the sub-stack of 1329 image slices processed from the X-ray CT, a montage of every 37 images is shown in Figure 4.5.5, starting at the top feed region of the LSM sample through to the glass at the bottom. The protocol for the image processing is described in Chapter 3, section 3.7.3.

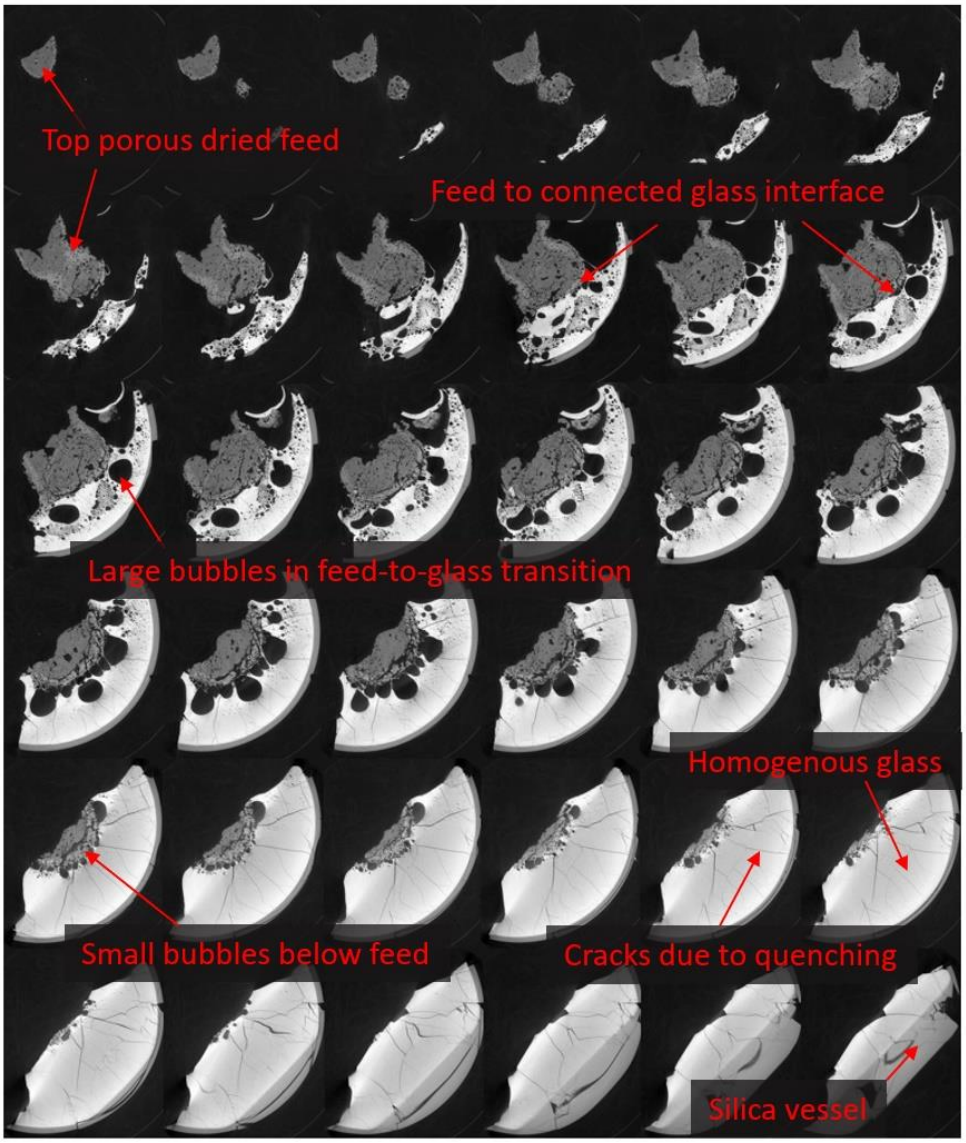

Figure 4.5.5. Montage of X-ray Tomography images of the HLW-NG-Fe2-II LSM sample, from the top porous feed region in the top left image, through the feed-to-glass transition. Showing the different densities of the feed and glass, and emergence of large and smaller bubbles. The bottom right image shows the homogenous glass in the bottom of the silica crucible.

The closed porosity through the height of the sample, shown in Figure 4.5.6, resembles the HLW-NG-Fe2-II feed volume expansion curve in Figure 4.3.4. There is a sharp peak of maximum porosity followed by a plateau of high porosity and a similar exponential-like decay to 0 porosity at the bottom of the sample. As discussed in the

research methods, Chapter 3, section 3.7.3, there is a balance during segmentation of the images in the middle feed-to-glass where there is a combination of dense glass (the brighter section of the images) and less dense feed region (the mid-range contrast) in Figure 4.5.5. In these images some of the smallest bubbles in the glass were segmented out of the final processed image so as to not overestimate the porosity by counting some darker areas of the feed region. The values presented are conservative for the total number of bubbles, particularly biased against the smallest bubbles.

Figure 4.5.7 shows that a small number of large bubbles do not necessarily contribute significantly to the porosity, Figure 4.5.5. The relatively small bubbles in the lower section of the sample are numerous enough to contribute to significant porosity between 10 and 5 cm down through the height of the sample. Similarly, in previous X-ray CT of a pellet expansion test of the HLW-Al-19 melter feed, the volume of the segmented bubbles did not account for the total measured porosity of the sample, those smaller bubbles that could not be segmented accounted for approximately half of the porosity at maximum foam temperature (Luksic et al. 2021).

The decrease in consistency of the circularity of the bubbles with height through the cold cap aligns with the models of bubbles rising through a liquid, those near surface and within the feed layer will deform due to the change in viscosity of the surrounding melt (Amaya-Bower and Lee 2010; Abboud and Guillen 2016).

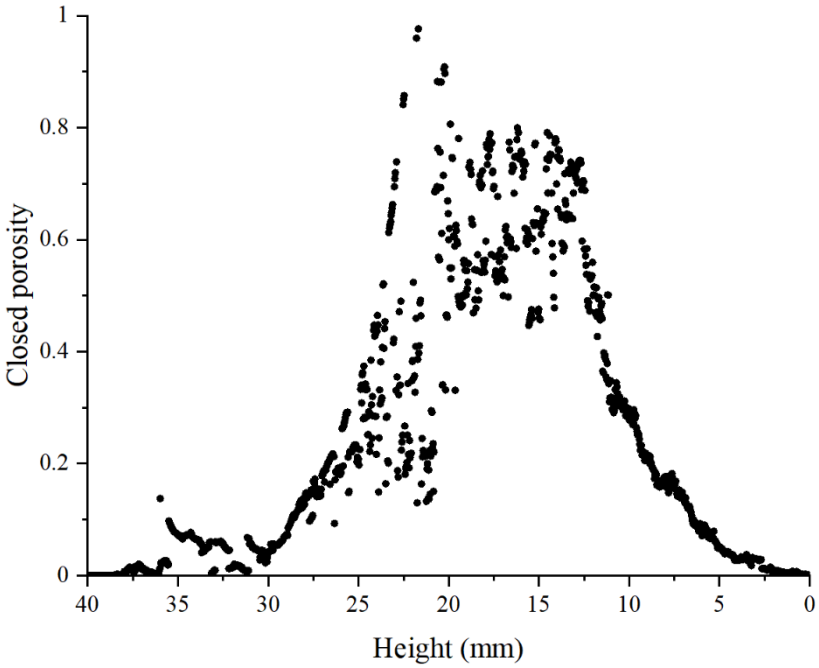

Figure 4.5.6. Closed porosity of the LSM sample by image analysis of X-ray Tomography, in ImageJ, showing large peak porosity followed by sustained lower porosity further down in the sample.

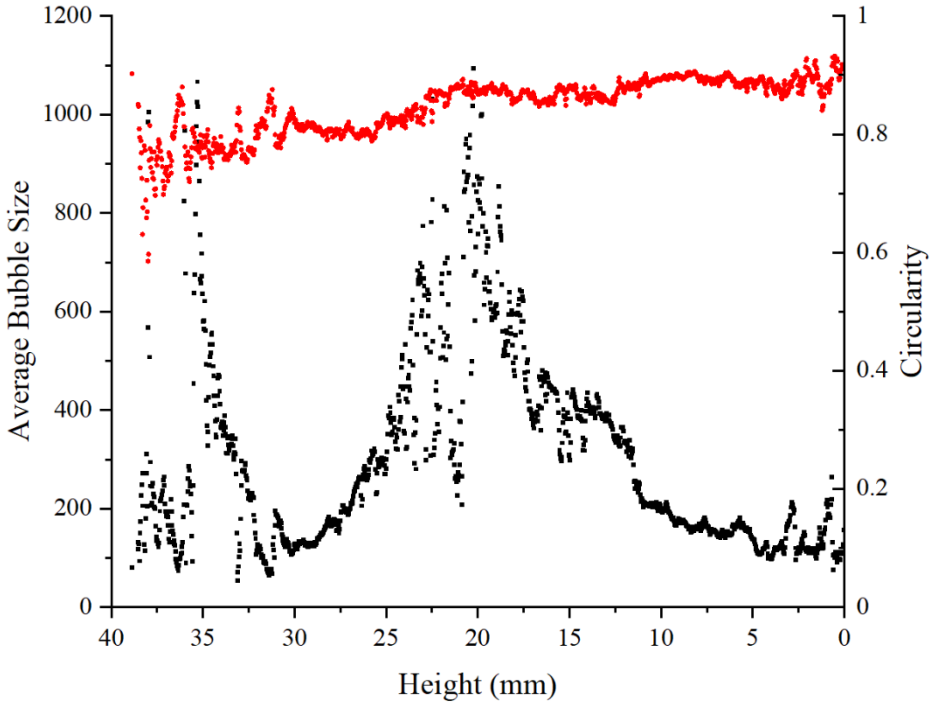

Figure 4.5.7. Average bubble size (black) and circularity (red) through slices of the LSM sample by X-ray Tomography showing large bubbles at the surface of the sample as well as in the centre. Those at the sample surface are least circular.

4.6 Summary

4.6.1 Foaming and gas evolution

Using a reduced raw material for iron in the HLW-NG-Fe2 feed reduced the foaming during melting to 50 ± 10.8 % of the original. The reduction in foaming agrees with previous studies of carbon addition and change of raw materials during vitrification, discussed in the literature review, sections 2.5.3 and 2.6.2. The difference in the volume of primary foam, in Figure 4.3.4, is due to evolving more CO and CO_2 at lower temperatures before the glass melt was viscous, by TGA and EGA, section 4.3.2. In the HLW-NG-Fe2 feed the earlier connection of a viscous melt means that a larger quantity of gases are trapped, forming bubbles and causing the much larger expansion.

Based on the thermal analysis results, section 4.3.2, in combination with the structural analysis, section 4.4, we here propose potential decomposition pathways for the iron-bearing raw materials in each of the feeds. It is likely that both raw materials dehydrate by ~350 ℃, shown in Figure 4.3.5, by the reactions

$$FeC_2O_4{\cdot}2H_2O \rightarrow FeC_2O_4 + 2H_2O \quad (28)$$

$$2Fe(OH)_3 \rightarrow Fe_2O_3 + 3H_2O \quad (29)$$

XRD patterns of HLW-NG-Fe2 during melting in Figure 4.4.2 show that by 600 ℃ both Fe_2O_3 and iron containing spinel structures have formed, as observed previously with this feed (Guillen et al. 2020), and they increase in relative abundance at temperatures up to 800 ℃. At temperatures above 800 ℃ the Fe-containing crystals dissolve into the melt, leaving traces of spinel crystals at 1150 ℃, by the reaction,

$$3Fe_2O_3 \rightarrow 2Fe_3O_4 + ½\ O_2 \quad (30)$$

There are two potential pathways for FeC_2O_4 to decompose proposed in the literature, Chapter 2, section 2.6.3 (López, Tirado, and Pérez Vicente 2013; Carles et al. 1999; Ogasawara and Koga 2014).

$$FeC_2O_4 \rightarrow FeO + CO + CO_2 \quad (31)$$

$$CO + \frac{1}{2} O_2 \rightarrow CO_2 \quad (32)$$

$$2FeO + \frac{1}{2} O_2 \rightarrow Fe_2O_3 \quad (33)$$

$$3FeC_2O_4 \rightarrow Fe_3O_4 + 4CO + 2CO_2 \quad (34)$$

Increased evolution of CO and CO_2 is consistent with either or both of these reactions. The suppression of O_2 evolution, measured by EGA, also supports the consumption of O_2 in the first reaction Equations (31), (32) and (33). From XRD (Figure 4.4.1 and Figure 4.4.2), spinel crystals form at 700 ℃ and then haematite forms at 800 ℃. This would suggest that the reaction in Equation (34) occurs, and that some spinel oxidises to form haematite, Fe_2O_3, by 800 ℃. While there is no change in the redox state of the paramagnetic Fe with melting in the HLW-NG-Fe2 feed, by ^{57}Fe Mössbauer spectroscopy, section 4.4.4, O_2 will be evolved during the formation of Fe_3O_4, and the redox state of other multivalent species in this feed has not been assessed, which could account for generation of some O_2. O_2 evolution is entirely suppressed in the HLW-NG-Fe2-II feed above 800 ℃ due to consumption of O_2 in reactions with CO and FeO.

4.6.2 Structure of the feeds during melting

The form of iron during melting may play a key role in melting reactions and foam evolution in these feeds. The Raman spectroscopy, section 4.4.3, and XRD, section 4.4.1, show the $Fe(OH)_3$ iron raw material has decomposed to a mixture of haematite, Fe_2O_3, and iron-bearing spinel, by 600 ℃. The ratio of haematite to spinel phase decreases with increasing temperature. The structural study of the HLW-NG-Fe2-II samples support decomposition of the remaining FeC_2O_4 to unstable FeO, and Fe^{3+} in the paramagnetic phase, by ^{57}Fe Mössbauer spectroscopy, section 4.4.4, followed by the formation of crystalline Fe_2O_3, in section 4.4.4 and the XRD in section 4.4.1. The same behaviour was observed in the decomposition of FeC_2O_4 in air (Smrčka et al. 2016).

Fe_3O_4 is present in greater quantities throughout melting in the HLW-NG-Fe2-II feed, by XRD, section 4.4.1, compared with the original HLW-NG-Fe2 feed, showing a lack of oxygen available.

With increasing temperature, the reduction in crystalline components by XRD, section 4.4.1 and magnetic iron phases by ^{57}Fe Mössbauer, section 4.4.4, are consistent with the amorphization of the melt and dissolution of crystalline raw materials and intermediate phases. The Raman spectra also show the dissolution of crystalline raw materials and amorphization of the melt, by the emergence of the Q^n species region and other borosilicate modes, Figure 4.4.5 and Figure 4.4.6. By XRD there is no significant difference in the melting rate of the silica or in the proportion of the amorphous phase, however the Raman suggests that the recognisable borosilicate structures form at 900 °C in the HLW-NG-Fe2 and not until 1000 °C in the -II samples.

At melt temperature the two glasses are structurally similar but not identical: the difference in the structure is only observed in the 610 cm^{-1} band in Raman spectroscopy, attributed to danburite-like ring structures, potentially dependent on the form of iron. Neither of the final glasses contain Fe^{2+} iron, within the detection limits of ^{57}Fe Mössbauer spectroscopy and approximately equal quantities of spinel phase were present in the final glass by ^{57}Fe Mössbauer spectroscopy and XRD.

4.6.3 Laboratory Scale Melter sample

The Laboratory Scale Melter run for the HLW-NG-Fe2-II feed produced a sufficient LSM sample, which was examined by SEM/EDX and X-ray CT. SEM/EDX compared the sample to the SoM samples of the same feed between 800 and 1150 °C, with some agreement in morphology between 1000 and 1150 °C. Analysed X-ray tomography images through the height of the sample correlated with the foaming curve by the feed volume expansion tests.

The feed volume expansion tests employed in this study were designed to represent a single particle of feed travelling vertically downwards through the cold cap (Lee, Hrma, Pokorný, et al. 2017; Hrma and Pokorný 2016). Secondary gases evolve from the feed pellet; however, they are not trapped beneath a primary foam layer as they would be within the cold cap inside a melter. This limitation of the experiment may cause underestimation of the significance of secondary foaming to overall foaming and heat transfer. The high porosity due to small bubbles observed, beyond the maximum foam region in the X-Ray-CT of the LSM sample, Figure 4.5.6 and Figure 4.5.7 support this being the case. Understanding the morphology of foaming of the cold cap helps to model the heat transfer to the reacting feed.

Evaluating the use of a reduced iron raw material is more academic than practical, since the iron source comes directly from the waste tank rather than being added as a glass former (G. L. Smith et al. 2001). It is not possible to change the initial iron raw material, and impractical to change the initial oxidation state. However, the value in comparing the two feeds with the alternative raw materials is in addressing the aim of understanding the mechanisms of foam production, providing an important contribution to the ongoing research into developing cold cap models.

4.7 References

Abboud, A. W. and Guillen, D. P. (2016) 'Computational fluid dynamics modeling of bubbling in a viscous fluid for validation of waste glass melter modeling', International Topical Meeting on Advances in Thermal Hydraulics 2016, ATH 2016, pp. 527–538.

Ahmadzadeh, M., Scrimshire, A., Bingham, P. A. and Goel, A. (2018) 'Structural Role of Iron in Nepheline-based Aluminosilicates for Nuclear Waste Applications.' WM2018 Conference, Phoenix, AZ (United States).

Amaya-Bower, Luz, and Taehun Lee. (2010) 'Single Bubble Rising Dynamics for Moderate Reynolds Number Using Lattice Boltzmann Method.' Computers and Fluids 39(7), pp. 1191–1207.

Andrzejewski, B., W. Bednarski, M. Kaźmierczak, K. Pogorzelec-Glaser, B. Hilczer, S. Jurga, M. Matczak, B. Łęska, R. Pankiewicz, and L. Kępiński. 2014. Magnetization Enhancement in Magnetite Nanoparticles Capped with Alginic Acid. Composites Part B: Engineering, 64, pp. 147–54.

Barth, S. and Feltz, A. (1989) 'Structure and ionic conduction in solids. VII. Ion conducting glasses in the system $Na_2ONb_2O_5P_2O_5$.' Solid State Ion. 34, 41–45

Bell, A. M. T., Backhouse, D. J., Deng, W., Eales, J. D., Kilinc, E., Love, K., Rautiyal, P., Rigby, J. C., Stone, A. H., Vaishnav, S., Wei-Addo, G. and Bingham, P. A. (2020) 'X-ray fluorescence analysis of feldspars and silicate glass: Effects of melting time on fused bead consistency and volatilisation.' Minerals, 10(5).

Bickford, D. F., Applewhite-Ramsey, A., Jantzen, C. M. and Brown, K. G., (1990.) 'Control of Radioactive Waste Glass Melters: I, Preliminary General Limits at Savannah River.' Journal of the American Ceramic Society, 73, 2896–2902.

Bonnenfant, A., J. M. Friedt, M. Maurer, and J. P. Sanchez. (1982) ‘Magnetic and Structural Properties of Iron-Based Oxide Glasses, Fe_2O_3-BaO-B_2O_3, from ^{57}Fe Mossbauer Spectroscopy.’ Journal de Physique 43(10) pp. 1475–87.

Brik, M. G., Suchocki, A. and Kamińska, A. (2014) ‘Lattice parameters and stability of the spinel compounds in relation to the ionic radii and electronegativities of constituting chemical elements’, Inorganic Chemistry, 53(10), pp. 5088–5099.

Carles, V., Alphonse, P., Tailhades, P. and Rousset, A. (1999) ‘Study of thermal decomposition of $FeC_2O_4.2H_2O$ under hydrogen’, Thermochimica Acta, 334(1–2), pp. 107–113.

Chen, L., Zhang, D. F., Lv, P., Zhang, J. D., Du, X., Yuan, W., Nan, S., Zhu, Z. H. and Wang, T. S. (2016) ‘Evolutions of molecular oxygen formation and sodium migration in Xe ion irradiated borosilicate glasses’, Journal of Non-Crystalline Solids, 448, pp. 6–10.

Cochain, B., Neuville, D. R., Henderson, G. S., McCammon, C. A., Pinet, O. and Richet, P. (2012) ‘Effects of the iron content and redox state on the structure of sodium borosilicate glasses: A Raman, Mössbauer and boron K-edge XANES spectroscopy study’, Journal of the American Ceramic Society, 95(3), pp. 962–971.

Cochain, B. and Neuville, D. R. (2008) ‘Determination of iron redox ratio in borosilicate glasses and melts from Raman spectra’, in Atalante, Montpellier (France).

D’Antonio, M. C. Wladimirsky, A. Palacios, D. Coggiola, L. González-Baró, A. C. Baran, E. J. Mercader, R. C. (2009) ‘Spectroscopic investigations of iron(II) and iron(III) oxalates.’ Journal of the Brazilian Chemical Society. 20, pp. 445–450.

Darby Dyar, M. (1985) ‘A review of Mössbauer data on inorganic glasses: The effects of composition on iron valency and coordination’, The American mineralogist, 70(3), pp. 304–316.

Darby Dyar, M., Agresti, D. G., Schaefer, M. W., Grant, C. A. and Sklute, E. C. (2006) ‘Mössbauer Spectroscopy of Earth and Planetary Materials.’ Annual Review of Earth and Planetary Sciences. 34, pp. 83–125.

Deshkar, A. Ahmadzadeh, M. Scrimshire, A. Han, E. Bingham, P. A. Post Guillen, D. McCloy, J. Goel, A. (2018) ‘Crystallization behavior of iron- and boron-containing nepheline ($Na_2O{\cdot}Al_2O_3{\cdot}2SiO_2$) based model high-level nuclear waste glasses.’ Journal of the American Ceramics Society. 4, pp. 1–21.

de Faria, D. L. A. and Lopes, F. N. (2007) ‘Heated goethite and natural hematite: Can Raman spectroscopy be used to differentiate them?’, Vibrational Spectroscopy, 45(2), pp. 117–121.

Fultz, B. (2012) ‘Mössbauer Spectrometry.’ In Kaufman, E. N. (ed.), ‘Characterisation of Materials.’ Hoboken, MJ (United States): John Wiley & Sons, Ltd.

Garcia-Muñoz, P., Fresno, F., de la Peña O’Shea, V. A. and Keller, N. (2020) ‘Ferrite Materials for Photoassisted Environmental and Solar Fuels Applications.’ In: Muñoz-Batista, M., Navarrete Muñoz, A., Luque, R. (eds) ‘Heterogeneous Photocatalysis. Topics in Current Chemistry Collections.’ Springer, Cham. (Switzerland), pp. 107–162.

Giles, H. L., Hurley, P. W. and Webster, H. W. M. (1995) ‘Simple approach to the analysis of oxides, silicates and carbonates using X-ray fluorescence spectrometry.’ X-Ray Spectrometry, 4(24), 205–218.

Gorski, C. A. and Scherer, M. M. (2010) ‘Determination of nanoparticulate magnetite stoichiometry by Mössbauer spectroscopy, acidic dissolution, and powder X-ray diffraction: A critical review.’ Am. Mineral. 95, pp. 1017–1026.

Guillen, D. P., Lee, S., Hrma, P., Traverso, J., Pokorný, R., Kloužek, J. and Kruger, A. A. (2020) 'Evolution of chromium, manganese and iron oxidation state during conversion of nuclear waste melter feed to molten glass.' Journal of Non-Crystalline Solids, 531, 119860.

Hrma, P. and Pokorný, R. (2016) 'The Office of River Protection Cold Cap and Melt Dynamics Technology Development and Research Plan.' PNNL-25350. Pacific Northwest National Laboratory, Richland, WA (United States).

Hrma, P., Pokorný, R., Lee, S. M. and Kruger, A. A. (2018) 'Heat transfer from glass melt to cold cap: Melting rate correlation equation.' International Journal of Applied Glass Science, (August) pp. 1–8.

Hrma, P., Schill, P. and Nemec, L. (2002) 'Settling of Spinel in a High-Level Waste Glass Melter.' PNNL-13747. Pacific Northwest National Laboratory, Richland, WA (United States).

Jin, T. Chun, J. Dixon, D. R. Kim, D-S. Crum, J. V. Bonham, C. C. VanderVeer, B. J. Rodriguez, C. P. Weese, B. L. Schweiger, M. J. Kruger, A. A. Hrma, P. (2018) 'Melter feed viscosity during conversion to glass: Comparison between low-activity waste and high-level waste feeds.' Journal of the American Ceramics Society. 101, pp. 1880–1891.

Jubb, A. M. and Allen, H. C. (2010) 'Vibrational spectroscopic characterization of hematite, maghemite, and magnetite thin films produced by vapor deposition', ACS Applied Materials and Interfaces, 2(10), pp. 2804–2812.

Kim, D. -S., Schweiger, M. J., Buchmiller, W. C. and Matyáš, J. (2012) 'Laboratory scale melter for determination of melting rate of waste glass feeds.' PNNL-21005. Pacific Northwest National Laboratory, Richland, WA. (United States).

Krolop, P., Jantschke, A., Gilbricht, S., Niiranen, K. and Seifert, T. (2019) 'Mineralogical imaging for characterization of the per geijer apatite iron ores in

the Kiruna district, northern Sweden: A comparative study of mineral liberation analysis and raman imaging', Minerals, 9(9), pp. 7–11.

Lee, S., Hrma, P., Pokorný, R., Kloužek, J., Eaton, W. C. and Kruger, A. A. (2019) 'Glass production rate in electric furnaces for radioactive waste vitrification', Journal of the American Ceramics Society. 102(10). pp. 5828–5842.

Lee, S., Hrma, P., Pokorný, R., Kloužek, J., VanderVeer, B. J., Dixon, D. R., Luksic, S. A., Rodriguez, C., Chun, J., Schweiger, M. J. and Kruger, A. A. (2017) 'Effect of melter feed foaming on heat flux to the cold cap', Journal of Nuclear Materials. 496, pp. 54–65.

Li, J. M. and Huan, A. (2000) 'Interface effects on magnetoresistance and magnetic-field-reduced Raman scattering in magnetite–, Physical Review B - Condensed Matter and Materials Physics, 61(10), pp. 6876–6878.

López, M. C., Tirado, J. L. and Pérez Vicente, C. (2013) 'Structural and comparative electrochemical study of M(II) oxalates, M = Mn, Fe, Co, Ni, Cu, Zn', Journal of Power Sources, 227, pp. 65–71.

Luksic, S. A., Pokorny, R., Hrma, P., Varga, T., Rivers, E. L., Buchko, A. C., Kloužek, J. and Kruger, A. A. (2021) 'Through a glass darkly: In-situ X-ray computed tomography imaging of feed melting in continuously fed laboratory-scale glass melter', Ceramics International. Elsevier Ltd, 47(11), pp. 15807–15818.

Marcial, J., Chun, J., Hrma, P. and Schweiger, M. J. (2014) 'Effect of bubbles and silica dissolution on melter feed rheology during conversion to glass', Environmental Science and Technology, 48(20), pp. 12173–12180.

Marcial, J., Pokorný, R., Kloužek, J., Vernerová, M., Lee, S., Hrma, P. and Kruger, A. (2021) 'Effect of water vapor and thermal history on nuclear waste feed conversion to glass', International Journal of Applied Glass Science, 12(1), pp. 145–157.

Marcial, J., Kloužek, J., Vernerová, M., Ferkl, P., Lee, S., Cutforth, D., Hrma, P., Kruger, A. and Pokorný, R. (2021) 'Effect of Al and Fe sources on conversion of high-level nuclear waste feed to glass', Journal of Nuclear Materials, 559(153423).

Nelson, J. L. (2010) 'IHLW Waste Form Qualification Report for the Hanford Tank Waste Treatment and Immobilization Plant.' 24590-HLW-RPT-RT-08-001 Rev. 0., US Department of Energy, Office of River Protection, Richland, WA (United States).

Nishida, T. (1994) '^{57}Fe and ^{119}Sn-Mössbauer effect of oxide glasses.' Journal of Radioanalytical and Nuclear Chemistry. 182, pp. 451–476.

Ogasawara, H. and Koga, N. (2014) 'Kinetic modeling for thermal dehydration of ferrous oxalate dihydrate polymorphs: A combined model for induction period-surface reaction-phase boundary reaction', Journal of Physical Chemistry A, 118(13), pp. 2401–2412.

Oh, S. J., Cook, D. C. and Townsend, H. E. (1998) 'Characterisation of iron oxides commonly formed as corrosion products on steel', Hyperfine Interactions, 112, pp. 59–65.

Osipov, A. A., Osipova, L. M. and Eremyashev, V. E. (2013) 'Structure of alkali borosilicate glasses and melts according to Raman spectroscopy data', Glass Physics and Chemistry, 39(2), pp. 105–112.

Parkinson, B. G. Holland, D. Smith, M. E. Larson, C. Doerr, J. Affatigato, M. Feller, S. A. Howes, A. P. Scales, C. R. (2008) 'Quantitative measurement of Q^3 species in silicate and borosilicate glasses using Raman spectroscopy', Journal of Non-Crystalline Solids, 354(17), pp. 1936–1942.

Petrova, E. V., Maksimova, A. A., Chukin, A. V. and Oshtrakh, M. I. (2019) 'X-ray diffraction and Mössbauer spectroscopy of Gandom Beryan 008 ordinary chondrite', Hyperfine Interactions. Hyperfine Interactions, 240(1), pp. 1–9.

Pokorný, R. and Hrma, P. (2011) 'Mathematical Model of Cold Cap — Preliminary One-Dimensional Model Development.' PNNL-20278. Pacific Northwest National Laboratory, Richland, WA (United States).

Pokorny, R., Kruger, A. A. and Hrma, P. (2014) 'Mathematical Modeling of Cold Cap: Effect of Bubbling on Melting Rate', Ceramics - Silikaty, 58(4), pp. 296–302.

Schreiber, H. D., Kozak, S. J., Merkel, R. C., Balazs, G. B. and Jones, P. W. (1986) 'Redox equilibria and kinetics of iron in a borosilicate glass-forming melt.' Journal of Non-Crystalline Solids, 84(1–3). pp. 186–195.

Sharma, K., Singh, S., Prajapat, C. L., Bhattacharya, S., Jagannath, Singh, M. R., Yusuf, S. M. and Kothiyal, G. P. (2009) 'Preparation and study of magnetic properties of silico phosphate glass and glass-ceramics having iron and zinc oxide', Journal of Magnetism and Magnetic Materials, 321(22), pp. 3821–3828.

Shrotri, J. J., Deshpande, C. E., Date, S. K. and Ogale, S. B. (1986) 'Chemical passivation of unstable FeO - A Mössbauer study', Hyperfine Interactions, 28(1–4), pp. 733–736.

Sickafus, K. E., Wills, J. M. and Grimes, N. W. (1999) 'Structure of spinel', Journal of the American Ceramic Society, 82(12), pp. 3279–3292.

Slavov, L. Abrashev, M. V. Merodiiska, T. Gelev, C. Vandenberghe, R. E. Markova-Deneva, I. Nedkov, I. (2010) 'Raman spectroscopy investigation of magnetite nanoparticles in ferrofluids.' Journal of Magnetism and Magnetic Materials. 322, pp. 1904–1911.

Smith, G. L. Bates, D. J., Goles, R. W., Greenwood, L. R., Lettau, R. C., Piepel, G. F., Schweiger, M. J., Smith, H. D., Urie, M. W., Wagner, J. J. (2001) 'Vitrification

and Product Testing of C-104 and AZ-102 Pretreated Sludge Mixed with Flowsheet Quantities of Secondary Wastes.' PNNL-13452. Pacific Northwest National Laboratory. Richland, WA (United States).

Smrčka, D., Procházka, V., Novák, P., Kašlík, J. & Vrba, V. (2016) 'Iron oxalate decomposition process by means of Mössbauer spectroscopy and nuclear forward scattering.' American Institute of Physics Conference Proceedings. 1781, 020012

Testa-Anta, M., Ramos-Docampo, M. A., Comesaña-Hermo, M., Rivas-Murias, B. and Salgueiriño, V. (2019) 'Raman spectroscopy to unravel the magnetic properties of iron oxide nanocrystals for bio-related applications', Nanoscale Advances, 1, pp. 2086–2103.

Winsett, J., Moilanen, A., Paudel, K., Kamali, S., Ding, K., Cribb, W., Seifu, D. and Neupane, S. (2019) 'Quantitative determination of magnetite and maghemite in iron oxide nanoparticles using Mössbauer spectroscopy', SN Applied Sciences. Springer International Publishing, 1(12), pp. 1–8.

Yadav, A. K. and Singh, P. (2015) 'A review of the structures of oxide glasses by Raman spectroscopy', RSC Adv. Royal Society of Chemistry, 5(83), pp. 67583–67609.

Yun, Y. H. and Bray, P. J. (1978) 'Nuclear magnetic resonance studies of the glasses in the system $K_2OB_2O_3P_2O_5$.' Journal of Non-Crystalline Solids. 30, pp. 45–60.

5 Alternative Reductants – Foaming and Gas Evolution

5.1 Overview

Additives to feeds present a more accessible and more developed method to reduce foaming, than a change of raw material, as discussed in Chapter 4. Sucrose is the baseline reductant at the Hanford site, based on balancing the C/N ratios in high-nitrate feeds from experience at the Defense Waste Processing Facility (DWPF), SC, and Hanford Low-Activity Waste feed research (Lee, Hrma, Kloužek, et al. 2017; Hujová, Pokorný, et al. 2018; Appel et al. 2019). In the early evaluation of alternative reductants on the Hanford site waste glasses, particularly using carboxylic acids, the effect on redox behaviour of mixed multivalent species feeds was not well understood (Seymour 1995). Seymour, in 1995, suggested that fine tuning of the interrelationship of the complex redox chemistry of the cold cap and melt pool should be pursued (Seymour 1995). In Low-Activity (LAW) feeds ratios up to C:N = 1.2 have seen large reductions in foaming (Appel et al. 2019; Hrma, Marcial, et al. 2011; Hrma et al. 2010). However, nitrates are not the key issue in High-Level (HLW) feeds. As discussed in section 2.6, the original HLW-NG-Fe2 feed less than 0.5 wt% nitrates, without significant quantities of nitrates in the feed, the models used to determine the amount of sugar to add to high-nitrate LAW feeds needs to be modified for HLW feeds high in multivalent species such as Fe, and further testing is required to better define the relationship between different sources of carbon and melting behaviour (Kruger, Matlack, Pegg, et al. 2012). As discussed in the previous chapter, Chapter 4, high-temperature evolution of O_2 may contribute more to foam behaviour in the HLW-NG-Fe2 feed, than in low-multivalent

species LAW feeds. Redox manipulation of the feeds becomes important in this case (Bickford 1986; Pinet, Hugon, and Mure 2014).

In Chapter 2, section 2.8, alternative reductants from both the industrial glass melting industry and previous waste vitrification programs are discussed. The reductants in Table 3.2.3: sucrose, graphite, coke, formic acid and HEDTA, were selected based on this review of the literature, to provide a range of reductants to explore foaming behaviour and redox manipulation in the HLW-NG-Fe2 feed. The HLW-NG-Fe2 feeds with added carbon-based reductants, are discussed collectively as the HLW-NG-Fe2-R feeds. The coke used in the study is ~93.3 wt% C according to XRF, with 3.1 wt% O, 1.1 wt% Si, 0.8 wt% Al, 0.6 wt% Fe, 0.4 wt% S, 0.3 wt% Ca, 0.1 wt% Mg and 0.1 wt% Ti, with trace amounts of P, Na, Cl, Ba, Sr, Mn, Cr, Ru and Ni.

5.2 Graphite Study

To determine the wt% addition to the feeds, a series of HLW-NG-Fe2 glasses were melted with 0.5, 1, 2, 3, 4, 5, and 6 wt% graphite addition to the feed, and XRD was performed to determine the extent of crystallinity, and whether any metallic phases formed which must be avoided (Appel et al. 2019; Jantzen et al. 2003; Jantzen 2011). Graphite, having the highest carbon content per gram of compound, was used as the "worst case" scenario as it was expected to most strongly reduce the melt.

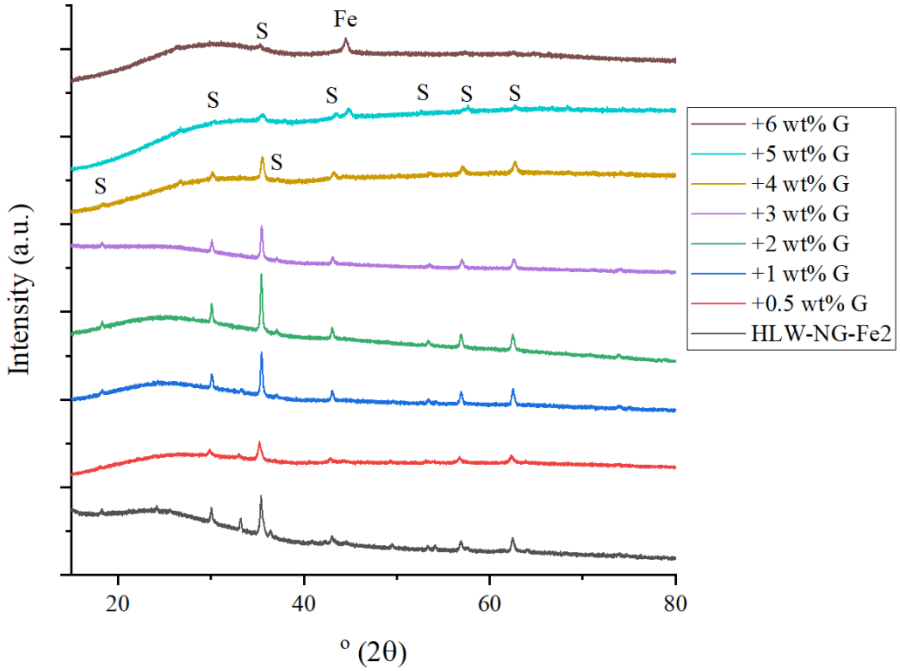

Figure 5.2.1. XRD patterns of the HLW-NG-Fe2 glass with varying levels of graphite added to the feed. An Fe_3O_4 spinel is identified in all samples (S) and the main peak for Fe in this region (Fe) emerges for the 5 and 6 wt% samples.

At 0-4 wt%, a similar level of crystallinity is observed, and the peaks are identified as Fe_3O_4, which has been observed previously in the HLW-NG-Fe2 glass (Matlack et al. 2012; Guillen et al. 2020; Matlack, Kot, et al. 2015). At 5 and 6 wt% graphite addition, the main peak emerges in this angular range for metallic Fe (ICDD Powder Diffraction File ref. 6-696), at 44.674 ° 2θ (Gates-Rector and Blanton 2019). To avoid the chance of precipitating any metallic Fe in the glasses, 3 wt% addition was chosen for all reductants for the remainder of the study.

5.3 Feed Volume Expansion

Feed expansion tests in Figure 5.3.1 show the range of foaming behaviours of the 6 different feeds. The maximum foam volume is compared with the carbon content per gram of compound in Figure 5.3.2, showing an approximately linear relationship with R^2 = 0.903. Coke and graphite are most effective in reducing the maximum foam volume, as well as the integrated foam volume over the temperature range, given in Table 5.3.1.

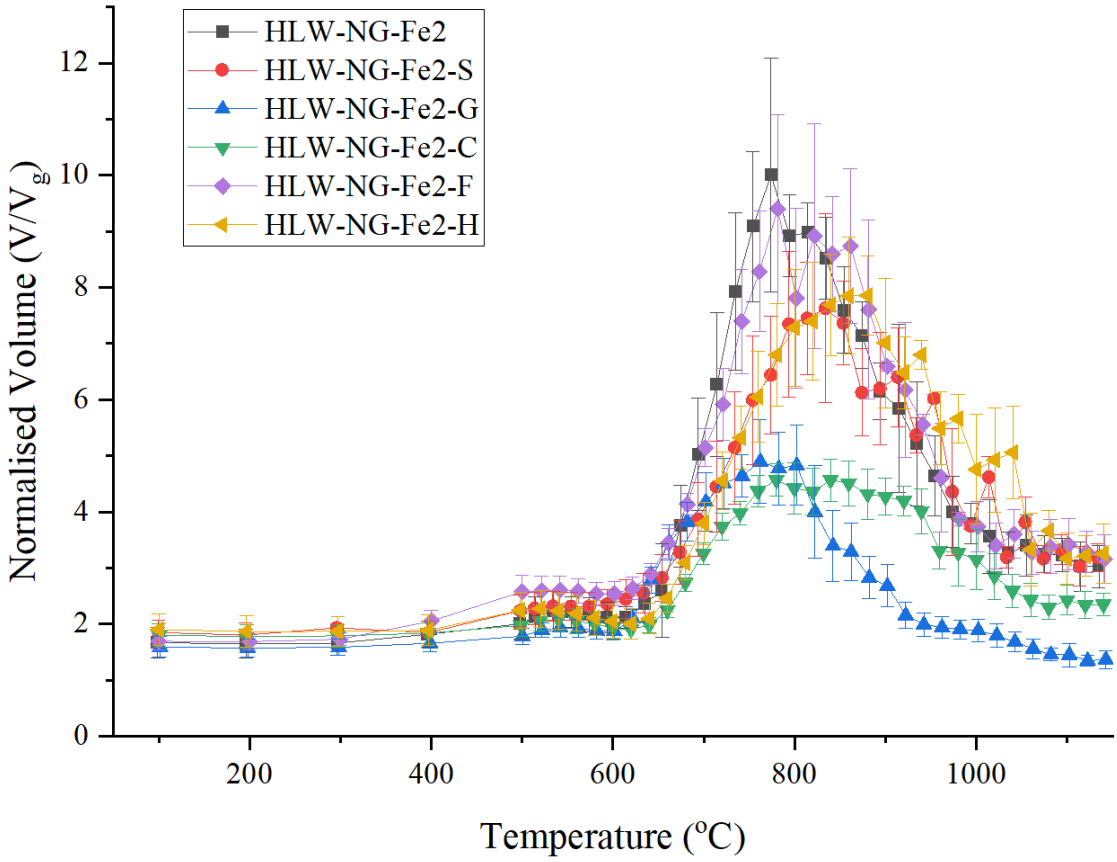

Figure 5.3.1. Normalised volume of pellets during Feed Expansion Test with different reductant and raw material feeds showing the evolution of primary foaming and foam collapse for the HLW-NG-Fe2-R feeds. Both primary and secondary foaming are considerably supressed in the HLW-NG-Fe2-G and -C feeds.

As discussed in Chapter 4, section 4.3.1 the temperature of foam collapse, T_{FB}, is a parameter used in the melt rate correlation equation (Hrma et al. 2018). The implication

of a lower T_{FB} in isolation is an increased melting rate. The temperature of T_{FB} is disputed, as it is likely that those feeds where foaming is significant at higher temperatures, after the collapse of the primary foam peak, will have a reduction in melting rate. This is discussed in Chapter 2, section 2.4.3.

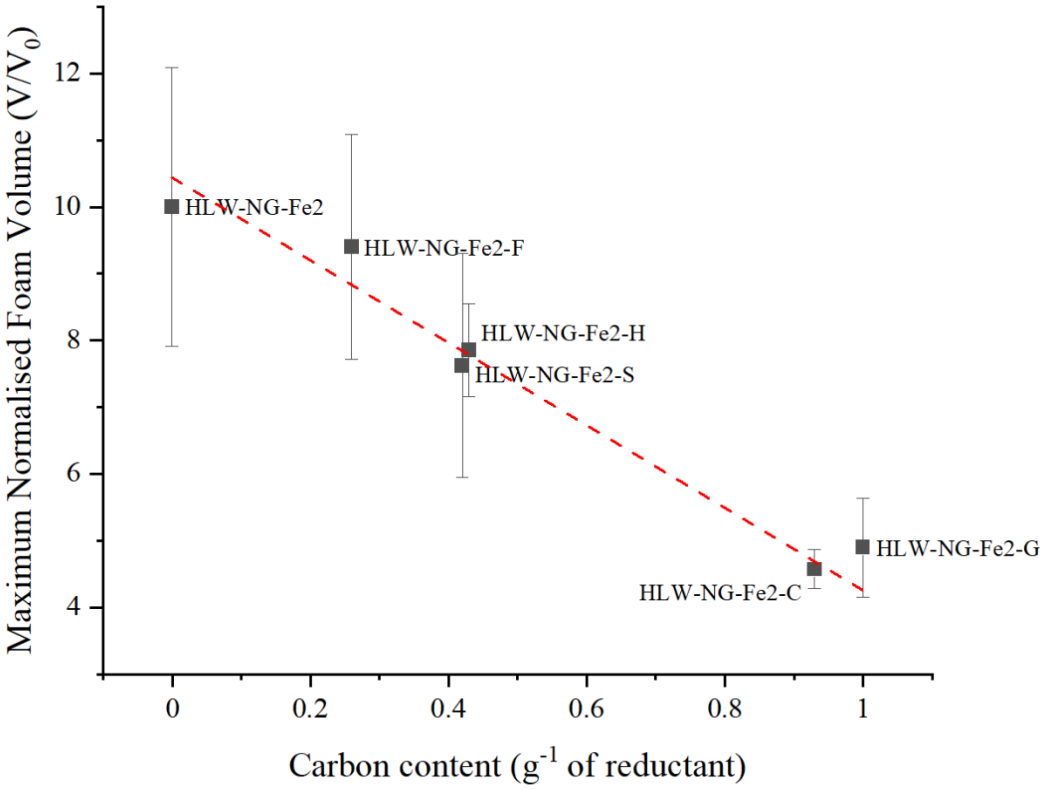

Figure 5.3.2. Normalised maximum foam volume of HLW-NG-Fe2 and HLW-NG-Fe2-R feeds with carbon content of reductant g^{-1}. A linear fit of the data with a $R^2 = 0.903$.

Table 5.3.1. Foaming behaviour of feeds during melting from FETs.

	Normalised Maximum Foam Volume	Normalised Total Integrated Foam Volume	Temperature of foam onset (°C)	Temperature of foam collapse* (°C)
HLW-NG-Fe2	10.0 ± 2.1	3725 ± 23	674.3 ± 10.1	774.0 ± 10.6
HLW-NG-Fe2-S	7.6 ± 1.7	3561 ± 19	673.7 ± 8.3	834.0 ± 8.5
HLW-NG-Fe2-G	4.9 ± 0.7	2385 ± 11	642.0 ± 1.6	762.3 ± 1.2
HLW-NG-Fe2-C	4.6 ± 0.3	2739 ± 10	679.7 ± 0.9	780.0 ± 1.4
HLW-NG-Fe2-F	9.4 ± 1.7	3918 ± 21	661.3 ± 1.9	781.3 ± 1.9
HLW-NG-Fe2-H	7.9 ± 0.7	3722 ± 20	679.7 ± 0.9	880.3 ± 0.5

*Measured at peak foam height.

5.4 Thermal Analysis

5.4.1 Thermogravimetric Analysis

Sucrose, graphite, coke and HEDTA raw materials were subject to TGA to determine the temperatures of mass-loss events. Derivatives of the TGA for those reductants and the HLW-NG-Fe2 and HLW-NG-Fe2-R feeds are shown in Figure 5.4.1. No measurements were taken on formic acid due to potential damage to the equipment.

Most gas evolution, therefore, decomposition, of the sucrose and HEDTA samples occurs prior to 500 °C. No literature was available on the decomposition of formic acid, however based on the behaviour of sucrose and HEDTA, we assume the decomposition to be in the 200-600 °C temperature range. Minimal gas evolution from coke or graphite was detected within the temperature range measured.

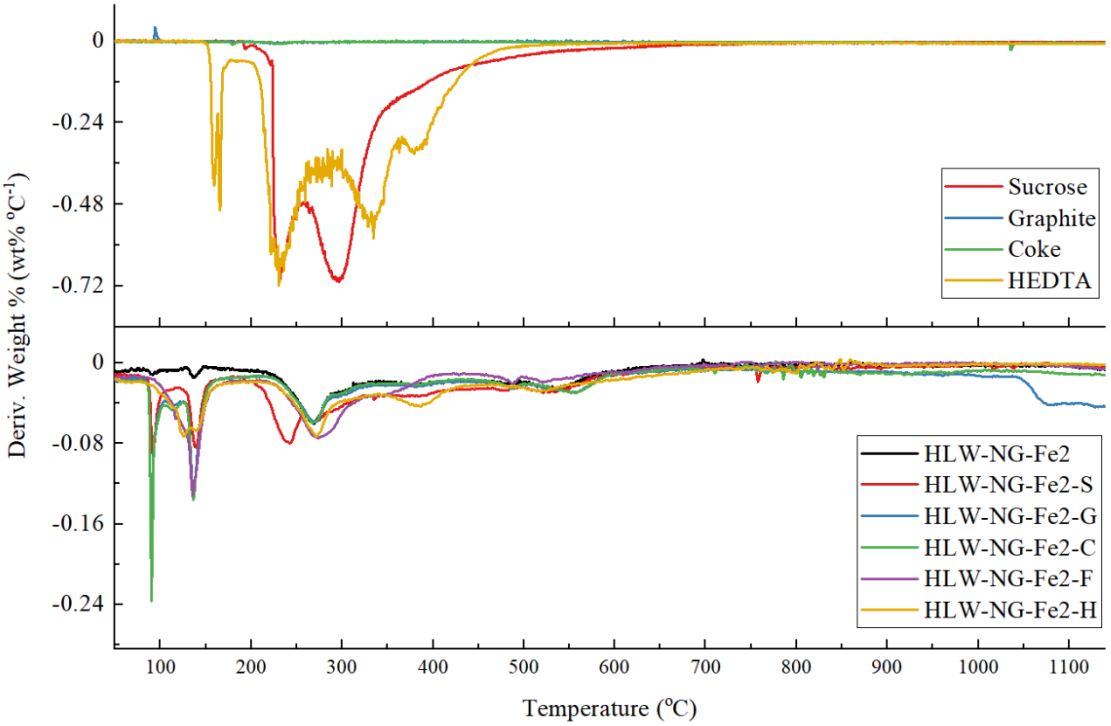

Figure 5.4.1. Derivative of the TGA (DTG) of some of the reductants (top) and feeds with added reductants (bottom) between room temperature and 1150 °C. Sucrose and HEDTA decompose between 200 and 500 °C, where coke does not decompose in the temperature range measured and graphite only begins to react in the feed ~1050 °C.

In the HLW-NG-Fe2 feed with the added reductants, the bottom graph in Figure 5.4.1, gas evolution peaks in the range 200-600 ℃ are similar for the HLW-NG-Fe2 and HLW-NG-Fe-2-G and C feeds. Variation in behaviour prior to 600 ℃ in the HLW-NG-Fe2-S and H feeds can be attributed to reactions involving the reductants added based on the results in the above graph in Figure 5.4.1, and HLW-NG-Fe2-F behaves similarly. The HLW-NG-Fe2-G feed has a mass-loss above 1000 ℃, where graphite has begun to take effect earlier in the glass melt atmosphere, than when isolated.

5.4.2 Differential Thermal Analysis

The DTA prior to foaming onset, from room temperature up to 600 ℃ is shown in Figure 5.4.2, and the DTA during foaming up to melt temperature is shown in Figure 5.4.3. Prior to the onset of foam, Figure 5.4.2, there are a number of low-temperature endothermic decomposition reactions between ~50 and 350 ℃, most of these reactions show the same heat flow profiles with temperature. Endothermic peaks in unique to the HLW-NG-Fe2-S feed, ~ 200 ℃, and HLW-NG-Fe2-F feed ~250 ℃, are likely reactions involving the reductant. A small, endothermic peak corresponding to glass transition temperature is visible in this region at just less than 600 ℃, representing the connection and amorphization of the main glass-forming melt. Foaming initiates just beyond this temperature as there is a connected melt. Smaller reactions below to T_g in some of the feeds likely represents melting of some of the earlier glass formic eutectics.

Beyond 600 ℃, the increasingly negative heat flow is representative of melting of the bulk material, with different melt temperatures, T_m, for different raw materials (Ray et al. 2005). The exothermic reactions in this temperature region, discussed in Chapter 4, section 4.3.2, are reactions with organics in the feed, and exothermic crystallisation peaks. There are also small endothermic peaks in the HLW-NG-Fe2-G, -C and -H curves along with the HLW-NG-Fe2 curve, also discussed in Chapter 4, section 4.3.2, and attributed to redox changes during melting.

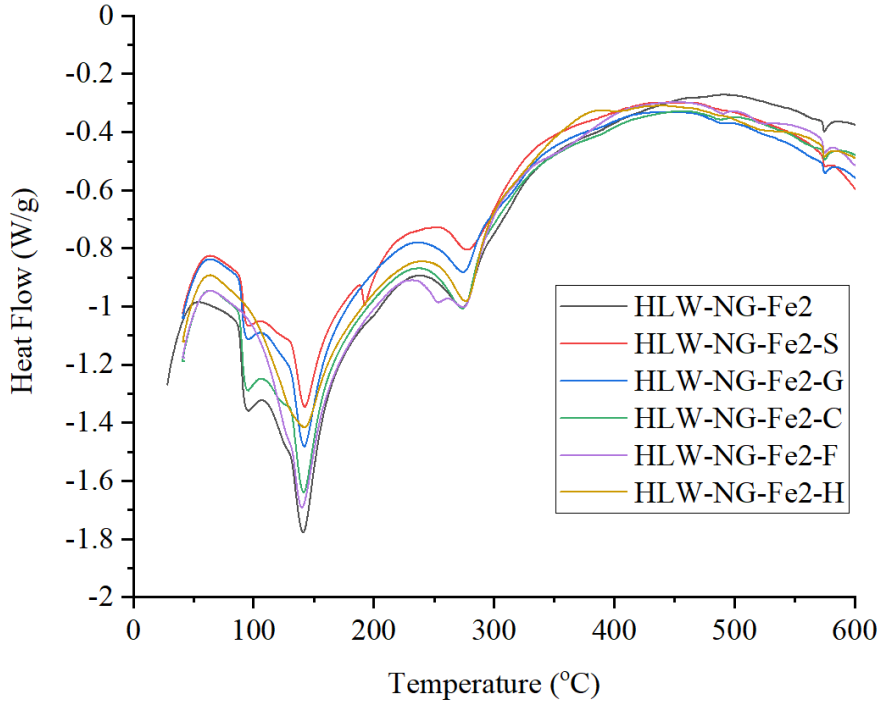

Figure 5.4.2. DTA of the HLW-NG-Fe2 and HLW-NG-Fe2-R feeds from room temperature to 600 ℃, showing endothermic dehydration reactions up to 350 ℃ and connection of the glass-forming melt between 550 and 600 ℃.

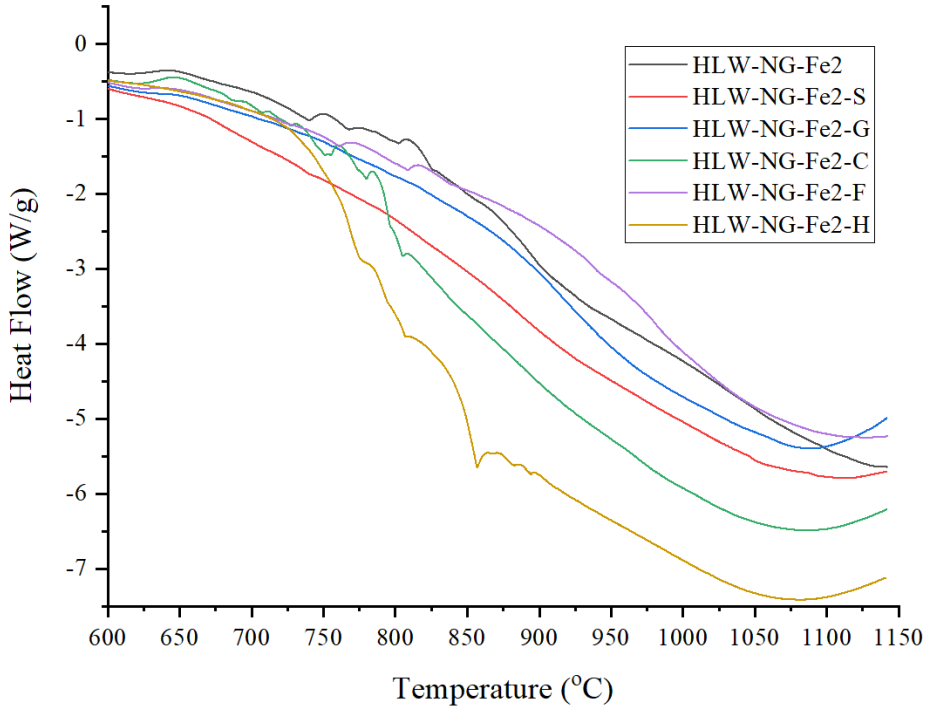

Figure 5.4.3. DTA of the HLW-NG-Fe2 and HLW-NG-Fe2-R feeds from 600 to 1150 ℃ showing the enthalpy of melting for each of the feeds. Endothermic peaks indicating high-temperature reactions, 700-900 ℃, are absent in the HLW-NG-Fe2-S and -G feeds.

The heat flux during melting, ΔH, in the MRC equation, can be explored using DTA. Enthalpy was measured by integrating the DTA curve between room temperature and the temperature of foam onset, as in (Lee, Hrma, Pokorný, Kloužek, et al. 2019; Hrma et al. 2018), to provide the enthalpy of the reacting feed for the ΔH term in the MRC, which takes the form (Hrma et al. 2018):

$$\Delta H = \Delta H_W + \Delta H_R + c_p \Delta T \quad (35)$$

where, ΔH_W, is the enthalpy due to physical water evaporation in the feed slurry, ΔH_R, is the enthalpy due to the reacting feed, and $c_p \Delta T$, is the sensible heat for average heat capacity, c_p = 1.1 J g^{-1} K^{-1} (Lee, Hrma, Pokorný, et al. 2017; Lee, Hrma, Pokorný, Kloužek, et al. 2019). For ΔT = 1000 °C, ΔH_S = 1.1 kJ g^{-1} K. ΔH_W is determined by the free water mass in the feeds per mass of glass, w_G, and the enthalpy of water evaporation, ΔH_E = 2.256 J kg^{-1}. Due to issues with the viscosity of the $Fe(OH)_3$ slurry when batching the HLW-NG-Fe2 feed, and therefore subsequent HLW-NG-Fe2-R feeds, discussed in Chapter 3, section 3.3.1, there is a much higher water content in these feeds than batched previously. The outcome of this is a higher ΔH_w value than previously reported for HLW-NG-Fe2 (Hrma et al. 2018; Lee, Hrma, Pokorný, Kloužek, et al. 2019).

Table 5.4.1. Enthalpy of reacting feed by DTA.

Feed	**ΔH_R (kJ g^{-1})**	**w_G**	**ΔH_w (kJ g^{-1})**	**ΔH (kJ g^{-1})**
HLW-NG-Fe2	0.44	4.55	10.26	11.80
HLW-NG-Fe2-S	0.41	4.55	10.35	11.86
HLW-NG-Fe2-G	0.40	4.55	10.35	11.85
HLW-NG-Fe2-C	0.45	4.55	10.35	11.89
HLW-NG-Fe2-F	0.44	4.55	10.35	11.89
HLW-NG-Fe2-H	0.43	4.55	10.35	11.88

5.5 Gas Evolution

5.5.1 Gas balance Calculations

From the raw batch materials, stoichiometric calculations of the volatiles expected to evolve for each batch were calculated. For the initial calculations, it was assumed that the feed had oxygen available for each of the reactions containing carbon:

$$C + O_2 \rightarrow CO_2 \quad (36)$$

$$CO + ½\ O_2 \rightarrow CO_2. \quad (37)$$

For nitrate and nitrite reactions, the following was assumed:

$$NaNO_2 \rightarrow ½\ Na_2O + ½\ NO + ½\ NO_2 \quad (38)$$

$$NaNO_3 \rightarrow ½\ Na_2O + ½\ NO + ½\ NO_2 + ½\ O_2. \quad (39)$$

For each of the reductants, the following reactions were assumed:

$$C_{12}H_{22}O_{11}\ (\text{Sucrose}) + 6O_2 \rightarrow 12CO_2 + 11H_2O \quad (40)$$

$$C\ (\text{Graphite}) + O_2 \rightarrow CO_2 \quad (41)$$

$$0.93C\ (\text{Coke}) + 0.93O_2 \rightarrow 0.93CO_2 \quad (42)$$

$$CH_2O_2\ (\text{Formic Acid}) + ½\ O_2 \rightarrow CO_2 + H_2O \quad (43)$$

$$C_{10}H_{18}N_2O_7 + 12O_2 \rightarrow 10CO_2 + 9H_2O + 2NO. \quad (44)$$

Using the total mass of each component evolving, the expected off-gas for the HLW-NG-Fe2 feed and the HLW-NG-Fe2-R feeds are given in Table 5.5.1. The variety of atmospheres used to in the gas evolution measurements described in the following sections make it difficult to determine exact quantities of evolved and consumed gases. However, these calculations give an indication of the total volume of evolved gases expected by each feed.

Table 5.5.1. Calculated evolved gases based on stoichiometric calculations of the HLW-NG-Fe2 feed, and HLW-NG-Fe2-R feeds.

Feed	Theoretical Evolved Gases (mg kg^{-1} glass)						
	CO_2	CO	O_2	SO_2	H_2O	NO_2	NO
HLW-NG-Fe2	45377	0	772.65	0	273594	1254	818
HLW-NG-Fe2-II	252400	0	-55673	0	263497	1254	818
HLW-NG-Fe2-S	84052	0	-13430	0	285499	1247	813
HLW-NG-Fe2-G	189923	0	-104625	0	270974	1247	813
HLW-NG-Fe2-C	168176	0	-97246.1	0	270974	1247	813
HLW-NG-Fe2-F	82777	0	-12966	0	286462	1247	813
HLW-NG-Fe2-H	209652	0	-286630	0	358993	1247	2373

5.5.2 EGA

Evolved gas analysis by gas chromatography was used to quantify the off-gas from the feeds during melting, Figure 5.5.1-5. Most of the CO_2 evolution occurs prior to the onset of foaming, ~ 640 - 680 ℃ by Table 5.3.1. Earlier evolution of CO_2 occurs in the HLW-NG-Fe2-S, -F and -H feeds, predicted by the early mass loss events in TGA in Figure 5.4.1. Residual CO_2 is trapped within the foam. At ~ 760 – 880 ℃ spikes of CO_2 evolution, particularly evident in the HLW-NG-Fe2-F feed, show release of CO_2 trapped in bubbles. Significant evolution of CO_2 continues up to ~1050 ℃ in the HLW-NG-Fe2-G and -C feeds where we expect carbon to begin reacting based on the TGA results in Figure 5.4.1.

The HLW-NG-Fe2-H feed has a large CO evolution, Figure 5.5.2, beginning after most of the CO_2 evolution, showing by ~700 ℃ there is insufficient oxygen to evolve large quantities of CO_2. For the HLW-NG-Fe2-G and -C feeds there are significant quantities of CO evolved at high temperature, 1000 – 1150 ℃, where it is proposed that the reductant sources are beginning to react, this is occurs beyond the final release of CO_2.

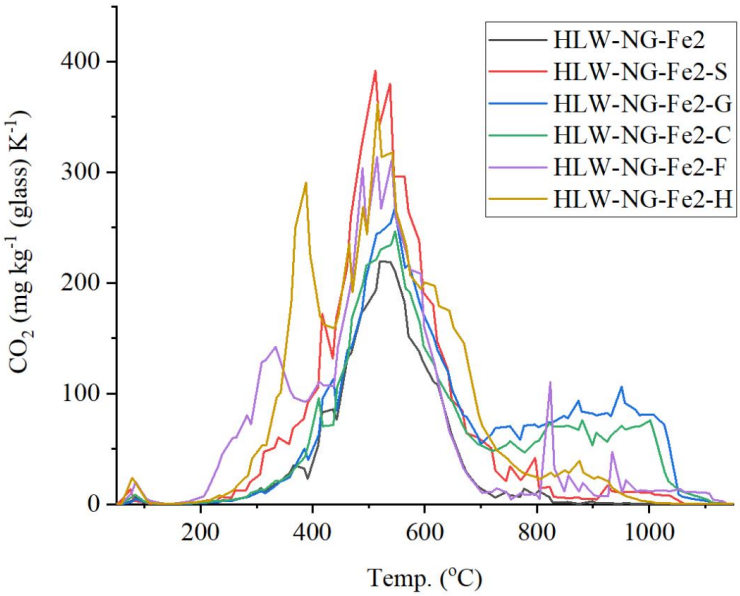

Figure 5.5.1. CO_2 evolution from the feeds by gas chromatography. The main CO_2 peak evolution is similar for all feeds, however HLW-NG-Fe2-G and -C have sustained CO_2 evolution up to ~1100 °C.

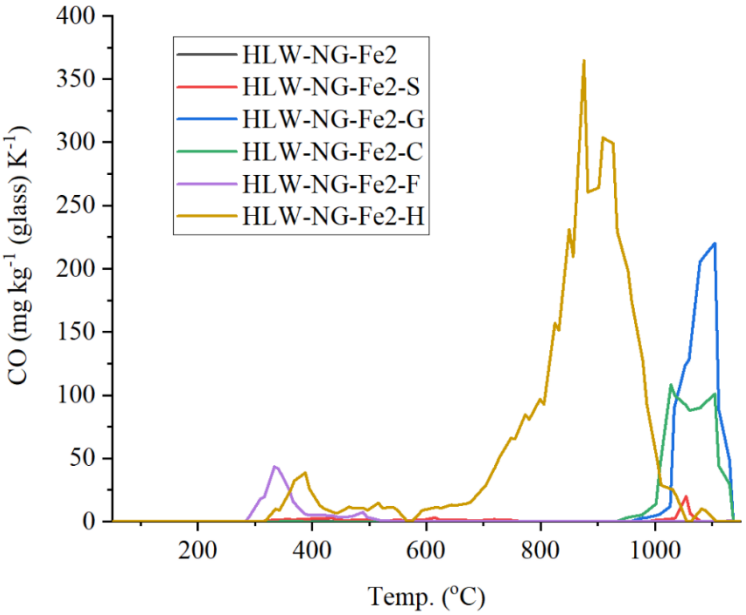

Figure 5.5.2. CO evolution from the feeds by gas chromatography. CO is evolved at temperatures above foam collapse in the HLW-NG-Fe2-H, -G and -C feeds, evolution in the -G and -C feeds is up to melting temperature.

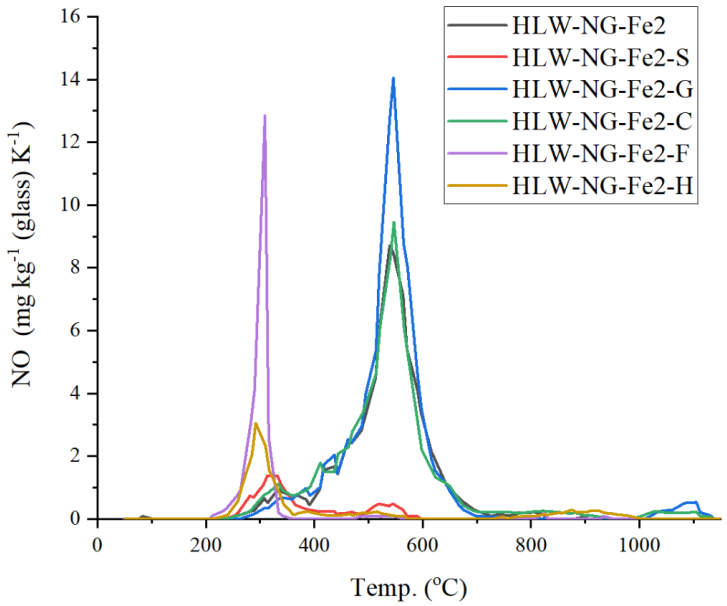

Figure 5.5.3. NO evolution from the feeds by gas chromatography, showing earlier evolution of NO in the HLW-NG-Fe2-S and -F feeds.

No SO_2 evolution was detected in the HLW-NG-Fe2-H feed. The HLW-NG-Fe2-S and -F feeds release SO_2 at a similar rate to the HLW-NG-Fe2 feed, however in the HLW-NG-Fe2-F feed the SO_2 begins to evolve at lower temperature therefore accumulating higher total evolution. The HLW-NG-Fe2-C and -G feeds evolve the most SO_2, with a distinct lower temperature peak ~ 800 °C and a second large peak in the HLW-NG-Fe2-G feed ~1000 °C.

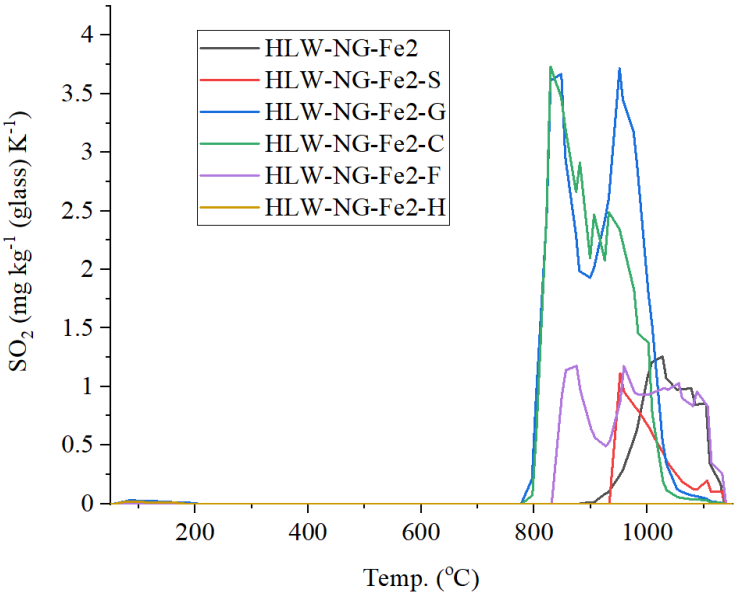

Figure 5.5.4. SO_2 evolution from the feeds by gas chromatography, showing much greater overall evolution in the HLW-NG-Fe2-G and -C feeds.

The small spikes in O_2 evolution from the HLW-NG-Fe2-G and -C feeds are considered indistinguishable from background, otherwise O_2 is suppressed in all HLW-NG-Fe2-R feeds. The total quantity of each gas evolved is given in Table 5.5.2.

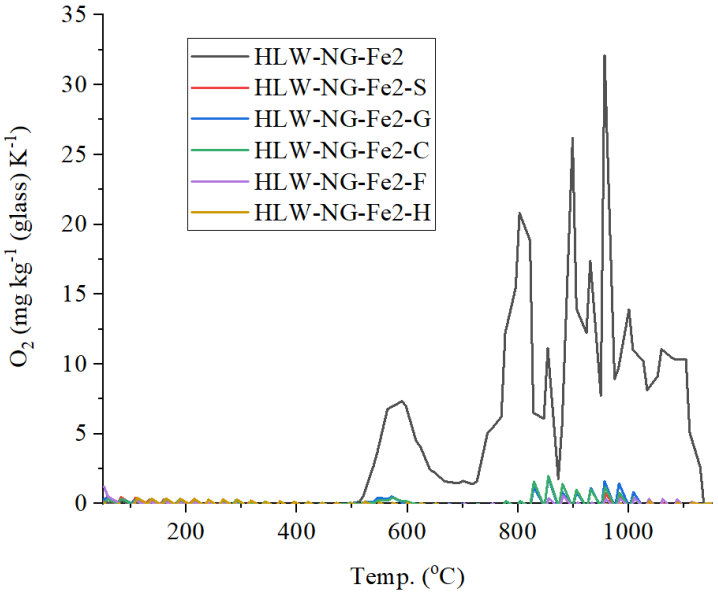

Figure 5.5.5. O_2 evolution from the feeds by gas chromatography showing suppression of O_2 evolution in all of the HLW-NG-Fe2-R feeds.

Table 5.5.2. Evolved gases by EGA for the HLW-NG-Fe2 and HLW-NG-Fe2-R feeds.

Feed	**Evolved Gases by EGA (mg kg^{-1} glass)**				
	CO_2	**CO**	**O_2**	**SO_2**	**NO**
HLW-NG-Fe2	46300	13	6633	200	1200
HLW-NG-Fe2-S	76900	1000	0	100	200
HLW-NG-Fe2-G	75600	22400	0	600	1300
HLW-NG-Fe2-C	67900	15400	0	500	1100
HLW-NG-Fe2-F	72400	2900	0	300	300
HLW-NG-Fe2-H	86600	52700	0	0	200

5.5.3 Gas Balance

The release of SO_2, from Table 5.5.2, was used in the following calculations of O_2, where in Table 5.5.1, it was assumed that all SO_3 is retained in the melt. This is corrected for the O_2 evolution from:

$$SO_3 \rightarrow SO_2 + ½\ O_2 \qquad (45)$$

in Table 5.5.3. This offers little consolation for the highly negative O_2 evolution predicted from the batch gases.

Table 5.5.3. Evolution of O_2 by evolved SO_2 measured by EGA.

	SO_2 evolution (mg kg^{-1} glass)	**Calculated O_2 from SO_2 evolution (mg kg^{-1} glass)**
HLW-NG-Fe2	200	50
HLW-NG-Fe2-S	100	30
HLW-NG-Fe2-G	600	150
HLW-NG-Fe2-C	500	130
HLW-NG-Fe2-F	300	70
HLW-NG-Fe2-H	0	0

NO evolved from the HLW-NG-Fe2 feed is greater than predicted based on equations (38) and (39). The proposed decomposition of $NaNO_2$ or $NaNO_3$ is inaccurate. It is likely, that the NO_2 evolution is lower than predicted. Based on the results in Figure 5.5.3, it is assumed in Table 5.5.4, that the remaining N batched in the feeds evolves as NO_2. This concept was also applied to the CO_2/CO evolution in based on the measured values of CO_2 and CO by EGA.

Table 5.5.4. Expected NO_2 evolution based on measured NO evolved by EGA.

Feed	**Calculated NO_2 from batch gases** (mg kg^{-1} glass)	**Calculated NO from batch gases** (mg kg^{-1} glass)	**NO evolved by EGA** (mg kg^{-1} glass)	**Recalculated NO_2** (mg kg^{-1} glass)	**O_2 difference** (mg kg^{-1} glass)
HLW-NG-Fe2	1254	818	890	1144	19
HLW-NG-Fe2-S	1247	813	119	2325	-187
HLW-NG-Fe2-G	1247	813	980	1005	42
HLW-NG-Fe2-C	1247	813	834	1229	3
HLW-NG-Fe2-F	1247	813	214	2179	-162
HLW-NG-Fe2-H	1247	2373	170	2247	-174

Table 5.5.5. Expected O_2 evolution based on measured CO and CO_2 evolved.

Feed	**Calculated CO_2 from batch gases** (mg kg^{-1} glass)	**Calculated CO from batch gases** (mg kg^{-1} glass)	**CO_2 evolved by EGA** (mg kg^{-1} glass)	**CO evolved by EGA** (mg kg^{-1} glass)	**O_2 difference** (mg kg^{-1} glass)
HLW-NG-Fe2	45400	0	46300	0	0
HLW-NG-Fe2-S	84100	0	76900	1000	600
HLW-NG-Fe2-G	189900	0	75600	22400	12800
HLW-NG-Fe2-C	168200	0	67900	15400	8800
HLW-NG-Fe2-F	82800	0	72400	2900	1700
HLW-NG-Fe2-H	209700	0	86600	52700	30000

5.6 Melt Rate Correlation

The melt rate correlation equation, discussed in detail in Chapter 2, section 2.4.3, takes the following form:

$$j = \xi_0 \left(\frac{\eta_{MO}}{\eta_R}\right)^{-\alpha} \left(1 + \frac{u_B}{u_0}\right)^{\beta} (T_{MO} - T_{FB}) \Delta H^{-1}. \quad (46)$$

From the results in this section from FETs, Table 5.3.1, and thermal analysis, Table 5.4.1, the feed-dependent parameters for the MRC have been derived, apart from the viscosity at melt temperature. The viscosity is the parameter for which the model is most sensitive, and therefore most effects the melting rate of the feed (Lee, Hrma, Pokorný, Kloužek, et al. 2019). In the absence of measured viscosity, it is assumed that the same viscosity for all feeds, and the previously measured value used for HLW-NG-Fe2, η_{MO} = 3.04, also using value for forced bubbling u_B = 4.94 as previously (Lee, Hrma, Pokorný, Kloužek, et al. 2019). T_{MO} = 1150 °C for all feeds. The estimated heating rates based on these parameters is given in Table 5.6.1. These are much lower than j = 19.1 g m^{-2} s^{-1} measured previously: the influencing factor in this is the water content of the feed slurry (Lee, Hrma, Pokorný, Kloužek, et al. 2019). There is a slight increase in melting rate using formic acid, and a large decrease using coke. These are influenced by the foam collapse temperature, T_{FB} as the enthalpy of the reacting feed is similar for HLW-NG-Fe2-F and -C.

Table 5.6.1. Expected melting rate from the measured parameters for the MRC.

Feed	***ΔH* (kJ g^{-1})**	***T*$_{FB}$ (°C)**	***Q* (*kW m*$^{-2}$)**	***j* (*g m*$^{-2}$ *s*$^{-1}$)**	***j* (*kg m*$^{-2}$ *day*$^{-1}$)**
HLW-NG-Fe2	11.80	774.0 ± 10.6	90.65 ± 1.24	8.40 ± 0.11	726 ± 6
HLW-NG-Fe2-S	11.86	834.0 ± 8.5	76.19 ± 0.78	7.02 ± 0.07	607 ± 1
HLW-NG-Fe2-G	11.85	762.3 ± 1.2	93.54 ± 0.15	8.36 ± 0.01	722 ± 1
HLW-NG-Fe2-C	11.89	780.0 ± 1.4	89.20 ± 0.16	5.98 ± 0.01	516 ± 1
HLW-NG-Fe2-F	11.89	781.3 ± 1.9	88.96 ± 0.22	8.60 ± 0.01	743 ± 1
HLW-NG-Fe2-H	11.88	880.3 ± 0.5	65.10 ± 0.04	8.21 ± 0.01	710 ± 1

5.7 Summary

5.7.1 Foaming behaviour

The order of normalised maximum volume expansion (V/V_g) for the HLW-NG-Fe2 and HLW-NG-Fe2-R feeds, by feed expansion tests, was as follows:

Original (10.0±2.1) > Formic Acid (9.4±1.7) > HEDTA (7.9±0.7) > Sucrose (7.6±1.7) > Graphite (4.9±0.7) > Coke (4.6±0.3).

For HLW-NG-Fe2, HLW-NG-Fe2-S, -H, and -F, the order of maximum foam reduction correlates with the carbon content per gram of reductant added. The maximum foam volume only accounts for the primary foaming and the effect on secondary foaming is of most interest to this project. For both graphite and coke additions to the HLW-NG-Fe2 feed, there is a great effect on the overall foam volume expansion, including the secondary foam region between ~800 and 1150 °C.

The main contributions to this secondary foaming behaviour, based on EGA, are residual CO and CO_2. The explanation for the sustained effects of these reductants at high temperature can be found in the TGA of the reductants Figure 5.4.1. Sucrose and HEDTA are shown to decompose between 100 and 500 °C and in the TGA of the feeds they appear to interact with the components of the feeds in the same temperature region, i.e., prior to the onset of primary foam. They have the effect of the early elimination of nitrates (Bickford, Hrma, and Bowan 1990; Ryan 1995) which precludes any efficient high-temperature reduction of multivalent species (P. A. Smith, Vienna, and Merz 1996). Graphite and coke do not show any significant decomposition in isolation in the temperature range from 0 to 1150 °C. When in the feeds, the graphite feed has some evidence of decomposition above 1000 °C, while the coke does not.

5.7.2 Balance of Oxygen

The total O_2 balance, from the batched raw-materials in the feeds, and taking into account the evolution of SO_2, CO over CO_2, and NO over NO_2, provides a strongly negative value for O_2 for all HLW-NG-Fe2-R feeds, Table 5.7.1. This is supported by zero O_2 evolution from these feeds by EGA, section 5.5. HLW-NG-Fe2 has increased in final expected O_2, however, not enough to account for over double the amount detected by EGA. O_2 evolved in the HLW-NG-Fe2 feed must come from trapped air in the dried feed prior to melting, or reduction of multivalent species in the feed releasing O_2. For the HLW-NG-Fe2-R feeds the O_2 balance is less negative once the reactions of other batch gases are taken into account, but still negative, such that it must be assumed that there has been a substantial reduction in the multivalent species in the feeds during melting. This is particularly the case for HLW-NG-Fe2-H where negative oxygen balance is an order of magnitude greater than the other HLW-NG-Fe2-R species.

In the O_2 balance calculated for the high-alumina waste feed with different alumina raw materials, (Lee, Hrma, Kloužek, et al. 2017), there was more O_2 released by EGA than predicted by the O_2 balance. They concluded that the redox state of iron was the largest results of this balance of O_2, and in that study the contribution to O_2 evolution by formation of spinel from haematite was considered negligible. In the following Chapters 6 and 7, all possible contributions are taken into account.

Table 5.7.1. Comparison of evolved O_2 with expected O_2 based on batched feed raw materials and evolution of O_2 by reactions with SO_x, NO_x and CO_x measured by EGA.

	O_2 balance initial (mg kg^{-1} glass)	**O_2 balance final** (mg kg^{-1} glass)	**O_2 evolved by EGA** (mg kg^{-1} glass)
HLW-NG-Fe2	772.65	841.65	6633
HLW-NG-Fe2-S	-13430	-12987	0
HLW-NG-Fe2-G	-104625	-91633	0
HLW-NG-Fe2-C	-96562.3	-88629.3	0
HLW-NG-Fe2-F	-12966	-11358	0
HLW-NG-Fe2-H	-286630	-256456	0

5.7.3 Melting Rate

By DTA, the enthalpy change of melting in the feeds, while not quantified, Figure 5.4.3, is greatest in the HLW-NG-Fe2-H feed followed by -C and -S. Otherwise by DTA, the main melting reactions are at similar temperatures, apart from some reactions between 700 and 900 ℃, attributed to redox reactions in Chapter 4, section 4.3.2. Based on the MRC calculations, section 5.6, the effect of the reductants on the melting rate of the feeds (kg m^{-2} day^{-1}) is as follows:

Coke (516±1) < Sucrose (607±1) < HEDTA (710±1) < Graphite (722±1)

< Original (726 ± 6) < Formic Acid (743±1)

Without viscosity data for the feeds at melting temperature, these values may not represent the feed melting rate, since viscosity is the most influential parameter (Hrma et al. 2018; Lee, Hrma, Pokorný, Kloužek, et al. 2019). However, with the values that are available using the present techniques, t(he addition of formic acid slightly improves the melting rate, while the other additives have a negative effect.

5.8 References

Appel, C. J., Kloužek, J. Jani, N., Lee, S., Dixon, D. R., Hrma, P., Pokorný, R., Schweiger, M. J. and Kruger, A. A., (2019) 'Effect of sucrose on foaming and melting behavior of a low-activity waste melter feed', Journal of the American Ceramic Society, 102(12), pp. 7594–7605.

Bickford, D. F. (1986) 'Redox control Of electric melters with complex feed compositions II. Preliminary limits for radioactive waste melters', Journal of Non-Crystalline Solids, 84, pp. 285–291.

Bickford, D. F., Hrma, P. and Bowan, B. W. (1990) 'Control of Radioactive Waste Glass Melters: II, Residence Time and Melt Rate Limitations', Journal of the American Ceramic Society, 73(10). pp. 2903–2915.

Gates-Rector, S. D. and Blanton, T. N. (2019) 'The Powder Diffraction File: A Quality Materials Characterisation Database', Powder Diffraction, 34(4), pp. 352–60.

Guillen, D. P. Lee, S., Hrma, P., Traverso, J., Pokorny, R., Kloužek, J., and Kruger, A. A., (2020) 'Evolution of chromium, manganese and iron oxidation state during conversion of nuclear waste melter feed to molten glass', Journal of Non-Crystalline Solids. Elsevier, 531(December 2019), p. 119860.

Hrma, P., Marcial, J., Swearingen, K. J., Henager, S. H., Schweiger, M. J., and Tegrotenhuis, N. E. (2011) 'Conversion of batch to molten glass, II: Dissolution of quartz particles', Journal of Non-Crystalline Solids. Elsevier B.V., 357(3), pp. 820–828.

Hrma, P., Pokorný, R., Lee, S. M. and Kruger, A. A. (2018) 'Heat transfer from glass melt to cold cap: Melting rate correlation equation.' International Journal of Applied Glass Science, (August) pp. 1–8.

Hrma, P. R. Schweiger, M. J., Humrickhouse, C. J., Moody, J. A., Tate, R. M., Rainsdon, T. T., Tegrotenhuis, N. E., Arrigoni, B. M., Marcial, J., Rodriguez, C.

P. and Tincher, B. H. (2010) ‘Effect of glass-batch makeup on the melting process’, Ceramics - Silikaty, 54(3), pp. 193–211.

Hujová, M., Pokorný, R., Kloužek, J., Lee, S., Traverso, J. J., Schweiger, M. J., Kruger, A. A. and Hrma, P. (2018) ‘Foaming during nuclear waste melter feeds conversion to glass: Application of evolved gas analysis’, International Journal of Applied Glass Science, 9(4), pp. 487–498.

Jantzen, C. M., Koopman, D. C., Herman, C. C., Pickett, J. B. and Zamecni, J. R. (2003) ‘Electron Equivalents Redox Model for High Level Waste Vitrification’, in Symposium on Waste Management Technologies in Ceramic and Nuclear Industries, American Ceramic Society. Westerville, Ohio: Westinghouse Savannah River Company, Aiken, SC (United States).

Jantzen, C. M. (2011) ‘Development of glass matrices for high level radioactive wastes’, in Handbook of Advanced Radioactive Waste Conditi^{on}ing Technologies. 1st ed. Aiken, SC (United States): Woodhead Publishing Limited, pp. 230–292.

Kruger, A. A., Matlack, K. S., Pegg, I. L., Kot, W. K. and Joseph, I. (2012) ‘Redox Control for Hanford HLW Feeds.’ VSL-12R2530-12. Office of River Protection, Richland, WA (United States).

Lee, S., Hrma, P. R., Kloužek, J., Pokorný, R., Hujová, M., Dixon, D. R., Schweiger, M. J. and Kruger, A. A. (2017) ‘Balance of oxygen throughout the conversion of a high-level waste melter feed to glass’, Ceramics International, 43(16), pp. 13113–13118.

Lee, S., Hrma, P., Pokorný, R., Kloužek, J., VanderVeer, B. J., Dixon, D. R., Luksic, S. A., Rodriguez, C., Chun, J., Schweiger, M. J. and Kruger, A. A. (2017) ‘Effect of melter feed foaming on heat flux to the cold cap’, Journal of Nuclear Materials. 496, pp. 54–65.

Lee, S., Hrma, P., Pokorný, R., Kloužek, J., Eaton, W. C. and Kruger, A. A. (2019) 'Glass production rate in electric furnaces for radioactive waste vitrification', Journal of the American Ceramics Society. 102(10). pp. 5828–5842.

Matlack, K. S., Gan, H., Chaudhuri, M., Kot, W. K., Pegg, I. L., Joseph, I. and Kruger, A. A. (2012) 'Melter Throughput Enhancements for High-Iron HLW.' ORP-54002. Vitreous State Laboratory, Washington, D. C. (United States).

Matlack, K. S., Kot, W. K., Pegg, I. L. and Joseph, I. (2015) 'Support–for HLW Direct Feed - Phase 2 VSL-15R3440-1.' Vitreous State Laboratory, Washington, D. C. (United States).

Pinet, O., Hugon, I. and Mure, S. (2014) 'Redox Control of Nuclear Glass', Procedia Materials Science. Elsevier B.V., 7, pp. 124–130.

Ray, C. S., Reis, S. T., Brow, R. K., Höland, W. and Rheinberger, V. (2005) 'A New DTA Method for Measuring Critical Cooling Rate for Glass Formation.' Journal of Non-Crystalline Solids 351. pp. 1350–58.

Ryan, J. L. (1995) 'Redox Reactions and Foaming in Nuclear Waste Glass Melting.' PNL-10510. Pacific Northwest National Laboratory. Richland, WA (United States).

Seymour, R. G. (1995) 'Evaluation of Alternative Chemical Additives for High-Level Waste Vitrification Feed Preparation Processing.' WHC-SD-WM-SP-009. Westinghouse Hanford Company, Oak Ridge, TN (United States).

Smith, P. A., Vienna, J. D. and Merz, M. D. (1996) 'NCAW Feed Chemistry: Effect of Starting Chemistry on Melter Offgas and Iron Redox.' PNL-10517. Pacific Northwest National Laboratory, Richland, WA (United States).

6 Alternative Reductants: Structural changes during melting

6.1 Overview

The structural changes during melting underpin the gas evolving reactions and melting rate of waste feeds. To study the evolution of structure during melting, SoM samples were prepared by heating dried feed to 600, 800, 1000, and 1150 ℃ and quenching them at temperature for snapshots of the melting behaviour vertically in the cold cap, this is described in detail in Chapter 3, section 3.3.3. The temperature range was chosen to represent the foaming temperatures, as shown in Chapter 5 section 5.3. The reactions of waste feeds prior to 700 ℃ have been explored previously (Xu et al. 2015). The dissolution of silica is a key indicator of the viscosity of the glass-forming melt; the more silica dissolved in the melt the higher the expected viscosity (Marcial et al. 2014a; Hujová, Pokorný, et al. 2018; Bacon and Hasapis 1959).

In this chapter we explore the glass-forming reactions in the 600-1150 ℃ temperature range using XRD for phase identification and proportions, to determine the dissolution of phases during melting and the form of Fe and other multivalent species. Raman spectroscopy of each of the SoM samples provides information on the structure of the melt, particularly in the bonding of major glass-formers: SiO_2 and B_2O_3. The form of Fe, and the other multivalent species are explored, Fe by ^{57}Fe Mössbauer in this chapter, and then Fe, Cr, Mn, Ce and Ni by XANES in the following chapter, Chapter 7.

6.2 XRD and phase evolution during melting

The phases formed between the key temperatures of interest, 600 – 1150 ℃, were identified using HighScore Plus to search the ICDD Powder Diffraction File Database. Phases were then fit to the spectra using the Rietveld refinement functions as described in section 3.6.1. At 600 ℃ there are a number of unidentified intermediate phases formed in the HLW-NG-Fe2-G, C and F samples, making full Rietveld refinement of the patterns, and quantification of phases impossible. The other remaining phases are quartz (SiO_2), haematite (Fe_2O_3), and spinel (AB_2O_4), these peaks are labelled in Figure 6.2.1 along with the Si peaks used to determine the phase proportions, Figure 6.2.2.

With increase in quench temperature, in all feeds, there is broadening of crystalline peaks and the emergence of an amorphous hump region, which we expect with the amorphization of the melt (Yalmali et al. 2007; Rehman et al. 2021). Dissolution rate of silica is similar amongst all of the feeds, Figure 6.2.2.

The rate of Fe_2O_3 dissolution is slowest in the HLW-NG-Fe2 feed, all other feeds show less than 5 wt% at 1000 ℃. By 1000 ℃ there is no Fe_2O_3 detected in the HLW-NG-Fe2-G, C and -H feeds, but a significant increase in spinel phase in the HLW-NG-Fe2-C feed. In the final glasses, the spinel phases remain prevalent. There is also some indication of remaining SiO_2 and Fe_2O_3 in the HLW-NG-Fe2-S, -C and -F feeds. There are only enough peaks to confirm the presence of 3.6 ± 0.2 wt% Fe_2O_3 in the HLW-NG-Fe2-S pattern and 0.24 ± 0.02 wt% in the HLW-NG-Fe2-F pattern. HLW-NG-Fe2-C has the highest amount of spinel in the final glass, whereas HLW-NG-Fe2-F has only slightly more than HLW-NG-Fe2. As with the spinels identified in Chapter 4, section 4.4.1., the elements on each of the spinel sites cannot be accurately determined by this method and there is likely a mixture of spinel structures in each sample containing Fe, Mn, Cr, Ni and O.

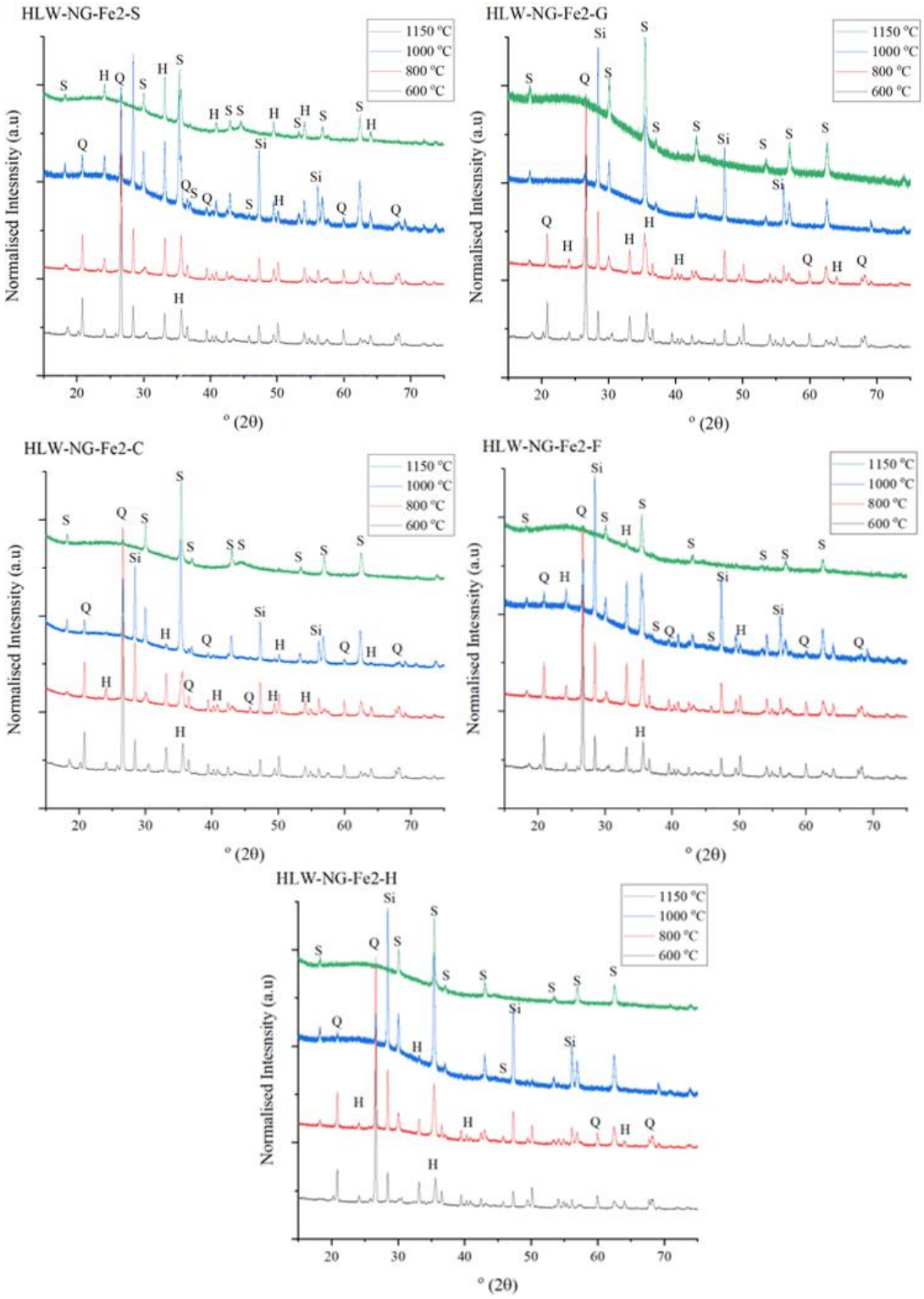

Figure 6.2.1. XRD patterns for HLW-NG-Fe2-S, G, C, F and H 600, 800 1000 and 1150 ℃ showing quartz (Q) and haematite (H) phases present up to 1150 ℃ in the HLW-NG-Fe2-S and -F samples compared to the HLW-NG-Fe2-G and -H samples were there is little to no remaining quartz or haematite at 1000 ℃. Spinels (S) are present in all feeds up to 1150 ℃.

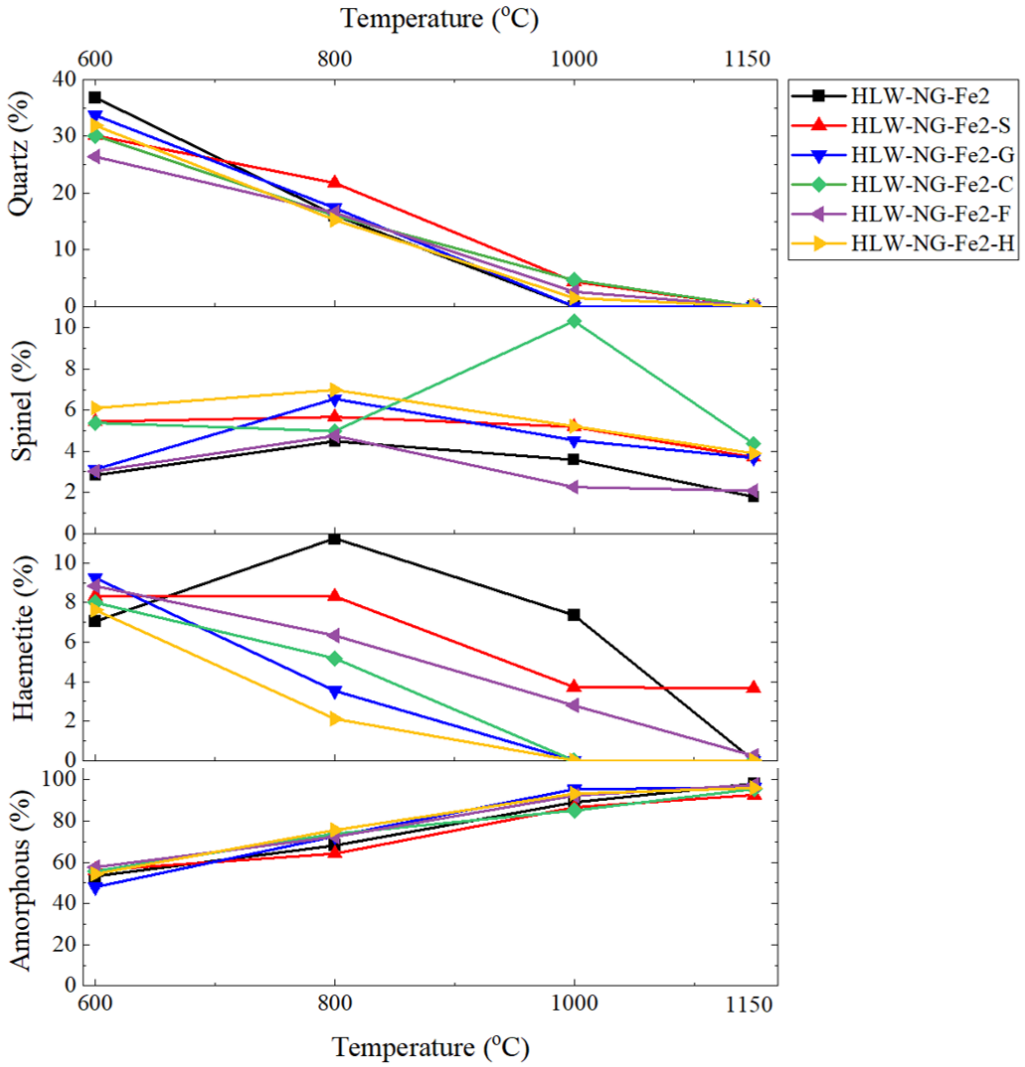

Figure 6.2.2. Quantity of phases determined by semi-quantitative analysis of refined phases identified in XRD patterns, compared with 5 wt% Si powder as an internal standard, for each of the feeds studied at 600, 800 1000 and 1150 °C. Quartz dissolution and amorphization of the melt occur at similar temperatures in all feeds, the feeds vary in the form of iron with temperature: the ratio of haematite to spinel.

6.3 Raman Spectroscopy

6.3.1 600-1000 °C

Raman spectra collected for the HLW-NG-Fe2-R SoM samples quenched at 600, 800 and 1000 °C are compared with the equivalent HLW-NG-Fe2 and -II samples from section 4.4.3 in Figure 6.3.1. Noise is highest in inhomogeneous samples, where merged spectra were significantly different, this has the greatest effect on the 600 °C samples.

As discussed in section 4.4.3, the emergence of the broad Si-O (Al-O, Fe-O) Q^n-species region between 800 and 1200 cm^{-1} (Parkinson et al. 2008; Yadav and Singh 2015), indicates amorphous melt formation. For the feeds studied, these features, along with the characteristic bands of the borosilicate network, between 350 and 600 cm^{-1} and 1200 – 1500 cm^{-1} (Parkinson et al. 2008; Yadav and Singh 2015), are apparent by 1000 °C in the HLW-NG-Fe2, HLW-NG-Fe2-F and -H feeds, where in the other feeds they become apparent only by 1150 °C.

In the 600 °C samples the broadest peak, and most intense in all but the HLW-NG-Fe2-G feeds, is between 1200 and 1400 cm^{-1}, attributed to; the haematite band centred around 1320 cm^{-1}, in Table 4.4.2 (Krolop et al. 2019; de Faria and Lopes 2007). This band broadens and reduces in intensity, coupled with an increase in intensity of the Si-O, Fe-O, Al-O Q^n region (Parkinson et al. 2008; Yadav and Singh 2015; Neuville and Mysen 1996), at different temperatures in each sample. Haematite bands are not present in the HLW-NG-Fe2-II sample at 600 °C, where haematite has not formed by XRD phase identification in Chapter 4, section 4.4.1. However, correlating to the XRD, it has fully formed by 800 °C. There is a sharp band dominating the HLW-NG-Fe2-G 800 °C sample at 1600 cm^{-1} which is a merged spectrum of multiple regions, this suggests that the majority of this sample is crystalline, at least at the surface measured.

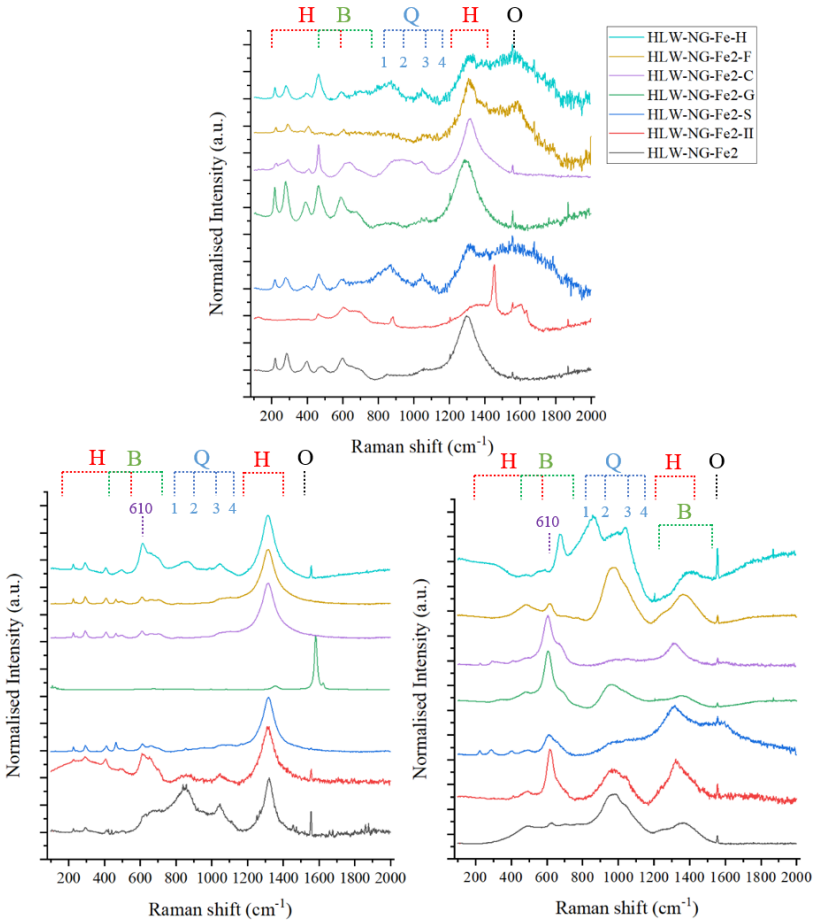

Figure 6.3.1. Raman spectra for HLW-NG-Fe2, HLW-NG-Fe2-II and HLW-NG-Fe2-R feeds of samples quenched at 600 ℃ (top), 800 ℃ (bottom left) and 1000 ℃ (bottom right). Raman mode assignments are labelled H = haematite, B = borate/borosilicate structures, Q = Q^n species and O = O – O in molecular oxygen. The spectra show the evolution from sharp crystalline peaks and haematite bands to the emergence of borosilicate structures, notably the 610 cm^{-1} band and the Q^n species region.

Broad bands in the 500 – 700 cm^{-1} region, which we attributed in Chapter 4, Table 4.4.2, to borate and borosilicate structures (Parkinson et al. 2008; Yadav and Singh 2015) develop by 1000 ℃ in all samples. The sharper band in this region is the emergence of the 610 cm^{-1} band which we suggested in Chapter 4, section 4.4.3, was due to danburite-like ring structures (Testa-Anta et al. 2019; Cochain and Neuville 2008; Cochain et al. 2012). This band is prevalent in the HLW-NG-Fe2-II, -C, -G and -H samples at 1000 ℃.

6.3.2 Final glasses

In all glasses Figure 6.3.2, the broad Si-O (Al-O, Fe-O) Q^n-species region is centred around 970 cm^{-1} (Parkinson et al. 2008; Yadav and Singh 2015; Neuville and Mysen 1996). A 970 cm^{-1} band can be attributed to the $^{IV}Fe^{3+}$-O stretching (Cochain et al. 2012) as well as silica Q^n structural units, and Si-O-Al interlinking (Yadav and Singh 2015; Parkinson et al. 2008; Neuville and Mysen 1996; Di Genova et al. 2017). Full deconvolution of the spectra is complicated by the presence of Si, Fe and Al bonds in this region (Neuville and Mysen 1996). An attempt is made to deconvolute the Raman spectrum qualitatively, fitting 4 Gaussian peaks to the 800-1250 cm^{-1} region, with limits on the half-width to 30-80 cm^{-1} and area > 100. Spectral deconvolution and fit parameters are given in Appendix C, Figures 1-7 and Tables 1-7. Estimated proportions of the Q^n species for each of the HLW-NG-Fe2 series glasses is given in Table 6.3.1.

Based on the assumption, discussed in section 2.2.3, that $^{IV}Fe^{3+}$ and $^{1V}Al^{3+}$ ions form $[MO_4]^-$ network polyhedra, whereas $^{VI}Fe^{2+}$ acts as a network modifier we can qualitatively interpret a shift from the 1150 cm^{-1} Q^4 band and the 970 cm^{-1} Q^4/Fe^{3+} to 1065 cm^{-1} Q^3 and 925 cm^{-1} Q^2 bands as depolymerisation of the network, and potential changes in Fe/Al coordination or oxidation state (Parkinson et al. 2008; Neuville and Mysen 1996; Cochain and Neuville 2008). From the tabulated results, Table 6.3.1, the HLW-NG-Fe2-F sample could be highly polymerised, followed by HLW-NG-Fe2-S and HLW-NG-Fe2-II. HLW-NG-Fe2-C and HLW-NG-Fe2-G have a greater proportion of Q^2 than HLW-NG-Fe2, but a similar level of the Q^4 and Q^4/Fe band. HLW-NG-Fe2-H is highly depolymerised with the majority of the region leaning towards Q^2.

The low wavenumber region of the spectra, 200 – 800 cm^{-1} was fitted with a main broad peak centred ~480 cm^{-1}, and not deconvoluted further as it covers a range of borate and borosilicate vibrational modes, Table 4.4.2. The significant difference in all of the spectra in this region is in the intensity of the 610 cm^{-1} peak, shown by the Raman

difference spectra in Figure 6.3.3 (right). The positions and areas of each of the ~610 cm^{-1} peaks are given in Appendix C, Table 8. This peak is loosely attributed to a change in the danburite-like ring structures in Chapter 4, section 4.4.3 based on literature of iron-bearing borosilicate glasses, in Chapter 2, section 2.2.2.4 and 2.2.3 (Cochain et al. 2012; Cochain and Neuville 2008; Manara, Grandjean, and Neuville 2009a).

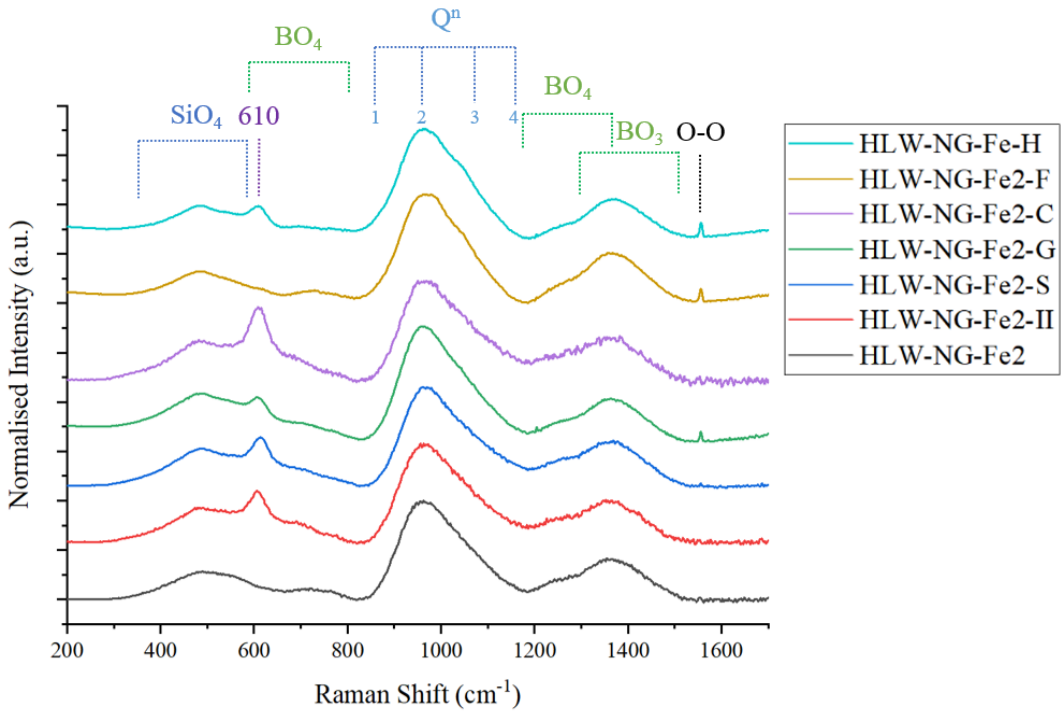

Figure 6.3.2. Raman spectra of HLW-NG-Fe2, -II and -R 1150 °C samples. More detailed Raman mode assignments are labelled including individual borate and silicate modes. The 610 cm^{-1} peak is the main difference between the spectra. There is no defined shift in Q^n species and other modes remain similar between the spectra.

Table 6.3.1. Relative proportions of Q^n species by Raman spectral deconvolution.

Glass	**%Q^2 (~925 cm^{-1})**	**Q^4/Fe^3 (~970 cm^{-1})**	**%Q^3 (~1065 cm^{-1})**	**%Q^4 (1100 cm^{-1})**
HLW-NG-Fe2	22.6	32.1	40.5	4.8
HLW-NG-Fe2-II	7.9	32.3	34.6	25.2
HLW-NG-Fe2-S	5.6	34.1	32.5	27.8
HLW-NG-Fe2-G	38.1	32.9	29.0	0.0
HLW-NG-Fe2-C	36.1	37.5	26.4	0.0
HLW-NG-Fe2-F	0.0	75.1	20.7	4.3
HLW-NG-Fe2-H	0	61.1	34.5	4.4

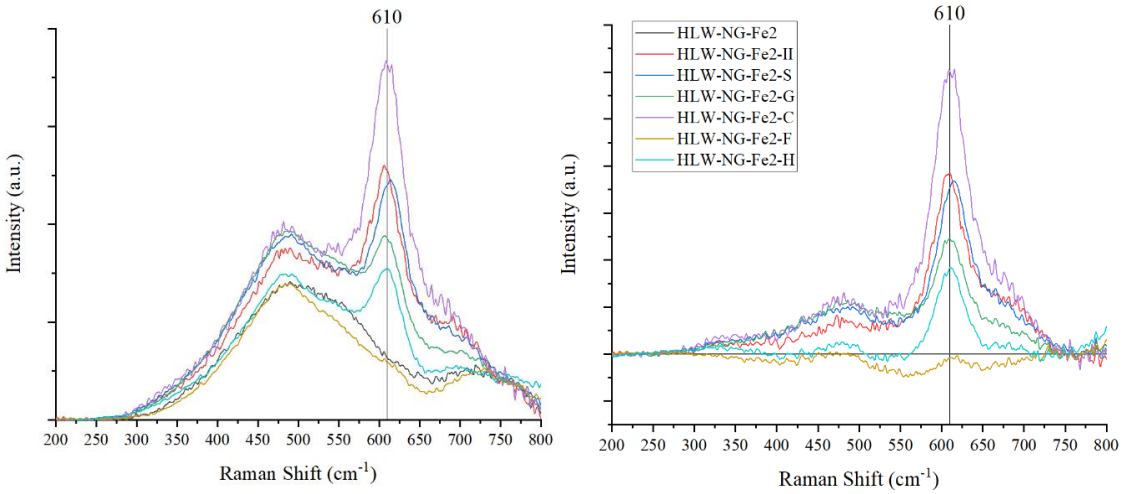

Figure 6.3.3. Raman spectra (left) and difference spectra (right) between 200-800 cm^{-1} showing the main difference in the spectra low wave-number region is the 610 cm^{-1} peak which is most intense in the HLW-NG-Fe2-C spectra followed by -II, -S, -G and -H. The feature is absent from the HLW-NG-Fe2 and -F spectra.

6.3.3 Graphite series

To further investigate the stipulation that this danburite-like ring structure changes with the bonding of Fe to the borosilicate network, Raman spectroscopy was performed on the samples from the study of increasing graphite addition from Chapter 5, section 5.2. For these samples the graphite addition to the HLW-NG-Fe2 varied from 0.5-6 wt%, Figure 6.3.4, providing a likely scenario where the more graphite added the more reduced the Fe in the glass (Zhernovaya, Onishchuk, and Davydoglu 2007; Kruger, Matlack, Pegg, et al. 2012). The variation in in the intensity of the ~610 cm^{-1} Figure 6.3.4 peak correlates with the presence of spinel phases in the glass up to 4 wt%, as shown by XRD, in Chapter 5, section 5.2. In the XRD, it is suspected that at 5 and 6 wt% graphite, the samples contain metallic Fe and significantly less spinel. The Raman supports this being the case, if the presence of Fe^{2+} increases the intensity of the danburite-like peak at 610 cm^{-1}, then the 5 and 6 wt% samples, where the Fe^{2+} is further reduced to metal, the danburite-like peak would decrease once again.

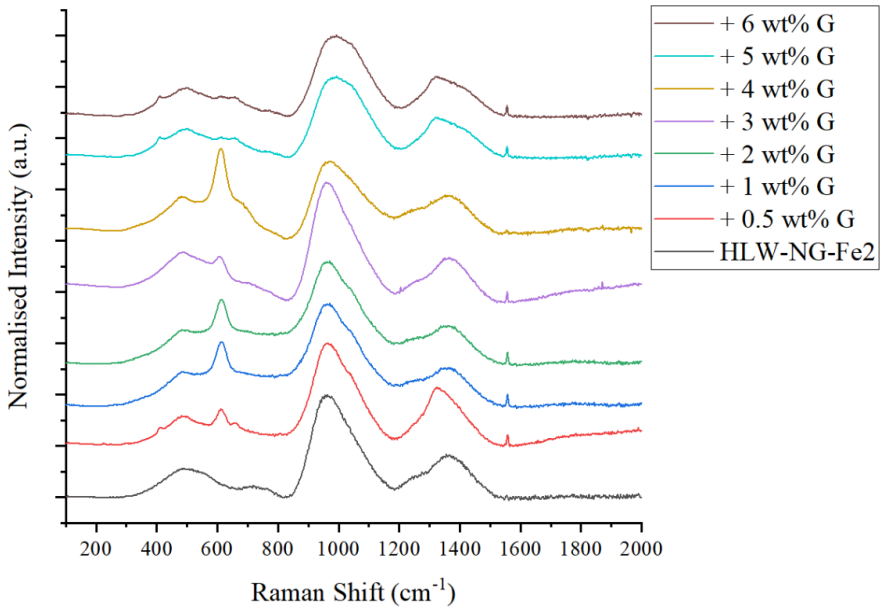

Figure 6.3.4. Raman spectra for HLW-NG-Fe2 and HLW-NG-Fe2-G for 0.5 – 6 wt% Graphite collected on samples quenched at 1150 ℃ showing the increase in intensity of the 610 cm^{-1} band up to most intense at 4 wt% graphite addition, at 5 and 6 wt% addition the band is no longer visible.

6.4 ^{57}Fe Mössbauer Spectroscopy

^{57}Fe Mössbauer spectroscopy has the capability to explore only Fe in the feeds and separate out iron on the paramagnetic and magnetic sites. As explained in Chapter 3, section 3.6.4 and Chapter 4, section 4.4.4, broader paramagnetic doublets are representative of the glassy Fe phase and the sharp magnetic sextets represent the magnetic crystalline phases. Throughout the feeds we see the paramagnetic doublets increase in intensity with quench temperature, relative to the sextets, reflecting the increase in amorphous phase content and decrease in crystalline iron components in the XRD, section 6.2, and Raman spectroscopy, section 6.3.

6.4.1 HLW-NG-Fe2, -S and -F

The spectra shown in Figure 6.4.1 are the HLW-NG-Fe2, HLW-NG-Fe2-S and -F feeds quenched at 600-1150 ℃. From 600-800 ℃ paramagnetic phases in these spectra are all Fe^{3+} based on the centre shift (CS) and quadrupole splitting (QS) values, detailed in Table 6.4.1. At 600 ℃ and 800 ℃ only one paramagnetic phase is resolvable, however, there are consistently a minimum of 2 resolvable sites resolved at 1000 and 1150 ℃. The two common sites between all three samples are tetrahedral paramagnetic Fe^{3+} sites with a CS between 0.25-0.27 mm s^{-1} and QS of 0.75-0.79 mm s^{-1} and 1.05-1.38 mm s^{-1}. The CS values of these sites are all within the range of tetrahedral Fe^{3+} (Darby Dyar 1985) each sample has a site with relatively lower and higher QS, indicating a site where the electron cloud symmetry is distorted by local bonding, e.g. rather than Fe-O-Fe there are Fe-O-M bonds where M is an atom with a different electronegativity (Stevens, Travis, and DeVoe 1972). In the HLW-NG-Fe2-S sample at 1000 ℃ there is a $^{IV}Fe^{2+}$ phase contributing 2.4 ± 2 % to the spectral area, which is only slightly above error. There is no Fe^{2+} phase detected in the 1150 ℃ sample.

Magnetically ordered dominant sextets at 600 and 800 ℃ belong to α-Fe_2O_3, with smaller contributions from Fe-bearing spinels with Fe^{3+} on the B site, and Fe, Mn or Ni

likely on the A site (Oh, Cook, and Townsend 1998). The relative proportion of the spinel phases increases with decrease in the α-Fe_2O_3, in line with the previous discussion in Chapter 4, section 4.4.4, and the XRD section 6.2. In the final glass samples, at 1150 ℃ 24.8 ± 2 % of the Fe in the HLW-NG-Fe2-S sample, and 14 ± 2 % in the HLW-NG-Fe2-F sample, is in the α-Fe_2O_3 phase. There is a small amount of Fe_2O_3 detected in the HLW-NG-Fe2-S sample correlating with the XRD, section 6.2.

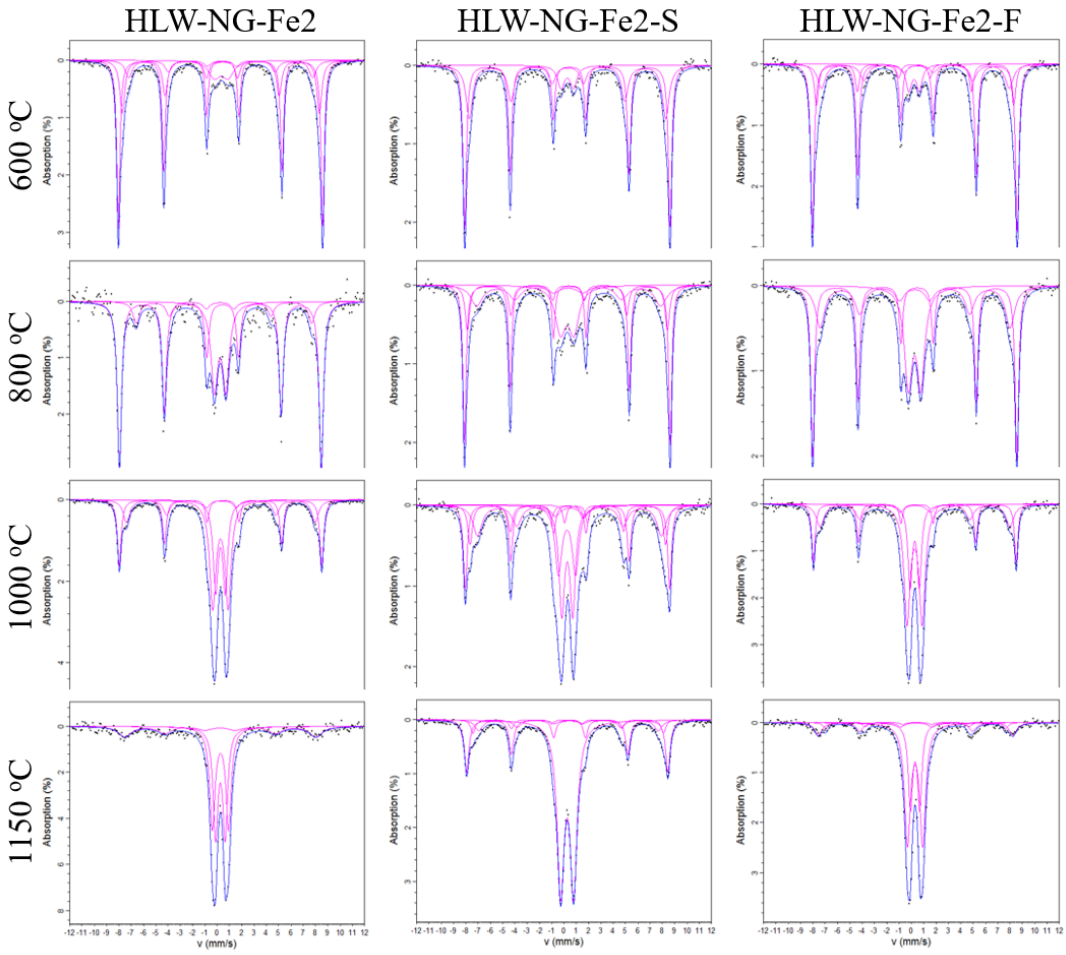

Figure 6.4.1. ^{57}Fe Mössbauer spectra of the HLW-NG-Fe2, HLW-NG-Fe2-S and -F feeds quenched at 600, 800, 1000 and 1150 ℃ showing the evolution of the form of iron during melting from magnetic to paramagnetic. Fe^{2+} is observed in the HLW-NG-Fe2-S sample at 1000 ℃, but only Fe^{3+} is resolvable at 1150 ℃.

Table 6.4.1. ^{57}Fe Mössbauer fit parameters for HLW-NG-Fe2, HLW-NG-Fe2-S, and HLW-NG-Fe2-F SoM samples. CS, relative to α-Fe, ± 0.02 mm s^{-1}. QS, ± 2 mm s^{-1}, H, ± 0.5 T, Area ± 2 %.

Feed	Temp (°C)	Signal	CS (mm s^{-1})	Δ (mm s^{-1})	H (T)	Area (%)	ID
HLW-NG-Fe2	600	Doublet 1	0.33	1.12		9.1	IV Fe^{3+}
		Sextet 1	0.37		51.6	53.0	α-Fe_2O_3
		Sextet 2	0.36		49.7	26.0	(Fe,Ni)Fe_2O_4
		Sextet 3	0.35		46.4	11.9	Fe_3O_4
	800	Doublet 1	0.25	0.95		25.0	IV Fe^{3+}
		Sextet 1	0.36		50.9	62.6	α-Fe_2O_3
		Sextet 2	0.41		44.3	12.4	(Fe,Mn)Fe_2O_4
	1000	Doublet 1	0.27	1.25		34.3	IV Fe^{3+}
		Doublet 2	0.27	0.79		23.0	IV Fe^{3+}
		Sextet 1	0.38		51.1	26.5	α-Fe_2O_3
		Sextet 2	0.33		47.6	16.1	Fe_3O_4
	1150	Doublet 1	0.26	0.78		39.0	IV Fe^{3+}
		Doublet 2	0.27	1.33		41.0	IV Fe^{3+}
		Sextet 1	0.25		48.2	20.0	Fe_3O_4
HLW-NG-Fe2-S	600	Doublet 1	0.27	1.01		7.5	IV Fe^{3+}
		Sextet 1	0.31		49.6	36.5	Fe_3O_4
		Sextet 2	0.37		51.8	56.0	α-Fe_2O_3
	800	Doublet 1	0.26	1.08		19.5	IV Fe^{3+}
		Sextet 1	0.37		52	42.1	α-Fe_2O_3
		Sextet 2	0.33		50.5	18	Fe_3O_4
		Sextet 3	0.37		46.5	20.9	Fe_3O_4
	1000	Doublet 1	0.27	0.88		22.0	IV Fe^{3+}
		Doublet 2	0.25	1.38		17.0	IV Fe^{3+}
		Doublet 3	0.99	1.87		2.4	VI Fe^{2+}
		Sextet 1	0.39		51.6	24.0	α-Fe_2O_3
		Sextet 2	0.28		49.4	13.6	Fe_3O_4
		Sextet 3	0.47		46.4	21.1	~Fe_3O_4
	1150	Doublet 1	0.26	1.05		60.3	IV Fe^{3+}
		Doublet 2	0.25	0.79		22.0	IV Fe^{3+}
		Sextet 1	0.37		50.80	24.8	α-Fe_2O_3
		Sextet 2	0.29		48.12	6.0	Fe_3O_4
		Sextet 3	0.39		45.35	9.3	Fe_3O_4
HLW-NG-Fe2-F	600	Doublet 1	0.22	0.85		7.37	IV Fe^{3+}
		Sextet 1	0.37		51.6	56.4	α-Fe_2O_3
		Sextet 2	0.28		49.7	17.1	Fe_3O_4
		Sextet 3	0.45		47.3	19.1	(Fe,Mn)Fe_2O_4
	800	Doublet 1	0.26	1.0		27.1	IV Fe^{3+}
		Sextet 1	0.37		51.4	44.8	α-Fe_2O_3
		Sextet 2	0.29		47.8	28.1	Fe_3O_4
	1000	Doublet 1	0.27	0.75		19	IV Fe^{3+}
		Doublet 2	0.27	1.22		40	IV Fe^{3+}
		Sextet 1	0.38		51.1	21.8	α-Fe_2O_3
		Sextet 2	0.3		47.8	19.6	Fe_3O_4
	1150	Doublet 1	0.31	1.24		54	VI Fe^{3+}
		Doublet 2	0.3	0.75		27	VI Fe^{3+}
		Sextet 1	0.37		49.0	14	α-Fe_2O_3
		Sextet 2	0.42		45.3	4.6	Fe_3O_4

6.4.2 HLW-NG-Fe2-G, -C and -H

^{57}Fe Mössbauer spectra for the HLW-NG-Fe2-G, -C and -H SoM samples are grouped in Figure 6.4.2. During melting of these three feeds, there is emergence of Fe^{2+} paramagnetic doublets. The Fe^{2+} paramagnetic doublet, characterised by its higher CS and QS (Darby Dyar 1985), is resolvable by 800 ℃. Amorphous $^{VI}Fe^{2+}$ acts as a network modifier in the glasses, whereas crystalline $^{VI}Fe^{2+}$ could be a component of Fe on the B site of a spinel, for example. Glasses quenched at 1150 ℃ show significant proportions of $^{VI}Fe^{2+}$, contributing 38.8 ± 2, 21.3 ± 2 and 11.8 ± 2 % to the total spectral area for the HLW-NG-Fe2-G, -C and -H glasses, respectively.

The transition from α-Fe_2O_3 dominating the magnetically ordered components to Fe_3O_4-like spinels (Oh, Cook, and Townsend 1998), occurs by 800 ℃ in the HLW-NG-Fe2-G and -H feeds, earlier than all of the other feeds, and 1000 ℃ in the HLW-NG-Fe2-C feed. This order is in agreement with the XRD in section 6.2. All of the magnetic sextets in the 1150 ℃ samples are attributed to spinel-type phases.

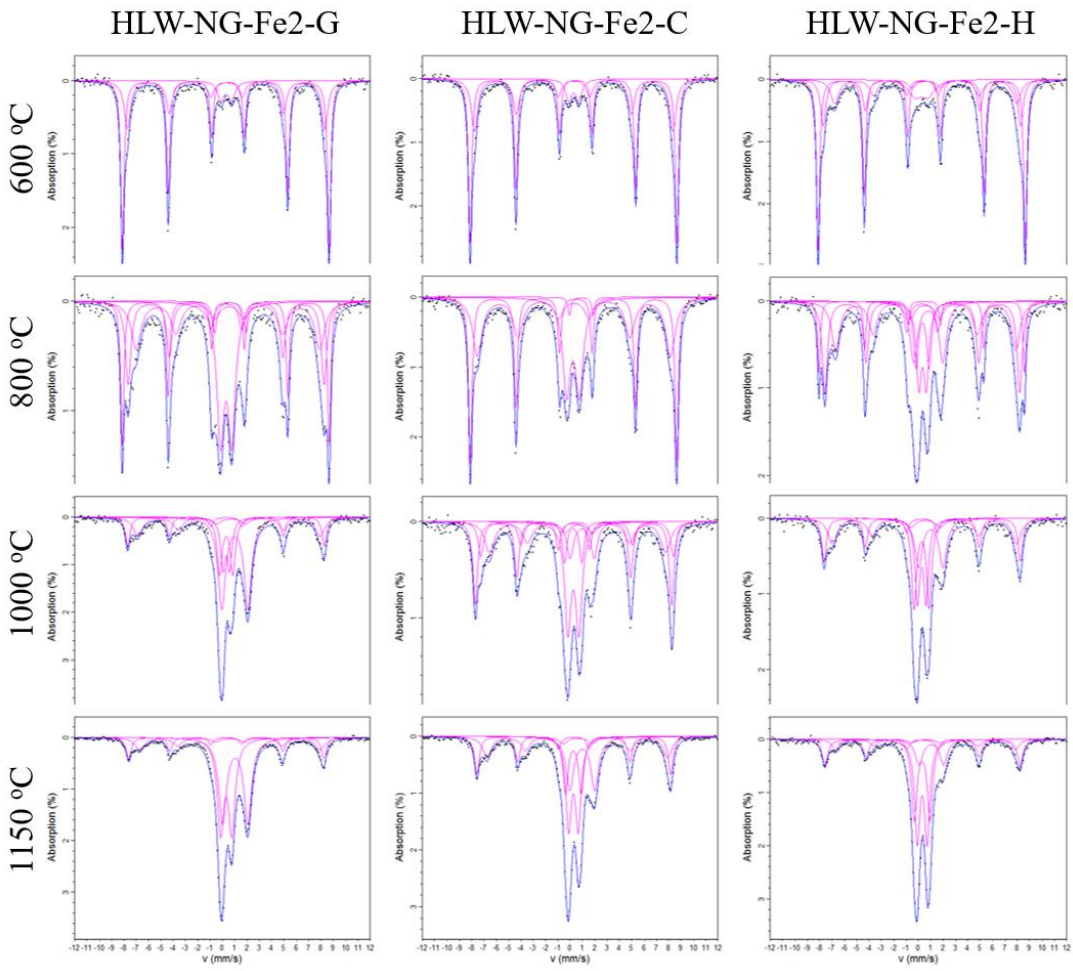

Figure 6.4.2. ^{57}Fe Mössbauer spectra of the HLW-NG-Fe2-G, HLW-NG-Fe2-C and -H feeds quenched at 600, 800, 1000 and 1150 °C, showing the presence of Fe^{2+} iron in all of the feeds during melting resolvable by 800 °C. Magnetic components remain prevalent up to 1150 °C indicating high levels of spinel present.

Table 6.4.2. ^{57}Fe Mössbauer fit parameters for HLW-NG-Fe2-G and HLW-NG-Fe2-C. CS, relative to α-Fe, ± 0.02 mm s^{-1}. QS, ± 2 mm s^{-1}, H, ± 0.5 T, Area ± 2 %.

Feed	Temp (°C)	Signal	CS (mm s^{-1})	Δ (mm s^{-1})	H (T)	Area (%)	ID
HLW-NG-Fe2-G	600 °C	Doublet 1	0.31	0.87		6.88	IV Fe^{3+}
		Sextet 1	0.37		52	60.7	α-Fe_2O_3
		Sextet 2	0.32		49.7	32.4	Fe_3O_4
	800 °C	Doublet 1	0.31	0.91		25	IV Fe^{3+}
		Doublet 2	0.65	2.56		3.7	VI Fe^{2+}
		Sextet 1	0.37		52	23.5	α-Fe_2O_3
		Sextet 2	0.51		46.2	24.2	(Fe,Mn)Fe_2O_4
		Sextet 3	0.31		49.4	23.7	Fe_3O_4
	1000 °C	Doublet 1	0.33	0.55		12	IV Fe^{3+}
		Doublet 2	1.01	2.12		39.1	VI Fe^{2+}
		Doublet 3	0.32	1.09		16	IV Fe^{3+}
		Sextet 1	0.31		49.5	14.4	Fe_3O_4
		Sextet 2	0.62		45.9	19.4	Fe_3O_4
	1150 °C	Doublet 1	0.31	0.92		34.9	IV Fe^{3+}
		Doublet 2	1.04	2.04		38.8	VI Fe^{2+}
		Sextet 1	0.32		49.1	12.4	Fe_3O_4
		Sextet 2	0.61		45.5	13.9	Fe_3O_4
HLW-NG-Fe2-C	600 °C	Doublet 1	0.3	0.81		6.74	IV Fe^{3+}
		Sextet 1	0.37		52.1	57.7	α-Fe_2O_3
		Sextet 2	0.3		50	35.6	Fe_3O_4
	800 °C	Doublet 1	0.92	1.92		1.77	IV Fe^{2+}
		Doublet 2	0.24	1.04		23.4	IV Fe^{3+}
		Sextet 1	0.37		52	37.9	α-Fe_2O_3
		Sextet 2	0.32		48.6	37	Fe_3O_4
	1000 °C	Doublet 1	0.25	1.4		6	IV Fe^{3+}
		Doublet 2	1	1.95		8.6	VI Fe^{2+}
		Doublet 3	0.27	0.89		23	IV Fe^{3+}
		Sextet 1	0.29		49.5	27.3	Fe_3O_4
		Sextet 2	0.65		44.3	20.5	Fe_3O_4
		Sextet 3	0.55		48.5	13.7	Fe_3O_4
	1150 °C	Doublet 1	0.28	0.78		25.5	IV Fe^{3+}
		Doublet 2	0.27	1.27		14.9	IV Fe^{3+}
		Doublet 3	0.99		2.02	21.3	VI Fe^{2+}
		Sextet 1	0.3		48.8	19.2	Fe_3O_4
		Sextet 2	0.61		45.44	19.1	Fe_3O_4
HLW-NG-Fe2-H	600 °C	Doublet 1	0.25	1.04		9.2	IV Fe^{3+}
		Sextet 1	0.37		52.0	49.9	α-Fe_2O_3
		Sextet 2	0.32		49.6	23	Fe_3O_4
		Sextet 3	0.63		45.7	17.9	Fe_3O_4
	800 °C	Doublet 1	0.34	0.59		12	IV Fe^{3+}
		Doublet 2	0.8	2.36		13.5	VI Fe^{2+}
		Doublet 3	0.34	1.05		9	IV Fe^{3+}
		Sextet 1	0.38		51.6	11.8	α-Fe_2O_3
		Sextet 2	0.32		48.9	28.8	Fe_3O_4
		Sextet 3	0.58		45.3	24.1	Fe_3O_4
	1000 °C	Doublet 1	0.27	1.21		21	IV Fe^{3+}
		Doublet 2	0.27	0.69		19	IV Fe^{3+}
		Doublet 3	1.01	1.97		17.7	VI Fe^{2+}
		Sextet 1	0.31		49.3	20.1	Fe_3O_4
		Sextet 2	0.53		46.2	22.4	(Fe,Mn)Fe_2O_4
	1150 °C	Doublet 1	0.31	0.79		32	IV Fe^{3+}
		Doublet 2	0.31	1.27		27	IV Fe^{3+}
		Doublet 3	1.04	2.0		11.8	VI Fe^{2+}
		Sextet 1	0.59		41.2	9.8	(Fe,Mn)Fe_2O_4
		Sextet 2	0.34		49.0	19.2	Fe_3O_4

6.5 Summary

6.5.1 Structural changes during melting

From XRD, section 6.2, and Raman spectroscopy, section 6.3.1-2, the amorphization of the remaining crystalline materials at 600 ℃ to almost entirely glass was observed in each of the samples by 1150 ℃. XRD suggests the rate of amorphization is slightly slower in the HLW-NG-Fe2 and HLW-NG-Fe2-S feed, based on the rates of silica and haematite dissolution, and the amorphous phase fraction. By Raman spectroscopy, section 6.3.1, there is a more distinct difference between the amorphization of the feeds. The emergence of the broad Si-O (Al-O, Fe-O) Q^n-species region between 800 and 1200 cm^{-1} (Parkinson et al. 2008; Yadav and Singh 2015), occurs by 1000 ℃ in the HLW-NG-Fe2, HLW-NG-Fe2-F and -H feeds, and not until 1150 ℃ in the other feeds, section 6.3.2. These differences may indicate different melting rates of the feeds. At 1150 ℃ there is remaining Fe_2O_3 in the HLW-NG-Fe2-S and -F glasses showing that these feeds have not completely melted by 1150 ℃. In the other glasses the transition from Fe_2O_3 to iron-bearing spinel is observed during melting, by both XRD, section 6.2, and ^{57}Fe Mössbauer, section 6.4, which precipitates out in the final glasses.

6.5.2 The form of iron during melting

The change of the form of iron during melting, is not only a useful indicator of the melting rate of the feeds, but also impacts the total O_2 evolution in cases where a proportion of the initially Fe^{3+} raw material has reduced Fe^{2+} in the paramagnetic melt phase, or precipitated out as Fe_3O_4. Quantification of these phases changes is provided by ^{57}Fe Mössbauer spectroscopy, section 6.4, and XRD, section 6.2 and the net contribution to O_2 evolution calculated.

For the HLW-NG-Fe2-R feeds, the rate of dissolution of Fe_2O_3 varies significantly during melting. The slowest rate of dissolution of Fe_2O_3 in the HLW-NG-Fe2 feed is as

predicted in the absence of additional reducing species (Karamanov et al. 2000). The spinels in the final HLW-NG-Fe2-R glass samples, similar those the HLW-NG-Fe2 and HLW-NG-Fe2-II samples, they have a range of lattice parameters similar to that of magnetite, Fe_3O_4, a = b = c = 8.394, but are likely to also contain Mn, Cr and Ni.

By ^{57}Fe Mössbauer spectroscopy we observe a change in the redox state of iron in the paramagnetic phase in the HLW-NG-Fe2-S, -G, -C and -H samples. In the HLW-NG-Fe2-S sample the paramagnetic iron is reduced at 1000 ℃ and re-oxidises, in the other samples there remains considerable Fe^{2+} in the final glasses.

6.5.3 Contributions to O_2 evolution

Both reduction of iron in the paramagnetic phase and the formation of spinel structures are considered here for their contribution to the O_2 balance instigated in 5.5.3. The contribution of the spinel formation was considered negligible in a previous O_2 balance in a HLW feed, from which there was ~1 wt% spinel in the final glass (Lee, Hrma, Kloužek, et al. 2017). Spinels contribute up to 4.15 wt% of the HLW-NG-Fe2-R samples, therefore the O_2 release could be appreciable. All spinels formed during melting and in the final glasses were assumed to be Fe_3O_4 for simplification of the calculation of the reaction:

$$3Fe_2O_3 \rightarrow 2Fe_3O_4 + ½\ O2 \qquad (47)$$

This is the most common identified spinel in both ^{57}Fe Mössbauer and XRD, although mass changes in the cations would influence the quantity of O_2 evolved. Estimations of the O_2 evolution from the feeds where spinel phases have formed from haematite, are given in Table 6.5.1. The O_2 evolution in the 1150 ℃ samples should be used at the net O_2 evolution contribution, and the intermediate samples as the temperatures at which O_2 is evolved.

Table 6.5.1. O_2 contributions from the formation of Fe_3O_4 over Fe_2O_3 measured by XRD. The net O_2 evolution by the change in crystalline phase of iron is shown in bold.

Feed	Temperature	O_2 contribution	
	°C	mg kg^{-1} glass	Error
HLW-NG-Fe2	600	496.90	17.48
	800	784.00	15.74
	1000	625.73	34.97
	1150	**312.87**	**6.99**
HLW-NG-Fe2-S	600	949.64	13.99
	800	990.13	15.74
	1000	905.47	10.49
	1150	**647.82**	**3.50**
HLW-NG-Fe2-G	600	546.59	8.74
	800	1142.88	10.49
	1000	793.21	6.99
	1150	**642.30**	**3.50**
HLW-NG-Fe2-C	600	938.60	174.84
	800	870.50	13.99
	1000	1803.58	8.74
	1150	**763.76**	**5.25**
HLW-NG-Fe2-F	600	530.03	5.25
	800	830.01	12.24
	1000	395.68	5.25
	1150	**364.40**	**3.50**
HLW-NG-Fe2-H	600	1065.58	13.99
	800	1218.33	8.74
	1000	909.15	6.99
	1150	**680.94**	**5.25**

Table 6.5.2 provides the redox states of the Fe in the paramagnetic phase determined by ^{57}Fe Mössbauer spectroscopy. The redox ratios were determined by the proportion of Fe in each of the two paramagnetic phases, assuming that the that the recoil-free fraction ratio f(Fe3+/Fe2+)=1.0. This assumption may overestimate the Fe3+/FeT values (H. L. Zhang et al. 2018). The intermediate stages give indications of the temperatures at which the O2 is evolved by these structural changes, which are of interest for foam evolution, discussed in Chapter 5, section 5.7.1.

From these calculations, it has been determined that the HLW-NG-Fe2-G feed has the highest net O_2 contribution based on the form of Fe in the melt. HLW-NG-Fe2, HLW-NG-Fe2-S and -F feeds have no net change of redox state in the paramagnetic phase, and therefore no net O_2 contribution by this mechanism. By the change of Fe_2O_3 to Fe_3O_4, the HLW-NG-Fe2-C feed has the highest net contribution to O_2 evolution,

followed by HLW-NG-Fe2-S, G and H, and HLW-NG-Fe2-F evolves a similar amount to the HLW-NG-Fe2 feed.

Table 6.5.2. Redox state in the amorphous phase in each sample measured by ^{57}Fe Mössbauer spectroscopy and estimated O_2 evolution contribution from these redox changes. The net O_2 evolution by the change in redox state of iron is shown in bold.

Feed	**Temperature**	**Redox Ratio**		**O_2 "evolution"**	
	°C	**Fe^{3+}/Fe_T**	**Error**	**mg kg^{-1} glass**	**Error**
HLW-NG-Fe2	600	1.00	0.020	0	0
	800	1.00	0.020	0	0
	1000	1.00	0.020	0	0
	1150	**1.00**	**0.020**	**0**	**0**
HLW-NG-Fe2-S	600	1.00	0.020	0	0
	800	1.00	0.020	0	0
	1000	0.94	0.019	1000	20
	1150	**1.00**	**0.020**	**0**	**0**
HLW-NG-Fe2-G	600	1.00	0.020	0	0
	800	0.87	0.017	2407	48
	1000	0.42	0.008	22707	454
	1150	**0.47**	**0.009**	**18078**	**362**
HLW-NG-Fe2-C	600	1.00	0.020	0	0
	800	0.93	0.019	1230	25
	1000	0.77	0.015	4822	96
	1150	**0.65**	**0.013**	**8573**	**171**
HLW-NG-Fe2-F	600	1.00	0.020	0	0
	800	1.00	0.020	0	0
	1000	1.00	0.020	0	0
	1150	**1.00**	**0.020**	**0**	**0**
HLW-NG-Fe2-H	600	1.00	0.020	0	0
	800	0.61	0.012	10453	209
	1000	0.69	0.014	7195	144
	1150	**0.83**	**0.017**	**3252**	**65**

These contributions to O_2 evolution begin to explain the highly negative O_2 balance for the reductant added feeds discussed in Chapter 5. Further contributions involving other redox-active multivalent species are explored by X-ray Absorption Near-Edge spectroscopy in Chapter 7.

6.6 References

Bacon, J. F. and Hasapis, A. A. (1959) 'Viscosity of molten silica', Journal of Applied Physics, 30(9), pp. 1470–1471.

Cochain, B., Neuville, D. R., Henderson, G. S., McCammon, C. A., Pinet, O. and Richet, P. (2012) 'Effects of the iron content and redox state on the structure of sodium borosilicate glasses: A Raman, Mössbauer and boron K-edge XANES spectroscopy study', Journal of the American Ceramic Society, 95(3), pp. 962–971.

Cochain, B. and Neuville, D. R. (2008) 'Determination of iron redox ratio in borosilicate glasses and melts from Raman spectra', in Atalante, Montpellier (France).

Darby Dyar, M. (1985) 'A review of Mössbauer data on inorganic glasses: The effects of composition on iron valency and coordination', The American mineralogist, 70(3), pp. 304–316.

de Faria, D. L. A. and Lopes, F. N. (2007) 'Heated goethite and natural hematite: Can Raman spectroscopy be used to differentiate them?', Vibrational Spectroscopy, 45(2), pp. 117–121.

Di Genova, D., Sicola, S., Romano, C., Vona, A., Fanara, S. and Spina, L. (2017) 'Effect of iron and nanolites on Raman spectra of volcanic glasses: A reassessment of existing strategies to estimate the water content', Chemical Geology. Elsevier, 475(October), pp. 76–86.

Hujová, M., Pokorný, R., Kloužek, J., Lee, S., Traverso, J. J., Schweiger, M. J., Kruger, A. A. and Hrma, P. (2018) 'Foaming during nuclear waste melter feeds conversion to glass: Application of evolved gas analysis', International Journal of Applied Glass Science, 9(4), pp. 487–498.

Karamanov, A., Pisciella, P., Cantalini, C. and Pelino, M. (2000) ‘Iron-Rich Glasses Made with Industrial Wastes.’ Journal of the American Ceramic Society 83(12), pp. 3153–3157.

Krolop, P., Jantschke, A., Gilbricht, S., Niiranen, K. and Seifert, T. (2019) ‘Mineralogical imaging for characterization of the per geijer apatite iron ores in the Kiruna district, northern Sweden: A comparative study of mineral liberation analysis and raman imaging’, Minerals, 9(9), pp. 7–11.

Kruger, A. A., Matlack, K. S., Pegg, I. L., Kot, W. K. and Joseph, I. (2012) ‘Redox Control for Hanford HLW Feeds.’ VSL-12R2530-12. Office of River Protection, Richland, WA (United States).

Lee, S. M., Hrma, P. R., Kloužek, J., Pokorný, R., Hujová, M., Dixon, D. R., Schweiger, M. J. and Kruger, A. A. (2017) ‘Balance of oxygen throughout the conversion of a high-level waste melter feed to glass’, Ceramics International, 43(16), pp. 13113–13118.

Manara, D., Grandjean, A. & Neuville, D. R. (2009) ‘Advances in understanding the structure of borosilicate glasses: A raman spectroscopy study’, American Mineralogist, 94(5–6), pp. 777–784.

Marcial, J., Chun, J., Hrma, P. and Schweiger, M. J. (2014) ‘Effect of bubbles and silica dissolution on melter feed rheology during conversion to glass’, Environmental Science and Technology, 48(20), pp. 12173–12180.

Neuville, D. R. and Mysen, B. O. (1996) ‘Role of aluminium in the silicate network: In situ, high-temperature study of glasses and melts on the join SiO_2-$NaAlO_2$.’ Geochimica et Cosmochimica Acta, 60(10). pp. 1727–1737.

Oh, S. J., Cook, D. C. and Townsend, H. E. (1998) ‘Characterisation of iron oxides commonly formed as corrosion products on steel’, Hyperfine Interactions, 112, pp. 59–65.

Parkinson, B. G. Holland, D. Smith, M. E. Larson, C. Doerr, J. Affatigato, M. Feller, S. A. Howes, A. P. Scales, C. R. (2008) 'Quantitative measurement of Q^3 species in silicate and borosilicate glasses using Raman spectroscopy', Journal of Non-Crystalline Solids, 354(17), pp. 1936–1942.

Rehman, Z. U., Ullah, S., Qayyum, H., Irfan, M., Tran, K. A., Suk, H., Qayyum, A. and Janulewicz, K. A. (2021) 'Phase transformations initiated by optical breakdown in bulk of fused silica', Optics and Laser Technology. Elsevier Ltd, 134, 106630.

Stevens, J. G., Travis, J. C. and DeVoe, J. R. (1972) 'Mössbauer Spectrometry.' Analytical Chemistry, 44(5). pp. 384–406.

Testa-Anta, M., Ramos-Docampo, M. A., Comesaña-Hermo, M., Rivas-Murias, B. and Salgueiriño, V. (2019) 'Raman spectroscopy to unravel the magnetic properties of iron oxide nanocrystals for bio-related applications', Nanoscale Advances, 1(6), pp. 2086–2103.

Xu, K., Hrma, P., Rice, J., Riley, B. J., Schweiger, M. J. and Crum, J. V. (2015) 'Melter Feed Reactions at T ≤ 700 °C for Nuclear Waste Vitrification', Journal of the American Ceramic Society, 98(10), pp. 3105–3111.

Yadav, A. K. and Singh, P. (2015) 'A review of the structures of oxide glasses by Raman spectroscopy', RSC Adv. Royal Society of Chemistry, 5(83), pp. 67583–67609.

Yalmali, V. S., Deshingkar, D. S., Wattal, P. K. and Bharadwaj, S. R. (2007) 'Preparation and characterization of vitrified glass matrix for high level waste from MOX fuel processing', Journal of Non-Crystalline Solids, 353(52–54), pp. 4647–4653.

Zhang, H. L., Cottrell, E., Solheid, P. A., Kelley, K. A. and Hirschmann, M. M. (2018) 'Determination of $Fe^{3+}/\Sigma Fe$ of XANES basaltic glass standards by Mössbauer

spectroscopy and its application to the oxidation state of iron in MORB', Chemical Geology. Elsevier, 479(January), pp. 166–175.

Zhernovaya, N. F., Onishchuk, V. I. and Davydoglu, B. (2007) 'Color control and redox balance monitoring in container glass', Glass and Ceramics (English translation of Steklo i Keramika), 64(3–4), pp. 111–114.

7 Alternative Reductants: Redox behaviour of multivalent species

7.1 Overview

In the previous chapter, Chapter 6, the structural changes during melting were explored by XRD, Raman spectroscopy and ^{57}Fe Mössbauer spectroscopy. The structure of Fe during melting is of particular importance in the HLW-NG-Fe2 feed, due to its high Fe content dictating much of its variation in melting behaviour. However, the negative O_2 balance, calculated in Chapter 5, section 5.5, likely affects the redox states of the all multivalent species in the melt (Lee, Hrma, Kloužek, et al. 2017).

A previous 2020 X-ray Absorption Near-Edge Spectroscopy (XANES) study (Guillen et al. 2020) study showed changes in the oxidation state of Fe and Mn in the HLW-NG-Fe2 feed during melting by XANES. The levels of Fe^{2+} increased with heat-treatment temperature between 500-1150 °C with a final redox state Fe^{3+}/Fe_T = 0.627, and Mn reduced from MnO_2 to MnO in the temperature range 500-850 °C. The final redox state of Fe in the HLW-NG-Fe2 feed is lower than we found in the previous chapter, Chapter 6, section 6.4.1 by ^{57}Fe Mössbauer spectroscopy.

A complete understanding of the redox changes in multivalent species during melting in the study in this chapter will not just be useful to incorporate all possible sources of oxygen into the O_2 balance for this feed, but also to provide a matrix of glass melts, with different reducing conditions, to explore redox changes, adding to the material systems explored by Schreiber (Schreiber et al. 1986; Schreiber 1986; Schreiber and Hockman 1987) and others since (Lee, Hrma, Kloužek, et al. 2017; Kloužek and Rohanová 1999; Pinet, Hugon, and Mure 2014; McKeown et al. 2002; Gan et al. 2009), discussed in Chapter 2 section 2.7.

7.2 Expected redox behaviour

The electron redox potentials, E^*_M, Table 2.7.1, derived by Schreiber, by equation (13), in Chapter 2, section 2.7.3, provide the order in which the multivalent species will reduce (Schreiber and Balazs 1985; Schreiber et al. 1987). For the HLW-NG-Fe2, and derivative glasses, the order is Cr^{6+}/Cr^{3+} > Ce^{3+}/Ce^{4+} > Mn^{3+}/Mn^{2+} > Fe^{3+}/Fe^{2+} (Schreiber and Balazs 1985; Mirhadi and Mehdikhani 2011b; Thiemsorn et al. 2008b; Schreiber et al. 1984; Brückner 1985; Pinet et al. 2008). Cr^{6+} to Cr^{3+} has a reduction potential of -0.04, making oxidation from the initial Cr^{3+} raw material to Cr^{6+} possible. The potentials for reduction to metallic Fe and Ni are -1.27 and -1.06, respectively, these are unlikely to occur unless the conditions are extremely reducing.

If the reactions stated above are completed, the total O_2 evolution is given in, Table 7.2.1. Approximately 30 % of the O_2 evolution would come from a reduction of Mn^{4+} to Mn^{2+}, preceding reduction of Fe^{3+} to Fe^{2+} (Schreiber and Balazs 1985). In Chapter 6, section 6.4.1, there is no net change in the redox state of Fe in the HLW-NG-Fe2, -S and -F samples. Therefore, investigation of Mn, and other multivalent species are necessary to provide a complete O_2 balance and understanding of structural changes.

Table 7.2.1. Theoretical O_2 evolution if multivalent species were reduced g kg^{-1} glass, calculated by taking the contributions of each reduction reaction weighted by the quantity of the oxidised species in the batch. While Fe contributes most to the theoretical O_2 evolution, Mn is still a considerable quantity.

Multivalent element	**O_2 evolution (g kg^{-1} glass)**	
	Species reduced to metal – highly reducing conditions	**Species reduced according to redox potentials – moderate reducing conditions**
Total	43.92	23.49
Fe	32.31	16.16
Mn	10.92	7.28
Cr	0.53	0.00
Ni	0.51	0.00
Ce	0.17	0.06

7.3 Fe K-edge X-ray Absorption Near-Edge Spectroscopy

Each merged, normalised Fe K-edge XANES spectra is shown for HLW-NG-Fe2 and -R feeds at 600 – 1150 ℃ in Figure 7.3.1. Analysis of the pre-edge features, described in Chapter 3, section 3.6.3.5, was used to compare the Fe oxidation state and coordination with the ^{57}Fe Mössbauer spectroscopy, in section 6.4. The greater the energy separation between the pre-edge and absorption edge, the higher the Fe^{2+} content in the sample (Berry et al. 2003; Wilke et al. 2001). Tetrahedrally coordinated Fe^{3+} and Fe^{2+} generally have higher intensity transitions than octahedrally coordinated (Berry et al. 2003).

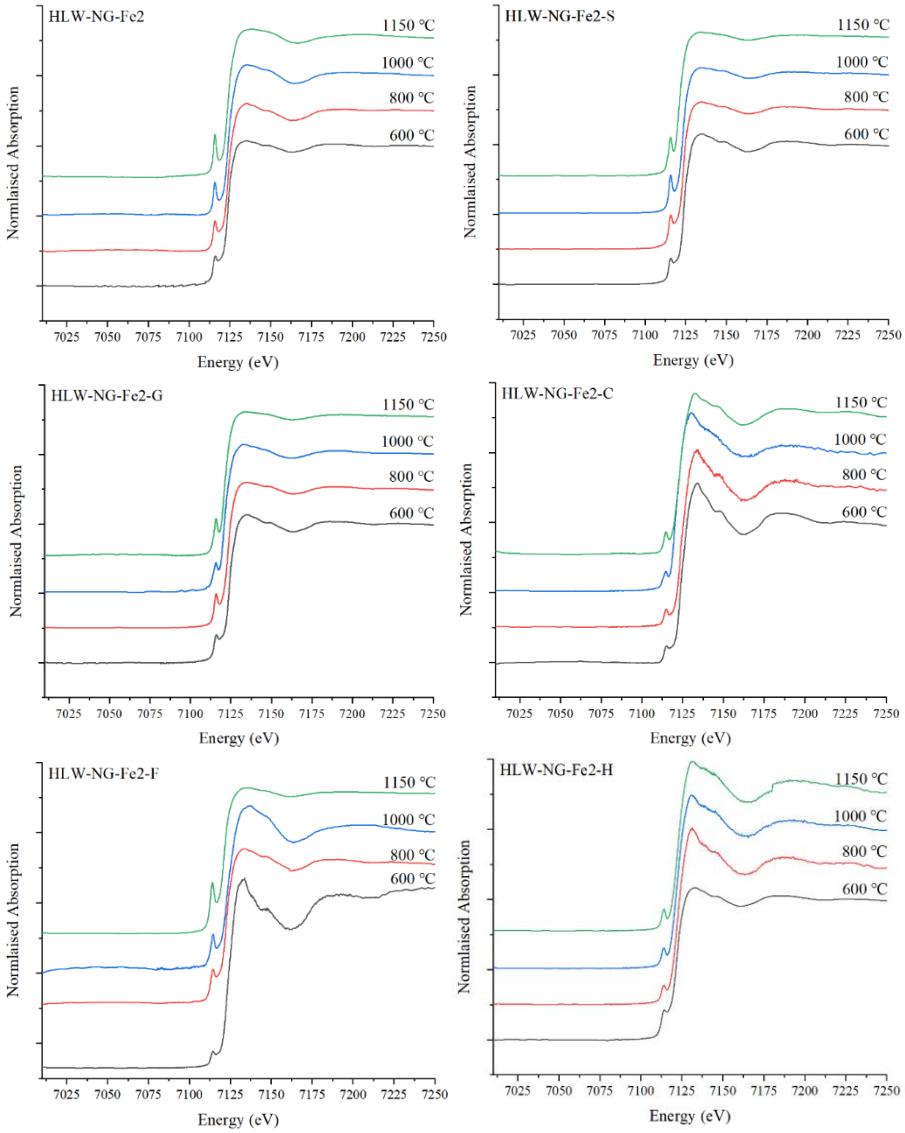

Figure 7.3.1. Fe K-edge XANES Spectra for HLW-NG-Fe2 and HLW-NG-Fe2-R samples quenched at 600, 800, 1000 and 1150 ℃.

7.3.1 Fe Wilkes Diagram

Approximate oxidation state and coordination of each of the samples were identified by plotting the centroid positions and integrated intensities of the pre-edge features on a diagram developed by Wilke et al. (Wilke et al. 2004, 2001), Figure 7.3.2, along with the positions of measured reference materials; wüstite (FeO), Fe_2O_3, Fe_3O_4, $^{IV}Fe^{2+}$ staurolite ($Fe_{1.5}Mg_{0.7}Cr_{1.4}Al_{0.5}O_4$), $^{V}Fe^{2+}$ grandidierite ($(Mg,Fe)Al_3(BO_4)(SiO_4)O$), $^{VI}Fe^{2+}$ siderite ($FeCO_3$), $^{IV}Fe^{3+}$ berlinite ($FePO_4$), and $^{VI}Fe^{3+}$ aegirine ($NaFeSi_2O_6$), for comparison. The weighted average of each of the centroid position of each of the contributing peaks was used to give an average Fe redox state in the sample (Wilke et al. 2004, 2001).

Since the spectra contains information on all of the iron in the sample, these plots display and average of all of the magnetic and paramagnetic iron in the samples. By phase ID of the XRD patterns, in Chapter 6, section 6.2, multiple Fe containing phases were identified for many of the SoM samples from 600 – 1000 °C. Thus, most samples likely contain a mixture of crystalline and amorphous Fe, which causes overlapping peaks in the pre-edge (Wilke et al. 2004; Farges et al. 2005). Error bars were generated using the error on the values of position and intensity of the pre-edge peak in the peak fitting function in OriginPro ®, combined with the uncertainty in eV from the step size (0.15 eV for those performed at ESRF and 0.1 eV for those at Diamond Light Source).

The HLW-NG-Fe2 feed contains almost entirely Fe^{3+} throughout the temperature range by comparison with the standards on the Wilke diagram, Figure 7.3.2. Deviation from the Fe^{3+} line may indicate a proportion of Fe_3O_4 or similar spinel in the sample which we have identified using XRD, Fe_3O_4 contains 33 % Fe^{2+}. With increasing temperature there is a slight increase in the Fe^{2+} content and a gradual change from octahedral to tetrahedral coordination, consistent with previous measurements (Guillen et al. 2020).

The sucrose feed is reduced at 1150 °C so it would have been expected to find some reduced Fe in the ^{57}Fe Mössbauer spectra of the sucrose at 1150 °C. The coordination state of the iron in the sucrose feed appears to remain octahedral throughout. Graphite appears to contain tetrahedral Fe^{3+} at 600 °C which then becomes reduced and octahedrally coordinated with temperature, reaching maximum quantities of Fe^{2+} at 1000 °C before oxidising again slightly.

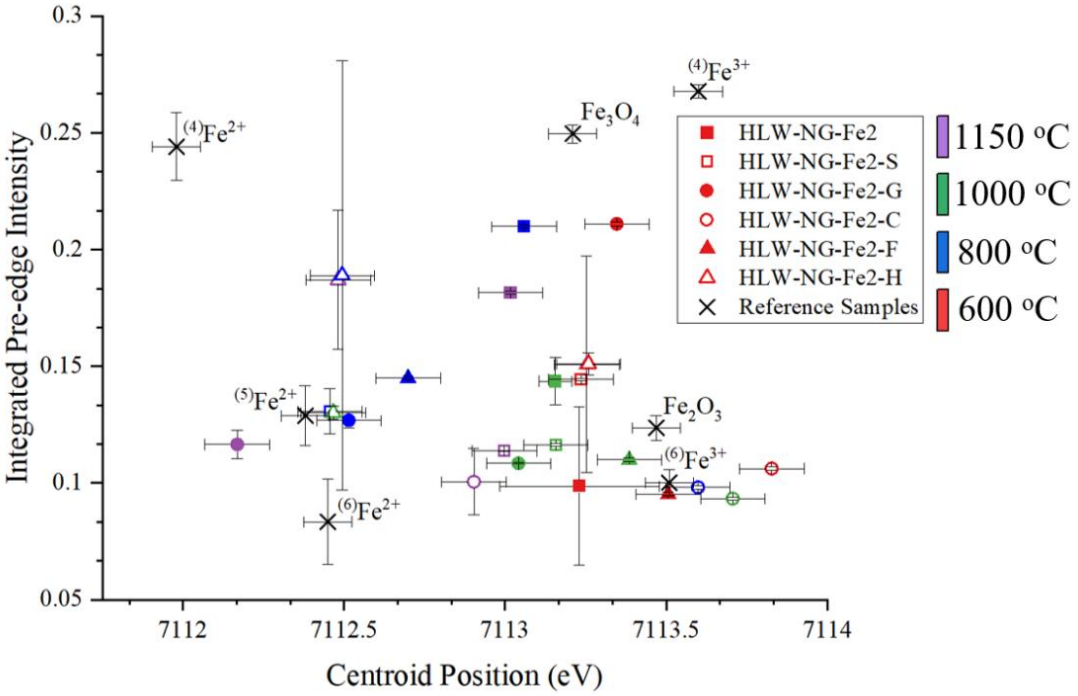

Figure 7.3.2. Integrated intensity and centroid positions of Fe K-edge pre-edge peaks for each of the HLW-NG-Fe2 and -R feeds and the measured standards labelled. The position of the datapoints indicate that most of the samples are $^{VI}Fe^{3+}$ or high in Fe_2O_3, those that contain considerable amounts of Fe^{2+} are -G at 800 and 1150 °C, -H from 800 - 1150 °C and -S at 800 °C.

Iron in the coke-reduced sample remains octahedrally Fe^{3+} coordinated at all temperatures apart from 1000 °C which contains a considerable amount of Fe^{2+}, which is in contrast to the high proportion of Fe^{2+} observed in the glass ^{57}Fe Mössbauer spectra. According to XANES, the formic acid reduced sample has more Fe^{2+} in the final glass than the glass produced from the coke feed, and a similar amount to graphite.

The coordination Fe in both coke and formic acid feed samples does not change considerably with temperature. HEDTA appears reduced at 800-1150 ℃, which is consistent with the 1150 ℃ Mössbauer. At 1000 and 1150 ℃ there is also an increase in tetrahedrally coordinated Fe.

Heamatite and magnetite were identified in the samples by XRD, Chapter 6, section 6.2. The pre-edge position for magnetite should theoretically show a mixture of tetrahedral and octahedral Fe^{3+} and octahedral Fe^{2+}, although the measured standard lies close to tetrahedral Fe^{3+} (Wilke et al. 2001). Haematite has a characteristically intense shoulder between the main pre-edge peak and the absorption edge ~7116 eV, relating to the 1s → 4s transition (Berry et al. 2003; Magnien et al. 2004), although multiple contributing peaks have previously been fitted to this shoulder (Wilke et al. 2001). For the data collected, this means that the centroid position is shifted to a higher energy when haematite is present in the sample, and this shoulder emerges, for example in the 600 °C and 800 ℃ HLW-NG-Fe2-S samples displayed in Figure 3.6.10. The exact states of each of the forms of iron in the samples is not precisely determined by this deconvolution of pre-edge peaks.

7.3.2 Comparison with Mössbauer

Pre-edge positions and intensities are effected by both the crystalline and amorphous phases in the sample, so the average centroid position and integrated intensity values are an average of the entire material. The ^{57}Fe Mössbauer spectroscopy, Chapter 6, section 6.4, gives a more accurate representation of the oxidation states and coordination of the individual iron sites. Table 7.3.1 compares the oxidation states as determined by XANES and ^{57}Fe Mössbauer spectroscopy.

The differences are most apparent in the HLW-NG-Fe2-S 1150 ℃, HLW-NG-Fe2-C 1000 ℃, and all of the HLW-NG-Fe2-F and -H samples. By XRD these samples all have a considerable amount of spinel and/or haematite present. Taking the HLW-NG-

Fe2-C 1000 ℃ sample as an example, there is twice the amount of spinel phase present than any of the other feeds.

Table 7.3.1. Table of comparison of the ^{57}Fe Mössbauer and Fe K-edge XANES redox state predictions.

Sample	**Fe Oxidation State (Fe^{3+}/Fe_T)**		**Difference**
	^{57}Fe Mossbauer	Fe K-edge XANES	
HLW-NG-Fe2 600 ℃	1.00	1.00	0.00
HLW-NG-Fe2 800 ℃	1.00	0.98	0.02
HLW-NG-Fe2 1000 ℃	1.00	0.96	0.04
HLW-NG-Fe2 1150 ℃	1.00	0.90	0.10
HLW-NG-Fe2-S 600 ℃	1.00	1.00	0.00
HLW-NG-Fe2-S 800 ℃	1.00	0.96	0.04
HLW-NG-Fe2-S 1000 ℃	0.94	0.90	0.04
HLW-NG-Fe2-S 1150 ℃	1.00	0.63	0.37
HLW-NG-Fe2-G 600 ℃	1.00	0.99	0.01
HLW-NG-Fe2-G 800 ℃	0.87	0.91	-0.04
HLW-NG-Fe2-G 1000 ℃	0.42	0.48	-0.06
HLW-NG-Fe2-G 1150 ℃	0.47	0.64	-0.17
HLW-NG-Fe2-C 600 ℃	1.00	1.00	0.00
HLW-NG-Fe2-C 800 ℃	0.93	0.85	0.08
HLW-NG-Fe2-C 1000 ℃	0.77	0.27	0.50
HLW-NG-Fe2-C 1150 ℃	0.65	0.63	0.02
HLW-NG-Fe2-F 600 ℃	1.00	0.60	0.40
HLW-NG-Fe2-F 800 ℃	1.00	0.54	0.46
HLW-NG-Fe2-F 1000 ℃	1.00	0.32	0.68
HLW-NG-Fe2-F 1150 ℃	1.00	0.17	0.83
HLW-NG-Fe2-H 600 ℃	1.00	0.30	0.70
HLW-NG-Fe2-H 800 ℃	0.61	0.01	0.60
HLW-NG-Fe2-H 1000 ℃	0.69	-0.01	0.70
HLW-NG-Fe2-H 1150 ℃	0.83	0.07	0.76

7.4 Mn K-edge X-ray Absorption Near-Edge Spectroscopy

For processing of Mn K-edge spectra, multiple scans (up to 20) for each sample were corrected for outliers, merged and normalised in Athena ® processing software. The merged and normalised spectra were calibrated by calibrating the absorption edge position of the measured standards, Mn-foil, MnO, Mn_2O_3 and MnO_2 to literature values (McKeown et al. 2003; Belli et al. 1980) and applying any shift in eV to the rest of the collected data. Each calibrated spectrum is shown for each of the feeds at each temperature in Figure 7.4.1.

7.4.1 Linear fits of data

Qualitatively the absorption edge in Mn spectra shifts linearly with oxidation state; this method has been used to obtain a quantitative estimate of Mn oxidation state in previous studies (Abuín et al. 2013; McKeown et al. 2003; Scheinost et al. 2001; Guillen et al. 2020). The first inflection point of each of the Mn K-edge spectra was plotted against a linear fit of the first inflection point of each of the standards and their known oxidation states (Figueroa et al. 2005; Guillen et al. 2020). The fit was used to approximate an average Mn oxidation state. Error bars are the uncertainty in the eV value due to the step size used since minimal processing was required to generate the datapoints.

All of the feeds were batched with MnO_2 (Mn^{4+}). The feeds quenched at 600 ℃ all contain approximately Mn^{4+}, with only HLW-NG-Fe2-H showing a percentage of lower oxidation state. All but HLW-NG-Fe2-H samples at 600 ℃ lie some distance above the edge position for the Mn^{4+} standard. The Mn^{5+} oxidation state is unstable in aqueous solutions, particularly at elevated temperatures (X. Zhang et al. 2017; Iyel, Oktem, and Akmaz 2014), and oxidation to Mn^{6+} and Mn^{7+} is also unlikely at this temperature, with the added carbon to the feeds.

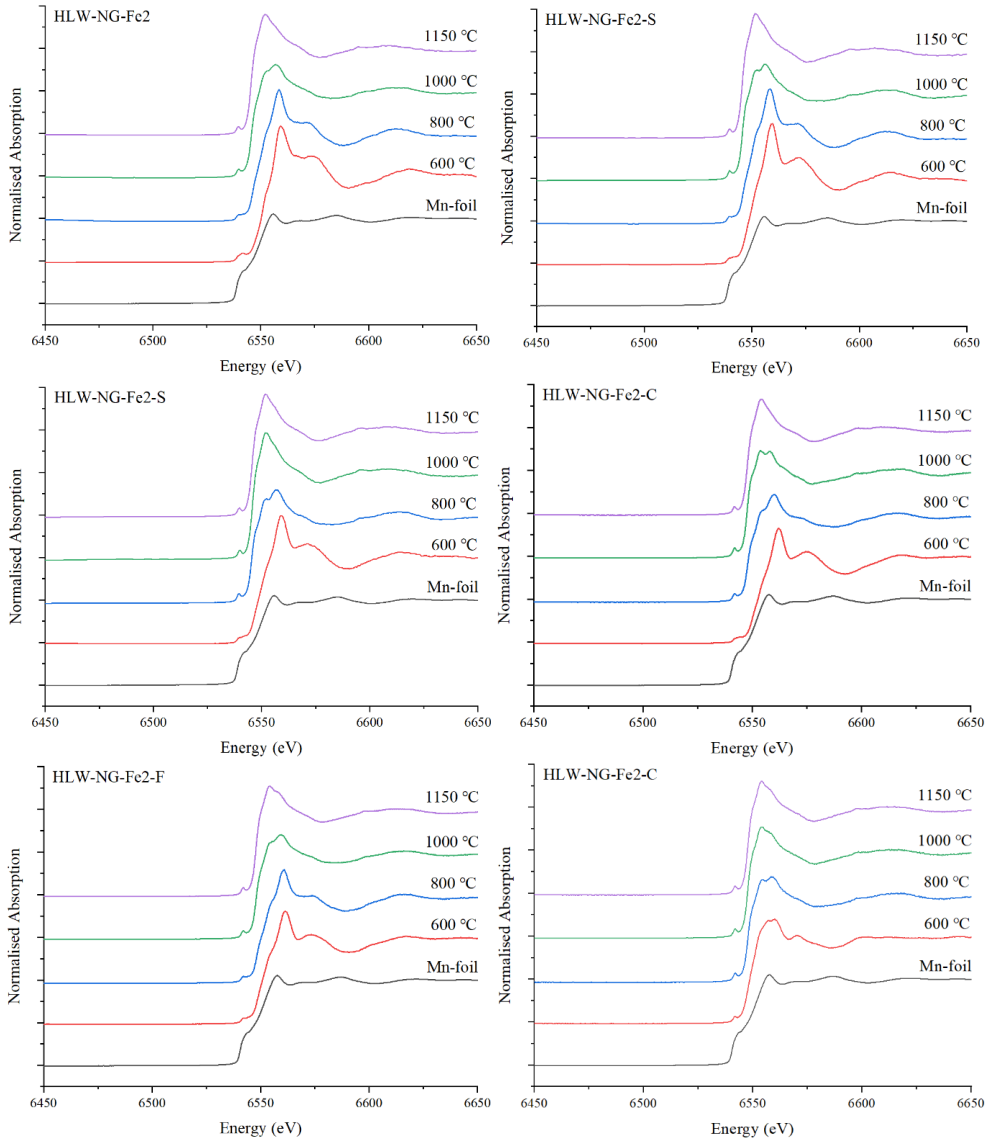

Figure 7.4.1. Mn K-edge XANES Spectra for HLW-NG-Fe2 and HLW-NG-Fe2-R samples quenched at 600, 800, 1000 and 1150 °C.

Increased heat-treatment temperature had the effect of reducing MnO_2, to MnO in the final glass. For HLW-NG-Fe2-G, -C and -H the main reduction occurred between 800 and 1000 °C. Whereas the HLW-NG-Fe2, HLW-NG-Fe2-S and -F feeds reduced most significantly between 1000 and 1150 °C. All of the final glasses are below the Mn^{2+} standard in edge position, which would indicate that they contain a proportion of metallic-Mn. However, they are a similar distance to those above Mn^{4+} at 600 °C, and there is no indication of metallic precipitation by XRD, Chapter 6, section 6.2. It is

therefore more likely that the errors are greater in the oxidation states than the error bars shown, and in fact there is solely MnO in the glass product.

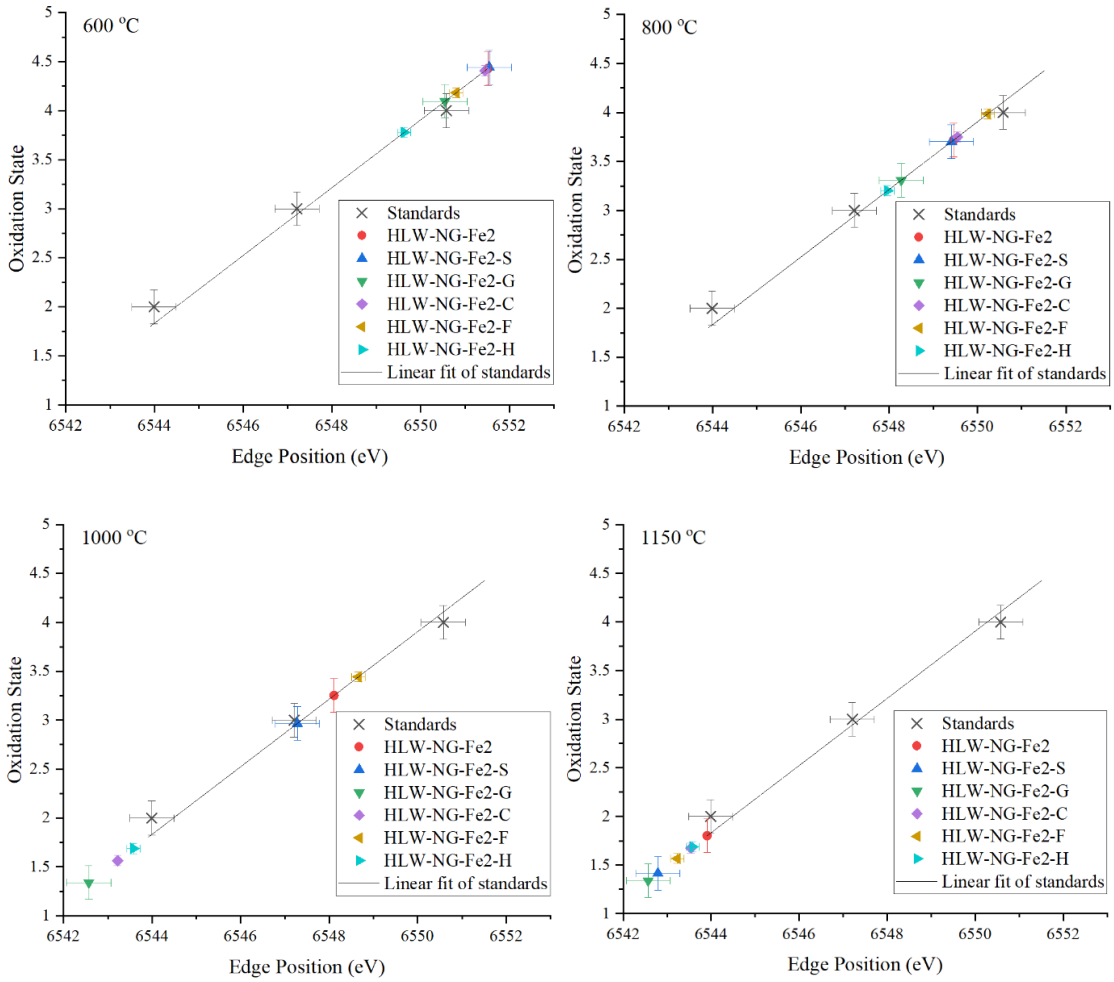

Figure 7.4.2. Mn K-edge positions plotted as a linear function of the reference standards and associated oxidation states for each of the HLW-NG-Fe2 and HLW-NG-Fe2-R samples at 600, 800, 1000 and 1150 °C. Mn reduces from Mn^{4+} to Mn^{2+} with temperature, reduction is at higher temperature in the HLW-NG-Fe2, -S and -F feeds.

7.5 Cr K-edge X-ray Absorption Near-Edge Spectroscopy

Multiple scans of the Cr K-edge (up to 20) for each sample were collected, corrected for outliers, merged and normalised in Athena ® processing software. The spectra were processed as described in Chapter 3, section 3.6.3.5. Each calibrated spectrum is shown for the feeds at each temperature in Figure 7.5.1, along with the measured standards.

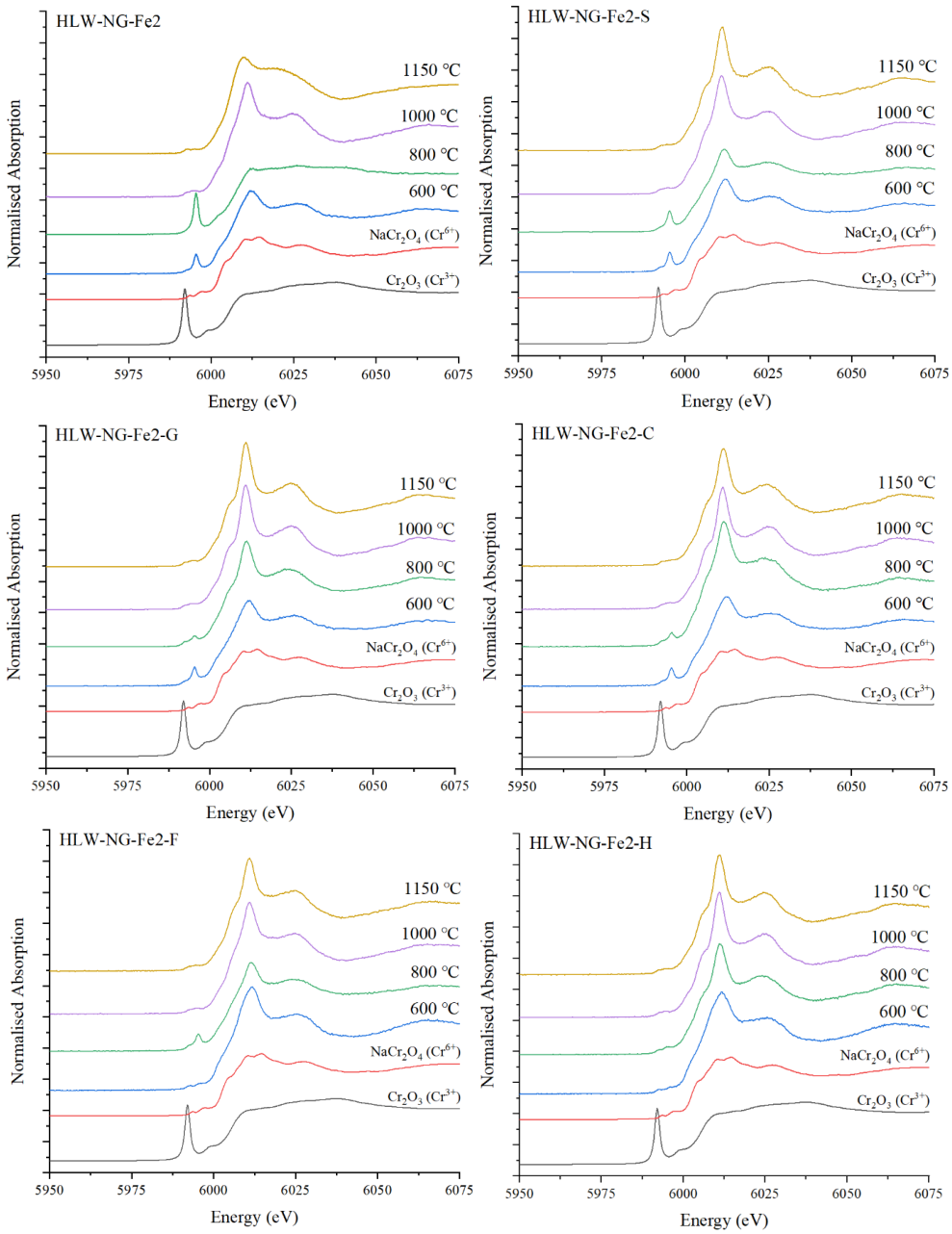

Figure 7.5.1. Cr K-edge XANES Spectra for the HLW-NG-Fe2 and HLW-NG-Fe2-R samples quenched at 600, 800, 1000 and 1150 °C, with the reference standards for Cr^{3+} (Cr_2O_3) and Cr^{6+} ($NaCr_2O_4$). The sharp pre-edge feature reduces with melt temperature.

7.5.1 Linear Combination Fitting results

Results of the proportion of each redox state in the sample, determined by the LCF of Cr^{3+} and Cr^{6+} standards, are shown in Figure 7.5.2. Connecting lines between the sample quench temperatures are a guide for the eye, there is no collected data for the intermediate temperatures. Error bars were generated using the residual of the LCF combined with the uncertainty in eV due to the step size.

As shown in the example LCF fit in Figure 7.5.2 beyond the absorption edge, the LCF was not a suitable method to apply to the data. However, by focussing on the XANES region, particularly the pre-edge peak characteristic of $1s \rightarrow 3d$ transitions in Cr^{6+} and weak in Cr^{3+} (Berry and O'Neill 2004). The fitting function was able to determine the relative amounts of Cr^{3+} and Cr^{6+} in each sample, based on the relative height of this peak to the absorption edge (Villain et al. 2007). All fits had a reduced χ^2 values < 0.02, showing the suitability of the LCF for this purpose.

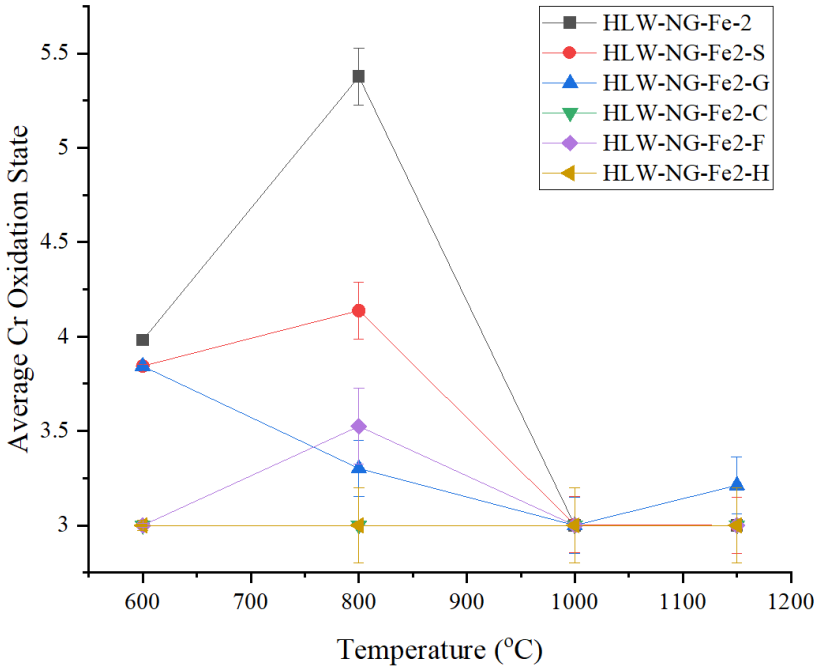

Figure 7.5.2. Cr K-edge positions plotted as a linear function of the standards and associated oxidation states for the samples at 600 - 1150 °C. Oxidation of Cr^{3+} to Cr^{6+} is observed between 600 and 800 °C in the HLW-NG-Fe2, -S and -F samples, followed by reduction. Reoxidation may have occurred in the HLW-NG-Fe2-G sample at 1150 °C.

A proportion of the batched Cr^{3+} in the HLW-NG-Fe2 feed oxidises to Cr^{6+} by 600 ℃, then further at 800 and 1000 ℃ up to a maximum of ~60 % Cr^{6+}. At 1150 ℃ the chromium is reduced back down to entirely Cr^{3+}. A less prominent occurrence of this oxidation at 800 ℃ can be observed in the HLW-NG-Fe2-S and -F feeds. For HLW-NG-Fe2-G, the peak oxidation is at 600 ℃, within the range of temperature measured, followed by reduction to 100 % Cr^{3+} at 1000 ℃. Reoxidation at 1150 ℃ occurs only in the HLW-NG-Fe2-G feed. HLW-NG-Fe2-C and -H remain Cr^{3+} throughout the temperatures measured.

7.6 Ce L_{III}-edge X-ray Absorption Near-Edge Spectroscopy

Multiple scans of the Ce L_{III}-edge (up to 20) for each sample were collected, and processed as described in Chapter 3, section 3.6.3.5. Each calibrated spectrum is shown for the feeds at each temperature in Figure 7.6.1, along with the measured standards.

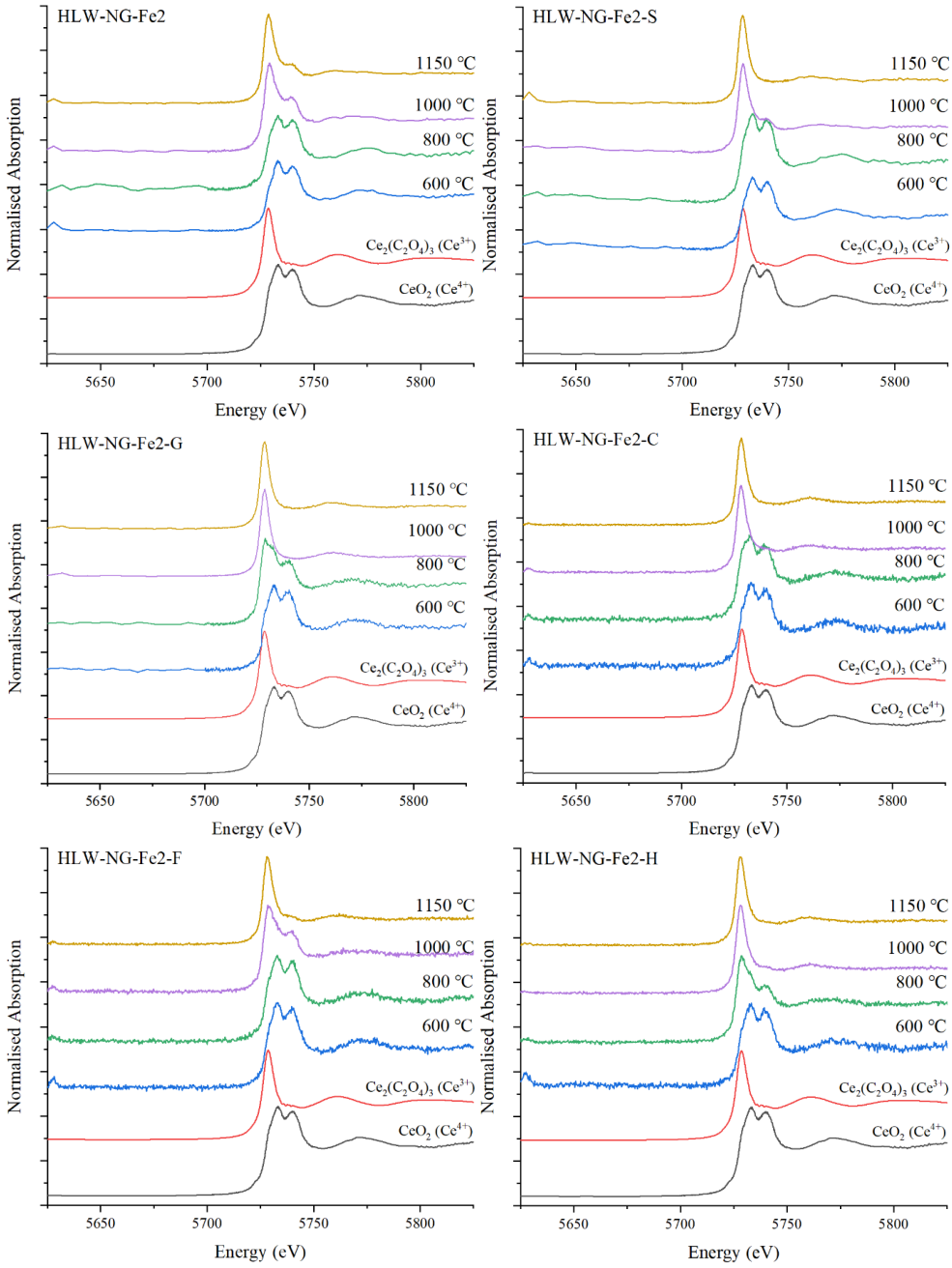

Figure 7.6.1. Ce L_{III}-edge XANES Spectra for the HLW-NG-Fe2 and HLW-NG-Fe2-R samples quenched at 600 - 1150 °C, with the reference standards for Ce^{3+} ($Ce_2(C_2O_4)_3$) and Ce^{4+} (CeO_2). The two absorption edge features converge with temperature.

7.6.1 Linear Combination Fits

Results of the proportion of each redox state in the sample, determined by the LCF of Ce^{3+} and Ce^{4+} standards, are shown in Figure 7.6.2. Connecting lines are a guide for the eye, no data was collected for the intermediate temperatures. Error bars were generated using the residual of the LCF and the uncertainty in eV due to the step size. The fits give the proportion of Ce^{4+} and Ce^{3+} in the samples by the shape of the absorption edge features (Pereira 2021; Dantelle et al. 2020; Norman et al. 2001). The single absorption peak in the Ce^{3+} arises from the $5d \rightarrow 4f$ emission (Ranasinghe et al. 2019). Two higher energy peaks representative of the $2p \rightarrow 5d$ transitions are characteristic of Ce^{4+}, with the *4f* shell unoccupied (Benedetti et al. 2018).

Cerium is reduced from Ce^{4+} to Ce^{3+} with temperature amongst all of the feeds. A proportion of the HLW-NG-Fe2-H, -G, and -C reduces by 800 ℃, where the others begin to reduce by 1000 ℃. The HLW-NG-Fe2-S feed reduces entirely from Ce^{4+} to Ce^{3+} between 800 and 1000 ℃. HLW-NG-Fe2-F follows the same trend as the HLW-NG-Fe2 feed between 600 and 1000 ℃, but where HLW-NG-Fe-F is entirely reduced by 1150 ℃, there is 23 % Ce^{4+} remaining in the HLW-NG-Fe2 feed.

The redox potential of the $Ce^{4+} + e \rightarrow Ce^{3+}$ reaction is 1.72, greater than that of the other expected reactions of the multivalent species studied in this feed (Vanysek 2000; Schreiber and Todd Coolbaugh 1995). The earlier reduction of Ce, compared with Cr, Fe and Mn, is expected by the electromotive force series, section 7.2. Significant quantities of trivalent Ce^{3+} are often found in glasses made with CeO_2 due to its high reducibility (Ranasinghe et al. 2019; Schreiber et al. 1994; Lopez et al. 2003), studies have shown that both increasing the melting temperature can increase the proportion of Ce^{3+} present in some glasses (Ranasinghe et al. 2019; Lopez et al. 2003; Wondergem-de Best 1994), as well as the choice of raw materials (Ranasinghe et al. 2019).

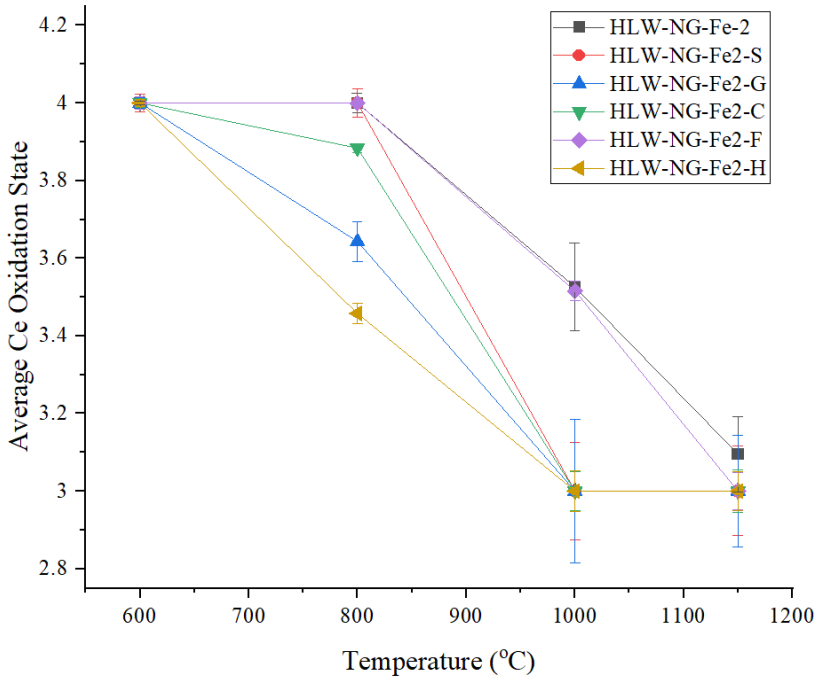

Figure 7.6.2. Ce L_{III}-edge positions plotted as a linear function of the standards and associated oxidation states for each of the samples at 600, 800, 1000 and 1150 ℃. Reduction to Ce^{3+} occurs by 1000 ℃ for the HLW-NG-Fe2-S, -G, -C, and -H samples. In the HLW-NG-Fe2 sample complete reduction to Ce^{3+} is not reached at 1150 ℃.

7.7 Ni K-edge X-ray Absorption Near-Edge Spectroscopy

Normalised and merged spectra for the Ni K-edge XANES collected of all HLW-NG-Fe2 and HLW-NG-Fe2-R samples are shown in Figure 7.7.1, The HLW-NG-Fe2-H sample quenched at 600 ℃ is omitted due to extreme noise in the spectra. The signal to noise ratio in all of the samples collected was low, making the pre-edge feature, *1s* → *3d* transition (Anspoks and Kuzmin 2011), undiscernible. There are no distinguishing shifts in the main absorption peak or pre-edge features (N. Zhang et al. 2015; Anspoks and Kuzmin 2011).

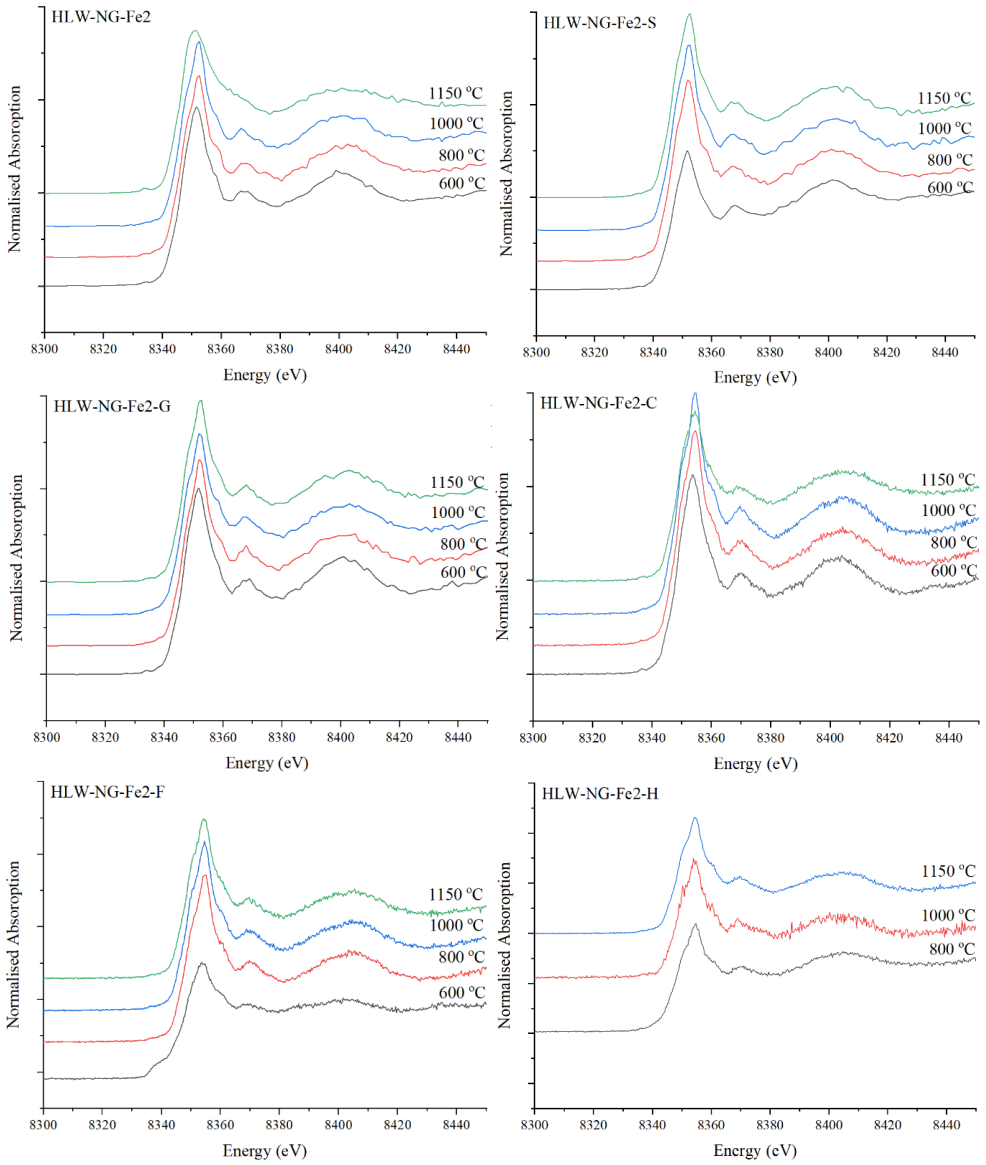

Figure 7.7.1. Ni K-edge XANES Spectra for HLW-NG-Fe2 feed samples heated to 600, 800, 1000 and 1150 ℃ and the NiO reference material.

7.8 Partial Pressure of Oxygen

Patrial pressure of oxygen can be inferred by the redox state of the melt, often using only the redox state of Fe (H. L. Zhang et al. 2018). Using Schreiber's relationship, in section 7.2, and comparisons with literature (Schreiber, Wilk, and Schreiber 1999; Schreiber and Balazs 1985; Schreiber et al. 1986), estimations of the partial pressure in the final glass melts are in Table 7.8.1. The values are based predominantly on the Fe redox state, as it has the most control over oxygen partial pressure (Guillen et al. 2020). A summary of the percentage conversion of each species at each temperature in each feed is given in Appendix B, Table 2.

Table 7.8.1. Estimated -log(f_{O2}) at 1150 °C by Fe^{3+}/Fe_T by ^{57}Fe Mössbauer spectroscopy, Cr K-edge, Ce L_{III}-edge and Mn K-edge XANES spectroscopy (Schreiber and Hockman 1987; Schreiber et al. 1986).

Glass	**% Reduced Fe (^{57}Fe Mössbauer)**	**% Reduced Cr (XANES)**	**% Reduced Ce (XANES)**	**% Reduced Mn (XANES)**	**Estimated -log(f_{O_2})**
HLW-NG-Fe2	0 ± 7	100.0 ± 0.3	90.5 ± 3.2	100 ± 12	2
HLW-NG-Fe2-S	0 ± 0.1	100.0 ± 0.1	100.0 ± 3.8	100 ± 16	2
HLW-NG-Fe2-G	53 ± 0.2	92.9 ± 1.1	100.0 ± 4.8	100 ± 16	8
HLW-NG-Fe2-C	35 ± 7	100.0 ± 0.3	100.0 ± 1.8	100 ± 17	7
HLW-NG-Fe2-F	0 ± 7	100.0 ± 0.2	100.0 ± 1.6	100 ± 14	2
HLW-NG-Fe2-H	17 ± 9	100.0 ± 0.8	100.0 ± 1.7	100 ± 13	5-6

7.9 Revised O_2 Balance

O_2 contributions by the proportion of reduced Fe, Mn, Cr and Ce species at each temperature are given in Table 7.9.1. Net O_2 contributions by redox reactions were determined by calculation of the total reduced percentage of each reaction between the batched raw material and the sample quenched at 1150 °C. Values from ^{57}Fe Mössbauer spectroscopy were used for Fe, and from XANES for Mn, Cr and Ce. The reduced proportions of each species and the theoretical O_2 liberated by each reaction are shown in Figure 7.9.1 and used to calculate the total balance of O_2 in Table 7.9.2.

Table 7.9.1. O_2 evolution from redox reactions observed by XANES and ^{57}Fe Mössbauer spectroscopy.

Oxide	Reaction	O_2 mass in compound	Feed	% Reacted	O_2 liberated
		g kg^{-1} glass			g kg^{-1} glass
Fe_2O_3	Fe^{3+}/Fe^{2+}	48.47	HLW-NG-Fe2	0	0
			HLW-NG-Fe2-S	0	0
			HLW-NG-Fe2-G	52.6 ± 1.4	8.5 ± 0.02
			HLW-NG-Fe2-C	34.5 ± 4.2	5.6 ± 0.7
			HLW-NG-Fe2-F	0	0
			HLW-NG-Fe2-H	16.7 ± 5.7	2.7 ± 0.9
MnO_2	Mn^{4+}/Mn^{2+}	14.56	HLW-NG-Fe2	100 ± 17	8.0 ± 1.2
			HLW-NG-Fe2-S	100 ± 22	9.4 ± 1.6
			HLW-NG-Fe2-G	100 ± 23	9.7 ± 1.7
			HLW-NG-Fe2-C	100 ± 18	8.5 ± 1.4
			HLW-NG-Fe2-F	100 ± 20	8.9 ± 1.5
			HLW-NG-Fe2-H	100 ± 19	8.4 ± 1.4
CeO_2	Ce^{4+}/Ce^{3+}	0.22	HLW-NG-Fe2	90.5 ± 2.9	0.050 ± 0.002
			HLW-NG-Fe2-S	100 ± 3.8	0.055 ± 0.002
			HLW-NG-Fe2-G	100 ± 4.8	0.055 ± 0.002
			HLW-NG-Fe2-C	100 ± 1.8	0.055 ± 0.001
			HLW-NG-Fe2-F	100 ± 1.6	0.055 ± 0.001
			HLW-NG-Fe2-H	100 ± 1.7	0.055 ± 0.001
Cr_2O_3	Cr^{3+}/Cr^{6+}	0.80	HLW-NG-Fe2	0	0
			HLW-NG-Fe2-S	0	0
			HLW-NG-Fe2-G	7.1 ± 4.2	-0.001± 0.0002
			HLW-NG-Fe2-C	0	0
			HLW-NG-Fe2-F	0	0
			HLW-NG-Fe2-H	0	0

As hypothesised, in section 7.2 net contributions from reduction of Mn^{4+}/Mn^{2+} outweigh the contribution from Fe^{3+}/Fe^{2+} in the HLW-NG-Fe2, -S, -C, -F and -H feeds, Figure 7.9.1, and are within the uncertainties of the Fe contribution in the -G feed. The

O_2 evolved from Ce^{4+}/Ce^{3+} is negligible due to the small amount of CeO_2 in the sample, and there is no net positive O_2 evolution by Cr redox in any of the feeds. The total O_2 balance, from section 5.5.3, is revised in Table 7.9.2 to include the expected O_2 from redox reactions determined in this chapter.

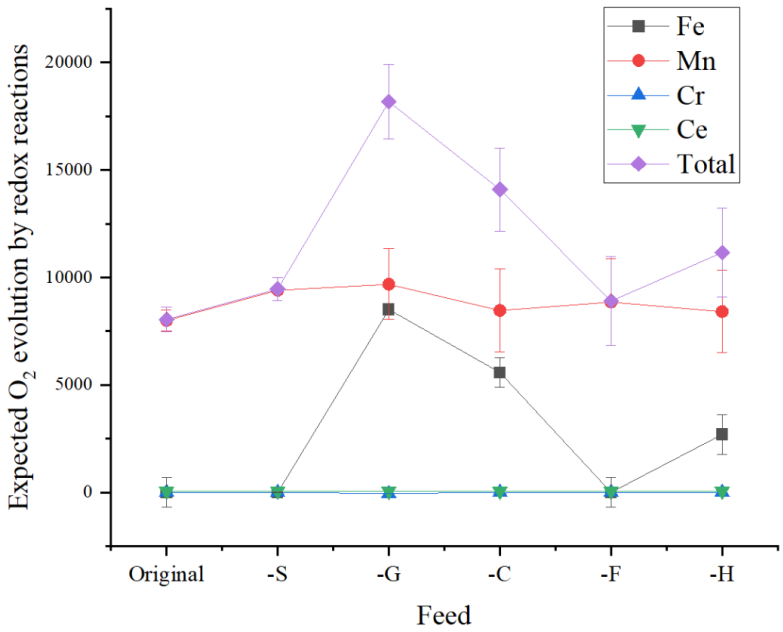

Figure 7.9.1. Summary of the net contributions to O_2 evolutions by all of the multivalent species for the HLW-NG-Fe2, HLW-NG-Fe2-II and HLW-NG-Fe2-R samples, showing the Mn redox change contributes most to O_2 evolution for all but the HLW-NG-Fe2-G feed, for which it is equivalent to Fe within error.

Table 7.9.2. O_2 balance measured by EGA, with O_2 evolution from batched feed raw materials and redox reactions of Fe, Mn, Cr and Ce by XANES and ^{57}Fe Mössbauer.

Feed	**Expected O_2 evolution from all batch gasses** mg kg^{-1} glass	**O_2 from redox reactions *** mg kg^{-1} glass	**Total expected O_2 evolution** mg kg^{-1} glass	**O_2 evolved by EGA** mg kg^{-1} glass
HLW-NG-Fe2	800	8000 ± 900	8800 ± 900	6600
HLW-NG-Fe2-S	-12900	9500 ± 400	-3400 ± 400	0
HLW-NG-Fe2-G	-91800	18200 ± 500	-73700 ± 500	0
HLW-NG-Fe2-C	-80000	14100 ± 700	-65900 ± 700	0
HLW-NG-Fe2-F	-11300	8900 ± 700	-2400 ± 700	0
HLW-NG-Fe2-H	-256500	11200 ± 900	-245400 ± 900	0

** with ^{57}Fe Mössbauer spectroscopy used for Fe, and XANES for Mn, Cr and Ce.

7.10 Summary

7.10.1 Redox behaviour of iron

The iron redox state estimated by Fe K-edge XANES for each of the reductant-added samples, Chapter 7, section 7.3, does not correlate with the foam volume or carbon content per gramme of substance, in Chapter 5, section 5.3. The ^{57}Fe Mössbauer correlates more closely with the expected reduction, as shown in Figure 7.10.1.

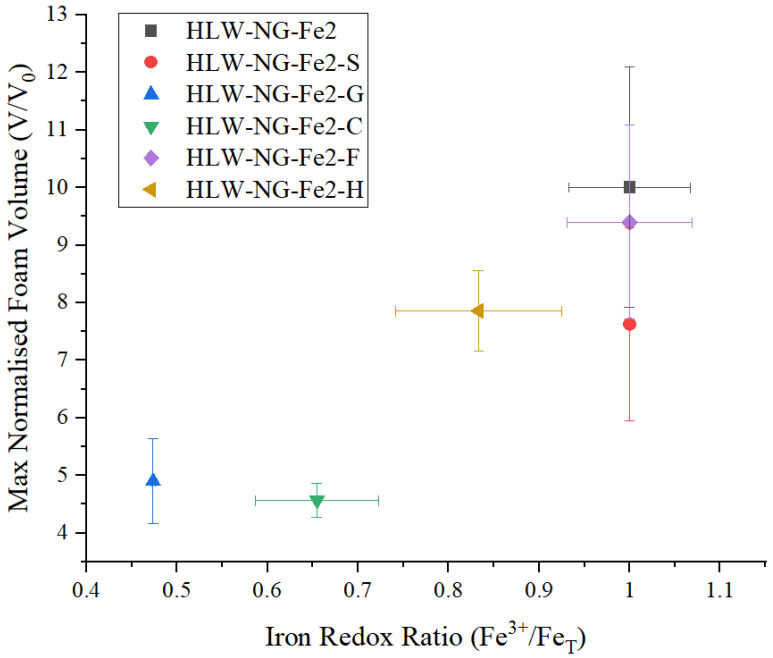

Figure 7.10.1. Maximum normalised foam volume with Fe^{3+}/Fe_T by ^{57}Fe Mössbauer spectroscopy of the final glasses for the HLW-NG-Fe2 and HLW-NG-Fe2-R feeds showing that the samples containing reduced Fe correlated to reduced foam volume

As was observed in most previous studies of iron in borosilicate glasses (Farges et al. 2005; Ahmadzadeh, Scrimshire, Bingham, Goel, et al. 2018; Cochain et al. 2012), ^{57}Fe Mössbauer spectroscopy suggests that the iron either exists as $^{IV}Fe^{3+}$ or $^{VI}Fe^{2+}$, Chapter 6, section 6.4. Where other coordination numbers appear to exist in the Fe K-edge XANES spectroscopy results, section 7.3.1, it is likely that there is a mixture of those two iron sites/oxidation states present, along with the crystalline iron, contributing to distortion of the pre-edge feature.

By Fe K-edge XANES, Figure 7.3.2, there was a significant reduction of Fe observed for both the HLW-NG-Fe2-S and -F feeds at 1000 and 1150 ℃, which was inconsistent with the ^{57}Fe Mössbauer spectroscopy, section 6.4.1. Studies of sucrose additions to waste feeds have shown high levels of Fe^{2+} in the final glass (Hujová, Pokorný, et al. 2018; Appel et al. 2019; Muller et al. 2009; Blair and Lukacs 1980), and a number of studies using formic acid also show ferrous iron contents up to $Fe^{3+}/Fe_T = 0$ (Bickford and Diemer Jr 1986) and 0.4 (Weimers 1996). However, ^{57}Fe Mössbauer spectroscopy, section 6.4.1 suggests that there is an overestimation of the reduction in the HLW-NG-Fe2-F feed in particular: there is no evidence of Fe^{2+} present at any of the temperatures in the paramagnetic phase, and only at 1000 ℃ in the HLW-NG-Fe2-S feed.

Studies of waste feeds that have contained HEDTA, have focussed on the addition of sucrose, and no literature specifically reports its effects on iron redox (Matlack, Gong, and Pegg 2003; Kruger, Matlack, Gong, et al. 2012; Matlack et al. 2006). The reduction of Fe in the HEDTA feed occurs most significantly between 600 and 800 ℃ by ^{57}Fe Mössbauer spectroscopy. The lower temperature redox change correlates with the earlier decomposition by TGA, Chapter 5, section 5.4.1, Figure 5.4.1 and is consistent with the reduced oxygen availability leading to a large evolution of CO Chapter 5, section Figure 5.5.1 and Figure 5.5.2.

The HLW-NG-Fe2-G and -C feeds show similar reduction of Fe by ^{57}Fe Mössbauer spectroscopy, in section 6.4.2. At 600 ℃, the HLW-NG-Fe2-G sample contains iron as tetrahedral Fe^{3+}. At 800 ℃ 23 % of the iron is present as $^{VI}Fe^{2+}$, continuing to increase to 58% at 1000 ℃, before reducing slightly to $Fe^{3+}/Fe_T = 0.47$. At 600 ℃ the HLW-NG-Fe2-C feed also contains $^{IV}Fe^{3+}$, but the reduction is gradual from $Fe^{3+}/Fe_T = 1 \rightarrow 0.65$ with increasing temperature up to $Fe^{3+}/Fe_T = 0.65$ at 1150 ℃. The HLW-NG-Fe2-G feed shows some decomposition by TGA, Chapter 5, Figure 5.4.1, between 1000 and 1150 ℃, where the coke shows very little decomposition in the high-temperature

region. This may be the cause of the consistent reduction in the HLW-NG-Fe2-C feed, rather than the re-oxidation observed in HLW-NG-Fe2-G.

7.10.2 Redox behaviour of multivalent species

A summary of the percentage of each species reduced at each temperature for each of the samples is shown in Figure 7.10.2. In all of the feeds, the oxidation of Cr^{3+} to Cr^{6+} and subsequent reduction to Cr^{3+} precedes the reduction of the other species in the melt, as predicted by Schreiber's work, discussed in section 7.2 (Schreiber and Balazs 1985; Mirhadi and Mehdikhani 2011b; Thiemsorn et al. 2008b; Schreiber et al. 1984; Brückner 1985; Pinet et al. 2008). The only deviation from this behaviour is observed in the HLW-NG-Fe2-G feed, where there is a re-oxidation of some Cr^{6+} at 1150 °C. This behaviour is not adequately described by the models of redox behaviour in reducing conditions and at elevated temperatures.

Reduction of $Mn^{4+} \rightarrow Mn^{2+}$ follows, before any reduction of Ce^{4+}, at 800 °C, in the HLW-NG-Fe2, HLW-NG-Fe2-S and -H feeds. This is contradictory to the order predicted by the electromotive force series (Schreiber and Todd Coolbaugh 1995; Schreiber and Balazs 1985). For all feeds, the proportion of reduced of Mn and Ce follows a very similar path with increasing temperature, particularly in the HLW-NG-Fe2-G and -C feeds. In the HLW-NG-Fe2 feed, the reduction to Ce^{2+} is incomplete by 1150 °C, where Mn^{4+} has fully reduced to Mn^{2+}.

The Linear Combination Fitting (LCF) method of fitting the XANES spectra, applied to the Cr K-edge and Ce L_{III}-edge, provided significantly more accurate results than the linear fits of the Mn K-edge and the ^{57}Fe Mössbauer data from Chapter 6, section 6.4. The final oxidation state of Fe in the HLW-NG-Fe2 feed as determined by Fe K-edge XANES is Fe^{3+}/Fe_T = 0.9, and by ^{57}Fe Mossbauer spectroscopy Fe^{3+}/Fe_T = 1. Some reduction of Fe as a function of heat treatment temperature was reported in the previous Fe K-edge XANES study (Guillen et al. 2020). The Fe^{3+} to Fe^{2+} reduction is the least

complete reaction in all of the feeds with increasing temperature, reaching a maximum Fe^{2+} content of 42 ± 7 % in the HLW-NG-Fe2-G sample at 1000 ℃.

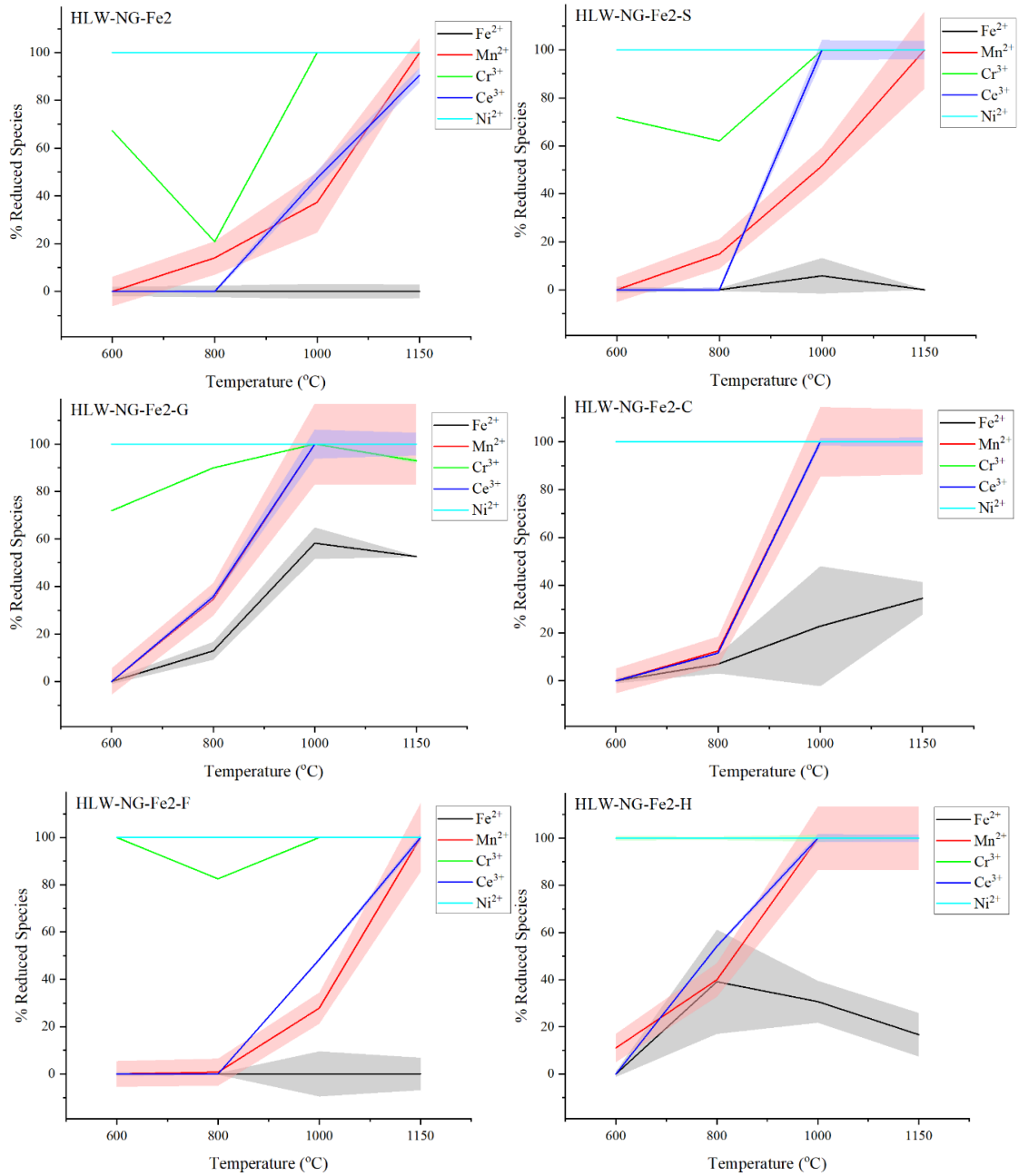

Figure 7.10.2. Summary of the percentage of Fe, Cr, Mn, Ni and Ce in the reduced state, Fe^{2+}, Cr^{3+}, Mn^{2+}, Ce^{3+} and Ni^{2+} for the HLW-NG-Fe2 and HLW-NG-Fe2-R feeds at 600, 800, 1000 and 1150 ℃. Errors are shown in the filled area around each line. Where the error area is not visible, the errors are within the lines shown. The reduction of the Cr precedes, Mn and Ce. Fe is the least reduced in all of the samples.

In the present study, the manganese is approximately Mn^{4+} at 600 ℃ in the HLW-NG-Fe2 feed, consistent with the previous results for which the Mn^{4+} oxidation state was observed at 500 ℃ (Guillen et al. 2020). However, the same study of the feed quenched at 850 ℃ showed reduction to almost entirely Mn^{2+}, where the main reduction of Mn occurs between 1000 and 1150 ℃ in Figure 7.10.2. Collection of the Cr K-edge in the XANES study of the HLW-NG-Fe2 feed was not reported along with Mn and Fe K-edges as there was too much noise in the data (Guillen et al. 2020). However, that study did observe a similar trend in the HLW-E-M09 simulated waste feed as shown by the data in section 7.5.1, mostly Cr^{3+} was observed at 500 ℃, and then a large increase occurred at 700 ℃ to over 80 % Cr^{6+}, then at higher temperatures, the Cr reduced again down to over 90 % Cr^{3+} in the final glass (Guillen et al. 2020).

7.11 References

Abuín, M., Serrano, A., Chaboy, J., García, M. A. and Carmona, N. (2013) 'XAS study of Mn, Fe and Cu as indicators of historical glass decay', Journal of Analytical Atomic Spectrometry, 28(7), pp. 1118–1124.

Ahmadzadeh, M., Scrimshire, A., Bingham, P. A. and Goel, A. (2018) 'Structural Role of Iron in Nepheline-based Aluminosilicates for Nuclear Waste Applications.' WM2018 Conference. Phoenix, AZ (United States).

Anspoks, A. and Kuzmin, A. (2011) 'Interpretation of the Ni K-edge EXAFS in nanocrystalline nickel oxide using molecular dynamics simulations', Journal of Non-Crystalline Solids, 357(14), pp. 2604–2610.

Appel, C. J., Kloužek, J., Jani, N. Lee, S., Dixon, D. R., Hrma, P., Pokorný R., Kruger A. A. and Schweiger, M. J. (2019) 'Effect of sucrose on foaming and melting behavior of a low-activity waste melter feed.' Journal of the American Ceramic Society, 102(12), pp. 7594–7605.

Belli, M., Scafati, A., Bianconi, A., Mobilio, S., Palladino, L., Reale, A. and Burattini, E. (1980) 'X-ray absorption near edge structures (XANES) in simple and complex Mn compounds.' Solid State Communications, 35(4). pp. 355–361.

Benedetti, F. Amidani, L., Pelli Cresi, J. S., Boscherini, F., Valeri, S., D'Addato, S., Nicolini, V., Malavasi, G. and Luches, P. (2018) 'Role of cerium oxide in bioactive glasses during catalytic dissociation of hydrogen peroxide', Physical Chemistry Chemical Physics. Royal Society of Chemistry, 20(36), pp. 23507–23514.

Berry, A. J., O'Neill, H. S. C., Jayasuriya, K. D., Campbell, S. J. and Foran, G. J. (2003) 'XANES calibrations for the oxidation state of iron in a silicate glass.' American Mineralogist, 88(7). pp. 967–977.

Berry, A. J. and O'Neill, H. S. C. (2004) 'A XANES determination of the oxidation state of chromium in silicate glasses', American Mineralogist, 89(5–6), pp. 790–798.

Bickford, D. F. and Diemer Jr, R. B. (1986) 'Redox control of electric melters with complex feed compositions I. Analytical methods and models', Journal of Non-Crystalline Solids, 84, pp. 276–284.

Blair, H. T. and Lukacs, J. M. (1980) 'Investigation of foaming during nuclear defense waste solidification by electric melting PNL-3552. Pacific Northwest National Laboratory, Richland, WA (United States).

Brückner, R. (1985) 'Redox Ratio Shifts and Electrical Transport Properties in Redox Pairs Containing Glasses.' Journal of Non-Crystalline Solids, 71. pp. 49–57.

Cochain, B., Neuville, D. R., Henderson, G. S., McCammon, C. A., Pinet, O. and Richet, P. (2012) 'Effects of the iron content and redox state on the structure of sodium borosilicate glasses: A Raman, Mössbauer and boron K-edge XANES spectroscopy study', Journal of the American Ceramic Society, 95(3), pp. 962–971.

Dantelle, G., Boulon, G., Guyot, Y., Testemale, D., Guzik, M., Kurosawa, S., Kamada, K. and Yoshikawa, A. (2020) 'Research on Efficient Fast Scintillators: Evidence and X-Ray Absorption Near Edge Spectroscopy Characterization of Ce^{4+} in Ce^{3+}, Mg^{2+}-Co-Doped $Gd_3Al_2Ga_3O_{12}$ Garnet Crystal', Physica Status Solidi (B) Basic Research, 257(8), pp. 1–7.

Farges, F., Rossano, S., Lefrère, Y., Wilke, M. and Brown, G. E. (2005) 'Iron in silicate glasses: A systematic analysis of pre-edge, XANES and EXAFS features', Physica Scripta T, T115, pp. 957–959.

Figueroa, S. J. A., Requejo, F. G., Lede, E. J., Lamaita, L., Peluso, M. A. and Sambeth, J. E. (2005) 'XANES study of electronic and structural nature of Mn-sites in

manganese oxides with catalytic properties', Catalysis Today, 107–108, pp. 849–855.

Gan, H., Viragh, C., McKeown, D. A., Muller, I. S., Cecil, R., Kot, Wing K., Joseph, I., Wang, C., Pegg, I. L., Chaudhuri, M., Zhao, W. and Feng, Z. (2009) 'Crystal Settling, Redox, and High Temperature Properties of ORP HLW and LAW Glasses.' VSL-09R1510-1. Vitreous State Laboratory, Washington, D. C. (United States).

Guillen, D. P. Lee, S., Hrma, P., Traverso, J., Pokorny, R., Kloužek, J., and Kruger, A. A., (2020) 'Evolution of chromium, manganese and iron oxidation state during conversion of nuclear waste melter feed to molten glass', Journal of Non-Crystalline Solids. Elsevier, 531(December 2019), p. 119860.

Hujová, M., Pokorný, R., Kloužek, J., Lee, S., Traverso, J. J., Schweiger, M. J., Kruger, A. A. and Hrma, P. (2018) 'Foaming during nuclear waste melter feeds conversion to glass: Application of evolved gas analysis', International Journal of Applied Glass Science, 9(4), pp. 487–498.

Iyel, A., Oktem, D. and Akmaz, F. (2014) 'Parameters Affecting the Color Mechanism of Manganese Containing Colored Glasses', Journal of Chemistry and Chemical Engineering. 8, pp. 849–858.

Kloužek, J. and Rohanová, D. (1999) 'The measurement of oxygen partial pressure and characterisation of oxidation-reduction equilibria in glass melts', Ceramics - Silikaty, 43(3), pp. 94–98.

Kruger, A. A., Matlack, K. S., Gong, W. and Pegg, I. L. (2012) 'Small-Scale Melter Testing with LAW Simulants to Assess the Impact of Higher Temperature Melter Operations.' ORP-51809/VSL-04R4980-1. Office of River Protection, Richland, WA (United States).

Lee, S. M., Hrma, P. R., Kloužek, J., Pokorný, R., Hujová, M., Dixon, D. R., Schweiger, M. J. and Kruger, A. A. (2017) 'Balance of oxygen throughout the conversion of a high-level waste melter feed to glass', Ceramics International, 43(16), pp. 13113–13118.

Lopez, C., Deschanels, X., Bart, J. M. and Levrau, C. (2003) 'Solubility of Plutonium Surrogates in Nuclear Glasses', Scientific Research on the Back-end of the Fuel Cycle for the 21. Century, (Table I), pp. 1–5.

Magnien, V. Neuville, D. R., Cormier, L., Mysen, B. O., Briois, V., Belin, S., Pinet, O. and Richet, P. (2004) 'Kinetics of iron oxidation in silicate melts: A preliminary XANES study', Chemical Geology., 213, pp. 253–263.

Matlack, K. S., Gong, W. and Pegg, I. L. (2003) 'Final Report: Compositional Variation Tests on DuraMelter 100 with LAW Sub-Envelope A3 Feed in Support of the LAW Pilot Melter.' VSL-01R62N0-1, Rev. 2. Vitreous State Laboratory, Washington, D. C. (United States).

Matlack, K. S., Muller, I. S., Gong, W., Pegg, I. L. and Kruger, A. A. (2006) 'Final Report - DuraMelter 100 Tests to Support LAW Glass Formulation Correlation Development.' VSL-06R6480-1. Vitreous State Laboratory, Washington, D. C. (United States).

McKeown, D. A., Muller, I. S., Matlack, K. S. and Pegg, I. L. (2002) 'X-ray absorption studies of vanadium valence and local environment in in borosilicate waste glasses using vanadium sulfide, silicate, and oxide standards', Journal of Non-Crystalline Solids, 298, pp. 160–175.

McKeown, D. A., Kot, W. K., Gan, H. and Pegg, I. L. (2003) 'X-ray absorption studies of manganese valence and local environment in borosilicate waste glasses.' Journal of Non-Crystalline Solids, 328. pp. 71–89.

Mirhadi, B. and Mehdikhani, B. (2011) ‘Effect of manganese oxide on redox iron in sodium silicate glasses’, Journal of Optoelectronics and Advanced Materials, 13(10), pp. 1309–1312.

Muller, I. S., Viragh, C., Gan, H., Matlack, K. S. and Pegg, I. L. (2009) ‘Iron Mössbauer redox and relation to technetium retention during vitrification’, Hyperfine Interactions, 191(1–3), pp. 17–24.

Norman, A., Perrichon, V., Bensaddik, A., Lemaux, S., Bitter, H. and Koningsberger, D. S. (2001) ‘Study of the reducibility of Pt or Pd on ceria–zirconia catalysts by XANES measured at the Ce L_{III} edge and magnetic susceptibility measurements’, Topics in Catalysis, 16/17(1–4).

Pereira, L. D. P. (2021) ‘Mechanisms of oxygen bubble formation in a glass melt in the nuclear waste vitrification context.’ PhD Thesis. Université Paris sciences et lettres, Paris (France).

Pinet, O. Guirat, R., Phalippou, J., Advocat, T. (2008) ‘Development of Models to Predict the Redox State of Nuclear Waste Containment Glass’, in Nuclear fuel cycle for a sustainable future. Atalante, Montpellier (France).

Pinet, O., Hugon, I. and Mure, S. (2014) ‘Redox Control of Nuclear Glass’, Procedia Materials Science. Elsevier B.V., 7, pp. 124–130.

Ranasinghe, K. S., Singh, R., Day, D. E., Attenkofer, K., Stavitski, E., Quinn, L. A., Patterson, D. and Duenas, A. (2019) ‘Evidence of the coexistence of multivalence cerium oxide nano-particles in a sodium borate glass’, Journal of Non-Crystalline Solids, 515(June), pp. 75–81.

Scheinost, A. C., Stanjek, H., Schulze, D. G., Gasser, U. & Sparks, D. L. (2001) ‘Structural environment and oxidation state of Mn in goethic-groutite solid-solutions’, American Mineralogist, 86(1–2), pp. 139–146.

Schreiber, H. D., Balazs, G. B., Carpenter, B. E., Kirkley, J. E., Minnix, L. M., Jamison, P. L. and Mason, T. O. (1984) 'An Electromotive Force Series in a Borosilicate Glass-Forming Melt', Journal of the American Ceramic Society, 67(6), p. C-106-C-108.

Schreiber, H. D., Kozak, S. J., Merkel, R. C., Balazs, G. B. and Jones, P. W. (1986) 'Redox equilibria and kinetics of iron in a borosilicate glass-forming melt.' Journal of Non-Crystalline Solids, 84(1–3). pp. 186–195.

Schreiber, Henry D. (1986) 'Redox processes in glass-forming melts.' Journal of Non-Crystalline Solids, 84(1–3). pp. 129–141.

Schreiber, H. D. Merkel Jr., R. C., Schreiber, V. L. and Balazs, G. B. (1987) 'Mutual Interactions of Redox Couples Via Electron Exchange in Silicate Melts: Models for Geochemical Melt Systems', Journal of Geophysical Research, 92(B9), pp. 9233–9245.

Schreiber, H. D., Kochanowski, B. K., Schreiber, C. W., Morgan, A. B., Coolbaugh, M. T. and Dunlap, T. G. (1994) 'Compositional dependence of redox equilibria in sodium silicate glasses', Journal of Non-Crystalline Solids, 177(C), pp. 340–346.

Schreiber, H. D. and Balazs, G. B. (1985) 'An Electromotive Force Series for Redox Couples in a Borosilicate Melt: The Basis for Electron Exchange Interactions of the Redox Couples', Journal of Non-Crystalline Solids, 71, pp. 59–67.

Schreiber, H. D. and Hockman, A. L. (1987) 'Redox Chemistry in Candidate Glasses for Nuclear Waste Immobilization', Journal of the American Ceramic Society, 70(8), pp. 591–594.

Schreiber, H. D. and Todd Coolbaugh, M. (1995) 'Solvations of redox ions in glass-forming silicate melts', Journal of Non-Crystalline Solids, 181(3), pp. 225–230.

Schreiber, H. D., Wilk, N. R. and Schreiber, C. W. (1999) 'Comprehensive electromotive force series of redox couples in soda-lime-silicate glass', Journal of Non-Crystalline Solids, 253(1–3), pp. 68–75.

Thiemsorn, W., Keowkamnerd, K., Phanichphant, S., Suwannathada, P. and Hessenkemper, H. (2008) 'Influence of glass basicity on redox interactions of iron-manganese-copper ion pairs in soda-lime-silica glass', Glass Physics and Chemistry, 34(1), pp. 19–29.

Vanysek, P. (2002) 'Electrochemical Series.' in 'CRC handbook of chemistry and physics' (ed. Technology), D. R. L. (National I. of S.) 23–33, CRC Press: Boca Raton.

Villain, O., Calas, G., Galoisy, L. and Cormier, L. (2007) 'XANES determination of chromium oxidation states in glasses: comparison with optical absorption spectroscopy', Journal of the American Ceramic Society, 90(11), pp. 1–23.

Weimers, K. D. (1998) 'The Effect of HWVP Feed Nitrate and Carbonate Content on Glass Redox Adjustment.' PNNL-11044. Pacific Northwest National Laboratory, Richland, WA (United States).

Wilke, M., Farges, F., Petit, P. E., Brown, G. E. and Martin, F. (2001) 'Oxidation state and coordination of Fe in minerals: An Fe K-XANES spectroscopic study.' American Mineralogist, 86(5–6). pp. 714–730.

Wilke, M., Partzsch, G. M., Bernhardt, R. and Lattard, D. (2004) 'Determination of the iron oxidation state in basaltic glasses using XANES at the K-edge.' Chemical Geology, 213(1–3), pp. 71–87.

Wondergem-de Best, A. (1994) 'Redox behaviour and fining of molten glass.' Ph. D. Thesis. Eindhoven University of Technology, Eindhoven, The Netherlands.

Zhang, H. L., Cottrell, E., Solheid, P. A., Kelley, K. A. and Hirschmann, M. M. (2018) 'Determination of $Fe^{3+}/\Sigma Fe$ of XANES basaltic glass standards by Mössbauer

spectroscopy and its application to the oxidation state of iron in MORB', Chemical Geology. Elsevier, 479(January), pp. 166–175.

Zhang, N., Brugger, J., Etschmann, B., Ngothai, Y. and Zeng, D. (2015) 'Thermodynamic modeling of poorly complexing metals in concentrated electrolyte solutions: An X-ray absorption and UV-Vis spectroscopic study of Ni(II) in the $NiCl_2$-$MgCl_2$-H_2O system', PLoS ONE, 10(4).

Zhang, X., Li, Y., Hu, Z., Chen, Z. and Qiu, J. (2017) 'A general strategy for controllable synthesis of $Ba_3(MO_4)_2$:Mn^{5+} (M=V, P) nanoparticles', RSC Advances. Royal Society of Chemistry, 7(17), pp. 10564–10569.

8 Alternative Reductants: Final Glass Product

8.1 Overview

In this chapter we explore the implications of the structural differences between the feeds, Chapter 6 and 7, on the properties of the final glasses, in the context of ensuring the glasses are suitable hosts for immobilisation of radioactive wastes. Any changes to the processing flow-sheet, to use this work as an example, the addition of reductants, must be justified by vigorous laboratory-based testing and produce a comparable quality of waste product.

Desired waste glass properties are outlined in Chapter 2, section 2.3.3. General requirements include long-term mechanical, thermal, chemical and radiation stability and the ability to incorporate a range of wasteform elements into the microstructure (Caurant et al. 2009; Gin et al. 2013; Vienna et al. 2013; Ojovan and Lee 2014a; I. W. Donald 1997). The HLW-NG-Fe2 glass was designed with these in mind (Matlack et al. 2012). There addition of reductants causes structural changes in the final glass, the contract limits for Hanford HLW glasses, discussed in section 2.3.3, must be operated within (Matlack et al. 2012; Piepel et al. 2008, 2007).

In this chapter the iron redox state, spinel phase precipitation and leach rates are considered. Viscosity at 1100 ℃ is not measured explicitly, as the available techniques for glass viscosity measurements available rely on their not being crystal precipitation in the glass. However thermal analysis provides indication of the viscosity. Previous measurement of the HLW-NG-Fe2 glass at 1100 ℃ had a viscosity of 3.04 Pa.s (Matlack et al. 2012). There are also limits on the corrosion to melter components. This was measured for the corrosion on Inconel 690 and MA758 for different sulphate contents in the HLW-NG-Fe2 glass, for a 7-day corrosion test at 1150 ℃ (Matlack et al. 2012). The effect of the reductant additions on the corrosion behaviour is outside the

scope of this project. The readily available information on the influence of the Fe redox state on SO_3 retention, by EGA and compositional analysis of the glasses is explored in this chapter. Retention of semi-volatiles in the glass is essential for immobilising radioactive isotopes (Bibler et al. 2000; George, Kim, and Kruger 2020), SO_3 has limited solubility in borosilicate glasses, and can segregate into salt phases in the cold cap and accumulate causing corrosion to melter materials (Jin et al. 2015; Vienna 2010). One method of ensuring sulphate immobilisation is actually by promoting sulphate volatilisation and recirculation (Kruger et al. 2013).

8.2 Glass Characterisation

8.2.1 Compositional Analysis

The compositions of the final glasses were determined by XRF and are compared to the target composition in Table 8.2.1. Nominal values were used for CeO_2, ZnO and La_2O_3 as these were not available in the OXI program used for analysis (Giles, Hurley, and Webster 1995a). Values for Li_2O and B_2O_3, not detectable by XRF, were measured using ICP-MS.

Deviations from the target wt% occurred most prominently for MgO and SO_3. MgO was consistently more than double the target value, for all glasses. SO_3 was only retained in the HLW-NG-Fe2-F and -H glass samples, within the limits of detection of the instrument. 15 – 35 % losses in Na_2O and 15 – 25 % losses in Li_2O could be attributed to volatilisation during melting or XRF sample preparation (Bell et al. 2020), however, interestingly, the B_2O_3 content is up by an average of 7.5 %, which we would also expect to volatilise since it is lighter than Na_2O. Na_2O is also approaching the lowest detection limit of the XRF instrument. Fe_2O_3 is increased by an average of 9 % amongst all the feeds, highest increase is in the HLW-NG-Fe2-S glass and lowest in the HLW-NG-Fe2-H glass. As a percentage increase this is lower than the deviation in most of the other elements, so while it is a significant wt% quantity increase in the glass, it is not as significant relative to the total amount added. All glasses are between 17 and 47 % higher in alumina content than the target composition, suggesting contamination during melting from the alumina crucibles. This affects the HLW-NG-Fe2-F sample the most and HLW-NG-Fe2-H sample the least. The compositions are considerably more internally consistent, than they are with the target composition. The internal consistency is satisfactory for comparison between the samples.

Table 8.2.1. Analysed compositions of HLW-NG-Fe2 and reductant-added glasses by XRF spectroscopy compared with the nominal composition.

Oxide	Nominal Composition (wt%)	Fe2 (wt%)	Fe2-II (wt%)	Fe2-S (wt%)	Fe2-G (wt%)	Fe2-C (wt%)	Fe2-F (wt%)	Fe2-H (wt%)
SiO_2	41.02	41.2(2)	41.13(2)	41.9(3)	41.1(2)	41.8(2)	40.5(2)	40.1(3)
Na_2O	13.36	10.1(2)	11.1(2)	8.8(2)	10.5(2)	9.5(2)	10.4(2)	11.4(2)
B_2O_3	13.79	15.49*	14.46*	14.65*	14.13*	15.10*	14.46*	15.10*
Li_2O	1.56	1.18*	1.38*	1.24*	1.27*	1.27*	1.21*	1.31*
MgO	0.16	0.36(2)	0.00	0.33(2)	0.32(2)	0.34(2)	0.33(2)	0.33(2)
Fe_2O_3	16.12	17.9(3)	17.86(3)	18.06(3)	17.71(3)	17.63(7)	17.43(3)	16.91(3)
Al_2O_3	5.59	6.6(1)	6.03(1)	7.9(1)	8.0(1)	7.4(1)	8.2(1)	7.8(1)
CaO	0.52	0.61(1)	0.60(1)	0.63(1)	0.60(1)	0.63(1)	0.62(1)	0.58(1)
ZrO_2	1.13	0.94(03)	1.18(03)	0.937(3)	0.903(2)	0.91(1)	0.901(2)	0.882(3)
SrO	0.20	0.16(01)	0.16(01)	0.161(1)	0.161(1)	0.159(1)	0.164(1)	0.157(1)
SO_3	0.22	0.00	0.00	0.00	0.00	0.00	0.36(2)	0.30(2)
P_2O_5	0.78	0.60(3)	0.65(3)	0.60(3)	0.56(3)	0.59(3)	0.58(3)	0.55(3)
MnO_2	3.98	3.20(3)	3.63(1)	3.20(1)	3.11(1)	3.11(7)	3.11(1)	3.02(1)
PbO	0.63	0.66(05)	0.73(5)	0.63(1)	0.647(5)	0.62(2)	0.658(5)	0.64(1)
NiO	0.47	0.45(04)	0.54(4)	0.475(4)	0.448(4)	0.429(1)	0.443(4)	0.434(4)
Cr_2O_3	0.25	0.25(1)	0.29(1)	0.28(1)	0.28(1)	0.27(1)	0.26(1)	0.25(1)
CeO_2	0.12	0.12**	0.12**	0.12**	0.12**	0.12**	0.12**	0.12**
ZnO	0.03	0.03**	0.03(01)	0.03**	0.03**	0.03**	0.03**	0.03**
La_2O_3	0.09	0.09**	0.09**	0.09**	0.09**	0.09**	0.09**	0.09**
Total	100.00	100.00	100.00	100.00	100.00	100.00	100.00	100.00

* Measured using ICP-MS

** Nominal values

8.2.2 Density

Measured densities of all glasses are given in Table 8.2.2, compared with the crystal phase wt% as measured by XRD. No correlation between the increase in the amount of crystalline phase present and the density of the sample exists, implying that the bulk glass density is decreasing. There are large errors on the HLW-NG-Fe2-S and -C glasses where there were only small samples available for measurement.

Table 8.2.2. Measured density of the HLW-NG-Fe2 and HLW-NG-Fe2-R glasses as well as wt% crystalline phase by XRD.

Glass	Density g cm^{-1}	Crystal Phase wt%
HLW-NG-Fe2	2.672 ± 0.006	1.79 ± 0.04
HLW-NG-Fe2-II	2.797 ± 0.056	1.89 ± 0.01
HLW-NG-Fe2-S	2.473 ± 0.238	3.71 ± 0.02
HLW-NG-Fe2-G	2.620 ± 0.058	3.67 ± 0.02
HLW-NG-Fe2-C	2.590 ± 0.204	4.37 ± 0.03
HLW-NG-Fe2-F	2.580 ± 0.004	2.08 ± 0.02
HLW-NG-Fe2-H	2.703 ± 0.002	3.89 ± 0.03

8.3 Iron Redox

8.3.1 ^{57}Fe Mössbauer Spectroscopy

The limit of $0.09 < Fe^{2+}/Fe_T < 0.33$ (Larson 1996; Jantzen 2011) is suggested to avoid excessive foaming at the low end and precipitation of metallic species at the high end. Higher FeO quantities in the glass have also been linked to reductions in chemical durability (Peeler and Edwards 2004). No metallic species were identified in any of the HLW-NG-Fe2-R samples in Chapter 6. As discussed in Chapter 7, ^{57}Fe Mössbauer spectroscopy is the most reliable source of data for the redox state of Fe in the final glasses. The spectra collected for the glass samples and hyperfine parameters are given in Chapter 6, section 6.4. The redox states of the glasses are given in Table 8.3.1.

Table 8.3.1. Redox state of iron in the final HLW-NG-Fe2, -II and -R glasses.

Glass sample	**Fe^{3+}/Fe_T**
HLW-NG-Fe2	1.00 ± 0.07
HLW-NG-Fe2-II	1.00 ± 0.07
HLW-NG-Fe2-S	1.00 ± 0.09
HLW-NG-Fe2-G	0.47 ± 0.02
HLW-NG-Fe2-C	0.65 ± 0.02
HLW-NG-Fe2-F	1.00 ± 0.11
HLW-NG-Fe2-H	0.83 ± 0.07

8.3.2 Sulphate Retention

The relationship between the Fe^{3+}/Fe_T redox and SO_3 retention is explored using the available data from the studies so far. The Fe^{3+}/Fe_T redox ratio was provided by ^{57}Fe Mössbauer spectroscopy, section 8.3.1. Both evolved gas analysis, Chapter 5, section 5.5, and XRF, section 8.2.1, of the glasses provide information on the retention of SO_3. Evolved SO_2 by EGA is plotted on the left y-axis in Figure 8.3.1 and SO_3 retained in the glass by XRF on the right y-axis.

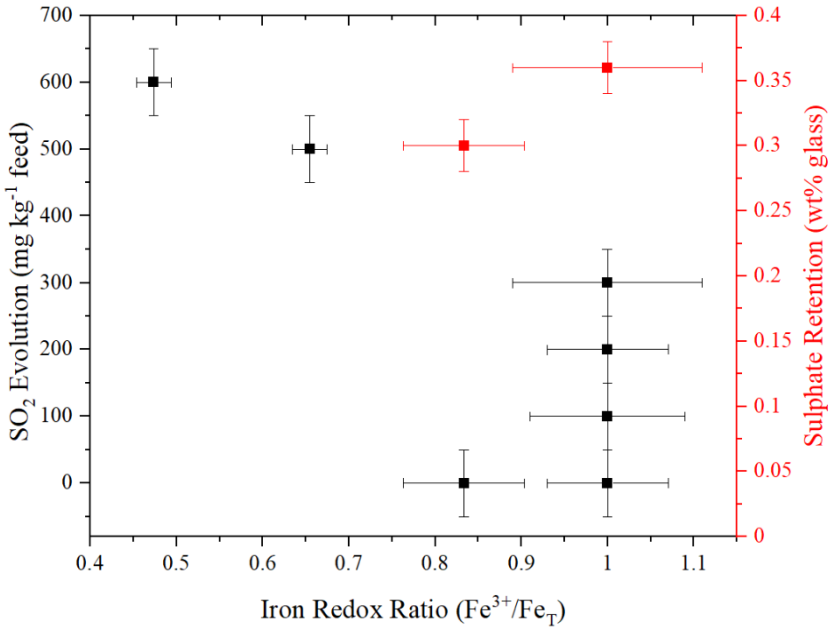

Figure 8.3.1. Evolution and retention of sulphates in the final glass samples as a function of redox state of Fe, showing that the evolved SO_2 and retained SO_3 do not correlate. Evolved SO_2 is highest for the feeds with the lowest final iron redox states.

The HLW-NG-Fe2-F feed has apparently retained 0.36 ± 0.02 wt% SO3 and lost ~300 mg kg-1 (glass). 300 mg kg-1 (glass) equates to 0.03 g 100 g^{-1} glass or equivalent wt% SO_2, which is only 16 % of the total SO_3 batched. 16 % loss of SO_3 is not reflected in the XRF data, Table 8.2.1. The wt% of SO_3 increases for both HLW-NG-Fe2-F and HLW-NG-Fe2-H relative to the rest of the composition.

The highest SO_2 evolution is observed in the HLW-NG-Fe2-G and -C feeds, which is the same behaviour experienced with Fe^{2+}/Fe_T ratio in the soda-lime-silicate glasses (Beerkens 1999; Hubert et al. 2017), where a minimum retention is observed at Fe^{3+}/Fe_T ~ 0.4-0.8. A thorough study of the effect of coke addition on sulphur redox in glass melts showed that the more reduced the melt the more SO_2 bubbles were produced, the study only explored up to 0.1 wt% coke additions to the batch (Kloužek, Arkosiová, and Němec 2006), extrapolation of the data suggests that this would only increase at higher wt%. It is therefore not surprising that 3 wt% of coke and graphite additions to the HLW-NG-Fe2 feed produce the most SO_2 gas.

8.4 Spinel Phase Precipitation

8.4.1 XRD

One of the main concerns around the quality of the final glasses the precipitation of unstable crystal phases that could compromise the quality of the final glass, particularly if these phases are likely to carry radionuclides (Miekina 2018; Rodriguez et al. 2011; G. L. Smith et al. 2001). The presence of a spinel phase is not inherently detrimental to the quality of the final glass products, as explored in a recent study (Lonergan et al. 2022), but the crystallinity is currently limited to 1 vol% at 950 ℃ (Matlack et al. 2012). Precipitation and settling of spinel crystals is a concern for processing, as they may cause shorting of electrodes or blockages to melter components (Lonergan et al. 2022).

In the final glass products, appear to be two distinct stages of spinel precipitation as a function of the carbon content g^{-1} of reductant added, Figure 8.4.1. Between 0-0.32 g (C) g^{-1} compound, the spinel precipitation is 1.78-2.08 wt %, and 0.42-1 g (C) g^{-1} the proportion approximately doubles to 3.71-4.36 wt%. For the HLW-NG-Fe2-II glass, the carbon content g^{-1} of reductant was calculated as the carbon content in the excess mass added by the $FeC_2O_4 \cdot 2H_2O$ raw material compared with the $Fe(OH)_3$. The HLW-NG-Fe2-S and -F samples also contain some Fe_2O_3, a considerable amount in the HLW-NG-Fe2-S sample, which could have adverse effects on the glass properties such as durability, if Fe^{3+} bonds have been removed from the bulk glass matrix.

As identified in Chapter 6, section 6.2, there are a number of possibilities for the compositions of the spinel phases in the final glasses based on refinement of XRD patterns alone. The lattice constants range from a = b = c = 8.391 to 8.404 Å, suggesting that some of the spinels are not pure Fe_3O_4, and instead have Mn or Ni on the A (2+) site, or Cr on the B (3+) site. This was also ambiguous in the ^{57}Fe Mössbauer analysis in Chapter 6, section 6.2.

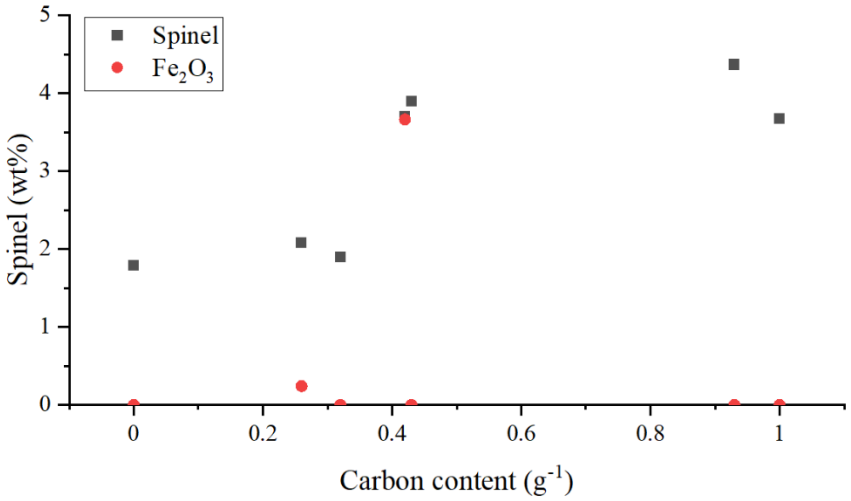

Figure 8.4.1. Quantity of crystalline phases identified by XRD patterns as a function of carbon content g^{-1} of reductant added.

8.4.2 SEM/EDX

SEM/EDX of the glasses, allows for a semi-quantitative compositional analysis of the spinels in isolation from the bulk glass. Backscattered electron images and EDX maps in Figure 8.4.2 shows examples of the cubic shape of these spinel crystals against the bulk glass matrix in the HLW-NG-Fe2-C sample. The remaining images are shown in the Appendix D, Figure 4-9. The composition of the spinels are consistent within the spinels measured in the HLW-NG-Fe2-G, -C and -H glasses. 28 % O is consistent with the expected O content of all suggested spinels, containing Fe, Mn, Cr and Ni. Spinels in the HLW-NG-Fe2, and HLW-NG-Fe2-F and -H glasses have lower Fe content. HLW-NG-Fe2-S and -F are also higher in Mn than Ni or Cr, where the others have a higher abundance of Ni in the spinels.

For the HLW-NG-Fe2-S sample, Figure 8.4.3, and Figure 8.4.4, some areas are rich in Fe and O, and Fe, Mn and O, but not Ni or Cr. Point identification of an area of the HLW-NG-Fe2-S samples is shown in Figure 8.4.4. Some of these regions reflect the Fe_2O_3 present in the HLW-NG-Fe2-S sample, detected by XRD, section 6.2. There are also Si and O rich phases, suggesting SiO_2 crystals, however these were not identified in XRD patterns ins section 6.2.

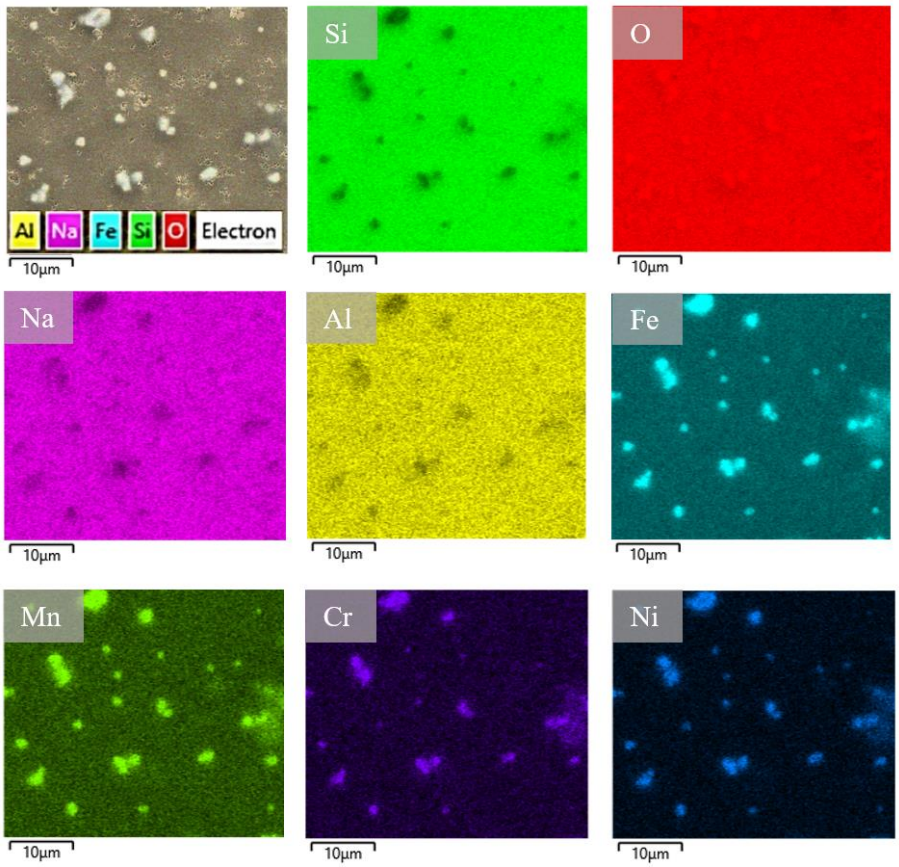

Figure 8.4.2. Elemental maps by EDX of the HLW-NG-Fe2-C showing dispersed spinel crystals rich in Fe, Mn, Ni and Cr in an inhomogeneous matrix.

Table 8.4.1. Spinel composition by average point scans by EDX and average spinel size.

Element	**NG-Fe2**	**NG-Fe2-S**	**NG-Fe2-G**	**NG-Fe2-C**	**NG-Fe2-F**	**NG-Fe2-H**
O	22.0 ± 3.0	24.7 ± 8.3	21.1 ± 2.2	27.0 ± 1.9	26.5 ± 1.8	26.6 ± 1.2
Fe	47.7 ± 5.6	54.8 ±18.1	60.9 ± 4.3	55.3 ± 5.6	45.0 ± 3.7	48.3 ± 3.9
Cr	8.5 ± 1.9	2.0 ± 2.3	4.0 ± 2.6	4.0 ± 0.9	6.1 ± 1.1	7.2 ± 1.9
Mn	8.5 ± 1.1	11.7 ± 7.7	4.7 ± 0.7	5.3 ± 0.4	11.5 ± 1.3	7.4 ± 0.5
Ni	13.4 ± 2.1	6.7 ± 7.4	9.3 ± 2.2	8.4 ± 1.6	10.8 ± 1.7	10.5 ± 1.2
Average Size (μm^3)	1.39	1.40	1.95	1.87	1.69	1.60

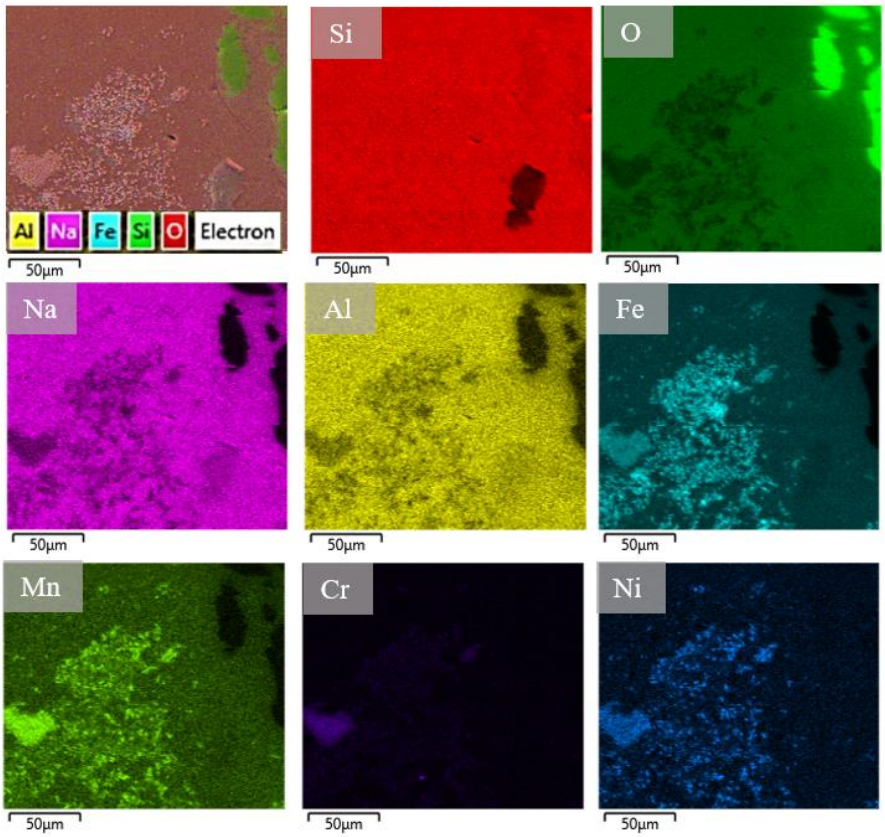

Figure 8.4.3. Elemental maps by EDX of the HLW-NG-Fe2-S showing regions rich in O, Fe, Mn and Ni, and Cr, as well as regions of only O, Fe, Mn and Ni. Si and O rich regions are also observed.

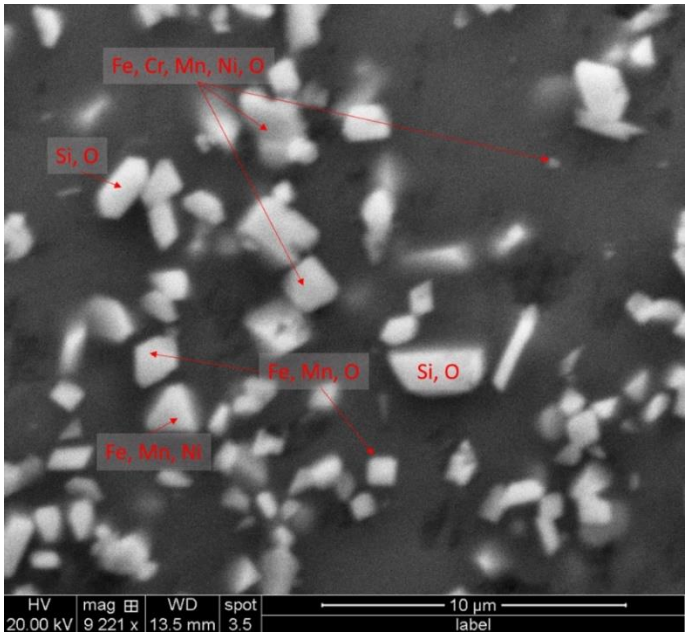

Figure 8.4.4. Elemental point identification of the crystalline phases on the backscattered electron image HLW-NG-Fe2-S quenched at 1150 ℃ identifying SiO_2 crystals and spinels containing mixtures of Fe, Mn, Cr and Ni.

8.4.3 Spinel Phase precipitation at 950 ℃

As discussed in sections 2.3.38.1 there is a limit of < 1 vol% spinel crystals at 950 ℃ employed at the WTPs (Matlack et al. 2007). Previous measurement of the HLW-NG-Fe2 glass under this regime showed 0.65 wt% spinel formation (Matlack et al. 2012). Quantification of phases formed during the heat-treatment, described in section 3.8.2, are shown in Figure 8.4.5. Both spinel and Fe_2O_3 phases were identified in all samples apart from the HLW-NG-Fe2-G sample, which only contained a spinel phase.

Heat-treatments were ~480 ℃ above the glass transition temperature, section 8.5.1. It is, therefore, not surprising that devitrification of Fe_2O_3 occurs. Growth of the spinel phases present in the glass and likely formation of more spinels, will occur as discussed 2.2.4, increasing the total crystallinity in the sample. In the HLW-NG-Fe2, HLW-NG-Fe2-S and -F samples that had the least negative oxygen partial pressure in the glass, estimated in Chapter 7, section 7.8, there is considerably higher Fe_2O_3 precipitation. The HLW-NG-Fe2-G and -C heat-treated samples, which had the most negative oxygen partial pressure, produce more spinel phase, and zero or little Fe_2O_3, respectively.

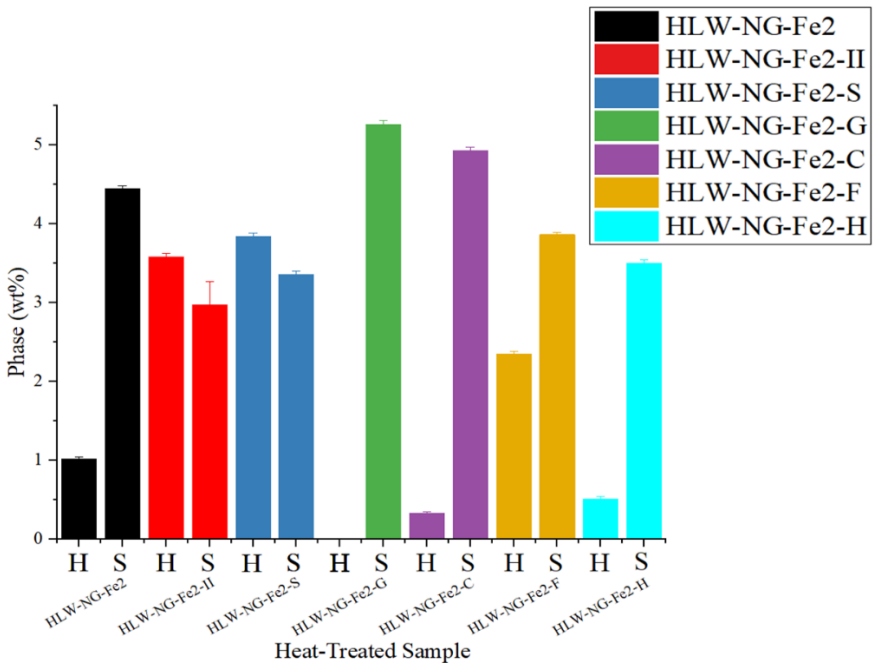

Figure 8.4.5. Crystalline phase wt% by XRD of the heat-treated glass samples. Highest spinel phase precipitation and lowest haematite in the HLW-NG-Fe2-G and -C samples.

Table 8.4.2. Measured density of the HLW-NG-Fe2 and HLW-NG-Fe2-R glasses, compared with the samples heat treated to 950 ℃ for 24 hours as well as wt% crystalline phase by XRD.

Glass	**Density g cm^{-1}**		**Crystal Phase wt%**	
	Glass	**HT (950 ℃)**	**Glass**	**HT (950 ℃)**
HLW-NG-Fe2	2.672 ± 0.006	2.725 ± 0.060	1.79 ± 0.04	5.46 ± 0.06
HLW-NG-Fe2-II	2.797 ± 0.056	2.941 ± 0.431	1.89 ± 0.01	6.55 ± 0.34
HLW-NG-Fe2-S	2.473 ± 0.238	2.627 ± 0.037	3.71 ± 0.02	7.20 ± 0.08
HLW-NG-Fe2-G	2.620 ± 0.058	2.929 ± 0.439	3.67 ± 0.02	5.26 ± 0.05
HLW-NG-Fe2-C	2.590 ± 0.204	2.670 ± 0.011	4.37 ± 0.03	5.26 ± 0.06
HLW-NG-Fe2-F	2.580 ± 0.004	2.693 ± 0.015	2.08 ± 0.02	6.21 ± 0.06
HLW-NG-Fe2-H	2.703 ± 0.002	2.678 ± 0.001	3.89 ± 0.03	4.01 ± 0.07

Table 8.4.3. Crystalline phase vol% in heat-treated glass samples.

Heat-treated sample	**vol% crystallinity**
HLW-NG-Fe2	0.9 ± 0.1
HLW-NG-Fe2-II	1.1 ± 0.1
HLW-NG-Fe2-S	1.2 ± 0.3
HLW-NG-Fe2-G	0.9 ± 0.2
HLW-NG-Fe2-C	0.9 ± 0.2
HLW-NG-Fe2-F	1.0 ± 0.2
HLW-NG-Fe2-H	0.7 ± 0.2

8.5 Thermal Properties

8.5.1 Glass Transition Temperature

Changes in the structure of the glasses impact the glass properties. DTA of the glasses informs the thermal behaviour with increasing temperature. The glass transition temperature, T_g, located in the insert of Figure 8.5.1, is a property that relates to high temperature stability, and behaviour on cooling. Below T_g the glass structure is "locked" in place, on cooling the melt must reach below T_g at a sufficient rate to avoid formation of crystalline phases (Yalmali et al. 2007), as discussed in Chapter 2, section 2.2.2. As mentioned with alkali effects in silica glasses, 2.2.2.2, there is a strong relationship reported between the glass transition temperature and glass viscosity (Cormier, Neuville, and Calas 2005; Angell 1988; Yue 2008).

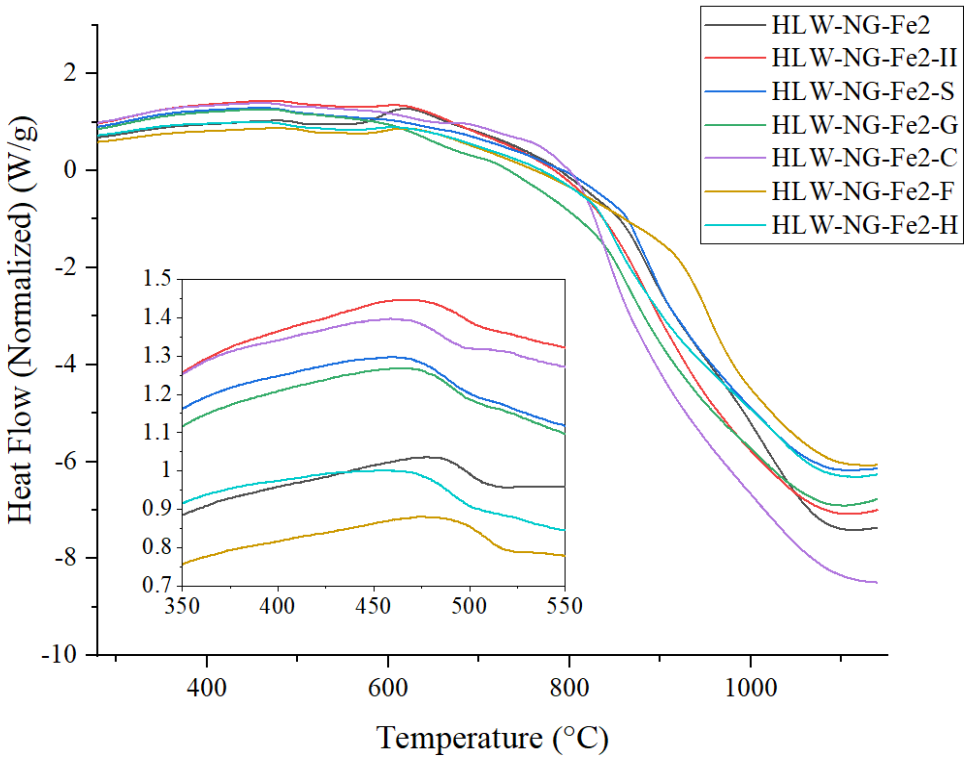

Figure 8.5.1. DTA of HLW-NG-Fe2, HLW-NG-Fe2-II and HLW-NG-Fe2-R glass samples. Insert magnified curves showing onset of T_g. The temperatures of T_g onset are lower in the HLW-NG-Fe2-S, -G, -C and -H samples than the HLW-NG-Fe2 sample.

The T_g values, tabulated in Table 8.5.1, are all within 20 °C. The difference in the HLW-NG-Fe2 and HLW-NG-Fe2-F glass from the other glasses is likely to indicate some change in the behaviour on cooling and the viscosity of the glasses (Cormier, Neuville, and Calas 2005; Angell 1988; Yue 2008). Additionally, the correlation between T_g and the Fe^{3+} content in the glass, shown in Figure 8.5.2, alludes to a subtle property change which may impact the chemical durability (Goel et al. 2012; Cunnane et al. 1994). Figure 8.5.2 shows the relationship between T_g onset and the Fe^{3+} iron content in the glass. The Fe^{3+} iron content was calculated by the quantity of Fe_2O_3 in the glasses by XRF, minus the Fe^{2+} content in the glass by ^{57}Fe Mössbauer spectroscopy. The binding energies of Fe – O, Si – O and Al – O linkages are 407 kJ mol^{-1}, 502 kJ mol^{-1} and 800 kJ mol^{-1}, respectively. Direct replacement of Fe_2O_3 with Al_2O_3 in a glasses, has been shown to lead to "weaker" glass matrices, reflected in a reduction in glass transition temperature (Hansen et al. 2022; Deshkar et al. 2019). If the Fe^{3+} in these glasses was tetrahedrally coordinated and acting as a network former, we may expect the aforementioned relationship to apply, however the inverse appears to be true. Those with higher T_g, HLW-NG-Fe2 and HLW-NG-Fe2-F have a higher Fe^{3+} content than the other HLW-NG-Fe2-R glasses with lower T_g.

Table 8.5.1. Temperature of T_g onset and midpoint for the HLW-NG-Fe2, HLW-NG-Fe2-II and HLW-NG-Fe2-R glasses measured by DTA.

Heat-treated sample	**T_g Onset (°C)**	**T_g Midpoint (°C)**
HLW-NG-Fe2	486 ± 3	497 ± 3
HLW-NG-Fe2-II	474 ± 3	490 ± 3
HLW-NG-Fe2-S	471 ± 3	484 ± 3
HLW-NG-Fe2-G	472 ± 3	485 ± 3
HLW-NG-Fe2-C	471 ± 3	483 ± 3
HLW-NG-Fe2-F	490 ± 3	503 ± 3
HLW-NG-Fe2-H	471 ± 3	485 ± 3

There may, in fact be a “stronger” influence of the network-modifying characteristics of octahedrally coordinated Fe^{2+} or Fe^{3+}. Reduced glasses, “tend to be less durable and less viscous than oxidised glasses” (Cunnane et al. 1994), this is attributed to iron becoming network forming under oxidising conditions, presumably network modifying with reducing conditions.

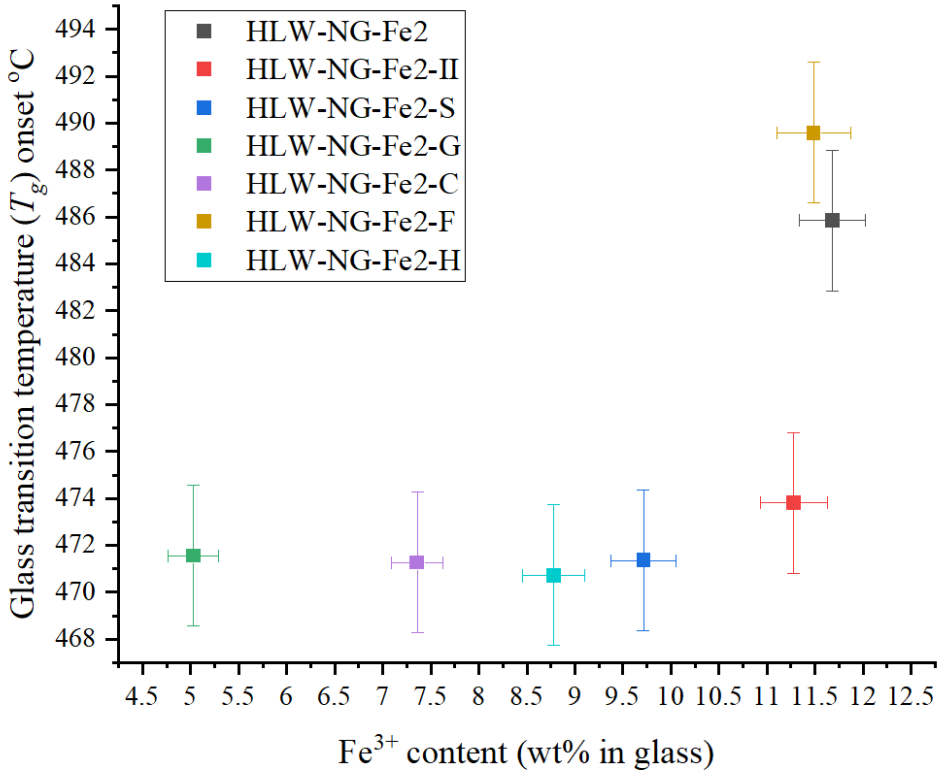

Figure 8.5.2. Temperature of onset of T_g, for HLW-NG-Fe2, HLW-NG-Fe2-II and HLW-NG-Fe2-R glass samples showing a decrease in T_g for the samples with lower Fe^{3+} contents in the final glasses.

8.6 Product Consistency Test

The Product Consistency Test -B was employed to qualify the chemical durability behaviour of the HLW-NG-Fe2-II, -G and -F glasses. The test protocol is described in Chapter 3, section 3.8.1. Measurements of the pH of the blank samples, and the leachates are detailed in Table 8.6.1. These samples were selected to form a matrix to compare the results with those for original HLW-NG-Fe2 glass, measured previously (Matlack et al. 2012). The matrix consists of a range of foaming behaviours during melting, from little foam reduction in the HLW-NG-Fe2-F feed, to ~ 50 % foam reduction in the HLW-NG-Fe2-II and -G feeds, and further to compare with the range of redox states $Fe^{3+}/Fe_T = 1$ in the HLW-NG-Fe2-II and -F samples and $Fe^{3+}/Fe_T = 0.47$ in the HLW-NG-Fe2-G feed. The HLW-NG-Fe2-II feed provides an example with both foam reduction and no change in Fe redox state.

Table 8.6.1. pH measurements of the leachates before and after the 7-day PCT-B test.

Sample	**pH**		
	No.	**Initial**	**After 7 day PCT**
Blank	1	6.34	10.8
	2		10.2
	3		10.9
HLW-NG-Fe2-II	1	6.08	10.2
	2		10.2
	3		10.4
HLW-NG-Fe2-G	1	6.07	9.78
	2		9.76
	3		9.73
HLW-NG-Fe2-F	1	6.03	9.93
	2		9.94
	3		9.88

There is an increase in pH of all samples after the test, including the blank samples. ICP-OES off the blank samples after the test showed considerable amounts of Si and

Na, data provided in Appendix B, Table 4. There was no test response for any of the glasses from Si or Na, by section 25.1.2 of the ASTM C1285-21. The amount of each element detected in the waste leachate must be more than 3 standard deviations from the test value to be considered statistically significant. That is not to say that no Si or Na was leached from the glasses, just that the quantity is not able to be determined by the ICP-OES values measured due to high values of Na and Si in the blank sample.

The raw ICP-MS measurements and processed PCT-B response data are given in Appendix B, Tables 5 – 9. Of the valid data collected during the experiment, the Li and B values were measured previously for HLW-NG-Fe2, the comparison of the measured data in this study with the earlier study of HLW-NG-Fe2 (Matlack et al. 2012), is given in Table 8.6.2. As is a continuing theme in this chapter, the HLW-NG-Fe2-F feed has similarly low losses of Li and B to the original HLW-NG-Fe2 feed, in fact considerably lower for Li. The HLW-NG-Fe2-II and -G samples are higher for both Li and B losses. The B loss in HLW-NG-Fe2-G is approaching the contract limit of < 4 g L^{-1} (Piepel et al. 2007; Kirkbride et al. 2009; Piepel et al. 2005; Muller et al. 2013).

Table 8.6.2. Average normalised concentrations (NC_i), of elements leached during 7-day PCT-B test.

Element	**NC_i g_{waste} $L^{-1}_{leachant}$**			
	HLW-NG-Fe2 (Matlack et al. 2012)	**HLW-NG-Fe2-II This study**	**HLW-NG-Fe2-G This study**	**HLW-NG-Fe2-F This study**
Si	0.318	0*	0*	0*
Na	0.817	0*	0*	0*
B	0.986	1.443	3.151	0.925
Li	0.833	1.476	1.952	0.183

*No viable data by the ASTM C1285-21, 2021 Standard.

Leach rates of Al, Ca, Cr, Fe, Mg, Mn, Ni, P, Pb, S, Sr and Zr were also collected by ICP-OES from the leachate samples, the average normalised losses per day are plotted in Figure 8.6.1. The other notable losses occur for Al, in the HLW-NG-Fe2-II and -F

glasses, Fe, Mn and P in the HLW-NG-Fe2-G glass, and Ni amongst all glasses, but HLW-NG-Fe2-F most distinctly. Those elements, in particular, may indicate some leaching of spinel crystals, or iron phosphate containing phases. As discussed in sections and 8.4.2 the spinel phase precipitation is not necessarily an issue for chemical durability as spinels are chemically stable (Lonergan et al. 2022).

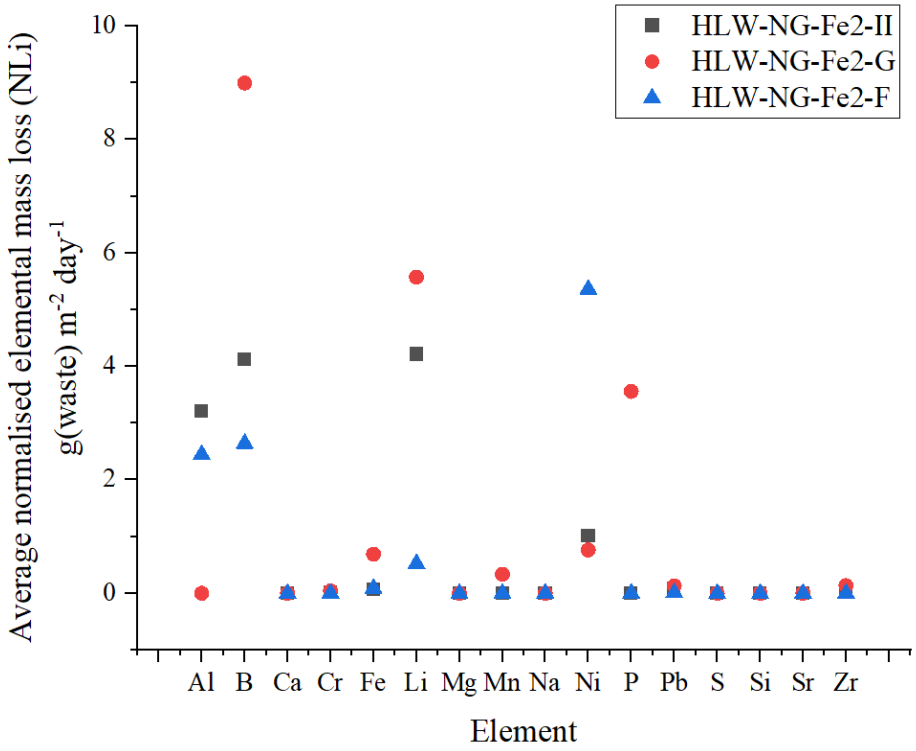

Figure 8.6.1. Average normalised elemental mass loss by calculations of values from ICP-OES of leachate samples following a 7-day PCT-B showing high losses of Al, P and Ni as well as the B and Li.

8.7 Summary

8.7.1 Glass product quality

Of the quality requirements of the glasses outlined in section 8.1, this chapter has explored the redox state of the glasses, the spinel phase precipitation in the glasses, and the crystalline phase precipitation in heat treated samples, and the chemical durability by PCT-B. The viscosity has not been explicitly measured, but thermal analysis by DTA was employed to explore the effect of the structure of the glasses on the thermal behaviour.

At least at the crucible scale, the HLW-NG-Fe2, HLW-NG-Fe2-S, HLW-NG-Fe2-F and HLW-NG-Fe2-H glasses remain within the contract limits employed at the WTPs, stated in Chapter 8, section 8.1, for redox state, $Fe^{2+}/Fe_T < 0.33$ (Larson 1996; Jantzen 2011; Peeler and Edwards 2004). The oxidation states during melting of manganese, nickel, chromium and cerium were explored in Chapter 7, sections 0-7.7, by XANES. There are no stated limits on the redox states of these species, apart from avoiding metallic precipitation (Seymour 1995), which was the case for all feeds studied within the detection limits of XRD, in section 6.2.

From the 7-day PCT-B tests performed, section 8.6, the HLW-NG-Fe2 (Matlack et al. 2012), HLW-NG-Fe2-F and HLW-NG-Fe2-G feed glasses were within the contract limits for normalised loss of B, < 4 g L^{-1} (2 g m^{-2}) by PCT of Si, B and Na (Piepel et al. 2007; Kirkbride et al. 2009; Piepel et al. 2005; Muller et al. 2013), but the Si and Na were unreported. The selection of these glasses provided a matrix of redox states to compare with the original glass which had been tested previously (Matlack et al. 2012). Boron had the highest leaching rate of the previously measured HLW-NG-Fe2 glass (Matlack et al. 2012), therefore it is reasonable to approximate that the Si and Na leach rates would be lower than the B in the other glasses. The other HLW-NG-Fe2-R glasses were not measured.

Of the valid data presented here in the PCT-B study of the glasses, there is inferior chemical durability observed in the HLW-NG-Fe2-II and -G glasses, compared to the HLW-NG-Fe2 and -F glasses. This is consistent with the suggestions in the literature that higher Fe^{2+} content is associated with lower chemical durability (Peeler and Edwards 2004) for the HLW-NG-Fe2-G glass. Of the other elements analysed during ICP analysis of the PCT leachates, section 8.6, there was also some aluminium, nickel and iron leached, as well as phosphorus in the graphite glass. These could be leached from the glass, from partitioned spinel phases, or from other secondary phases and while they are not necessarily detrimental to the glass properties, they will require monitoring when scaling up.

All of the HLW-NG-Fe2-R glasses were close to the control limit for spinel crystallisation, < 1 vol% at 950 °C (Matlack et al. 2012; Piepel et al. 2007; Gan et al. 2009). Only the HLW-NG-Fe2-H glass sample would be confidently below this limit. However, the HLW-NG-Fe2 glass was subject to this test previously, experiencing only 0.65 vol% spinel crystallisation (Matlack, Viragh, et al. 2015).

8.7.2 Sulphate Retention

SO_3 retention in the glass, or the evolution of SO_2, has been shown to be related to the partial pressure of the glass melt, determined in most studies by the redox state of Fe (Appel et al. 2019; Beerkens 1999; Arkosiová, Kloužek, and Němec 2008). In the HLW-NG-Fe2 glass a study was performed on the sulphate retention with time held at melt temperature (1150 °C), where sulphate reduced from 0.36 wt% to 0.12 wt% with 20+ hours of melting (Gan et al. 2013).

The sulphate retention correlates with redox states at the low Fe^{3+}/Fe_T end of the data, in section 8.3.2 agreeing with the literature values, however the data in inconclusive for those with high Fe^{3+}/Fe_T. The solubility of SO_3 is also a property of interest to the Hanford site (Vienna, Kim, Muller, Piepel, and Kruger 2014; Jantzen 2011; Kruger,

Pegg, et al. 2012; Kruger et al. 2006), and other commercial and radioactive waste vitrification programs (Kaushik et al. 2006, 2004; Kloužek, Arkosiová, and Němec 2006). There is also interest in retention other species with redox dependent solubility, such as ^{99}Tc (Jantzen 2011; Um et al. 2017; Dixon et al. 2022; George, Kim, and Kruger 2020)

.Figure 8.3.1, shows the sulphur evolution and sulphate retention against Fe^{3+}/Fe_T. There is discrepancy between the released SO_2 and detected SO_3 in the glasses, particularly for the HLW-NG-Fe2-F feed sample, for which it appears that the highest amount of SO_3 has been retained in the glass, but this sample also has the 3rd highest mass of SO_2 evolved from the HLW-NG-Fe2-R feeds. Considering alone the evolution by EGA results, the evolution of SO_2 is consistent with the redox-dependence observed in the literature for a variety of glass compositions (Soderquist et al. 2014; Vienna, Kim, Muller, Piepel, Kruger, et al. 2014; Langowski, Darab, and Smith 1996; Bibler et al. 2000; Beerkens 1999; Hubert et al. 2017).

8.8 References

Angell, C. A. (1988) ‘Perspective on the Glass Transition.’ Journal of Physics and Chemistry of Solids 49 (8): 863–71.

Appel, C. J., Kloužek, J. Jani, N., Lee, S., Dixon, D. R., Hrma, P., Pokorný, R., Schweiger, M. J. and Kruger, A. A., (2019) ‘Effect of sucrose on foaming and melting behavior of a low-activity waste melter feed’, Journal of the American Ceramic Society, 102(12), pp. 7594–7605.

Arkosiová, M., Kloužek, J. and Nìmec, L. (2008) ‘The Role of Sulfur in Glass Melting Processes’, Ceramics - Silikaty, 52(1), pp. 155–159.

Beerkens, R. (1999) ‘Redox and sulphur reactions in glass melting processes’, Ceramics - Silikaty, 43(3), pp. 123–131.

Bell, A. M. T., Backhouse, D. J., Deng, W., Eales, J. D., Kilinc, E., Love, K., Rautiyal, P., Rigby, J. C., Stone, A. H., Vaishnav, S., Wei-Addo, G. and Bingham, P. A. (2020) ‘X-ray fluorescence analysis of feldspars and silicate glass: Effects of melting time on fused bead consistency and volatilisation.’ Minerals, 10(5).

Bibler, N. E., Fellinger, T. L., Marra, S. L., O'Driscoll, R. J., Ray, J. W. and Boyce, W. T. (2000) ‘Tc-99 and Cs-137 volatility from the DWPF production melter during vitrification of the first macrobatch of HLW sludge at the Savannah River Site’, in Materials Research Society Symposium - Proceedings. Aiken, SC (United States), pp. 697–702.

Caurant, D., Loiseau, P., Majerus, O., Aubin-Chevaldonnet, V., Bardez, I. and Quintas, A. (2009) ‘Glasses, Glass-Ceramics and Ceramics for Immobilization of Highly Radioactive Nuclear Wastes.’ New York, NY (United States): Nova Science Publishers, Inc.

Cormier, L., Neuville, D. R. and Calas, G. (2005) ‘Relationship between Structure and Glass Transition Temperature in Low-Silica Calcium Aluminosilicate Glasses:

The Origin of the Anomaly at Low Silica Content.' Journal of the American Ceramics Society.88 (8), pp. 2292–99.

Cunnane, J. C., Bates, J. K., Bradley, C. R., Buck, E. C., Ebert, W. L., Feng, X., Mazer, J. J., Wronkiewicz, D. J., Sproull, J., Bourcier, W. L., McGrail, B. P. and Altenhofen, M. K. (1994) "High Level Waste Borosilicate Glass: A Compendium of Corrosion Characteristics Volume 2" Office of Waste Management, United States Department of Energy. Argonne National Laboratory, IL (United States).

Deshkar, A. Ahmadzadeh, M. Scrimshire, A. Han, E. Bingham, P. A. Post Guillen, D. McCloy, J. Goel, A. (2018) 'Crystallization behavior of iron- and boron-containing nepheline ($Na_2O{\cdot}Al_2O_3{\cdot}2SiO_2$) based model high-level nuclear waste glasses.' Journal of the American Ceramics Society. 4, pp. 1–21.

Dixon, D. R., Hall, M. A., Lang, J. B., Cutforth, D. A., Stewart, C. M. and Eaton, W. C. (2022) 'Retention analysis from vitrified low-activity waste and simulants in a laboratory-scale melter,' Ceramics International, 48(5). pp. 5955–5964.

Donald, I. W. (1997) 'Review: The immobilization of high level radioactive wastes using ceramics and glasses', Journal of Materials Science, 32(22), pp. 5851–7.

Gan, H., Viragh, C., McKeown, D. A., Muller, I. S., Cecil, R., Kot, Wing K., Joseph, I., Wang, C., Pegg, I. L., Chaudhuri, M., Zhao, W. and Feng, Z. (2009) 'Crystal Settling, Redox, and High Temperature Properties of ORP HLW and LAW Glasses.' VSL-09R1510-1. Vitreous State Laboratory, Washington, D. C. (United States).

Gan, H., Pegg, I. L., Joseph, I., Matlack, K. S. and Feng, Z. (2013) 'Management of High Sulfur HLW' VSL-13R2920-1. Richland, WA. (United States).

Gates-Rector, S. D. and Blanton, T. N. (2019) 'The Powder Diffraction File: A Quality Materials Characterisation Database', Powder Diffraction, 34(4), pp. 352–60.

George, J. L., Kim, D. -S and Kruger, A. A. (2020) ‘Effects of iron oxalate on rhenium incorporation into low-activity waste glass’, Journal of Non-Crystalline Solids. Elsevier, 545(June), p. 120257.

Giles, H. L., Hurley, P. W. and Webster, H. W. M. (1995) ‘Simple approach to the analysis of oxides, silicates and carbonates using X-ray fluorescence spectrometry.’ X-Ray Spectrometry, 4(24), 205–218.

Gin, S. Abdelouas, A., Criscenti, L. J., Ebert, W. L., Ferrand, K., Geisler, T., Harrison, M. T., Inagaki, Y., Mitsui, S., Mueller, K. T., Marra, J. C., Pantano, C. G., Pierce, E. M., Ryan, J. V., Schofield, J. M., Steefel, C. I. and Vienna, J. D. (2013) ‘An international initiative on long-term behavior of high-level nuclear waste glass’, Materials Today. Elsevier Ltd., 16(6), pp. 243–248.

Goel, A., McCloy, J. S., Fox, K. M., Leslie, C. J., Riley, B. J., Rodriguez, C. and Schweiger, M. J. (2012) ‘Structural analysis of some sodium and alumina rich high-level nuclear waste glasses’, Journal of Non-Crystalline Solids. Elsevier B.V., 358(3), pp. 674–679.

Hansen, E., Perret, D., Bardez-Giboire, I., Diliberto, S. and Rapin. C. (2022) ‘Iron Enriched Peraluminous Glasses: Incorporation Limit and Effect of Iron on Glass Transition Temperature and Viscosity.’ Journal of Non-Crystalline Solids 584(12152).

Hubert, M., Faber, A. J., Sesigur, H., Akmaz, F., Kahl, S. R., Alejandro, E. and Maehara, T. (2017) ‘Impact of Redox in industrial glass melting and importance of redox control’, Ceramic Engineering and Science Proceedings, 38(1), pp. 115–128.

Jantzen, C. M. (2011) ‘Development of glass matrices for high level radioactive wastes’, in Handbook of Advanced Radioactive Waste Conditioning

Technologies. 1st ed. Aiken, SC (United States): Woodhead Publishing Limited, pp. 230–292.

Jin, T., Kim, D., Tucker, A. E., Schweiger, M. J. and Kruger, A. A. (2015) 'Reactions during melting of low-activity waste glasses and their effects on the retention of rhenium as a surrogate for technetium-99', Journal of Non-Crystalline Solids. Elsevier B.V., 425, pp. 28–45.

Kaushik, C. P., Mishra, R. K., Sengupta, P., Kumar, A., Das, D., Kale, G. B. and Raj, K. (2006) 'Barium borosilicate glass - a potential matrix for immobilization of sulfate bearing high-level radioactive liquid waste', Journal of Nuclear Materials, 358(2–3), pp. 129–138.

Kaushik, C. P., Mishra, R. K., Thorat, V., Ramchandran, M., Kumar, A., Ozarde, P. D., Raj, K. and Das, D. (2004) 'Development of a Glass Matrix for Vitrification of Sulphate Bearing High Level Radioactive Liquid Waste.' BARC--2004/E/018. Bhabha Atomic Research Centre, Mumbai (India).

Kirkbride, R. A., Allen, G. K., Lowy, R. M. and Bergmann, L. M. (2009) 'Hanford Tank Waste Operations Simulator (HTWOS) Model Design.' RPP-17152. Richland, WA (United States).

Kloužek, J., Arkosiová, M. and Němec, L. (2006) 'Redox equilibria of sulphur in glass melts', Ceramics - Silikaty, 50(3), pp. 134–139.

Kruger, A. A., Gan, H., Pegg, I. L., Kot, W. K. and Feng, Z. (2006) 'Final Report - Sulfate Solubility in RPP-WTP HLW Glasses.' ORP-56325, Office of River Protection, Richland, WA (United States).

Kruger, A. A., Matlack, K. A., Pegg, Ian L. and Gong, W. (2013) 'Final Report - Glass Formulation Testing to Increase Sulfate Volatilization from Melter.' VSL-04R4970-1, Rev. 0. Office of River Protection, Richland, WA (United States).

Langowski, M. H., Darab, J. G. and Smith, P. A. (1996) 'Volatility Literature of Chlorine, Iodine, Strontium, Technetium, and Rhenium: Technetium and Rhenium Volatility Testing.' PNNL-11052. Pacific Northwest National Laboratory, Richland, WA (United States).

Larson, D. E. (1996) 'Hanford High-Level Waste Vitrification Program at the Pacific Northwest National Laboratory: Technology Development - Annotated Bibliography.' Pacific Northwest National Laboratory, Richland, WA (United States).

Lonergan, C. E., Rice, J., Skidmore, C., Schweiger, M. J. and Hrma, P. (2022) 'The effects of mixing multi-component HLW glasses on spinel crystal size', Journal of Nuclear Materials. Elsevier B.V., 558, p. 153318.

Matlack, K. S., Gan, H., Gong, W., Pegg, I. L., Champman, C. C., Joseph, I. and Kruger, A. A. (2007) 'Final Report - High Level Waste Vitrification System Improvements.' VSL-07R1010-1, Rev 0, dated 04/16/07. Vitreous State Laboratory, Washington, D. C. (United States).

Matlack, K. S., Gan, H., Chaudhuri, M., Kot, W. K., Pegg, I. L., Joseph, I. and Kruger, A. A. (2012) 'Melter Throughput Enhancements for High-Iron HLW.' ORP-54002. Vitreous State Laboratory, Washington, D. C. (United States).

Matlack, K. S., Viragh, C., Kot, W. K., Pegg, I. L. and Joseph, I. (2015) 'Effect of the Form of Iron on HLW Melt Rate.' VSL-15R3430-1. Vitreous State Laboratory, Washington, D. C. (United States).

Miekina, M. (2018) 'Crystal formation during the vitrification of HLW in Ca/Zn base glass.' PhD Thesis. University of Sheffield, Sheffield, UK.

Muller, I. S., Gilbo, K., Joseph, I. and Pegg, Ian L. (2013) 'Final Report- Enhanced LAW Glass Property-Composition Models- Phase 1.' VSL-13R2940-1. Richland, WA (United States).

Ojovan, M. I. and Lee, W. E. (2014) ‘Principles of Nuclear Waste Management’, in An Introduction to Nuclear Waste Immobilisation. Oxford, (UK): Elsevier, pp. 65–74.

Peeler, D. K. and Edwards, T. B. (2004) ‘Impact of redox on glass durability: the glass selection process.’ WSRC-TR-2004-00135, Savannah River Technology Center, Aiken, SC (United States).

Piepel, G., Cooley, S. K., Muller, I. S., Gan, H., Joseph, I. and Pegg, I. L. (2007) ‘ILAW PCT, VHT, Viscosity, and Electrical Conductivity Model Development. VSL-07R1230-1, Rev. 0’, (June 2017).

Piepel, G. F., Amidan, B. G., Heredia-langner, A., Weier, D. R. and Cooley, S. K. (2005) ‘Statistical Methods and Results for WTP IHLW and ILAW Compliance.’ PNWD-3568., Battelle—Pacific Northwest Division Richland, WA. (United States).

Piepel, G. F., Cooley, S. K., Heredia-langner, A. Landmesser, S. M., Kot, W. T., Gan, H. and Pegg, I. L. (2008) ‘Final Report IHLW PCT, Spinel $T_{1\%}$, Electrical Conductivity, and Viscosity Model Development.’ VSL-07R1240-4, Pacific Northwest National Laboratory, Richland, WA. (United States).

Rodriguez, C. P., McCloy, J. S., Schweiger, M. J., Crum, J. V. and Winschell, A. (2011) ‘Optical Basicity and Nepheline Crystallization in High Alumina Glasses’, (February), p. 92.

Seymour, R. G. (1995) ‘Evaluation of Alternative Chemical Additives for High-Level Waste Vitrification Feed Preparation Processing.’ WHC-SD-WM-SP-009. Westinghouse Hanford Company, Oak Ridge, TN (United States).

Smith, G. L. Bates, D. J., Goles, R. W., Greenwood, L. R., Lettau, R. C., Piepel, G. F., Schweiger, M. J., Smith, H. D., Urie, M. W., Wagner, J. J. (2001) ‘Vitrification and Product Testing of C-104 and AZ-102 Pretreated Sludge Mixed with

Flowsheet Quantities of Secondary Wastes.' PNNL-13452. Pacific Northwest National Laboratory. Richland, WA (United States).

Soderquist, C. Z., Schweiger, M. J., Kim, D. -S., Lukens, W. W. and McCloy, J. S. (2014) 'Redox-dependent solubility of technetium in low activity waste glass', Journal of Nuclear Materials. Elsevier B.V., 449(1–3), pp. 173–180.

Um, W., Luksic, S. A., Wang, G., Saslow, S., Kim, D.-S., Schweiger, M. J., Soderquist, C. Z., Bowden, M. E., Lukens, W. W. and Kruger, A. A. (2017) 'Enhanced ^{99}Tc retention in glass waste form using Tc(IV)-incorporated Fe minerals', Journal of Nuclear Materials, 495, pp. 455–462.

Vienna, J. D. (2010) 'Nuclear Waste Vitrification in the United States: Recent Developments and Future Options', International Journal of Applied Glass Science, 1(3), pp. 309–321.

Vienna, J. D., Skorski, D. C., Kim, D. -S. and Matyáš, J. (2013) 'Glass Property Models and Constraints for Estimating the Glass to be Produced at Hanford by Implementing Current Advanced Glass Formulation Efforts PNNL-22631, Rev. 1', Pacific Northwest National Laboratory, Richland, WA (United States).

Vienna, J. D., Kim, D.-S., Muller, I. S., Piepel, G. F. and Kruger, A. A. (2014) 'Toward Understanding the Effect of Nuclear Waste Glass Composition on Sulfur Solubility', Journal of the American Ceramic Society, 97(10), 3136–3142.

Yalmali, V. S., Deshingkar, D. S., Wattal, P. K. and Bharadwaj, S. R. (2007) 'Preparation and characterization of vitrified glass matrix for high level waste from MOX fuel processing', Journal of Non-Crystalline Solids, 353(52–54), pp. 4647–4653.

Yue, Yuan-Zheng. (2008) 'Characteristic Temperatures of Enthalpy Relaxation in Glass.' Journal of Non-Crystalline Solids 354 (12–13): 1112–18.

9 Discussion

9.1 Overview

As stated in the introduction, section 1.1, improved understanding of foam mechanisms and redox behaviour in simulated radioactive waste feeds will help to develop protocols for relevant issues that may arise during vitrification of Hanford radioactive wastes (Peeler et al. 2015; Gephart 2010). Thus far, many of the properties of generic waste stream behaviour inside Joule-heated ceramic melters have been modelled (Guillen 2015; Guillen et al. 2018; Abboud, Guillen, and Pokorný 2016). However, the work is incomplete; these models must be able to demonstrate effective processing "across the full WTP compositional envelope" (Peeler et al. 2015). The following sections describe how each of the experiments performed here address the question of understanding the melting behaviour of waste feeds high in multivalent components, in the context of previous literature, and in scaling up the ideas presented to larger experiments and, ultimately, potential adaptation or implementation at the Hanford Site.

9.2 Effect of carbon content and source on melting behaviour

9.2.1 Effect of raw material change on foaming

In the two studies which analysed the melting rate (Matlack, Viragh, et al. 2015) and melting behaviour (Marcial, Kloužek, et al. 2021) with iron hydroxide $Fe(OH)_3$, goethite (FeOOH), haematite (Fe_2O_3) and magnetite (Fe_3O_4) raw materials for iron, there was no correlation between the raw materials that produced the most foam and those that had the slowest melting rate, or with the form of iron in the Fe_3O_4 raw material. Those two studies in particular highlight the unpredictability of feed behaviour inside the melters. The attempt to model the melting rate of feeds based on the temperature of foam collapse, amongst other feed parameters, by the melt rate correlation equation (MRC), overestimates the melting rate for the original feed with the $Fe(OH)_3$ slurry raw material. Two possibilities are stipulated by (Marcial, Kloužek, et al. 2021) to explain the discontinuity with the melting rates, first that the chemically bound water content (H_2O/Fe) has a greater influence on the melting rate than previously understood and second that the melt viscosity is changing.

Out of those previous studies came the motivation for an entirely reduced iron source, $FeC_2O_4 \cdot 2H_2O$, which showed promising foam reduction in the HLW-Al-19 feed (Guillen et al. 2020; Hujová, Pokorný, et al. 2018). The remainder of Chapter 4 compares the melting behaviour of HLW-NG-Fe2 with the original $Fe(OH)_3$ slurry raw material and HLW-NG-Fe2-II with $FeC_2O_4 \cdot 2H_2O$, for foaming behaviour, structural behaviour of iron and some of the melting rate parameters.

By using $FeC_2O_4 \cdot 2H_2O$ as a raw material in the HLW-NG-Fe2 feed, rather than $Fe(OH)_3$, we observed a reduction in peak foaming of 50.6 ± 5.1 % and of total foaming during melting of 43.8 ± 4.4 %, from section 4.3, Table 4.3.1. The effect on foam reduction in the HLW-NG-Fe2 feed using this raw material was greater than in the HLW-Al-19 feed measured previously, Chapter 2, section 2.5.3 (Guillen et al. 2020;

Hujová, Pokorný, et al. 2018). This is due to an increased amount of carbon through the raw material used for the higher wt% Fe_2O_3 in the glass, Chapter 2, section 2.6. Other factors that may be influential are the chemically-bound water content of the raw material and melt viscosity, as stipulated previously (Marcial, Kloužek, et al. 2021), however, these have not been investigated in the present work. From the impact of carbon addition emerges the following study in Chapters 5-8 on the addition of carbon-based reductants.

9.2.2 Effect of reductant addition on foaming

There is considerable literature to support the successful application of foam reducing agents, discussed in Chapter 2, section 2.8.1 (Bickford and Diemer Jr 1986; Goldman 1986; Drobnik 1972; Ross 1978; Blair 1976; Straub 1973). While sucrose is accepted as the baseline reductant for LAW feeds (Matlack et al. 2006; Muller et al. 2009; Hrma, Pokorný, et al. 2011; Appel et al. 2019), it is highlighted that the mechanism of foam production is different in HLW feeds with much lower nitrate contents (Kruger, Matlack, Pegg, et al. 2012). Investigation of alternative reductants for high-foaming HLW feeds, will help to feed new algorithms for high-foaming HLW feeds, by adding to the "limited amount" of testing of organic compounds in WTP HLW feeds (Kruger, Matlack, Pegg, et al. 2012; Matlack, Kruger, et al. 2011; Seymour 1995). In Chapters 5-8 the addition of 3 wt% sucrose in HLW-NG-Fe2 is compared with additions of 3 wt% formic acid, graphite, coke (93 wt% C) and N'(-2 hydroxyethyl) ethylenediamine-NNN' triacetic acid (HEDTA), for effects on foaming and structural behaviour and redox state during melting.

The feed volume expansion tests of the 6 feeds in section 5.3 uncover a relatively linear relationship between the carbon content per gramme of reductant added and the maximum foam volume, Figure 5.3.2. This linearity may be suggested taking a holistic view of the studies on sucrose additions to HLW (Kruger, Matlack, Pegg, et al. 2012;

Seymour 1995; Henager et al. 2011; Josephs and Stone 2001), however, it has not been directly observed before. These findings support the idea that the amount of carbon added to each feed is the most influential factor when choosing a reductant. However, given that addition to the feed at an equal carbon content was not tested in this study, the specific effects of each carbon source based on its chemical nature, decoupled from total carbon content, have not yet been addressed and this question is suggested for future research. For high-multivalent species feeds, where gas evolving reactions are continuing to occur beyond primary foaming, the reductants must not dissociate prior to the temperature of these reactions (Knavish and Harrell 1991). High-temperature interaction of the reductants with the melt are demonstrated by the HLW-NG-Fe2-G, -C and -H feeds in the thermal analysis, section 5.4, and gas evolution, section 5.5.

The mechanism of foam reduction with both carbon addition via reductants and raw material, is largely due to be the earlier release of gases that would otherwise be trapped within the foam, (Ryan 1995; Bickford, Hrma, and Bowan 1990). The addition of carbon to a feed alters the gas profiles, Figure 5.5.1-5. More CO_2 evolved prior to the foam onset in the HLW-NG-Fe2-S, -F and -H feeds than in the HLW-NG-Fe2 feed. While HLW-NG-Fe2-C and -G feeds had sustained CO and CO_2 release at higher temperature. The decomposition of coke and graphite appears to be reaching the temperatures at which redox reactions are energetically favourable (Kruger et al. 2013; Ryan 1995; Seymour 1995). As suggested in the literature (Fedorov and Pilon 2002), an increase in primary foaming to supress secondary foaming, may be preferential for melting rate of the feeds. The evolution of CO, Figure 5.5.2, and the complete suppression of O_2, Figure 5.5.5, is the most striking difference between the HLW-NG-Fe2-R feeds, and is indicative of the available oxygen in the feeds at the different temperatures, and therefore preferential evolution of CO/CO_2. The gas balance performed based on theoretical calculations of evolved gases compared to the EGA,

Table 5.5.3-5, shows the effect of a reducing atmosphere on the quantities of CO, NO and SO_2 evolved, as well as the source of the highly negative O_2 balance.

9.2.3 Melt Rate Correlation Equation

The MRC overestimates the melting rate of the HLW-NG-Fe2 feed when compared to the measured melting rate (Hrma et al. 2018), discussed in Chapter 2, section 2.4.3. Most of the feeds for which the MRC overestimates the melting rate are particularly high in multivalent species (Lee, Hrma, Pokorný, Kloužek, et al. 2019), indicating that the impact of secondary foam behaviour is not understood to the point where it is accurately included in models, as discussed in section 9.2.2.

Using thermal analysis in combination with the FETs, the melting and foaming behaviour of the feeds were explored and it was possible to estimate relative melting rates of each of the feeds using the MRC equation, in section 5.7. The HLW-NG-Fe2-F feed was shown to have a slightly improved melting rate. The study did not take into account varying the use of bubblers, which would require a research-scale melter system: the stability of foam would be decreased with bubbling through the melt and therefore melting rate improved (Pokorný et al. 2015; Abboud and Guillen 2016; Abboud, Guillen, and Pokorný 2016; Lee, Hrma, Pokorný, Kloužek, et al. 2019).

The feed volume expansion test may underestimate the impact of secondary foaming on the heat transfer. Since parameters of the MRC are based on the FET curve analysis, this could explain the underestimation of the melting rate in HLW-NG-Fe2. In particular the temperature of the bottom of the foam, T_{FB}, would be affected in this theory. This is an often disputed parameter, commonly taken as the maximum foaming temperature, i.e., the collapse of the primary foam. However, where there is prevalent secondary foaming this will not be the case, the effects of "gas bubbles from redox reactions and the dissolving residues of solid particles" should be taken into account in a complete model (Hrma et al. 2018).

9.3 Evolution of the local environment of multivalent species during melting

The form of iron during melting is the most distinct feature between the HLW-NG-Fe2-R feeds. For each feed, quenched at 600, 800, 1000 and 1150 ℃ the proportions of amorphous Fe^{3+} and Fe^{2+} were calculated by ^{57}Fe Mössbauer spectroscopy, sections 6.4.1 and 6.4.2, and the proportions of Fe_2O_3 and $(Mn,Ni,Fe)Fe_2O_4$ by both XRD, section 6.2, and ^{57}Fe Mössbauer spectroscopy. The measurements of crystalline Fe phase, between the two techniques have a standard deviation of 1.0 and 1.3 wt% for Fe_2O_3 and $(Mn,Ni,Fe)Fe_2O_4$, respectively.

9.3.1 Iron-bearing crystalline phase evolution

As discussed in Chapter 2, section iron-bearing spinels are not a concern to processing or final glass quality at < 1 vol% at 950 ℃ (Matlack et al. 2012; Kruger et al. 2009; Matlack, Kot, et al. 2015). Under reducing conditions, by addition of carbon, an increase in spinel/Fe_2O_3 was observed along with an overall increase in crystallisation (Karamanov et al. 2000).

With increasing temperature during melting, the transition from haematite to the formation of spinels is common in HLW feeds (Xu et al. 2015; Guillen et al. 2020; Dixon et al. 2015b), measured on quenched samples of feed at different temperatures, as in the present study, sections 4.4.1 and 6.2. In-situ, high-temperature XRD would allow analysis of the amount of spinel forming during melting, however, the volume change of the samples during melting renders it difficult to obtain accurate measurements. From the quenched crucible melt studies in the present work, the spinel quantity observed is the amount of spinels precipitated during quenching, (Xu et al. 2015; Guillen et al. 2020; Dixon et al. 2015b) which is likely higher than the amount present during melting at the higher temperatures where a considerable amount would have dissolved. All

crucible samples were melted and quenched under the same conditions so it is reasonable to compare spinels the SoM samples and glasses in Chapters 4-8.

In the HLW-NG-Fe2 samples, at 600, 800, 1000 and 1150 ℃, the iron is present as tetrahedral Fe^{3+}, by ^{57}Fe Mössbauer spectroscopy, Chapter 6 section 6.4.1, while X-ray Absorption Near-Edge Spectroscopy indicates a movement from octahedral Fe^{3+} to tetrahedral Fe^{3+} with increasing temperature, and a proportion of Fe^{2+} also present. The Fe K-edge XANES data more closely represents the interpretation of the Fe K-edge XANES measured previously (Guillen et al. 2020) – there is an increase in coordination number and Fe^{2+} content between 600 and 800 ℃ (samples quenched at 500 ℃, and 850 ℃ were measured in place of 600 ℃ and 800 ℃ in (Guillen et al. 2020)). The mixture of crystalline and amorphous iron in the samples makes the uncertainties associated with the XANES interpretation large. The ^{57}Fe Mössbauer data can resolve these constituents independently, and the resolution of the paramagnetic doublets is reduced when there is a significant amount of crystalline material (the 600 and 800 ℃ samples). In a previous investigation of the C-106/AY-102 feed under different redox conditions, by varying addition of nitrates and oxalates, up to 10 % Fe^{2+}/Fe_T was observed with 50 g oxalate added per kg of glass (Kruger, Matlack, Pegg, et al. 2012).

Crystalline spinel precipitation in the final glasses was found in Chapter 8, section 8.4.1 to be highest in feeds with the highest oxygen partial pressure, HLW-NG-Fe2-S, G, C and -H, Chapter 7, section 7.8. This behaviour is reflected in the spinel precipitation in the heat treated samples in Chapter 8, section 8.4.3.

9.3.2 Structure of iron in the final glasses

As discussed in Chapter 2, section 2.2.3, the coordination number and redox state of iron in the amorphous phase determines how the iron functions in the glass network, as a network former or modifier (Farges et al. 2005; Ahmadzadeh, Scrimshire, Bingham, Goel, et al. 2018; Cochain et al. 2012). In general, it is expected that tetrahedral Fe^{3+} is

network forming and octahedral Fe^{2+} is network modifying, (Cochain et al. 2012; Cochain and Neuville 2008; Shaharyar et al. 2016; Mysen and Virgo 1989; Greaves, Binsted, and Henderson 1984). The structure of iron is important when understanding properties of the glass (section 9.4.1).

Apart from the reduction of Fe^{3+}/Fe_T in the HLW-NG-Fe2-G, C and -H feeds, discussed in Chapter 7, section 7.10.1 and Chapter 8, section 8.3.1, one of the only indicators of fundamental structural changes in the glass is identified by Raman spectroscopy, in the peak ~ 610 cm^{-1}, Chapter 6, section 6.3.2, Figure 6.3.2. The danburite-like ring structure peak, discussed in Chapter 4, section 4.4.3 and Chapter 6, section 6.3.2, is explained by the theory that Fe^{3+} and BO_4 units are competing for charge compensation by Na^+, allowing more danburite-like ring units to form in the absence of Fe^{3+}, causing the 610 cm^{-1} peak to emerge (Koroleva, Shabunina, and Bykov 2011; Hubert and Faber 2014; Cochain et al. 2012). Plotting the peak area against redox state of Fe is insufficient due to variation in Fe content of the final glasses by XRF, Chapter 8, section 8.2.1, and the spinel quantity, by XRD, Chapter 8, section 8.4.1, with varying levels of Fe^{2+} and Fe^{3+} present. Assuming that all of the 3+ 'B' sites in the identified 'AB_2O_4' spinels are Fe^{3+} the ~610 cm^{-1} peak area was plotted against the total Fe^{3+} content in the glass, Figure 9.3.1, The assumption likely overestimates total Fe^{3+} content as it is known from Chapter 8, section 8.4.1, that some spinels contain Cr, presumably as Cr^{3+} on the B site. There is some correlation observed between the quantity of Fe^{3+} in the glass and the integrated peak area, that is not followed by the HLW-NG-Fe2-G sample. The 3 wt% G is also the outlier in the HLW-NG-Fe2-G series, in Chapter 6, section 6.3.2, having a reduced 610 cm^{-1} peak area compared to the 2, 3 and 5 wt% graphite samples.

There is little literature on the relationship between Fe^{3+} content and danburite-like ring structures in the range Fe^{3+}/Fe_T 0-0.6, however, one study suggested that this Raman band increased further for Fe^{3+}/Fe_T = 0.15, than it had at > 0.6 (Cochain et al. 2012).

The reason for the decrease in the danburite-like peak area is not clear from the analysis performed, if indeed this band can be attributed to danburite-like rings. Further research is needed to establish this. The transient nature of the band in the Raman spectra was investigated in Chapter 4, 0.

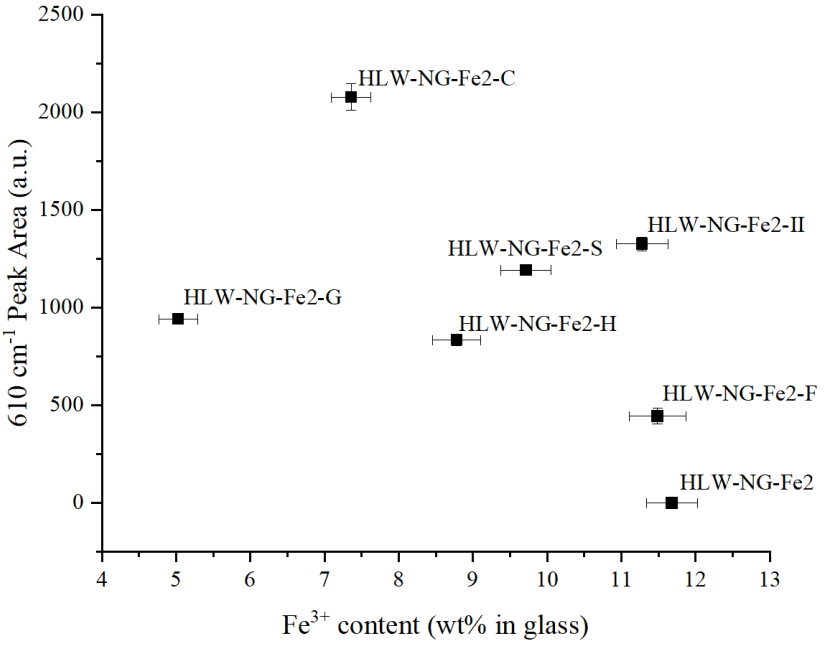

Figure 9.3.1. Area of the 610 cm^{-1} danburite-like ring peak for each of the HLW-NG-Fe2 glasses made with each of the reductants. Above 6 wt% Fe^{3+} content there is a negative relationship in the area of the peak with increasing iron content. HLW-NG-Fe2-G has low Fe^{3+} content but a moderate peak area.

The structural change is also apparent in the glass transition temperature, and therefore potential glass viscosity, in the glasses in section 8.5.1. This is explained by iron becoming network modifying (octahedrally coordinated Fe^{2+} or Fe^{3+}) in reduced glasses (Cunnane et al. 1994). In light of the other structural relationships identified by Raman spectroscopy, there is a potential further mechanism at play related to the proportion of Fe^{3+} tetrahedra and BO_4 units. AlO_4 and BO_4 in aluminoborate glasses (Klyuev and Pevzner 2002). Perhaps this is also the case with FeO_4 tetrahedra. A higher quantity of BO_4 units is expected in reduced glasses (Cochain et al. 2012), where there is less competition by Fe^{3+} tetrahedra for BO_4 tetrahedra.

The deviation from the relationship in the danburite-like peak with Fe^{3+} content in the HLW-NG-Fe2-G glass, may be indicate a limit for which the relationship applies, that also means there is a minimum reduction in glass transition temperature and viscosity. Otherwise, we might expect the T_g to have reduced even further in the HLW-NG-Fe2-G and -C glasses than the HLW-NG-Fe2-S and -H glasses. To understand the deviation from this behaviour in the HLW-NG-Fe2-G glass, ^{11}B Magic Angle Spinning – Nuclear Magnetic Resonance (MAS-NMR) or B K-edge XANES would enable a more comprehensive understanding of the influence of the form of iron on the structure of boron in the glass (Ollier et al. 2004; Cochain et al. 2012).

9.3.3 Evolution of Fe, Mn, Ni, Cr and Ce during melting

The redox state of a feed, or melt, influences more than just the O_2 contribution to foaming: the redox state can affect the retention of volatile species (Kruger, Matlack, Pegg, et al. 2012; Pinet, Hugon, and Mure 2014; George, Kim, and Kruger 2020) furnace refractory corrosion (Pinet, Hugon, and Mure 2014; Bingham et al. 2011; Gan et al. 2009), melt conductivity (Kruger, Matlack, Pegg, et al. 2012; Goldman 1986), chemical durability (Peeler and Edwards 2004) and, as discussed in section 9.3.1, the amount of crystallinity (Gan et al. 2009; Karamanov et al. 2000).

The iron redox state is often used as the measure of redox in a glass batch, and to quantify the oxygen partial pressure (Hujová, Pokorný, et al. 2018; Zhernovaya, Onishchuk, and Davydoglu 2007; Bickford et al. 1990), which is a reasonable approximation for waste streams, or industrial glass batches and melts that contain high levels of iron, and insignificant amounts of other multivalent oxides. In work by Goldman (Goldman 1986), even when there is no detected ferrous iron in the glasses, there is oxygen evolution associated with other redox species such as chromium, cerium and manganese. Other multivalent species, Mn, Cr, Ni and Ce, have been investigated for a range of properties in commercial glass melting (Hubert et al. 2014, 2017;

Bingham and Jackson 2008; Wondergem-de Best 1994; Villain et al. 2007) and in radioactive waste streams (Hrma et al. 2006; Jantzen and Stone 2007; Jantzen et al. 2003). The development of understanding of mixed multivalent species effects in complex glass systems glasses is presented in Chapter 2, section 2.7.3.

These tools are used in the following discussion to help interpret the redox behaviour of the HLW-NG-Fe2 feed. Other models of redox behaviour developed to particularly address redox reactions within the cold cap for US waste treatment programs (Hanford and Savannah River sites) have been developed since (Jantzen et al. 2003). The results of this work aim to provide further data to improve these model predictions for wastes high in multivalent species.

The majority of the redox changes observed by XANES in this chapter 7, were predicted by the modelling work performed on previous mixed-multivalent species glasses. Where there were limitations on the accuracy of the XANES data the interpretation is qualitative. This applied to the measured Fe and Mn K-edges XANES. For Fe, ^{57}Fe Mössbauer spectroscopy provides complimentary data.

Two interesting deviations in the expected behaviour occurred. The first in the HLW-NG-Fe2 feed, for which Mn^{4+} preferentially reduced to Mn^{2+}, to completion, over the Ce^{4+}/Ce^{3+} reaction, leaving some oxidised Ce^{4+} in the final glass. The second incidence is in the HLW-NG-Fe2-G feed where there is a reoxidation of some Cr^{3+} to Cr^{6+} at 1150 °C. The analytical techniques used in this study are inadequate in providing a complete understanding of the redox behaviour of the complex feed compositions. Further limiting the interpretation of the data, O_2 is available during melting in the electric furnace. Where the EGA was performed in a He atmosphere, the samples quenched for XANES were melted in electric furnaces in air.

The overall trends in reduction of the multivalent species with heat-treatment temperature, to differing extents based on their reduction potentials is observed, and

provides estimates of the melt partial pressure and evolution of O_2. The *f(O_2)* values, reported in Chapter 7, section 7.8, while still estimations based on the average redox states of the multivalent species, are consistent with previous studies of glasses bearing similar levels of Fe_2O_3 (Pinet, Hugon, and Mure 2014; Hubert et al. 2017; Thiemsorn et al. 2008b; Jantzen and Stone 2007; Hujová, Pokorný, et al. 2018). Intuitively, the reductants which had the most negative effect on oxygen balance, graphite, coke and HEDTA, section 7.8, also had the most negative effect on the oxygen partial pressure.

9.3.4 Balance of Oxygen

Including O_2 from redox reactions in the balance of oxygen, in Chapter 7, Table 7.9.2, overcompensates for the previous lack of O_2 calculated for the HLW-NG-Fe2 feed calculated in Chapter 5, section 5.5.3. The values are now far more consistent. The O_2 contributions for the HLW-NG-Fe2-R feeds compensate somewhat for the highly negative O_2 balance, but not sufficiently to be consistent with the EGA results.

Many studies of redox reactions in the cold cap, and glass melting in general, have focussed on the Fe redox alone in balancing oxygen in the melt (Lee, Hrma, Kloužek, et al. 2017; George, Kim, and Kruger 2020; P. A. Smith, Vienna, and Hrma 1995; Hujová, Pokorný, et al. 2018). In this work, we have shown that the other multivalent species, if not at least the Mn in this feed, must be considered when examining contributions to oxygen evolution. At the sample sizes used in this study the difference in O_2 evolution between the feeds may not appear significant, however, in a full-scale melter, where these O_2 bubbles are trapped by the cold cap, suppression of O_2 and SO_2 evolution could have much greater consequences, as discussed in section 9.2.2. The effects of O_2 and SO_2 evolution on foaming behaviour in commercial glass melts and calcined waste glasses are easier to predict (Beerkens 1999; Arkosiová, Kloužek, and Němec 2008; Hujová and Vernerová 2017) than in complex radioactive waste feeds during direct feed vitrification, with multiple overlapping reactions (Hrma et al. 2010).

9.4 Application and scale-up of the range of foam controlling techniques

As well as the academic investigations of foaming and redox behaviour, this research has provided a range of options for foam control, with suitable supportive data to understand their effects on the glass melting and foaming behaviour, as well as the properties of the final glass. Quality control of the final glass products is the subject of much research, and property models are used to design waste glass compositions prior to testing (Vienna, Kim, and Hrma 2002; Vienna et al. 2013; Muller et al. 2013; Vienna et al. 2016; Piepel et al. 1993). The exploration of the extreme case of foaming for the HLW-NG-Fe2 feed, compared with other waste feeds, will be of interest to modelling the vitrification process, but also provides an interesting case to explore foaming issues that appear in many commercial glass-melting processes (Wondergem-de Best 1994; Beerkens 1999; Manring and Diken 1980).

As discussed in section 4.6.3, an alternative raw material is not a practical flowsheet change, since the iron hydroxide arises from the waste in the HLW-NG-Fe2 feed (G. L. Smith et al. 2001). However, the implications of starting with a reduced raw material on the glass properties will be of interest to studies of some LAW glasses (where iron is added to the feeds), and will expand the literature on raw-material options for iron-containing commercial glasses and other industrial waste glasses (Mirhadi and Mehdikhani 2011a; Deng et al. 2020; Romero and Rincón 1998).

9.4.1 Final Glass Product Quality

By initial characterisation of the HLW-NG-Fe2 and HLW-NG-Fe2-II glasses, Chapter 4, section 4.6.2, the glasses are structurally similar by XRD and ^{57}Fe Mössbauer spectroscopy, indicating no immediate threat to the product quality posed by the alteration of the raw material for iron. The Raman spectroscopy, section 4.4.3,

highlighted a structural change in the glass which is linked to the content of glass-forming Fe^{3+}, section 9.3.2. PCT-B of the HLW-NG-Fe2 and HLW-NG-Fe2-II glass samples, Chapter 8, section 8.6 show an increase in the leaching rates of B and Li in the HLW-NG-Fe2-II sample compared with the previously measured HLW-NG-Fe2 glass (Matlack et al. 2012). While the leaching rates are within the < 4 g L^{-1} limit (Piepel et al. 2007), the reduction in chemical durability, and glass transition temperature (section 8.5.1) and the transient Raman band feature, all suggest that there is a structural change in the final HLW-NG-Fe2-II glass that has not been explained by a change in the iron redox state within the detection limit of the ^{57}Fe Mössbauer spectroscopy, or any significant change in the level of crystallinity. Similar structure-properties relationships were explored in the HLW-NG-Fe2-R glasses, discussed in section 9.3.2.

Chapter 8 provides the evidence to support the view that the adoption of the reductants to the vitrification flowsheet would have varying effects on the final glass properties depending on the total carbon content of the reductant employed. The results of the measured glass properties in Chapter 8 are summarised in Figure 9.4.1, along with the contract limits employed at the WTPs and the maximum normalised foam volume to demonstrate reductant effectiveness on reducing foam.

The influence of redox state on the chemical durability was explored, comparing the HLW-NG-Fe2-II, -F and -G glasses to the HLW-NG-Fe2 by PCT-B. There is insufficient evidence collected in the present study to conclude structure-property relationships, however it does provide some interesting scenarios for future exploration. There are seemingly multiple mechanisms at play, not only the redox state of Fe, and its structural implications, but other structural changes that are perhaps observed in the increase in danburite-like ring structures in the HLW-NG-Fe2-II glass, without a reduction in Fe^{3+} content, that lead to a reduction in chemical durability.

The melt viscosity plays a significant role in the processing of the feeds (Lee, Hrma, Pokorný, Kloužek, et al. 2019) and the contract limits are set at 1 - 15 Pa.s at 1100 ℃ (Piepel et al. 2007). The glass transition temperature, T_g, indicates that there is reduced viscosity in the HLW-NG-Fe2-II, S, G, C and H glasses compared to the HLW-NG-Fe2 and HLW-NG-Fe2-F glasses. Viscosity measurements would be required to confirm whether these glasses are still within the viscosity limits.

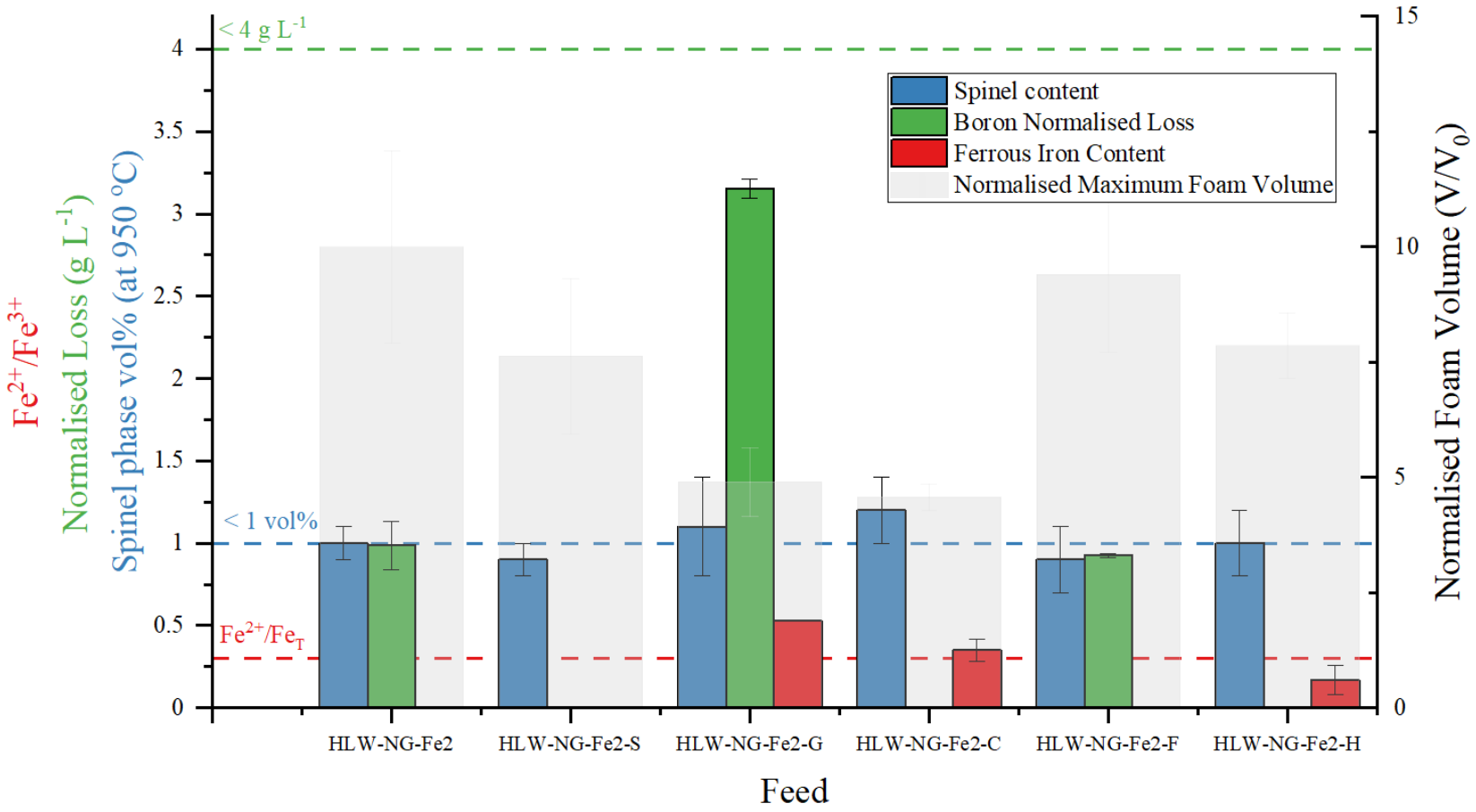

Figure 9.4.1. Summary of the measured glass properties of the HLW-NG-Fe2-R feeds, along with the contract limits for these properties employed at the Waste Treatment Plants, and the maximum normalised foam volume for each of the feeds during melting.

9.4.2 Scale-up to Laboratory Scale Melter System

In Chapter 4, section 4.5 the successful scale-up from crucible studies to the Laboratory Scale Melter (LSM) system was demonstrated for the HLW-NG-Fe2-II feed. The melter run produced a sufficient sample with no feeding or excessive foaming issues. The HLW-NG-Fe2 feed was deemed unsuitable for testing in this melter due to the high feed rheology. Although increased viscosity of the HLW-NG-Fe2 feed with Fe(OH)3 was reported, previous demonstrations of this feed in larger melter systems report no feeding issues (Kruger, Matlack, Pegg, et al. 2012; Matlack, Viragh, et al. 2015; Matlack et al. 2012). The diameter of the tubing in the LSM was likely the bottleneck, Chapter 3, section 3.3.4. Since the addition of 3 wt% of each of the reductants, Chapter 5, section 5.1, is unlikely to significantly affect the feed rheology, only the HLW-NG-Fe2-II feed was suitable for testing via this method.

Comparison of the quenched LSM sample with the crucible melts at different temperatures, Figure 4.5.3, showed that the structure and morphology of the LSM sample was representative of the higher temperature crucible melts > 800 ℃. By X-ray tomography of the LSM sample some novel methods of analysing bubble distributions throughout the cold cap were explored (Luksic et al. 2021, 2020; Harris et al. 2017). The porosity with height through the cold cap, Figure 4.5.6, was shown to correlate well with the feed volume expansion test, Figure 4.3.4, for both the main primary foam peak and the sustained secondary foaming beyond the first peak. This has been observed once before in a study on the HLW-Al-19 feed (Luksic et al. 2021), and is shown in more clarity in this HLW-NG-Fe2-II feed. The average size of the bubbles contributing to this sustained secondary foaming is significantly lower than those contributing to the primary foaming. As discussed in section 9.2.2, the amount of secondary foam bubbles can be underestimated for their effect on heat transfer and overall foam expansion by

feed volume expansion tests. In this X-ray tomography study of the HLW-NG-Fe2-II sample, the impact of these small bubbles on overall porosity is conclusively presented. Running only the HLW-NG-Fe2-II feed is a largely academic exercise, however, the confirmation that some of the analysed properties of the SoM samples apply also to the LSM sample is promising for scale up of the HLW-NG-Fe2-R feeds. A full analysis of the scale-up of the crucible studies to the Laboratory Scale Melter sample analysis is beyond the scope of this work. However, Chapter 4 provided some additional data using novel analytical tools that may be useful for future analysis of these, or related, samples. The Laboratory Scale Melter system itself is a dynamic system and there is great value in running tests with this system to observe the cold cap creation (Dixon et al. 2015b; Riley et al. 2009; D. S. Kim et al. 2012). However, there are limitations to how accurately the smaller melter system represents full-scale melting, particularly in bridging of the cold cap and creation of large vent holes, which may be influenced by the melt surface area (Hrma 1990b; Pokorný and Hrma 2011; Guillen and Agarwal 2013). Much of the relevant work in the present study was performed on the quenched cold cap, post melter run. This quenched cold cap has the limitations of being a snapshot in the complex dynamic melting process, and subject to quenching effects, both limiting the applicability of the results to the full-scale system (Harris et al. 2017; Guillen et al. 2018; Choi et al. 2017). Furthermore, the use of bubblers to break up foaming is beyond the scope of this study. Bubbling is an important mechanism for influencing both foam volume and heat transfer (Pokorný, Kruger, and Hrma 2014; Hrma et al. 2018). For these reasons discussed, scale up of the research in this study would need to include research scale melters (Matlack, Gan, et al. 2009; Matlack, Viragh, et al. 2015).

9.4.3 Suitability of reductants for further study

The feed volume expansion results, section 5.3, show the most effective additives for reduction of foam during melting. Graphite and coke reduced the total foam volume more effectively, although as noted previously, the amount of carbon in each reductant differed due to differences in reductant chemistry. Formic acid did not have a great effect on the foam volume expansion, and sucrose and HEDTA had some effect. Figure 7.10.1 summarises the relationship between the redox state of the final glass and the reduction in normalised maximum foam volume for each of the feeds, showing that the reductants that had a significantly reducing effect on the iron in the final glass, also had a reducing effect on the peak foam volume, but not vice versa.

In terms of suitability for processing, all samples were close to the limit for spinel concentration. The glass viscosity, indicated by T_g section 8.5.1, suggests that the lower Fe^{3+} content in the HLW-NG-Fe2-S, -G, -C, and -H glasses would lead to a lower viscosity than those with higher Fe^{3+} content, HLW-NG-Fe2, HLW-NG-Fe2-II and -F. HLW-NG-Fe2-G and -C are outside of the contract limits for redox state of Fe (Larson 1996; Jantzen 2011; Peeler and Edwards 2004), however, HLW-NG-Fe2-II, -F and -G glasses within the limits for leaching rates of the glasses for long-term immobilisation of radioactive wastes, for those elements measured, namely Li and B. The experiment would need to be repeated to determine values of Si and Na.

The most effective reductants, graphite and coke, compromise on the redox state of iron and precipitation of Fe, Mn, Cr and Ni -bearing spinels. There is also evidence of reduced viscosity and chemical durability in the HLW-NG-Fe2-G glass. The limit is considered conservative in (Weimers et al. 1996; Seymour 1995), and since no metallic precipitation was observed in any of the glasses, this study provides further evidence that may be the case. There is, however, evidence provided for reduced chemical durability with reduced iron redox state.

Considering the effects on the redox state of iron and chemical durability, the amount of graphite or coke added to the feed could be decreased. In further work, studies of incremental additions of coke and graphite to the feeds may be considered. It is conceivable that at a lower wt% addition, effects on foam volume would be appreciable without negatively impacting the desired properties of the final glass. Optimisations of the wt% addition, along with the particle size of the reductant, are suggested for further work (Liukkonen, Penttilä, and Koukkari 2012; Yu et al. 2014; Ryan 1995).

Due to practical considerations, this research does not provide a comprehensive review of the carbon-based reductant additions to all HLW feeds, only the HLW-NG-Fe2 feed, and redox control of HLW feeds should be treated on an individual basis until a complete predictive model is obtained. However, in a feed with considerable levels of multivalent species, the lack of metallic precipitation at 3 wt% reductant addition is promising for application in other HLW feeds and glass batches high in these species.

9.4.4 Environmental impact and impact on project lifetime

The environmental impacts of nuclear fuel production were evaluated in Chapter 2, section 2.1.1 (World Nuclear Association 2011; International Atomic Energy Agency 2017; Adamantiades and Kessides 2009; Köne and Büke 2010). However, the environmental impacts of legacy waste clean-up are not often reported alongside these estimates. With the volume of research required for these legacy waste projects, the Hanford project in particular being the largest and most complex (Guillen et al. 2018; Guillen and Agarwal 2013; Harvey 2000; Washington Department of Ecology State of Washington 2018), there is promise that lessons learned in recycling (Adamantiades and Kessides 2009; US Department of Energy 1999), and immobilisation of radioactive wastes will prove valuable for the future nuclear fuel cycle.

The estimated cost of the remaining clean-up, covering the years 2022-2095, exceeds 300 billion US dollars (Richland Operations Office 2022). The cost and schedule of

waste treatment at the Hanford site WTPs is highly dependent upon the waste loading of the vitrified wasteform and the rate of glass production (Hrma and Pokorný 2016). Improvements to the vitrification process could have positive impacts on the cost and efficiency of the project (Guillen and Agarwal 2013; Marcial, Kloužek, et al. 2021; Kruger et al. 2008). Coke, the most effective reductant for reducing foaming identified in this study is a by-product of many other industrial processes (Pilon 2012; Nemanova et al. 2014; Dankwah, Amoah, and Fosu 2016; Babich and Senk 2018). This may prove to be an environmentally preferable and cost-effective additive for foam reduction.

However, neither coke nor graphite improved the melting rates of the feeds based on the MRC equation parameters measured in this study, section 9.2.3. In fact, formic acid, with the least effect on foam volume, had the highest theoretical melting rate. This highlights that viscosity measurements are necessary to predict melting rate, and relying on most of the sensitivity from the disputed foam bottom temperature is insufficient.

For a melt surface area, in the WTP melters, of 3.75 m (Matlack, Viragh, et al. 2015), the excess CO/CO_2 released per day from addition of each reductant can be calculated. The greatest increase compared to the original feed is in HLW-NG-Fe2-H, with a 104 kg day^{-1} increase in CO_2 and 140 kg day^{-1} increase in CO. The HLW-NG-Fe2-C emits only 6 kg^{-1} of excess CO_2 and 30 kg day^{-1} excess CO, however, this is due to the lower estimated melting rate. Over the lifetime of the feed in the melter, the HLW-NG-Fe2-C will both emit a similar level of CO_2 and CO emissions from batch reactions and use more energy. The increase in CO_2 emissions from the use of formic acid may be offset by the increased melting rate, depending on emissions associated with energy generation to power the melter, and the total time to process the feeds. Application of the reductants would require further evaluation of the benefit to the project timeline, environmental and cost impact overall.

9.5 References

Abboud, A. W. and Guillen, D. P. (2016) 'Computational fluid dynamics modeling of bubbling in a viscous fluid for validation of waste glass melter modeling', International Topical Meeting on Advances in Thermal Hydraulics 2016, ATH 2016, pp. 527–538.

Abboud, A. W., Post Guillen, D. and Pokorný, R. (2016) 'Heat Transfer Model of a Small-Scale Waste Glass Melter with Cold Cap Layer', in 11th International Topical Meeting on Nuclear Thermal Hydraulics, Operation and Safety. (NURETH-11), Avignon (France).

Ahmadzadeh, M., Scrimshire, A., Bingham, P. A. and Goel, A. (2018) 'Structural Role of Iron in Nepheline-based Aluminosilicates for Nuclear Waste Applications.' WM2018 Conference. Phoenix, AZ (United States).

Appel, C. J., Kloužek, J., Jani, N. Lee, S., Dixon, D. R., Hrma, P., Pokorný R., Kruger A. A. and Schweiger, M. J. (2019) 'Effect of sucrose on foaming and melting behavior of a low-activity waste melter feed', Journal of the American Ceramic Society, 102(12), pp. 7594–7605.

Arkosiová, M., Kloužek, J. and Nìmec, L. (2008) 'The Role of Sulfur in Glass Melting Processes', Ceramics - Silikaty, 52(1), pp. 155–159.

Beerkens, R. (1999) 'Redox and sulphur reactions in glass melting processes', Ceramics - Silikaty, 43(3), pp. 123–131.

Bickford, D. F., Applewhite-Ramsey, A., Jantzen, C. M. and Brown, K. G. (1990.) Control of Radioactive Waste Glass Melters: I, Preliminary General Limits at Savannah River. Journal of the American Ceramic Society, 73, 2896–2902.

Bickford, D. F. and Diemer Jr, R. B. (1986) 'Redox control of electric melters with complex feed compositions I. Analytical methods and models', Journal of Non-Crystalline Solids, 84, pp. 276–284.

Bickford, D. F., Hrma, P. and Bowan, B. W. (1990) 'Control of Radioactive Waste Glass Melters: II, Residence Time and Melt Rate Limitations', Journal of the American Ceramic Society, 73(10). pp. 2903–2915.

Bingham, P. A. and Jackson, C. M. (2008) 'Roman blue-green bottle glass: chemical-optical analysis and high temperature viscosity modelling', Journal of Archaeological Science, 35(2), pp. 302–309.

Bingham, Paul A., Connelly, A. J., Hyatt, N. C. and Hand, R. J. (2011) 'Corrosion of glass contact refractories for the vitrification of radioactive wastes: a review', International Materials Reviews, 56(4), pp. 226–242.

Blair, H. T. (1976) 'Vitrification of Nuclear Waste Calcines by In-Can Melting.' BNWL-2061. Battelle-Northwest, Pacific Northwest National Laboratories, Richland, WA (United States).

Cochain, B., Neuville, D. R., Henderson, G. S., McCammon, C. A., Pinet, O. and Richet, P. (2012) 'Effects of the iron content and redox state on the structure of sodium borosilicate glasses: A Raman, Mössbauer and boron K-edge XANES spectroscopy study', Journal of the American Ceramic Society, 95(3), pp. 962–971.

Cochain, B. and Neuville, D. R. (2008) 'Determination of iron redox ratio in borosilicate glasses and melts from Raman spectra', in Atalante, Montpellier (France).

Cunnane, J. C., Bates, J. K., Bradley, C. R., Buck, E. C., Ebert, W. L., Feng, X., Mazer, J. J., Wronkiewicz, D. J., Sproull, J., Bourcier, W. L., McGrail, B. P. and Altenhofen, M. K. (1994) "High Level Waste Borosilicate Glass: A Compendium of Corrosion Characteristics Volume 2" Office of Waste Management, United States Department of Energy. Argonne National Laboratory, IL (United States).

Deng, W., Spathi, C., Coulbeck, T., Erhan, K., Backhouse, D., Marshall, M., Ireson, R. and Bingham, P. A. (2020) 'Exploratory research in alternative raw material sources and reformulation for industrial soda-lime-silica glass batches', International Journal of Applied Glass Science, 11(2), pp. 340–356.

Dixon, D. R., Schweiger, M. J., Riley, B. J., Pokorný, R. and Hrma, P. R. (2015) 'Temperature Distribution within a Cold Cap during Nuclear Waste Vitrification', Environmental Science and Technology, 49(14). pp. 8856–8863.

Drobnik, S. (1991) 'Method of removing nitric acid, nitrate ions and nitrite ions out of aqueous waste solutions.' United States: United States Patent Office: US3,673,086

Farges, F., Rossano, S., Lefrère, Y., Wilke, M. and Brown, G. E. (2005) 'Iron in silicate glasses: A systematic analysis of pre-edge, XANES and EXAFS features', Physica Scripta T, T115, pp. 957–959.

Fedorov, A. G. and Pilon, L. (2002) 'Glass foams: Formation, transport properties, and heat, mass, and radiation transfer', Journal of Non-Crystalline Solids, 311(2), pp. 154–173.

Gan, H., Viragh, C., McKeown, D. A., Muller, I. S., Cecil, R., Kot, Wing K., Joseph, I., Wang, C., Pegg, I. L., Chaudhuri, M., Zhao, W. and Feng, Z. (2009) 'Crystal Settling, Redox, and High Temperature Properties of ORP HLW and LAW Glasses.' VSL-09R1510-1. Vitreous State Laboratory, Washington, D. C. (United States).

George, J. L., Kim, D. -S and Kruger, A. A. (2020) 'Effects of iron oxalate on rhenium incorporation into low-activity waste glass', Journal of Non-Crystalline Solids. Elsevier, 545(June), p. 120257.

Gephart, R. E. (2010) 'A short history of waste management at the Hanford Site', Physics and Chemistry of the Earth. Elsevier Ltd, 35(6–8), pp. 298–306.

Goldman, D. S. (1986) ‘Melt foaming, foam stability and redox in nuclear waste vitrification’, Journal of Non-Crystalline Solids, 84(1–3), pp. 292–298.

Greaves, G. N., Binsted, N. and Henderson, C. M. B. (1984) ‘The Environments of Modifiers in Oxide Glasses’, EXAFS and Near Edge Structure III. Springer Proceedings in Physics., 2, pp. 297–301.

Guillen, D. P. (2015) ‘Bubbling behavior in a waste glass melter’, in 8th International Conference on Computational and Experimental Methods in Multiphase Flow. Valencia, Spain.

Guillen, D. P. Lee, S., Hrma, P., Traverso, J., Pokorny, R., Kloužek, J. and Kruger, A. A., (2020) ‘Evolution of chromium, manganese and iron oxidation state during conversion of nuclear waste melter feed to molten glass’, Journal of Non-Crystalline Solids. Elsevier, 531(December 2019), p. 119860.

Guillen, D. P., Pokorný, R., Eaton, W. C., Dixon, D. R., Fox, K. and Kruger, A. A. (2018) ‘Development of a Validation Approach for an Integrated Waste Glass Melter Model’, Nuclear Technology. Taylor & Francis, 203(3), pp. 244–260.

Henager, S. H., Hrma, P., Swearingen, K. J., Schweiger, M. J., Marcial, J. and TeGrotenhuis, N. E. (2011) ‘Conversion of batch to molten glass, I: Volume expansion’, Journal of Non-Crystalline Solids. Elsevier B.V., 357(3), pp. 829–835.

Hrma, P., Marcial, J., Swearingen, K. J., Henager, S. H., Schweiger, M. J. and Tegrotenhuis, N. E. (2011) ‘Conversion of batch to molten glass, II: Dissolution of quartz particles’, Journal of Non-Crystalline Solids. Elsevier B.V., 357(3), pp. 820–828.

Hrma, P., Vienna, J. D., Wilson, B. K., Plaisted, T. J. and Heald, S. M. (2006) ‘Chromium phase behavior in a multi-component borosilicate glass melt’, Journal of Non-Crystalline Solids, 352(21–22), pp. 2114–2122.

Hrma, P., Pokorný, R., Lee, S. M. and Kruger, A. A. (2018) ‘Heat transfer from glass melt to cold cap: Melting rate correlation equation.’ International Journal of Applied Glass Science, (August) pp. 1–8.

Hrma, P. R. Schweiger, M. J., Humrickhouse, C. J., Moody, J. A., Tate, R. M., Rainsdon, T. T., Tegrotenhuis, N. E., Arrigoni, B. M., Marcial, J., Rodriguez, C. P. and Tincher, B. H. (2010) ‘Effect of glass-batch makeup on the melting process’, Ceramics - Silikaty, 54(3), pp. 193–211.

Hubert, M., Faber, A. J., Sesigur, H., Akmaz, F., Kahl, S. R., Alejandro, E. and Maehara, T. (2017) ‘Impact of Redox in industrial glass melting and importance of redox control’, Ceramic Engineering and Science Proceedings, 38(1), pp. 115–128.

Hubert, M, Faber, A. J., Akmaz, F., Sesigur, H., Alejandro, E., Maehara, T. and Kahl, S. R. (2014) ‘Stabilization of divalent chromium Cr(II) in soda–lime–silicate glasses’, Journal of Non-Crystalline Solids, 403, pp. 23–29.

Hubert, M. and Faber, A. J. (2014) ‘On the structural role of boron in borosilicate glasses’, Physics and Chemistry of Glasses: European Journal of Glass Science and Technology Part B, 55(3), pp. 136–158.

Hujová, M., Pokorný, R., Kloužek, J., Lee, S., Traverso, J. J., Schweiger, M. J., Kruger, A. A. and Hrma, P. (2018) ‘Foaming during nuclear waste melter feeds conversion to glass: Application of evolved gas analysis’, International Journal of Applied Glass Science, 9(4), pp. 487–498.

Hujová, M. and Vernerová, M. (2017) ‘Influence of fining agents on glass melting: A review, part 2’, Ceramics - Silikaty, 61(3), pp. 202–208.

Jantzen, C. M., Koopman, D. C., Herman, C. C., Pickett, J. B. and Zamecni, J. R. (2003) ‘Electron Equivalents Redox Model for High Level Waste Vitrification.’

In Symposium on Waste Management Technologies in Ceramic and Nuclear Industries, American Ceramic Society. Westerville, Ohio (United States):

Jantzen, C. M. and Stone, M. E. (2007) 'Role of Manganese Reduction/Oxidation (REDOX) on Foaming and Melt Rate in High Level Waste (HLW) Melters (U).' WSRC-STI-2006-00066. Savannah River National Laboratory, Aiken, SC (United States).

Josephs, J. E. and Stone, M. E. (2001) 'Melt Rate Improvement for DWPF MB3: Sugar Addition Test (U).' WSRC-TR-2001-00158, Revision 0. Aiken, SC (United States).

Karamanov, A., Pisciella, P., Cantalini, C. and Pelino, M. (2000) 'Iron-Rich Glasses Made with Industrial Wastes.' Journal of the American Ceramic Society 83(12), pp. 3153–3157.

Klyuev, V. and Pevzner, B. (2002) 'The Influence of Aluminum Oxide on the Thermal Expansion, Glass Transition Temperature, and Viscosity of Lithium and Sodium Aluminoborate Glasses.' Glass Physics and Chemistry 28(4), pp. 207–20.

Knavish, L. A. and Harrell, W. C. (1991) 'Melting Glass with Oxidation Control and Lowered Emissions.' United States: United States Patent Office: US5006144

Koroleva, O. N., Shabunina, L. A. and Bykov, V. N. (2011) 'Structure of borosilicate glass according to Raman spectroscopy data', Glass and Ceramics (English translation of Steklo i Keramika), 67(11–12), pp. 340–342.

Kruger, A. A., Matlack, K. A., Pegg, Ian L. and Gong, W. (2013) 'Final Report - Glass Formulation Testing to Increase Sulfate Volatilization from Melter.' VSL-04R4970-1, Rev. 0. Office of River Protection, Richland, WA (United States).

Kruger, A. A., Matlack, K. S., Pegg, I. L., Kot, W. K. and Joseph, I. (2012) 'Redox Control for Hanford HLW Feeds.' VSL-12R2530-12. Office of River Protection, Richland, WA (United States).

Kruger, A. A., Pegg, I. L., Matlack, K. S., Chaudhuri, M., Kot, W. and Lutze, W. (2009) 'Effects of High Spinel and Chromium Oxide Crystal Contents on Simulated HLW Vitrification in DM100 Melter Tests.' VSL-09R1520-1 Rev. 0. Richland, WA.

Lee, S., Hrma, P., Pokorný, R., Kloužek, J., Eaton, W. C. and Kruger, A. A. (2019) 'Glass production rate in electric furnaces for radioactive waste vitrification', Journal of the American Ceramics Society. 102(10). pp. 5828–5842.

Lee, S. M., Hrma, P. R., Kloužek, J., Pokorný, R., Hujová, M., Dixon, D. R., Schweiger, M. J. and Kruger, A. A. (2017) 'Balance of oxygen throughout the conversion of a high-level waste melter feed to glass', Ceramics International, 43(16), pp. 13113–13118.

Manring, W. H. and Diken, G. M. (1980) 'A practical approach to evaluating redox phenomena involved in the melting-fining of soda-lime glasses', Journal of Non-Crystalline Solids, 38–39, pp. 813–818.

Marcial, J., Kloužek, J., Vernerová, M., Ferkl, P., Lee, S., Cutforth, D., Hrma, P., Kruger, A. and Pokorný, R. (2021) 'Effect of Al and Fe sources on conversion of high-level nuclear waste feed to glass', Journal of Nuclear Materials, 559(153423).

Matlack, K. S., Gan, H., Chaudhuri, M., Kot, W. K., Pegg, I. L., Joseph, I. and Kruger, A. A. (2012) 'Melter Throughput Enhancements for High-Iron HLW.' ORP-54002. Vitreous State Laboratory, Washington, D. C. (United States).

Matlack, K. S., Kruger, A. A., Gong, W., Bardakci, T., D'Angelo, N. A., Kot, W. K. and Pegg, I. L. (2011) 'Integrated DM1200 Melter Testing of HLW C-106/AY-102 Composition Using Bubblers.' VSL-03R3800-1. Vitreous State Laboratory, Washington, D. C. (United States).

Matlack, K. S., Kot, W. K., Pegg, I. L. and Joseph, I. (2015) 'Support for HLW Direct Feed - Phase 2.' VSL-15R3440-1. Vitreous State Laboratory, Washington, D. C. (United States).

Matlack, K. S., Muller, I. S., Gong, W., Pegg, I. L. and Kruger, A. A. (2006) 'Final Report - DuraMelter 100 Tests to Support LAW Glass Formulation Correlation Development.' VSL-06R6480-1. Vitreous State Laboratory, Washington, D. C. (United States).

Matlack, K. S., Viragh, C., Kot, W. K., Pegg, I. L. and Joseph, I. (2015) 'Effect of the Form of Iron on HLW Melt Rate.' VSL-15R3430-1. Vitreous State Laboratory, Washington, D. C. (United States).

Mirhadi, B. and Mehdikhani, B. (2011a) 'Effect of batch melting temperature and raw material on iron redox state in sodium silicate glasses', Journal of the Korean Ceramic Society, 48(2), pp. 117–120.

Muller, I. S., Viragh, C., Gan, H., Matlack, K. S. and Pegg, I. L. (2009) 'Iron Mössbauer redox and relation to technetium retention during vitrification', Hyperfine Interactions, 191(1–3), pp. 17–24.

Muller, I. S., Gilbo, K., Joseph, I. and Pegg, Ian L. (2013) 'Final Report- Enhanced LAW Glass Property-Composition Models- Phase 1.' VSL-13R2940-1. Richland, WA (United States).

Mysen, B. O. and Virgo, D. (1989) 'Redox equilibria, structure, and properties of Fe-bearing aluminosilicate melts; relationships among temperature, composition, and oxygen fugacity in the system Na_2O-Al_2O_3-SiO_2-FeO', American Mineralogist, 74(1–2), pp. 58–76.

Ollier, N., Charpentier, T., Boizot, B., Wallez, G. and Ghaleb, D. (2004) 'A Raman and MAS NMR study of mixed alkali Na-K and Na-Li aluminoborosilicate glasses', Journal of Non-Crystalline Solids, 341(1–3), pp. 26–34.

Peeler, D. K. and Edwards, T. B. (2004) ‘Impact of redox on glass durability: the glass selection process.’ WSRC-TR-2004-00135, Savannah River Technology Center, Aiken, SC (United States).

Peeler, D. K., Vienna, J. D., Schweiger, M. J. and Fox, K. M. (2015) ‘Advanced High-Level Waste Glass Research and Development Plan.’ Pacific Northwest National Laboratory. Richland, WA (United States).

Piepel, G., Cooley, S. K., Muller, I. S., Gan, H., Joseph, I. and Pegg, I. L. (2007) ‘ILAW PCT, VHT, Viscosity, and Electrical Conductivity Model Development. VSL-07R1230-1, Rev. 0’, (June 2017).

Piepel, G. F., Hrma, P., Bates, O., Schweiger, M. J. and Smith, D. E. (1993) ‘First-Order Study of Property/Composition Relationships for Hanford Waste Vitrification Plant Glasses.’ PNL-8502. Pacific Northwest National Laboratory, Richland, WA. (United States).

Pinet, O., Hugon, I. and Mure, S. (2014) ‘Redox Control of Nuclear Glass’, Procedia Materials Science. Elsevier B.V., 7, pp. 124–130.

Pokorný, R., Hilliard, Z. J., Dixon, D. R., Schweiger, M. J., Post Guillen, D., Kruger, A. A. and Hrma, P. (2015) ‘One-Dimensional Cold Cap Model for Melters with Bubblers.’ Journal of the American Ceramic Society, 98(10). pp. 3112–3118.

Romero, M. and Rincón, J. M. (1998) ‘Preparation and Properties of High Iron Oxide Content Glasses Obtained from Industrial Wastes’, Journal of the European Ceramic Society, 18(2), pp. 153–160.

Ross, W. A. (1978) ‘Process for solidifying high-level nuclear waste.’ United States: United States Patent Office: US4,094,809.

Ryan, J. L. (1995) ‘Redox Reactions and Foaming in Nuclear Waste Glass Melting.’ PNL-10510. Pacific Northwest National Laboratory. Richland, WA (United States).

Seymour, R. G. (1995) ‘Evaluation of Alternative Chemical Additives for High-Level Waste Vitrification Feed Preparation Processing.’ WHC-SD-WM-SP-009. Westinghouse Hanford Company, Oak Ridge, TN (United States).

Shaharyar, Y. Cheng, J. Y., Han, E., Maron, A., Weaver, J., Marcial, J., McCloy, J. S. and Goel, A. (2016) ‘Elucidating the Effect of Iron Speciation (Fe^{2+}/Fe^{3+}) on Crystallization Kinetics of Sodium Aluminosilicate Glasses’, Journal of the American Ceramic Society, 99(7), pp. 2306–2315.

Smith, G. L. Bates, D. J., Goles, R. W., Greenwood, L. R., Lettau, R. C., Piepel, G. F., Schweiger, M. J., Smith, H. D., Urie, M. W., Wagner, J. J. (2001) ‘Vitrification and Product Testing of C-104 and AZ-102 Pretreated Sludge Mixed with Flowsheet Quantities of Secondary Wastes.’ PNNL-13452. Pacific Northwest National Laboratory. Richland, WA (United States).

Smith, P. A., Vienna, J. D. and Merz, M. D. (1996) ‘NCAW Feed Chemistry: Effect of Starting Chemistry on Melter Offgas and Iron Redox.’ PNL-10517. Pacific Northwest National Laboratory, Richland, WA (United States).

Straub, C. P. (1973) ‘Radioactive Wastes.’ Water Pollution Control Federation, 45(6), pp. 1202–1215.

Thiemsorn, W., Keowkamnerd, K., Phanichphant, S., Suwannathada, P. and Hessenkemper, H. (2008) ‘Influence of glass basicity on redox interactions of iron-manganese-copper ion pairs in soda-lime-silica glass’, Glass Physics and Chemistry, 34(1), pp. 19–29.

Vienna, J. D., Kim, D.-S. and Hrma, P. (2002) ‘Database and Interim Glass Property Models for Hanford HLW Glasses’ PNNL-14060. Pacific Northwest National Laboratory, Richland. WA. (United States).

Vienna, J. D., Skorski, D. C., Kim, D. -S. and Matyáš, J. (2013) ‘Glass Property Models and Constraints for Estimating the Glass to be Produced at Hanford by

Implementing Current Advanced Glass Formulation Efforts PNNL-22631, Rev. 1', Pacific Northwest National Laboratory, Richland, WA (United States).

Vienna, J. D., Stanfill, B. A., Piepel, G. F., Riley, B. J., Kim, D. -S., Cooley, S. K., Crum, J. V., Jin, T. and Lonergan, C. E. (2016) 2016 Update of Hanford Glass Property Models and Constraints for Use in Estimating the Glass Mass to be Produced at Hanford by Implementing Current Enhanced Glass Formulation Efforts PNNL-25835 2016. Pacific Northwest National Laboratory, Richland, WA (United States).

Villain, O., Calas, G., Galoisy, L. and Cormier, L. (2007) 'XANES determination of chromium oxidation states in glasses: comparison with optical absorption spectroscopy', Journal of the American Ceramic Society, 90(11), pp. 1–23.

Wondergem-de Best, A. (1994) 'Redox behaviour and fining of molten glass.' PhD. Thesis. Eindhoven University of Technology, Eindhoven, (The Netherlands).

Xu, K., Hrma, P., Rice, J., Riley, B. J., Schweiger, M. J. and Crum, J. V. (2015) 'Melter Feed Reactions at T ≤ 700 ℃ for Nuclear Waste Vitrification′, Journal of the American Ceramic Society, 98(10), pp. 3105–3111.

Zhernovaya, N. F., Onishchuk, V. I. and Davydoglu, B. (2007) 'Color control and redox balance monitoring in container glass', Glass and Ceramics (English translation of Steklo i Keramika), 64(3–4), pp. 111–114.

10 Conclusions

The high-iron HLW-NG-Fe2 waste stream explored in this thesis is a rare case of high foaming of the high-level waste (HLW) streams, and relatively fast melting rate. Foaming beneath the cold cap, discussed in Chapter 2, section 2.4.2, is an issue for heat transfer through the cold cap and therefore efficiency of melting. Foaming, in extreme cases, also poses a risk of blockages to melter components. The aims outlined in Chapter 1, section 1.2 include: understanding the mechanisms of foaming, and exploring foam reduction methods in high-multivalent species feeds. The outcome of the research carried out on the HLW-NG-Fe2 feed in Chapters 4-8, is evaluation of some of the parameters that impact the melting rate, and the extent to which it is influenced by foaming.

As well as being an extreme case of foaming behaviour for HLW feeds, the high-multivalent species content, including Fe, Mn, Ni, Cr and Ce is used to explore mixed multivalent species reactions during melting. Investigation of the high-iron HLW-NG-Fe2 simulated waste feed during melting with a reduced iron raw material, $FeC_2O_4 \cdot 2H_2O$ (Chapter 4), and addition of 5 different carbon-based reductants, sucrose, coke, formic acid and HEDTA (Chapters 5-8) was employed to address the aims detailed in Chapter 1. By robust characterisation of feed samples, crucible scale melts, glass samples and scaled up laboratory-scale melter (LSM) samples, the melting behaviour of the HLW-NG-Fe2 feed under different redox conditions is uncovered, as well as the impact of redox manipulation on the structure and properties of the final glass (Chapter 9). A full analysis of the scale-up of the crucible studies to the Laboratory Scale Melter sample analysis is beyond the scope of this work. However, Chapter 4 provided some analytical tools that may be useful for future analysis of these samples.

The most effective reductants in reducing foaming were coke and graphite, at 3 wt% addition to the HLW-NG-Fe2 feed. This result was consistent with expectations, due to the high carbon content of these reductants compared to sucrose, formic acid and HEDTA. The linearity in maximum foam volume reduction and carbon content per gramme of reductant added was demonstrated for the first time. Evaluation of the compromises made when adding high-carbon based reductants to the HLW-NG-Fe2 feed, to the final glass properties, is recommended for further research. However, this thesis provides much of the supportive data to aid these decisions.

The mechanisms of primary and secondary foaming were explored in great detail by drawing connections between the structure of the feeds during melting and the gas evolution. Redox specific advanced analytical techniques, ^{57}Fe Mössbauer spectroscopy and X-ray Absorption Near-Edge spectroscopy, provided insight into the local structure of the multivalent species in the feed at different quench temperatures. This allowed for comparison of redox changes with O_2 evolution, to underpin the mechanism of secondary foaming, as well as exploration of the mixed multivalent species effects in glass melts. Providing more literature on these multivalent species in complex feed compositions and glasses will support not only the high-multivalent species content waste feeds at the Hanford site, but also many other industrial and waste glass production systems with mixed multivalent species.

This thesis delivers variety of reductant options for use in the HLW-NG-Fe2 feed, along with many of the important properties of the cold cap and final glass products for each reductant. Due to practical considerations, this research does not provide a comprehensive review of the carbon-based reductant additions to all HLW feeds and redox control of HLW feeds should be treated on an individual basis until a complete predictive model is obtained. Where the results of this study are directly and particularly applicable to the Hanford WTPs is in improved understanding of the melting process,

melt rate-controlling reactions and predictability of the melters. This understanding will aid safety and efficiency of running the melters and reduce melter downtime.

Further research should involve viscosity measurements of the glass melts to accurately apply the Melt Rate Correlation Equation to the feed with different reductant additions. Further investigation of the boron speciation in the glasses by ^{11}B Magic Angle Spinning – Nuclear Magnetic Resonance (MAS-NMR) or B K-edge XANES is required to underpin the structural origin of the changes in the 610 cm^{-1} Raman band.

The reductant additives and approaches described in this thesis should be applied to other high-multivalent species feeds. Further optimisation of the reductants for foaming and glass properties can be performed by varying the amount of reductant added and the reductant particle size, providing two more dimensions to the matrix of data. Also equating the reductants for carbon content would enable specific identification of any chemical effects of the different reductants, separate from the total carbon content. Finally, the research presented here should be tested in larger research-scale melters to confirm the melter processing rates and to ensure that the quality of the final glass products explored in this study are representative of those at the WTPs.

11 Appendices

A – Image Processing Macro

M1:

```
run("Duplicate...", "title=[File]+input");
run("Duplicate...", "title=[Glass Mask]");
setAutoThreshold("Intermodes dark");
run("Threshold...");
setThreshold(100, 255);
setOption("BlackBackground", true);
run("Convert to Mask");
run("Close");
run("Duplicate...", "title=Holes");
run("Fill Holes");
run("Invert");
selectWindow("Glass Mask");
imageCalculator("Add create", "Glass Mask","Holes");
selectWindow("Result of Glass Mask");
rename("Bubbles");
run("Dilate");
run("Invert");
run("Dilate");
run("Watershed");
run("Analyze Particles...", "size=0.002-Infinity circularity=0.20-1.00 display summarize
add in_situ");
```

B – Raw Data

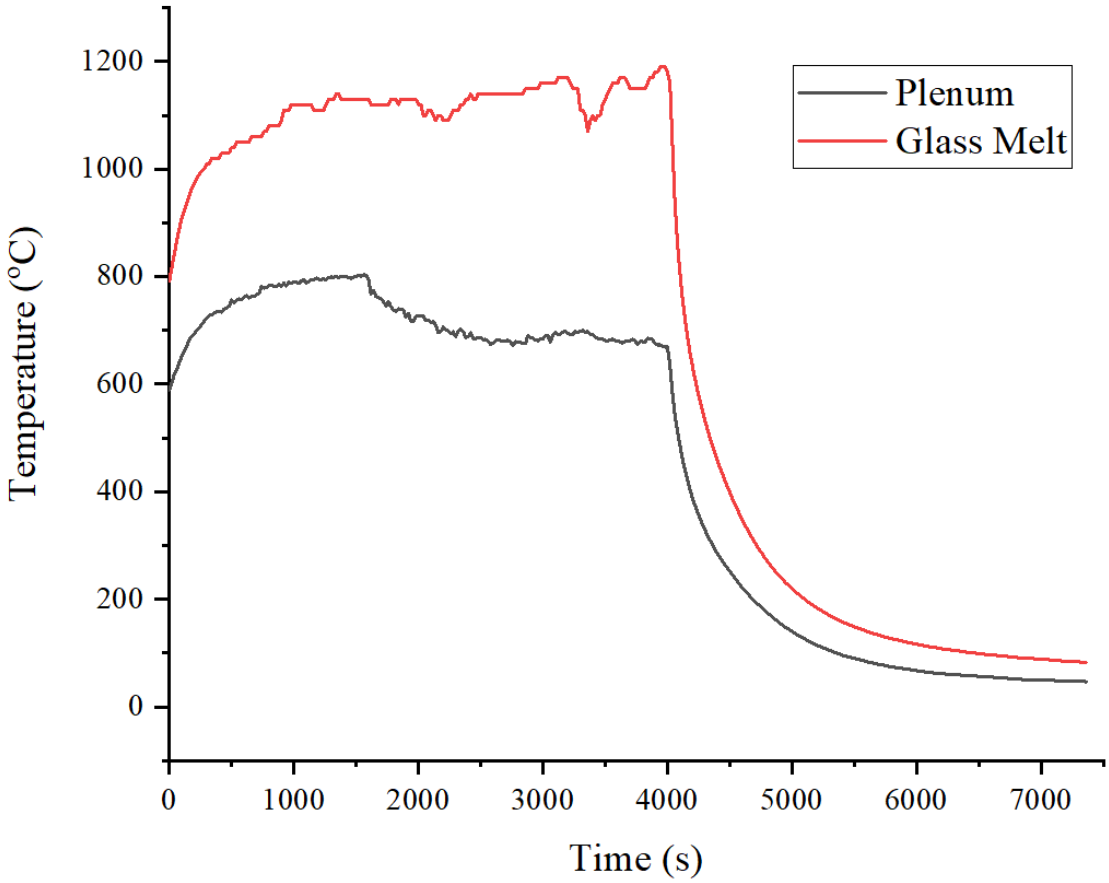

Figure 1. Temperature recordings from thermocouples placed in the plenum and the glass melt during the Laboratory Scale Melter run for the HLW-NG-Fe2-II feed.

Table 1. Phase Proportions determined by comparison of the Phases identified in XRD patterns with 5 wt% Si powders as an internal standard for all HLW-NG-Fe2, HLW-NG-Fe2-II and HLW-NG-Fe2-R feeds at all measured quench temperatures.

Reductant	Temp.	Quartz	Err	Spinel	Err	Haematite	Err	Other	Err	Amorphous	Err
Original	Feed	20.2	0.2	0.00	0.00	4.20	0.10	3.81	0.2	66.80	0.20
	600	36.84	1.0	2.84	0.10	7.05	0.30			53.26	0.093
	700	28.21	0.4	3.37	0.10	7.26	0.10			61.16	0.04
	800	16.11	0.2	4.48	0.09	11.26	0.20			68.15	0.033
	900	5.47	0.1	2.95	0.10	6.00	0.10			85.58	0.020
	1000	0.00	0.0	3.58	0.10	0.00	0.00			89.05	0.020
	1100	0.00	0.0	2.04	0.06	1.67	0.05			96.28	0.007
	1150	0.00	0.0	1.79	0.04	0.00	0.00			98.21	0.003
	HT	0.00	0.0	4.67	0.04	1.07	0.02			94.25	0.004
Oxalate	Feed	18.0	1.0	0.00	0.00	0.00	0.00	36.3	1.7	41.00	1.00
	600	31.58	1.0	0.00	0.00	0.00	0.00			67.05	0.087
	700	26.42	0.4	13.37	0.20	0.00	0.00			60.21	0.04
	800	13.89	0.2	4.40	0.08	8.00	0.10			73.71	0.025
	900	2.55	0.1	3.68	0.10	3.58	0.10			90.19	0.018
	1000	2.53	0.2	6.32	0.40	2.11	0.20			89.05	0.053
	1100	0.00	0.0	2.56	0.04	0.00	0.00			97.44	0.003
	1150	0.00	0.0	1.89	0.10	0.00	0.00			98.11	0.007
	HT	0.00	0.0	3.13	0.03	3.77	0.04			93.11	0.005
Sucrose	600	30.11	0.3	5.43	0.08	8.34	0.09			56.13	0.031
	800	21.79	0.2	5.66	0.09	8.32	0.09			64.23	0.025
	1000	4.38	0.1	5.18	0.06	3.73	0.05			86.72	0.011
	1150	0.00	0.0	3.71	0.02	0.00	0.00			96.29	0.001
	HT	0.00	0.0	3.54	0.04	4.04	0.04			92.42	0.005
Graphite	600	33.68	1.0	3.13	0.05	9.26	0.20			47.98	0.107
	800	17.37	0.1	6.54	0.06	3.53	0.04			72.57	0.013
	1000	0.00	0.0	4.54	0.04	0.00	0.00			95.46	0.003
	1150	0.00	0.0	3.67	0.02	0.00	0.00			96.33	0.003
	HT	0.00	0.0	5.54	0.05	0.00	0.00			94.46	0.003
Coke	600	30.11	0.4	5.37	1.00	8.00	0.10			55.69	0.103
	800	16.00	0.2	4.98	0.08	5.18	0.08			73.84	0.024
	1000	4.62	0.0	10.32	0.05	0.00	0.00			85.06	0.005
	1150	0.00	0.0	4.37	0.03	0.00	0.00			95.63	0.002
	HT	0.00	0.0	5.19	0.04	0.34	0.02			94.47	0.004
Formic Acid	600	26.42	0.3	3.03	0.03	8.84	0.10			57.60	0.042
	800	16.53	0.2	4.75	0.07	6.34	0.08			72.39	0.023
	1000	2.57	0.0	2.26	0.03	2.79	0.04			92.38	0.007
	1150	0.00	0.0	2.08	0.02	0.00	0.00			97.92	0.001
	HT	0.00	0.0	4.06	0.03	2.47	0.03			93.46	0.004
HEDTA	600	31.89	0.3	6.09	0.08	7.63	0.08			54.38	0.028
	800	15.26	0.1	6.97	0.05	2.12	0.03			75.65	0.012
	1000	1.49	0.0	5.20	0.04	5.20	0.04			88.11	0.007
	1150	0.00	0.0	3.89	0.03	0.00	0.00			96.11	0.002
	HT	0.00	0.0	3.68	0.04	0.54	0.03			95.78	0.004

Table 2. Summary of oxidation/reduction reactions in the HLW-NG-Fe2 and HLW-NG-Fe2-R feeds at 600, 800, 1000 and 1150 ℃.

Feed	Redox reaction	Temperature		% Conversion
		Onset	Complete	
HLW-NG-Fe2	Fe^{3+}/Fe^{2+}	-	-	0
	Mn^{4+}/Mn^{3+}	600	1150	100
	Cr^{3+}/Cr^{6+}	0	800	79.2
	Cr^{6+}/Cr^{3+}	800	1000	100
	Ce^{4+}/Ce^{3+}	800	1150	90.5
HLW-NG-Fe2-S	Fe^{3+}/Fe^{2+}	800	1000	5.8
	Fe^{2+}/Fe^{3+}	1000	1150	100
	Mn^{4+}/Mn^{3+}	600	1150	100
	Cr^{3+}/Cr^{6+}	0	800	37.9
	Cr^{6+}/Cr^{3+}	800	1150	100
	Ce^{4+}/Ce^{3+}	800	1000	1000
HLW-NG-Fe2-G	Fe^{3+}/Fe^{2+}	600	1000	58.2
	Fe^{2+}/Fe^{3+}	1000	1150	47.4
	Mn^{4+}/Mn^{3+}	600	1000	100
	Cr^{3+}/Cr^{6+}	0	600	28.1
	Cr^{6+}/Cr^{3+}	600	1000	100
	Cr^{3+}/Cr^{6+}	1000	1150	7.1
	Ce^{4+}/Ce^{3+}	600	1000	100
HLW-NG-Fe2-C	Fe^{3+}/Fe^{2+}	600	1150	34.5
	Mn^{4+}/Mn^{3+}	600	1000	100
	Cr^{3+}/Cr^{6+}	-	-	0
	Cr^{6+}/Cr^{3+}	-	-	100
	Ce^{4+}/Ce^{3+}	600	1000	100
HLW-NG-Fe2-F	Fe^{3+}/Fe^{2+}	-	-	0
	Mn^{4+}/Mn^{3+}	600	1150	100
	Cr^{3+}/Cr^{6+}	600	800	17.5
	Cr^{6+}/Cr^{3+}	800	1000	100
	Ce^{4+}/Ce^{3+}	800	1150	100
HLW-NG-Fe2-H	Fe^{3+}/Fe^{2+}	600	800	39.1
	Fe^{2+}/Fe^{3+}	800	1150	83.3
	Mn^{4+}/Mn^{3+}	600	1000	100
	Cr^{3+}/Cr^{6+}	-	-	0
	Cr^{6+}/Cr^{3+}	-	-	0
	Ce^{4+}/Ce^{3+}	600	1000	100

Table 3. Density of crystals identified in heat treated samples of HLW-NG-Fe2, HLW-NG-Fe2-II and HLW-NG-Fe2-R glasses.

Glass	Phase ID ICDD		Density	
	Fe_2O_3	Fe_3O_4	Fe_2O_3	Fe_3O_4
HLW-NG-Fe2	01-089-0597	04-023-8319	5.27(2)	5.18(3)
HLW-NG-Fe2-II	01-079-1741	04-015-0157	5.27(2)	5.16(2)
HLW-NG-Fe2-S	01-089-0597	019-079-1500	5.27(3)	4.90(2)
HLW-NG-Fe2-G		04-020-9332		4.74(4)
HLW-NG-Fe2-C	04-015-9579	04-018-9791	5.27(2)	5.06(3)
HLW-NG-Fe2-F	01-089-0597	04-018-9791	5.27(2)	5.05(2)
HLW-NG-Fe2-H	01-089-0596	04-006-0436	5.27(3)	5.38(3)

Table 4. ICP-MS results of blank samples used in PCT-B after 7-days.

Element	B1	B2	B3
	$g\ L^{-1}$	$g\ L^{-1}$	$g\ L^{-1}$
Al	0.311	0.199	0.448
B	0.305	0.207	0.567
Ca	0.973	0.626	0.529
Cr	0	0	0
Fe	0.039	0.056	0.025
Li	0.007	0.011	0.072
Mg	0.39	0.255	0.253
Mn	0.009	0.027	0.185
Na	28.8792	9.01448	31.5
Ni	0	0	0
P	0.044	0.027	0
Pb	0	0	0
S	0.19	0.121	0
Si	5.491	2.965	4.57
Sr	0	0	0.014
Zr	0.003	0.006	0

Table 5. ICP-MS results of HLW-NG-Fe2-II, HLW-NG-Fe2-G (G) and HLW-NG-Fe2-F (F) after 7-day PCT-B.

Element	HLW-NG-Fe2-II			HLW-NG-Fe2-G			HLW-NG-Fe2-F		
	g L^{-1}			g L^{-1}			g L^{-1}		
	1	2	3	1	2	3	1	2	3
Al	36.7	36.7	27.2	8.19	7.19	7.35	26.3	25.5	25.2
B	66.1	67.1	53.3	136	132	138	27.9	27.3	28
Ca	1.25	1.1	1.83	3.47	2.66	3.34	0.944	1.13	1.46
Cr	0.005	0.014	0.007	0.026	0.023	0.023	0	0.005	0.006
Fe	2.46	2.81	2.18	30.6	23.9	27.2	1.35	1.29	1.42
Li	11.4	11.6	9.08	14.4	13.9	14.1	5.42	5.41	5.48
Mg	0.034	0.034	0.084	1.76	1.35	1.5	0	0.034	0.084
Mn	0.598	0.799	0.483	8.82	6.87	7.52	0.112	0.127	0.122
Na	136	134	119	207	198	203	54.1	56	53.2
Ni	0.031	0.049	0.032	0.492	0.361	0.404	0.011	0.013	0.011
P	1.09	1.07	1.08	4.35	3.97	4.46	0.933	0.862	0.84
Pb	0.183	0.173	0.178	0.26	0.26	0.28	0.071	0.06	0.125
S	0.604	0.583	0.477	0.59	0.56	0.66	0.467	0.456	0.483
Si	40.1	41	34.5	79.7	71.8	76.3	40.1	39.9	39.4
Sr	0.014	0.023	0.014	0.03	0.02	0.03	0	0.005	0.009
Zr	0.235	0.252	0.337	0.38	0.39	0.4	0.137	0.156	0.148

Table 6. PCT-B Data Normalised elemental mass loss (NLi) - g(waste form)m^{-2}

Element	HLW-NG-Fe2-II			HLW-NG-Fe2-G			HLW-NG-Fe2-F		
	g m^{-2}			g m^{-2}			g m^{-2}		
	1	2	3	1	2	3	1	2	3
Al	24.771	24.771	18.385	0	0	0	17.765	17.225	17.031
B	30.818	31.284	24.886	63.361	61.592	64.392	18.846	18.441	18.924
Ca	0	0	0	0	0	0	0	0	0
Cr	0.058	0.161	0.081	0.3	0.266	0.266	0	0.003	0.004
Fe	0.436	0.498	0.387	5.415	4.236	4.821	0.912	0	0.96
Li	31.518	32.071	25.14	39.784	38.461	39.015	3.661	3.654	3.704
Mg	0	0	0	0	0	0	0	0	0
Mn	0	0	0	7.044	0	0	0	0	0
Na	0	0	0	0	0	0	0	0	0
Ni	10.763	0	10.778	64.532	21.543	10.772	0	0	0
P	0	0	0	25.546	23.35	26.232	0	0	0
Pb	0.629	0.595	0.613	0.886	0.887	0.96	0.048	0.041	0.084
S	0	0	0	0	0	0	0	0	0
Si	0	0	0	0	0	0	0	0	0
Sr	0	0	0	0	0	0	0	0	0
Zr	0	0.604	0.809	0.915	0.946	0.962	0	0	0

Table 7. PCT Data Average normalised elemental mass loss (NLi) - g(waste form) m^{-2}

Element	Normalised Loss (g m^{-2})		
	HLW-NG-Fe2-II	HLW-NG-Fe2-G	HLW-NG-Fe2-F
Al	22.642	0	17.341
B	28.996	63.115	18.737
Ca	0	0	0
Cr	0.1	0.277	0.002
Fe	0.44	4.824	0.624
Li	29.577	39.087	3.673
Mg	0	0	0
Mn	0	2.348	0
Na	0	0	0
Ni	7.181	5.389	37.655
P	0	25.043	0
Pb	0.612	0.911	0.058
S	0	0	0
Si	0	0	0
Sr	0	0	0
Zr	0.471	0.941	0

Table 8. PCT Data Average normalised elemental mass loss (NLi) - g(waste form) m^{-2} day^{-1}

Element	Normalised Loss (g m^{-2})		
	HLW-NG-Fe2-II	HLW-NG-Fe2-G	HLW-NG-Fe2-F
Al	3.235	0	2.477
B	4.142	9.016	2.677
Ca	0	0	0
Cr	0.014	0.04	0
Fe	0.063	0.689	0.089
Li	4.225	5.584	0.525
Mg	0	0	0
Mn	0	0.335	0
Na	0	0	0
Ni	1.026	0.77	5.379
P	0	3.578	0
Pb	0.087	0.13	0.008
S	0	0	0
Si	0	0	0
Sr	0	0	0
Zr	0.067	0.134	0

Table 9. PCT Data Average Standard deviations of NLi

HLW-NG-	Al	B	Ca	Cr	Fe	Li	Mg	Mn
Fe2-II	3.010	2.913	0.000	0.044	0.045	3.145	0.000	0.000
Fe2-G	0.000	0.885	0.000	0.017	0.590	0.661	0.000	3.522
Fe2-F	8.883	22.773	0.000	0.133	1.955	17.677	0.000	0.000
HLW-NG-	Na	Ni	P	Pb	S	Si	Sr	Zr
Fe2-II	0.000	5.077	0.000	0.014	0.000	0.000	0.000	0.344
Fe2-G	0.000	5.389	1.098	0.009	0.000	0.000	0.000	0.102
Fe2-F	0.000	26.877	13.116	0.137	0.000	0.000	0.000	0.053

Table 10. Measured glass properties of the HLW-NG-Fe2-R feeds, along with the control limits for these properties employed at the Waste Treatment Plants, and the maximum normalised foam volume for each of the feeds during melting.

Feed Name	**Reductant Carbon Source**	**Carbon content g^{-1}**	**Maximum Normalised Foam Vol**	**Spinel phase vol% at 950 °C**	**PCT – B Normalised B Loss day^{-1} ($g\ L^{-1}$)**	**Fe^{2+}/Fe_T**
Limits				1.0	4	0.3
HLW-NG-Fe2	-	0	10.0	0.9(1)	0.986*	0.0
HLW-NG-Fe2-S	Sucrose	0.42	9.40	1.1(1)		0.0
HLW-NG-Fe2-G	Graphite	1	4.90	1.2(3)	3.151	0.53
HLW-NG-Fe2-C	Coke Dust	0.93	4.57	0.9(2)		0.35
HLW-NG-Fe2-F	Formic Acid	0.26	7.63	0.9(2)	0.925	0.0
HLW-NG-Fe2-H	HEDTA	0.43	7.86	1.0(2)		0.17

* Literature value from (Matlack et al. 2012).

Table 11. Phases identified as starting models in the final glasses.

Feed	Phase ID	ICDD Ref.	Lattice Constants (Å)
HLW-NG-Fe2	Fe_3O_4	01-076-1849	8.401(04)
HLW-NG-Fe2-II	Fe_3O_4	01-088-0866	8.391(2)
HLW-NG-Fe2-S	Fe_3O_4	04-014-4322	8.392(1)
HLW-NG-Fe2-G	Fe_3O_4	04-009-4255	8.395(1)
HLW-NG-Fe2-C	Fe_3O_4	00-019-0629	8.395(1)
HLW-NG-Fe2-F	Fe_3O_4	04-008-4511	8.404(1)
HLW-NG-Fe2-H	Fe_3O_4	01-087-2334	8.398(1)

C – Deconvolution of Raman glass spectra

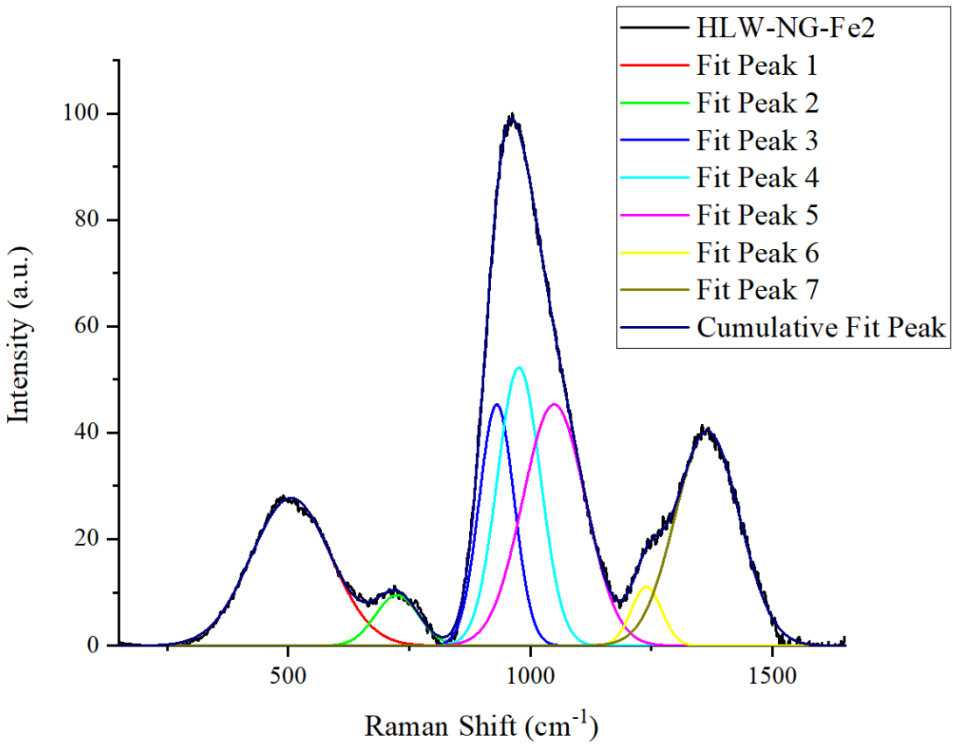

Figure 1. Deconvolution of Raman spectrum for HLW-NG-Fe2 glass

Table 1. Fit values for deconvolution of Raman spectrum for HLW-NG-Fe2 glass.

	xc	xc	A	A	w	w	Statistics	
	Value	Standard Error	Value	Standard Error	Value	Standard Error	Reduced Chi-Sqr	Adj. R-Square
Peak1	505.8	0.4	5740.3	27.6	194.4	1.0	0.927	0.998
Peak2	724.6	0.8	1064.5	19.3	105.4	2.0		
Peak3	930.6	11.3	4098.3	7011.7	85.0	12.8		
Peak4	976.6	39.8	5836.8	10355.9	104.9	51.3		
Peak5	1049.1	28.3	7366.2	3592.0	152.7	22.2		
Peak6	1239.7	1.0	870.3	47.8	73.8	2.5		
Peak7	1365.4	0.4	6706.2	38.2	156.3	0.9		

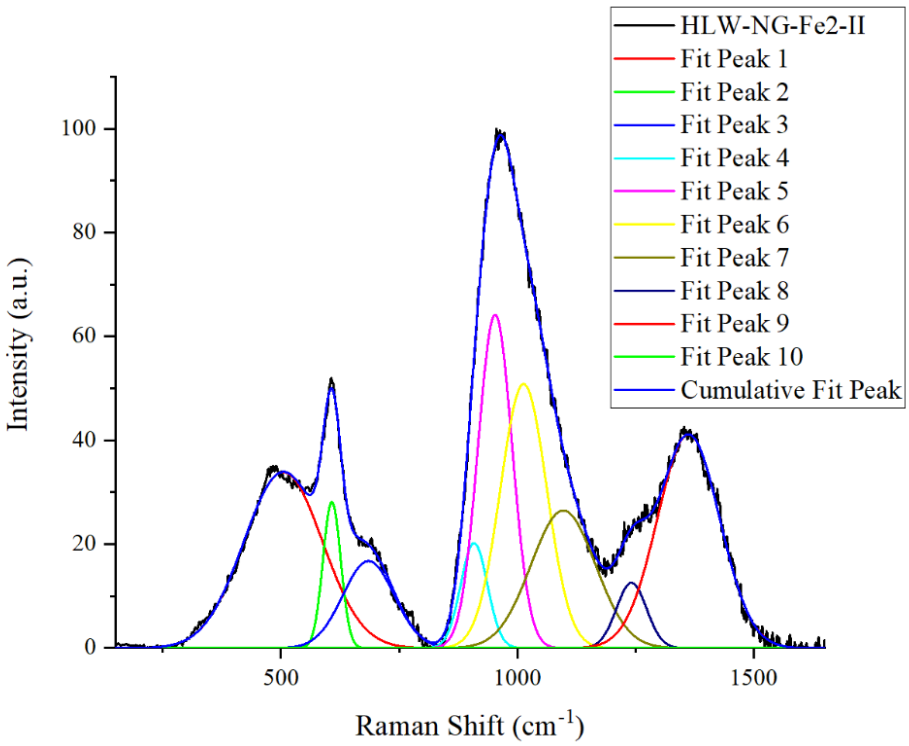

Figure 2. Deconvolution of Raman spectrum for HLW-NG-Fe2-II glass

Table 2. Fit values for deconvolution of Raman spectrum for HLW-NG-Fe2-II glass.

	xc	xc	A	A	w	w	Statistics	
Intensity	Value	Standard Error	Value	Standard Error	Value	Standard Error	Reduced Chi-Sqr	Adj R-Square
Peake	504.6	0.8	7060.9	65.2	195.7	1.7	1.314	0.998
Peak2	607.6	0.2	1325.5	35.9	44.2	0.7		
Peak3	685.1	1.5	2291.8	66.4	128.5	3.0		
Peak4	908.3	19.5	1430.1	4331.9	66.4	19.0		
Peak5	952.8	9.2	5810.6	18546.3	85.0	60.9		
Peak6	1013.1	66.4	6240.1	34349.3	115.2	185.6		
Peak7	1096.9	283.5	4530.1	20866.2	160.7	280.3		
Peak8	1241.2	3.4	1004.4	521.2	75.0	9.4		
Peak9	1361.9	0.9	6798.6	84.3	155.1	1.4		
Peak10	1779.2	5.3	206.2	24.1	119.7	13.8		

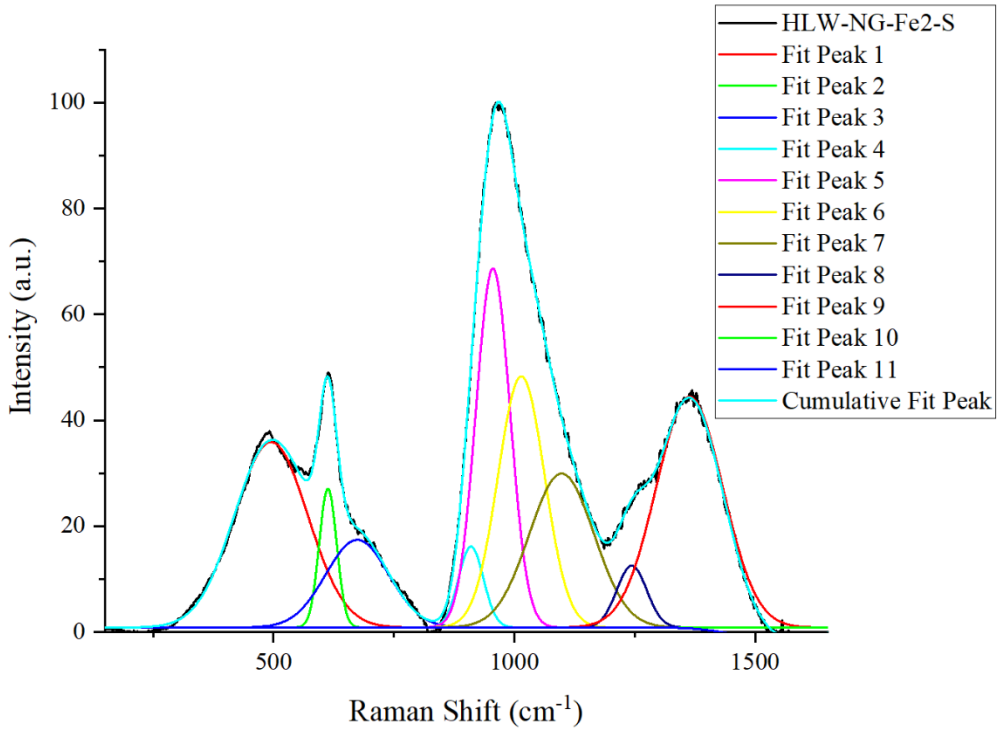

Figure 3. Deconvolution of Raman spectrum for HLW-NG-Fe2-S glass

Table 3. Fit values for deconvolution of Raman spectrum for HLW-NG-Fe2-S glass.

	xc	xc	A	A	w	w	Statistics	
Intensity	Value	Standard Error	Value	Standard Error	Value	Standard Error	Reduced Chi-Sqr	Adj. R-Square
Peak1	494.94	0.83	6674.90	67.98	179.10	1.33	0.67	0.99
Peak2	612.98	0.16	1192.01	26.56	42.73	0.56		
Peak3	673.87	2.19	2708.62	86.52	153.93	3.15		
Peak4	909.90	9.48	990.45	1661.97	60.97	12.26		
Peak5	955.56	4.82	6015.56	10082.2	83.38	30.19		
Peak6	1014.39	43.55	5734.92	19163.9	113.61	115.07		
Peak7	1098.21	138.78	4897.54	11154.3	158.34	135.84		
Peak8	1243.69	2.20	908.05	268.14	73.07	5.73		
Peak9	1363.54	0.63	7564.62	133.86	163.12	2.31		
Peak10	-	-	-	-	-	--		
Peak11	1545.24	15.38	506.79	94.84	186.93	23.22		

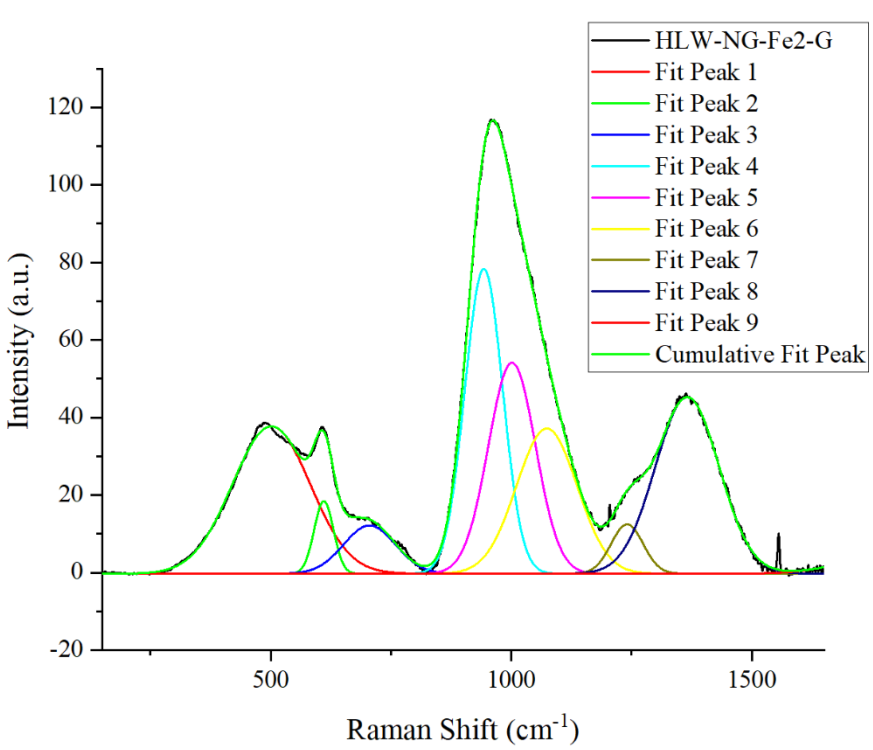

Figure 4. Deconvolution of Raman spectrum for HLW-NG-Fe2-G glass

Table 4. Fit values for deconvolution of Raman spectrum for HLW-NG-Fe2-G glass.

	xc	xc	A	A	w	w	Statistics	
Intensiry	Value	Standard Error	Value	Standard Error	Value	Standard Error	Reduced Chi-Sqr	Adj. R-Square
Peak1	501.0	0.4	7726.0	41.6	191.0	1.0	0.65	0.999
Peak2	610.2	0.3	941.6	22.4	47.3	0.7		
Peak3	705.3	0.9	1675.6	28.7	126.6	2.2		
Peak4	942.9	6.0	7747.7	5279.1	92.6	5.6		
Peak5	1001.4	14.8	6691.8	14774.8	115.4	65.7		
Peak6	1073.8	86.3	5905.6	9755.2	148.1	63.8		
Peak7	1240.7	1.5	1061.8	100.1	78.4	3.1		
Peak8	1365.8	0.3	7569.1	39.3	156.1	0.8		
Peak9	1775.7	1.9	983.2	30.1	216.8	5.6		

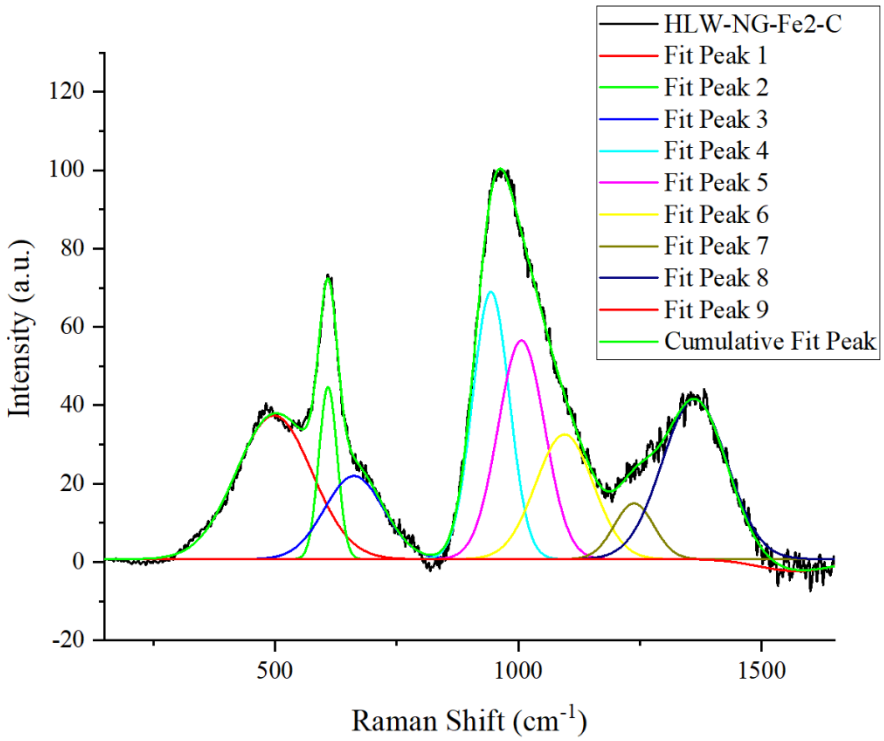

Figure 5. Deconvolution of Raman spectrum for HLW-NG-Fe2-C glass

Table 5. Fit values for deconvolution of Raman spectrum for HLW-NG-Fe2-C glass.

	xc	xc	A	A	w	w	Statistics	
Intensiry	Value	Standard Error	Value	Standard Error	Value	Standard Error	Reduced Chi-Sqr	Adj. R-Square
Peak1	498.0	2.1	7159.0	178.4	183.6	3.2	2.9	1.0
Peak2	609.1	0.2	2077.3	68.3	44.4	0.8		
Peak3	662.5	4.2	3221.2	227.0	142.7	5.3		
Peak4	943.9	9.5	6446.7	6384.7	88.8	8.9		
Peak5	1006.4	12.7	6696.7	16275.7	112.7	91.9		
Peak6	1094.8	113.1	4709.7	10533.6	139.1	123.0		
Peak7	1237.7	7.8	1442.5	603.8	95.6	14.1		
Peak8	1362.2	1.6	6815.1	244.8	156.8	4.9		
Peak9	1571.0	13.7	-590.3	102.0	182.2	27.5		

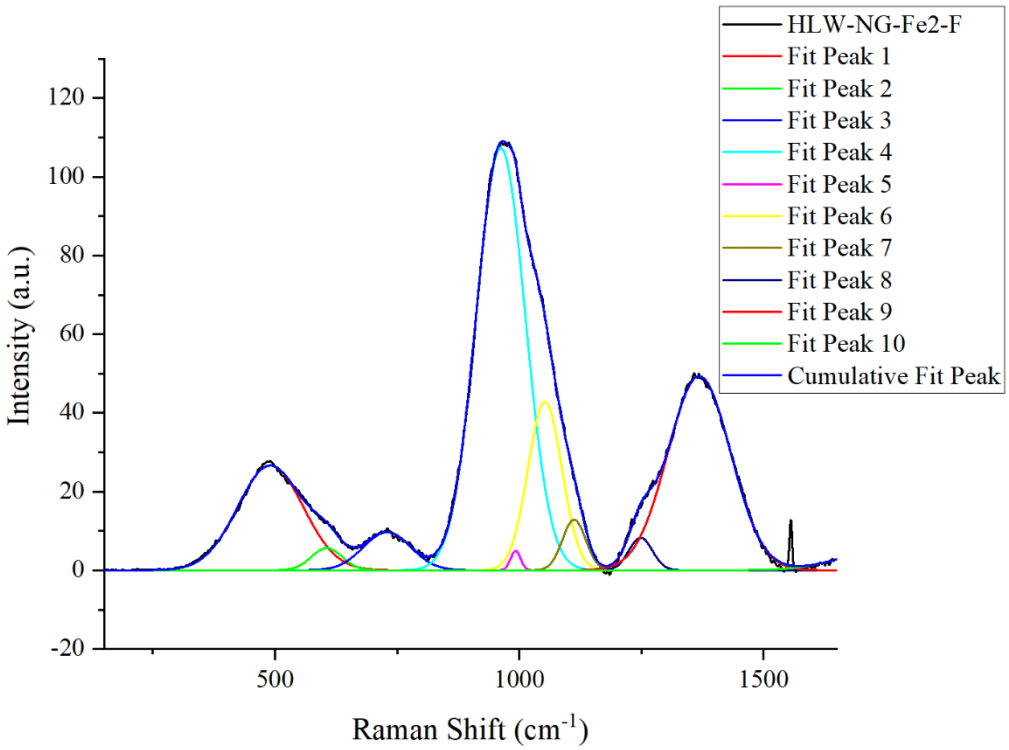

Figure 6. Deconvolution of Raman spectrum for HLW-NG-Fe2-F glass

Table 6. Fit values for deconvolution of Raman spectrum for HLW-NG-Fe2-F glass.

	xc	xc	A	A	w	w	Statistics	
Intensiry	Value	Standard Error	Value	Standard Error	Value	Standard Error	Reduced Chi-Sqr	Adj. R-Square
Peak1	490.7	0.7	4477	44.7	158.1	1.5	0.7	1.0
Peak2	606.0	1.4	444.4	39.4	74.2	4.0		
Peak3	729.4	0.9	1178.7	23.3	114.6	2.5		
Peak4	961.9	0.5	13493.5	131.8	118.2	0.7		
Peak5	992.4	0.7	124.8	20.8	23.8	2.3		
Peak6	1052.5	1.0	3719.8	235.9	81.8	3.4		
Peak7	1112.2	2.1	765.5	135.1	56.0	2.7		
Peak8	1248.3	0.6	497.2	18.1	56.5	1.6		
Peak9	1368.3	0.2	7956.9	28.2	151.6	0.6		
Peak10	1759.5	1.5	1316.2	30.2	219.6	4.3		

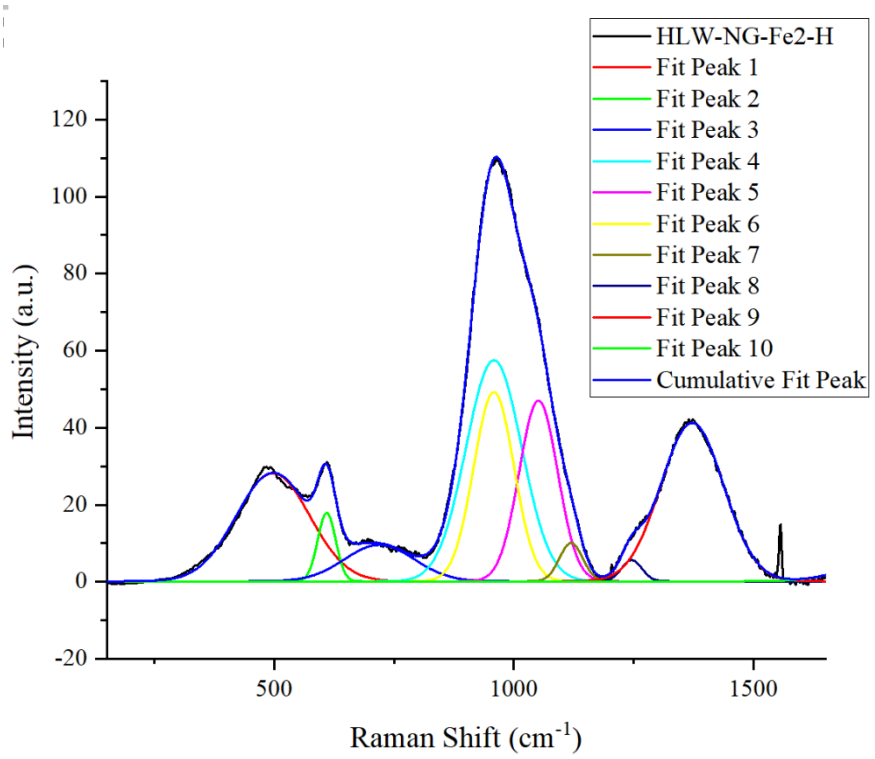

Figure 7. Deconvolution of Raman spectrum for HLW-NG-Fe2-H glass

Table 7. Fit values for deconvolution of Raman spectrum for HLW-NG-Fe2-H glass.

	xc	xc	A	A	w	w	Statistics	
Intensiry	Value	Standard Error	Value	Standard Error	Value	Standard Error	Reduced Chi-Sqr	Adj. R-Square
Peak1	497.0	0.8	5392.5	58.9	180.6	1.7	0.97	0.999
Peak2	609.2	0.3	834.0	27.6	44.2	0.9		
Peak3	719.2	2.2	1718.1	119.7	170.9	12.6		
Peak4	958.2	168.1	8354.5	47753.7	136.8	52.3		
Peak5	1051.2	46.1	4725.9	14769.0	94.6	51.4		
Peak6	958.2	59.2	5172.5	33541.9	99.0	72.9		
Peak7	1119.4	4.5	601.5	427.7	56.9	7.9		
Peak8	1245.8	1.0	292.7	16.9	50.2	2.5		
Peak9	1372.1	0.3	6768.6	31.4	154.7	0.7		
Peak10	1783.3	1.7	1185.6	33.3	197.8	4.8		

Table 8. Peak positions and areas of borate and borosilicate related Raman bands.

Glass	Danburite (610 cm^{-1})	$B\text{-}O^-$ in BO_4 units	
	Peak area	Peak area	Peak position (cm^{-1})
HLW-NG-Fe2	0	6706	1365
HLW-NG-Fe2-II	1325	6799	1362
HLW-NG-Fe2-S	1192	7565	1364
HLW-NG-Fe2-G	942	7569	1366
HLW-NG-Fe2-C	2077	6815	1362
HLW-NG-Fe2-F	444	7957	1368
HLW-NG-Fe2-H	834	6769	1372

*assignment of bands is tentative (see main thesis).

D – SEM/EDX and X-Ray CT Images

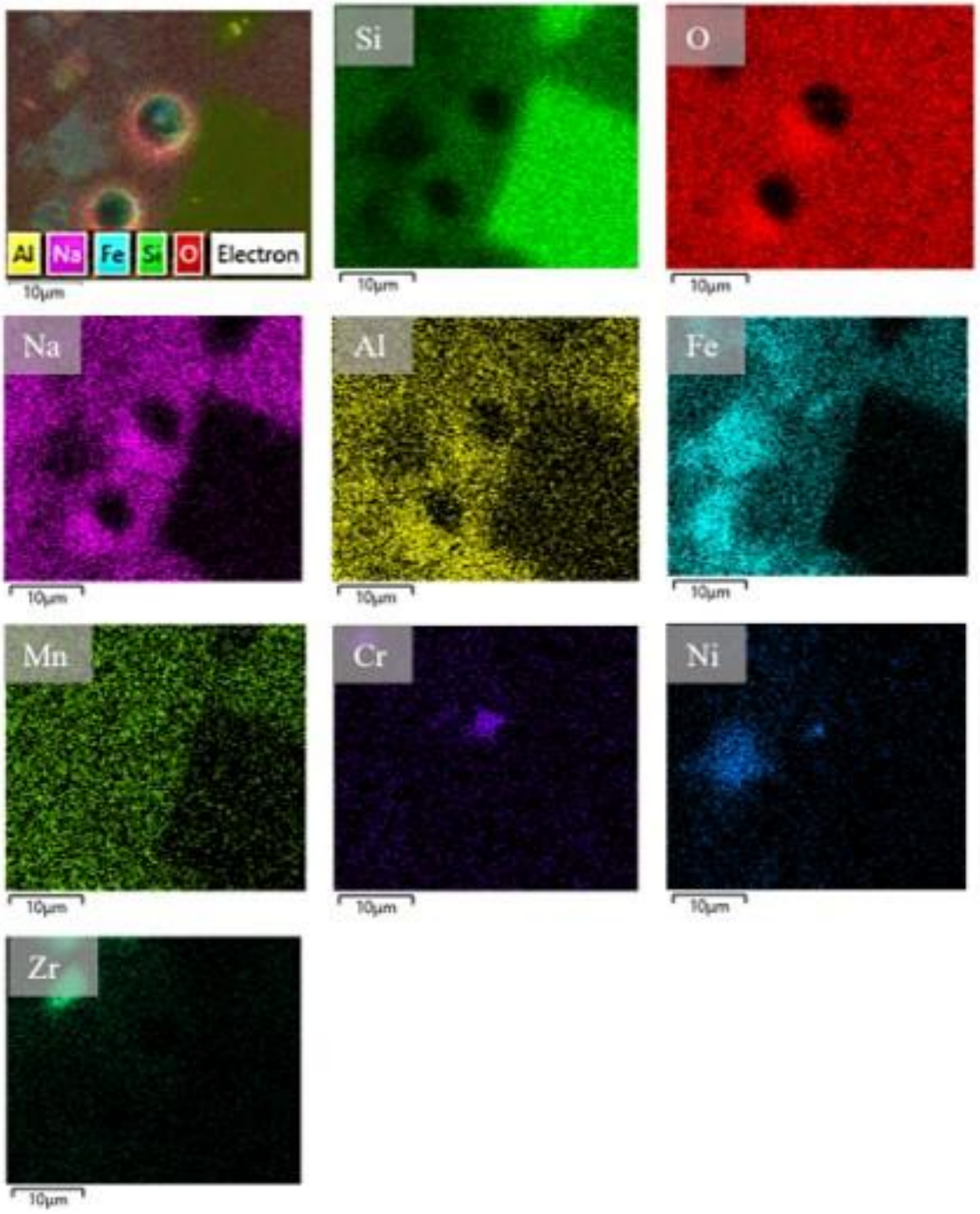

Figure 1. EDX maps of the top feed portion of the HLW-NG-Fe2 Laboratory Scale Melter sample.

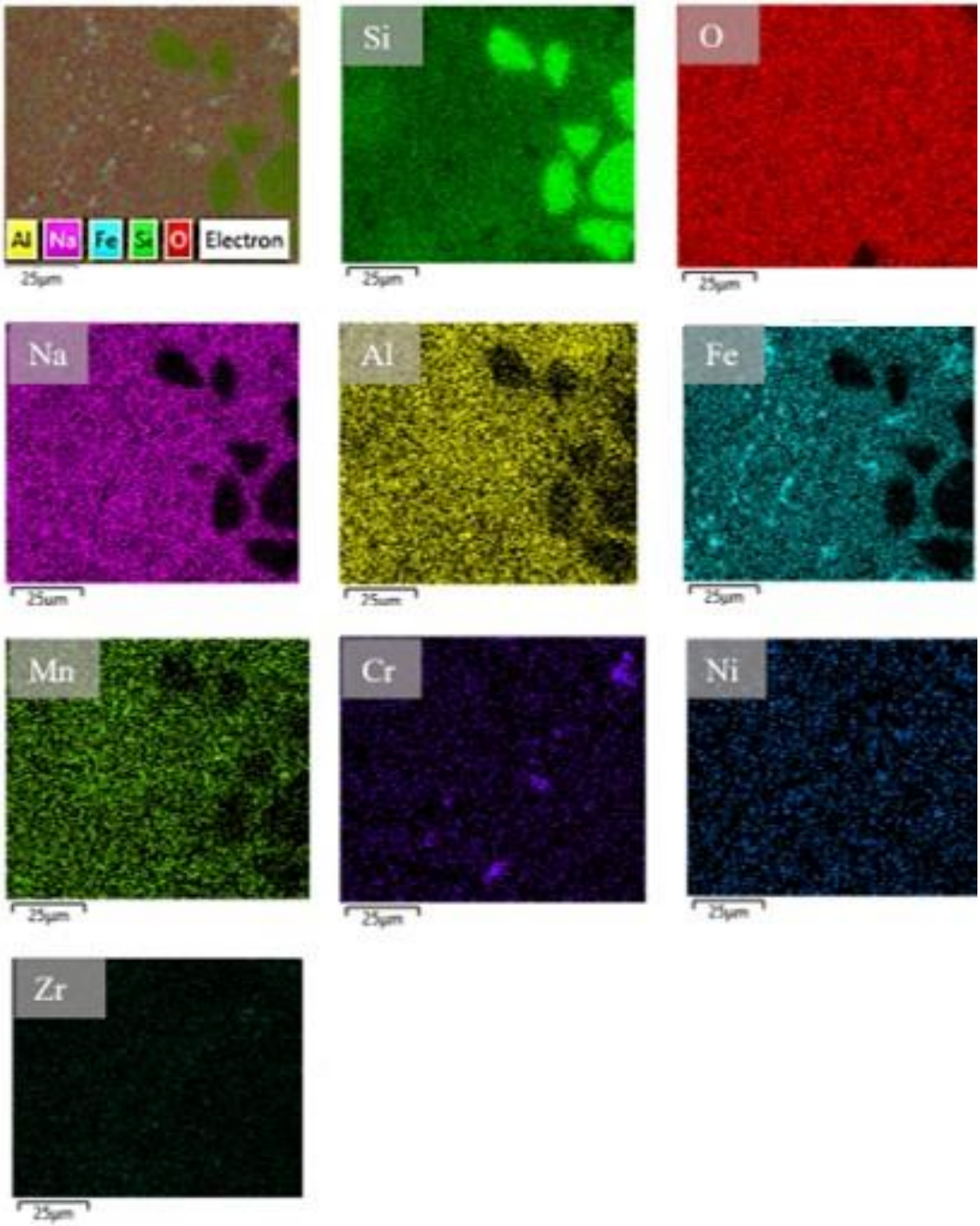

Figure 2. EDX maps of the middle feed-to-glass portion of the HLW-NG-Fe2 Laboratory Scale Melter sample.

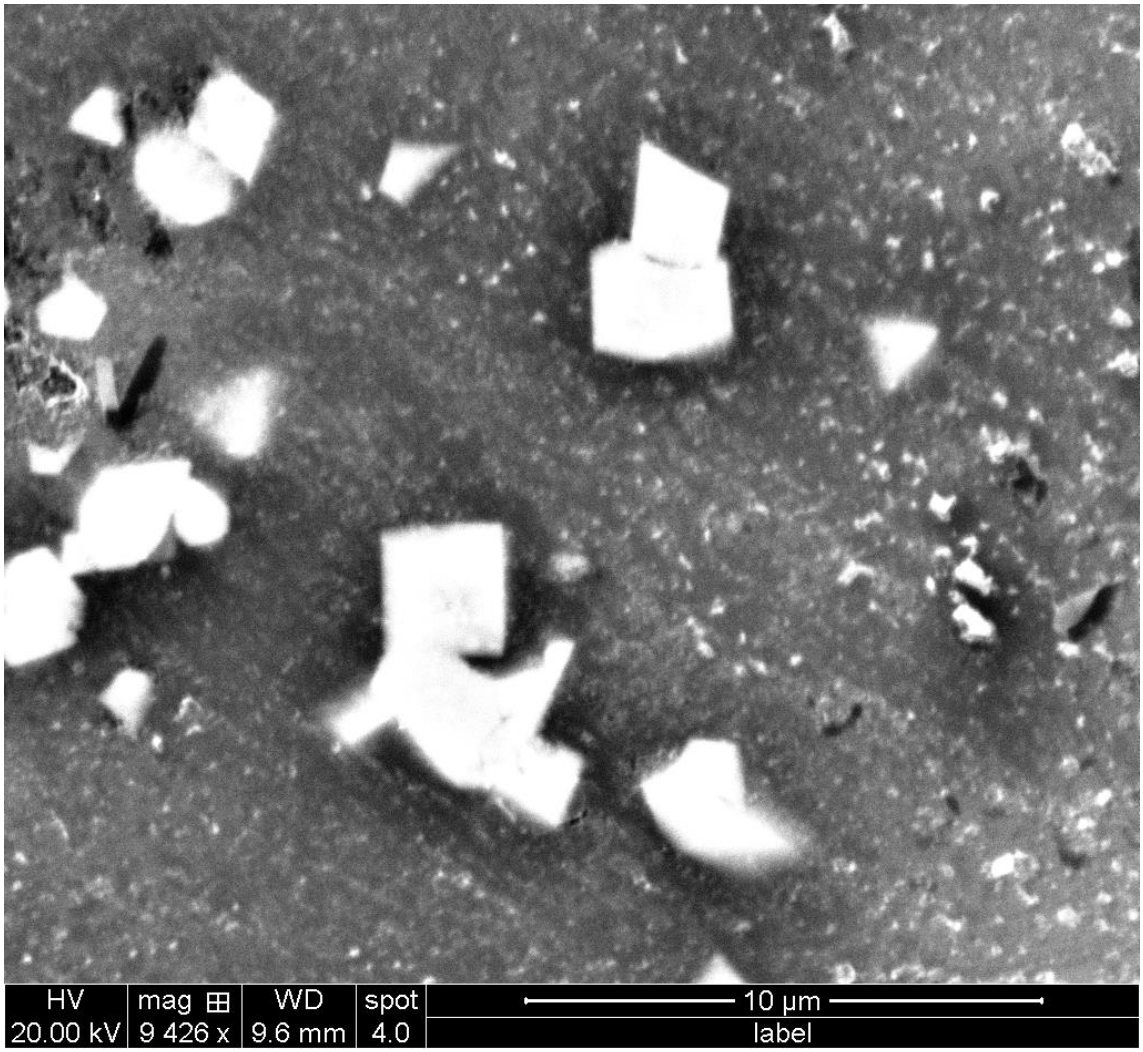

Figure 4. HLW-NG-Fe2-G Backscattered Electron SEM Image at 10,000 X.

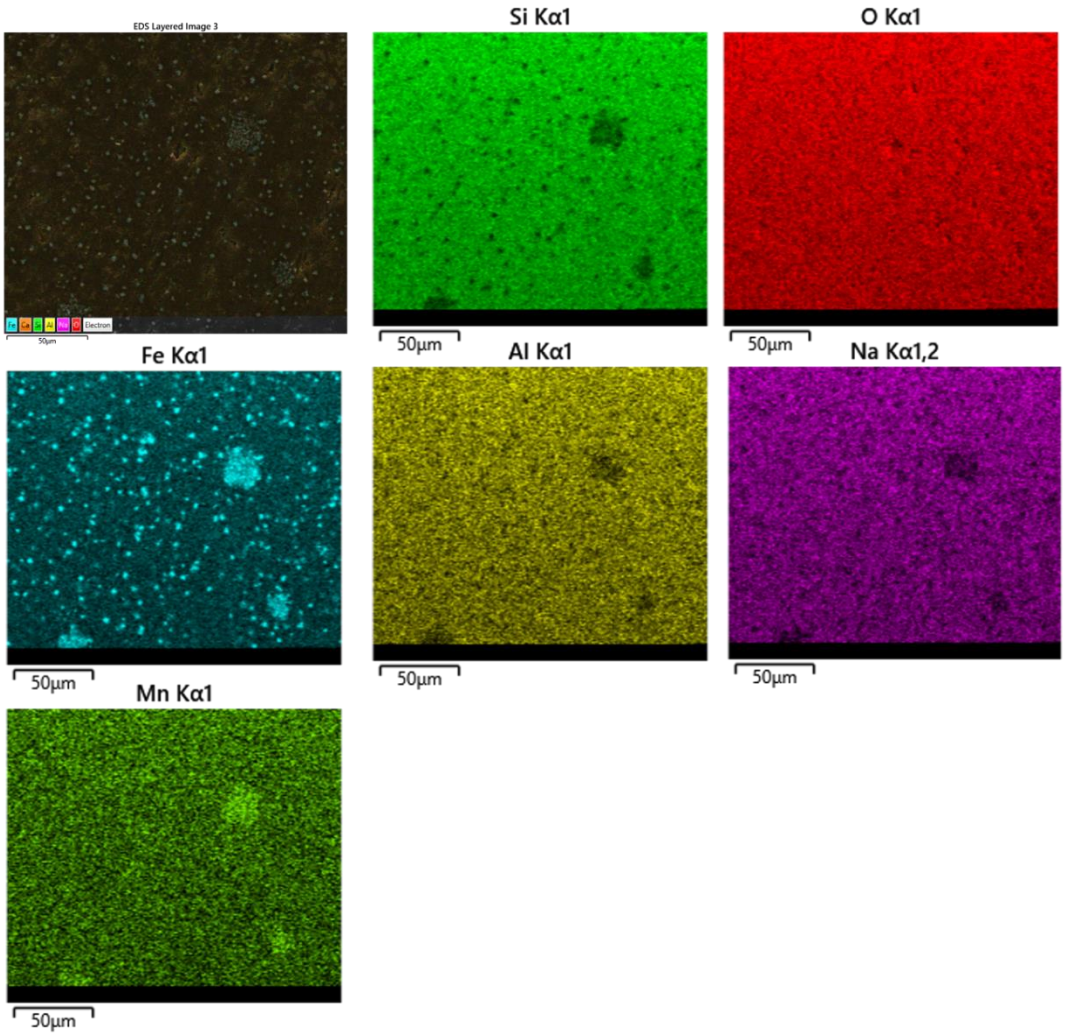

Figure 5. HLW-NG-Fe2-G EDX Maps.

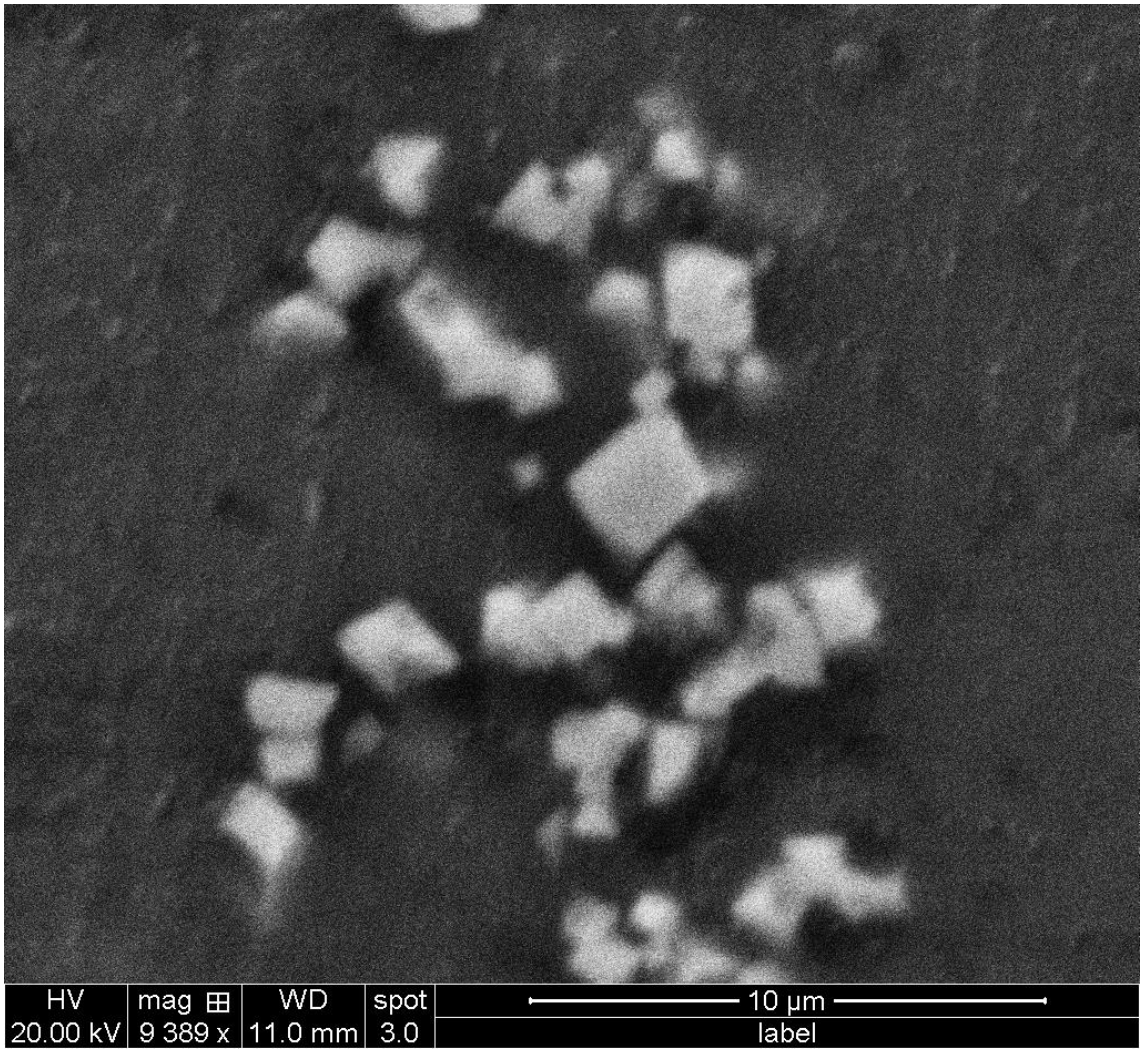

Figure 6. HLW-NG-Fe2-F Backscattered Electron SEM Image at 10,000 X.

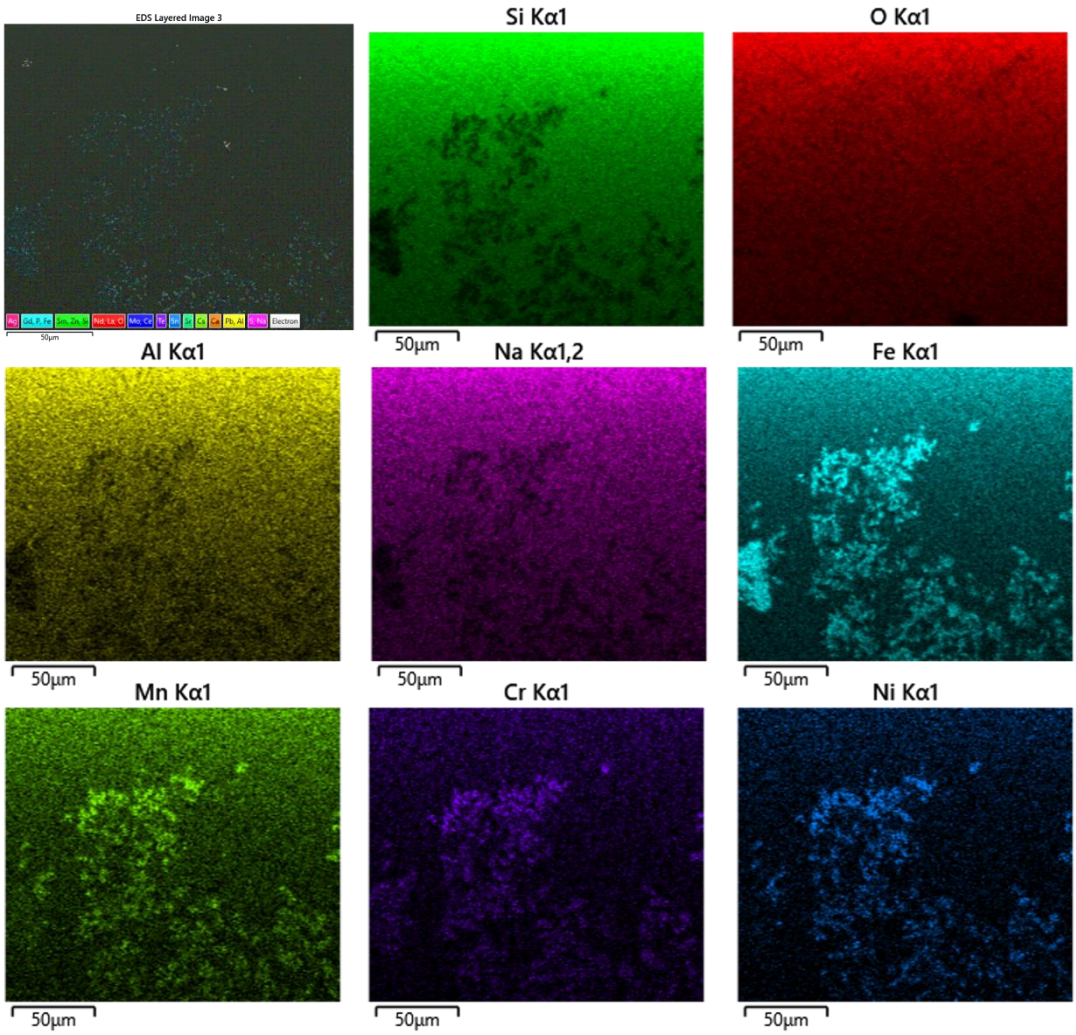

Figure 7. HLW-NG-Fe2-F EDX Maps.

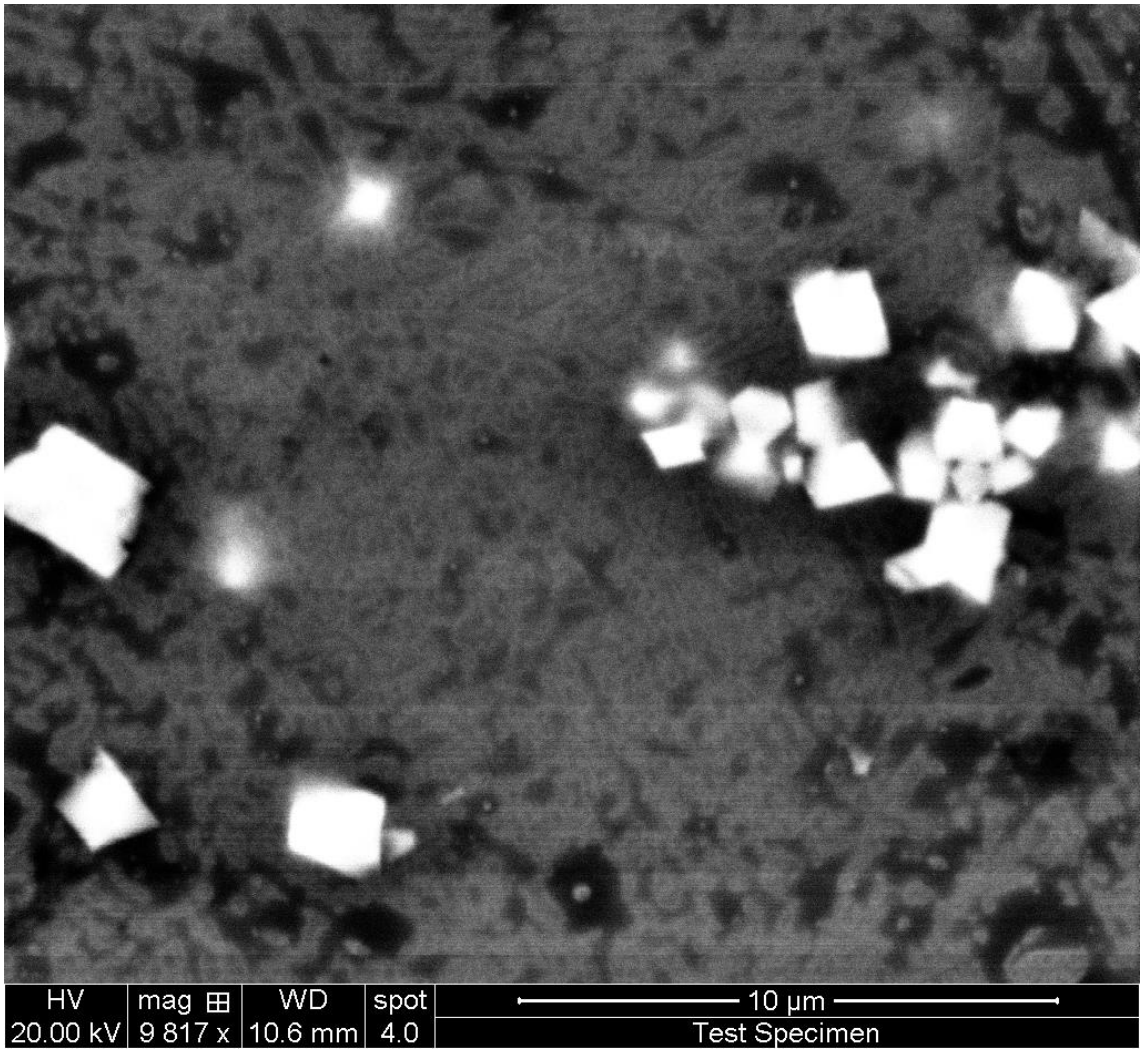

Figure 8. HLW-NG-Fe2-H Backscattered Electron SEM Image at 10,000 X.

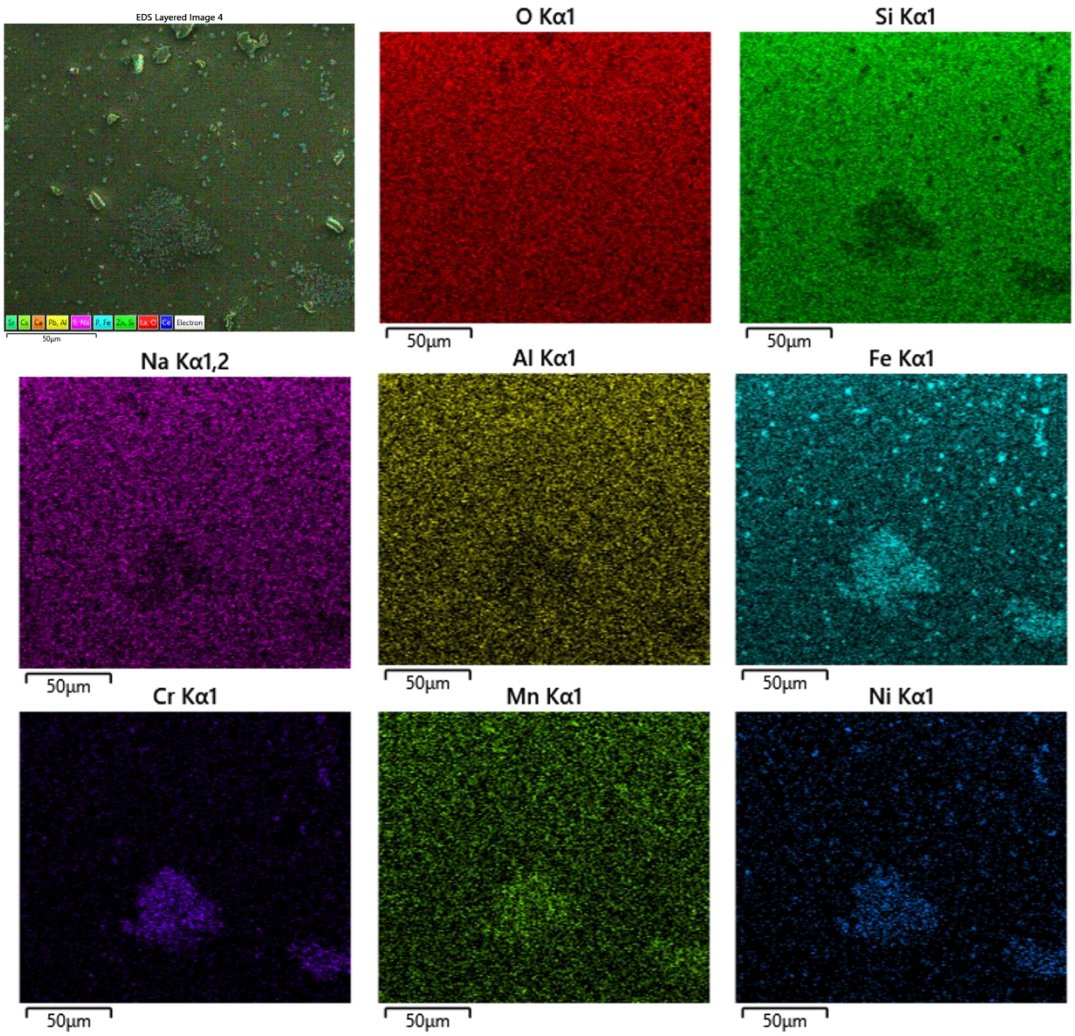

Figure 9. HLW-NG-Fe2-H EDX Maps.